Springer Series in Chemical Physics 118

Kaoru Yamanouchi · Philippe Martin
Marc Sentis · Li Ruxin
Didier Normand *Editors*

Progress in Ultrafast Intense Laser Science XIV

Springer
PUILS
JILS

Springer Series in Chemical Physics

Progress in Ultrafast Intense Laser Science

Volume 118

Series editors

A. W. Castleman Jr., University Park, USA
J. P. Toennies, Göttingen, Germany
K. Yamanouchi, Tokyo, Japan
W. Zinth, München, Germany

The purpose of this series is to provide comprehensive up-to-date monographs in both well established disciplines and emerging research areas within the broad fields of chemical physics and physical chemistry. The books deal with both fundamental science and applications, and may have either a theoretical or an experimental emphasis. They are aimed primarily at researchers and graduate students in chemical physics and related fields.

More information about this series at http://www.springer.com/series/11752

Kaoru Yamanouchi · Philippe Martin
Marc Sentis · Li Ruxin · Didier Normand
Editors

Progress in Ultrafast Intense Laser Science

Volume XIV

Springer

Editors
Kaoru Yamanouchi
Department of Chemistry
School of Science
The University of Tokyo
Tokyo, Japan

Philippe Martin
Lasers Interactions and Dynamics
Laboratory (LIDYL)
Gif-sur-Yvette, France

Marc Sentis
CNRS
Aix Marseille University
Marseille, France

Li Ruxin
Shanghai Institute of Optics and Fine
Mechanics
Chinese Academy of Sciences (CAS)
Shanghai, China

Didier Normand
CEA Saclay-IRAMIS
Gif-sur-Yvette, France

ISSN 0172-6218
Springer Series in Chemical Physics
Progress in Ultrafast Intense Laser Science
ISBN 978-3-030-03785-7 ISBN 978-3-030-03786-4 (eBook)
https://doi.org/10.1007/978-3-030-03786-4

Library of Congress Control Number: 2018960749

© Springer Nature Switzerland AG 2018
This work is subject to copyright. All rights are reserved by the Publisher, whether the whole or part of the material is concerned, specifically the rights of translation, reprinting, reuse of illustrations, recitation, broadcasting, reproduction on microfilms or in any other physical way, and transmission or information storage and retrieval, electronic adaptation, computer software, or by similar or dissimilar methodology now known or hereafter developed.
The use of general descriptive names, registered names, trademarks, service marks, etc. in this publication does not imply, even in the absence of a specific statement, that such names are exempt from the relevant protective laws and regulations and therefore free for general use.
The publisher, the authors and the editors are safe to assume that the advice and information in this book are believed to be true and accurate at the date of publication. Neither the publisher nor the authors or the editors give a warranty, express or implied, with respect to the material contained herein or for any errors or omissions that may have been made. The publisher remains neutral with regard to jurisdictional claims in published maps and institutional affiliations.

This Springer imprint is published by the registered company Springer Nature Switzerland AG
The registered company address is: Gewerbestrasse 11, 6330 Cham, Switzerland

Preface

We are pleased to present the fourteenth volume of Progress in Ultrafast Intense Laser Science. As the frontiers of ultrafast intense laser science rapidly expand ever outward, there continues to be a growing demand for an introduction to this interdisciplinary research field that is at once widely accessible and capable of delivering cutting-edge developments. Our series aims to respond to this call by providing a compilation of concise review-style articles written by researchers at the forefront of this research field, so that researchers with different backgrounds as well as graduate students can easily grasp the essential aspects.

As in previous volumes of PUILS, each chapter of this book begins with an introductory part, in which a clear and concise overview of the topic and its significance is given, and moves onto a description of the authors' most recent research results. All chapters are peer-reviewed. The articles of this fourteenth volume cover a diverse range of the interdisciplinary research field, and the topics may be grouped into four categories: atoms and molecules interacting with an ultrashort intense laser field (Chaps. 1–8); propagation of intense laser pulses in a gaseous medium and its applications (Chaps. 9 and 10); generation of high-order harmonics and attosecond pulses and their applications (Chaps. 11–13); and intense laser matter interactions (Chaps. 14 and 15).

From the third volume, the PUILS series has been edited in liaison with the activities of the Center for Ultrafast Intense Laser Science at the University of Tokyo, which has also been responsible for sponsoring the series and making the regular publication of its volumes possible. From the fifth volume, the Consortium on Education and Research on Advanced Laser Science, the University of Tokyo, has joined this publication activity as one of the sponsoring programs. The series, designed to stimulate interdisciplinary discussion at the forefront of ultrafast intense laser science, has also collaborated since its inception with the annual symposium series of ISUILS (http://www.isuils.jp/), sponsored by Japan Intense Light Field Science Society (JILS).

We would like to take this opportunity to thank all of the authors who have kindly contributed to the PUILS series by describing their most recent work at the frontiers of ultrafast intense laser science. We also thank the reviewers who have

read the submitted manuscripts carefully. One of the co-editors (KY) thanks Ms. Mihoshi Abe for her help with the editing processes. Last but not least, our gratitude goes out to Dr. Claus Ascheron, Physics Editor of Springer-Verlag at Heidelberg, for his kind support over the years until his retirement in this February.

We hope this volume will convey the excitement of ultrafast intense laser science to the readers and stimulate interdisciplinary interactions among researchers, thus paving the way to explorations of new frontiers.

Tokyo, Japan — Kaoru Yamanouchi
Gif-sur-Yvette, France — Philippe Martin
Marseille, France — Marc Sentis
Shanghai, China — Li Ruxin
Gif-sur-Yvette, France — Didier Normand

Contents

Contributors

Yuta Arakawa Department of Chemistry, Graduate School of Science, Tohoku University, Sendai, Japan

Dimitri Batani Université Bordeaux, CNRS, CEA, CELIA, UMR 5107, Talence, France; Department of Plasma Physics, National Research Nuclear University MEPhI, Moscow, Russia

Xue-Bin Bian State Key Laboratory of Magnetic Resonance and Atomic and Molecular Physics, Wuhan Institute of Physics and Mathematics, Chinese Academy of Sciences, Wuhan, China

F. Billard Laboratoire Interdisciplinaire CARNOT de Bourgogne, UMR 6303 CNRS-Université Bourgogne Franche-Comté, Dijon, France

D. Charalambidis Foundation for Research and Technology—Hellas, Institute of Electronic Structure and Laser, Heraklion (Crete), Greece; Department of Physics, University of Crete, Heraklion, Greece; ELI-ALPS, ELI-Hu Kft, Szeged, Hungary

S. Chatziathanasiou Foundation for Research and Technology—Hellas, Institute of Electronic Structure and Laser, Heraklion (Crete), Greece; Department of Physics, University of Crete, Heraklion, Greece

See Leang Chin Center for Optics, Photonics and Laser (COPL) and Department of Physics, Engineering Physics and Optics, Laval University, Quebec City, Canada

Aditya K. Dharmadhikari Tata Institute of Fundamental Research, Mumbai, India

Jayashree A. Dharmadhikari Department of Atomic and Molecular Physics, Manipal Academy of Higher Education, Manipal, India

Tao-Yuan Du State Key Laboratory of Magnetic Resonance and Atomic and Molecular Physics, Wuhan Institute of Physics and Mathematics, Chinese Academy of Sciences, Wuhan, China

F. H. M. Faisal Fakultät für Physik, Universität Bielefeld, Bielefeld, Germany; Optical Sciences Center, University of Arizona, Tucson, AZ, USA

O. Faucher Laboratoire Interdisciplinaire CARNOT de Bourgogne, UMR 6303 CNRS-Université Bourgogne Franche-Comté, Dijon, France

Hideki Gotoh Quantum Optical Physics Research Group, Optical Science Laboratory, NTT Basic Research Laboratories, NTT Corporation, Atsugi, Kanagawa, Japan

E. Hertz Laboratoire Interdisciplinaire CARNOT de Bourgogne, UMR 6303 CNRS-Université Bourgogne Franche-Comté, Dijon, France

Xiao-Huan Huang Hubei Key Laboratory of Pollutant Analysis and Reuse Technology, College of Chemistry and Chemical Engineering, Hubei Normal University, Huangshi, China

Kenichi L. Ishikawa Department of Nuclear Engineering and Management, Graduate School of Engineering, The University of Tokyo, Bunkyo-ku, Tokyo, Japan

Katarzyna Jakubowska IPPLM, Warsaw, Poland

Mark Hyunpong Jhon Institute of High Performance Computing, A*STAR, Singapore, Singapore

Guang-Rui Jia State Key Laboratory of Magnetic Resonance and Atomic and Molecular Physics, Wuhan Institute of Physics and Mathematics, Chinese Academy of Sciences, Wuhan, China

B. Lavorel Laboratoire Interdisciplinaire CARNOT de Bourgogne, UMR 6303 CNRS-Université Bourgogne Franche-Comté, Dijon, France

Helong Li State Key Laboratory of Integrated Optoelectronics, College of Electronic Science and Engineering, Jilin University, Changchun, China

Jialin Li Division of Chemistry and Biological Chemistry, Division of Physics and Applied Physics, School of Physical and Mathematical Sciences, Nanyang Technological University, Singapore, Singapore

ChunMei Liu Institut für Chemie und Biochemie, Freie Universität Berlin, Berlin, Germany

Zhi-Heng Loh Division of Chemistry and Biological Chemistry, Division of Physics and Applied Physics, School of Physical and Mathematical Sciences, Centre for Optical Fibre Technology, The Photonics Institute, Nanyang Technological University, Singapore, Singapore

I. Makos Foundation for Research and Technology—Hellas, Institute of Electronic Structure and Laser, Heraklion (Crete), Greece; Department of Physics, University of Crete, Heraklion, Greece

Jörn Manz Institut für Chemie und Biochemie, Freie Universität Berlin, Berlin, Germany; State Key Laboratory of Quantum Optics and Quantum Optics Devices, Collaborative Innovation Center of Extreme Optics, Institute of Laser Spectroscopy, Shanxi University, Taiyuan, China

Hiroki Mashiko Quantum Optical Physics Research Group, Optical Science Laboratory, NTT Basic Research Laboratories, NTT Corporation, Atsugi, Kanagawa, Japan

Katsumi Midorikawa Attosecond Science Research Team, RIKEN Center for Advanced Photonics, Wako-shi, Saitama, Japan

Yasuo Nabekawa Attosecond Science Research Team, RIKEN Center for Advanced Photonics, Wako-shi, Saitama, Japan

Katsuya Oguri Quantum Optical Physics Research Group, Optical Science Laboratory, NTT Basic Research Laboratories, NTT Corporation, Atsugi, Kanagawa, Japan

Yukiyoshi Ohtsuki Department of Chemistry, Graduate School of Science, Tohoku University, Sendai, Japan

Tomoya Okino Attosecond Science Research Team, RIKEN Center for Advanced Photonics, Wako-shi, Saitama, Japan; JST PRESTO, Wako-shi, Saitama, Japan

I. Orfanos Foundation for Research and Technology—Hellas, Institute of Electronic Structure and Laser, Heraklion (Crete), Greece; Department of Physics, University of Crete, Heraklion, Greece

Yuki Orimo Department of Nuclear Engineering and Management, Graduate School of Engineering, The University of Tokyo, Bunkyo-ku, Tokyo, Japan

Takeshi Sato Department of Nuclear Engineering and Management, Graduate School of Engineering, The University of Tokyo, Bunkyo-ku, Tokyo, Japan

Soo Teck See Division of Chemistry and Biological Chemistry, Division of Physics and Applied Physics, School of Physical and Mathematical Sciences, Nanyang Technological University, Singapore, Singapore

Fan Shi Key Laboratory of Magnetic Resonance in Biological Systems, State Key Laboratory of Magnetic Resonance and Atomic and Molecular Physics, National Center for Magnetic Resonance in Wuhan, Wuhan Institute of Physics and Mathematics, Chinese Academy of Sciences, Wuhan, China

E. Skantzakis Foundation for Research and Technology—Hellas, Institute of Electronic Structure and Laser, Heraklion (Crete), Greece

Akira Suda Department of Physics, Faculty of Science and Technology, Tokyo University of Science, Yamazaki, Noda, Chiba, Japan

Tamás Szidarovszky Department of Chemistry, School of Science, The University of Tokyo, Tokyo, Japan; Laboratory of Molecular Structure and Dynamics, Institute of Chemistry, Eötvös Loránd University and MTA-ELTE Complex Chemical Systems Research Group, Budapest, Hungary

Takuma Teramura Department of Nuclear Engineering and Management, Graduate School of Engineering, The University of Tokyo, Bunkyo-ku, Tokyo, Japan

Jean Christophe Tremblay Institut für Chemie und Biochemie, Freie Universität Berlin, Berlin, Germany

N. Tsatrafyllis Foundation for Research and Technology—Hellas, Institute of Electronic Structure and Laser, Heraklion (Crete), Greece; Department of Physics, University of Crete, Heraklion, Greece

Oyunbileg Tugs Department of Nuclear Engineering and Management, Graduate School of Engineering, The University of Tokyo, Bunkyo-ku, Tokyo, Japan

P. Tzallas Foundation for Research and Technology—Hellas, Institute of Electronic Structure and Laser, Heraklion (Crete), Greece; ELI-ALPS, ELI-Hu Kft, Szeged, Hungary

Lin Wang Division of Chemistry and Biological Chemistry, Division of Physics and Applied Physics, School of Physical and Mathematical Sciences, Nanyang Technological University, Singapore, Singapore

Zhengrong Wei Division of Chemistry and Biological Chemistry, Division of Physics and Applied Physics, School of Physical and Mathematical Sciences, Nanyang Technological University, Singapore, Singapore

Huailiang Xu State Key Laboratory of Precision Spectroscopy, East China Normal University, Shanghai, China; State Key Laboratory of Integrated Optoelectronics, College of Electronic Science and Engineering, Jilin University, Changchun, China

Kaoru Yamanouchi Department of Chemistry, School of Science, The University of Tokyo, Bunkyo-ku, Tokyo, Japan

Minghui Yang Key Laboratory of Magnetic Resonance in Biological Systems, State Key Laboratory of Magnetic Resonance and Atomic and Molecular Physics, National Center for Magnetic Resonance in Wuhan, Wuhan Institute of Physics and Mathematics, Chinese Academy of Sciences, Wuhan, China

Masataka Yoshida Department of Chemistry, Graduate School of Science, Tohoku University, Sendai, Japan

Hongwei Zang State Key Laboratory of Integrated Optoelectronics, College of Electronic Science and Engineering, Jilin University, Changchun, China

Yingfeng Zhang Key Laboratory of Magnetic Resonance in Biological Systems, State Key Laboratory of Magnetic Resonance and Atomic and Molecular Physics, National Center for Magnetic Resonance in Wuhan, Wuhan Institute of Physics and Mathematics, Chinese Academy of Sciences, Wuhan, China

Chapter 1
Strong-Field Threshold Ionization: An Asymptotic Wavefunction Ansatz

F. H. M. Faisal

Abstract We discuss an analytic model of threshold ionization in an intense laser field. It is based on a strong-field wavefunction Ansatz that satisfies the long range asymptotic behavior of Coulomb wave plus the laser field at large distances. Results of illustrative calculations of the energy and momentum distributions of the electrons, from ionization of a hydrogenic atom by intense mid-infrared laser field, are presented and discussed. The results indicate that the energy distribution of ionization reaches a finite non-zero value at the threshold (at zero kinetic energy) and, approaches it in an oscillatory way. The parallel momentum distribution close to the polarization axis is characterised by a two-peak structure and show rapid high-amplitude oscillations very close to the threshold. Integrated over small values of the perpendicular momentum, it shows a sharp maximum at zero parallel momentum. The perpendicular momentum distribution close to a direction transverse to the polarization axis shows a cusp-like fall-off at the threshold momentum. Integrated over small values of the parallel momentum, the transverse distribution is dominated by the sharp cusp-structure at the threshold. These prominent qualitative behavior of the ionization energy and momentum distributions at and near the threshold are associated with the long-range Coulomb interaction included in the present wavefunction Ansatz. It contrast, they are absent in the corresponding distributions given by the usual "strong-field approximation" (or SFA) that is based on the final plane-wave Volkov state.

F. H. M. Faisal (✉)
Fakultät für Physik, Universität Bielefeld, 33501 Bielefeld, Germany
e-mail: ffaisal@physik.uni-bielefeld.de

F. H. M. Faisal
Optical Sciences Center, University of Arizona, Tucson, AZ 85721, USA

© Springer Nature Switzerland AG 2018

K. Yamanouchi et al. (eds.), *Progress in Ultrafast Intense Laser Science XIV*,
Springer Series in Chemical Physics 118,
https://doi.org/10.1007/978-3-030-03786-4_1

1.1 Introduction

Strong-field ionization is one of the most ubiquitous phenomena that arise when intense laser light interacts with atoms and molecules. Over the last many years much has been learned both experimentally and theoretically about the nature of the highly non-linear laser interaction involved in these processes (e.g. [1]). Along with direct numerical simulation of the Schrödinger equation, whenever feasible, and the so-called strong-field approximation or SFA, also known as KFR approximation ([2–4]), have been among the most popular approaches to analyze these processes in the past. Recently, advances in experimental techniques are allowing to investigate strong-field ionization with low frequency fields at low energies (e.g. [5–7]) that is approaching near to the ionization threshold (e.g. [8–11]). Thus, a universal low energy structure (LES) in the ionization spectra of atoms and molecules at near infrared wavelengths was reported in 2009 by Blaga et al. [5] and Quan et al. [6]. This structure was never observed or had appeared in simulations before, neither was it predicted by the SFA. Immediately after the discovery of LES it was suggested (based on the nature of the long-range Coulomb interaction and a graphical consideration of the electron motion) [12] that, the observed low energy structure could arise from a forward scattering of the low energy electrons with the core in the presence of the field and could be investigated by the second order extension of the strong field KFR approximation (KFR2). This is unlike the back-scattering, popularly known as "rescattering" [13] in the presence of the field, which is known to enhance the probability of high energy electron emission. A subsequent classical analysis [14] of the phase space in the presence of the field showed a sharp low energy structure at about 0.1 U_p (U_p is the ponderomotive potential) that well agreed with the observed position of the prominent LES; in addition, this analysis predicted an infinite sequence of peaks with decreasing spacings with decreasing energy. Physically, the dominant first peak as well as the sequence of peaks were found to arise from a forward scattering process, as anticipated in [12], albeit associated with the so-called "soft-collision" trajectories [14]. A similar sequence of forward scattering peaks have since been found to appear at low energies in the second order strong-field amplitude (or KFR2) as well [15]. Experimentally, additional low energy peaks were observed (e.g. [6, 8, 9]) below the main LES and were dubbed "very low energy structures" (or VLES) to distinguish them from the prominent LES. Subsequent experiments (e.g. [10, 11] and references cited therein) have reported extra peak structures in the energy and momentum distributions of the ionized electron at even lower energies, which include a peak structure at the hitherto lowest energy near the threshold, that is dubbed a "zero energy structure" or ZES [10]. At present it seems to be not completely clear whether all these additional observed peaks (except the prominent LES peak) belong to the above mentioned sequence of the forward "soft-collision" peaks or not. It is also not clear whether the total number of the observable low energy peaks form an infinite sequence that converge at the threshold. It is more likely that there is a finite number of observable peaks whose number depends on the number of cycles in the incident pulse. Another complication with the observed intense field

ionization signal at low energies is the issue of the mixing of the primary ionization process with contributions from the secondary ionization of the electrons that are first excited by the laser field in the high lying Rydberg states e.g. [10, 16], and subsequently emitted by the weak electric field of the apparatus. Finally, at present no definite answer is known even to the following simple question: is the strong-field ionization probability *at* the threshold of ionization is zero or finite (non-zero)? To answer this question theoretically, the usual numerical simulation techniques become increasingly difficult to carry out as the electron kinetic energy diminishes towards zero at the threshold. The difficulty is due to the increasing importance of the asymptotically longer distances in the coordinate space in a Coulomb + laser field with the decreasing values of the momentum of the electron which demands an increasingly larger grid size that makes the usual numerical simulation un-practicable, at the threshold. Nevertheless, one may hope to investigate the intriguing question of the nature of the strong-field ionization probability *at* the threshold of ionization, as far as may be possible, by analytical means. The well known analytical model of the strong-field approximation (SFA) shows that the ionization probability goes down to zero at the threshold. This, however, might not be the case in reality, since the SFA, which is based on the plane wave Volkov-solution, does *not* account for the unavoidable final-state Coulomb interaction between the ejected electron and the core. As can be seen from Fig. 1.1, a short range Yukawa potential (orange line) with a typical atomic range ($\lambda = 1$ Bohr) falls off rapidly, while the infinite-range ($\lambda = 0$) Coulomb potential (blue line) remains significant even beyond 100 Bohr. To see the influence of the two potentials on the ionization probability at the threshold, it is worthwhile to recall how the ordinary one-photon ionization probability (photo-effect) depends on the choice of the final state of the system i.e. whether it is a plane wave final-state, appropriate for a short range potential, or it is a Coulomb wave final-state, appropriate for a long range Coulomb potential, keeping the initial bound state of the system the same. The ionization amplitude within the first order perturbation theory is defined (in the "length gauge", with a linearly polarized laser field, $\mathbf{F}(t) = \hat{\varepsilon}_z F \cos \omega t$, in the dipole approximation) by

$$\mathscr{A}^{(1)}(\mathbf{k}) = -\frac{i}{\hbar} \int_{-\infty}^{\infty} \mathrm{d}t \mathrm{e}^{\frac{i}{\hbar} E_k t} \langle \psi^{(-)*}(\mathbf{k}, \mathbf{r}) | - \mathrm{e} \hat{\varepsilon_z} \cdot \mathbf{r} \frac{F}{2} \mathrm{e}^{-i\omega t} | N_b \mathrm{e}^{-k_b r} \rangle \mathrm{e}^{\frac{i}{\hbar} E_b t} \quad (1.1)$$

where $\psi^{(-)}(\mathbf{k}, \mathbf{r})$ is the ingoing Coulomb wave (CW) final state, with the kinetic energy $E_k = \frac{\hbar^2 k^2}{2m}$, and $N_b \mathrm{e}^{-k_b r}$ is the initial bound state, the binding energy $E_b = \frac{\hbar^2 k_b^2}{2m}$; $\hat{\varepsilon_z}$ is the unit polarization vector along the z-axis and N_b is the bound state normalization factor. We evaluate the spatial integral with the CW final state in (1.1) by Nordsieck's method [17] and obtain the transition dipole moment, $D_z(\mathbf{k})$, along the polarization direction,

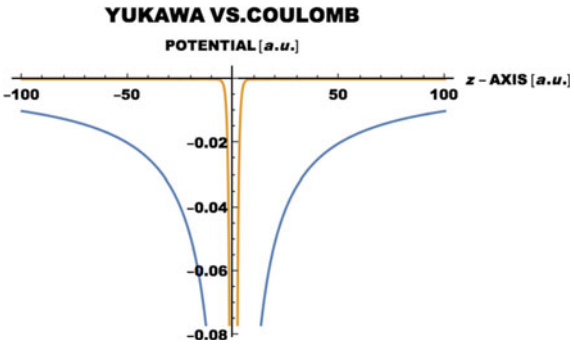

Fig. 1.1 A graphical representation of a short-range Yukawa potential (orange line) versus the log-range Coulomb potential (blue line): $V_{\text{Yukawa}}(r) = -Ze^2 e^{-\lambda r}/r$ $(Z = 1, \lambda = 1)$ and, $V_{\text{Coulomb}}(r) = -Ze^2/r$ $(Z = 1, \lambda = 0)$. Clearly, the long-range Coulomb potential remains significantly large at large distances far beyond the typical atomic range of the Yukawa potential

$$
\begin{aligned}
D_z(\mathbf{k}) &= \langle N_{k\,1}^* F_1[i\eta_k, 1, i(kr + \mathbf{k}\cdot\mathbf{z})]\mathrm{e}^{-i\mathbf{k}\cdot\mathbf{r}}|(-\mathrm{e}z)|\mathrm{e}^{-k_b r} N_b\rangle \\
&= -\mathrm{e}\frac{16i\pi(1 - i\eta_k)(\eta_{k_b} - 2)k_b k\cos\theta_k}{(k_b^2 + k^2)^3}\mathrm{e}^{-2\eta_k \times \arctan(k/k_b)} N_k^* N_b, \\
N_k^* &= \mathrm{e}^{\frac{\pi}{2}\eta_k}\Gamma(1 - i\eta_k), \\
\eta_k &= \frac{Z}{ka_0}, \\
\eta_{k_b} &= \frac{Z}{k_b a_0}, \\
N_b &= \sqrt{\frac{k_b^3}{\pi}}.
\end{aligned}
\tag{1.2}
$$

The angle brackets above imply integrations with respect to the coordinates $\mathbf{r}$ and, $a_0 = 0.52918 \times 10^{-8}$ cm, is the Bohr radius. Therefore, the differential probability of ionization per unit time (or the rate of ionization) is given as usual by the Fermi golden rule,

$$
\mathrm{dRate}(\mathbf{k}) = \frac{2\pi}{\hbar}|\frac{F}{2}D_z(\mathbf{k})|^2\delta\left(\frac{\hbar^2 k^2}{2m} + E_b - \hbar\omega\right)\frac{\mathrm{d}^3 k}{(2\pi)^3} \tag{1.3}
$$

The corresponding cross-section is obtained by dividing the rate with the incident photon flux which is defined by the number of photons crossing unit area across the target atom in unit time or, $\text{Flux} = \frac{\text{Intensity}}{\hbar\omega} = \frac{F^2 c}{8\pi\hbar\omega}$. We note that by the energy conserving δ-function we have $\hbar\omega = \frac{\hbar^2}{2m}(k^2 + k_b^2)$. Thus, finally, using (1.2) in (1.3) and dividing by the flux and, simplifying, we get the one-photon ionization probability for a Coulomb wave final state (expressed in terms of the differential cross-section)

$$\frac{\mathrm{d}\sigma_{CW}(\mathbf{k})}{\mathrm{d}\Omega_k} = \alpha 128\pi \frac{\eta_k}{(1-\mathrm{e}^{-2\pi\eta_k})} \frac{(\eta_{k_b}-2)^2}{(k_b a_0)^2} \frac{(1+\eta_k^2)}{[1+(k/k_b)^2]^5} \times \mathrm{e}^{-4\eta_k \times \arctan(k/k_b)} (k/k_b)^3 \cos^2\theta_k a_0^2 \tag{1.4}$$

where $\mathrm{d}\Omega_k$ is the element of solid angle in the direction of $\mathbf{k}$. For the short-range potential with the plane-wave (PW) final state we get the cross-section by simply taking the limit $Z = 0$ or, $(\eta_k, \eta_{k_b}) = 0$, in (1.4) above

$$\frac{\mathrm{d}\sigma_{PW}(\mathbf{k})}{\mathrm{d}\Omega_k} = \alpha 256 \frac{1}{(k_b a_0)^2} \frac{1}{[1+(k/k_b)^2]^5} (k/k_b)^3 \cos^2\theta_k a_0^2 \tag{1.5}$$

where, $\alpha = \frac{e^2}{\hbar c} = 137.036$, is the fine structure constant and, $\mathrm{d}\Omega_k$ is the element of solid angle in the direction of $\mathbf{k}$. We may note that in the above formulas the pre-factors of a_0^2 are dimensionless and hence the cross-sections are proportional to $(a_0 = \text{Bohr radius})^2$ i.e. 1 a.u. $= 2.8 \times 10^{-17}\,\mathrm{cm}^2$. The long range of the Coulomb potential (compared to all other atomic potentials) drastically alters the probability of one-photon ionization (or, photo-effect) both near and at the threshold. This can be seen from Fig. 1.2, where we compare the cross-sections for photo-effect calculated from the above formulas for the Coulomb-wave final state (blue line) and the plane-wave final state (orange line). Clearly, the ionization cross-section vanishes at the threshold for the plane-wave case (orange). In contrast, the cross-section for the Coulomb-wave final state (blue) yields a finite (non-zero) magnitude at the threshold. It is clear from this simple example that the correct asymptotic behaviour of the final state wavefunction is of central importance in determining the probability of ionization at and near the threshold. Thus, the question of our present interest is: what happens to the ionization probability, in intense low-frequency laser fields, near and *at* the threshold of ionization, when the ionization becomes highly non-linear in such

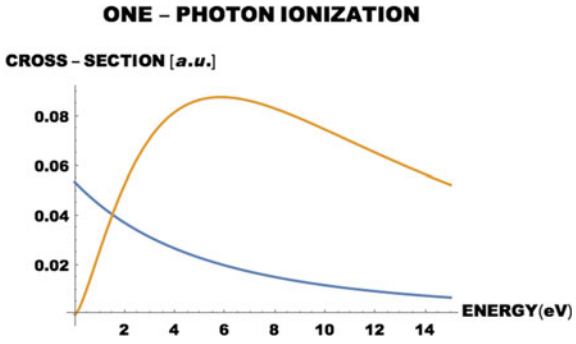

Fig. 1.2 Comparison of weak-field one-photon ionization cross-section (or photo-effect) in a Coulomb potential (blue line) versus in a short-range potential (orange line). Note the finite (non-zero) photo-ionization probability at the threshold for Coulomb-wave final state (blue) versus the zero probability at the threshold for a plane-wave final state (orange)

fields? Below, we investigate the problem using an approximate strong-field Ansatz of the wavefunction that satisfies the asymptotic boundary condition for the final state Coulomb interaction in the presence of the field.

1.2 An Asymptotic Strong-Field Wave Function with Coulomb Boundary Condition

Consider the prototype problem of a single active electron (hydrogenic) atom interacting with an intense laser field. The Schrödinger equation of the interacting system is

$$i\hbar\frac{\partial}{\partial t}\Psi(t) = \left(\frac{\mathbf{p}_{op}^2}{2m} - \frac{Ze^2}{r} - \frac{e}{mc}\mathbf{A}(t)\cdot\mathbf{p}_{op} + \frac{e^2A^2(t)}{2mc^2}\right)\Psi(t) \tag{1.6}$$

where, Z is the ionic core charge and, the laser-atom interaction is assumed in the minimal coupling gauge (in "dipole" approximation)

$$V_i(t) = \left(-\frac{e}{mc}\mathbf{A}(t)\cdot\mathbf{p}_{op} + \frac{e^2A^2(t)}{2mc^2}\right) \tag{1.7}$$

$\mathbf{A}(t)$ is the vector potential, and $\mathbf{p}_{op} \equiv -i\hbar\nabla$. No explicit solution of the apparently simple looking (1.6) is known. In order to proceed analytically and to develop an approximate but asymptotically correct wavefunction, we rewrite the equation as

$$i\hbar\frac{\partial}{\partial t}\Psi(t) = \left[\left(\frac{\mathbf{p}_{op}^2}{2m} - \frac{Ze^2}{|\mathbf{r}+\mathbf{s}(t)|} - \frac{e}{mc}\mathbf{A}(t)\cdot\mathbf{p}_{op} + \frac{e^2A^2(t)}{2mc^2}\right) + \mathscr{V}(\mathbf{r},t)\right]\Psi(t) \tag{1.8}$$

where we have introduced the instantaneous quiver radius $\mathbf{s}(t) = \frac{e}{mc}\int^t \mathbf{A}(t')\mathrm{d}t''$, and the quantity in the parentheses defines the asymptotically appropriate reference Hamiltonian,

$$H_1(t) = \left(\frac{\mathbf{p}_{op}^2}{2m} - \frac{Ze^2}{|\mathbf{r}+\mathbf{s}(t)|} - \frac{e}{mc}\mathbf{A}(t)\cdot\mathbf{p}_{op} + \frac{e^2A^2(t)}{2mc^2}\right) \tag{1.9}$$

for, the rest interaction

$$\mathscr{V}(\mathbf{r},t) \equiv \frac{Ze^2}{|\mathbf{r}+\mathbf{s}(t)|} - \frac{Ze^2}{|\mathbf{r}|} \tag{1.10}$$

$$= 0\left(\frac{1}{r^2}\right), \qquad r\to\infty. \tag{1.11}$$

Note that the rest interaction $\mathscr{V}(\mathbf{r}, t)$ falls off asymptotically faster than the Coulomb potential and hence the model Hamiltonian $H_1(\mathbf{r}, t)$ and the solution of the associated Schrödiger equation have the appropriate asymptotic form for ionization. The Hamiltonian $H_1(t)$ has both continuum and bound state solutions in the presence of the laser field. In fact the complete set of linearly independent time-dependent solutions of the Schrödinger equation governed by H_1,

$$i\hbar\frac{\partial}{\partial t}\psi(t) = \left(\frac{\mathbf{p}_{op}^2}{2m} - \frac{Ze^2}{|\mathbf{r}+\mathbf{s}(t)|} - \frac{e}{mc}\mathbf{A}(t)\cdot\mathbf{p}_{op} + \frac{e^2A^2(t)}{2mc^2}\right)\psi(t), \tag{1.12}$$

can be readily obtained by a space-translation method , as has been shown a long time ago [3, 18], or it can be verified by direct substitution in the above equation. Thus, for example, the continuum solution of (1.12) with a given momentum $\hbar\mathbf{k}$ and satisfying the ingoing Coulomb-wave boundary condition is

$$\psi_{\mathbf{k}}^{(-)}(\mathbf{r}, t) = \phi_{\mathbf{k}}^{(-)}(\mathbf{r}+\mathbf{s}(t))\mathrm{e}^{-\frac{i}{\hbar}\int_{t'}^{t}\frac{1}{2m}\left(\hbar\mathbf{k}-\frac{e}{c}\mathbf{A}(t'')\right)^2 dt''} \tag{1.13}$$

where, $\phi_{\mathbf{k}}^{(-)}(\mathbf{x}(t))$ is given by

$$\begin{aligned}\phi_{\mathbf{k}}^{(-)}(\mathbf{x}(t)) = \mathrm{e}^{\frac{\pi}{2}\eta_k}\Gamma(1+i\eta_k)\mathrm{e}^{i\mathbf{k}\cdot\mathbf{r}} \\ \times {}_1F_1[-i\eta_k, 1, -i(kx(t)+\mathbf{k}\cdot\mathbf{x}(t))]\end{aligned} \tag{1.14}$$

with $\mathbf{x}(t) = \mathbf{r}+\mathbf{s}(t)$, and $\eta_k = \frac{Z}{ka_0}$ is the Sommerfeld parameter. We have also defined the instantaneous "quiver radius" $\mathbf{s}(t) = \frac{e}{mc}\int^t \mathbf{A}(t')\mathrm{d}t'$; if we chose a vector potential $\mathbf{A}(t) = -\hat{\varepsilon}_z A_0 \sin\omega t$, then, $\mathbf{s}(t) = \hat{\varepsilon}_z\alpha_0\cos\omega t$, with $\alpha_0 = \frac{eF}{m\omega^2}$, $F = A_0\omega/c$ is the maximum field strength. The bound state solutions of (1.12) are

$$\psi_{nlm}(\mathbf{r}, t) = \phi_{nlm}(\mathbf{x}(t))\mathrm{e}^{-\frac{i}{\hbar}\int_{t'}^{t}(E_{nl}+\frac{e^2}{2mc^2}A^2(t''))dt''} \tag{1.15}$$

where the functions ϕ_{nlm} are the same as the well-known stationary bound states of the hydrogenic atom (e.g. [19, 20]), with eigenvalues E_{nl}. In fact, the complete set of solutions of (1.12) can be used to construct the propagator or the Green's function, $G_1(t, t')$, associated with the reference Hamiltonian $H_1(t)$, that satisfies the inhomogeneous equation

$$\left(i\hbar\frac{\partial}{\partial t} - H_1(t)\right)G_1(\mathbf{r}t, \mathbf{r}'t') = \delta(t-t')\delta(\mathbf{r}-\mathbf{r}') \tag{1.16}$$

The solution of interest of (1.16) is

$$
\begin{aligned}
G_1^{(-)}(t,t') = -\frac{i}{\hbar}\theta(t-t') \\
&\times \left\{ \sum_{\mathbf{k}} \phi_{\mathbf{k}}^{(-)}(\mathbf{r}+\mathbf{s}(t)) \mathrm{e}^{-\frac{i}{\hbar}\int_{t'}^{t} \frac{1}{2m}\left(\hbar\mathbf{k}-\frac{e}{c}\mathbf{A}(t'')\right)^2 dt''} \right. \\
&\times \phi_{\mathbf{k}}^{(-)*}(\mathbf{r}+\mathbf{s}(t')) \\
&+ \sum_{nlm} \phi_{nlm}(\mathbf{r}+\mathbf{s}(t)) \mathrm{e}^{-\frac{i}{\hbar}\int_{t'}^{t}\left(E_{nl}+\frac{e^2}{2mc^2}A^2(t'')\right)\mathrm{d}t''} \\
&\left. \times \phi_{nlm}^{*}(\mathbf{r}+\mathbf{s}(t')) \right\} \qquad (1.17)
\end{aligned}
$$

where, $\Sigma_{\mathbf{k}} \equiv \frac{1}{(2\pi)^3}\int \mathrm{d}^3k$. An exact definition of the amplitude of ionization from the unperturbed initial state $\phi_i(t)$ is given by the integral

$$
\mathscr{A}(\mathbf{k}) = -\frac{i}{\hbar}\int_{-\infty}^{\infty} \mathrm{d}t \langle \Psi_{\mathbf{k}}^{(-)}(t)|V_i(t)|\phi_i(t)\rangle \qquad (1.18)
$$

where, $\Psi_{\mathbf{k}}(t)$ stands for the total wavefunction satisfying the ionization final state ingoing boundary condition, at the momentum $\hbar\mathbf{k}$, and

$$
V_i(t) = -\frac{e}{mc}\mathbf{A}(t)\cdot\mathbf{p}_{op} + \frac{e^2A^2(t)}{2mc^2} \qquad (1.19)
$$

is the rest-interaction with respect to the (unperturbed) initial state, in the so-called "velocity-gauge". In the present model we approximate the full $\Psi_{\mathbf{k}}^{(-)}(t)$ by the state $\psi_{\mathbf{k}}^{(-)}(t)$ which satisfies the important property of asymptotically correct Coulomb wave boundary condition in the presence of the field. As discussed earlier above, this requirement is important for the behavior of the ionization probability near the threshold. Thus, with the above Ansatz for the interacting wavefunction we define the strong-field ionization amplitude of the present model,

$$
\mathscr{A}(\mathbf{k}) = -\frac{i}{\hbar}\int_{-\infty}^{\infty} \mathrm{d}t \langle \psi_{\mathbf{k}}^{(-)}(t)|V_i(t)|\phi_i(t)\rangle \qquad (1.20)
$$

In the alternative so-called "length-gauge", the Schrödinger equation of the interacting system (1.6) is governed by the dipolar laser-atom interaction energy

$$
V(\mathbf{r},t) = -e\mathbf{F}(t)\cdot\mathbf{r} \qquad (1.21)
$$

(instead of the velocity-gauge interaction $V_i(t)$, defined above). There is no difficulty in obtaining the corresponding solutions in the length gauge. The simplest way to

obtain them now in the length-gauge is to apply the gauge transformation factor $\mathrm{e}^{-i\frac{e}{\hbar c}\mathbf{A}(t)\cdot\mathbf{r}}$ to the solutions in the velocity-gauge. Thus, we get the asymptotic solution of the model Schrödinger equation (1.12), with $H_1(t)$ in the length gauge, as

$$\begin{aligned}\psi_{\mathbf{k}}^{(-)}(\mathbf{r},t) = \mathrm{e}^{\frac{\pi}{2}\eta_k}\Gamma(1+i\eta_k)\mathrm{e}^{-\frac{i}{\hbar}\int^t\left(\frac{\hbar^2\mathbf{k}^2}{2m}-\frac{e\hbar}{mc}\mathbf{A}(t'')\cdot\mathbf{k}+\frac{e^2}{2mc^2}\mathbf{A}^2(t'')\right)dt''} \\ \times\mathrm{e}^{-i\frac{e}{\hbar c}\mathbf{A}(t)\cdot\mathbf{r}}\mathrm{e}^{i\mathbf{k}\cdot\mathbf{r}} \\ \times{}_1F_1[-i\eta_k,1,-i(k|\mathbf{r}+\mathbf{s}(t)|-\mathbf{k}\cdot(\mathbf{r}+\mathbf{s}(t)))] \qquad (1.22)\end{aligned}$$

1.3 Derivation of Energy and Momentum Distributions

To be specific, below we shall calculate the energy and momentum distributions of the electron in the length-gauge. The ionization amplitude in this model in the length gauge is:

$$\mathscr{A}(\mathbf{k}) = -\frac{i}{\hbar}\int_{-\infty}^{\infty}\mathrm{d}t\int\mathrm{d}^3r\,\psi_{\mathbf{k}}^{(-)*}(\mathbf{r},t)(-e\mathbf{F}(t)\cdot\mathbf{r})\phi_i(\mathbf{r},t) \qquad (1.23)$$

where the binding energy E_b of the ground state is taken equal to the ionization potential I_p ($E_b \equiv \frac{\hbar^2k_b^2}{2m} = I_p$). Next, we may expand the periodic part of the integrand in a Fourier series and evaluate the time integral in terms of the delta-function and write the amplitude, $\mathscr{A}$ in the form

$$\mathscr{A}(\mathbf{k}) = -2\pi i\sum_n\delta\left(\frac{\hbar^2(k^2+k_b^2)}{2m}+U_p-n\hbar\omega\right)T^{(n)}(\mathbf{k}) \qquad (1.24)$$

where $U_p = e^2F^2/(4m\omega^2)$ is the ponderomotive potential. The Fourier component $T^{(n)}(\mathbf{k})$ (the so-called "T-matrix" element) physically corresponds to the probability amplitude for ionization of the atom by absorption of n photons from the laser field, and an electron ejected with the momentum $\hbar\mathbf{k}$. The corresponding differential probability of ionization per unit time (i.e. the differential ionization *rate*) is given by,

$$\mathrm{dRate}(\mathbf{k}) = \frac{2\pi}{\hbar}\sum_{n=n_0}^{\infty}|T^{(n)}(\mathbf{k})|^2\delta\left(\frac{\hbar^2(k^2+k_b^2)}{2m}+U_p-n\hbar\omega\right)\frac{\mathrm{d}^3k}{(2\pi)^3} \qquad (1.25)$$

where, $n_0 = \mathrm{Int.part}[\frac{E_b+U_p}{\hbar\omega}]+1$ is the minimum number of photons needed to be absorbed to overcome the ionization potential. The energy distribution is thus given by

$$\mathrm{dRate}(\mathbf{k})/\mathrm{d}\Omega_k = \frac{2\pi}{\hbar}\sum_{n=n_0}^{\infty}|T^{(n)}(\mathbf{k})|^2\rho(E_k) \tag{1.26}$$

where $\mathrm{d}\Omega_p$ is the element of solid angle about the momentum $\hbar\mathbf{k}$, and $\rho(E_k) = \frac{mk}{\hbar^2}$ is the density of the continuum energy states per unit energy and unit volume. More explicitly, the n-photon T-matrix is given by the four-dimensional space-time integral,

$$\begin{aligned} T^{(n)}(\mathbf{k}) = 1/T \int_0^T \mathrm{d}t \mathrm{e}^{\frac{i}{\hbar}\int^t \frac{\hbar^2}{2m}\left(k(t'')^2+k_b^2\right)dt''} \\ \times \int \mathrm{d}^3 r \mathrm{e}^{\frac{\pi}{2}\eta_k}\Gamma(1-i\eta_k)\mathrm{e}^{-i\mathbf{k}(t)\cdot\mathbf{r}} \\ \times {}_1F_1(i\eta_k, 1, i(k|\mathbf{r}+\mathbf{s}(t)| + \mathbf{k}\cdot(\mathbf{r}+\mathbf{s}(t)))) \\ \times(-e\mathbf{F}(t)\cdot\mathbf{r})\phi_i(\mathbf{r})\mathrm{e}^{\frac{i}{\hbar}E_b t} \end{aligned} \tag{1.27}$$

where, $\mathbf{k}(t) \equiv \mathbf{k} - \frac{e}{\hbar c}\mathbf{A}(t)$; $T = 2\pi/\omega$ is the laser period. The spatial integral above is rather complicated (due to the presence of the shifted coordinates in the confluent hypergeometric function). However, an approximate analytic estimate of the integral may be obtained quite easily by noting that the radial range of the integrand is strongly limited by the presence of the bound state wavefunction with the usual factor of the form $\mathrm{e}^{-k_b r}$, which decreases exponentially beyond a distance of the order of $r = < r > \approx 1/k_b$. On the other hand, for a typical intense laser field in the long wavelength domain (e.g. mid-infrared), the quiver amplitude of $s(t)$ is of the order of $\alpha_0 = eF/(m\omega^2) >> < r >$. For example, for a typically intense, 150 TW/cm^2, 2000 nm, mid-infrared laser, $\alpha_0 \approx 124$ a.u. $>> < r > \approx 1$ a.u. Therefore, for the present analytic estimate we shall neglect the r-dependence in the argument of the Hypergeometric function where it appears in relation to α_0. We assume that the bound state of the atomic model is of the form (cf. [21, 22]) $\phi_i(\mathbf{r}) = N_b(\nu, l)r^{(\nu-1)}\mathrm{e}^{-k_b r}Y_{l,m}(\hat{r})$ where the normalization factor is $N_b(\nu, l) = k_b^{\nu+1/2}2^\nu/\sqrt{\nu\Gamma(\nu-l)\Gamma(\nu+l+1)}$. This form of the bound state wavefunction has the correct asymptotic behavior and the correct binding energy. The $\mathbf{r}$-integration could be performed analytically by an asymptotic method [22] and the time-integration, by the stationary phase method (cf. [21, 22]). There are two stationary points per period, hence, adding their contributions we get the result (in atomic units, a.u., $e = m = \hbar = \alpha \times c = 1$),

$$
\begin{aligned}
T^{(n)}(\mathbf{k}) &= T_{+}^{(n)} + T_{-}^{(n)} \\
T_{\mathbf{k}}^{(n)} &= M(\mathbf{k}, t_{\pm}) \frac{e^{if_{\pm}}}{(-if_{\pm}'')^{(\nu+1)/2}} \\
M(\mathbf{k}, t_{\pm}) &= N_{k}^{*}{}_1F_1(i\eta_k, 1, i(ks(t_{\pm}) + \mathbf{k}\cdot\mathbf{s}(t_{\pm}))) \\
&\quad \times(-\sqrt{2\pi}) N_b(\nu, l)(\pm 1)^l Y_{l,m}(\Theta_k, \phi_k) \\
&\quad \times (k_b)^{\nu} \omega \Gamma\left(\frac{\nu+2}{2}\right) 2^{\nu/2} \\
if_{\pm} &= n \times ln(c_{\pm} + is_{\pm}) - ic_{\pm}(\alpha_0 k_{\parallel} + (U_p/\omega)s_{\pm}) \\
(-if_{\pm}'') &= F\sqrt{(k_b^2 + k_{\perp}^2)(1 - s_{\pm}^2)} \\
N_{\mathbf{k}}^{*} &= \mathrm{e}^{\pi\eta_k/2}\Gamma(1 - i\eta_k) \\
\eta_k &= Z/k \\
N_b(\nu, l) &= k_b^{\nu+1/2} 2^{\nu} / \sqrt{\nu\Gamma(\nu - l)\Gamma(\nu + l + 1)} \\
\nu &= Z/k_b \\
\alpha_0 &= F/\omega^2 \\
s_{\pm} &= \omega/F\left(-k_{\parallel} \pm i\sqrt{k_b^2 + k_{\perp}^2}\right) \\
c_{\pm} &= \pm\sqrt{1 - s_{\pm}^2} \\
t_{\pm} &= -\frac{i}{\omega}\ln(c_{\pm} + is_{\pm}) \\
\cos\Theta_k &= \sqrt{1 + (k_{\perp}/k_{\parallel})^2} \\
k &= \sqrt{k_{\perp}^2 + k_{\parallel}^2} = \sqrt{2(n\omega - E_b - U_p)}
\end{aligned}
\tag{1.28}
$$

1.4 Results and Discussions

In Fig. 1.3 we present the energy distribution $\frac{\mathrm{d\,Rate}(E_k,\theta)}{\mathrm{d}\Omega_k}$ in the forward direction ($\theta = 0°$) from the threshold to 60 eV. The distribution calculated from the present Coulomb model (blue line) is compared with the corresponding distribution from the SFA (orange line). It can be seen that the zero probability at the threshold (orange) given by the SFA, is changed into a finite (non-zero) probability by the present model with Coulomb wave final state (blue) at the threshold. Furthermore the Coulomb model shows rapid oscillations of the probability as the threshold is approached; the SFA does not show this behavior either. In Fig. 1.4, the same distribution is shown at lower energies with a greater resolution. The phase of the oscillations are seen to approach each other at about 10 eV but the probabilities remain significantly different in magnitude. In Fig. 1.5 we compare the parallel momentum distributions

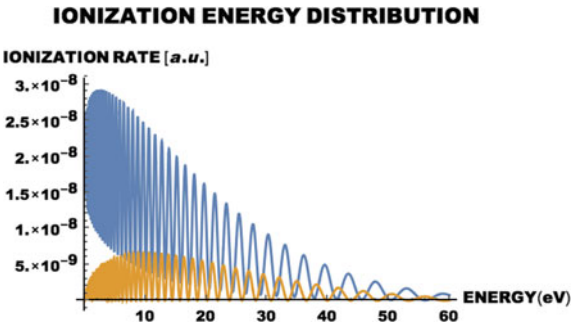

Fig. 1.3 Comparison of the calculated energy distributions parallel to the polarization axis ($\theta_k = 0°$) as a function of electron energy (in eV): the present Coulomb model (blue line) versus SFA (orange line); wavelength, 2000 nm, intensity 150 TW/cm^2. Note that a non-zero value of ionization probability at the threshold is predicted by the Coulomb model. In contrast, the usual SFA gives zero probability at the threshold

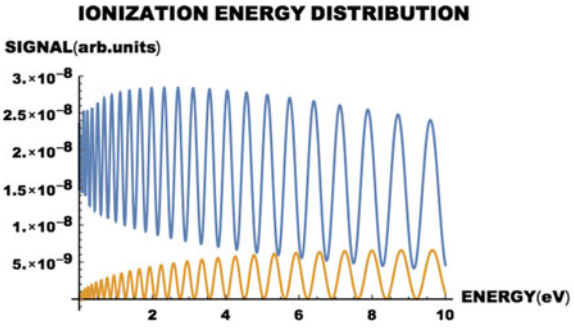

Fig. 1.4 Comparison of the energy distributions of the electron along the polarization axis ($\theta_k = 0°$) shown at a higher resolution (than in Fig. 1.3) between 0 and 10 eV; wavelength 2000 nm, and intensity, 150 TW/cm^2. The ionization probability in the Coulomb field (blue line) is generally larger than the probability given by the SFA (orange line), while the phase of the probability oscillations approach each other above 10 eV

calculated from the Coulomb model (blue line) and the usual SFA (orange line) for a small value of $P_x = 0.001$ a.u., and $P_y = 0$. The SFA distribution is much lower in magnitude and shows a rather uniformly oscillating probability (orange line) compared to the distribution obtained from the Coulomb model (blue line). Clearly, the Coulomb effect enhances the distribution strength significantly and gives rise to two prominent peak structures about the threshold; this is analogous to the double-peak structures that were observed earlier experimentally [10, 23]. It also shows a rapid high-amplitude oscillation close to the threshold. In Fig. 1.6 we present the parallel momentum (P_z) distribution of the ionization rate integrated over the perpendicular momentum P_x between -0.01 and 0.01 a.u., and $P_y = 0$. The result shows a sharp maximum at the threshold and two humps on either side of it. In Fig. 1.7 we compare the perpendicular momentum distribution of the Coulomb model (blue line) with

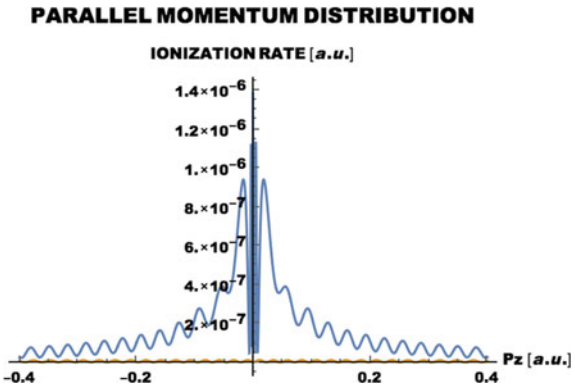

Fig. 1.5 Parallel momentum distribution close to the polarization axis ($P_x = 0.001$ a.u., $P_y = 0$) and near the threshold. Results of the Coulomb model (blue line) versus the usual SFA (orange line); laser wavelength 2000 nm, intensity 150 TW/cm^2. Note the qualitatively different behavior of the parallel momentum distribution in the two cases near and at the threshold – the SFA gives generally much lower probability which oscillates rather uniformly across the threshold. In contrast, the Coulomb model shows an increasing probability with decreasing magnitude of momentum and, a strong high amplitude oscillation very close to the threshold. It also exhibits two prominent peak structures close to the threshold (in the forward and the backward directions)

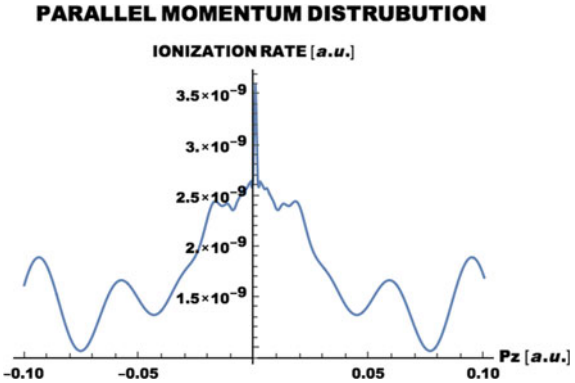

Fig. 1.6 Integrated parallel momentum (P_z) distributions close to the polarization axis for the Coulomb model near the threshold (it is integrated over P_x from -0.01 to 0.01 a.u., $P_y = 0$). The laser parameters are as in Fig. 1.5. Note the sharp maximum of the parallel momentum distribution at the threshold $P_z = 0.0$ and two side peaks near it. Result is shown for the Coulomb model (blue line); laser wavelength 2000 nm, intensity 150 TW/cm^2

the SFA (orange line) at and near the threshold momentum. The Coulomb model is characterised by a cusp-like decrease of the probability from its peak value at the threshold; this is analogous to the earlier experimental findings (e.g. [10, 23]). In contrast, the SFA (orange line) does not show the cusp-structure but changes smoothly over the threshold. For the higher values of the perpendicular momentum both distributions show similar oscillatory behavior with prominent minima. However, they differ in the positions and depths of the minima – the minima of the Coulomb model

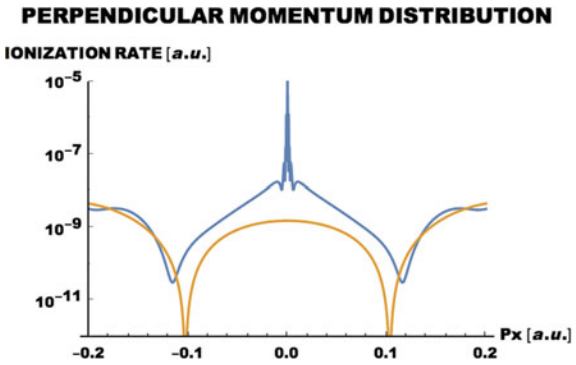

Fig. 1.7 Perpendicular momentum distributions near the threshold ($P_z = 0.001$ a.u., $P_y = 0$): Coulomb model (blue line) versus SFA (orange line). The laser wavelength is 2000 nm, and the laser intensity is 150 TW/cm^2. Note, that the Coulomb model shows a cusp-like fall-off of the probability from its peak value at the threshold; no such cusp at the threshold arises in the case of SFA (orange line) which is based on the plane-wave Volkov state

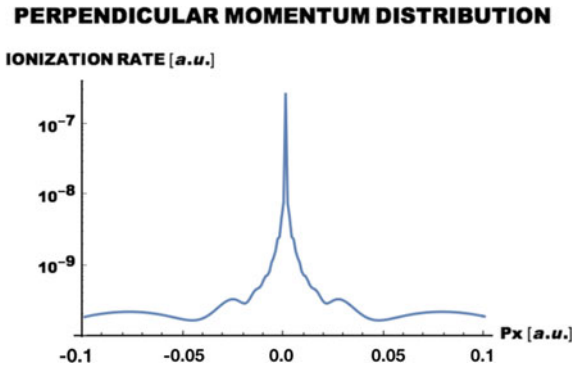

Fig. 1.8 Integrated perpendicular momentum distributions near the threshold for the Coulomb model (blue line) – integrated over P_z from -0.01 to 0.01 a.u., $P_y = 0$. The laser parameters are the same as in Fig. 1.7. Note the cusp-like fall-off of the distribution at the threshold momentum $P_x = 0$

are some what higher than the SFA minima, as well as are shifted somewhat away from SFA minima. Finally, in Fig. 1.8 we present the transverse momentum (P_x) distribution integrated over P_z between -0.01 and 0.01 a.u., and $P_y = 0$, for the Coulomb model. This distribution is marked by the appearance of a characteristic finite cusp-structure at the transverse momentum threshold, $P_x = 0$. It should be noted that in the un-integrated parallel P_z-momentum distribution and transverse P_x-momentum distribution (shown in Figs. 1.5 and 1.7, respectively), we have avoided the point ($P_x = 0$, or $P_z = 0$, respectively, when $P_y = 0$), for numerically the point $(P_x, P_y, P_z) = 0$ appears to be a singular point of the two distributions. It is also interesting to note that the apparent singularity at the exact threshold momentum is

removed by a sharp maximum or a sharp cusp in the corresponding integrated distributions (integrated over a small domain of P_x or P_z) in Figs. 1.6 and 1.8, respectively. We note further that there is no singularity at the zero energy threshold in the energy distributions along the forward direction (Figs. 1.3 and 1.4). This is due to the presence of the density of energy states factor $\rho(E_k) = \frac{mk}{\hbar^2}$ in the energy distributions, while in the P_z and, P_x differential rates with respect to the momentum along these axes (Figs. 1.5 and 1.7) this factor does not arise.

We conclude by summarising that the present model calculations suggest that the long-range Coulomb potential can qualitatively affect the energy and momentum distributions of electrons from ionization of atoms in intense long wavelength laser fields at and near the threshold. It yields a non-zero probability at the threshold of ionization, that oscillates faster as the threshold energy is approached. The Coulomb effect on the parallel momentum distribution is seen to develop a two-peak structure near the threshold, while its effect on the perpendicular momentum distribution is to develop a cusp-like structure at the threshold, that seem to be consistent with earlier experimental findings. In contrast, the SFA (based, as it is, on the final-state plane-wave Volkov wavefunction) has a zero probability at the threshold energy and does not show a sharp maximum or a cusp structure in the parallel or perpendicular momentum distributions. Before ending, we further note that although the present model analysis clearly separates out the effect of the long-range Coulomb potential on the threshold behaviour of energy and momentum distributions, by comparison with respect to the SFA, in its present form it does not account for the specific rescattering induced effects that are associated with the isolated "low energy structures" discussed in the introduction. It is hoped that the present approximate investigation of the issue of threshold behavior of the strong-field ionization probability would stimulate more accurate investigations, e.g., using the recently derived systematic Coulomb-Volkov S-matrix series [20] and/or alternative methods, in the future.

References

1. A. Becker, F.H.M. Faisal, J. Phys. B: At. Mol. Opt. Phys. **38**, R1 (2005)
2. L.V. Keldysh, Zh. Eksp. Teor. Fiz. **47**, 1945 (1964) [Sov. Phys.-JETP **20**, 1307 (1965)]
3. F.H.M. Faisal, J. Phys. B: At. Mol. Opt. Phys. **6**, L89 (1973)
4. H.R. Reiss, Phys. Rev. A **22**, 1786 (1980)
5. C.I. Blaga et al., Nat. Phys. **5**, 335 (2008)
6. W. Quan et al., Phys. Rev. Lett. **103**, 093001 (2009)
7. T.-M. Yan et al., Phys. Rev. Lett. **105**, 253002 (2010)
8. C. Wu et al., Phys. Rev. Lett. **109**, 043001 (2012)
9. H. Liu et al., Phys. Rev. Lett. **109**, 093001 (2012)
10. J. Dura et al., Nat. Sci. Rep. **3**, Art. No. 2675 (2013)
11. B. Wolter et al., Phys. Rev. A **90**, 063424 (2014)
12. F.H.M. Faisal, Nat. Phys. **5**, 319 (2009)
13. K.J. Schafer, B. Yang, L.F. DiMauro, K.C. Kulander, Phys. Rev. Lett. **70**, 1599 (1993)
14. A. Kästner, U. Saalmann, J.M. Rost, Phys. Rev. Lett. **108**, 033201 (2012)
15. W. Becker et al., J. Phys. B: At. Mol. Opt. Phys. **47**, 204022 (2014)
16. T. Nubbemayer et al., Phys. Rev. Lett. **101**, 233001 (2008)

17. A. Nordsieck, Phys. Rev. **93**, 785 (1954)
18. F.H.M. Faisal, Multiple absorption of laser photons by atoms for 40 years and more (in Viewpoints). J. Phys. B: At. Mol. Opt. Phys. **49**, No. 22 (28 November 2016)
19. L.D. Landau, E.M. Lifshitz, *Quantum Mechanics* (Pergamon Press, Oxford, 1965)
20. F.H.M. Faisal, Phys. Rev. A **94**, 031401 (R) (2016)
21. G.F. Gribakin, MYu. Kuchiev, Phys. Rev. A **55**, 3760 (1997)
22. F.H.M. Faisal, G. Schlegel, J. Phys. B 38, L223 (2005); J. Mod. Opt. **53**, 207 (2006)
23. A. Rudenko et al., J. Phys. B **37**, L407 (2004)

Chapter 2
Laser-Induced Alignment and Orientation Dynamics Beyond the Rigid-Rotor Approximation

Tamás Szidarovszky and Kaoru Yamanouchi

Abstract We introduce theoretical methods we developed, with which the laser-induced alignment and/or orientation dynamics of polyatomic molecules can be investigated beyond the rigid rotor approximation. The time-dependent Schrödinger equation is solved by expanding the laser-induced wave packet in terms of the field-free rovibrational eigenstates of the system. We present the results of highly accurate numerical calculations on the laser-induced alignment dynamics of floppy and weakly-bound H_2He^+ and rigid- and strongly-bound H_2O, and investigate the effect of the vibrational excitations on the alignment dynamics. We show that one-photon vibrational excitations induce changes in the light-induced alignment and orientation dynamics through the changes in the molecular structure, leading to the breakdown of the rigid rotor approximation, and through the changes in the optical selections in the rotational excitation.

2.1 Introduction

The developments of laser technologies in these decades have enabled researchers to align and orient molecules in space by ultrashort laser pulses, and a variety of experimental studies have been performed on the alignment and orientation of molecules. Theoretical studies on the mechanisms of the alignment and orientation processes have also been carried out intensively, and the experimental results have been interpreted successfully by numerical simulations [1–3]. Indeed, as many as three chapters have been devoted to this topic in this book series [4–6], demonstrating the high-level interest on the laser-induced orientation and/or alignment dynamics of molecules in

T. Szidarovszky (✉) · K. Yamanouchi
Department of Chemistry, School of Science, The University of Tokyo, Tokyo, Japan
e-mail: tamas821@caesar.elte.hu

T. Szidarovszky
Laboratory of Molecular Structure and Dynamics, Institute of Chemistry, Eötvös Loránd University and MTA-ELTE Complex Chemical Systems Research Group, Pázmány Péter sétány 1/A, Budapest 1117, Hungary

© Springer Nature Switzerland AG 2018

K. Yamanouchi et al. (eds.), *Progress in Ultrafast Intense Laser Science XIV*,
Springer Series in Chemical Physics 118,
https://doi.org/10.1007/978-3-030-03786-4_2

the research field of ultrafast and intense laser science. It is expected that an ensemble of non-randomly aligned and/or oriented molecules will be used for initiating stereochemically specific bimolecular reactions, leading to new ways of controlling chemical reaction processes.

In the framework of quantum mechanics, spatial alignment and orientation can be understood as the result of a coherent superposition of rotational states. In most of the previous theoretical studies on alignment and orientation of molecules, molecules were treated as rigid or semi-rigid bodies, whose geometrical structure does not change largely in the course of the alignment and/or orientation, that is, the rigid rotor approximation with its perturbative corrections was adopted. The detailed description of such approaches can be found in related review articles or book chapters [1, 2, 6], and a user-friendly software is available for conducting such computations [7]. Simulations on polyatomic molecules beyond the rigid rotor model and its perturbative corrections have also been made in some cases [8–11]. The rigid rotor approach can be rationalized as long as the light induced alignment is achieved by light pulses being off-resonant with any optical transitions, leading to very low dipole transition amplitudes. In this case, the most dominant optical excitation processes are two-photon Raman-type transitions, leading only to the rotational excitation. For rigid or semi-rigid molecules, the laser-induced rotational excitation can be accurately described within the rigid rotor approximation.

When we treat molecular alignment and orientation processes beyond the rigid rotor approximation, there may be two different cases. In the first case, when the frequency range of the alignment and/or orientation pulse covers within its band width vibrational transition frequencies, the vibrational excitations are induced simultaneously with the Raman-type rotational excitations. As will be discussed below in detail, these rovibrational excitations can lead to significant changes in the populations in the rovibrational stationary states in the generated wave packet, which can affect the alignment and orientation dynamics. In the second case, when molecules are floppy, that is, when molecules have one or more large-amplitude vibrational modes, the rigid rotor approximation and its perturbative corrections fail to describe the rotational dynamics of the system, which has been known well in molecular spectroscopy [12]. The strong rovibrational couplings can lead to substantial changes in the energy level structure and the rotational constants of the system. Therefore, it becomes necessary to introduce non-perturbative approaches, in which accurate potential energy surfaces, exact kinetic energy operators and variational wavefunction expansions are employed [13, 14].

In our recent study, we have formulated a general theoretical framework, which enables us to simulate the laser-induced rovibrational motion and spatial alignment and/or orientation of polyatomic molecules beyond the rigid rotor approximation [15]. The method is based on solving the time-dependent Schrödinger equation (TDSE) by expanding the laser-induced wave packet with the field-free rovibrational eigenstates of the system. By this approach we are able to obtain not only the exact solution of the TDSE but also its approximated solution, depending on the choices of the method for determining the field-free eigenstates. The field-free eigenstates can be computed directly, or alternatively, for some molecular species,

those obtained by previous accurate calculations can also be used. For example, in [11, 16] the accurate data from spectroscopic databases were used for the simulation of the light-induced dynamics of NH_3 and H_2O, respectively.

In the following sections, we review the general theoretical approach explored in [15], with which the laser-induced rovibrational dynamics of polyatomic molecules can be simulated. We then introduce our highly accurate numerical demonstration on the laser-induced rovibronic dynamics of the weakly bound H_2He^+ [17, 18] and the strongly bound H_2O [19] molecules, through which we examine the effect of the vibrational excitations on the alignment dynamics.

2.2 Theoretical Methods

2.2.1 Laser-Induced Rovibrational Dynamics

The theoretical approach outlined below closely follows that presented in [15]. In order to simulate light-induced alignment dynamics of molecules, we solve the time-dependent Schrödinger equation (TDSE),

$$i\hbar\frac{\partial|\Psi(t)\rangle}{\partial t} = \widehat{H}(t)|\Psi(t)\rangle, \quad \widehat{H}(t) = \widehat{H}_0 - \boldsymbol{\varepsilon}(t)\boldsymbol{\mu} - \frac{1}{2}\boldsymbol{\varepsilon}(t)(\boldsymbol{\alpha}\boldsymbol{\varepsilon}(t)), \tag{2.1}$$

where $\widehat{H}_0$, $\boldsymbol{\mu}$, $\boldsymbol{\alpha}$ and $\boldsymbol{\varepsilon}(t)$ are the field-free rovibrational Hamiltonian, the permanent dipole moment, the first polarizability, and the electric field of the external field, respectively. In certain cases, higher order polarizability terms also need to be considered [6], but these are neglected here.

The most straightforward approach for solving (2.1) is to expand the time-dependent wavefunction as a superposition of time-independent basis functions with time-dependent coefficients, i.e., $|\Psi(t)\rangle = \sum_n C_n(t)|\Psi_n\rangle$. Because alignment dynamics can be understood as the dynamics created by a coherent superposition of stationary rovibrational states, we regard $|\Psi_n\rangle$ as the bound rovibrational states, satisfying the time-independent nuclear Schrödinger equation,

$$\widehat{H}_0|\Psi_n\rangle = E_n|\Psi_n\rangle. \tag{2.2}$$

Compared with grid-based rovibrational basis sets, this choice leads to a set of basis functions with a modest size, leading to a compact matrix representation of the Hamiltonian, with which time-propagation can be carried out in a straightforward manner. On the other hand, as long as we adopt the stationary states as basis functions, we need to solve the time-independent Schrödinger equation (2.2). The accuracy and approximations made in solving (2.2) will limit the accuracy of the time-dependent calculations.

Naturally, approximations commonly adopted in theoretical molecular spectroscopy such as the harmonic oscillator and rigid rotor approximations, their perturbative extensions [12, 20], using, for example, effective Hamiltonians, can be introduced in solving (2.2). In order to obtain more accurate bound rovibrational states, a preferable approach is to perform variational rovibrational calculations, which can also be used for floppy molecular species to which the rigid rotor approximation could not be adopted. In the case of triatomic molecules, we may be able to compute many hundreds or thousands of bound rovibrational states with full-dimensional variational methods with an acceptable computational cost, and obtain a numerically exact basis set to represent the laser-induced time-dependent rovibrational dynamics. However, for larger molecular systems having four or more atoms, accurate rovibrational calculations are in general very demanding, and consequently, we are compelled to adopt less accurate methods. Nonetheless, some efficient methods and computer codes [13, 21, 22] are available for larger molecular systems. Alternatively, in order to reduce the computational cost, reduced-dimensional approaches [23] may also be adopted, in which only selected degrees of freedom that are most relevant for describing the laser-induced dynamics of the molecule are taken into account.

In most of the theoretical approaches and corresponding computer codes that have been developed for solving (2.2), the full- or reduced-dimensional rovibrational wavefunctions of a field-free molecular system are generated by expanding the nuclear wave function as

$$\left|\Psi^{JMn}\right\rangle = \sum_{K,v} C_{Kv}^{Jn} \left|v\right\rangle \left|JKM\right\rangle, \tag{2.3}$$

where C_{Kv}^{Jn} is an expansion coefficient, $|v\rangle$ is the vth vibrational basis function, $|JKM\rangle$ is a symmetric-top eigenfunction [24], J is the rotational quantum number, K is the projection of the rotational angular momentum onto the body-fixed (BF) z-axis, M is the projection of the rotational angular momentum onto the laboratory-fixed (LF) z-axis, and n is "all other" quantum numbers. The quantum numbers, J and M, are good quantum numbers under field-free conditions. In coordinate representation, (2.3) takes the form of

$$\Psi^{JMn}(Q_1, \ldots, Q_d, \varphi, \vartheta, \chi) = \sqrt{\frac{2J+1}{8\pi^2}} \sum_{K,v} C_{Kv}^{Jn} \psi_v(Q_1, \ldots, Q_d) D_{MK}^{J*}(\varphi, \vartheta, \chi), \tag{2.4}$$

where $\psi_v(Q_1, \ldots, Q_d)$ is the vth vibrational basis function having d vibrational degrees of freedom and $D_{MK}^{J}(\varphi, \vartheta, \chi)$ is a Wigner matrix [24]. The variables, φ, ϑ and χ are the three Euler-angles, describing the orientation of the BF coordinate frame with respect to the LF frame.

After the field-free states $\left|\Psi^{JMn}\right\rangle$ of (2.2) are obtained and expressed in the form of (2.3), the matrix representation of the Hamiltonian of (2.1) can be constructed using the field-free basis states. We express the external field $\boldsymbol{\varepsilon}(t)$ and the molecular

properties $\boldsymbol{\mu}$ and $\boldsymbol{\alpha}$ in (2.1) in the LF frame, because $\boldsymbol{\varepsilon}(t)$ is given in most cases in the LF frame. However, in quantum chemistry calculations, $\boldsymbol{\mu}$ and $\boldsymbol{\alpha}$ are commonly obtained in the BF frame. Therefore, we transform $\boldsymbol{\mu}$ and $\boldsymbol{\alpha}$ given in the BF frame into those in the LF frame. Such transformation can be carried out conveniently by changing from the Cartesian representation to the spherical-basis [24] representation using the transformation formulae $\mu^{(1,0)} = \mu_3$, $\mu^{(1,\pm1)} = \frac{1}{\sqrt{2}}(\mp\mu_1 - i\mu_2)$, $\alpha^{(0)} = -\frac{1}{\sqrt{3}}(\alpha_{11}+\alpha_{22}+\alpha_{33}) = -\frac{1}{\sqrt{3}}\mathrm{Tr}[\boldsymbol{\alpha}]$, $\alpha^{(2,\pm2)} = \frac{1}{2}[\alpha_{11}-\alpha_{22} \pm i(\alpha_{12}+\alpha_{21})]$, $\alpha^{(2,\pm1)} = \frac{1}{2}[\mp(\alpha_{13}+\alpha_{31}) - i(\alpha_{23}+\alpha_{32})]$, and $\alpha^{(2,0)} = \frac{1}{\sqrt{6}}[2\alpha_{33}-\alpha_{22}-\alpha_{11}]$. In the spherical-basis representation, the transformation between the BF frame and the LF frame can be performed by the transformation using the Wigner matrices, i.e., the jth component of a spherical tensor of rank l in the LF frame $T^{\mathrm{LF},(l,j)}$ is obtained from the body-fixed components $T^{\mathrm{BF},(l,k)}$ by the transformation represented as [24]

$$T^{\mathrm{LF},(l,j)} = \sum_{k=-l}^{l} D^{l*}_{jk}(\varphi,\vartheta,\chi)T^{\mathrm{BF},(l,k)}. \tag{2.5}$$

If one adopts a linearly polarized external field $\boldsymbol{\varepsilon}^{\mathrm{LF}} = (0,0,\varepsilon)$, the interaction terms in (2.1) can be expressed using (2.5) as

$$\boldsymbol{\varepsilon}^{\mathrm{LF}}\boldsymbol{\mu}^{\mathrm{LF}} = \varepsilon\mu_3^{\mathrm{LF}} = \varepsilon\mu^{\mathrm{LF},(1,0)} = \varepsilon\sum_{k=-1}^{1} D^{1*}_{0k}(\varphi,\vartheta,\chi)\mu^{\mathrm{BF},(1,k)}$$

$$\begin{aligned}\boldsymbol{\varepsilon}^{\mathrm{LF}}\left(\boldsymbol{\alpha}^{\mathrm{LF}}\boldsymbol{\varepsilon}^{\mathrm{LF}}\right) &= \varepsilon^2\alpha_{33}^{\mathrm{LF}} \\ &= \varepsilon^2\frac{\sqrt{6}}{3}\left(\alpha^{\mathrm{LF},(2,0)} - \frac{1}{\sqrt{2}}\alpha^{\mathrm{LF},(0)}\right) \\ &= \varepsilon^2\frac{\sqrt{6}}{3}\left[\sum_{k=-2}^{2} D^{2*}_{0k}(\varphi,\vartheta,\chi)\alpha^{\mathrm{BF},(2,k)} - \frac{1}{\sqrt{2}}\alpha^{\mathrm{BF},(0)}\right].\end{aligned}$$

By taking into account the integral formula of the Wigner-matrices expressed using 3j-symbols [24],

$$\int D^{J_1}_{M_1'M_1}(R)D^{J_2}_{M_2'M_2}(R)D^{J_3}_{M_3'M_3}(R)\mathrm{d}R = 8\pi^2\begin{pmatrix} J_1 & J_2 & J_3 \\ M_1' & M_2' & M_3' \end{pmatrix}\begin{pmatrix} J_1 & J_2 & J_3 \\ M_1 & M_2 & M_3 \end{pmatrix}, \tag{2.6}$$

where R represents an operation in the SO(3) rotation group, and by using (2.3), (2.4), and (2.5), the matrix elements of the Hamiltonian of (2.1) can be expressed as

$$
\begin{aligned}
\langle \Psi^{JMn}|\widehat{H}|\Psi^{J'M'n'}\rangle &= E^{Jn}\delta_{JJ'}\delta_{nn'}\delta_{MM'} - \varepsilon(t)\sum_{k=-1}^{1}\langle \Psi^{JMn}|D_{0k}^{1*}\mu^{\mathrm{BF},(1,k)}|\Psi^{J'M'n'}\rangle \\
&\quad - \frac{\varepsilon(t)^2}{\sqrt{6}}\Bigg[\sum_{k=-2}^{2}\langle \Psi^{JMn}|D_{0k}^{2*}\alpha^{\mathrm{BF},(2,k)}|\Psi^{J'M'n'}\rangle \\
&\quad - \frac{1}{\sqrt{2}}\langle \Psi^{JMn}|\alpha^{\mathrm{BF},(0)}|\Psi^{J'M'n'}\rangle\Bigg] \\
&= E^{Jn}\delta_{JJ'}\delta_{nn'}\delta_{MM'} \\
&\quad - \delta_{MM'}\varepsilon(t)\sum_{k=-1}^{1}\Bigg(\sum_{v,v'}\langle v|\mu^{\mathrm{BF},(1,k)}|v'\rangle\sum_{K,K'}C_{Kv}^{Jn*}C_{K'v'}^{J'n'}(2J+1)^{\frac{1}{2}} \\
&\quad (2J'+1)^{\frac{1}{2}}(-1)^{-k+M-K'}\begin{pmatrix} J & 1 & J' \\ M & 0 & -M \end{pmatrix}\begin{pmatrix} J & 1 & J' \\ K & -k & -K' \end{pmatrix}\Bigg) \\
&\quad - \delta_{MM'}\frac{\varepsilon^2(t)}{\sqrt{6}}\sum_{k=-2}^{2}\Bigg(\sum_{v,v'}\langle v|\alpha^{\mathrm{BF},(2,k)}|v'\rangle\sum_{K,K'}C_{Kv}^{Jn*}C_{K'v'}^{J'n'}(2J+1)^{\frac{1}{2}} \\
&\quad (2J'+1)^{\frac{1}{2}}(-1)^{-k+M-K'}\begin{pmatrix} J & 2 & J' \\ M & 0 & -M \end{pmatrix}\begin{pmatrix} J & 2 & J' \\ K & -k & -K' \end{pmatrix}\Bigg) \\
&\quad + \delta_{JJ'}\delta_{MM'}\frac{\varepsilon^2(t)}{\sqrt{12}}\sum_{v,v'}\sum_{K}C_{Kv}^{Jn*}C_{Kv'}^{J'n'}\langle v|\alpha^{\mathrm{BF},(0)}|v'\rangle, \qquad (2.7)
\end{aligned}
$$

where E^{Jn} are the field-free eigenenergies of the system. In determining the matrix elements of (2.7), the bound rovibrational eigenvalues E^{Jn}, the eigenvector coefficients C_{Kv}^{Jn} and the $\langle v|\mu^{\mathrm{BF}}|v'\rangle$ dipole and $\langle v|\alpha^{\mathrm{BF}}|v'\rangle$ polarizability matrix elements need to be given. The latter two are obtained as $\langle v|\mu^{\mathrm{BF}}|v'\rangle \equiv \int \psi_v^*(Q_1,\ldots,Q_d)\mu^{\mathrm{BF}}(Q_1,\ldots,Q_d)\psi_{v'}(Q_1,\ldots,Q_d)\mathrm{d}Q_1,\ldots,\mathrm{d}Q_d$ and $\langle v|\alpha^{\mathrm{BF}}|v'\rangle \equiv \int \psi_v^*(Q_1,\ldots,Q_d)\alpha^{\mathrm{BF}}(Q_1,\ldots,Q_d)\psi_{v'}(Q_1,\ldots,Q_d)\mathrm{d}Q_1,\ldots,\mathrm{d}Q_d$.

Then, the TDSE of (2.1) expressed with the matrix representation is solved and the temporal evolution of physical quantities can be monitored by computing their expectation values with the time-dependent rovibrational wavepacket at different times. The expectation values can be evaluated efficiently if the matrix representation of the respective physical quantities in the field-free basis states are available. Using (2.3), the matrix elements of an operator, which is a $f(Q_1,\ldots,Q_d)$ function of the internal coordinates, can be written as

$$
\left\langle \Psi^{JMn}|f(Q_1,\ldots,Q_d)|\Psi^{J'M'n'}\right\rangle = \delta_{JJ'}\delta_{MM'}\sum_{v,v'}\sum_{K}C_{Kv}^{Jn*}C_{Kv'}^{J'n'}\langle v|f(Q_1,\ldots,Q_d)|v'\rangle. \qquad (2.8)
$$

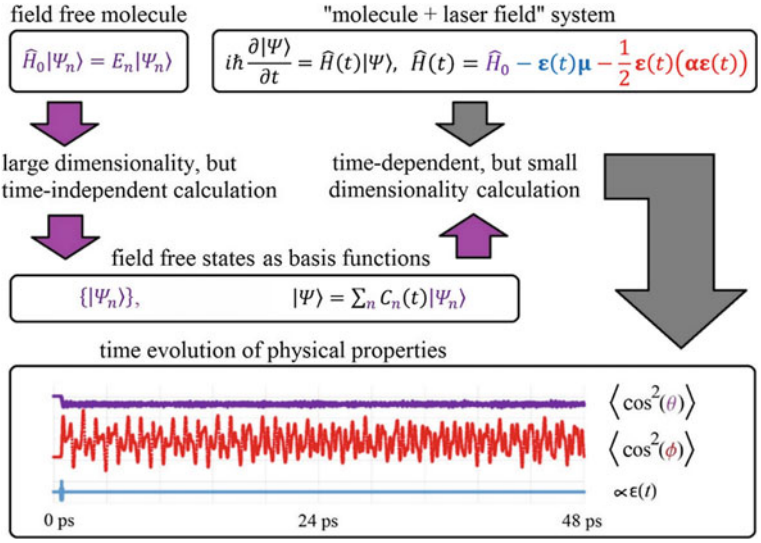

Fig. 2.1 Summary of the theoretical approach of [15] for calculating laser-induced alignment dynamics of polyatomic molecules. See text for the definitions of $\widehat{H}_0, E_n$, $|\Psi_n\rangle$, $\boldsymbol{\mu}$, $\boldsymbol{\alpha}$, $\boldsymbol{\varepsilon}(t)$, and $|\Psi\rangle$. The angle ϕ describes the spatial alignment and the angle θ is the variable representing an internal degree of freedom

The degree of alignment can be given using the angle ϕ between the z-axis of the BF frame and Z-axis of the LF coordinate frames. The matrixelements of $\cos^2\phi$ can be expressed as [25]

$$\begin{aligned}&\langle\Psi^{JMn}|\cos^2\phi|\Psi^{J'M'n'}\rangle\\&= \sum_v \sum_{K,K'} C_{Kv}^{Jn*} C_{K'v}^{J'n'}\left[\frac{1}{3}\delta_{JJ'}\delta_{KK'}\delta_{MM'}\right.\\&\left.+\frac{2}{3}(2J+1)^{\frac{1}{2}}\left(2J'+1\right)^{\frac{1}{2}}(-1)^{M'+K'}\begin{pmatrix} J & 2 & J' \\ M & 0 & -M' \end{pmatrix}\begin{pmatrix} J & 2 & J' \\ K & 0 & -K' \end{pmatrix}\right].\end{aligned} \tag{2.9}$$

A pictorial summary of the theoretical approach is presented in Fig. 2.1.

2.2.2 *Bound State Calculations*

In this section, we present the laser-induced rovibrational dynamics of the weakly bound H_2He^+ and the strongly bound H_2O molecules. According to the theoretical framework detailed above, the first step is to solve the time-independent rovibrational Schrödinger-equation (2.2) for obtaining the field-free bound rovibrational

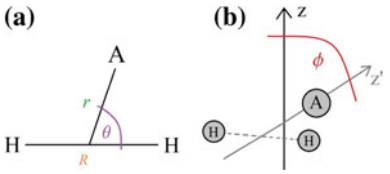

Fig. 2.2 The Jacobi-coordinates (**a**) and the angle between the laboratory-fixed and body-fixed z-axes (**b**). The atom labelled with the letter "A" is "He" for H_2He^+ and "H" for H_2O

states of these two systems. This was carried out by full-dimensional variational computations in the Jacobi coordinates [26] shown in Fig. 2.2 with the D^{2}FOPI program suite [27]. D^{2}FOPI utilizes an iterative eigensolver, a mixed discrete variable representation (DVR) [28] and finite basis representation (FBR) [28] for the vibrational degrees of freedom, and symmetry-adopted Wigner-matrices constructed by the rotational basis functions for the rotational degrees of freedom. The calculations were performed using the C_{2v}(M) molecular symmetry [12] as described in [29]. The electronic potential energy surfaces (PES) used for the rovibrational calculations were the accurate PESs called MRCI8 [17], for H_2He^+ and CVRQD [30] for H_2O.

2.2.3 Computational Details

The parameters used during the computation of the bound rovibrational states of H_2He^+ are detailed in [15]. During the computations on H_2O, for each irreducible representation of the C_{2v}(M) molecular symmetry group, we employed (i) a complete set of rotational basis functions whose size varies depending on the given value of the J rotational quantum number, (ii) 35 potential-optimized (PO) spherical-DVR basis functions [27] along the R and r coordinates, and (iii) 15 associated-Legendre functions along the θ coordinate. The coordinate ranges used in the present calculations were $R/\text{bohr} \in (0, 4.5)$ and $r/\text{bohr} \in (0, 3.5)$, and the nuclear masses $m_H = 1.00727647$ u and $m_O = 15.990526$ u were employed. With these parameters all rovibrational eigenenergies are converged to within 0.01 cm^{-1}.

The dipole moment μ^{BF} surfaces and the polarizability α^{BF} surfaces used for H_2He^+ were described in [15]. For H_2O, the dipole moment surface was taken from [31] while the polarizability surface was taken from [32].

The matrix elements of the Hamiltonian of (2.1) were computed according to (2.7) using the bound rovibrational states that were computed before. Because the size of the final Hamiltonian is small, time propagation during the interaction with the external field was carried out using the simple formula $\mathbf{\Psi}(t + \mathrm{d}t) = \mathrm{e}^{-\frac{i}{\hbar}\mathbf{H}(t)\mathrm{d}t}\mathbf{\Psi}(t)$, where $\mathrm{e}^{-\frac{i}{\hbar}\mathbf{H}(t)\mathrm{d}t}$ is explicitly constructed by the diagonalization of $\mathbf{H}(t)$ at each timestep, for which $\mathrm{d}t = 5$ a.u. was used. Time propagation under the field-free conditions was performed in a straightforward manner using the basis of the field-free eigenstates.

2.3 Results and Discussion

2.3.1 H_2He^+ Bound States

Based on the theoretical studies of [17, 33], H_2He^+ has been known to have two equivalent linear equilibrium structures. In terms of the Jacobi-coordinates, these are located near the H–H distance of $R = 2.09$ bohr and the H_2^+–He distance of $r = 2.96$ bohr with $\theta = 0$ or π. The lowest spectroscopic dissociation energy of H_2He^+ is estimated to be only about 1780 cm^{-1}. Theoretical computations on the rovibrational energies and rovibrational transitions of H_2He^+ have already been made [15, 18, 34–36], and only the most important features of the bound rovibrational states will be reviewed here.

Because H_2He^+ is so weekly bound, the ground state PES supports only 16 bound vibrational states up to the first dissociation limit. Figure 2.3 shows the contour plots of the wavefunctions for the two selected vibrational states. It can be seen in Fig. 2.3a that the lowest energy eigenstate exhibits a very narrow distribution along the θ coordinate around $\theta = 0$ and π, indicating H_2He^+ takes a linear structure. Figure 2.3b on the other hand shows that, when H_2He^+ is vibrationally highly excited, He is delocalized to a large extent around the H_2^+ moiety and the wavefunction is very diffuse along the r coordinate.

The total number of bound rovibrational states is found to be about 420. The eigenenergies of all computed rovibrational states are presented in Fig. 2.4. Vibrational and rotational quantum numbers assigned to the eigenstates are taken from [15]. The notation $\left(v_{\text{strech}}^{H_2} v_{\text{bend}}^{H_2-He} v_{\text{strech}}^{H_2-He}\right)[J\,K]$, which was employed in [36], is adopted, where $v_{\text{strech}}^{H_2}$ and $v_{\text{strech}}^{H_2-He}$ are the quantum numbers for the stretching motion along the R and r coordinates, respectively, $v_{\text{bend}}^{H_2-He}$ is the quantum number for the bending along θ. The variables, J and K, are the total rotational quantum number and the projection of the rotational angular momentum onto the body-fixed z-axis, respectively. Based on the assignments shown in Fig. 2.4, it can be seen that there is a group of eigenstates with the quantum numbers (0 0 0)[J 0], corresponding to non-vibrating linear rotor states with purely rotational excitations. On the other hand, in the vibrationally excited (0 0 1)[0 0] state and in the rotationally excited (0 0 0)[1 1] state shown in Fig. 2.4, the vibrational energy and the rotational energy are on the same magnitude, indicating that, even at this low energy region, the rigid rotor approximation could not be applied because of the strong coupling between the rotational and vibrational degrees of freedom.

2.3.2 H_2He^+ Alignment Dynamics

Based on the theoretical methods detailed in the Section *Theoretical methods*, we simulated in [15] the laser-induced rovibrational dynamics of H_2He^+ under selected

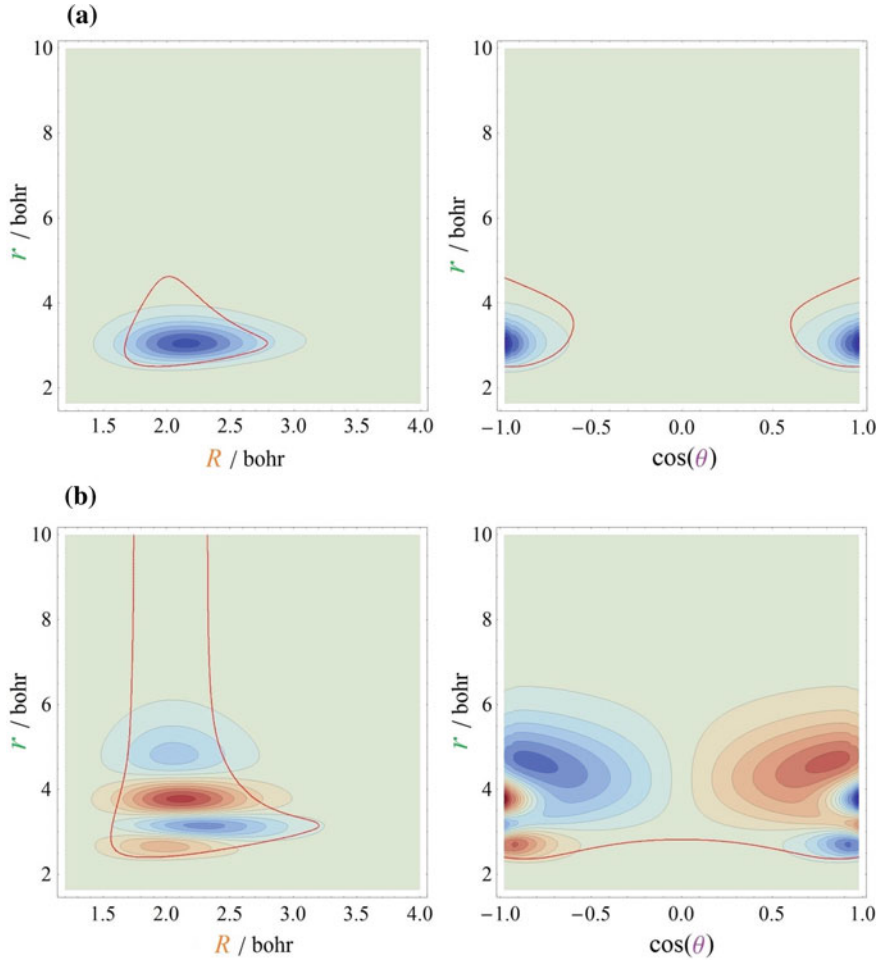

Fig. 2.3 Contour plots of the wave functions of the two selected vibrational states of H_2He^+: **a** the ground vibrational state with energy 2107.00 cm^{-1} and **b** the ninth excited vibrational state with energy 3653.34 cm^{-1}

laser conditions starting from its rovibrational ground state. In the expansion of the wavepacket, all the bound rovibrational states were included as the basis functions. The results of the simulation of the alignment dynamics presented here for H_2He^+ have already been reported in [15].

In Fig. 2.5, the non-adiabatic alignment dynamics of H_2He^+ can be seen, which is obtained when H_2He^+ is exposed to a linearly polarized Gaussian laser pulse [$\lambda = 800$ nm, $I = 2 \times 10^{13}$ W cm^{-2}, and FWHM (full-width at half-maximum) = 330 fs]. Figure 2.5 demonstrates that the interaction with the laser pulse starts making $\langle \cos^2(\phi) \rangle$ oscillate around $\langle \cos^2(\phi) \rangle = 1/3$, representing the isotropic spatial distri-

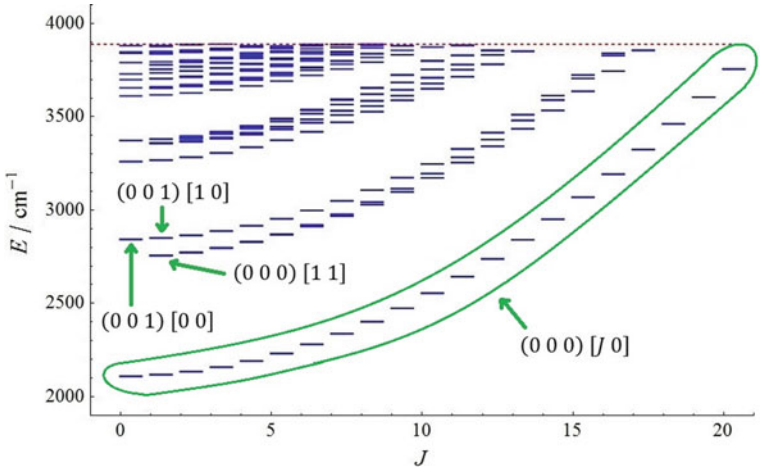

Fig. 2.4 The rovibrational energy levels of H_2He^+ represented by blue horizontal bars, supported by the PES of De Fazio et al. [17] as a function of the J rotational quantum number. The horizontal dashed red line represents the first dissociation energy

bution of the z-axis of the BF frame in the LF frame, exhibiting the time-dependent field-free alignment dynamics. On the other hand, no significant laser-induced structural change can be seen in Fig. 2.5, indicating that a purely rotationally excited wavepacket is created. This can be confirmed by the inspection of the populations in the different rovibrational eigenstates forming the laser-induced wavepacket as shown in Fig. 2.6a. The states having a non-negligible population in Fig. 2.6a are all labelled with the quantum numbers $(0\,0\,0)[J\ 0]$, representing purely rotationally excited states.

When H_2He^+ is exposed to a linearly polarized Gaussian laser pulse (λ = 25,000 nm, $I = 10^{12}$ W cm^{-2}, and FWHM = 240 fs), whose carrier frequency corresponds to a photon energy of the same magnitude as the vibrational transition energies, the non-adiabatic alignment dynamics of H_2He^+ becomes as shown in Fig. 2.7. It can be seen in Fig. 2.7 that the molecule undergoes substantial vibrational excitationalso see Fig. 2.6b, and structural deformation. The expectation values of the structural parameters vary as a function of time as seen in Fig. 2.7, reflecting the temporal evolution of the wavepacket created as the superposition of the vibrational eigenstates. These variations in the structural parameters result in the temporal change in the rotational constants, leading to the alignment dynamics with no evident revival times.

In Fig. 2.8, we compare the results of the simulation obtained within the rigid rotor approximation with those obtained with the full-dimensional calculations presented above. The upper panel of Fig. 2.8 shows the alignment dynamics of H_2He^+ when it is exposed to a laser pulse ($I = 5 \times 10^{13}$ W cm^{-2}, FWHM = 165 fs) whose wavelength is 800 nm. Because only the rovibrational states characterized by the quantum numbers $(0\,0\,0)[J\ 0]$ are populated in this case, the two simulations are in good agreement

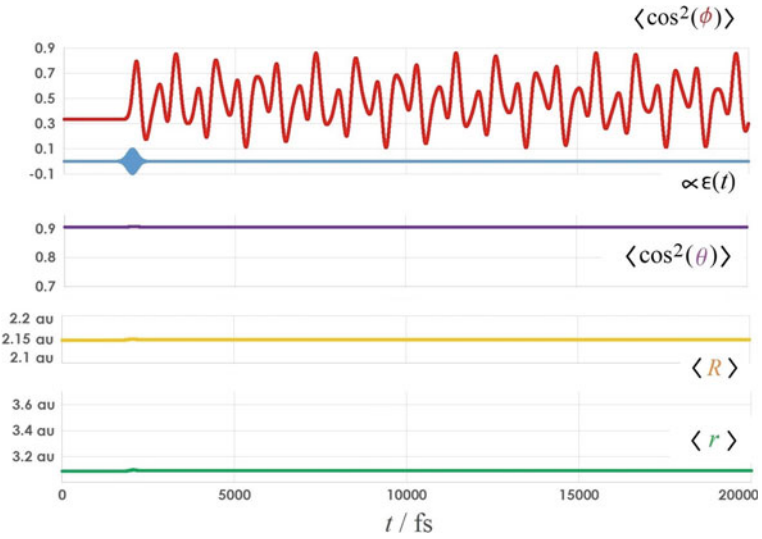

Fig. 2.5 The temporal evolution of the spatial alignment and that of the structural parameters of H_2He^+ obtained when H_2He^+ is exposed to a laser field characterized by the parameters of $\lambda =$ 800 nm, $I = 2 \times 10^{13}$ W cm^{-2}, and FWHM = 330 fs

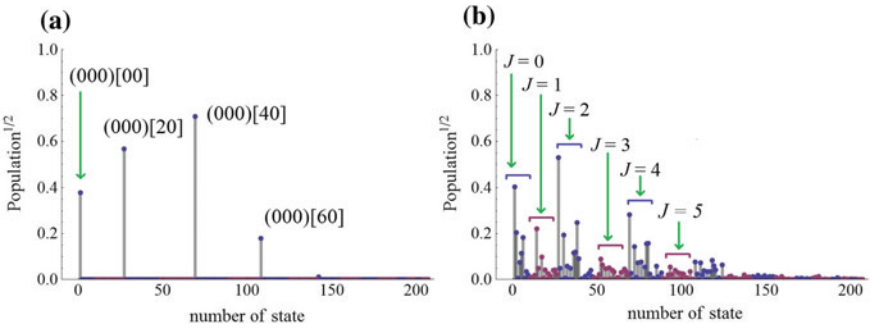

Fig. 2.6 The square root of the relative populations in the different rovibrational states of H_2He^+ obtained when its wavepacket is generated by a laser pulse with the parameter sets of **a** $\lambda = 800$ nm, $I = 2 \times 10^{13}$ W cm^{-2}, FWHM = 330 fs and **b** $\lambda = 25{,}000$ nm, $I = 10^{12}$ W cm^{-2}, FWHM = 240 fs. The square root of the populations is plotted for enhancing the visibility of the populations in the rotational levels populated only to a small extent

with each other up to a few picoseconds after the interaction with the laser pulse. However, because of the weakly bound nature of H_2He^+, the centrifugal distortion shifts the rotational energies considerably to the lower values in the full-dimensional calculations, which eventually lead to large differences in the relative phases of the eigenstates in the wavepacket, and consequently, as time goes on, the results of the simulation in these two cases deviate from each other as shown in the upper panel of Fig. 2.8. The lower panel of Fig. 2.8 shows the results obtained when H_2He^+ is

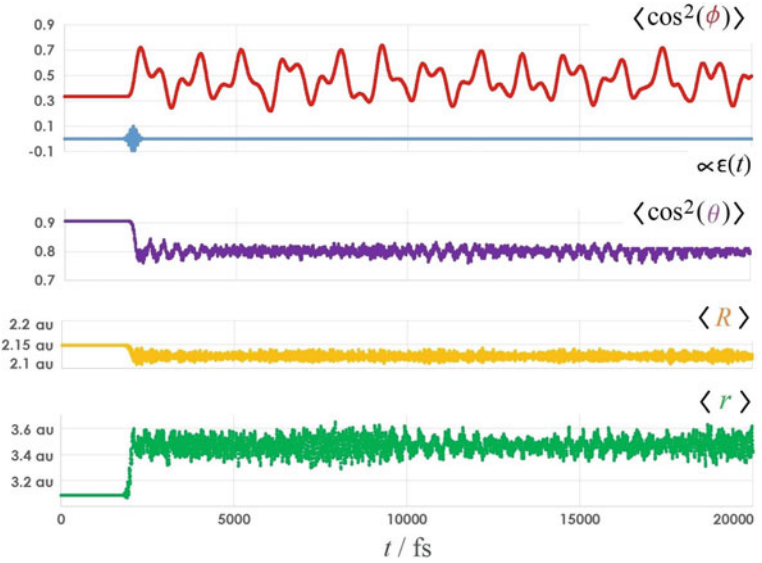

Fig. 2.7 The temporal evolutions of the alignment and structural parameters of H_2He^+ obtained when H_2He^+ is exposed to a laser field characterized by the parameters of $\lambda = 25{,}000$ nm, $I = 10^{12}$ W cm^{-2}, FWHM = 240 fs

irradiated with a laser pulse ($I = 10^{12}$ W cm^{-2}, FWHM = 240 fs) whose wavelength is 25,000 nm. Because the large structural changes are induced in the full-dimensional model associated with significant vibrational excitation in addition to the rotational excitation, the rigid rotor model is no longer a good approximation in this case.

2.3.3 H_2O Bound States

The accurate theoretical calculations of the rovibrational levels of H_2O as well as the transitions among these rovibrational levels have been investigated intensively as seen in [19, 37], for example. In this section, we focus our attention on a few characteristic features of H_2O that are relevant to the light induced alignment dynamics. Differently from H_2He^+, H_2O is a strongly bound molecule, having the first dissociation energy of about 41,100 cm^{-1} [19]. In its equilibrium structure, the O–H internuclear distance is 0.958 Å and the H–O–H bond angle is 104.5° [38]. Because the rigidity of H_2O is high, the vibrational excitation by a few quanta could not result in significant structural changes [39]. The rovibrational states of water are conventionally labeled by $(v_1 v_2 v_3)[J K_a K_c]$, where v_1, v_2 and v_3 are the normal mode quantum numbers for the symmetric stretch, bending and antisymmetric stretch normal modes, respectively, while J, K_a and K_c are the standard asymmetric top quantum numbers [12].

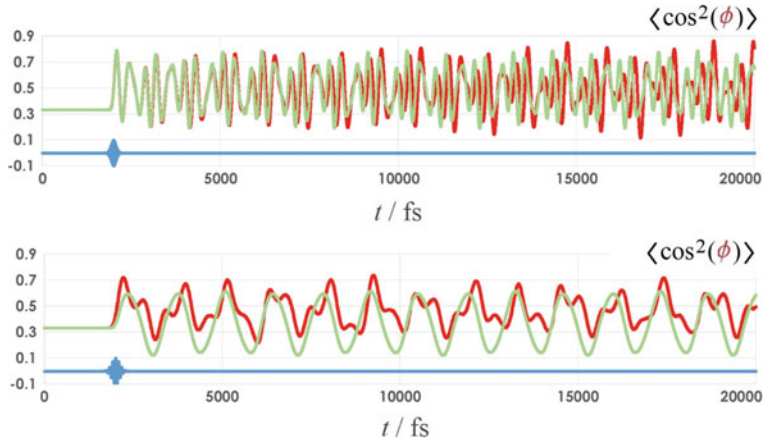

Fig. 2.8 The temporal evolution of the expectation values of the alignment of H_2He^+ computed with the rigid rotor approximation (green curves) and that computed with the full-dimensional approach (red curves). The blue curve represents the temporal variation of the electric field of the laser pulse. The temporal evolutions in the upper panel were obtained with the set of laser parameters; $\lambda = 800$ nm, $I = 5 \times 10^{13}$ W cm^{-2}, and FWHM = 165 fs and the temporal evolutions in the lower panel were obtained with the set of laser parameters; $\lambda = 25{,}000$ nm, $I = 10^{12}$ W cm^{-2}, and FWHM = 240 fs

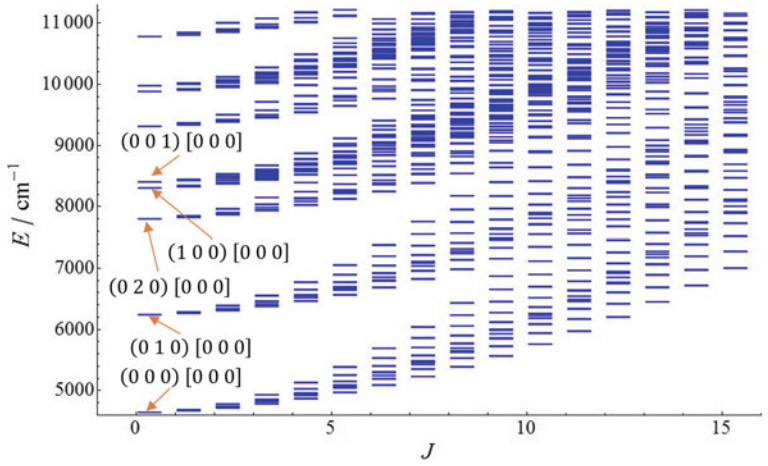

Fig. 2.9 The rovibrational energy levels of H_2O represented by blue horizontal bars, supported by the PES obtained by Barletta et al. [30] as a function of the rotational quantum number J

Figure 2.9 shows the computed bound rovibrational energies of H_2O as a function of the rotational quantum number J.

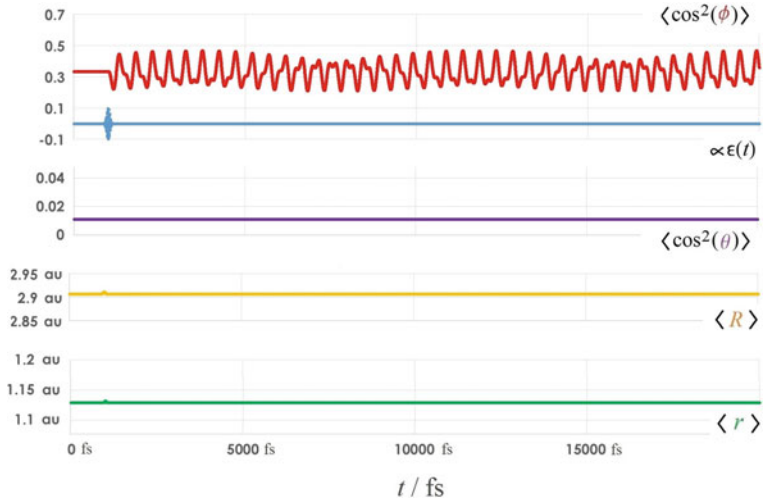

Fig. 2.10 The temporal evolution of the expectation values of the structural parameters and the alignment of H_2O obtained when H_2O is exposed to a laser field whose parameters are $\lambda = 800$ nm, $I = 5 \times 10^{13}$ W cm^{-2}, and FWHM = 96 fs

2.3.4 *H_2O Alignment Dynamics*

Based on the theoretical methods detailed in the Section *Theoretical methods*, we simulated the laser-induced rovibrational dynamics of H_2O under selected laser conditions starting from its rovibrational ground state. In the expansion of the rovibrational wavepacket, all bound states whose energies are smaller than 12,000 cm^{-1} and whose rotational quantum number J fulfills $J \leq 15$ were adopted as the basis functions, so that the total number of the basis functions becomes 758.

In Fig. 2.10, the non-adiabatic field-free alignment dynamics of H_2O with no significant laser-induced structural changes can be seen when H_2O is exposed to a linearly polarized Gaussian laser pulse ($\lambda = 800$ nm, $I = 5 \times 10^{13}$ W cm^{-2}, and FWHM = 96 fs). The populations in the different rovibrational eigenstates in the laser-induced wavepacket presented in Fig. 2.11a show that a purely rotationally excited wavepacket is created. The five most populated states are labelled by (0 0 0)[0 0 0], (0 0 0)[2 0 2], (0 0 0)[2 2 0], (0 0 0)[4 0 4] and (0 0 0)[4 2 2], indicating that the excitation process is dominated by two-photon Raman-type transitions.

When H_2O is exposed to a linearly polarized Gaussian laser pulse ($\lambda = 2500$ nm, $I = 5 \times 10^{13}$ W cm^{-2}, and FWHM = 160 fs) whose carrier frequency is near resonant with the fundamental of the asymmetric stretching mode, the non-adiabatic alignment dynamics of H_2O becomes as shown in Fig. 2.12. It can be seen in Fig. 2.12 that the molecule does not experience substantial structural change, even though the vibrational excitation proceeds as demonstrated in Fig. 2.11b. The most populated rovibrational states are labelled by (0 0 0)[0 0 0], (0 0 0)[2 0 2], (0 0 0)[2 2 0], (1 0 0)[3 3 1],

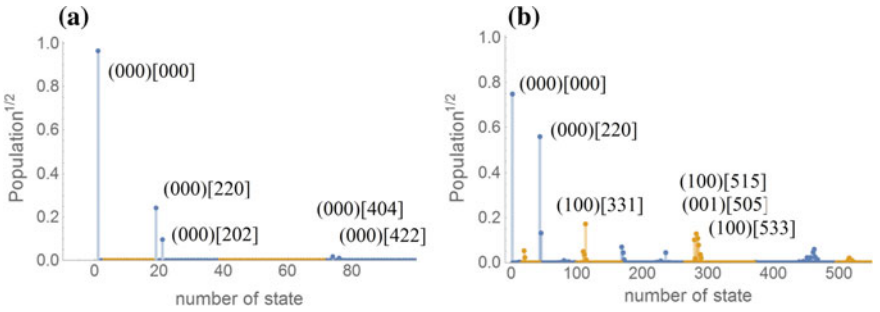

Fig. 2.11 The square root of the relative populations in the different rovibrational states of H_2O obtained when its wavepacket is generated by a laser pulse with the parameter sets of **a** $\lambda = 800$ nm, $I = 5 \times 10^{13}$ W cm^{-2}, FWHM = 96 fs and **b** $\lambda = 2500$ nm, $I = 5 \times 10^{13}$ W cm^{-2}, FWHM = 160 fs. The square roots of the populations are plotted for enhancing the visibility of the populations in the rotational levels populated only to a small extent

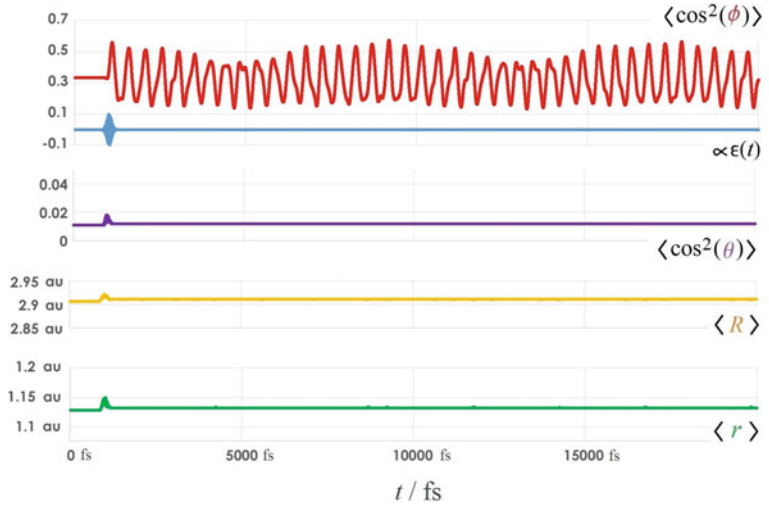

Fig. 2.12 The temporal evolution of the expectation values of the alignment and the structural parameters of H_2O obtained when H_2O is exposed to a laser field whose parameters are $\lambda = 2500$ nm, $I = 5 \times 10^{13}$ W cm^{-2}, and FWHM = 160 fs

(1 0 0)[5 1 5], (0 0 1)[5 0 5], and (1 0 0)[5 3 3], showing that two-photon Raman-type transitions as well as one-photon dipole transitions contribute to the creation of the rovibrational wavepacket.

In Fig. 2.13, we compare the light-induced dynamics of H_2O obtained within the rigid-rotor approximation with that obtained by our highly accurate full-dimensional calculations. It can be seen in the upper panel of Fig. 2.13 that, when H_2O is excited by an 800 nm wavelength pulse, the result obtained by the rigid rotor approximation is only slightly different from that obtained by the full-dimensional calculations,

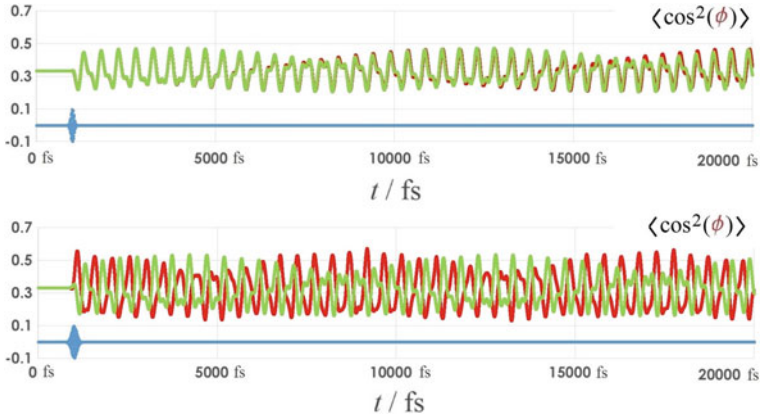

Fig. 2.13 The temporal evolution of the expectation values of the alignment of H_2O obtained by the rigid rotor approximation (green curves) and those obtained by our full-dimensional calculations (red curves). The blue curve represents the temporal variation of the electric field of the laser pulse. The temporal evolution shown in the upper panel was obtained with a laser pulse whose parameters are $\lambda = 800$ nm, $I = 5 \times 10^{13}$ W cm^{-2}, and FWHM = 96 fs, and that shown in the lower panel was obtained with a laser pulse whose parameters are $\lambda = 2500$ nm, $I = 5 \times 10^{13}$ W cm^{-2}, and FWHM = 160 fs

showing that H_2O behaves as a rigid rotor to a good approximation. However, it can be seen in the lower panel of Fig. 2.13 that, when the wavelength of the excitation pulse is red shifted to 2500 nm, the results obtained by the rigid rotor approximation become largely different from those obtained by the highly accurate full-dimensional calculation. Because no significant structural change can be identified in Fig. 2.12, this difference does not originate from the structural changes induced by the light field but from the differences in the optical transitions in the two cases.

In the rigid-rotor approximation, only the light-induced rotational excitations dominated by two-photon Raman-type transitions are allowed while, in the full-dimensional calculations, not only the Raman-type rotational transitions but also the one-photon vibrational transitions are allowed, leading to the changes in the distribution of populations in the rovibrational eigenstates. It should be noted here that the light-induced populations in the rotational states in a vibrationally excited state are influenced by the rovibrational symmetry. The total symmetry of the rovibrational wave function is determined not only by the vibrational symmetry but also by the rotational symmetry. Therefore, depending on the symmetry of the vibrational state being prepared by an allowed one-photon transition, the rotational state prepared in the vibrationally excited state could vary. For example, as shown in Fig. 2.11b, the vibrational transition to (1 0 0) can lead to the population of the [5 1 5] rotational state while the vibrational transition to (0 0 1) leads to the population of the [5 0 5] rotational state.

As shown above, the one-photon vibrational excitations not only induce structural changes but also alter the optical selection rules in the rotational excitation, leading to

the changes in the light-induced alignment and orientation dynamics. Therefore, the descriptions beyond the rigid rotor approximation are necessary for treating strongly-bound rigid molecules like H_2O as well as for treating floppy molecules like H_2He^+.

2.4 Summary and Conclusion

We overviewed the simple and general theoretical framework of [15], which can be applied to the numerical simulation of laser-induced alignment and orientation dynamics of non-rigid polyatomic molecules. This method is based on solving the TDSE using the field-free rovibrational eigenstates of the system as the basis functions. If the field-free eigenstates are obtained with high accuracy, highly accurate solutions of the TDSE can be obtained.

As numerical examples, the laser-induced alignment dynamics of weakly-bound H_2He^+ and strongly bound H_2O were presented. By the full-dimensional computations on the nuclear motion with high-accuracy, the bound rovibrational eigenstates of the two molecular species were computed and used as basis functions for describing their laser-induced alignment dynamics. The results presented in this chapter can be summarized as follows:

(i) In the case of floppy molecules like H_2He^+, the light-matter interaction can induce considerable centrifugal distortion and structural change, and therefore, it becomes necessary to take into account vibrational motion and rovibrational couplings for accurate descriptions of its laser-induced alignment dynamics.

(ii) When H_2He^+ is exposed to a laser pulse whose parameters are $\lambda = 800$ nm, FWHM = 330 fs, and $I = 2 \times 10^{13}$ W cm^{-2}, a purely rotational wavepacket is created, in which all the significantly populated states can be labelled by $(0\,0\,0)[J\,0]$.

(iii) By changing the wavelength of a laser pulse to be closer to that for a one-photon vibrational transition ($\lambda = 25{,}000$ nm, FWHM = 240 fs, $I = 10^{12}$ W cm^{-2}), H_2He^+ undergoes significant structural changes. The temporal variation of the geometrical structure of H_2He^+ leads to the variation in the rotational constants, and consequently, no evident revival times can be found in the non-adiabatic rotational dynamics of H_2He^+.

(iv) When H_2He^+ is irradiated with a 800 nm wavelength light pulse ($I = 5 \times 10^{13}$ W cm^{-2}, FWHM = 165 fs), the results obtained by the rigid-rotor approximation show good agreement with those obtained by the full-dimensional calculations up to a few picoseconds. However, in the later period, the deviations become evident because of the effect of the centrifugal distortion.

(v) When H_2He^+ is irradiated with a 25,000 nm wavelength laser pulse ($I = 10^{12}$ W cm^{-2}, and FWHM = 240 fs), which induces both rotational and vibrational excitations, it becomes necessary to adopt the full-dimensional approach in

order to obtain accurate results on the alignment dynamics because the rigid rotor approximation is no longer applicable.

(vi) When H_2O is exposed to a laser pulse whose parameters are $\lambda = 800$ nm, FWHM = 96 fs, and $I = 5 \times 10^{13}$ W cm^{-2}, a purely rotational wavepacket is created, in which all the significantly populated states can be labelled by the sets of the quantum numbers, (0 0 0)[0 0 0], (0 0 0)[2 0 2], (0 0 0)[2 2 0], (0 0 0)[4 0 4] and (0 0 0)[4 2 2], which show that the excitation process is dominated by two-photon Raman-type transitions.

(vii) When the laser wavelength of a laser pulse (FWHM = 160 fs, $I = 5 \times 10^{13}$ W cm^{-2}) is set to be 2500 nm, which is in near resonant with the asymmetric stretching fundamental, it is found that H_2O undergoes vibrational excitations as well as rotational excitations, but no substantial structural changes during these excitation processes. The most populated rovibrational states are labelled by the sets of the quantum numbers, (0 0 0)[0 0 0], (0 0 0)[2 0 2], (0 0 0)[2 2 0], (1 0 0)[3 3 1], (1 0 0)[5 1 5], (0 0 1)[5 0 5], and (1 0 0)[5 3 3], showing that not only two-photon Raman-type transitions but also one-photon dipole transitions contribute to the creation of the wavepacket.

(viii) A comparison of the alignment dynamics of H_2O obtained by the full-dimensional calculations with those obtained by the rigid rotor approximation shows that the alignment dynamics of H_2O can be described accurately by the rigid-rotor approximation as long as the interaction with the laser pulse induces only the rotational excitations. On the other hand, when vibrational excitations are induced, the rigid-rotor approximation could not describe the alignment dynamics well because of its failure in describing the rotational excitations associated with one-photon vibrational transitions, which shows that the theoretical treatment beyond the rigid-rotor approximation becomes necessary not only for weakly-bound floppy molecules but also for strongly-bound rigid molecules when both rotational and vibrational excitations proceed.

(ix) The theoretical framework of [15] introduced here can be applied to a wide range of molecules as long as their accurate rovibrational eigenstates necessary for describing the laser-induced dynamics are prepared.

Acknowledgements The authors thank the support from the Grant-in-Aid (Tokubetsu Kenkyuin Shorei-hi) scientific research fund of JSPS (Japan Society for the Promotion of Science), project number 26-04333, the JSPS KAKENHI Grant No. 15H05696, and the NKFIH Grant No. PD124623.

References

1. H. Stapefeldt, T. Seideman, Rev. Mod. Phys. **75**, 543 (2003)
2. Y. Ohshima, H. Hasegawa, Int. Rev. Phys. Chem. **29**, 619 (2010)
3. M. Lemeshko, R.V. Krems, J.M. Doyle, S. Kais, Mol. Phys. **111**, 1648 (2013)
4. A. Rouze´e, A. Gijsbertsen, M.J.J. Vrakking, in *Progress in Ultrafast Intense Laser Science*, vol VI, Chap. 3 (Springer, Berlin, Heidelberg, 2010)

5. O. Faucher, B. Lavorel, E. Hertz, F. Chaussard, in *Progress in Ultrafast Intense Laser Science*, vol VII, Chap. 4 (Springer, Berlin, Heidelberg, 2011)
6. H. Hasegawa, Y. Ohshima, in *Progress in Ultrafast Intense Laser Science*, vol XII, Chap. 3 (Springer International Publishing, Switzerland, 2015)
7. T. Szidarovszky, M. Jono, K. Yamanouchi, Comput. Phys. Commun. **228**, 219 (2018)
8. J. Floß, T. Grohmann, M. Leibscher, T. Seideman, J. Chem. Phys. **136**, 084309 (2012)
9. C.M. Dion, A. Keller, O. Atabek, A.D. Bandrauk, Phys. Rev. A **59**, 1382 (1999)
10. A.A. Søndergaard, R.E. Zillich, H. Stapelfeldt, J. Chem. Phys. **147**, 074304 (2017)
11. A. Owens, E.J. Zak, K.L. Chubb, S.N. Yurchenko, J. Tennyson, A. Yachmenev, Sci. Rep. **7**, 45068 (2017)
12. P.R. Bunker, P. Jensen, *Molecular Symmetry and Spectroscopy* (NRC Research Press, Ottawa, 1998)
13. A.G. Császár, C. Fábri, T. Szidarovszky, E. Mátyus, T. Furtenbacher, G. Czakó, Phys. Chem. Chem. Phys. **14**, 1085 (2012). and references therein
14. J. Tennyson, J. Chem. Phys. **145**, 120901 (2016). and references therein
15. T. Szidarovszky, K. Yamanouchi, Mol. Phys. (André D. Bandrauk Special Issue) **115**, 1916 (2017)
16. K. Schuh, P. Rosenow, M. Kolesik, E.M. Wright, S.W. Koch, J.V. Moloney, Phys. Rev. A **96**, 043818 (2017)
17. D. De Fazio, M. de Castro-Vitores, A. Aguado, V. Aquilanti, S. Cavalli, J. Chem. Phys. **137**, 244306 (2012)
18. D. Papp, A.G. Császár, K. Yamanouchi, T. Szidarovszky, J. Chem. Theory Comput. **14**, 1523 (2018)
19. A.G. Császár, E. Mátyus, T. Szidarovszky, L. Lodi, N.F. Zobov, S.V. Shirin, O.L. Polyansky, J. Tennyson, J. Quant. Spectr. Rad. Transfer **111**(9), 1043–1064 (2010)
20. V. Barone, M. Biczysko, J. Blonio, Phys. Chem. Chem. Phys. **16**, 1759 (2014)
21. S.N. Yurchenko, W. Thiel, P. Jensen, Mol. Spectrosc. **245**, 126 (2007)
22. J.M. Bowman, S. Carter, X.-C. Huang, Int. Rev. Phys. Chem. **22**, 533 (2003)
23. C. Fábri, E. Mátyus, A. G. Császár, J. Chem. Phys. **134**, 074105 (2011)
24. R.N. Zare, *Angular Momentum* (Wiley, New York, 1988)
25. V. Makhija, X. Ren, V. Kumarappan, Phys. Rev. A **85**, 033425 (2012)
26. C.G.J. Jacobi, Cr. Hebd, Acad. Sci. **15**, 236 (1842)
27. T. Szidarovszky, A.G. Császár, G. Czakó, Phys. Chem. Chem. Phys. **12**, 8373 (2010)
28. J.C. Light, T. Carrington Jr., Adv. Chem. Phys. **114**, 263 (2000)
29. T. Szidarovszky, A.G. Császár, Mol. Phys. (Martin Quack Special Issue) **111**, 2131 (2013)
30. P. Barletta, S.V. Shirin, N.F. Zobov, O.L. Polyansky, J. Tennyson, E.F. Valeev, A.G. Császár, J. Chem. Phys. **125**, 204307 (2006)
31. L. Lodi, J. Tennyson, O.L. Polyansky, J. Chem. Phys. **135**, 034113 (2011)
32. G. Avila, J. Chem. Phys. **122**, 144310 (2005)
33. P. Palmieri, C. Puzzarini, V. Aquilanti, G. Capecchi, S. Cavalli, D. DeFazio, A. Aguilar, X. Giménez, J.M. Lucas, Mol. Phys. **98**, 1835 (2000)
34. M. Juřek, V. Špirko, W.P. Kraemer, J. Mol. Sprectrosc. **182**, 364 (1997)
35. M. Šindelka, V. Špirko, W.P. Kraemer, Theor. Chem. Acc. **110**, 170 (2003)
36. J. Tennyson, S. Miller, J. Chem. Phys. **87**, 6648 (1987)
37. J. Tennyson, P.F. Bernath, L.R. Brown, A. Campargue, M.R. Carleer, A.G. Császár, L. Daumont, R.R. Gamache, J.T. Hodges, O.V. Naumenko, O.L. Polyansky, L.S. Rothmam, A.C. Vandaele, N.F. Zobov, A.R. Al Derzi, C. Fábri, A.Z. Fazliev, T. Furtenbacher, I.E. Gordon, L. Lodi, I.I. Mizus, J. Quant. Spectrosc. Radiat. Transfer **117**, 29 (2013)
38. A.G. Császár, G. Czakó, T. Furtenbacher, J. Tennyson, V. Szalay, S.V. Shirin, N.F. Zobov, O.L. Polyansky, J. Chem. Phys. **122**, 214305 (2005)
39. G. Czakó, E. Mátyus, A.G. Császár, J. Phys. Chem. A **113**, 11665–11678 (2009)

Chapter 3
Linear and Nonlinear Optics in Coherently Spinning Molecules

O. Faucher, E. Hertz, B. Lavorel and F. Billard

Abstract Over the last two decades, coherently spinning molecules induced by laser have been a subject of current growing interest motivated by their unique individual and collective properties. From a fundamental aspect, spinning molecules had also led to a better understanding of the mechanisms at play when molecular rotors are strongly driven by an external field. In this chapter, we describe new strategies for designing laser pulses enabling the production of spinning molecules. Two rationalized approaches are first discussed highlighting major assets and flaws. In order to implement them, simple and compact optical arrangements are proposed together with the use of a pulse shaper device that provides a greater flexibility. A more sophisticated strategy relying on a non-standard pulse shaper arrangement is also discussed. Laser pulses exhibiting a twisted linear polarization are then applied to control the rotation of linear molecules subsequently used as ultrafast phase modulators. The rotational Doppler shifts resulting from the linear and nonlinear scattering of a circularly polarized laser pulse with fast spinning molecules are investigated both experimentally and numerically.

3.1 Introduction

Manipulating matter with light at the microscopic level has been a long pursued goal since the discovery of the laser. The coherent properties of the laser light allows to exert elaborated control over the internal and external degrees of freedom of a wide class of quantum systems ranging from isolated atoms to molecules merged in a complex environment [1, 2]. With the advent of femtosecond laser technology, it became possible to steer electronic and nuclear wavepackets into a target state by

O. Faucher (✉) · E. Hertz · B. Lavorel · F. Billard
Laboratoire Interdisciplinaire CARNOT de Bourgogne, UMR 6303
CNRS-Université Bourgogne Franche-Comté, 9 Av. A. Savary, BP 47870,
21078 Dijon Cedex, France
e-mail: olivier.faucher@u-bourgogne.fr

E. Hertz
e-mail: edouard.hertz@u-bourgogne.fr

© Springer Nature Switzerland AG 2018

K. Yamanouchi et al. (eds.), *Progress in Ultrafast Intense Laser Science XIV*,
Springer Series in Chemical Physics 118,
https://doi.org/10.1007/978-3-030-03786-4_3

extending control strategies to ultrafast phenomena [1, 3]. Among the most spectacular achievements performed in this direction, one concerns the control of temporal rotational dynamics in molecules. During the two last decades, the effect of strong laser pulses on molecules has been extensively studied with final goal to control the angular distribution of the molecular axes. One of the most recognized effect of this type is laser induced molecular alignment [4, 5]. Therein, a laser pulse is used to bring the axis of a molecule along a fixed direction of space, eventually applying a control over its orientation [6, 7] when non symmetric molecules are concerned. In planar alignment [8, 9], the laser field aligns the rotational angular momentum **J** of the molecule instead of its axis, meaning that the molecule is confined in a plane perpendicular to J. Furthermore, the rotation within the plane can be forced to a unique direction by orienting the angular momentum of the molecule. Gases of fast spinning molecules with a preferred sense of rotation has attracted considerable attention because of their singular optical, magnetic, and kinetic properties [10–22].

Diverse schemes have been implemented toward the production of unidirectionally rotating (UDR) molecules. The methods relying on the polarization shaping of a fast laser pulse include the optical centrifuge for the creation of superrotors [11–13, 23–25], the chiral pulse train [26, 27], the molecular propeller [28–30], and more recently the twisted linear polarization [25]. The present chapter is related to the realization of this last category of pulses and its application to the spectral shift of short laser pulses. It was recently demonstrated that spinning molecules can be used as ultrafast phase modulators enabling terahertz optical shifts of a short laser pulse with a carrier frequency spanning from infrared [12, 13, 25] to ultraviolet [31, 32], revealing also potential extensions toward the modification of extreme ultraviolet (EUV) coherent radiations [33].

3.2 Strategies for Producing Pulse Exhibiting Twisted Linear Polarization

Different strategies can be implemented for the production of femtosecond pulses with twisted linear polarization. In the first part of this section, two different optical setups enabling to reach this objective are presented. The performances and main shortcomings of these arrangements are discussed. These methods, based on a limited number of control parameters, offer a low versatility. This limitation can be overcome by the use of programmable pulse shaper devices [34] operating in polarization shaping, which allows the production of almost any arbitrary time-dependent polarization profile within the pulse [35]. After a short introduction to the standard spatial light modulator based on liquid crystal display, the potentialities offered by this device with respect to the generation of femtosecond laser pulses with twisted linear polarization are investigated. For a suitable comparison, all the methods are assessed considering the specifications of our laser system delivering Gaussian pulses of 100 fs duration.

3.2.1 Polarization Shaping from Basic Optical Schemes

3.2.1.1 Method 1: Two Perpendicularly Polarized Time-Delayed Pulses

As reported in our previous work [25], the production of a pulse with a twisted linear polarization can be achieved by means of a multiple-order wave plate (MOWP) combined with a Berek compensator (BC). A femtosecond pulse, polarized at 45° with respect to the slow (**x**) and fast (**y**) axes of the MOWP, propagates through the latter. At the exit, the pulse is splitted in two identical time-delayed and orthogonally polarized pulses, as a result of the group velocity difference. The BC is used to control the phase difference between the two pulses at the sub-cycle level. The component of the electric field along **x** and **y** can be written as

$$\begin{aligned} E_x(t) &= \mathscr{E}(t-T)\cos(\omega(t-T)-\varphi_0) = \mathscr{E}(t-T)\cos(\omega t-\xi) \\ E_y(t) &= \mathscr{E}(t)\cos(\omega t), \end{aligned} \tag{3.1}$$

where ω is the angular frequency, T the interpulse separation, φ_0 the additional phase difference induced by the Berek compensator, and ξ the total phase difference between the two polarization directions. The delay T is chosen so as to ensure a significant overlap between the two field envelopes. For a gaussian pulse of duration Δt at full width at half maximum (FWHM), a suitable delay is $T \approx \sqrt{2}\Delta t$ (i.e. T is approximately equal to the field envelope duration). As depicted in Fig. 3.1, the leading and trailing edge of the pulse are linearly polarized along **y** and **x**, respectively. The polarization in the overlapping region, for its part, depends on the relative phase ξ which can be finely adjusted by the BC. For $\xi = 0\ [2\pi]$, the polarization remains linear but is "twisted" from **y** to **x** due to the gradual variation of the relative field-amplitude between these axes. The pump pulse exhibits therefore a twisted linear polarization in the clockwise direction. For $\xi = \pi\ [2\pi]$, the polarization is twisted in

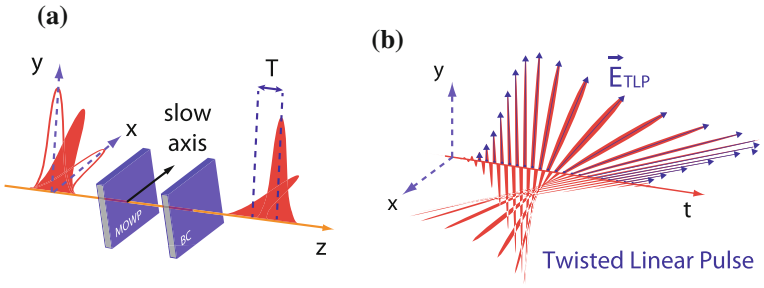

Fig. 3.1 **a** Experimental scheme for the production of pulses of twisted linear polarization: the multiple-order wave plate (MOWP) produces two orthogonally polarized delayed pulses whose phase difference is controlled by a Berek compensator (BC) **b** Schematic representation of the time-dependent polarization profile for $\xi = \pi$

the opposite direction, while any other phases produce an elliptical polarization in the middle of the pulse. The value of the phase ξ can be evaluated by measuring the spectral fringes after a polarizer set at 45° with respect to **x** and **y**, respectively (see [25]).

In order to assess the quality of the polarization shaping, the ellipticity $\varepsilon(t)$ and orientation angle α(t) of the field are calculated at any time during the pulse. Assuming an elliptical polarization, the ellipticity ε is defined as the ratio between the minor and major axis of the ellipse so that $\varepsilon = 0$ (resp. 1) for a linear (resp. circular) polarization. The orientation angle α corresponds to the orientation of the ellipse, i.e. the angle between the semi-major axis of the ellipse and the x-axis. In order to calculate $\varepsilon(t)$ and $\alpha(t)$ the following procedure is applied all along this section. The electric fields $E_x(t)$ and $E_y(t)$ are calculated within the pulse together with the parameters $r(t) = \left|E_y(t)\right| / |E_x(t)|$ and $\varphi(t) = \arg[E_y(t)] - \arg[E_x(t)]$. The ellipticity ε(t) and orientation angle $\alpha(t)$ are then calculated from $r(t)$ and $\varphi(t)$ via the relations

$$\varepsilon(t) = \tan\left(\frac{1}{2}\arcsin\left[\frac{2r(t)\sin(\varphi(t))}{1+r(t)^2}\right]\right) \tag{3.2}$$

$$\tan[2\alpha(t)] = \frac{2r(t)\cos(\varphi(t))}{1-r(t)^2}. \tag{3.3}$$

The present strategy is evaluated with a pulse of 100 fs FWHM duration, a delay T = 150 fs, and a phase ξ = 0. The ellipticity $\varepsilon(t)$ is depicted in Fig. 3.2a together with the normalized electric field envelope $E(t) \propto \sqrt{|E_x(t)|^2 + \left|E_y(t)\right|^2}$. As shown, $\varepsilon(t) = 0$ at any times during the pulse, confirming hence the linear polarization state during the pulse. The orientation angle $\alpha(t)$, shown in Fig. 3.2b, exhibits a linear variation in the middle of the pulse with a twist from 90° to 0°, as expected. It is however approximately constant during the leading and trailing edge of the pulse where only one component is present. From the tangent to the curve shown with

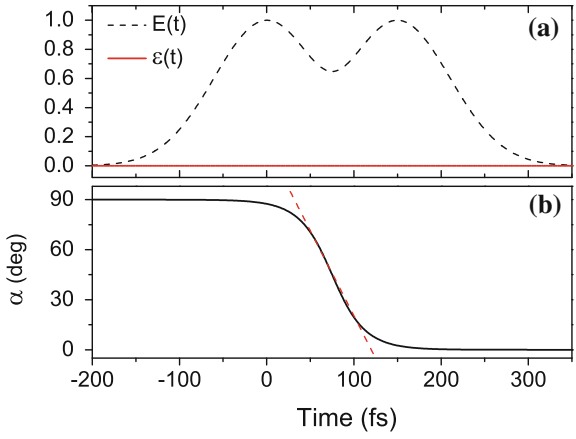

Fig. 3.2 **a** Normalized electric field envelope $E(t)$ (black dashed line) and ellipticity $\varepsilon(t)$ (red solid line). **b** Polarization angle $\alpha(t)$ (black solid line) with the tangent to the curve (red dashed line) giving the rotational period $T_{\text{rot}} \approx 350$ fs

a dashed line in Fig. 3.2b, the rotational period of the spinning polarization in the middle of the pulse is found to be $T_{\mathrm{rot}} \approx 350$ fs.

This method allows, through a simple and compact optical arrangement, the production of twisted linear polarization of rather good quality. It features nevertheless several limitations. First, the speed of rotation is mainly determined by T, the delay between the two pulses. For a given pulse duration Δt, T is limited and cannot exceed $2\Delta t$ for keeping a reasonable overlap between the field envelopes. Second, the twist is related to the gradual variation of the relative field amplitude between the x and y axis so that the overall angular range of rotation cannot exceed $\pi/2$. Third, the stabilization of ξ (or φ_0) by the BC requires great care. Some of these limitations can be overcome by the method described in the next paragraph.

3.2.1.2 Method 2: Two Counter-Rotating Time-Delayed Chirped Pulses

A field of rotating linear polarization can be seen as a superposition of two counter-rotating circularly polarized (CP) fields with slightly different frequencies [23, 36]. For a frequency shift $\delta\omega$, the resulting field vector then rotates with a period $T_{\mathrm{rot}} = 4\pi/\delta\omega$. The method illustrated in Fig. 3.3 is based on this principle. It uses a sequence of two chirped pulses orthogonally polarized and temporally delayed by T. The delay T is chosen to insure a significant overlap between the two pulses which are sent into a zero-order quarter-wave plate (QWP) with neutral axes **x** and **y** set at 45° with respect of the incident pulse polarizations. The two outgoing pulses are therefore circularly polarized with opposite handedness. Each pulse presents an instantaneous frequency that varies linearly with the time so that the delay T between them introduces an effective constant frequency shift. The configuration is therefore equivalent to two counter-rotating CP field of different frequencies.

We consider for the calculation a Fourier-transform-limited gaussian pulse of FWHM duration Δt and of angular frequency ω_0, chirped with a quadratic chirp ϕ''. The electric field can be written as

$$E(t) = E_0 \mathrm{e}^{-\frac{t^2}{4\beta\gamma}} \mathrm{e}^{i\omega_0 t} \mathrm{e}^{i(at^2-\varepsilon)}, \tag{3.4}$$

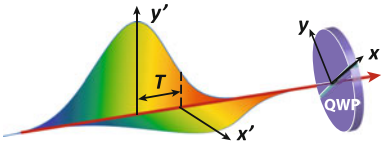

Fig. 3.3 Experimental scheme for the production of pulses of twisted linear polarization. Two chirped pulses are time-delayed by T providing a shift between their instantaneous frequencies. They propagate through a quarter-wave plate (QWP) and become circularly polarized with opposite handedness. The resulting field is linearly polarized with a rotating polarization

with $\beta = \frac{\Delta t^2}{8\ln 2}$, $\gamma = 1 + \frac{\phi''^2}{4\beta^2}$, $a = \frac{\phi''}{8\beta^2\gamma}$, and $\varepsilon = \frac{1}{2}\arctan(\frac{\phi''}{2\beta})$. The sequence of two orthogonally polarized and time-delayed pulses is then calculated. The two pulses are polarized along two axes called $\mathbf{x}'$ and $\mathbf{y}'$, respectively, and the delay between them is T:

$$\begin{aligned} E_{x'}(t) &= E_0 \mathrm{e}^{-\frac{(t+T/2)^2}{4\beta\gamma}} \mathrm{e}^{i\omega_0(t+\frac{T}{2})} \mathrm{e}^{i\left(a(t+\frac{T}{2})^2-\varepsilon\right)} \\ E_{y'}(t) &= E_0 \mathrm{e}^{-\frac{(t-T/2)^2}{4\beta\gamma}} \mathrm{e}^{i\omega_0(t-\frac{T}{2})} \mathrm{e}^{i\left(a(t-\frac{T}{2})^2-\varepsilon\right)}. \end{aligned} \tag{3.5}$$

In order to simplify the calculation, we consider that the envelope amplitude are about the same for each pulse:

$$\mathrm{e}^{-\frac{(t-T/2)^2}{4\beta\gamma}} \approx \mathrm{e}^{-\frac{(t+T/2)^2}{4\beta\gamma}} \approx \mathrm{e}^{-\frac{t^2}{4\beta\gamma}} = G_{\mathrm{ch}}(t). \tag{3.6}$$

This approximation is valid when $T << \Delta t_{\mathrm{ch}}$, with Δt_{ch} the duration of the Gaussian chirped pulses ($\Delta t_{\mathrm{ch}} = \Delta t\sqrt{1+\phi''^2 16\ln(2)^2/\Delta t^4}$). The two fields can thus be written

$$\begin{bmatrix} E_{x'}(t) \\ E_{y'}(t) \end{bmatrix} = E_0 G_{\mathrm{ch}}(t) \mathrm{e}^{i(\omega_0 t + at^2 + a\frac{T^2}{4} - \varepsilon)} \begin{bmatrix} \mathrm{e}^{+i(aTt+\omega_0\frac{T}{2})} \\ \mathrm{e}^{-i(aTt+\omega_0\frac{T}{2})} \end{bmatrix}. \tag{3.7}$$

It should be noted that the difference of instantaneous frequency between the 2 components $\delta\omega = 2aT$ is constant. After the zero-order QWP, the expression of the field along $\mathbf{x}$ and $\mathbf{y}$ becomes

$$\mathbf{E}(t) = \begin{bmatrix} E_x(t) \\ E_y(t) \end{bmatrix} = E_0 G_{\mathrm{ch}}(t) \mathrm{e}^{i(\omega_0 t + at^2 + a\frac{T^2}{4} - \varepsilon)} \sqrt{2} \begin{bmatrix} \cos\left(aTt + \omega_0\frac{T}{2}\right) \\ \sin\left(aTt + \omega_0\frac{T}{2}\right) \end{bmatrix}. \tag{3.8}$$

According to (3.8), the $\mathbf{x}$ and $\mathbf{y}$ field components are in phase leading to a linear polarization whose relative amplitude along $\mathbf{x}$ and $\mathbf{y}$ is governed by the time-dependent sinusoidal terms. This temporal dependency provides a spinning polarization of period $T_{\mathrm{rot}} = 4\pi/\delta\omega = 2\pi/(aT)$ which depends on the chirp and the delay T. The latter can be easily controlled using a standard delay line since the technique requires no need for interferometric stabilization. The main features of the polarization-shaped pulse, namely its duration and angular frequency of spinning polarization, can in principle be controlled through the two control parameters a and T. Nevertheless, the duration and angular frequency cannot be chosen independently since they both depend on a and T. Furthermore, the temporal delay must preserve a significant overlap between the two pulses. This additional condition limits the speed of spinning polarization that can be achieved. Considering a delay verifying $T < \sqrt{2}\Delta t_{\mathrm{ch}}$, one can calculate the lower limit of the rotational period. The latter is obtained when the chirp tends to infinity. It is found to be $T_{\mathrm{rot}} > \frac{\pi}{\sqrt{2}\ln(2)}\Delta t \approx 320$ fs for an input pulse duration Δt=100 fs. This value, comparable to the rotational period

found with Method 1 ($\approx$ 350 fs), is only obtained for large chirp and therefore shaped pulses of long duration.

The present method has been evaluated starting from a pulse of duration Δt = 100 fs, chirped with ϕ'' = 50,000 fs^2 (giving that Δt_{ch} = 1.39 ps FWHM) and splitted with a delay T = 200 fs. The period of spinning of the polarization is T_{rot} = 3.15 ps. The main results are depicted in Fig. 3.4 from which several conclusions can be drawn. First, the polarization shown in Fig. 3.4a can continuously rotate and the overall angular range of rotation is not limited. This point is evidenced in Fig. 3.4c depicting a linear increase of the field vector angle without any limitation. Second, the method presents a significant ellipticity flaw. As shown in Fig. 3.4b, the polarization is purely linear only at the center of the pulse and tends to become circular in the wings. This observation disagrees with (3.8) predicting that the field components along **x** and **y** are in principle self-phase synchronized (unlike Method 1 in which ξ must be adjusted by the BC). This flaw can be imputed to the validity of the assumption made in (3.6). In fact, the linear polarization can be achieved only for two counter-rotating CP fields of equal amplitude. This condition is fulfilled in the middle of the pulse, while at the beginning and the end of the shaped pulse each counter-rotating CP field prevails modifying the ellipticity.

To summarize, the present strategy is well suited for producing polarization-twisted pulses of rather long duration with potentially many turns and when the sensitivity upon ellipticity is not crucial. Furthermore, while the main feature of the polarization-shaped pulse can be controlled via the temporal delay and the chirp, the implementation of a pulse stretcher for a tunable linear chirp leads to a rather complex overall arrangement.

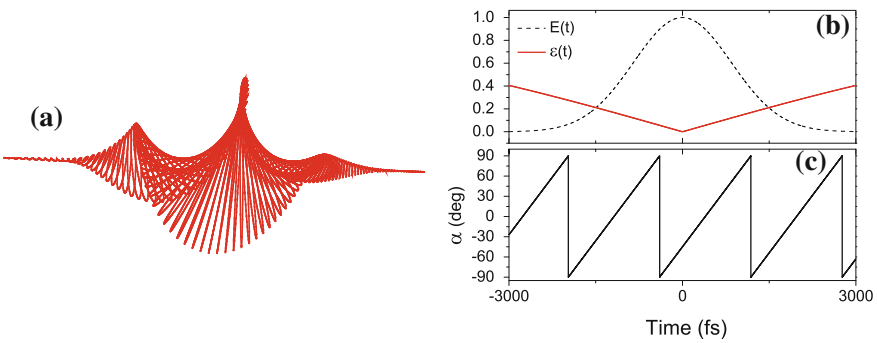

Fig. 3.4 **a** Representation of the electric field profile. **b** Normalized electric field envelope $E(t)$ and ellipticity $\varepsilon(t)$. **c** Polarization angle $\alpha(t)$

3.2.2 Polarization Shaping from Pulse Shaper Devices

3.2.2.1 Main Features of Pulse Shaper Devices

Different approaches have been reported for generating light fields with varying polarization states on a femtosecond timescale. This part is dedicated to the most successfully and widely employed method based on liquid crystal spatial light modulator (LC-SLM) [34–37]. A large number of papers has been published on this approach so that only main features are recalled here. The setup consists of a 4f-line where the modulation is realized by spectral manipulation of spatially dispersed frequency components. The shaping is performed in the middle of the arrangement, called Fourier plane, where the dispersed spectral components are focused. In this plane, a two-layer pixelated liquid crystal display (LCD) modulates the field independently for each pixel. The input light is polarized along the **x** axis. The axes of the LC molecules in the first (A) and second (B) layer are orientated in the xy-plane at $\pm 45°$ with respect to **x**. These axes are called **a** and **b** (Fig. 3.5).

By applying a voltage in the z-direction on a given pixel of the first or the second layer, electric dipoles are induced and the molecules rotate toward z causing a change in the refractive index along **a** and **b**. A LC cell behaves therefore as a variable wave plate with neutral axes **a** and **b** of fixed orientation whose phase φ_a and φ_b can be independently controlled through the applied voltage. Before the SLM, the electric field vector along **x** and **y** of a given frequency component ω is written

$$\mathbf{E}_{\text{in}}^{\omega}(t) = E(\omega)\mathrm{e}^{i(\omega t - kz)} \begin{pmatrix} 1 \\ 0 \end{pmatrix}. \tag{3.9}$$

After the modulator, the projections of the field along the **a** and **b** axis are

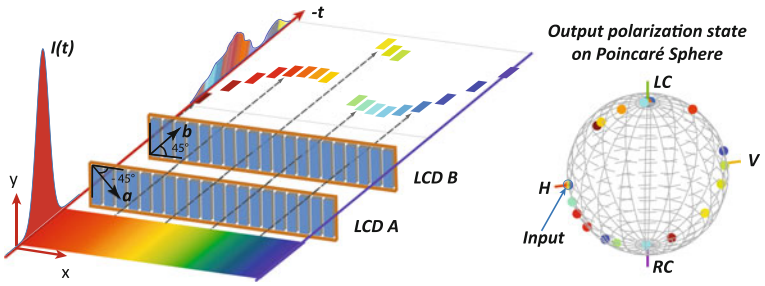

Fig. 3.5 Schematic layout of a dual layer LC-SLM providing phase and polarization shaping. The input polarization is horizontal. By controlling the phases φ_a and φ_b along **a** and **b**, respectively, the phase and polarization of the frequency components can be controlled as illustrated by the left and right drawing

$$\mathbf{E}^{\omega}_{\text{out}}(t) = \begin{bmatrix} E^{\omega}_{a}(t) \\ E^{\omega}_{b}(t) \end{bmatrix} = \frac{1}{\sqrt{2}} E(\omega) \mathrm{e}^{i(\omega t - kz)} \begin{bmatrix} \mathrm{e}^{i\varphi_a(\omega)} \\ \mathrm{e}^{i\varphi_b(\omega)} \end{bmatrix}, \tag{3.10}$$

whereas along the **x** and **y** axis, one can write

$$\mathbf{E}^{\omega}_{\text{out}}(t) = \begin{bmatrix} E^{\omega}_{x}(t) \\ E^{\omega}_{y}(t) \end{bmatrix} = E(\omega) \mathrm{e}^{i(\omega t - kz)} \mathrm{e}^{i\left(\frac{\varphi_a(\omega)+\varphi_b(\omega)}{2}\right)} \begin{bmatrix} \cos(\frac{\varphi_a(\omega)-\varphi_b(\omega)}{2}) \\ i \ \sin(\frac{\varphi_a(\omega)-\varphi_b(\omega)}{2}) \end{bmatrix}. \tag{3.11}$$

The phase of a spectral component can be controlled by the average phase retardance $\varphi(\omega) = \frac{\varphi_a(\omega)+\varphi_b(\omega)}{2}$ and the polarization by the difference $\delta(\omega) = \frac{\varphi_a(\omega)-\varphi_b(\omega)}{2}$. The polarization is controlled through a change of the relative field amplitude along **x** and **y** which are in phase quadrature. One limitation is therefore that the double-layer modulator is not able to create tilted linear or elliptical polarization with a given pixel. However since the shaping is independent for each pixel (in phase and polarization), the total electric field in the time domain after recombination of the different components can feature very complex polarization-shaped pulse without any restriction on the direction of the major axes. Another limitation of the double-layer modulator is that the spectral amplitude $E(\omega)$ cannot be controlled together with the polarization. Independent control over the phase, amplitude, and polarization can be obtained [38] via a specific scheme using a double pass through the SLM.

3.2.2.2 Field of Twisted Linear Polarization Produced by Pulse Shaper Devices

The ability of pulse shaper devices to produce light fields with varying polarization states offers a unique tool for generating the desired twisted linear polarization. Several approaches can be undertaken in order to identify the relevant spectral modulations to apply with the SLM. For instance, the two previous strategies using "two perpendicularly polarized time-delayed pulses" or "two counter-rotating time-delayed chirped pulses" can be reproduced with a pulse shaper. For an input pulse of carrier angular frequency ω_0, the shaping described in Sect. 3.2.1.1 can be replicated by applying the following spectral modulation

$$\begin{aligned} \varphi_a &= (\omega - \omega_c)T \\ \varphi_b &= 0. \end{aligned} \tag{3.12}$$

The resulting field is then composed of two identical time delayed pulses linearly polarized along the **a** and **b** axis, respectively. It can be easily shown that by choosing $\omega_c = \omega_0$, the polarization remains linear and sweeps therefore from $-45°$ to $+45°$.

To reproduce the polarization sweep depicted in Fig. 3.4, the spectral phases to apply with the pulse shaper are [36]

$$\varphi_a = \frac{\phi''}{2}(\omega - \omega_0)^2 + (\omega - \omega_0)\frac{T}{2} \qquad (3.13)$$
$$\varphi_b = \frac{\phi''}{2}(\omega - \omega_0)^2 - (\omega - \omega_0)\frac{T}{2}.$$

Such a shaping induces two time-delayed chirped pulses orthogonally polarized along **a** and **b**. By placing a zero-order quarter-wave plate with neutral axes along **x** and **y** at the exit of the setup, one obtain the criterion of two counter-rotating time-delayed chirped pulses required in Sect. 3.2.1.2.

The use of a computer-controlled pulse shaper for generating these two polarization shapings confers a better flexibility since the delay between the two pulses or the chirp can be adjusted at convenience. Nevertheless, the flaws and drawbacks pointed out in the previous sections still remain. In particular, the pulse shape (or duration) and angular frequency of the spinning polarization cannot be fully independently chosen by these streamlined approaches based on few control parameters. A reasonable question is to know which spectral filtering can provide a perfect and fully controllable pulse of twisted linear polarization and whether or not it can be produced by a pulse shaper. We consider for the discussion that the pulse to be generated along the **x** and **y** axis can be expressed as

$$\mathbf{E}(t) = \varepsilon(t)\mathrm{e}^{i\omega_0 t}\begin{bmatrix}\cos(\widetilde{\omega}t)\\ \sin(\widetilde{\omega}t)\end{bmatrix} \qquad (3.14)$$

where $\varepsilon(t)$ is the field envelope, ω_0 the angular frequency, and $\widetilde{\omega}$ the angular frequency of spinning polarization. This target field can be written as the superposition of two pulses sharing the same envelope $\varepsilon(t)$ but frequency shifted by $\pm\widetilde{\omega}$ and circularly polarized with opposite handedness:

$$\mathbf{E}(t) = \frac{\varepsilon(t)}{2}\begin{bmatrix}\mathrm{e}^{i(\omega_0+\widetilde{\omega})t} + \mathrm{e}^{i(\omega_0-\widetilde{\omega})t}\\ -i(\mathrm{e}^{i(\omega_0+\widetilde{\omega})t} - \mathrm{e}^{i(\omega_0-\widetilde{\omega})t})\end{bmatrix}. \qquad (3.15)$$

In order to test the ability of the pulse shaper to produce this field, we calculate the spectrum associated to $\mathbf{E}(t)$. In the spectral domain, the field writes:

$$E_x(\omega) = \frac{\varepsilon(\omega)}{2} \otimes [\delta(\omega - (\omega_0 + \widetilde{\omega})) + \delta(\omega - (\omega_0 - \widetilde{\omega}))] \qquad (3.16)$$
$$E_y(\omega) = \frac{\varepsilon(\omega)}{2} \otimes -i\,[\delta(\omega - (\omega_0 + \widetilde{\omega})) - \delta(\omega - (\omega_0 - \widetilde{\omega}))],$$

where $\otimes$ stands for the convolution product and $\delta(\omega)$ the Dirac delta function. The spectrum associated to $\mathbf{E}(t)$ will depend on the desired pulse shape $\varepsilon(t)$. We consider for the following discussion, the synthesis of a Gaussian pulse of duration τ_p. The spectral amplitude is therefore:

$$\varepsilon(\omega) = \mathrm{e}^{-\left(\frac{\omega}{\sigma}\right)^2} \qquad (3.17)$$

with $\sigma = \frac{2\sqrt{2\ln(2)}}{\tau_p}$. Under these conditions, the spectrum along the **x** and **y** coordinate can be written

$$\mathbf{E}(\boldsymbol{\omega}) = \begin{bmatrix} E_x(\omega) \\ E_y(\omega) \end{bmatrix} = \varepsilon(\omega - \omega_0) \mathrm{e}^{-\left(\frac{\widetilde{\omega}}{\sigma}\right)^2} \begin{bmatrix} \cosh\left(\frac{2(\omega-\omega_0)\widetilde{\omega}}{\sigma^2}\right) \\ -i \sinh\left(\frac{2(\omega-\omega_0)\widetilde{\omega}}{\sigma^2}\right) \end{bmatrix}. \tag{3.18}$$

Using the relation $\cosh^2(x) + \sinh^2(x) = \cosh(2x)$, the modulus of the spectral amplitude of our target field writes as

$$E(\omega) = \sqrt{|E_x(\omega)|^2 + \left|E_y(\omega)\right|^2} = \varepsilon(\omega - \omega_0) \mathrm{e}^{-\left(\frac{\widetilde{\omega}}{\sigma}\right)^2} \sqrt{\cosh\left(\frac{4(\omega - \omega_0)\widetilde{\omega}}{\sigma^2}\right)}. \tag{3.19}$$

It should be noted that the spectrum of the polarization shaped pulse $E(\omega)$ is broader than the spectrum of its Gaussian envelope $\varepsilon(\omega - \omega_0)$, namely the spectrum of the pulse with no polarization shaping. This point can be understood by the fact that any spectral shaping, and in particular polarization shaping, leads to a temporal broadening of the pulse. If one wants to produce a pulse of twisted linear polarization with an envelope $\varepsilon(t)$ of duration τ_p, the input pulse needs to be shorter than τ_p or its spectrum needs to be broader than $\varepsilon(\omega)$. The spectrum $E(\omega)$ can be easily visualized via (3.16) as the sum of two spectra shifted by $\pm\widetilde{\omega}$: $\varepsilon(\omega - \omega_0 - \widetilde{\omega}) + \varepsilon(\omega - \omega_0 + \widetilde{\omega})$. If we call $\Delta\omega_0$ the FWHM of $\varepsilon(\omega)$, the width $\Delta\omega$ of $E(\omega)$ is therefore larger than $\Delta\omega_0$ (typically $\Delta\omega \approx \Delta\omega_0 + 2\widetilde{\omega}$).

It can be shown that the spectrum defined by (3.18) and (3.19) can be rewritten as

$$\mathbf{E}(\boldsymbol{\omega}) = E(\omega) \begin{bmatrix} \cos[\delta(\omega)] \\ i \sin[\delta(\omega)] \end{bmatrix}, \tag{3.20}$$

with $\delta(\omega) = -\arctan\left(\tanh\left(\frac{2(\omega-\omega_0)\widetilde{\omega}}{\sigma^2}\right)\right)$. The expression of the spectrum $\mathbf{E}(\boldsymbol{\omega})$ in (3.20) is then comparable with the one that can be produced by a pulse shaper operating in polarization shaping [see (3.11)]. In particular, the fields along **x** and **y** are in phase quadrature, which is fully compatible with the ability of the pulse shaper. From (3.19) and (3.20), the main finding for the synthesis is that (i) the polarization state can be controlled using a standard pulse shaper operating in phase and polarization shaping and that (ii) the spectral amplitude must be simultaneously tailored in addition to the phase and polarization. As already mentioned, this can be achieved using a scheme with a double pass through the SLM [38]. The amplitude shaping is needed to design the spectrum $E(\omega)$ as given in (3.19), one inherent condition being to have an initial spectrum with a sufficient width.

The present strategy has been tested considering an input Gaussian pulse around 800 nm ($\omega_0 = 2.36 \times 10^{15}$ Hz) of 100 fs duration with the purpose of producing a Gaussian pulse of rotating polarization with $\tau_p = 200$ fs FWHM and $T_{\mathrm{rot}} = 2\pi/\widetilde{\omega} = 600$ fs. The calculation is conducted with a 320-pixels SLM [39]. The spectrum and phases (φ_a, φ_b) to apply to the SLM are depicted in Fig. 3.6. As shown from Fig. 3.6a,

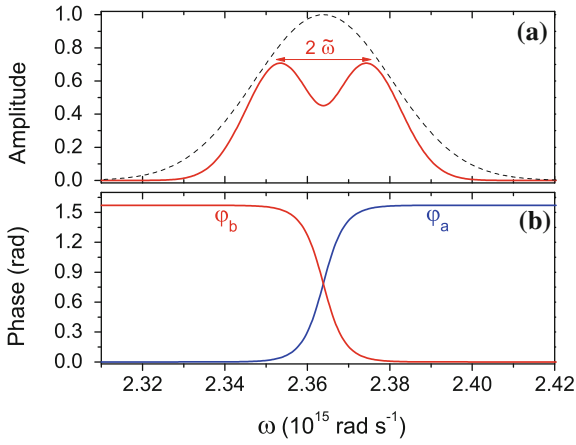

Fig. 3.6 Shaping for a pulse of rotating polarization with $\tau_p = 200$ fs and $T_{\text{rot}} = 600$ fs. **a** Spectral amplitude of the shaped pulse (solid line) and of the 100 fs Gaussian pulse (dashed line). **b** Phases φ_a and φ_b applied to the two LCD arrays

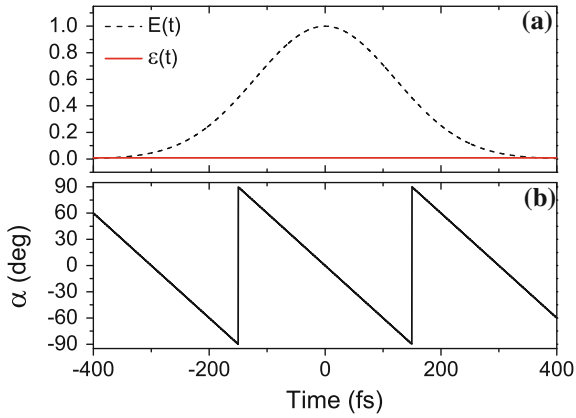

Fig. 3.7 **a** Normalized electric field envelope $E(t)$ (dashed line) and ellipticity $\varepsilon(t)$ (solid line). **b** Polarization angle $\alpha(t)$

the spectrum must be tailored in amplitude in order to get the suitable specific shape. The spectral amplitude of the 100 fs input pulse, depicted in dashed line, is broad enough for the present desired shaping but a broader spectrum would be required for larger angular frequencies of spinning polarization $\widetilde{\omega}$. The phases φ_a and φ_b to apply to the SLM, depicted in Fig. 3.6b, present a sigmoid function shape.

The produced electric field, depicted in Fig. 3.7, features as expected a Gaussian envelope and remains perfectly linearly polarized with a continuous increase of the polarization angle. This method presents therefore a great flexibility offering the generation of controllable pulses of twisted linear polarization.

Each method proposed in this section features advantages and disadvantages. While the last method based on shaping of spectral phase, amplitude, and polarization provides the best result in terms of final output and versatility, it requires the implementation of a non-standard and quite sophisticated pulse shaper arrangement. For this reason, the experiments presented in the second part of this chapter have been conducted using the Method 1 relying on two perpendicularly polarized time-

delayed pulses, as described in Sect. 3.2.1.1. This approach allows the production of twisted linear polarization of rather good quality that maintains a linear polarization during the pulse in contrast with Method 2. As already mentioned, the main drawback of this method is that the rotational period of the spinning polarization is not easily controllable. Nevertheless, it turns out that the angular frequency obtained under our experimental conditions fits well with the one needed for producing a unidirectional rotational motion of the molecules under consideration.

3.2.3 *Spinning Molecules with a Twisted Linear Polarization*

Unidirectional molecular rotation is characterized by evaluating the orientation of the rotational angular momentum **J** achieved by the field exhibiting a twisted linear polarization (TLP). This is achieved by solving the Liouville-von Neumann equation representing the evolution of the density operator ρ:

$$\frac{\mathrm{d}}{\mathrm{d}t}\rho(t) = \frac{1}{i\hbar}\left[H(t), \rho(t)\right]. \tag{3.21}$$

In this expression, the time-dependent Hamiltonian of the system is written

$$H(t) = H_0 + H_{\mathrm{int}}(t), \tag{3.22}$$

where

$$H_0 = BJ^2 - DJ^4, \tag{3.23}$$

is the Hamiltonian governing the rotational dynamics in the absence of external field, with J the angular momentum operator, B and D the rotational constants, and H_{int} is the Hamiltonian describing the interaction of the system with the TLP field. In the electric dipole approximation, the last term can be written in the form [40]

$$H_{\mathrm{int}}(t) = -\int_0^{E_{\mathrm{TLP}}} \boldsymbol{\mu} \cdot \mathrm{d}\mathbf{E} \tag{3.24}$$

with $\boldsymbol{\mu}$ the electric dipole coupled to the TLP field $\mathbf{E}_{\mathrm{TLP}}$. The electric dipole can be written as a sum of a permanent component $\boldsymbol{\mu}_0$ and a field-induced component $\overline{\alpha} \cdot \mathbf{E}(t)$

$$\boldsymbol{\mu}(t) = \boldsymbol{\mu}_0 + \overline{\alpha} \cdot \mathbf{E}(t), \tag{3.25}$$

where $\overline{\alpha}$ is the first-order polarizability tensor written in the space-fixed frame, neglecting higher-order terms. According to (3.24) and (3.25), the interaction Hamiltonian is given by

$$H_{\text{int}}(t) = -\boldsymbol{\mu}_0 \mathbf{E}_{\text{TLP}}(t) - \frac{1}{2}\mathbf{E}_{\text{TLP}}(t) \cdot \overline{\alpha} \cdot \mathbf{E}_{\text{TLP}}(t). \tag{3.26}$$

Defining the induced electric dipole moment

$$\boldsymbol{\mu}_{\text{i}}(t) = \overline{\alpha} \cdot \mathbf{E}_{\text{TLP}}(t), \tag{3.27}$$

(3.24) can be cast in the form

$$H_{\text{int}}(t) = -\boldsymbol{\mu}_0 \mathbf{E}_{\text{TLP}}(t) - \frac{1}{2}\boldsymbol{\mu}_{\text{i}}(t) \cdot \mathbf{E}_{\text{TLP}}(t). \tag{3.28}$$

The polarizability $\overline{\alpha}$ can be deduced from the polarizability α expressed in the molecule-fixed frame by using the rotation matrix involving the three Euler angles θ, ϕ, and χ

$$\overline{\alpha}_{ij} = \sum_{i',j'} c_{ii'} c_{jj'} \alpha_{i'j'}, \tag{3.29}$$

where $c_{ii'}$ are the direction cosines describing the orientation of any axis (i', $j' = 1, 2, 3$) of the molecule with respect to any axis (i, $j = x, y, z$) of the space-fixed Cartesian frame [41]. For a linear molecule with a molecular axis labeled 3, the elements of the polarizability tensor expressed in the space-fixed frame are given by the expression

$$\overline{\alpha}_{ij} = \alpha_0 \delta_{ij} + \Delta\alpha \left(c_{i3'} c_{j3'} - \delta_{ij}/3 \right), \tag{3.30}$$

where $\Delta\alpha = \alpha_{\parallel} - \alpha_{\perp}$ is the difference between the polarizability components $\alpha_{\parallel}$ and $\alpha_{\perp}$ parallel and perpendicular to the molecular axis, respectively, $\alpha_0 = \left(2\alpha_{\perp} + \alpha_{\parallel}\right)/3$ is the averaged polarizability, and δ_{ij} are the Kronecker deltas. The TLP electric field propagating along the z axis and polarized in the xy-plane is written

$$\mathbf{E}_{\text{TLP}}(t) = \mathscr{E}_x(t - T)\cos(\omega t - \xi)\mathbf{x} + \mathscr{E}_y(t)\cos(\omega t)\mathbf{y}. \tag{3.31}$$

The temporal envelope of the field along $\mathbf{x}$ and $\mathbf{y}$ are respectively written $\mathscr{E}_x(t)$ and $\mathscr{E}_y(t)$. The carrier frequency is ω. We recall that T and ξ define the temporal delay and the relative phase between the two spatial components of the field, respectively. The first term of (3.28) vanishes when averaged over the fast oscillations of the optical field. Under the high frequency approximation and taking into account (3.27)–(3.31), the interaction Hamiltonian can be written [31]

$$\begin{aligned} H_{\text{int}}(t) = -\frac{\Delta\alpha}{4} \Big\{ &\left(\cos^2\theta_x - 1/3\right) \mathscr{E}_x^2(t - T) \\ &+ \left(\cos^2\theta_y - 1/3\right) \mathscr{E}_y^2(t) + 2\cos\xi\cos\theta_x\cos\theta_y \mathscr{E}_x(t - T)\mathscr{E}_y(t) \Big\}, \end{aligned} \tag{3.32}$$

where θ_x and θ_y are the angle of the molecular axis with respect to **x** and **y**, respectively. For $\mathscr{E}_x = \mathscr{E}_y$ and in the absence of the third term in (3.32), i.e. for $\xi = \pi/2$ $[2\pi]$, it has been shown [31] that the first and second term of the Hamiltonian produce a superposition of two perfectly symmetric ensembles of molecules with opposite UDR. The inclusion of the third term breaks this symmetry, resulting in the orientation of the rotational angular momentum **J** that is maximized for $\xi = 0$ $[2\pi]$ or π $[2\pi]$, depending on the handedness of the TLP pulse.

In order to assess the degree of orientation achievable with the TLP field, we numerically solve (3.21) for parameters matching the experimental conditions. We consider room temperature molecules exposed to a TLP pulse produced from an initial pulse of 100 fs duration. Each pulse forming the TLP field has an intensity of 80 TW/cm^2. The delay T between the envelope related to each field component $\mathscr{E}_x$ and $\mathscr{E}_y$ is set to 145 fs. Figure 3.8a compares the temporal evolution of the expectation value $\langle J_z \rangle$ calculated for different linear molecules. As illustrated in Fig. 3.8b, J_z corresponds to the projection of **J** along the propagation direction z of the TLP pulse. The time origine is set at the maximum of $\mathscr{E}_y(t)$. As shown, the orientation of the angular momentum raises from the time the two cross polarized TLP components start to temporally overlap and then reaches its maximum value during the turn-off of the TLP pulse. For the investigated molecules, the amount of angular momentum transferred along the z axis increases with the anisotropy of polarizability. In N_2, O_2, and CO_2, $\langle J_z \rangle$ reaches 0.50, 1.13, and 1.96 $\hbar$ after the pulse turn-off, corresponding to about 4, 8, and 7% of the total angular momentum $\sqrt{\langle J^2 \rangle}$, respectively. It should be noted that unlike CO_2 and N_2, the O_2 molecule possesses an electron spin angular momentum resulting in a spin-rotation coupling [42] that is not taken into account by the Hamiltonian defined in (3.23). In fact, the interaction of the spin with the nuclear rotation being very weak, the influence of the electronic spin on the rotational dynamics can be neglected in the present study.

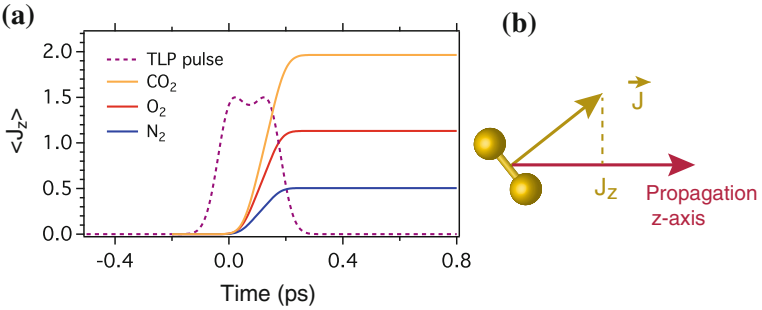

Fig. 3.8 **a** Expectation values of the angular momentum projection along z versus time (solid lines) induced by a linear twisted polarization (TLP) calculated for different molecules. The temporal envelope of the TLP pulse is depicted in dashed line. **b** Orientation of the rotational angular momentum **J** with z the propagation axis of the TLP pulse

3.3 Linear Scattering of Light by Spinning Molecules

This section concerns the linear interaction of a circularly polarized (CP) radiation with a gas of spinning molecules. The latter can be seen as an ultrafast light modulator with an associated bandwidth of few terahertz. The temporal phase modulation that spinning molecules apply to a short laser pulse leads to a spectral modification, as well as to a polarization change of the transmitted light. The effect can be interpreted in terms of the angular Doppler effect [43, 44] responsible for a rotational Doppler shift (RDS) of the incident radiation. To our best knowledge, the first direct observation of the RDS was performed by analysing the interaction of a circularly polarized electromagnetic wave with a rotating conducting electric dipole [45]. Later on the effect was also evidenced by analyzing the polarization of a HeNe laser transmitted through a rotating half-wave retardation plate [46]. Recently much larger RDS could be reported by using faster rotating bodies that are spinning molecules [12, 13, 25] as compared with slower rotating motorized optics [44–48].

The polarization and spectral change of the light scattered by the spinning molecules can be readily interpreted when considering a field polarized in the plane of rotation of the molecules. In this particular case, where the angular momentum related to the spin of the photon is collinear with the one associated with the molecular rotation, the carrier frequency and the polarization of the radiated photon can be directly inferred from conservation laws. Figure 3.9 illustrates for instance left CP photons interacting with spinning molecules co-rotating with an angular velocity Ω. The spinning molecule acts as a rotating wave plate converting the polarization of the incident light from left to right handed. In Fig. 3.9a the polarization of the photon is conserved and so its energy. In Fig. 3.9b, the polarization of the radiated photon is reversed, resulting in a change $\Delta L_{\text{photon}} = -2\hbar$ of the total angular momentum associated with the photons. This mismatch is balanced by an opposite change of the angular momentum $\Delta L_{\text{mol}} = 2\hbar$ of the molecule resulting in a variation of the rotational energy by $\Delta E_{\text{mol}} = 2\hbar\Omega$. As the energy is fixed for a closed system, the rotational energy is altered at the cost of the scattered photon energy that is in turn changed by $\Delta E_{\text{mol}} = -2\hbar\Omega$, leading to a spectral shift $\Delta\omega = -2\Omega$ of the radiated photon. The same type of arguments can be applied to left-polarized photons interacting with counter-rotating molecules and leading to a frequency shift $\Delta\omega = +2\Omega$.

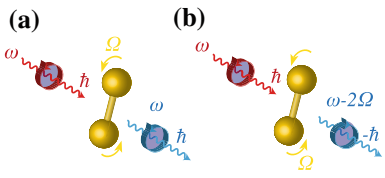

Fig. 3.9 Left circularly-polarized photons scattered by molecules spinning with an angular velocity Ω. **a** The angular momentum $+\hbar$ of the photons of frequency ω is conserved. **b** The angular momentum of the photon is changed from $+\hbar$ to $-\hbar$ resulting in a Doppler shift $\Delta\omega = -2\Omega$ of the transmitted photon

To summarize, the change in the helicity of the photon polarization is associated with a rotational Doppler shift of its frequency $\Delta\omega = \pm 2\Omega$, where the signs depend on the relative handedness of the incident polarization and molecular spinning.

In the next part of this section, we describe the experimental setup related to the time- and frequency-resolved measurement of a light pulse linearly scattered by a gas of spinning molecules. Next, we develop the theoretical model that is used in order to simulate the signal measured in the experiment. Finally, we present the experimental data, compare them to the theoretical predictions, and discuss the results.

3.3.1 Experimental Setup

The experiment is based on a femtosecond Ti:sapphire chirped pulse amplifier that delivers pulses of 100 fs duration, centered around 800 nm, at 100 Hz repetition rate. The setup is depicted in Fig. 3.10. The output energy of the amplifier is divided in two parts. The first part is used to generate a pulse with a twisted linear polarization illustrated in Fig. 3.1b, following the technique detailed in Sect. 3.2.1.1. As shown in Fig. 3.1a, the polarization shaping is achieved by combining two time delayed cross-polarized pulse of same amplitude, produced by the propagation of a linearly polarized pulse through a multiple-order wave plate MOWP. The thickness of the MOWP is such that the time separation between the two pulse replicas is fixed to $T = 145$ fs. A Berek compensator is introduced after the MOWP in order to control the relative phase between the two outgoing field projections independently of the length of the MOWP. The handedness of the twisted polarization can be controlled by setting the relative phase to an even or odd integer number of π. The second part of the laser energy is used to probe the spinning molecules. The two beams are crossed at small angle and focused inside a static cell filled with N_2 molecules at room

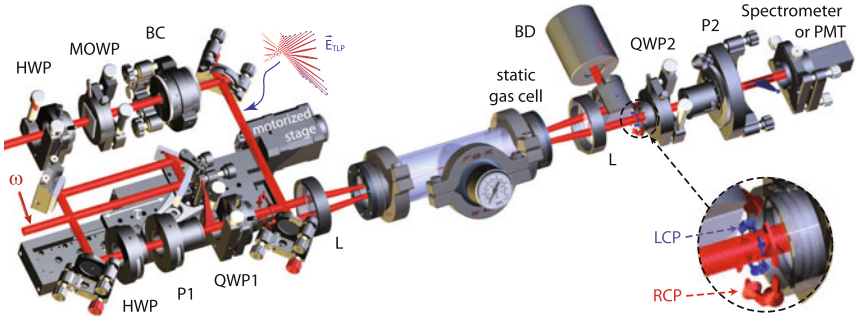

Fig. 3.10 Experimental setup. HWP: Half-wave plate; MOWP: Multiple-order wave plate; BC: Berek compensator; P: polarizer; QWP: quarter-wave plate; L: lens; BD: beam dump; PMT: photomultiplier tube. The polarization handedness of the left-handed circular polarization (LCP) or right-handed circular polarization (RCP) radiation is selected by a circular analyzer (QWP2, P2)

temperature. The temporal delay between the TLP and the probe pulse is adjusted via a motorized translation stage. The probe pulse is circularly polarized using the quarter-wave plate QWP1. The polarization of the transmitted probe is measured by a circular analyzer made of a second quarter-wave plate QWP2 combined with a second polarizer $P2$. The two quarter-wave plate slow axes are set perpendicular to each other so that the transmitted radiation produced with the same or opposite polarization to that of the probe is selected by orienting $P2$ parallel or perpendicular to $P1$, respectively. The light transmitted through $P2$ is measured by a photomultiplier tube or a spectrometer.

3.3.2 Detection and Model

The schematic of the detection including the notation for the different fields involved in the calculation of the signal is presented in Fig. 3.11. The incident probe field $\mathbf{E_0}$ on the first quarter-wave plate (QWP1) is linearly polarized at 45° with respect to the **x** and **y** axis

$$\mathbf{E}_0(t) = \frac{1}{\sqrt{2}} E_0(t)\,(\mathbf{x} + \mathbf{y})\,, \tag{3.33}$$

with $E_0(t)$ defining a real amplitude. After the retardation plate $\overline{\text{QWP1}} = \begin{pmatrix} i & 0 & 0 \\ 0 & 1 & 0 \\ 0 & 0 & 0 \end{pmatrix}$, where i denotes the imaginary unit, the circularly polarized field writes

$$\widetilde{\mathbf{E}}_1(t) = \overline{\text{QWP1}} \cdot \mathbf{E}_0 = \widetilde{E}_{1_x}\mathbf{x} + \widetilde{E}_{1_y}\mathbf{y} \simeq E_0(t)\,(i\mathbf{x} + \mathbf{y})\,, \tag{3.34}$$

where $\widetilde{E}_{1_x}$ and $\widetilde{E}_{1_y}$ are the spatial components of the complex field. The field then interacts with the molecular medium, inducing an electric dipole moment

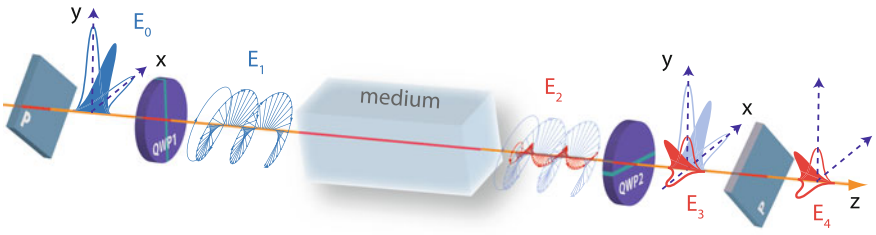

Fig. 3.11 Schematic of the detection. QWP: quarter-wave plate; P: polarizer; E_0: linearly-polarized incident probe field; E_1: circularly-polarized incident probe field; E_2: scattered field at the exit of the gas cell; E_3: field after the second quarter-wave plate; E_4: signal field

$$\boldsymbol{\mu}_1 = \overline{\alpha} \cdot \widetilde{\mathbf{E}}_1(t) \tag{3.35}$$

through excitation of the polarizability $\overline{\alpha}$. The linearly scattered field $\widetilde{\mathbf{E}}_2(t) \simeq \boldsymbol{\mu}_1$ is then passing through a second quarter-wave plate $\overline{\mathrm{QWP2}} = \begin{pmatrix} 1 & 0 & 0 \\ 0 & i & 0 \\ 0 & 0 & 0 \end{pmatrix}$ leading to the outgoing field

$$\widetilde{\mathbf{E}}_3(t) = \overline{\mathrm{QWP2}} \cdot \mathbf{E}_2 = \widetilde{E}_{3_x}\mathbf{x} + \widetilde{E}_{3_y}\mathbf{y}. \tag{3.36}$$

By replacing $\overline{\alpha}$ by its expression given in (3.30), it can be shown that the spatial components of the transmitted field write

$$\begin{aligned} \widetilde{E}_{3_x}(t) &\simeq \widetilde{E}_0(t)\left[i\alpha_0 + i\,\Delta\alpha\left(\cos^2\phi\sin^2\theta - 1/3\right) + \Delta\alpha/2\sin(2\phi)\sin^2\theta\right] \\ \widetilde{E}_{3_y}(t) &\simeq \widetilde{E}_0(t)\left[i\alpha_0 + i\,\Delta\alpha\left(\sin^2\phi\sin^2\theta - 1/3\right) - \Delta\alpha/2\sin(2\phi)\sin^2\theta\right], \end{aligned} \tag{3.37}$$

with θ and ϕ the Euler angles. θ describes the orientation of the molecular axis with respect to the z axis and ϕ corresponds to the rotation of the molecular frame around the z axis. The signal field measured after the second polarizer when $\overline{P2} = \frac{1}{\sqrt{2}}\begin{pmatrix} 1 \\ 1 \\ 0 \end{pmatrix}$ and $\overline{P1} = \frac{1}{\sqrt{2}}\begin{pmatrix} 1 \\ 1 \\ 0 \end{pmatrix}$ are set parallel is

$$\widetilde{\mathbf{E}}_4(t) = \overline{P2} \cdot \widetilde{\mathbf{E}}_3(t) \simeq i\,\widetilde{E}_0(t)\left(\alpha_\perp + \frac{\Delta\alpha}{2}\sin^2\theta\right), \tag{3.38}$$

whereas the signal field is written

$$\widetilde{\mathbf{E}}_4(t) \simeq i\,\widetilde{E}_0(t)\Delta\alpha\sin^2\theta \mathrm{e}^{-2i\phi} \tag{3.39}$$

when $\overline{P2} = \frac{1}{\sqrt{2}}\begin{pmatrix} 1 \\ -1 \\ 0 \end{pmatrix}$ and $\overline{P1} = \frac{1}{\sqrt{2}}\begin{pmatrix} 1 \\ 1 \\ 0 \end{pmatrix}$ are crossed.

The angular Doppler shift associated with the transmitted light can be easily identified from (3.37) by considering the classic limit where all molecules are confined in the plane of polarization of the incident CP light, meaning that $\theta = \pi/2$, and spinning with the angular velocity Ω such that $\phi = \pm\Omega t$, where the sign depends on the sense of rotation of the molecules. Assuming, for instance, that the field $\widetilde{\mathbf{E}}_1(t)$ of frequency ω is left polarized and defining $\mathscr{E}_0(t)$ the temporal envelope of the incident field

$$\widetilde{E}_0(t) = \mathscr{E}_0(t)\exp(i\omega t), \tag{3.40}$$

then (3.37) can be cast in the simple form

$$\begin{aligned}\widetilde{E}_{2_x}(t) &\simeq i\mathscr{E}_0(t)\left[(6\alpha_0+\Delta\alpha)\,\mathrm{e}^{i\omega t}+3\Delta\alpha\mathrm{e}^{i(\omega\mp 2\Omega)t}\right]\\ \widetilde{E}_{2_y}(t) &\simeq \mathscr{E}_0(t)\left[(6\alpha_0+\Delta\alpha)\,\mathrm{e}^{i\omega t}-3\Delta\alpha\mathrm{e}^{i(\omega\mp 2\Omega)t}\right].\end{aligned} \tag{3.41}$$

This set of equations reveals that the solution of a CP light transmitted through the molecular sample corresponds to a superposition of two CP radiations with different amplitudes and opposite handednesses. Moreover, the CP field generated with the same polarization as the incident light conserves the same frequency, whereas the one produced with an opposite polarization is frequency shifted by $\mp 2\Omega$. The down-shifted (up-shifted) frequency is obtained when the molecules are spinning in the same (opposite) direction as the incident field. These findings are consistent with the predictions based on conservation laws presented in Sect. 3.3.

The pump-probe signal produced by the Doppler shifted component $\pm 2\Omega$ can be derived from (3.39) through evaluation of the temporal convolution product

$$\mathscr{S}^{(2\Omega)}(\tau) \approx \int_{-\infty}^{\infty} \Delta\alpha^2 \left|\widetilde{E}_1(t-\tau)\langle \sin^2\theta \mathrm{e}^{-2i\phi}\rangle(t)\right|^2 \mathrm{d}t, \tag{3.42}$$

where τ is the temporal delay between the probe field $\mathbf{E_1}(t-\tau)$ and the TLP field $\mathbf{E}_{\mathrm{TLP}}(t)$ driving the molecular unidirectional rotation. The expectation value $\langle \sin^2\theta \mathrm{e}^{-2i\phi}\rangle$ can be estimated at any time t by solving (3.21) using a thermal distribution of molecules at temperature T as initial condition. The spectrum of the transmitted light is finally obtained by a Fourier transform of (3.39) taking into account the temporal delay τ.

3.3.3 Temporal and Spectral Analysis

Figure 3.12 presents the signal produced in N_2 by scanning the delay τ between the TLP and the probe pulse. The experiment is performed at room temperature and atmospheric pressure and the signal is recorded by a photomultiplier tube. The depicted temporal structures result from the modification of the angular distribution of the molecules exercised by the TLP field, leading to an induced transient birefringence responsible for the depolarization of the incident probe field [49, 50]. In the present context, we omit the signal produced at the temporal overlap of the two pulses and focus our study on the field-free revivals produced with a time interval $T_r/2 = 4.2\,\mathrm{ps}$, where T_r is the rotational revival time of the N_2 molecules [49]. As previously described, the transmitted probe field generated by a CP fundamental field is a superposition of two CP waves of opposite handedness. These two components are selected by the circular analyzer depicted in Figs. 3.10 and 3.11. In order to select the transmitted light produced with an helicity opposite to that of the fundamental one, i.e. the Doppler shifted component, $P2$ is oriented perpendicular to the original

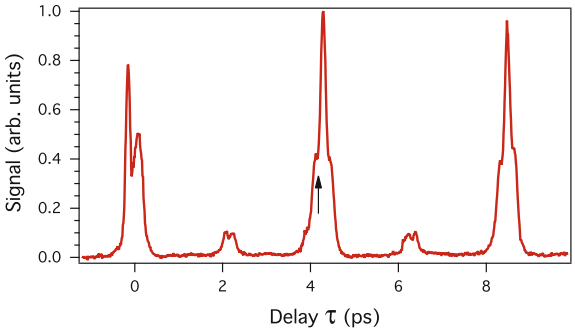

Fig. 3.12 Transmitted light through spinning N_2 molecules versus the delay between the TLP and the probe pulse. The TLP shaped pulse is composed of two equal pulses, each of intensity estimated to $I = 20\,\text{TW/cm}^2$, separated by $T = 145\,\text{fs}$. The black arrow indicates the delay where the spectra of Fig. 3.13 are recorded

direction of the incident field defined by $P1$. The spectrum shown in Fig. 3.13a is recorded when the molecules rotate in the same sense as the incident left-polarized field. It is obtained by setting to π $[2\pi]$ the relative phase ξ between the two spatial components of the field. As expected, the transmitted radiation is redshifted from its initial spectrum, represented in dashed line, in good agreement with the numerical simulation of (3.39) and (3.42) using $\Delta\alpha = 4.6$ a.u. [51]. The blueshifted radiation shown in Fig. 3.13b is observed by reversing the sense of rotation of the molecules, setting the phase of the Berek compensator to $\xi = 0$ $[2\pi]$. Both spectra shown in Fig. 3.13 have been recorded for a delay τ set at the local minimum of the first revival indicated by an arrow in Fig. 3.12, corresponding to the time where the angular Doppler shift is the largest [31, 32].

3.4 Third-Harmonic Generation in Spinning Molecules

The rotational Doppler effect is not restricted to linear optics. For instance, conservation laws applied to frequency up-conversion processes lead to a rich set of spectral shifts [52] depending on the nonlinear order of the process. These shifts are the direct manifestation of the rotational Doppler effect that were envisioned by Simon and Bloembergen in their early work on second-harmonic light generation [53]. These RDS were confirmed by two recent consecutive works; the first one is related to the second-harmonic generation in mechanically rotating nonlinear crystals [52], whereas the second one concerns the third-harmonic generation (THG) in spinning molecules [31]. In order to predict the spectral shifts of the THG radiation, we first consider, as in Sect. 3.3, left-polarized photons interacting with co-rotating molecules. In Fig. 3.14a, the THG photon is produced with the same polarization as the fundamental photon of frequency ω. The change $\Delta L_{\text{photon}} = -2\hbar$

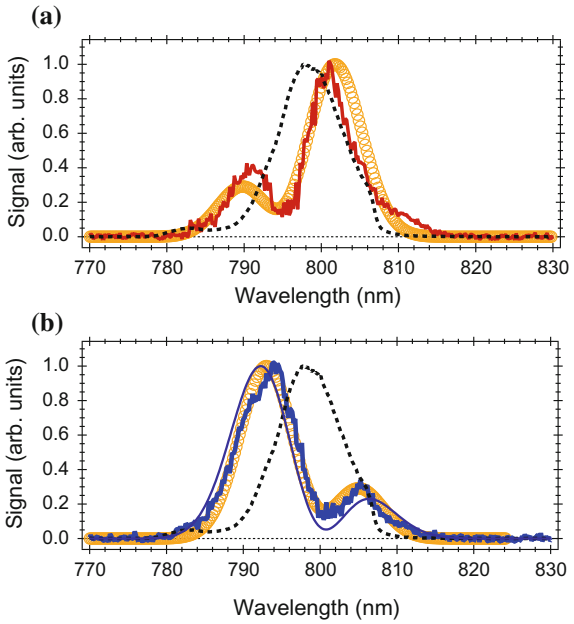

Fig. 3.13 Normalized spectra of the circularly-polarized transmitted probe beam recorded for N_2 molecules rotating **a** in the same (red line) and **b** in the opposite (blue line) direction to that of the incident field. The respective theoretical spectra are represented with orange solid circles. The input probe spectra are shown with a black dashed-line

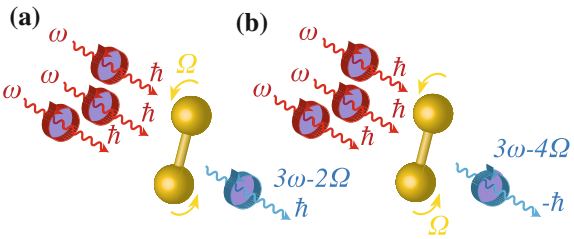

Fig. 3.14 Nonlinear photon scattering in molecules spinning with an angular velocity Ω. **a** The third-harmonic photon of frequency 3ω generated with the same polarization as the fundamental photon ω is downshifted by 2Ω. **b** The third-harmonic photon generated with the opposite polarization to that of the fundamental photon is downshifted by 4Ω

of the total angular momentum associated to the photons is balanced by a variation $\Delta E_{\mathrm{mol}} = 2\hbar\Omega$ of the rotational energy leading to a spectral shift $\Delta\omega = -2\Omega$ of the harmonic photon. The harmonic photon generated with the opposite polarization to that of the fundamental radiation is depicted in Fig. 3.14b. In that case, the angular momentum of the field is decreased by $-4\hbar$, whereas the rotational energy is proportionally increased by $4\hbar\Omega$, resulting in a Doppler shift of the THG photon by

-4Ω. The sign of the frequency shifts are reversed when considering left-polarized photons interacting with counter-rotating molecules. For a harmonic order n (the THG process corresponds to $n = 3$), it is easy to show that the rotational Doppler shifts are $\pm(n \pm 1)\Omega$ [32, 52].

The experimental setup used for the observation of the Doppler shifted THG spectra [32] is similar to the one depicted in Fig. 3.10, except that a UV band-pass filter is introduced between $P2$ and the spectrometer in order to reduce the amount of fundamental IR light reaching the detector.

3.4.1 Model

Using the same notations for the fields as in Sect. 3.3.2, the expression of the third-harmonic field $\mathbf{E}_2(t)$ produced after the medium interaction (see Fig. 3.11) can be estimated from the macroscopic nonlinear polarization $\mathbf{P}^{(3)}(t)$ induced by the fundamental electric field $\mathbf{E}_1$

$$\mathbf{P}^{(3)}(t) = \varepsilon_0 \chi^{(3)} \vdots \mathbf{E}_1(t)\mathbf{E}_1(t)\mathbf{E}_1(t), \tag{3.43}$$

where ε_0 is the vacuum permittivity and $\chi^{(3)} = \chi^{(3)}(-\omega_3; \omega, \omega, \omega)$ is the third-order nonlinear susceptibility of the medium. Assuming a nonresonant circularly polarized field as defined in (3.34), the spatial components of the THG field can be written

$$\widetilde{E}_{2_x}(t) \approx \varepsilon_0 \left(\chi^{(3)}_{xxxx} \widetilde{E}^3_{1_x} + 3\chi^{(3)}_{xxyy} \widetilde{E}_{1_x} \widetilde{E}^2_{1_y} + 3\chi^{(3)}_{xxxy} \widetilde{E}^2_{1_x} \widetilde{E}_{1_y} + \chi^{(3)}_{xyyy} \widetilde{E}^3_{1_y} \right) \tag{3.44}$$

and

$$\widetilde{E}_{2_y}(t) \approx \varepsilon_0 \left(\chi^{(3)}_{yyyy} \widetilde{E}^3_{1_y} + 3\chi^{(3)}_{yyyx} \widetilde{E}_{1_x} \widetilde{E}^2_{1_y} + 3\chi^{(3)}_{yyxx} \widetilde{E}^2_{1_x} \widetilde{E}_{1_y} + \chi^{(3)}_{yxxx} \widetilde{E}^3_{1_x} \right). \tag{3.45}$$

Using the rotation matrix $c_{ii'}$, the matrix elements of $\chi^{(3)}$ can be expressed in terms of the second-order hyperpolarizability tensor γ

$$\chi^{(3)}_{ijkl} = N_0 c_{ii'} c_{jj'} c_{kk'} c_{ll'} \gamma_{i'j'k'l'}, \tag{3.46}$$

with N_0 the number density. For linear molecules, only three elements are independent: $\gamma_{1122} = \gamma_{12}$, $\gamma_{1133} = \gamma_{13}$, and $\gamma_{3333} = \gamma_{33}$, with $\gamma_{13} = \gamma_{23}$.

As in Sect. 3.3.2, we can infer from the previous expressions the Doppler shifts experienced by the THG field by considering the classic limit where all molecules are confined in the plane of polarization of the incident CP light ($\theta = \pi/2$, $\phi = \pm\Omega t$). Using the expression of $\widetilde{E}_1(t)$ defined in (3.40), the spatial components of the THG field can be written

$$\widetilde{E}_{2_x} \approx \varepsilon_0 N_0 \mathscr{E}_1^3(t) \times \{(\Delta_2\gamma + 6\Delta\gamma)\sin(3\omega \mp 2\Omega)\,t + \Delta_2\gamma \sin(3\omega \mp 4\Omega)\,t\} \tag{3.47}$$

and

$$\widetilde{E}_{2_y} \approx -\varepsilon_0 N_0 \mathscr{E}_1^3(t) \times \{(\Delta_2\gamma + 6\Delta\gamma)\cos(3\omega \mp 2\Omega)\,t - \Delta_2\gamma \cos(3\omega \mp 4\Omega)\,t\}, \tag{3.48}$$

where $\Delta\gamma$ and $\Delta_2\gamma$ are defined by $\gamma_{13} - \gamma_{12}$ and $\gamma_{33} + 3\gamma_{12} - 6\gamma_{13}$, respectively. In contrast to the linear case treated in Sect. 3.3, the THG field is here obtained as a superposition of two frequency shifted CP components. In agreement with the predictions based on conservation laws, we can see that the smaller shifts $\mp 2\Omega$ are attached to the CP field produced with the same polarization helicity as the fundamental one, whereas the largest shifts $\mp 4\Omega$ correspond to THG field produced with opposite helicity.

The two CP components of the THG field are resolved by the circular analyzer depicted in Fig. 3.11. When P1 and P2 are set parallel, it can be shown from (3.44) and (3.45) that the analyser selects the $\mp 2\Omega$ shifted CP component:

$$\widetilde{E}_4^{(2\Omega)}(t) \approx \varepsilon_0 N_0 \widetilde{E}_1^3(t) \exp(-2i\phi)\left(\Delta_2\gamma \sin^4\theta + 6\Delta\gamma \sin^2\theta\right). \tag{3.49}$$

The THG component produced with the opposite polarization, i.e. frequency shifted by $\mp 4\Omega$ from 3ω, is obtained by setting $P2$ perpendicular to $P1$:

$$\widetilde{E}_4^{(4\Omega)}(t) \approx \varepsilon_0 N_0 \Delta_2\gamma\, \widetilde{E}_1^3(t) \exp(-4i\phi) \sin^4\theta. \tag{3.50}$$

The pump-probe signal produced by the Doppler shifted components is derived as in Sect. 3.3.2 through evaluation of the temporal convolution products

$$\mathscr{S}^{(2\Omega)}(\tau) \approx \int_{-\infty}^{\infty} \left|\widetilde{E}_1^3(t-\tau)\langle \exp(-2i\phi)\left(\Delta_2\gamma \sin^4\theta + 6\Delta\gamma \sin^2\theta\right)\rangle(t)\right|^2 \mathrm{d}t \tag{3.51}$$

and

$$\mathscr{S}^{(4\Omega)}(\tau) \approx \int_{-\infty}^{\infty} \left|\Delta_2\gamma\, \widetilde{E}_1^3(t-\tau)\langle \exp(-4i\phi) \sin^4\theta\rangle(t)\right|^2 \mathrm{d}t. \tag{3.52}$$

The THG spectra measured at a delay τ are obtained from the Fourier transform of (3.49) and (3.50), respectively.

3.4.2 *Harmonic Spectra*

Figure 3.15 presents the THG spectra of the 800 nm laser pulse produced in O_2 at room temperature. To allow the detection of both harmonic polarizations, the intensity of the CP fundamental light is set to ~80 TW/cm^2. The pressure is kept below 0.5 bar in order to limit spatiotemporal distorsion of the laser pulse during propagation. The spectra of the THG produced with the same polarization as the fundamental field is shown in Fig. 3.15a for both sense of rotation of the molecules. The redshifted spectrum is produced by molecules corotating with the fields, whereas the blueshifted one is generated by counter-rotating molecules. The absolute value of the spectral shift is 3.2 THz. In good agreement with the prediction based on conservation laws, approximately twice this value, 5.9 THz, is observed when the third harmonic is generated with a CP of opposite helicity, as shown in Fig. 3.15b. In that case, it has been shown that the THG process is driven by a higher-order nonlinear process as compared to the previous case [32], which explains the reduction of the harmonic intensity by a factor of about 20 between Fig. 3.15a, b. All observed spectra are well reproduced in position and amplitude by the Fourier transforms of (3.49) and (3.50) depicted in Figs. 3.15c, d, respectively. As in the linear case, the nonlinear Doppler shifts are maximized when the delay τ is set close to the local minimum of a revival (not shown).

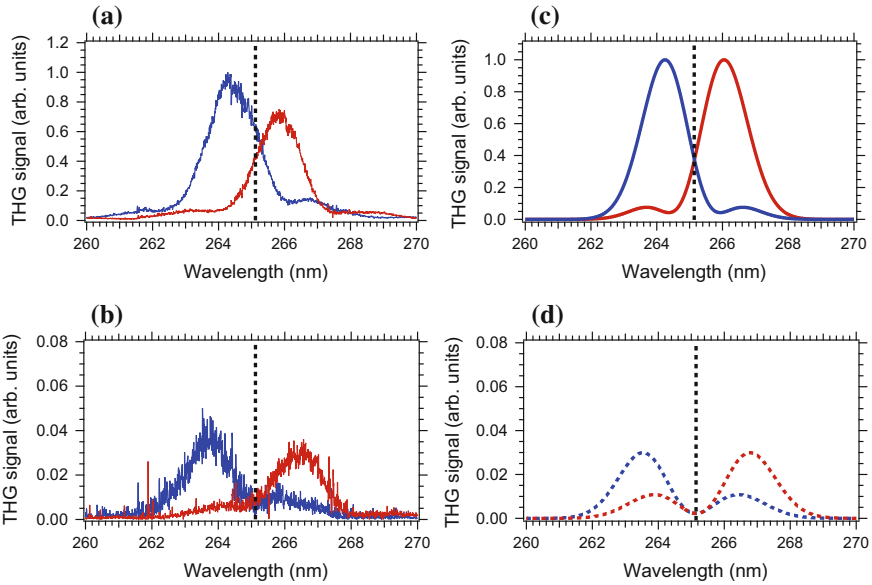

Fig. 3.15 **a** THG spectra generated by a circularly-polarized pulse interacting with O_2 molecules rotating in the same (red solid line) and in the opposite (blue solid line) direction to that of the fundamental field. The polarization of the fundamental and THG radiation is the same. **c** Corresponding theoretical spectra. **b**, **d** The same as **a**, **c**, except that the polarization of the THG radiation is reversed. The vertical dashed lines refer to the carrier frequency of the unshifted THG spectra

3.5 Summary

3.5.1 Conclusion

We have investigated the production of spinning molecules by synthesizing laser pulses with a twisted linear polarization. The first part of the chapter was devoted to the different strategies that can be implemented for polarization shaping. Two streamlined approaches that can be produced, either with simple and compact optical setups, or by means of pulse shaper devices have been assessed. The main strength and flaws of these methods to achieve the desired time-dependent field vector have been outlined. A more elaborated and effective strategy relying on a non-standard pulse shaping arrangement has also been discussed. Laser pulses with a twisted linear polarization have then been applied to control the rotation of linear molecules and the choice of the shaping method implemented experimentally has been discussed. Two experiments have been described, both aiming at observing the rotational Doppler shift exhibited by a circularly-polarized pulse subsequent to its interaction with the spinning molecules. In the first experiment, the spinning motion imparted to the molecules was monitored by analyzing the linear transmission of a circularly-polarized pulse through the medium. It was shown that the sense of rotation of the molecules can be inferred from the sign of the Doppler shift associated to the spectral component of the field produced with opposite polarization as compared to the incident one. In the second experiment, a circularly-polarized laser pulse drived a third-harmonic generation process through a nonlinear interaction with spinning molecules. In that case, the rotational Doppler shift was observed on both third-harmonic radiations produced with polarization the same as and opposite to that of the fundamental radiation. The sign and amplitude of the Doppler shifts were found to depend on the relative handedness of the incident polarization and molecular spinning. In agreement with the prediction based on conservation of energy and angular momentum, the shift imparted to the harmonic radiation generated with a reversed polarization was larger, i.e. about twice, than the one imparted to the harmonic produced with the same polarization as the fundamental pulse.

Molecules driven by twisted linear polarizations can serve as broadband phase modulators enabling the production of terahertz spectral shifts. Based on a non-resonant interaction process, they can be potentially employed with a wide range of short pulse ranging from infrared to ultraviolet. The spectral domain of applications can also be extended to the mid-infrared, through frequency down-conversion, and to the extreme ultraviolet, through high-harmonic generation in gases.

Acknowledgements Thanks are due to present and former Ph.D. students and postdoc fellowships G. Karras, M. Ndong, E. Prost, and H. Zhang for their contributions to a part of the work presented in this chapter. We would also like to thank I. S. Averbukh, P. Béjot, A. A. Milner, V. A. Milner, D. Sugny, and J. Zyss for their collaboration and valuable contributions.

References

1. C. Brif, R. Chakrabarti, H. Rabitz, New J. Phys. **12**, 075008 (2010)
2. S.J. Glaser, U. Boscain, T. Calarco, C.P. Koch, W. Kckenberger, R. Kosloff, I. Kuprov, B. Luy, S. Schirmer, T. Schulte-Herbrggen, D. Sugny, F.K. Wilhelm, Eur. Phys. J. D. **69**(12), 279 (2015)
3. T. Brixner, G. Gerber, ChemPhysChem. **4**(5), 418 (2003)
4. B. Friedrich, D. Herschbach, Phys. Rev. Lett. **74**(23), 4623 (1995)
5. H. Stapelfeldt, T. Seideman, Rev. Mod. Phys. **75**(2), 543 (2003)
6. H. Sakai, S. Minemoto, H. Nanjo, H. Tanji, T. Suzuki, Phys. Rev. Lett. **90**(8), 083001/1 (2003)
7. I. Nevo, L. Holmegaard, J.H. Nielsen, J.L. Hansen, H. Stapelfeldt, F. Filsinger, G. Meijer, J. Kupper, Phys. Chem. Chem. Phys. **11**(42), 9912 (2009)
8. M. Lapert, E. Hertz, S. Guérin, D. Sugny, Phys. Rev. A **80**, 051403 (2009)
9. M.Z. Hoque, M. Lapert, E. Hertz, F. Billard, D. Sugny, B. Lavorel, O. Faucher, Phys. Rev. A **84**, 013409 (2011)
10. L. Yuan, S.W. Teitelbaum, A. Robinson, A.S. Mullin, Proc. Natl. Acad. Sci. U.S.A. **108**(17), 6872 (2011)
11. A. Korobenko, A.A. Milner, V. Milner, Phys. Rev. Lett. **112**(11), 113004 (2014)
12. O. Korech, U. Steinitz, R.J. Gordon, I.S. Averbukh, Y. Prior, Nat. Photon. **7**(9), 711 (2013)
13. U. Steinitz, Y. Prior, I.S. Averbukh, Phys. Rev. Lett. **112**(1), 013004 (2014)
14. A.A. Milner, A. Korobenko, J. Flo, I.S. Averbukh, V. Milner, Phys. Rev. Lett. **115**(3), 033005 (2015)
15. Y. Khodorkovsky, U. Steinitz, J.M. Hartmann, I.S. Averbukh, Nat. Commun. **6** (2015)
16. K. Mizuse, K. Kitano, H. Hasegawa, Y. Ohshima, Sci. Adv. **1**(6) (2015)
17. M.J. Murray, H.M. Ogden, C. Toro, Q. Liu, D.A. Burns, M.H. Alexander, A.S. Mullin, J. Phys. Chem. A **119**(50), 12471 (2015)
18. K. Lin, Q. Song, X. Gong, Q. Ji, H. Pan, J. Ding, H. Zeng, J. Wu, Phys. Rev. A **92**(1), 013410 (2015)
19. A. Korobenko, V. Milner, Phys. Rev. Lett. **116**(18), 183001 (2016)
20. A.A. Milner, A. Korobenko, V. Milner, Phys. Rev. Lett. **118**(24), 243201 (2017)
21. E. Gershnabel, I.S. Averbukh, Phys. Rev. Lett. **120**(8), 083204 (2018)
22. I. Tutunnikov, E. Gershnabel, S. Gold, I.S. Averbukh, J. Phys. Chem. Lett. **9**:1105–1111 (2018)
23. J. Karczmarek, J. Wright, P. Corkum, M. Ivanov, Phys. Rev. Lett. **82**(17), 3420 (1999)
24. D.M. Villeneuve, S.A. Aseyev, P. Dietrich, M. Spanner, M.Y. Ivanov, P.B. Corkum, Phys. Rev. Lett. **85**(3), 542 (2000)
25. G. Karras, M. Ndong, E. Hertz, D. Sugny, F. Billard, B. Lavorel, O. Faucher, Phys. Rev. Lett. **114**(10), 103001 (2015)
26. S. Zhdanovich, A.A. Milner, C. Bloomquist, J. Floss, I.S. Averbukh, J.W. Hepburn, V. Milner, Phys. Rev. Lett. **107**(24), 243004 (2011)
27. C. Bloomquist, S. Zhdanovich, A.A. Milner, V. Milner, Phys. Rev. A **86**(6), 063413 (2012)
28. S. Fleischer, Y. Khodorkovsky, Y. Prior, I.S. Averbukh, New. J. Phys. **11**, 105039 (2009)
29. K. Kitano, H. Hasegawa, Y. Ohshima, Phys. Rev. Lett. **103**(22), 223002 (2009)
30. Y. Khodorkovsky, K. Kitano, H. Hasegawa, Y. Ohshima, I.S. Averbukh, Phys. Rev. A **83**(2), 023423 (2011)
31. O. Faucher, E. Prost, E. Hertz, F. Billard, B. Lavorel, A.A. Milner, V.A. Milner, J. Zyss, I.S. Averbukh, Phys. Rev. A **94**(5), 051402(R) (2016)
32. E. Prost, H. Zhang, E. Hertz, F. Billard, B. Lavorel, P. Bejot, J. Zyss, I.S. Averbukh, O. Faucher, Phys. Rev. A **96**(4), 043418 (2017)
33. E. Skantzakis, S. Chatziathanasiou, P.A. Carpeggiani, G. Sansone, A. Nayak, D. Gray, P. Tzallas, D. Charalambidis, E. Hertz, O. Faucher, Sci. Rep. **6**, 39295 (2016)
34. A.M. Weiner, Opt. Comm. **284**, 3669 (2011)
35. T. Brixner, G. Gerber, Opt. Lett. **8**(26), 557 (2001)
36. K. Misawa, Adv. Phys. X **1**(4), 544 (2016)
37. T. Brixner, G. Krampert, T. Pfeifer, R. Selle, G. Gerber, Phys. Rev. Lett. **92**(20), 208301 (2004)

38. M. Plewicki, S.M. Weber, F. Weise, A. Lindinger, Appl. Phys. B **86**(2), 259 (2007)
39. E. Hertz, F. Billard, G. Karras, P. Béjot, B. Lavorel, O. Faucher, Opt. Exp. **24**(24), 27702 (2016)
40. J.O. Hirschfelder, C.F. Curtiss, R.B. Bird, *Molecular Theory of Gases and Liquids* (Wiley, New York, 1954)
41. R.N. Zare, *Angular Momentum: Understanding Spatial Aspects in Chemistry and Physics* (Wiley-Interscience, New York, 1988)
42. G. Herzberg, *Molecular Spectra and Molecular Structure, Spectra of Diatomic Molecules*, vol. 1 (Van Nostrand Reinhold Company, New York, 1950)
43. B.A. Garetz, J. Opt. Soc. Am. **71**(5), 609 (1981)
44. I. Bialynicki-Birula, Z. Bialynicka-Birula, Phys. Rev. Lett. **78**(13), 2539 (1997)
45. P.J. Allen, Am. J. Phys. **34**(12), 1185 (1966)
46. B.A. Garetz, S. Arnold, Opt. Commun. **31**(1), 1 (1979)
47. F. Bretenaker, A. Le Floch, Phys. Rev. Lett. **65**(18), 2316 (1990)
48. J. Courtial, D.A. Robertson, K. Dholakia, L. Allen, M.J. Padgett, Phys. Rev. Lett. **81**(22), 4828 (1998)
49. V. Renard, M. Renard, S. Guérin, Y.T. Pashayan, B. Lavorel, O. Faucher, H.R. Jauslin, Phys. Rev. Lett. **90**(15), 153601 (2003)
50. A. Rouzée, E. Hertz, B. Lavorel, O. Faucher, J. Phys. B **41**, 074002 (2008)
51. G. Maroulis, J. Chem. Phys. **118**(6), 2673 (2003)
52. G. Li, T. Zentgraf, S. Zhang, Nat. Phys. **12**(8), 736 (2016)
53. H.J. Simon, N. Bloembergen, Phys. Rev. **171**(3), 1104 (1968)

Chapter 4
Optimal Control Approaches for Aligning/Orienting Asymmetric Top Molecules

Yukiyoshi Ohtsuki, Masataka Yoshida and Yuta Arakawa

Abstract We explain optimal control approaches with the aim of three-dimensional (3D) alignment/orientation of asymmetric molecules by using a combination of dipole and lowest-order-induced dipole interactions, the former of which mixes the rotational states with different parity. The present method enables the numerical design of an optimal temporal structure for the laser pulse including its time-dependent polarization on the basis of the molecular Hamiltonian together with the optimization algorithm. After explaining the theoretical framework, numerical details are examined through a case study of one-dimensional (1D) alignment control that is applied to SO_2.

4.1 Introduction

Quantum optimal control theory provides a first-principles method that simulates external-field-driven dynamics to best achieve a specified physical objective. This simulation, which will be referred to as optimal control simulation, requires knowledge of only the physical objective and the system Hamiltonian, and does not need a pre-determined external field. The design of the external field is involved in the simulation and the external field is semi-automatically derived by the optimization algorithm. It is applicable to all quantum systems ranging from a weak-field regime to a strong-field one, and from ultra-fast dynamics to long-time dynamics. The optimal control simulation was invented in the late 1980s in the field of physical chemistry [1, 2], in which laser pulses that interact with molecules through electric dipole

Y. Ohtsuki (✉) · M. Yoshida · Y. Arakawa
Department of Chemistry, Graduate School of Science, Tohoku University, 6-3 Aramaki Aza-Aoba, Aoba-Ku, Sendai 980-8578, Japan
e-mail: ohtsuki@m.tohoku.ac.jp

M. Yoshida
e-mail: m-yoshida@ms.ifoc.kyushu-u.ac.jp

Y. Arakawa
e-mail: yuta.arakawa.t8@dc.tohoku.ac.jp

© Springer Nature Switzerland AG 2018

K. Yamanouchi et al. (eds.), *Progress in Ultrafast Intense Laser Science XIV*,
Springer Series in Chemical Physics 118,
https://doi.org/10.1007/978-3-030-03786-4_4

interaction are often assumed as the external field. The basic idea is to define the optimal external field such that it maximizes the expectation value of a target operator that specifies the physical objective. We apply the calculus of variations to the expectation value to derive the so-called pulse-design equations, which are coupled nonlinear differential equations that need to be solved iteratively. To reduce computational cost, we usually adopt the effective solution algorithms, often called the monotonic convergence algorithms [3–6], as they guarantee monotonic convergence as a function of iteration steps.

Among a variety of applications of the optimal control simulation, molecular alignment/orientation induced by moderately strong laser pulses is one of the most interesting physical objectives. This is because the molecular alignment/orientation is a fundamental technique that enables us to observe and manipulate molecular wave functions in a molecule-fixed frame [7, 8]. Here, we use the terminology "orientation" ("alignment") when we distinguish (do not distinguish) the head and tail parts of molecules. To selectively control the rotational degrees of freedom without inducing vibrational or electronic excitation, we often use moderately strong non-resonant laser pulses. Then, the rotational dynamics is approximately described by the effective Hamiltonian, in which the molecules interact with the laser pulses through induced-dipole interactions [9–11]. If the temporal width of the laser pulse is much longer than the typical rotational period, the rotational motion is trapped in the induced-dipole potential, which leads to one- or three-dimensional (1D or 3D) alignment depending on the polarization of the laser pulse [12]. This control is often called an adiabatic method [13]. The drawback of using the trap potential is that molecules are not free from the laser fields, which may influence experimental results. To control the rotational motion in a field-free condition, we need to apply a laser pulse in a suitable manner, which is often called a non-adiabatic method [14]. In our recent review of the alignment and orientation control of linear molecules, we examined ways to design multiple laser pulses by using the optimal control simulation and discussed the underlying rotational dynamics [15]. In the present review, we explain the optimal control approach to align/orient asymmetric top molecules in a field-free condition, mainly focusing on the alignment control.

After impulsive laser-pulse excitation, linear and symmetric top molecules are characterized by a periodic motion called a (partial) revival [16–19]. The revival originates from the constructive interference among all or many excited rotational states. During the periods, the molecules are highly aligned/oriented in a field-free condition. The revivals also play a key role in determining the efficient relative timing of the multiple laser pulses to improve the degrees of alignment. The control schemes include the accumulative-squeezing [20, 21], child's-swing [22], repetitive-kick [23], and frequency-network schemes [24], to name a few. Although, rigorously speaking, no such periodic motion is expected for the asymmetric molecules because of the dephasing due to the irregular spacings between the energy eigenvalues, partially repeating alignment would appear, which decreases with time [17]. This suggests that the multiple-pulse excitation would be useful to enhance the degree of alignment of asymmetric top molecules as in the cases of linear/symmetric top molecules.

Here, we introduce some previous studies on the 3D alignment control of asymmetric top molecules. Underwood et al. [25] proposed a combination of two time-separated, linearly polarized laser pulses that have orthogonal polarization directions to achieve 3D alignment. The first laser pulse aligned the most polarizable axis along the polarization direction. When the degree of 1D alignment became a maximum, the second pulse was applied to align the second most polarizable axis while minimizing the torque upon the first aligned axis. In their subsequent study [26], the effectiveness of their scheme with slight modification was experimentally demonstrated by using SO_2 molecules (rotational temperature ~10 K), in which the second pulse appeared soon after the first pulse. As one of the keys to achieving this control is to prepare a highly 1D aligned state by the first pulse, Viftrup et al. [27, 28] adopted a temporally long, linearly polarized laser pulse to tightly hold the most polarizable axis along its polarization direction. Then, the second temporally short, linearly polarized laser pulse kicked the 1D aligned molecule to realize the 3D alignment. This control is called a hold-and-spin scheme. In the experimental realization, they used 3,5-difluoroiodobenzene (DFIB) and 3,4-dibromothiophene (DBT) and found that the maximum degrees of 3D alignment appeared soon after the second short pulse excitation. To realize the field-free 3D alignment control, they proposed a truncated-hold-and-spin scheme, in which the long pulse was turned off more rapidly than the rotational motion [29].

Referring to the adiabatic 3D alignment control, it would be natural to adopt a long elliptically polarized laser pulse with rapid truncation or a short elliptically polarized laser pulse to achieve the field-free 3D alignment. Note that the comparative numerical study using ethene at the rotational temperature of 4 K in [25] showed that the combination of linearly polarized laser pulses leads to a higher degree of 3D alignment than the schemes utilizing elliptically polarized laser pulses. The experiment by Takei et al. [30] adopted the former scheme as part of the combined-field approach to 3D-orient DBT in the presence of a weak static electric field. As for the latter, Rouzée et al. [31] experimentally and numerically demonstrated that a single short elliptically polarized laser pulse with optimal ellipticity may be advantageous to achieve the 3D alignment by using jet-cooled ethylene molecules. Pabst and Santra [32] numerically studied how the multiple elliptically polarized laser pulses with the same ellipticity enhanced the degree of alignment of SO_2 at the rotational temperature of 10 K, in which the number of pulses used in the simulation was from one to four. Their irradiation timings were determined on the basis of multiple-pulse excitation schemes that have been proposed to align linear molecules [20, 21, 23]. They concluded that the so-called accumulative squeezing scheme [20, 21] would be suitable to enhance the 3D alignment because of the lack of clear revivals of SO_2, although the degree of improvement was not significant. Artamonov and Seideman [33] assumed a pair of orthogonal Gaussian pulses and optimized their maximum amplitudes as well as temporal peak positions and widths to best achieve the 3D alignment of variable asymmetric top molecules modeled by rotational constants and polarizabilities. They found that the optimized laser pulses have a general form that consists of overlapping pulses with slightly displaced temporal peak positions, suggesting the advantage of the (truncated) hold-and-spin scheme [27, 28]. They also

noted that the optimized elliptically polarized single pulse [31] can likewise achieve a high degree of alignment, in which the difference between the two schemes is within 1%. Recently, Ren et al. [34] reported that multiple laser pulses with different ellipticities can lead to much better 3D alignment than a single elliptically polarized laser pulse, in which the irradiation timings of the multiple laser pulses are similar to those in [32]. They experimentally demonstrated the effectiveness of the combination of a linearly polarized laser pulse and a sequence of elliptically polarized laser pulses by using DFIB molecules at the rotational temperature of ~1 K. They also noted that the scheme is applicable to other asymmetric top molecules.

According to the above discussions, there still remains some degree of uncertainty regarding how to apply the multiple laser pulses to 3D-align asymmetric molecules, which would make the optimal control approaches useful to resolve the issue. Even if there is no general solution because of the complicated motion of asymmetric molecules, the optimal control simulation can be also useful to design a tailored laser pulse for a given asymmetric top molecule. In Sect. 4.2, we explain the optimal control simulation to 3D-align/orient asymmetric molecules in a general manner and examine the numerical details through a case study of 1D alignment control. In Sect. 4.3, we show numerical examples of 1D alignment of SO_2 molecules. In Sect. 4.4, we present a summary.

4.2 Optimal Control Simulation with Nonlinear Interactions

4.2.1 Hamiltonian of Asymmetric Top Molecules

We introduce the density operator, $\rho(t)$, to describe the time evolution of asymmetric top molecules interacting with laser pulses. The Liouville equation is given by

$$i\hbar\frac{\partial}{\partial t}\rho(t) = \left[H^t, \rho(t)\right], \tag{4.1}$$

where H^t is the total Hamiltonian composed of the molecular Hamiltonian, H_0, and the interaction between the molecules and the laser pulses, V^t,

$$H^t = H_0 + V^t. \tag{4.2}$$

Here, we specify the space-fixed XYZ-coordinate system by using a set of unit vectors, $\{\mathbf{e}_X, \mathbf{e}_Y, \mathbf{e}_Z\}$. The principal axes associated with the moment of inertia and those with the polarizability are referred to as the molecule-fixed abc-coordinate system with a set of unit vectors, $\{\mathbf{e}_a, \mathbf{e}_b, \mathbf{e}_c\}$, and the $\xi\eta\zeta$-coordinate system with a set of unit vectors, $\left\{\mathbf{e}_\xi, \mathbf{e}_\eta, \mathbf{e}_\zeta\right\}$, respectively. The molecular Hamiltonian is expressed as

$$H_0 = AJ_a^2 + BJ_b^2 + CJ_c^2$$
$$= \left(\frac{A+B}{2}\right)\boldsymbol{J}^2 + \left(C - \frac{A+B}{2}\right)J_c^2 + \left(\frac{A-B}{4}\right)\left(J_+^2 + J_-^2\right), \tag{4.3}$$

where A, B, and C are the rotational constants ($A > B > C$) and J_a, J_b, and J_c are the components of the angular momentum operator, $\boldsymbol{J}$, along the a-, b-, and c-axes. The raising and lowering operators in the molecule-fixed frame are defined by $J_\pm = J_a \pm i J_b$.

We consider the interaction, V^t, originating from the electric permanent dipole moment, $\boldsymbol{\mu}$, and the polarizability tensor, $\overleftrightarrow{\alpha}$. If we assume that they interact with different laser pulses, $\boldsymbol{E}_\mu(t)$ and $\boldsymbol{E}(t)$, we will have

$$V^t = V_\mu + V_\alpha = -\boldsymbol{\mu}\cdot\boldsymbol{E}_\mu(t) - \frac{1}{2}\overleftrightarrow{\alpha}\boldsymbol{E}(t)\boldsymbol{E}(t), \tag{4.4}$$

which would be justified by the following practical reason. As the electric dipole interaction, V_μ, and the polarizability interaction, V_α, induce resonant and non-resonant (Raman) transitions between the rotational states, respectively, the central frequencies of the two laser pulses,$\boldsymbol{E}_\mu(t)$ and $\boldsymbol{E}(t)$, are considerably different. In addition, the resonant electric field, $\boldsymbol{E}_\mu(t)$, is often weak enough to contribute little to the polarizability interaction. If this is not the case, we need to modify the polarizability interaction in (4.4), which, however, can be done in a straightforward manner.

We introduce a set of eigenstates of a symmetric top, $\{|JKM\rangle\}$, to calculate the time evolution, where J, K, and M are the quantum numbers of the operators, $\boldsymbol{J}^2$, J_c, and J_Z (space-fixed Z component), respectively. As the raising and lowering operators in (4.3) lead to the non-zero off-diagonal matrix elements

$$\langle JK \mp 2M|J_\pm^2|JKM\rangle$$
$$= \hbar^2\sqrt{J(J+1) - K(K\mp 1)}\sqrt{J(J+1) - (K\mp 1)(K\mp 2)}, \tag{4.5}$$

the eigenstate of the Hamiltonian in (4.3) is expressed as the linear combination of the symmetric top basis

$$H_0|J\tau M\rangle = H_0\sum_K |JKM\rangle a_{\tau K}^J = E_{J\tau}|J\tau M\rangle. \tag{4.6}$$

The initial Boltzmann distribution at rotational temperature, T, is, given by

$$\rho(0) = \sum_{J\tau M} |J\tau M\rangle p_{J\tau}(T)\langle J\tau M| \tag{4.7}$$

where $p_{J\tau}(T) \propto \exp(-E_{J\tau}/k_BT)$ with the Boltzmann constant, k_B.

4.2.2 Optimal Control Simulation

The first step of the optimal control simulation is to specify our physical objective by using a Hermitian operator, W, which is called a target operator, at a specified final time, t_f [1, 2, 15]. Then, the optimization problem ends up with the maximization problem of the objective functional

$$F[\boldsymbol{E}_\mu(t), \boldsymbol{E}(t)] = \mathrm{Tr}\{W\rho(t_\mathrm{f})\} - \int_0^{t_\mathrm{f}} \mathrm{d}t \frac{1}{\hbar A(t)} \big[\boldsymbol{E}_\mu(t)\big]^2, \tag{4.8}$$

where the positive function, $A(t)$, is an input parameter to adjust the penalty due to the pulse energy. We apply calculus of variations to (4.8) to derive the extremum conditions,

$$\boldsymbol{E}_\mu(t) = -A(t)\mathrm{ImTr}\{\Xi(t)\boldsymbol{\mu}\,\rho(t)\} \tag{4.9}$$

and

$$\mathrm{ImTr}\{\,\Xi(t)\vec{\alpha}\boldsymbol{E}(t)\,\rho(t)\} = 0. \tag{4.10}$$

Here, $\Xi(t)$ is the Lagrange multiplier that represents the constraint of (4.1) and obeys the equation of motion

$$i\hbar\frac{\partial}{\partial t}\Xi(t) = \big[(H^t)^\dagger, \Xi(t)\big], \tag{4.11}$$

where $(H^t)^\dagger$ means the Hermitian conjugate of H^t. The final condition is

$$\Xi(t_\mathrm{f}) = W. \tag{4.12}$$

Equations (4.1), (4.9), (4.10), and (4.11) compose the coupled pulse-design equations in the density matrix formalism, which can be solved by the monotonic convergence algorithm [35].

When we fully optimize $\boldsymbol{E}_\mu(t)$ and $\boldsymbol{E}(t)$ including their polarization conditions, it is convenient to set the polarization vectors on the space-fixed XY-plane,

$$\boldsymbol{E}_\mu(t) = E_{\mu X}(t)\mathbf{e}_X + E_{\mu Y}(t)\mathbf{e}_Y \text{ and } \boldsymbol{E}(t) = E_X(t)\mathbf{e}_X + E_Y(t)\mathbf{e}_Y. \tag{4.13}$$

The substitution of (4.13) into (4.9) yields

$$\begin{aligned} &E_{\mu X}(t) = -A(t)\mathrm{ImTr}\{\Xi(t)\mu_X\,\rho(t)\} \\ &\text{and}\quad E_{\mu Y}(t) = -A(t)\mathrm{ImTr}\{\Xi(t)\mu_Y\,\rho(t)\}. \end{aligned} \tag{4.14}$$

This suggests that the structure of $E_{\mu X}(t)$ is determined by $\mu_X = \boldsymbol{\mu} \cdot \mathbf{e}_X$ and indirectly influenced by $E_{\mu Y}(t)$ through $\rho(t)$ and $\Xi(t)$. Similarly, the optimality condition in (4.10) is reduced to

$$\begin{aligned} &\mathrm{ImTr}\{\Xi(t)(\alpha_{XX}E_X(t) + \alpha_{XY}E_Y(t))\rho(t)\} = 0 \\ &\text{and } \ \mathrm{ImTr}\{\Xi(t)(\alpha_{YX}E_X(t) + \alpha_{YY}E_Y(t))\rho(t)\} = 0 \end{aligned} \tag{4.15}$$

in which $E_X(t)$ and $E_Y(t)$ are directly connected to each other in (4.15).

If we could rewrite the pulse-design equations in the wave function form, we would be able to reduce the computational cost. For this purpose, we note that the density operator can be expressed, in terms of a set of wave functions, as

$$\rho(t) = \sum_{J\tau M} |\psi_{J\tau M}(t)\rangle\, p_{J\tau}(T)\langle\psi_{J\tau M}(t)|, \tag{4.16}$$

where each wave function is defined by the Schrödinger equation

$$i\hbar\frac{\partial}{\partial t}|\psi_{J\tau M}(t)\rangle = H^t|\psi_{J\tau M}(t)\rangle \tag{4.17}$$

with the initial condition $|\psi_{J\tau M}(0)\rangle = |J\tau M\rangle$. To replace the Lagrange multiplier operator, $\Xi(t)$, by a set of Lagrange multiplier wave functions, $\{|\xi_{J\tau M}(t)\rangle\}$, while keeping the monotonic convergence behavior of the iteration algorithm, we have to restrict ourselves to a non-negative target operator, W. The equation of motion of $|\xi_{J\tau M}(t)\rangle$ is

$$i\hbar\frac{\partial}{\partial t}|\xi_{J\tau M}(t)\rangle = (H^t)^\dagger|\xi_{J\tau M}(t)\rangle, \tag{4.18}$$

with the final condition, $|\xi_{J\tau M}(t_\mathrm{f})\rangle = W|\psi_{J\tau M}(t_\mathrm{f})\rangle$. According to these modifications, the extremum conditions in (4.9) and (4.10) are replaced by

$$\boldsymbol{E}_\mu(t) = -A(t)\mathrm{Im}\sum_{J\tau M} p_{J\tau}(T)\langle\xi_{J\tau M}(t)|\boldsymbol{\mu}|\psi_{J\tau M}(t)\rangle \tag{4.19}$$

and

$$\mathrm{Im}\sum_{J\tau M} p_{J\tau}(T)\langle\xi_{J\tau M}(t)|\vec{\alpha}\boldsymbol{E}(t)\,|\psi_{J\tau M}(t)\rangle = 0, \tag{4.20}$$

respectively. To deal with the nonlinear interaction with respect to $\boldsymbol{E}(t)$ in (4.4), we have proposed that $\boldsymbol{E}(t)$ should be divided into two artificial components, $\boldsymbol{E}_1(t)$ and $\boldsymbol{E}_2(t)$, such that the nonlinear interaction is expressed as the symmetrical sum of the artificial components [35]. The details will be explained through a case study in the next subsection.

So far, we have not imposed a penalty to the non-resonant laser pulse, $\boldsymbol{E}(t)$, as we have found that the penalty due to the pulse fluence seems to not work well in the case of the polarizability interaction [35]. We may introduce a non-Hermitian interaction potential that is proportional to $[\boldsymbol{E}(t)]^2$, which is referred to as the instantaneous penalty [24], so that intense laser pulses would reduce the norm of the wave functions, resulting in the decrease of the target expectation value. In practice, we replace the polarizability, $\vec{\vec{\alpha}}$, by the non-Hermitian polarizability, $\vec{\vec{\alpha}}_\gamma = \vec{\vec{\alpha}}(1 + i\gamma)$, where the positive constant, γ, determines the physical significance of the penalty. Note that this replacement keeps the monotonic convergence behavior of the iterative solution algorithm. As the instantaneous penalty is an artifact to suppress the maximum intensity of $\boldsymbol{E}(t)$, after obtaining the optimal laser pulses, we need to recalculate all the physical properties by using the original equation of motion ($\gamma = 0$). The instantaneous penalty can be actively utilized to specify the fluence of $\boldsymbol{E}(t)$ by using the iteration-step-dependent $\gamma^{(k)}$ [36]. If the fluence of $\boldsymbol{E}^{(k)}(t)$ at the kth iteration step is larger (smaller) than the target fluence, we may assume a larger (smaller) value of $\gamma^{(k+1)}$ in the next iteration step. We numerically showed that this procedure with an empirically chosen function can lead to optimal laser pulses with specified fluence [36].

4.2.3 *Special Case: 1D Alignment Control with Linearly Polarized Non-resonant Laser Pulses, $E(t)$*

The purpose of this subsection is to explain how to simulate optimal laser pulses in detail through a case study of the 1D alignment control of asymmetric molecules. When we consider a linearly polarized laser pulse, it is convenient to set the polarization vector along the space-fixed Z-axis, $\boldsymbol{E}(t) = E(t)\mathbf{e}_Z$, because of the conservation of the quantum number, M. The wave function is expanded as

$$|\psi_{J\tau M}(t)\rangle = \sum_{J',K'} \left|J'K'M\right\rangle C^{J'}_{MK'}(t) \text{ with } |\psi_{J\tau M}(0)\rangle = |J\tau M\rangle. \tag{4.21}$$

The quantum number, M, is also conserved in the expansion of the Lagrange multiplier, $|\xi_{J\tau M}(t)\rangle$. If we further assume a non-resonant laser pulse that solely induces the polarizability interaction, after the cycle average over the optical frequency, (4.4) is reduced to

$$V^t = V_\alpha = -\frac{1}{4}\alpha_{ZZ}[\varepsilon(t)]^2, \tag{4.22}$$

where $\varepsilon(t)$ is the envelope function of $E(t)$.

By using the notation of Zare [7], we briefly summarize how to calculate the matrix elements of the operator, α_{ZZ}, in our basis, $\{|JKM\rangle\}$. If we introduce the

Wigner rotation matrix, $D^J_{MK}(R)$, with $\hat{R} = (\theta, \phi, \chi)$ being the Euler angle, the eigenstate of a symmetric top, $|JKM\rangle$, is expressed as

$$\langle R \mid JKM\rangle = \sqrt{\frac{2J+1}{8\pi^2}} D^{J*}_{MK}(\hat{R}). \tag{4.23}$$

On the other hand, α_{ZZ} is expressed, in terms of the set of direction cosines, as

$$\alpha_{ZZ} = \left[\mathbf{e}_Z \cdot \mathbf{e}_a \;\; \mathbf{e}_Z \cdot \mathbf{e}_b \;\; \mathbf{e}_Z \cdot \mathbf{e}_c\right] \Omega \begin{bmatrix} \alpha_{\xi\xi} & 0 & 0 \\ 0 & \alpha_{\eta\eta} & 0 \\ 0 & 0 & \alpha_{\varsigma\varsigma} \end{bmatrix} \Omega^{-1} \begin{bmatrix} \mathbf{e}_a \cdot \mathbf{e}_Z \\ \mathbf{e}_b \cdot \mathbf{e}_Z \\ \mathbf{e}_c \cdot \mathbf{e}_Z \end{bmatrix}, \tag{4.24}$$

where the transformation matrix, Ω, that connects the *abc*-coordinate system to the $\xi\eta\zeta$-coordinate system is determined by the molecular structure and defined by

$$\Omega = \begin{bmatrix} \mathbf{e}_a \cdot \mathbf{e}_\xi & \mathbf{e}_a \cdot \mathbf{e}_\eta & \mathbf{e}_a \cdot \mathbf{e}_\varsigma \\ \mathbf{e}_b \cdot \mathbf{e}_\xi & \mathbf{e}_b \cdot \mathbf{e}_\eta & \mathbf{e}_b \cdot \mathbf{e}_\varsigma \\ \mathbf{e}_c \cdot \mathbf{e}_\xi & \mathbf{e}_c \cdot \mathbf{e}_\eta & \mathbf{e}_c \cdot \mathbf{e}_\varsigma \end{bmatrix}. \tag{4.25}$$

If we use the Wigner rotation matrix, (4.24) can be rewritten as

$$\begin{aligned} \alpha_{ZZ} = {} & (\alpha_{aa} + \alpha_{bb} + \alpha_{cc}) \frac{D^0_{00}(\hat{R})}{3} + (-\alpha_{aa} - \alpha_{bb} + 2\alpha_{cc}) \frac{D^2_{00}(\hat{R})}{3} \\ & + (\alpha_{aa} - \alpha_{bb} - 2i\alpha_{ab}) \frac{D^2_{02}(\hat{R})}{\sqrt{6}} + (\alpha_{aa} - \alpha_{bb} + 2i\alpha_{ab}) \frac{D^2_{0-2}(\hat{R})}{\sqrt{6}} \\ & + 2(\alpha_{ac} - i\alpha_{bc}) \frac{D^2_{01}(\hat{R})}{\sqrt{6}} - 2(\alpha_{ac} + i\alpha_{bc}) \frac{D^2_{0-1}(\hat{R})}{\sqrt{6}}, \end{aligned} \tag{4.26}$$

where we use the Clebsch-Gordan series. From (4.26), the calculation of the matrix elements ends up with the integral of the triple product of the Wigner rotational matrices. With these calculated matrix elements, we solve the differential equations (4.17–4.20) with respect to the expansion coefficients in (4.21) by employing a standard procedure, such as the Runge-Kutta method.

To solve the coupled pulse-design equations in the presence of the polarizability interaction, we divide the envelope function, $\varepsilon(t)$, into two artificial components, $\varepsilon_1(t)$ and $\varepsilon_2(t)$. The interaction in (4.22) is formally expressed as a symmetrical product of the artificial components, i.e., $V^t = -\alpha_{ZZ}\varepsilon_1(t)\varepsilon_2(t)/4$. Starting from the initial trial envelope functions, $\varepsilon_1^{(0)}(t)$ and $\varepsilon_2^{(0)}(t)$, we solve the pulse-design equations iteratively by using the monotonic convergence algorithms [35]. One member of the algorithms at the kth iteration step is summarized as follows:

$$i\hbar \frac{\partial}{\partial t} \left|\xi^{(k)}_{J\tau M}(t)\right\rangle = \left\{H_0 - \frac{1}{4}\alpha_{ZZ}(1 - i\gamma)\varepsilon_1^{(k)}\varepsilon_2^{(k-1)}\right\} \left|\xi^{(k)}_{J\tau M}(t)\right\rangle, \tag{4.27}$$

with the final condition, $\left|\xi^{(k)}_{J\tau M}(t_{\rm f})\right\rangle = W\left|\psi^{(k-1)}_{J\tau M}(t_{\rm f})\right\rangle$, and

$$i\hbar\frac{\partial}{\partial t}\left|\psi^{(k)}_{J\tau M}(t)\right\rangle = \left\{H_0 - \frac{1}{4}\alpha_{ZZ}(1+i\gamma)\varepsilon_1^{(k)}\varepsilon_2^{(k)}\right\}\left|\psi^{(k)}_{J\tau M}(t)\right\rangle \tag{4.28}$$

with the initial condition, $\left|\psi^{(k)}_{J\tau M}(0)\right\rangle = |J\tau M\rangle$, where γ is the instantaneous penalty parameter (see Sect. 4.2.2). The envelope functions are updated by

$$\begin{aligned}&\varepsilon_1^{(k)}(t) - \varepsilon_1^{(k-1)}(t)\\ &= -\lambda^{(k)}(t){\rm Im}\sum_{J\tau M} p_{J\tau}(T)\left\langle\xi^{(k)}_{J\tau M}(t)\right|\alpha_{ZZ}(1+i\gamma)\varepsilon_2^{(k-1)}(t)\left|\psi^{(k-1)}_{J\tau M}(t)\right\rangle\end{aligned} \tag{4.29}$$

and

$$\begin{aligned}&\varepsilon_2^{(k)}(t) - \varepsilon_2^{(k-1)}(t)\\ &= -\lambda^{(k)}(t){\rm Im}\sum_{J\tau M} p_{J\tau}(T)\left\langle\xi^{(k)}_{J\tau M}(t)\right|\alpha_{ZZ}(1+i\gamma)\varepsilon_1^{(k)}(t)\left|\psi^{(k)}_{J\tau M}(t)\right\rangle,\end{aligned} \tag{4.30}$$

where the positive function, $\lambda^{(k)}(t)$, is a parameter that characterizes the solution search speed and accuracy. If we adjust the pulse fluence, we may employ the iteration-step-dependent parameter, $\gamma^{(k)}$, instead of γ.

4.3 Numerical Example

For the sake of numerical illustration, we consider the 1D alignment control of SO_2 by linearly polarized laser pulses [37]. The SO_2 molecule has been studied to evaluate the effectiveness of the alignment control schemes [26, 32] and therefore, could be regarded as a "standard" molecule. We assume that the polarization vector is parallel to the space-fixed Z-axis. Because of the C_{2v} symmetry around the c-axis and the nuclear spin statistics of the oxygen atoms, the basis functions with even K numbers are used to expand the wave functions and the Lagrange multipliers. The rotational constants are $A = 2.028\ {\rm cm}^{-1}$, $B = 0.3442\ {\rm cm}^{-1}$, and $C = 0.2935\ {\rm cm}^{-1}$ [38]. The polarizability tensor has a diagonal form in the principal axis of inertia, the components of which are given in value by $\alpha_{aa} = 31.32$, $\alpha_{bb} = 20.80$, and $\alpha_{cc} = 18.66$ in units of ${\rm Å}^3$ [39].

Our control objectives are to align the a-axis and the b-axis along the Z-axis, in which the degrees of alignment are evaluated by the expectation values of the target operators, $W_a = (\mathbf{e}_a \cdot \mathbf{e}_Z)^2 = \cos^2\theta_{aZ}$ and $W_b = (\mathbf{e}_b \cdot \mathbf{e}_Z)^2 = \cos^2\theta_{bZ}$, respectively. We assume the rotational temperature, T=1 K. For convenience, time is measured in units of $T_{\rm rot} = 1/2(B+C) = 26.2$ ps and the final time is set to $t_{\rm f} = 4.0$. According to the procedure explained in Sect. 4.2.3, we solve the coupled pulse-design equations in which the initial trial envelope function is set to

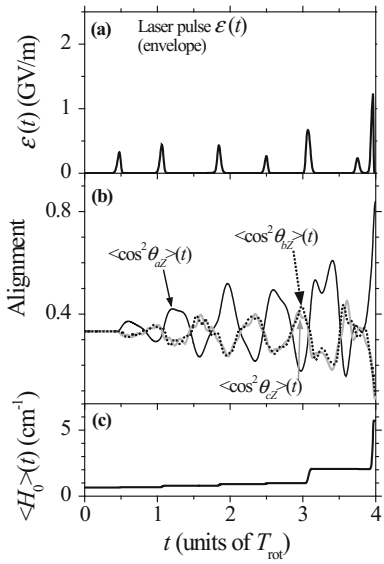

Fig. 4.1 Alignment control of the a-axis of SO_2 along the Z-axis. **a** Optimal envelope function, **b** time evolution of the expectation values of the squares of the direction cosines, and **c** that of the expectation value of H_0 as a function of time. Time is measured in units of T_{rot}

$$\varepsilon_1^{(0)}(t) = \varepsilon_2^{(0)}(t) = \begin{cases} \varepsilon_0 \sin(\pi t / 2\tau_0) & (0 \le t \le \tau_0) \\ \varepsilon_0 & (\tau_0 \le t \le t_{\mathrm{f}} - \tau_0) \\ \varepsilon_0 \sin[\pi(t_{\mathrm{f}} - t)/2\tau_0] & (t_{\mathrm{f}} - \tau_0 \le t \le t_{\mathrm{f}}) \end{cases}, \tag{4.31}$$

where $\tau_0 = 0.1$ and pulse fluence is set to 0.1 J/cm^2.

When the target operator and the target fluence are chosen as $W_a = \cos^2\theta_{aZ}$ and $f_0 = 0.3$ J/cm^2, we obtain the numerical results in Fig. 4.1. The optimal pulse in Fig. 4.1a is composed of several subpulses with almost regular time intervals of ~2/3 and leads to the optimal degree of alignment, $\mathrm{Tr}\{\rho(t_{\mathrm{f}})\cos^2\theta_{aZ}\} = 0.84$ [Fig. 4.1b]. The simple structure of the optimal pulse could be explained by the large rotational constant and the polarizability component along the a-axis, which are much larger than the other components. Because of this, SO_2 behaves like a linear or symmetric top molecule to some extent. In fact, the timing of each subpulse coincides with the timing when the change in time of $\mathrm{Tr}\{\rho(t)\cos^2\theta_{aZ}\}$ becomes locally maximum, which would be consistent with the child's swing control scheme [22] in the case of diatomic molecules.

A more interesting target would be to align the b-axis along the Z-axis as its rotational constant and the polarizability component is neither largest nor smallest. Figure 4.2 shows the results. Although the optimization conditions are the same as those in Fig. 4.1, we see that the optimal pulse has a much more complicated structure than that in Fig. 4.1a, leading to a lower degree of alignment,

$\mathrm{Tr}\{\rho(t_{\mathrm{f}})\cos^2\theta_{bZ}\} = 0.63$. By comparing Fig. 4.2a with b, we find that the timing of each subpulse again coincides with the timing when the change in time of $\mathrm{Tr}\{\rho(t)\cos^2\theta_{aZ}\}$, [not $\mathrm{Tr}\{\rho(t)\cos^2\theta_{bZ}\}$] becomes locally maximum. That means

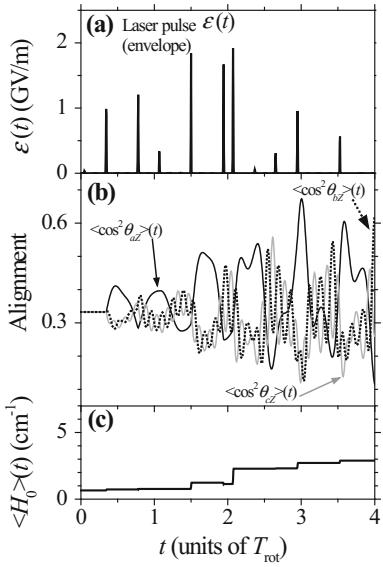

Fig. 4.2 Alignment control of the b-axis of SO_2 along the Z-axis. **a** Optimal envelope function, **b** time evolution of the expectation values of the squares of the direction cosines, and **c** that of the expectation value of H_0 as a function of time. Time is measured in units of T_{rot}

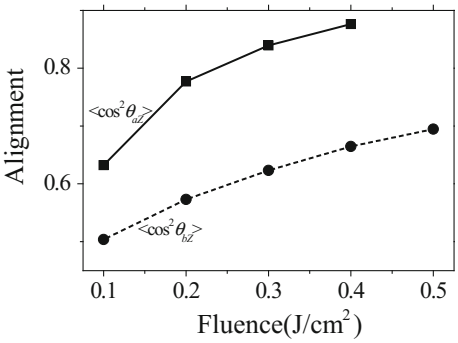

Fig. 4.3 Optimized degrees of alignment as a function of pulse fluence. The solid line with solid squares (dashed line with solid circles) shows the results when the a-axis (b-axis) alignment is chosen as the target

that the optimal pulse tends to indirectly align the b-axis mainly by utilizing the interaction through the a-component of the polarizability.

One may wonder if a laser pulse with a higher fluence may open the direct excitation control path to improve the degree of b-axis alignment. We, thus, optimize the laser pulses by assuming several values of the pulse fluence, the results of which are summarized in Fig. 4.3. We could conclude that the most polarizable axis (a-axis in the present case) dominates the alignment control. However, we could also see the increase of the degree of b-axis alignment with pulse fluence. This would suggest that we could align any molecular axis along a specified direction at the expense of a highly structured pulse with a high fluence.

In the above numerical examples, we have focused on the linearly polarized laser pulses to achieve the 1D alignment of SO_2. When controlling the 3D alignment of SO_2, we have to optimize the time-dependent polarization vectors in addition to the

temporal structures of the laser pulses. The optimal control simulation of the 3D alignment and orientation is currently under investigation [40].

Finally, we discuss practical limitations in the present optimal control simulations, which largely come from the long computing time since we need to iteratively solve the pulse-design equations. We empirically found that the number of the iteration steps to achieve the convergence is 10^3–10^4 when the iteration starts from the initial guess pulse with a flat envelope function (4.31). For the total computing time to be shorter than 10^3–10^4 min, the computing time of each iteration should be a few minutes at most. Because of this, if we adopt the eigenstates of a symmetric top as the basis, the maximum quantum number of J would be 10–20 due to the large number of the basis states, which imposes restrictions on the initial thermal distribution. To treat rotational dynamics at room temperature, we may have to rely on approximated methods such as introducing a random phase wave function (RPWF) [41].

4.4 Summary

We have explained optimal control approaches with the aim of 3D alignment/orientation of asymmetric molecules. We have assumed combined interactions originating from the electric permanent dipole moment and polarizability (lowest-order induced dipole), and examined how to optimize the laser pulses in a general manner (Sect. 4.2.2). To be more specific, we have considered 1D alignment by using a linearly polarized laser pulse to explain the numerical details (Sect. 4.2.3). As a numerical example, we have applied the optimal control simulation to the 1D control of SO_2 molecules and showed that the degree of complexity of the pulse structure largely depends on the choice of the target molecular axis. So far, we have considered isolated molecules. One recent study showed the adiabatic 3D alignment of 3,5-dichloroiodobenzene (DCIB) embedded inside helium nanodroplets by using 160 ps long, elliptically polarized laser pulses [42]. The long coherent rotational motion with revivals of I_2 embedded inside the helium nanodroplets was also reported although the duration was dependent on the pulse fluence [43]. The preset optimal control simulation can be straightforwardly extended to include such a dissipative environment [4, 44].

The 3D alignment/orientation control of asymmetric top molecules is a fundamental technique to observe and manipulate molecules in a molecule-fixed frame. As we avoid orientation averaging over the sample by using aligned molecules, for example, we can obtain high-contrast diffraction patterns, which is a key step toward making ultrafast "molecular movies" of chemical reactions [45]. In addition to the control of molecular rotational motion, the optimal control simulation numerically designs a laser pulse that best achieves a specified objective by solely using the system Hamiltonian at least in principle. It is, thus, especially useful to predict an effective control knob to manipulate complex systems and/or novel phenomena, in which our physical consideration does not necessarily lead to a satisfactory solution.

In this sense, ultrafast dynamics induced by attosecond laser pulses [46] would be a challenging and promising research subject for optimal control simulation.

Acknowledgements We thank Dr. N. Takemoto for stimulating discussions. YO acknowledges support from a Grant-in-Aid for Scientific Research (C) (15K05373) and partly from the Joint Usage/Research Program on Zero-Emission Energy Research, Institute of Advanced Energy, Kyoto University (ZE30B-16). This work is also partly supported by a Grant-in-Aid for JSPS Fellows (17J02010).

References

1. A.P. Peirce, M.A. Dahleh, H. Rabitz, Phys. Rev. A **37**, 4950 (1988)
2. R. Kosloff, S.A. Rice, P. Gaspard, S. Tersigni, D.J. Tannor, Chem. Phys. **139**, 201 (1989)
3. W. Zhu, J. Botina, H. Rabitz, J. Chem. Phys. **108**, 1953 (1998)
4. Y. Ohtsuki, W. Zhu, H. Rabitz, J. Chem. Phys. **110**, 9825 (1999)
5. Y. Ohtsuki, K. Nakagami, Y. Fujimura, W. Zhu, H. Rabitz, J. Chem. Phys. **114**, 8867 (2001)
6. Y. Ohtsuki, G. Turinici, H. Rabitz, J. Chem. Phys. **120**, 5509 (2004)
7. R.N. Zare, *Angular Momentum* (Wiley, New York, 1988)
8. D. Herschbach, Eur. Phys. J. D **38**, 3 (2006)
9. B. Friedrich, D. Herschbach, Phys. Rev. Lett. **74**, 4623 (1995)
10. B. Friedrich, D. Herschbach, J. Phys. Chem. **99**, 15686 (1995)
11. B. Friedrich, D. Herschbach, J. Phys. Chem. A **103**, 10280 (1999)
12. J.J. Larsen, K. Hald, N. Bjerre, H. Stapelfeldt, T. Seideman, Phys. Rev. Lett. **85**, 2470 (2000)
13. H. Stapelfeldt, T. Sideman, Rev. Mod. Phys. **75**, 543 (2003)
14. T. Seideman, E. Hamilton, Adv. At. Mol. Opt. Phys. **52**, 289 (2006)
15. Y. Ohtsuki, M. Yoshida, K. Nakashima, K. Arai, K. Nakajima, Adv. Multi-photon Process Spectro **13**, 55 (2016)
16. N. Mankoč-Borštnik, L. Fonda, B. Borštnik, Phys. Rev. A **35**, 4132 (1987)
17. P.M. Felker, J. Phys. Chem. **96**, 7844 (1992)
18. C. Leichtle, ISh Averbukh, W.P. Schleich, Phys. Rev. Lett. **77**, 3999 (1996)
19. T. Seideman, Phys. Rev. Lett. **83**, 4971 (1999)
20. M. Leibscher, ISh Averbukh, H. Rabitz, Phys. Rev. Lett. **90**, 213001 (2003)
21. M. Leibscher, ISh Averbukh, H. Rabitz, Phys. Rev. A **69**, 013402 (2004)
22. K.F. Lee, E.A. Shapiro, D.M. Villeneuve, P.B. Corkum, Phys. Rev. A **73**, 033403 (2006)
23. J.P. Cryan, P.H. Bucksbaum, R.N. Coffee, Phys. Rev. A **80**, 063412 (2009)
24. H. Abe, Y. Ohtsuki, Phys. Rev. A **83**, 053410 (2011)
25. J.G. Underwood, B.J. Sussman, A. Stolow, Phys. Rev. Lett. **94**, 143002 (2005)
26. K.F. Lee, D.M. Villeneuve, P.B. Corkum, A. Stolow, J.G. Underwood, Phys. Rev. Lett. **97**, 173001 (2006)
27. S.S. Viftrup, V. Kumarappan, S. Trippel, H. Stapelfeldt, E. Hamilton, T. Seideman, Phys. Rev. Lett. **99**, 143602 (2007)
28. S.S. Viftrup, V. Kumarappan, L. Holmegaard, C.Z. Bisgaard, H. Stapelfeldt, M. Artamonov, E. Hamilton, T. Seideman, Phys. Rev. A **79**, 023404 (2009)
29. J.G. Underwood, M. Spanner, MYu. Ivanov, J. Mottershead, B.J. Sussman, A. Stolow, Phys. Rev. Lett. **90**, 223001 (2003)
30. D. Takei, J.H. Mun, S. Minemoto, H. Sakai, Phys. Rev. A **94**, 013401 (2016)
31. A. Rouzée, S. Guérin, O. Faucher, B. Lavorel, Phys. Rev. A **77**, 043412 (2008)
32. S. Pabst, R. Santra, Phys. Rev. A **81**, 065401 (2010)
33. M. Artamonov, T. Seideman, Phys. Rev. A **82**, 023413 (2010)
34. X. Ren, V. Makhija, V. Kumarappan, Phys. Rev. Lett. **112**, 173602 (2014)

35. Y. Ohtsuki, K. Nakagami, Phys. Rev. A **77**, 033414 (2008)
36. M. Yoshida, Y. Ohtsuki, Phys. Rev. A **90**, 013415 (2014)
37. M. Yoshida, Y. Ohtsuki, unpublished
38. H.M. Frey, P. Beaud, T. Gerber, B. Mischler, P.P. Radi, A.P. Tzannis, J. Raman Spectro. **31**, 71 (2000)
39. D. Xenides, G. Maroulis, Chem. Phys. Lett. **319**, 618 (2000)
40. M. Yoshida, N. Takemoto, Y. Ohtsuki, Phys. Rev. A in press
41. R. Damari, S. Kallush, S. Fleischer, Phys. Rev. Lett. **117**, 103001 (2016)
42. A.S. Chatterley, B. Shepperson, H. Stapelfeldt, Phys. Rev. Lett. **119**, 073202 (2017)
43. B. Shepperson, A.A. Søndergaard, L. Christiansen, J. Kaczmarczyk, R.E. Zillich, M. Lemeshko, H. Stapelfeldt, Phys. Rev. Lett. **118**, 203203 (2017)
44. Y. Ohtsuki, J. Chem. Phys. **119**, 661 (2003)
45. R.J.D. Miller, Science **343**, 1108 (2014)
46. T. Okino, Y. Furukawa, T. Shimizu, Y. Nabekawa, K. Yamanouchi, K. Midorikawa, J. Phys. B: At. Mol. Opt. Phys. **47**, 124007 (2014)

Chapter 5
Elucidating the Origins of Vibrational Coherences of Polyatomic Molecules Induced by Intense Laser Fields

Zhengrong Wei, Jialin Li, Lin Wang, Soo Teck See, Mark Hyunpong Jhon, Yingfeng Zhang, Fan Shi, Minghui Yang and Zhi-Heng Loh

Abstract Strong-field laser-molecule interaction can be used to trigger and probe ultrafast quantum dynamics. Previous studies aimed at elucidating the origins of vibrational coherences induced by intense laser fields have been performed on diatomic molecules. Furthermore, in all cases examined to date, vibrational wave packet motion is found to be induced by *R*-selective depletion; wave packet motion launched by bond softening, though theoretically predicted, remains hitherto unobserved. Here, we exploit the exquisite sensitivity of femtosecond extreme ultraviolet absorption spectroscopy to sub-picometer structural changes to observe both bond softening-induced vibrational wave packets, launched by the interaction of intense laser pulses with iodomethane, as well as multimode vibrational motion of the parent ion produced by strong-field ionization. In addition, we show that the time-dependent wave packet-induced modulation of extreme ultraviolet transition energies directly

Adapted from the article "Elucidating the origins of multimode vibrational coherences of polyatomic molecules induced by intense laser fields" *Nat. Commun.* **8**, 735 (2017), published under the Creative Commons Attribution 4.0 International License (CC BY).

Z. Wei · J. Li · L. Wang · S. T. See · Z.-H. Loh (✉)
Division of Chemistry and Biological Chemistry, Division of Physics and Applied Physics, School of Physical and Mathematical Sciences, Nanyang Technological University, Singapore 637371, Singapore
e-mail: zhiheng@ntu.edu.sg

M. H. Jhon
Institute of High Performance Computing, A*STAR, 1 Fusionopolis Way #16-16 Connexis, Singapore 138632, Singapore

Y. Zhang · F. Shi · M. Yang
Key Laboratory of Magnetic Resonance in Biological Systems, State Key Laboratory of Magnetic Resonance and Atomic and Molecular Physics, National Center for Magnetic Resonance in Wuhan, Wuhan Institute of Physics and Mathematics, Chinese Academy of Sciences, Wuhan 430071, China

Z.-H. Loh
Centre for Optical Fibre Technology, The Photonics Institute, Nanyang Technological University, Singapore 639798, Singapore

© Springer Nature Switzerland AG 2018

K. Yamanouchi et al. (eds.), *Progress in Ultrafast Intense Laser Science XIV*, Springer Series in Chemical Physics 118,
https://doi.org/10.1007/978-3-030-03786-4_5

furnish vibronic coupling strengths involving core-level transitions, from which geometrical parameters of transient core-excited states can be obtained.

5.1 Introduction

Femtosecond intense laser-matter interaction [1] has emerged as a powerful tool for investigating the ultrafast quantum dynamics of molecules via processes such as high-order harmonic generation [2], above-threshold ionization [3], and laser-induced electron diffraction [4]. These phenomena have in turn been applied to, for example, the tomographic imaging of molecular orbitals [5, 6], the investigation of attosecond electronic wave packet dynamics [7–9], and the retrieval of transient molecular structures [10–12]. While the main emphasis of many of these studies is the investigation of electronic dynamics, it is important to realize that the intense laser-molecule interaction also induces vibrational motion, whose coupling to the electronic degrees of freedom will influence the outcome and analysis of experiments and theories that nominally seek to address electron dynamics [13–15]. Other factors that motivate the investigation of coherent vibrational dynamics in the strong-field regime include the possibility of using intense laser fields to manipulate molecular dynamics [16–19] and the identification of ion electronic states produced by strong-field ionization by measuring their vibrational quantum beat frequencies [20].

Beyond vibrational wave packet motion in ions triggered by strong-field ionization, the interaction of intense laser pulses with molecules can also generate vibrational coherences in the electronic ground state of neutral species. Two different mechanisms have been proposed: *R*-selective depletion [21] (Fig. 5.1a) and bond softening [22] (Fig. 5.1b). *R*-selective depletion emerges from the dependence of the strong-field ionization rate on the nuclear coordinate, which furnishes a vibrational probability density that is described by a non-stationary state after depletion of the ground-state population by ionization. On the other hand, bond softening arises from the field-induced distortion of the electronic ground-state potential, which drives the initially stationary vibrational probability density distribution away from its equilibrium position, hence initiating wave packet motion. Previous investigations of vibrational coherences induced on the electronic ground-state by intense laser fields have identified *R*-selective depletion as the dominant mechanism for their generation [23–25]. In pioneering studies by Ullrich et al., for example, an initial cosinusoidal oscillation phase of $(0.946 \pm 0.001)\pi$ rad in the temporal evolution of the D_2 bond length (Fig. 5.2) suggests the launching of the vibrational wave packet from the inner turning point of the D_2 potential [23]. This observation is consistent with the larger ionization potential, and hence, lower ionization rate, for D–D bond lengths shorter than the equilibrium bond length. Cosinusoidal phases approaching 0 mod π, indicative of *R*-selective depletion, are also observed for vibrational coherences generated in the electronic ground states of I_2 [24] and Br_2 [25]. These studies raise the question as to whether vibrational wave packets can be created by bond softening. Furthermore, the launching of vibrational wave packets in the electronic ground

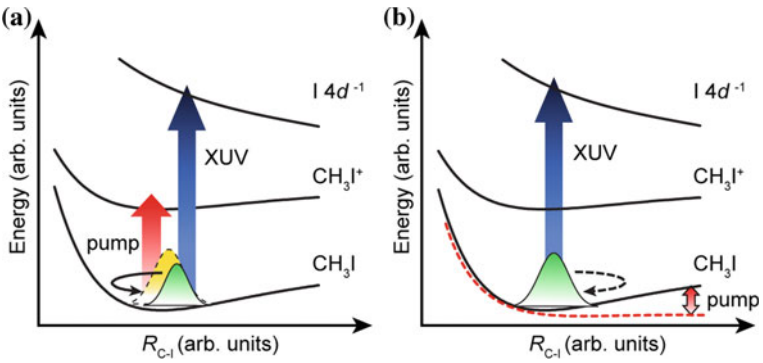

Fig. 5.1 Schematic illustration of vibrational wave packet generation along the C–I stretching mode in the electronic ground state of CH_3I by **a** *R*-selective depletion and **b** bond softening. Vibrational wave packet motion is induced by an intense laser field and is subsequently probed by XUV absorption

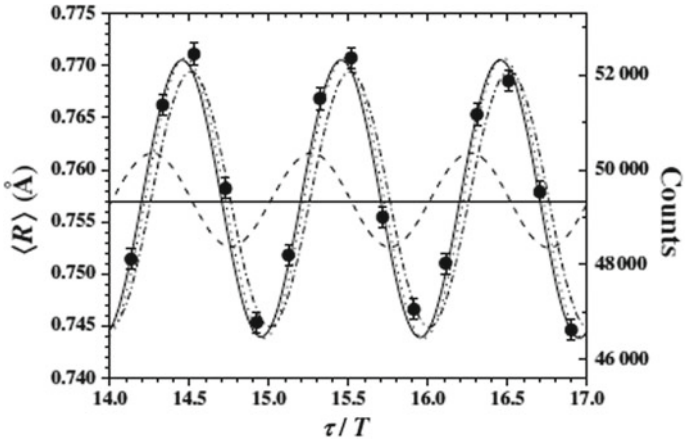

Fig. 5.2 Experimental evidence for vibrational wave packet generation by *R*-selective depletion in the electronic ground state of D_2. The change in the mean internuclear separation as a function of the delay between pump-probe time delay corresponds to an initial cosinusoidal phase of $(0.946 \pm 0.001)\,\pi$ rad. Reprinted with permission from [23]. Copyright (2006) American Physical Society

state of molecules by intense laser pulses remains to be generalized from diatomics to polyatomics. The ability to harness intense laser fields to drive vibrational coherences complements nonresonant impulsive stimulated Raman scattering, which operates in the perturbative limit at relatively low laser intensities [26].

Here, we employ femtosecond extreme ultraviolet (XUV) absorption spectroscopy [27, 28] to investigate multimode coherent vibrational motion induced by intense laser fields in neutral iodomethane (CH_3I) and its parent ion (CH_3I^+). XUV absorption spectroscopy is well-suited to the present study because it can distin-

guish, with electronic state resolution, the iodine (I) 4*d* core level transitions of CH_3I and CH_3I^+, as well as those of the atomic fragments I and I^+. In the case of the CH_3I $\tilde{X}\,^1A_1$ electronic ground state, analysis of the spectral modulations induced by C–I stretching motion (υ_3) yields the relative contributions of bond softening and *R*-selective depletion. In addition, wave packet motions along the C–I stretch (υ_3) and CH_3 umbrella (υ_2) modes are observed in the CH_3I^+ $\tilde{X}^+\,^2E_{3/2}$ parent ion. The results provide unambiguous evidence for the existence of bond softening-induced wave packets and demonstrate the sensitivity of femtosecond XUV absorption spectroscopy to structural changes on the sub-picometer scale. Furthermore, we show that the structural parameters of transient core-excited states can be retrieved from the time-dependent XUV absorption spectra.

5.2 Femtosecond XUV Absorption Spectroscopy

The experimental apparatus for femtosecond XUV absorption spectroscopy (Fig. 5.3a) is based on an amplified femtosecond laser system (Femtolasers GmbH) with an output center wavelength of 800 nm, pulse duration of 25 fs FWHM, and output pulse energy of 3 mJ at 1-kHz repetition rate. The laser output is spectrally broadened in a 1-m-long hollow-core fiber filled with 1.5 bar of helium gas before it is temporally recompressed by a set of chirped mirrors (Ultrafast Innovations GmbH). The visible-to-near-infrared (NIR) output from the chirped mirror compressor spans 553–962 nm at −10 dB (Fig. 5.3b), and has a carrier wavelength of 786 nm, a FWHM duration of 5.6 fs (Fig. 5.3c), and a pulse energy of 1.2 mJ.

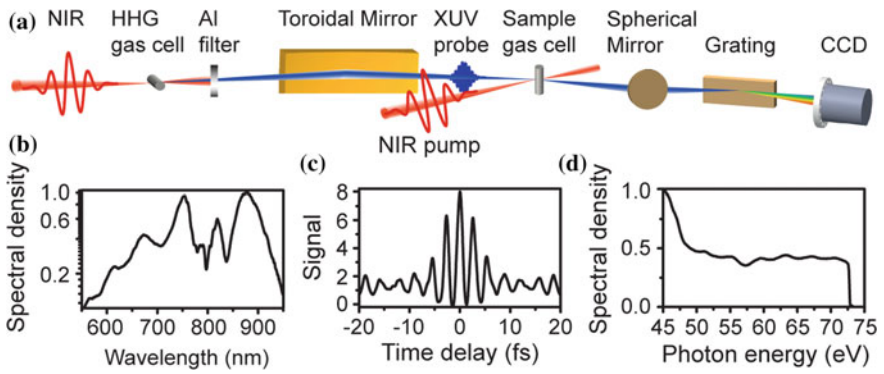

Fig. 5.3 **a** Schematic illustration of the experimental setup for femtosecond time-resolved XUV absorption spectroscopy. **b** The spectrum of the few-cycle laser pulse used to drive high-order harmonic generation (HHG) and strong-field ionization of the sample (plotted on a logarithmic scale). **c** Measured interferometric autocorrelation trace of a 5.6-fs FWHM laser pulse. **d** XUV spectrum generated from argon gas via HHG. The spectrum beyond 72.64 eV is blocked by the L_3 edge cut-off of the Al foils employed in the experiments

The XUV probe pulse is produced by focusing 0.8-mJ of the few-cycle output into a 2-mm-long argon gas cell with a quasi-static pressure of 54 mbar to drive high-order harmonic generation (HHG). The residual visible-NIR laser beam is removed by a 0.2-μm-thick Al foil positioned after the HHG gas cell. The XUV beam is refocused by a toroidal mirror (ARW Optical) that is designed for 1:1 relay-imaging of the XUV source onto the sample target. After the sample target, the transmitted XUV beam passes through another 0.2-μm-thick Al foil before it enters a home-built XUV spectrometer.

The XUV spectrometer is equipped with a concave mirror (ARW Optical), a varied-line-spaced grating (Hitachi), and a thermoelectrically cooled X-ray CCD camera (Princeton Instruments). A typical XUV probe spectrum produced by HHG with argon is shown in Fig. 5.3d. The spectrometer is calibrated by observing the positions of the $^2P_{3/2} \rightarrow {}^2D_{5/2}$ and $^2P_{1/2} \rightarrow {}^2D_{3/2}$ transitions [29] of Xe^+, located at 55.39 and 56.08 eV, respectively, the $4d^9\left(^2D_{5/2}\right)6p$, $4d^9\left(^2D_{5/2}\right)7p$, $4d^9\left(^2D_{3/2}\right)6p$, and $4d^9\left(^2D_{3/2}\right)7p$ resonances [30] of neutral Xe, located at 65.11, 66.37, 67.04, and 68.34 eV, respectively, and the aluminum L_3 edge [31] at 72.64 eV. The spectral resolution is determined from the fit of the Xe^+ $^2P_{3/2} \rightarrow {}^2D_{5/2}$ transition to a Voigt profile, where the Lorentzian linewidth is fixed as the natural linewidth of the transition (122 meV) [29] and the Gaussian width is determined by the spectrometer resolution. In this manner, the resolution is found to be 47 meV FWHM in the XUV photon energy range employed in the present study.

Pump pulses in the visible-NIR with 0.17-mJ energy and 5.6-fs FWHM duration are loosely focused by a 1-m focal length spherical mirror onto the sample target. The resultant peak intensity of 1.9×10^{14} W/cm^2 drives strong-field ionization of the sample. The sample target is a 3-mm path length quasi-static gas cell with 250-μm-diameter entrance and exit pinholes. The pump beam intersects the XUV probe beam at an angle of 1° at the sample target. For the present experiments, the gas cell is heated to 353 K and the CH_3I vapor pressure in the gas cell is 14 mbar. The CH_3I sample (Merck, >99% purity) was used as received. A variable time delay between the pump and probe pulses is introduced by means of a computer-controlled piezo-driven delay stage (Physik Instrumente GmbH) positioned in the path of the pump beam. At each time delay, the XUV spectra, $S(E, t)$, are accumulated over 0.5 s and referenced to the XUV spectrum collected at −500-fs time delay, $S(E, t = -500\,\text{fs})$, such that the differential absorption signal is given by $\Delta A(E, t) = -\log[S(E, t)/S(E, t = -500\,\text{fs})]$. The midpoint of the rise in the CH_3I^+ $\left(\tilde{X}^{+2}E_{3/2}\right)$ parent ion signal at 47.0 eV, when the instantaneous ionization rate is the highest, is used to define time-zero to a precision of $\Delta t_0 = 1.2$ fs. This timing jitter in turn contributes to the uncertainty in the initial phase of the wave packet-induced oscillation via $\Delta\phi = \omega\Delta t_0$, where ω is the oscillation frequency.

5.3 Experimental Results

The differential XUV absorption spectra collected as a function of pump-probe time delay is shown in Fig. 5.4. The XUV absorption in this energy range originates from transitions involving the spin-orbit-split I $4d$ core level to the unoccupied valence orbitals with primarily I $5p$ character. Modulations of the XUV absorption spectra as a function of time delay are observed in the region of the neutral CH_3I ground-state bleach transitions (~50–53 eV), i.e., the I $4d_j \rightarrow \sigma^*_{C-I}$ transitions [32] ($j = 3/2$ or $5/2$). The positive differential absorption signals observed in the ~46–49-eV range are due to the CH_3I^+ parent ion and the atomic I and I^+ photoproducts of dissociative ionization [33]. The I $4d_{5/2} \rightarrow e^{-1}_{3/2}$ transition of the CH_3I^+ $\tilde{X}^{+\,2}E_{3/2}$ parent ion appears as a prominent peak at 47.0 eV, consistent with the energetic difference between the binding energies of the I $4d_{5/2}$ core level [34] and the $e_{3/2}$ valence level [35] $\left(E_{4d_{5/2}} - E_{e_{3/2}} = 47.08\ \text{eV}\right)$. Analysis of the appearance times of I and I^+ reveals ultrafast dissociative ionization dynamics [36]. Here, we focus on the vibrational wave packet dynamics encoded in the I $4d_j \rightarrow \sigma^*_{C-I}$ and $4d_{5/2} \rightarrow e^{-1}_{3/2}$ transitions of CH_3I and CH_3I^+, respectively [37].

5.3.1 *Mechanism of Vibrational Wave Packet Generation in Neutral CH_3I*

The time-dependent spectral first-moment $\left\langle E_{CH_3I}(t)\right\rangle$ computed about the I $4d_j \rightarrow \sigma^*_{C-I}$ transition of neutral CH_3I reflects strong-field-induced wave packet motion along the C–I stretching mode in its electronic ground state (Fig. 5.5). Beyond the an energy offset $E^{(0)}_{CH_3I} = 50.6 \pm 0.1$ eV and a high-frequency oscillation, the presence of an envelope modulation suggests a fit to two oscillatory components, i.e., $\left\langle E_{CH_3I}(t)\right\rangle = E^{(0)}_{CH_3I} + \sum \left\langle E^{(i)}_{CH_3I}(0)\right\rangle \cos\left[\omega^{(i)}_{CH_3I} t + \phi^{(i)}_{CH_3I}\right]$ $(i = 1, 2)$. The first component, with an initial phase of $\phi^{(1)}_{CH_3I} = -(0.49 \pm 0.05)\pi$ rad, is consistent with

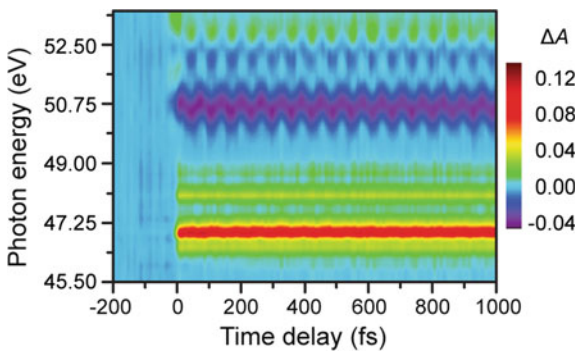

Fig. 5.4 Contour plot of the differential XUV absorption spectra collected as a function of pump-probe time delay

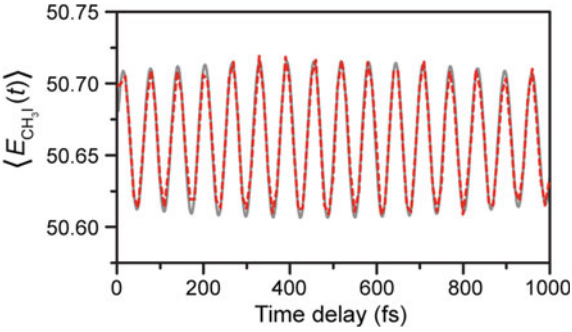

Fig. 5.5 Time-resolved spectral first-moments calculated about the neutral CH_3I I $4d_j \rightarrow \sigma^*_{C-I}$ resonance, $\langle E_{CH_3I}(t) \rangle$. The dashed red lines are the data and the solid grey lines are obtained from fits

bond softening-induced wave packet motion. Because the I $4d_j \rightarrow \sigma^*_{C-I}$ transition energy monotonically decreases with C–I bond length R_{C-I}, it can be inferred that an initial displacement towards larger R_{C-I} leads to $\phi = -\pi/2$ rad; conversely, initial displacement towards smaller R_{C-I} leads to $\phi = \pi/2$ rad. In the quasi-static limit of laser-molecule interaction, the intense laser field distorts the neutral ground state potential along the C–I coordinate. Within the Floquet picture, the one- and two-photon dressing of the neutral ground state by the dissociative $^3Q_{0^+}(A_1)$ state [19, 38] results in the softening of the ground-state C–I potential. Both quasi-static and Floquet pictures yield the same outcome: the intense laser field causes the equilibrium vibrational probability density to move initially towards larger R_{C-I}, hence launching wave packet motion that is characterized by $\phi^{(1)}_{CH_3I} = -\pi/2$ rad (Fig. 5.1b). The oscillation frequency $\omega^{(1)}_{CH_3I} = 533 \pm 1$ cm^{-1} is in excellent agreement with the literature value for the fundamental v_3 frequency (533 cm^{-1}) [39], consistent with the bond softening-induced wave packet motion being dominated by the coherent superposition of the vibrational ground state and the first-excited state.

The second component of $\langle E_{CH_3I}(t) \rangle$ has an initial phase of $\phi^{(2)}_{CH_3I} = -(0.09 \pm 0.12)\pi$ rad, indicative of wave packet motion launched by R-selective depletion from the outer turning point of the C–I potential (Fig. 5.1a). This observation can be rationalized by inspecting the energy gap between the spectroscopically reconstructed Morse potentials of the CH_3I and CH_3I^+ electronic ground states as a function of R_{C-I} (Fig. 5.6 top panel), which corresponds to the vertical ionization potential of CH_3I. In the vicinity of the equilibrium R_{C-I} for CH_3I, the vertical ionization potential exhibits a steep decrease for C–I bond lengths shorter than the equilibrium value. This trend favors strong-field ionization at the inner turning point of the C–I potential, hence launching wave packet motion from the outer turning point with a $\phi^{(2)}_{CH_3I} = 0$ rad. The measured oscillation frequency of $\omega^{(2)}_{CH_3I} = 518 \pm 3$ cm^{-1}, anharmonically shifted from the fundamental frequency of 533 cm^{-1}, suggests a vibrational coherence that involves mainly the $v = 2$ and $v = 3$ levels of the v_3 mode [40], whose estimated fractional populations at a vibrational temperature of 353 K are 0.0117 and 0.0014, respectively. R-selective depletion is dominated by the high-lying vibrational states because they possess higher probability densities near the turning points of the C–I potential, where strong-field ionization rates are larger.

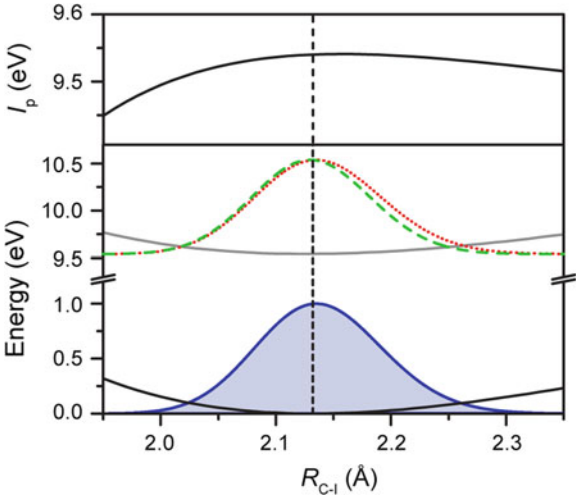

Fig. 5.6 The vertical ionization potential I_p of CH_3I as a function of C–I bond distance (top panel), as obtained from the energy gap between the Morse potentials of CH_3I (solid black line) and CH_3I^+ (solid grey line) along the C–I coordinate (bottom panel). The vertical dashed line denotes the CH_3I equilibrium C–I bond length. The vibrational probability densities for CH_3I, initially at thermal equilibrium (solid blue line), the CH_3I^+ fraction produced by strong-field ionization (red dotted line), and the CH_3I^+ $v = 0$ eigenstate (green dashed line) are also plotted. Strong-field ionization creates an initial vibrational probability density for CH_3I^+ that is noticeably different from that of the CH_3I^+ $v = 0$ eigenstate

5.3.2 *Observation and Origins of Multimode Coherent Vibrational Motion in CH_3I^+*

Aside from the vibrational wave packet initiated in neutral CH_3I by the intense laser field, the time-dependent spectral first-moment $\left\langle E_{CH_3I^+}(t)\right\rangle$ computed about the dominant CH_3I^+ resonance at 47.0 eV reveals oscillatory components that can be assigned to the C–I stretching (v_3) and CH_3 umbrella (v_2) modes of the $\tilde{X}^{+\,2}E_{3/2}$ state (Fig. 5.7). The $\left\langle E_{CH_3I^+}(t)\right\rangle$ time trace can be fit to an offset $E^{(0)}_{CH_3I^+} = 47.0 \pm 0.1$ eV and a sum of two damped cosinusoidal oscillations, i.e., $\left\langle E_{CH_3I^+}(t)\right\rangle = E^{(0)}_{CH_3I^+} + \sum E^{(i)}_{CH_3I^+}(0)\cos\left[\omega^{(i)}_{CH_3I^+}t + \phi^{(i)}_{CH_3I^+}\right]e^{-t/\tau^{(i)}_{CH_3I^+}}$ $(i = 1, 2)$. The retrieved vibrational frequencies, $\omega^{(1)}_{CH_3I^+} = 1253 \pm 1$ and $\omega^{(2)}_{CH_3I^+} = 475 \pm 1$ cm^{-1}, match those reported for the v_2 (1257 cm^{-1}) and v_3 (480 cm^{-1}) modes, respectively [41]. The vibrational wave packets have comparable damping times: $\tau^{(1)}_{CH_3I^+} = 1.8 \pm 0.6$ ps and $\tau^{(2)}_{CH_3I^+} = 1.7 \pm 0.4$ ps. The simultaneous appearance of both v_2 and v_3 modes in the vibrational wave packet stands in contrast to wave packet motion along a single vibrational coordinate that is observed in previous studies involving polyatomic molecular ions [42, 43].

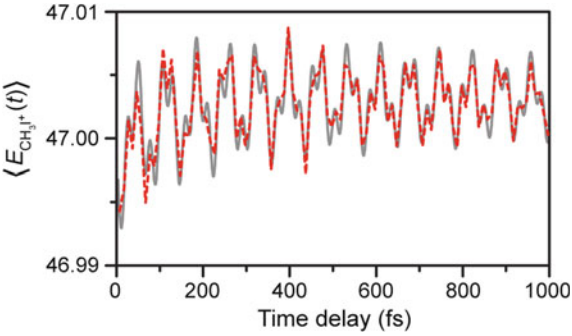

Fig. 5.7 Time-resolved spectral first-moments calculated about the CH_3I^+ I $4d_{5/2} \rightarrow e^{-1}_{3/2}$ resonance, $\langle E_{CH_3I^+}(t)\rangle$. The dashed red lines are the data and the solid grey lines are obtained from fits

The initial oscillation phase of $\phi^{(1)}_{CH_3I^+} = (0.13 \pm 0.12)\pi$ rad for the υ_2 mode is consistent with displacive excitation of the CH_3 umbrella mode wave packet. Displacive excitation occurs when the Franck-Condon region accessed by vertical ionization is displaced from the equilibrium geometry, such that the ensuing structural rearrangement that accompanies equilibration leads to wave packet motion with an initial phase of 0 mod π rad [44]. In this case, displacive excitation of the υ_2 mode is supported by the small but significant difference in the H–C–I bond angles between the neutral [44] and ion [45, 46] species: 107.7° in CH_3I vs. 108.3° in CH_3I^+. Interestingly, the measured oscillation phase $\phi^{(2)}_{CH_3I^+}$ of $(0.71 \pm 0.05)\,\pi$ rad for the C–I stretching mode deviates, beyond error, from phase values that would be expected for wave packet dynamics induced by either displacive excitation (π rad) or bond softening ($\pi/2$ rad). Here, we consider the simultaneous launching of wave packets by both displacive excitation and bond softening. It is conceivable that the same intense laser pulse that drives strong-field ionization can also induce the softening of the C–I potential of the resultant CH_3I^+ ions. Displacive excitation, on the other hand, is supported by the different equilibrium C–I bond lengths of CH_3I (2.132 Å) [45] and CH_3I^+ (2.126 Å) [46]. In this case, the overall oscillatory signal at $\omega^{(2)}_{CH_3I^+} = 475\ \mathrm{cm}^{-1}$ can be expressed as $\cos\left[\omega^{(2)}_{CH_3I^+}t + \phi^{(2)}_{CH_3I^+}\right] = \sin\phi^{(2)}_{CH_3I^+}\cos\left[\omega^{(2)}_{CH_3I^+}t + \pi/2\right] - \cos\phi^{(2)}_{CH_3I^+}\cos\left[\omega^{(2)}_{CH_3I^+}t + \pi\right]$, where the terms with amplitude coefficients $\sin\phi^{(2)}_{CH_3I^+}$ and $-\cos\phi^{(2)}_{CH_3I^+}$ arise from bond softening and displacive excitation, respectively. A phase value of $\phi^{(2)}_{CH_3I^+} = (0.71 \pm 0.05)\,\pi$ rad gives an amplitude ratio of $-\sin\phi^{(2)}_{CH_3I^+}/\cos\phi^{(2)}_{CH_3I^+} = 1.3 \pm 0.1$, suggesting that bond softening dominates over displacive excitation.

It is remarkable that the decrease in equilibrium C–I bond length of 0.006 Å, representing a change of merely 0.3%, can yield a discernible modulation of the XUV transition energy. For comparison, vibrational wave packets [47] or coherent phonons [44] detected by optical pump-probe spectroscopy typically involve changes in bond lengths of a few percent. *R*-selective depletion calculations that consider averaging over both thermal and laser-intensity distributions confirm that the initial vibrational probability density created in the CH_3I^+ $\tilde{X}^+\,^2E_{3/2}$ state indeed extends to larger

R_{C-I} compared to that of the $v = 0$ eigenstate (Fig. 5.6 bottom panel). The enhanced sensitivity of femtosecond XUV absorption spectroscopy to structural changes originates from the highly repulsive nature of the core hole-excited state, in this case, the I $4d_{5/2}^{-1}$ state of CH_3I^+. Access to such a repulsive potential upon absorption of the XUV probe pulse maps small geometrical distortions onto measurable shifts in XUV transition energies.

5.3.3 *Retrieval of Core-Excited-State Geometries from XUV Probing of Vibrational Wave Packets*

Aside from unraveling the mechanism of wave packet generation, quantitative analysis of the time-resolved XUV absorption spectra provides additional insight into the nature of the I $4d_{5/2}^{-1}$ core-excited state. The strength of the vibronic coupling between the CH_3I^+ I $4d_{5/2} \rightarrow e_{3/2}^{-1}$ XUV probe transition and the v_2 vibrational mode, as characterized by the Huang-Rhys factor S [48], is recovered from the oscillation amplitude via the relation $\left\langle E^{(1)}_{CH_3I^+}(0) \right\rangle = 2\lambda = 2\hbar\omega^{(1)}_{CH_3I^+} S$, where λ is the reorganization energy (Fig. 5.8). This relation between $\left\langle E^{(1)}_{CH_3I^+}(0) \right\rangle$ and S can be derived by considering two displaced harmonic potentials with the same curvatures [49]. (Note that the dissociative nature of the I $4d_{5/2}^{-1}$ core-excited state potential along the C–I stretch coordinate precludes the same analysis from being performed for the v_3 mode.) The experimentally determined amplitude of $\left\langle E^{(1)}_{CH_3I^+}(0) \right\rangle = 2.6 \pm 0.2$ meV yields a Huang-Rhys factor of $(8.3 \pm 0.7) \times 10^{-3}$, signifying weak vibronic coupling. Furthermore, combining the dimensionless displacement of $\Delta = \sqrt{2S} = 0.13 \pm 0.01$ with the measured phase $\phi^{(1)}_{CH_3I^+}$ of ~0 rad and the experimentally determined H–C–I angle of the CH_3I^+ $\tilde{X}^+ {}^2E_{3/2}$ state [46] $(108.3 \pm 0.3)°$ yields an equilibrium H–C–I angle of $(110.0 \pm 0.6)°$ for the I $4d_{5/2}^{-1}$ core-excited state of CH_3I^+.

5.4 Discussion

The emergence bond softening-induced coherent vibrational motion in the present work stands in stark contrast with earlier reports that attributed vibrational wave packet dynamics to R-selective depletion only [23–25]. In those cases, strong-field ionization removes either a bonding (D_2) or an anti-bonding electron (Br_2 and I_2). The change in the formal bond order induced by ionization leads to pronounced changes in the equilibrium bond length and vibrational frequency. For example, the equilibrium bond length of D_2 increases from 0.7415 to 1.0559 Å [50] upon ionization and its vibrational frequency decreases from 2993.60 to 1577.17 cm^{-1} [51, 52]. These changes in the relative displacement and curvatures of the neutral and ion potential

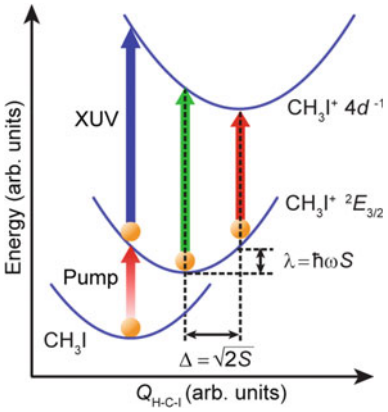

Fig. 5.8 Schematic illustration of potentials along the CH_3 umbrella (υ_2) mode for CH_3I, CH_3I^+ $\left(\tilde{X}^+\,^2E_{3/2}\right)$, and CH_3I^+ $\left(\mathrm{I}\,4d_{5/2}^{-1}\right)$. The amplitude of the component of $\left\langle E_{CH_3I^+}(t)\right\rangle$ that oscillates at the frequency υ_2 can be used to retrieve the Huang-Rhys factor S and the dimensionless displacement Δ between the two CH_3I^+ states, which in turn yields the equilibrium H–C–I angle for the I $4d$ core-excited CH_3I^+ species

energy curves yield a vertical ionization potential that is strongly dependent on bond length, hence favoring the generation of vibrational wave packets via R-selective depletion. In the case of CH_3I, however, strong-field ionization to the ion $\tilde{X}^+$ state corresponds to the removal of an electron from the nonbonding iodine $5p$ valence orbital [53]. Therefore, the C–I potential curves for neutral and ion species are mostly parallel atop one another, as evidenced by the minute differences in the experimental C–I bond lengths (2.132 Å for CH_3I vs. 2.126 Å for CH_3I^+) [45, 46] and υ_3 frequencies (533 cm^{-1} for CH_3I vs. 480 cm^{-1} for CH_3I^+) [39, 41], as well as the vanishingly small υ_3 vibrational progression in the $\tilde{X}^+\,^2E_{3/2}$ band of the CH_3I photoelectron spectrum [54]. The strongly suppressed R-selective depletion contribution allows the clear elucidation of bond softening-induced vibrational motion. Along these lines, the efficient launching of vibrational wave packets by bond softening is also expected for molecules for which valence ionization removes an electron from a nonbonding orbital. Examples of such molecules include HCl [4], H_2O [55], CO_2 [43], alcohols [56], and organic halides [19], some of which are routinely used in the study of strong-field phenomena.

The relative amplitudes of vibrational motion induced by bond softening and R-selective depletion should exhibit a distinct laser-intensity dependence. In general, bond softening dominates at lower intensities because of limited ionization depletion of the neutral ground state. In the case of D_2, for example, model calculations reveal that the relative contributions are reversed at a threshold intensity of $I_{th} \sim 2.5 \times 10^{14}$ W/cm^2, with R-selective depletion dominating the response for intensities $I > I_{th}$ [23]. Whether such an intensity threshold exists for CH_3I is unclear, given the negligible displacement between the equilibrium C–I distances

between the ground-state neutral and ion species ($\Delta R/R = 0.003$) and the similarity between the vibrational frequencies, and hence, the curvatures of the potentials of the two states ($\Delta\omega/\omega = 0.1$). In the extreme limit where both ΔR and $\Delta\omega/\omega$ are zero, R-selective depletion vanishes and only bond softening-induced wave packets can exist. In such cases, it is interesting to note that strong-field ionization to higher-lying electronically excited ion states could still result in vibrational motion launched by R-selective depletion. Future experiments that determine the relative contributions from bond softening and R-selective depletion as a function of laser intensity should address the existence of such an intensity threshold for CH_3I and if R-selective depletion involve electronically excited ion states.

The experimental determination of equilibrium geometries of core-excited states traditionally involves the analysis of vibronic progressions that appear in static core-level photoabsorption spectra to yield Franck-Condon factors. Such an approach was applied to determine the equilibrium geometries of the N $1s^{-1}$ core-excited N_2 [57] and Si $2p^{-1}$ core-excited SiH_4 [58]. However, this method is limited to core-hole states with sufficiently long lifetimes, whose narrow linewidths support clearly resolved vibronic features. For example, the natural linewidths of N $1s^{-1}$ and Si $2p^{-1}$ are 135 and 50 meV, respectively [57, 58], which are comparable to or smaller than the vibrational energy spacings in the vibronic progression. This frequency-domain approach breaks down for low-frequency vibrational modes and/or short-lived core-excited states, such as the I $4d^{-1}$ core levels probed herein (FWHM ~0.5 eV) [59]. Ab initio calculations of core-excited equilibrium geometries are similarly challenging due to the highly excited nature of the core-hole states [60, 61], making them beyond the reach of electronic structure methods, such as multi-reference configuration interaction and complete active-space self-consistent field, that are typically employed to determine the equilibrium geometries of valence-excited states. In the present work, we show that time-domain XUV probing of vibrational wave packet dynamics furnishes the vibronic coupling involving the core-level transition. The related dimensionless displacement parameter can in turn be used to recover the equilibrium geometry of the core-excited state. While our analysis is performed only for the υ_2 umbrella mode, it is important to note that the approach presented herein can be broadly generalized to the core-excited states of other molecules along their various vibrational coordinates. The ability to recover the molecular geometries of core-excited states will benefit efforts that are being pursued at X-ray free-electron lasers to investigate the ultrafast dynamics triggered by core-level excitation [62, 63].

Finally, we note that previous studies of vibrational wave packet dynamics in polyatomic molecular ions created by strong-field ionization have elucidated vibrational motion only along one vibrational mode [42, 43]. Strong-field-induced multimode vibrational coherences, such as those reported here for CH_3I^+ in the $\tilde{X}^+\,^2E_{3/2}$ state, is hitherto unobserved and can be attributed to multiple advantages offered by XUV absorption spectroscopy. First, XUV absorption probing permits the spectroscopic identification of both the chemical species that are produced by strong-field ionization as well as their electronic states [27]. Second, large shifts in the core-level transition energies accompany small structural changes, thus enabling spectrally resolved XUV absorption spectroscopy to detect small-amplitude coherent vibrational motion,

as demonstrated in the present work. Third, XUV absorption spectroscopy offers attosecond time resolution [64], which translates to a large detection bandwidth for coherent vibrational motion. Fourth, the use of few-cycle pulses for strong-field ionization triggers wave packet dynamics involving a large manifold of vibrational modes and provides a well-defined start time for the wave packet dynamics. The latter is crucial for establishing the initial phases of the wave packet oscillations and hence, the mechanisms for generating the vibrational coherences. The above factors favor femtosecond XUV absorption as a technique for investigating the multimode vibrational dynamics of transient molecular ions produced by intense laser-molecule interaction.

Acknowledgements This work is supported by a NTU start-up grant, the A*Star Science and Engineering Research Council Public Sector Funding (122-PSF-0011 and 122 360 0008), the Ministry of Education Academic Research Fund (MOE2014-T2-2-052 and RG105/17), and the award of a Nanyang Assistant Professorship to Z.-H.L. M.Y. acknowledges the financial support from National Natural Science of China (NSFC, Project No. 21373266). We are grateful to K. Yamanouchi, T. Kobayashi, S. L. Chin, and D. Mathur for useful discussions.

References

1. T. Brabec, F. Krausz, Intense few-cycle laser fields: frontiers of nonlinear optics. Rev. Mod. Phys. **72**, 545–591 (2000)
2. T. Popmintchev, M.-C. Chen, P. Arpin, M.M. Murnane, H.C. Kapteyn, The attosecond nonlinear optics of bright coherent X-ray generation. Nat. Photon. **4**, 822–832 (2010)
3. D.B. Milošević, G.G. Paulus, D. Bauer, W. Becker, Above-threshold ionization by few-cycle pulses. J. Phys. B **39**, R203 (2006)
4. M. Meckel, D. Comtois, D. Zeidler, A. Staudte, D. Pavičić, H.C. Bandulet et al., Laser-induced electron tunneling and diffraction. Science **320**, 1478 (2008)
5. J. Itatani, J. Levesque, D. Zeidler, H. Niikura, H. Pépin, J.C. Kieffer et al., Tomographic imaging of molecular orbitals. Nature **432**, 867–871 (2004)
6. C. Vozzi, M. Negro, F. Calegari, G. Sansone, M. Nisoli, S. De Silvestri et al., Generalized molecular orbital tomography. Nat. Phys. **7**, 822–826 (2011)
7. O. Smirnova, Y. Mairesse, S. Patchkovskii, N. Dudovich, D. Villeneuve, P. Corkum et al., High harmonic interferometry of multi-electron dynamics in molecules. Nature **460**, 972–977 (2009)
8. S. Haessler, J. Caillat, W. Boutu, C. Giovanetti-Teixeira, T. Ruchon, T. Auguste et al., Attosecond imaging of molecular electronic wavepackets. Nat. Phys. **6**, 200–206 (2010)
9. A.E. Boguslavskiy, J. Mikosch, A. Gijsbertsen, M. Spanner, S. Patchkovskii, N. Gador et al., The multielectron ionization dynamics underlying attosecond strong-field spectroscopies. Science **335**, 1336 (2012)
10. H.J. Wörner, J.B. Bertrand, D.V. Kartashov, P.B. Corkum, D.M. Villeneuve, Following a chemical reaction using high-harmonic interferometry. Nature **466**, 604–607 (2010)
11. C.I. Blaga, J. Xu, A.D. DiChiara, E. Sistrunk, K. Zhang, P. Agostini et al., Imaging ultrafast molecular dynamics with laser-induced electron diffraction. Nature **483**, 194–197 (2012)
12. S. Baker, J.S. Robinson, C.A. Haworth, H. Teng, R.A. Smith, C.C. Chirilă et al., Probing proton dynamics in molecules on an attosecond time scale. Science **312**, 424 (2006)
13. F. Lépine, M.Y. Ivanov, M.J.J. Vrakking, Attosecond molecular dynamics: fact or fiction? Nat. Photon. **8**, 195–204 (2014)

14. P.M. Kraus, B. Mignolet, D. Baykusheva, A. Rupenyan, L. Horný, E.F. Penka et al., Measurement and laser control of attosecond charge migration in ionized iodoacetylene. Science **350**, 790 (2015)
15. I.K. Alexander, S.C. Lorenz, Ultrafast correlation-driven electron dynamics. J. Phys. B **47**, 124002 (2014)
16. B. Sheehy, L.F. DiMauro, Atomic and molecular dynamics in intense optical fields. Annu. Rev. Phys. Chem. **47**, 463 (1996)
17. J.H. Posthumus, The dynamics of small molecules in intense laser fields. Rep. Prog. Phys. **67**, 623 (2004)
18. B.J. Sussman, D. Townsend, M.Y. Ivanov, A. Stolow, Dynamic stark control of photochemical processes. Science **314**, 278–281 (2006)
19. M.E. Corrales, J. González-Vázquez, G. Balerdi, I.R. Solá, R. de Nalda, L. Bañares, Control of ultrafast molecular photodissociation by laser-field-induced potentials. Nat. Chem. **6**, 785–790 (2014)
20. L. Fang, G.N. Gibson, Investigating excited electronic states of I_2^+ and I_2^{2+} produced by strong-field ionization using vibrational wave packets. Phys. Rev. A **75**, 063410 (2007)
21. E. Goll, G. Wunner, A. Saenz, Formation of ground-state vibrational wave packets in intense ultrashort laser pulses. Phys. Rev. Lett. **97**, 103003 (2006)
22. A. Saenz, Enhanced ionization of molecular hydrogen in very strong fields. Phys. Rev. A **61**, 051402 (2000)
23. T. Ergler, B. Feuerstein, A. Rudenko, K. Zrost, C.D. Schröter, R. Moshammer et al., Quantum-phase resolved mapping of ground-state vibrational D_2 wave packets via selective depletion in intense laser pulses. Phys. Rev. Lett. **97**, 103004 (2006)
24. L. Fang, G.N. Gibson, Strong-field induced vibrational coherence in the ground electronic state of hot I_2. Phys. Rev. Lett. **100**, 103003 (2008)
25. E.R. Hosler, S.R. Leone, Characterization of vibrational wave packets by core-level high-harmonic transient absorption spectroscopy. Phys. Rev. A **88**, 023420 (2013)
26. L. Dhar, J.A. Rogers, K.A. Nelson, Time-resolved vibrational spectroscopy in the impulsive limit. Chem. Rev. **94**, 157–193 (1994)
27. Z.-H. Loh, S.R. Leone, Capturing ultrafast quantum dynamics with femtosecond and attosecond X-ray core-level absorption spectroscopy. J. Phys. Chem. Lett. **4**, 292–302 (2013)
28. A.R. Attar, A. Bhattacherjee, C.D. Pemmaraju, K. Schnorr, K.D. Closser, D. Prendergast et al., Femtosecond X-ray spectroscopy of an electrocyclic ring-opening reaction. Science **356**, 54 (2017)
29. P. Andersen, T. Andersen, F. Folkmann, V.K. Ivanov, H. Kjeldsen, J.B. West, Absolute cross sections for the photoionization of 4*d* electrons in Xe^+ and Xe^{2+} ions. J. Phys. B **34**, 2009–2019 (2001)
30. D.L. Ederer, M. Manalis, Photoabsorption of the 4*d* electrons in xenon. J. Opt. Soc. Am. **65**, 634–637 (1975)
31. J. Seely, B. Kjornrattanawanich, Measurement of extreme-ultraviolet attenuation edges of magnesium, tin, and indium filters. Appl. Opt. **42**, 6374–6381 (2003)
32. T.N. Olney, G. Cooper, C.E. Brion, Quantitative studies of the photoabsorption (4.5–488 eV) and photoionization (9–59.5 eV) of methyl iodide using dipole electron impact techniques. Chem. Phys. **232**, 211–237 (1998)
33. G. O'Sullivan, C. McGuinness, J.T. Costello, E.T. Kennedy, B. Weinmann, Trends in 4*d*-subshell photoabsorption along the iodine isonuclear sequence: I, I^+ and I^{2+}. Phys. Rev. A **53**, 3211–3226 (1996)
34. J.N. Cutler, G.M. Bancroft, K.H. Tan, Ligand-field splittings and core-level linewidths in I 4*d* photoelectron spectra of iodine molecules. J. Chem. Phys. **97**, 7932–7943 (1992)
35. R. Locht, D. Dehareng, K. Hottmann, H.W. Jochims, H. Baumgärtel, B. Leyh, The photoionization dynamics of methyl iodide (CH_3I): a joint photoelectron and mass spectrometric investigation. J. Phys. B **43**, 105101 (2010)
36. Z. Wei, J. Li, S.T. See, Z.-H. Loh, Spin-orbit state-selective c-i dissociation dynamics of the CH3I+$\tilde{X}$ electronic state induced by intense few-cycle laser fields. J. Phys. Chem. Lett. **8**, 6067–6072 (2017)

37. Z. Wei, J. Li, L. Wang, S.-T. See, M.H. Jhon, Y. Zhang, F. Shi, M. Yang, Z.-H. Loh, Elucidating the origins of multimode vibrational coherences of polyatomic molecules induced by intense laser fields. Nat. Commun. **8**, 735 (2017)
38. R. de Nalda, J. Durá, A. García-Vela, J.G. Izquierdo, J. González-Vázquez, L. Bañares, A detailed experimental and theoretical study of the femtosecond A-band photodissociation of CH_3I. J. Chem. Phys. **128**, 244309 (2008)
39. T. Shimanouchi, *Tables of Molecular Vibrational Frequencies Consolidated* vol I (National Bureau of Standards, 1972)
40. J.L. Duncan, A.M. Ferguson, S. Mathews, Vibrational anharmonicity in CH_3I: a joint local and normal mode study. J. Chem. Phys. **91**, 783–790 (1989)
41. M. Lee, Y.J. Bae, M.S. Kim, *K* selection in one-photon mass-analyzed threshold ionization of CH_3I and CD_3I to the $\tilde{X}\,^2E_{3/2}$ state cations. J. Chem. Phys. **128**, 044310 (2008)
42. D. Geißler, B.J. Pearson, T. Weinacht, Wave packet driven dissociation and concerted elimination in CH_2I_2. J. Chem. Phys. **127**, 204305 (2007)
43. A. Rudenko, V. Makhija, A. Vajdi, T. Ergler, M. Schürholz, R.K. Kushawaha et al., Strong-field-induced wave packet dynamics in carbon dioxide molecule. Farad. Discuss. **194**, 463–478 (2016)
44. H.J. Zeiger, J. Vidal, T.K. Cheng, E.P. Ippen, G. Dresselhaus, M.S. Dresselhaus, Theory for displacive excitation of coherent phonons. Phys. Rev. B **45**, 768–778 (1992)
45. H. Matsuura, J. Overend, Equilibrium structure of methyl iodide. J. Chem. Phys. **56**, 5725–5727 (1972)
46. Y.J. Bae, M.S. Kim, Photodissociation spectroscopy of CD_3I^+ generated by mass-analyzed threshold ionization for structure determination. ChemPhysChem **9**, 1709–1714 (2008)
47. A. Yabushita, T. Kobayashi, Primary conformation change in bacteriorhodopsin on photoexcitation. Biophys. J. **96**, 1447–1461 (2009)
48. K. Huang, A. Rhys, Theory of light absorption and non-radiative transitions in F-centres. Proc. R. Soc. Lond. Ser. A **204**, 406–423 (1950)
49. M. Lax, The Franck-Condon principle and its application to crystals. J. Chem. Phys. **20**, 1752–1760 (1952)
50. K.P. Huber, G. Herzberg, *Constants of Diatomic Molecules* in NIST Chemistry WebBook, NIST Standard Reference Database Number 69. (National Institute of Standards and Technology) (1979)
51. P.J. Brannon, C.H. Church, C.W. Peters, Electric field induced spectra of molecular hydrogen, deuterium and deuterium hydride. J. Mol. Spectrosc. **27**, 44–54 (1968)
52. D.M. Bishop, R.W. Wetmore, Vibrational spacings for H_2^+, D_2^+ and H_2. Mol. Phys. **26**, 145–157 (1973)
53. S.G. Walt, N.B. Ram, A. von Conta, O.I. Tolstikhin, L.B. Madsen, F. Jensen et al., Role of multi-electron effects in the asymmetry of strong-field ionization and fragmentation of polar molecules: the methyl halide series. J. Phys. Chem. A **119**, 11772–11782 (2015)
54. L.S. Karlsson, R. Jadrny, L.H. Mattsson, F.T. Chau, K. Siegbahn, Vibrational and vibronic structure in the valence electron spectra of CH_3X molecules (X = F, Cl, Br, I, OH). Phys. Scripta **16**, 225 (1977)
55. J.P. Farrell, S. Petretti, J. Förster, B.K. McFarland, L.S. Spector, Y.V. Vanne et al., Strong field ionization to multiple electronic states in water. Phys. Rev. Lett. **107**, 083001 (2011)
56. T. Ando, A. Shimamoto, S. Miura, K. Nakai, H. Xu, A. Iwasaki et al., Wave packet bifurcation in ultrafast hydrogen migration in CH_3OH^+ by pump-probe coincidence momentum imaging with few-cycle laser pulses. Chem. Phys. Lett. **624**, 78–82 (2015)
57. C.T. Chen, Y. Ma, F. Sette, *K*-shell photoabsorption of the N_2 molecule. Phys. Rev. A **40**, 6737–6740 (1989)
58. R. Püttner, M. Domke, D. Lentz, G. Kaindl, Si 2*p* photoabsorption in SiH_4 and SiD_4: molecular distortion in core-excited silane. Phys. Rev. A **56**, 1228–1239 (1997)
59. G. O'Sullivan, The absorption spectrum of CH_3I in the extreme VUV. J. Phys. B **15**, L327–L330 (1982)

60. P. Norman, H. Ågren, Geometry optimization of core electron excited molecules. J. Mol. Struc. **401**, 107–115 (1997)
61. A.B. Trofimov, E.V. Gromov, T.E. Moskovskaya, J. Schirmer, Theoretical evidence for a bound doubly-excited $^1B_2$ (C 1 s, $n \rightarrow \pi^{*2}$) state in H_2CO below the C 1 s ionization threshold. J. Chem. Phys. **113**, 6716–6723 (2000)
62. B. Erk, R. Boll, S. Trippel, D. Anielski, L. Foucar, B. Rudek et al., Imaging charge transfer in iodomethane upon X-ray photoabsorption. Science **345**, 288 (2014)
63. B.K. McFarland, J.P. Farrell, S. Miyabe, F. Tarantelli, A. Aguilar, N. Berrah et al., Ultrafast X-ray auger probing of photoexcited molecular dynamics. Nat. Commun. **5**, 4235 (2014)
64. E. Goulielmakis, Z.-H. Loh, A. Wirth, R. Santra, N. Rohringer, V.S. Yakovlev et al., Real-time observation of valence electron motion. Nature **466**, 739–743 (2010)

Chapter 6
Real-Time Observation of Vibrational Wavepackets of Nitrogen Molecule Using A-Few-Pulse Attosecond Pulse Train

Tomoya Okino, Yasuo Nabekawa and Katsumi Midorikawa

Abstract Observation of quantum wavepackets in molecules is one of the vital steps in understanding chemical reactions occurring at femtosecond and attosecond timescales, because the broadband light sources inevitably coherently excite multiple quantum states. A-few-pulse attosecond pulse train generated via high-order harmonic generation in loose focusing geometry is sufficiently strong to induce multiphoton absorption processes and the pulse envelope is sufficiently short to resolve the nuclear motions. We investigated the vibrational wavepackets in a nitrogen molecule using a-few-pulse attosecond pulse train by measuring the pump-probe delay dependence of momentum images of fragment ions generated in singly charged manifolds via two-photon dissociative ionization processes using a velocity map imaging ion spectrometer. The time evolutions of vibrational wavepackets launched both in neutral and singly charged manifolds were projected using a frequency-resolved momentum imaging method.

6.1 Introduction

Monitoring the motion of nuclei in a molecule is among the essential steps in understanding the elementary processes of photochemical reactions. Because the period of nuclear motion in the bound electronic states in a molecule can be as short as 10 fs, the pulse duration of light sources for resolving the nuclear motion should be sub-10

T. Okino (✉) · Y. Nabekawa · K. Midorikawa
Attosecond Science Research Team, RIKEN Center for Advanced Photonics,
2-1 Hirosawa, Wako-shi, Saitama 351-0198, Japan
e-mail: tomoya.okino@riken.jp

Y. Nabekawa
e-mail: nabekawa@riken.jp

K. Midorikawa
e-mail: kmidori@riken.jp

T. Okino
JST PRESTO, 2-1 Hirosawa, Wako-shi, Saitama 351-0198, Japan

© Springer Nature Switzerland AG 2018

K. Yamanouchi et al. (eds.), *Progress in Ultrafast Intense Laser Science XIV*,
Springer Series in Chemical Physics 118,
https://doi.org/10.1007/978-3-030-03786-4_6

fs [1–3]. With such ultrashort optical pulses, several vibrational eigenstates in the bound electronic states of a molecule are coherently excited to form a vibrational wavepacket (VWP) because of the large spectral bandwidth of the optical pulses. The time evolution of a VWP depends on the potential shape of the electronic states and the range of the excited vibrational eigenstates, because of the anharmonicity of the excited electronic states, and it is regarded as a fingerprint of each electronic state [4, 5].

With the advent of attosecond light sources [6], it is possible to investigate ultrafast electron dynamics in a molecule at a sub-femtosecond temporal resolution [7, 8]. An attosecond light pulse is among the ideal light sources for simultaneously exciting multiple electronic states of a molecule, because the photon energy is sufficiently broad to excite multiple electronic states via the one-photon absorption process. In most cases, it is possible to launch VWPs in ionic manifolds because the photon energy of the attosecond pulse is greater than the ionization potential of the molecule. Furthermore, the attosecond pulse can coherently excite multiple electronic states to launch the electron wavepacket among the excited electronic states with one-photon absorption of the attosecond pulses, leading to intramolecular charge migration processes driven by the electron-electron correlation [9, 10].

Before the invention of attosecond light sources, VWPs in neutral manifolds were launched via the one-photon absorption of wavelength-tunable femtosecond light sources in the ultraviolet-visible (UV-VIS) wavelength region. The VWP in singly charged manifolds was launched via the multi-photon absorption of intense near infrared (NIR) pulses whose pulse duration was shorter than the vibrational period of the nuclei and the time evolution was monitored by recording the fragment ions generated from the Coulomb explosion process induced by the intense NIR probe pulse [11, 12]. When the intense NIR light pulse is used for creating VWPs in ionic manifolds, the electron(s) in the HOMO, HOMO-1, and HOMO-2 are mainly ejected. In other words, the electronic states in the singly charged manifolds excited by the intense NIR fields will be limited to several electronic states near the HOMO because the probability of tunnel ionization strongly depends on the potential energy of the electronic states.

In contrast, an attosecond pulse can launch VWPs both in neutral and singly charged manifolds without distorting the molecular potentials via the one-photon absorption process and the resultant vibrational state distribution coincides with that based on the Franck-Condon principle. However, it is still challenging to perform an attosecond-pump and attosecond-probe of a VWP because the repetition rate of the intense isolated attosecond light source whose pulse energy is sufficiently high to induce multi-photon processes [13] is too low to secure the sufficient data statistics.

The VWP can be observed in a real-time manner by detecting the pump-probe delay-dependent intensity of the photon and charged particles (ion and electron). The time evolution of a VWP launched in a low-lying excited state in a molecule has been probed by detecting the pump-probe delay-dependent laser-induced fluorescence [14, 15]. The attosecond transient absorption spectroscopy (ATAS) of VWPs launched in diatomic molecules is realized in which the multiple high-lying electronic states in the neutral manifolds are excited to create multiple VWPs via the one-photon absorption

of the extreme ultraviolet (XUV) pulse, and the time-delayed NIR pulse modulates the VWPs by coupling to neighboring electronic states [16]. In ATAS, the recorded XUV spectrum is modulated by the response of the molecule. Furthermore, it is proposed that a VWP can be probed by monitoring the change in the high harmonic spectrum from a diatomic molecule because the recombination efficiency depends on the internuclear distance of the molecule [17]. These schemes are effective in detecting VWPs mainly launched in the neutral manifolds.

Monitoring the time evolution of VWPs by recording the delay-dependent photoelectron signals is powerful for VWPs launched in neutral manifolds [18]. The advantage of recording the delay-dependent photoelectron signals is identifying the electronic state in the probe process. However, when a VWP is launched in singly charged manifolds, the photoelectron momentum image is composed of the photoelectrons generated from the pump process and those generated from the probe process. Because of the large spectral bandwidth of the attosecond pulses, there is a certain spectral overlap between the delay-independent signals originating from the one-photon process and the delay-dependent signals originating from the two-photon processes. Therefore, it is not effective to record the time evolution of a VWP launched in singly charged manifolds.

Detecting the delay-dependent fragment ion signals is an alternative means to observe the time evolution of a VWP with a femtosecond optical pulse [19–21] and XUV free-electron laser pulse [22]. By exciting into the repulsive electronic states in the singly charged or doubly charged manifolds, fragment ions can be generated, and the delay-dependent momentum images can be a measure of the VWPs.

Recently, Yang et al. demonstrated observations of a VWP launched in a bound electronic state of the neutral isolated iodine molecules using the ultrafast electron diffraction (UED) method [23] . Using this method, the pulsed electron beam generated by the optical pulse with the photoelectric effect is utilized as a probe pulse. However, it is currently impossible to observe a VWP with a sub-100 fs period because the temporal resolution of the UED method is several 100 fs because of the velocity mismatch between the electron and the light.

We recently demonstrated that the VWP of D_2^+ is generated using the attosecond pulse train (APT) via the one-photon absorption processes and the time evolution is probed in a real-time manner with a three-color probe laser pulse whose wavelength ranges from NIR to vacuum UV by measuring the delay-dependent momentum images of fragment ions [24–26].

In this work, we investigated the VWPs in a nitrogen molecule generated both in neutral and singly charged manifolds by pump-probe measurements using a-few-pulse attosecond pulse train. The pump-probe delay-dependent momentum images of the fragment ions were recorded using a velocity map imaging ion spectrometer [27].

6.2 Experimental

The experimental setup for the attosecond-pump and attosecond-probe measurement of VWPs in a nitrogen molecule is schematically shown in Fig. 6.1 [4]. There were three primary components: (i) an intense a-few-pulse APT, (ii) an attosecond interferometer termed an "atto-correlator", and (iii) a single-shot counting velocity map imaging ion spectrometer.

6.2.1 A-Few-Pulse Attosecond Pulse Train

An APT was generated using a sub-15 fs Ti:Sapphire laser system [28]. The output of a femtosecond laser system (800 nm, sub-15 fs, 40 mJ/pulse maximum, and 100 Hz) was loosely focused using a concave mirror ($f = 5$ m) onto a static gas cell filled with Xe to generate high harmonics. The resultant harmonic intensity distribution at the focal region is shown in the right panel of Fig. 6.2 in which the throughput of the XUV optics is considered. By tuning the central wavelength of the fundamental light, the harmonic distribution can be tuned for blue-shifted or red-shifted configurations. When the central wavelength of the fundamental light was in a blue-shift configuration, the resultant harmonic energy from the 3rd to 21st was also blue-shifted as shown in Fig. 6.2a. However, when the central wavelength of the fundamental light was in a red-shift configuration, the harmonic distribution was also

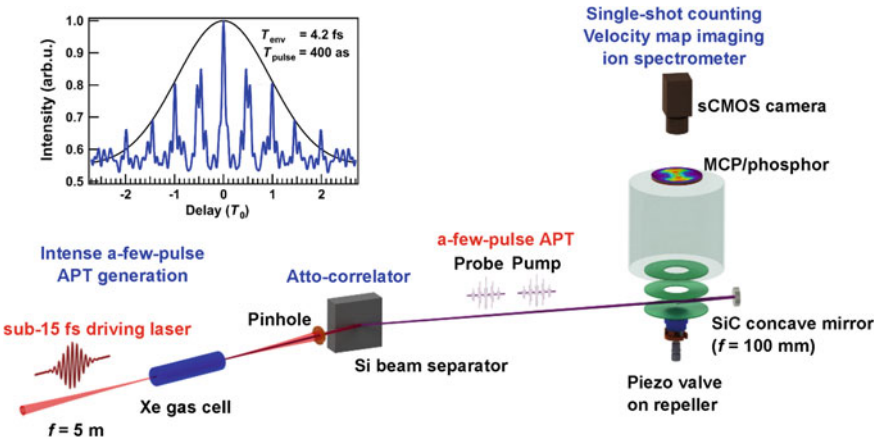

Fig. 6.1 Schematic drawing of the experimental setup for observing the VWPs in a nitrogen molecule with a-few-pulse APT. The experimental setup was composed of (i) intense a-few-pulse APT generation, (ii) an atto-correlator, and (iii) a single-shot-counting velocity-map-imaging ion spectrometer. The inset shows the IAC trace of a-few-pulse APT and its envelope, in which T_0 is the optical cycle of the fundamental pulse

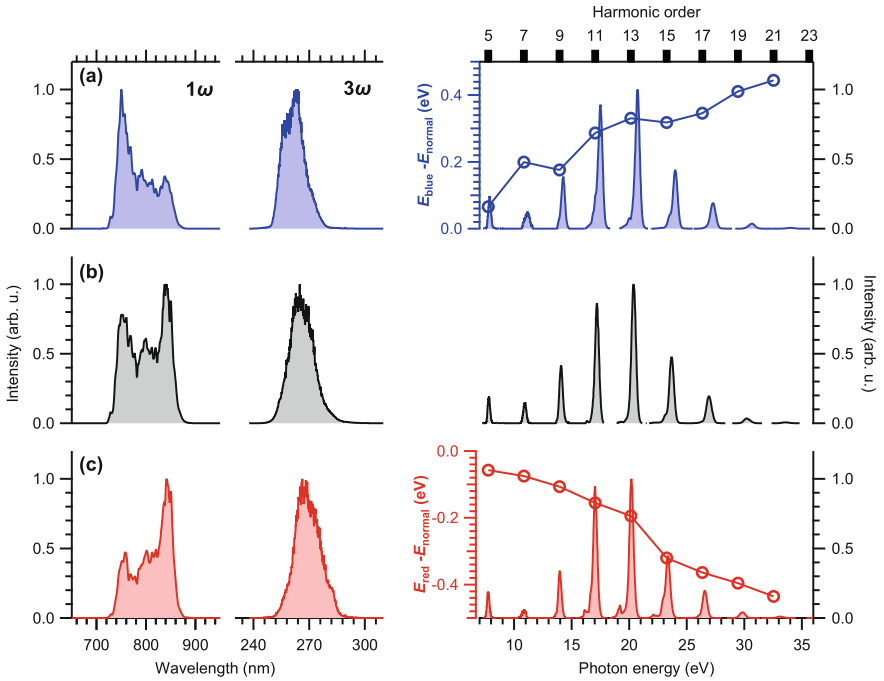

Fig. 6.2 Spectrum of fundamental light, the 3rd order harmonic, and the harmonic distribution from the 5th order harmonic to the 21st order harmonic for **a** blue-shift, **b** normal, and **c** red-shift wavelength configurations. The central photon energy of each harmonic order is compared to that in the normal wavelength configuration. The energy shift of the central photon energy of each harmonic is appended in (**a**) and (**c**)

red-shifted as shown in Fig. 6.2c. The energy shift was sufficiently large to change the vibrational state distribution in the neutral manifolds excited via the one-photon absorption process.

The temporal profile of the APT was characterized in situ by measuring the interferometric autocorrelation (IAC) trace using a nitrogen molecule as a nonlinear medium [29]. During the IAC measurement, the fragment ions generated from the two-photon dissociative ionization processes were recorded as a function of the delay between the two APT pulses. The delay was scanned every 36 as from −7 to +7 fs to record the IAC trace as shown in the inset of Fig. 6.1. Because the envelope of the APT was ∼4 fs, the number of attosecond pulses contained in the envelope was only a-few. Therefore, the generated APT can be referred to as a-few-pulse APT. The duration of the APT envelope was sufficiently short to resolve the nuclear motion of the N_2 molecule. A thin metal filter that is usually inserted for blocking the fundamental light and lower-order harmonics was not utilized in the present work to use the lower-order harmonics as a part of the probe pulse.

6.2.2 High-Throughput, High-Stability Interferometer: Atto-Correlator

The generated APT co-propagated approximately 6 m downstream with the unconverted fundamental light. Because the beam size of the harmonics was smaller than that of fundamental pulse, a large portion of the remnant fundamental light was blocked by inserting the aperture. After passing through the aperture, the APT and the unconverted fundamental light were coaxially incident on the Si mirrors so that the incident angle becomes the Brewster angle for the fundamental light, leading to the attenuation of the unconverted fundamental light via the absorption on the surface of the Si mirrors. In other words, the Si mirrors worked as a beam separator between the fundamental pulse and the harmonics. At the same time, the generated APT was spatially divided into two, the pump APT and probe APT pulses. One of the Si mirrors was mounted on a high-precision piezo linear one-axis translation stage to change the delay between the pump APT and probe APT pulses.

The delay between the two replicas of a-few-pulse APT was precisely adjusted by moving one of the Si mirrors on the piezo stage. To measure the IAC trace, the delay was scanned every 36 as from −7 to +7 fs corresponding to movement of the piezo stage (P-621.1CL, Physik Instrumente) in 20 nm steps. However, to measure the time evolution of the VWPs, the delay was scanned every 2 fs from 0 to 400 fs corresponding to a movement of the piezo stage (P-628.1CL, Physik Instrumente) in 1120 nm steps.

The thermal expansion of the capacitive position sensor integrated into the piezo stage deteriorated the stability of the interferometer. The delay instability was suppressed to be less than 10 as/hour by actively regulating the temperature of the piezo stage using a Peltier module sandwiched with Cu plates with 0.001 °C precision using a high-precision temperature controller (ILX Lightwave, LDT-5910C). The delay zero was experimentally confirmed by measuring the IAC trace of the a-few-pulse APT.

6.2.3 Single-Shot Counting Velocity Map Imaging Ion Spectrometer

For extracting the small changes in the angular distribution of the fragment ions, the signal-to-noise ratio of the velocity map imaging ion spectrometer (VMIS) should have been improved. There were three primary improvements on the configuration of our VMIS.

For increasing the sample density at the focal volume, the molecules were injected from a high-speed piezo valve [30] integrated into the rear side of a repeller electrode in the VMIS [31], in which the central part of the molecular beam of nitrogen molecules was skimmed by a pinhole (0.5 mmϕ). Because a high voltage up to 5 kV was applied to the repeller electrode, the piezo valve unit and the repeller electrode

were connected by ceramics for voltage isolation. The opening time of the piezo valve can be as short as 20 μs for reducing the load of the vacuum system in the VMIS. The backing pressure of the nitrogen molecules was regulated to realize the best signal-to-noise ratio while avoiding the distortion of momentum images induced by the space charge effect. The generated fragment ions were captured via microchannel plate (MCP)/phosphor (Photonis, 120 mmϕ) assembly composed of two MCPs and a phosphor screen (P47) and the resultant phosphorous image on the phosphor screen was recorded using a scientific CMOS (sCMOS) camera (Andor, Neo5.5). The signals assigned to be N^+ were securely selected by applying a high-voltage gating pulse to the MCPs. The sCMOS camera can read the image at the same repetition rate of the laser system (100 Hz) even with 2048 × 2048 image pixels without compromising the momentum resolution. Because the electron multiplication gain of MCP has a significant spatial distribution specified by the pulse height distribution, spot counting analysis was implemented to compensate for the spatial inhomogeneity. The aforementioned three improvements of the VMIS enabled us to record the small intensity variations in the signals as a function of the delay between the pump and probe pulses.

6.3 Frequency-Resolved Momentum Imaging of Vibrational Wavepackets

When the momentum images of the charged particles were recorded by scanning the delay Δt between the pump and probe pulses, the sequences of two-dimensional (2D) momentum images $I(x, y, \Delta t)$ could be obtained. The delay-dependent kinetic energy distribution of the charged particles $I(E, \Delta t)$ was obtained by integrating over the ejection angle θ defined as the angle between the polarization direction of the attosecond pulses and the ejection direction of the fragment ions. Alternatively, each pixel was characterized by the kinetic energy E and the ejection angle θ. A delay-dependent (E, θ) map $I(E, \theta, \Delta t)$ could be constructed in which the position (x, y) is converted into a set of energy and ejection angle (E, θ). In both cases, it accompanies the integration over some parameters.

If the signal-to-noise ratio for each pixel in the recorded momentum image was sufficiently high, the frequency spectrum $I(x, y, \omega)$ could be obtained for each pixel. In other words, a Fourier transformation of the delay-dependent signal $I(x, y, \Delta t)$ can be performed for each pixel. When the intensity variation in each pixel was filtered out by a certain frequency range (ω_1, ω_2), a frequency-resolved momentum image, $I(x, y; \omega_1, \omega_2)$, could be constructed.

In the present work, the momentum images of fragment ions N^+, $I(x, y, \Delta t)$, were recorded by scanning the delay Δt between the pump and probe pulses. The signals for each pixel were composed of (i) one-photon processes, (ii) two-photon processes from one beam (delay-independent signals) and (iii) two-photon processes from two beams. The momentum images of N^+, $J(x, y, \Delta t)$, were reconstructed in

each delay frame by the Abel inversion using the pBASEX algorithm [32]. The frequency spectrum $\tilde{J}(x, y, \omega)$ can be obtained by Fourier transformation for each pixel after subtracting the delay-averaged momentum image $\langle J(x, y, \Delta t)\rangle$ for each delay data as follows:

$$\tilde{J}(x, y, \omega) = \mathscr{F}[(J(x, y, \Delta t) - \langle J(x, y, \Delta t)\rangle] \tag{6.1}$$

The frequency-resolved momentum images $\tilde{J}(x, y; \omega_1, \omega_2)$ can be obtained by integrating over a certain frequency range (ω_1, ω_2) as follows:

$$\tilde{J}(x, y; \omega_1, \omega_2) = \int_{\omega_1}^{\omega_2} \tilde{J}(x, y, \omega) d\omega \tag{6.2}$$

It is noteworthy that the intensity appearing in the frequency-resolved momentum image was only based on delay-dependent nonlinear processes.

When frequency filtering is performed for each pixel data, the intensity variation with the single frequency $H(x, y, \Delta t; \omega)$, can be expressed as follows:

$$H(x, y, \Delta t; \omega) = A(x, y; \omega) \cos(\omega \Delta t + \Psi(x, y; \omega)) \tag{6.3}$$

where $A(x, y; \omega)$ is the proportional constant and $\Psi(x, y; \omega)$ is the phase of the oscillation depending on the pixel (x, y). A 2D phase map $\Psi(x, y; \omega)$ can be extracted from the frequency-filtered intensity variation in each pixel, $H(x, y, \Delta t; \omega)$. There is a one-to-one correspondence between the extracted phase and the internuclear distance. The extracted 2D phase map in each pixel is regarded as the internuclear distance at the moment of probing.

6.4 Results and Discussion

6.4.1 Vibrational Wavepackets in a Nitrogen Molecule

In the case of N_2, there are more than one bound electronic states both in the neutral and singly charged manifolds. The potential energy curves related to the generation of VWPs in a nitrogen molecule in this work are shown in Fig. 6.3 [4].

There are at least six bound electronic states excited by one-photon absorption of harmonics contained in the APT pump pulse. Two bound electronic states $b'^1\Sigma_u^+$, $b^1\Pi_u$ are in the neutral manifolds, and four bound electronic states $X^2\Sigma_g^+$, $A^2\Pi_u$, $B^2\Sigma_u^+$, and $C^2\Sigma_u^+$ states are in the singly charged manifolds. The one-photon absorption of the 9th order harmonic can create VWPs both in the $b^1\Pi_u$ and $b'^1\Sigma_u^+$ states and the one-photon absorption of 11th or higher order harmonics can generate VWPs in the $X^2\Sigma_g^+$ and $A^2\Pi_u$ states. In the case of the $B^2\Sigma_u^+$ and $C^2\Sigma_u^+$ states, the minimum harmonic order to generate the VWPs is 13th and 17th, respectively.

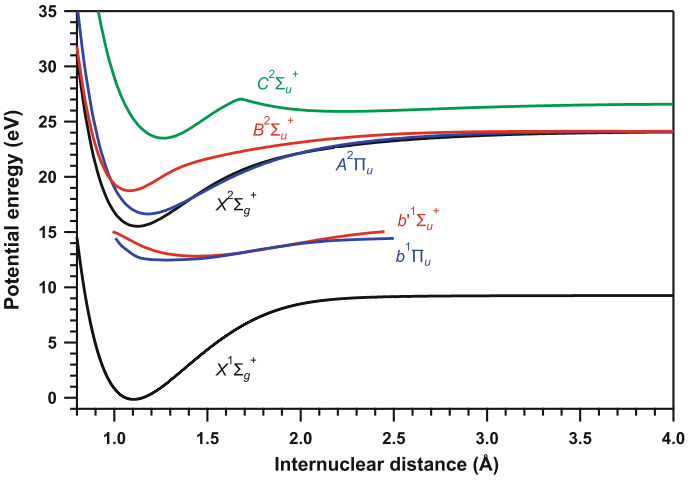

Fig. 6.3 Potential energy curves of the bound electronic states in N_2 and N_2^+. The potential energy of the $b^1\Pi_u$ and $b'^1\Sigma_u^+$ states in the neutral manifolds is adopted from the RKR potentials. The electronic states ($X^1\Sigma_g^+$, $X^2\Sigma_g^+$, $A^2\Pi_u$, $B^2\Sigma_u^+$, $C^2\Sigma_u^+$) were calculated using the Molpro quantum chemistry package

During all probing processes, fragment ions N^+ can be generated via the one-photon absorption of the APT probe pulse to excite into the repulsive electronic states in the singly charged manifolds. By measuring the delay-dependent kinetic energy release of N^+, the time evolutions of each VWP can be precisely tracked. Because there are several dissociation limits (L_3 and L_4) from the same repulsive electronic states, the kinetic energy distribution will be somewhat complicated.

It should be noted that it was difficult to create more than one VWP simultaneously using the conventional light source because the pulse duration was not sufficiently short to resolve and/or the spectral bandwidth was not sufficiently broad to cover more than one electronic states. However, the envelope of a-few-pulse APT (∼4 fs) was sufficiently short to resolve the VWPs formed both in the neutral and the singly charged manifolds and the spectrum could cover several electronic states.

The potential energy curves of the highly excited states of N_2^+ are necessary to assign the electronic states involved in the probe processes of the VWPs. Because there was no spectroscopic data for the highly excited electronic states of N_2^+, the electronic structure calculations of N_2^+ were conducted using the quantum chemistry program package MOLPRO [33]. All calculations were conducted in the D_{2h} point group. The potential energy curves of N_2^+ were calculated using the state-averaged complete active space self-consistent field (SA-CASSCF) approach followed by the internally contracted multireference single and double excitation configuration interaction (MRCI) method with the cc-pVTZ basis set, in which the $1s$ orbitals were treated as core orbitals and the $2s$ and $2p$ orbitals were incorporated into the active space. Because the D_{2h} point group has eight irreducible representations, 80 elec-

tronic states (10 electronic states for each symmetry representation) were included with an equal weight. Finally, five electronic states for each symmetry ($^2\Sigma_g^+$, $^2\Sigma_g^-$, $^2\Sigma_u^+$, $^2\Sigma_u^-$, $^2\Pi_g$, $^2\Pi_u$, $^2\Delta_g$, $^2\Delta_u$) were obtained. However, the potential energy curves of the $b^1\Pi_u$ and $b'^1\Sigma_u^+$ states in the neutral manifolds were adopted from the Rydberg-Klein-Rees (RKR) potentials [34] because the same basis set cannot reproduce the spectroscopic data.

6.4.2 *Vibrational Wavepackets in the Neutral Manifolds*

When the VWPs are formed in the neutral manifolds, the probe processes via the one-photon absorption of a-few-pulse APT accompany the ionization to induce the dissociation processes via excitation to the repulsive electronic states in the singly charged manifolds. Tuning the central wavelength of the driving laser for generating the APT can modify the central wavelength of each harmonic as shown in Fig. 6.2. Therefore, the vibrational state distributions in the neutral manifolds can be manipulated by changing the central wavelength of the fundamental light. The branching ratio of the VWPs formed with the pump APT pulse can also be manipulated by tuning the central wavelength of the fundamental light. Because the vibrational period depends on the energy spacing of the vibrational eigenstates or vibrational state distribution, different frequency spectrograms were obtained with the wavelength tuning of fundamental laser pulse.

In the case of the excited bound electronic states in the neutral manifolds of the nitrogen molecule, two electronic states, $b'^1\Sigma_u^+$, $b^1\Pi_u$, can be excited via the one-photon absorption of the 9th order harmonic contained in the pump APT pulse. Because the spectral bandwidth of the 9th order harmonic is nearly constant when changing the central wavelength of driving laser pulse, the number of vibrational eigenstates excited by the 9th order harmonic is nearly identical. The vibrational state distributions of the $b'^1\Sigma_u^+$ and $b^1\Pi_u$ states were estimated as shown in Fig. 6.4b considering the spectral distribution of the 9th order harmonic for three wavelength configurations. As the central wavelength of 9th order harmonic shortens, the fraction of $b^1\Pi_u$ state increases as shown in Fig. 6.4c because of the increase in the Franck-Condon overlap.

When the central wavelength of the driving laser pulse is tuned to the blue-shift configuration, higher vibrational eigenstates can be excited, leading to a longer vibrational period because of the anharmonicity of the electronic state. However, when the central wavelength of the driving laser pulse is tuned to the red-shift configuration, lower vibrational eigenstates can be excited, leading to a shorter vibrational period. These tendencies are clearly confirmed in the recorded delay-dependent kinetic energy distribution of the fragment ions for the three wavelength configurations as shown in Fig. 6.5. When the central wavelength of the driving laser is tuned to the normal or blue-shift configurations, there is only one frequency peak at approximately 18–20 THz as shown in Fig. 6.5a, b. The frequency peak is assigned to

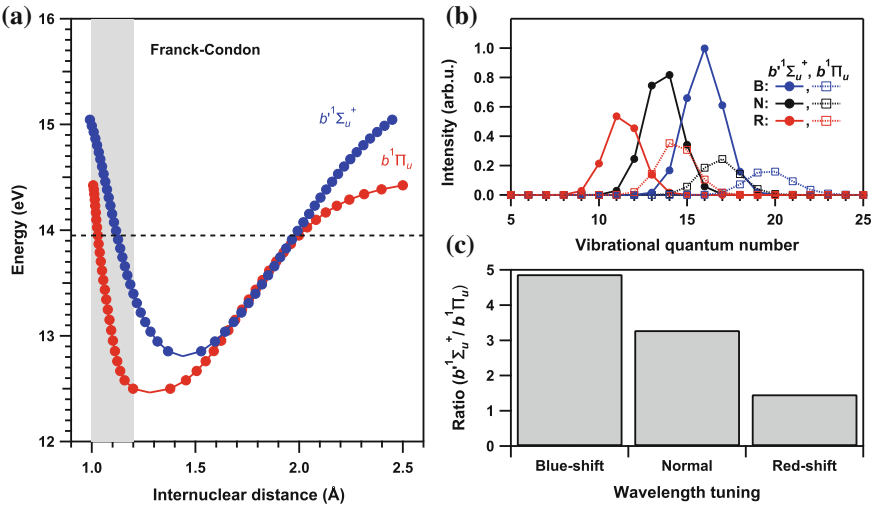

Fig. 6.4 **a** Potential energy curves of the $b'^1\Sigma_u^+$ and $b^1\Pi_u$ states adopted from the RKR potentials. The dotted line and hatched area show the central photon energy of the 9th order harmonic in the normal wavelength configuration and the Franck-Condon region of the ground electronic state $X^1\Sigma_g^+$, respectively. **b** Vibrational quantum number distributions for the $b'^1\Sigma_u^+$ and $b^1\Pi_u$ states with the three wavelength configurations shown in Fig. 6.2. **c** Ratio of the $b'^1\Sigma_u^+$ state to the $b^1\Pi_u$ state for three wavelength configurations

the VWP formed in the $b'^1\Sigma_u^+$ state. In these wavelength configurations, the fraction of the $b^1\Pi_u$ state excited by the pump APT pulse is negligibly small.

However, when the central wavelength of the driving laser pulse is tuned to the red-shift configuration, a new frequency peak at approximately 12 THz appears in addition to the frequency peaks shown at approximately 20 THz. The existence of two frequency contributions in the frequency spectrogram of the red-shift configuration supports that at least two bound electronic states ($b'^1\Sigma_u^+$ and $b^1\Pi_u$) are simultaneously excited to create the VWPs. Because the energy spacing between the vibrational eigenstates in $b^1\Pi_u$ is less than that in $b'^1\Sigma_u^+$, the frequency peak at approximately 12 THz is assigned to the VWP formed in the $b^1\Pi_u$ states.

The observed periodic nuclear motion $T_{vib} \sim 54$ fs ($\sim$18.5 THz) is ascribed to the VWP in the $b'^1\Sigma_u^+$ state in the neutral manifold. As shown schematically in Fig. 6.6a, the peaks B and C originate from N^+ generated by the excitation with 11th and higher-order harmonics at the outer turning well to the $5^2\Sigma_g^+$ state and dissociate into different dissociation limits (L_4 for peak B and L_3 for peak C).

However, peaks D and E originate from N^+ generated by the excitation with the 13th and higher-order harmonics at the inner turning well to the $3^2\Sigma_g^+$ state and dissociate into the dissociation limit L_4 for peak D and L_3 for peak E. The weak peak A at approximately $E = 0.2$ eV is assigned to N^+ generated by the excitation with the 7th or higher-order harmonics at the inner turning well to the $D^2\Pi_g$ state and dissociate into L_1.

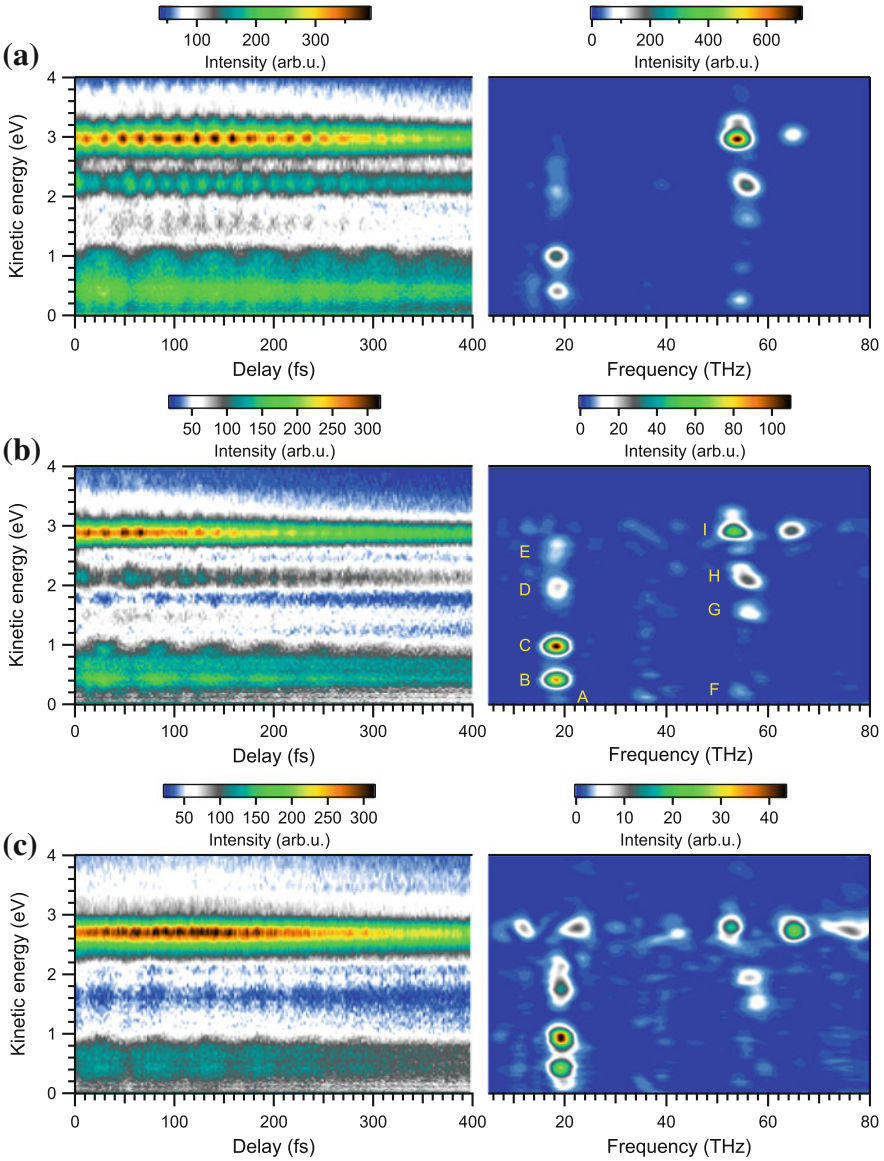

Fig. 6.5 Delay-dependent kinetic energy distributions of N^+ (left panel) and the kinetic energy dependent frequency spectrograms (right panel) for **a** blue-shift, **b** normal and **c** red-shift wavelength configurations. The labels from A to I are depicted for the assignments shown in Fig. 6.6

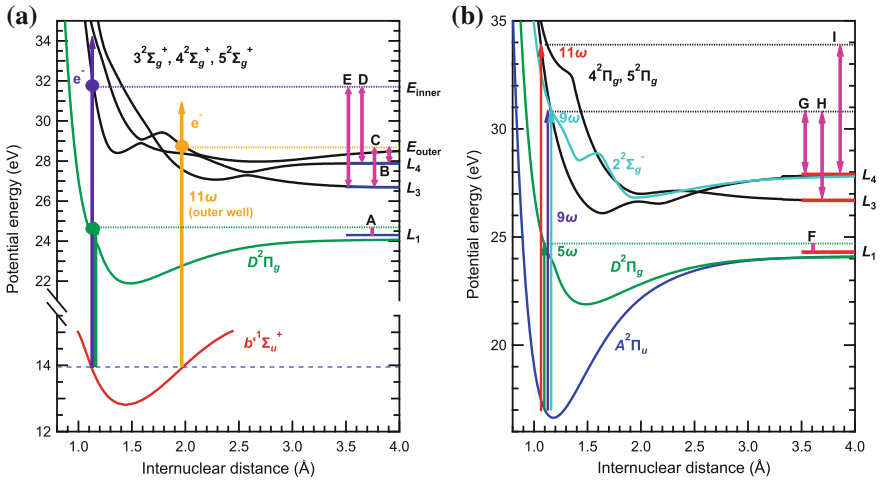

Fig. 6.6 **a** Probe scheme of a VWP formed in the $b'^1\Sigma_u^+$ state in the normal wavelength configuration. **b** Probe scheme of a VWP formed in the $A^2\Pi_u$ state in the normal wavelength configuration. L_1, L_3, and L_4 are dissociation limits. The labels from A to I correspond to the frequency peaks shown in the right panel of Fig. 6.5b. E_{inner} and E_{outer} are the potential energy accessed by the probe pulse at the inner and outer well of the $b'^1\Sigma_u^+$ state, respectively

6.4.3 *Vibrational Wavepackets in the Singly Charged Manifolds*

When the VWPs are generated in the singly charged manifolds, it is possible to probe their time evolutions without accompanying the further ionization processes during the probing processes by excitation into the repulsive electronic states in the singly charged manifolds. If the final electronic states excited by the probe pulse are the repulsive electronic states in the singly charged manifolds, the fragmentation processes will occur in the same manifolds. In this probe scheme, the probe pulse partially projects the nuclear density and the width of the projection is determined by the spectral bandwidth of the probe pulses. Because the spectrum of the APT is discrete, the nuclear density projection will also be discrete. As demonstrated in our previous works on the observation of VWPs in D_2 [24–26], there are several probing processes in which the VWPs are probed using the APT even if the final repulsive electronic state is the same. How precisely the nuclear density can be projected is determined by the slope of the repulsive final electronic state excited by the probe pulse because there is a one-to-one correspondence between the internuclear distance and the kinetic energy release of the fragment ions. If the slope is steep, the probe range is increased as long as the spectral bandwidth of the probe pulse is sufficiently broad.

Because the major probe processes in the VWPs formed in the singly charged manifolds are one-photon absorption processes, the excitation process is determined

by the electronic transition rule. If the intensity of the attosecond pulses utilized both for the pump and probe pulses is sufficiently high, it is possible to use the Coulomb explosion processes in the probe process. However, it is still challenging to induce the Coulomb explosion process excited to the Coulombic electronic state in the dication with the one-photon absorption of the attosecond pulse during the probing processes because the photon energy of the probe pulse will be larger than that of the pump pulse. Even if intense attosecond pulses are available, the kinetic energy distribution of the fragment ions generated in the single-charged manifold will have a certain overlap with those generated in the doubly-charged manifold.

In addition, more than one VWP is simultaneously created and probed by the Coulomb explosion process in the dication, and the probe processes are coherently superimposed exhibiting the electron wavepacket. This process can be utilized for probing the electron wavepacket, but it is not adequate to probe the time evolution of the respective VWPs. The electronic states in the probe process are well separated in energy so that they are separately observed. However, when the repulsive electronic states in the singly charged manifolds are excited, the demand for the probe pulse is significantly relaxed.

The KER distribution at the delay Δt as provided by [35, 36] is as follows:

$$f(E_{\mathrm{KER}}, \Delta t) = K|\Psi(R, \Delta t)|^2 \left|\frac{dE_f(R)}{dR}\right|^{-1} \tag{6.4}$$

where R is the internuclear distance and K is the proportional constant depending on the potentials of the intermediate electronic state E_i and final electronic state E_f and $|\Psi(R, \Delta t)|^2$ is the nuclear probability density at the delay Δt on the final electronic state E_f. Equation (6.4) indicates that the transition probability is larger when the slope of the final state potential energy curve is smaller.

Because the photon energy of the a-few-pulse APT utilized as a probe pulse is discrete, its spectrum $g(E_{\mathrm{probe}})$ should be considered in simulating the KER of the fragment ions. The KER distribution of the probe process at the delay time Δt on the dissociative adiabatic potential curve $E_f(R)$ is as follows:

$$F(E_{\mathrm{KER}}, g(E_{\mathrm{probe}}), \Delta t) = f(E_{\mathrm{KER}}, \Delta t)|g(E_{\mathrm{probe}})\delta(E_{\mathrm{probe}} - (E_f(R) - E_i))| \tag{6.5}$$

From the selection rule for the one-photon transition, the excitation from the $A^2\Pi_u$ state can populate the $^2\Sigma_g^+$, $^2\Sigma_g^-$, $^2\Pi_g$, or $^2\Delta_g$ states. The numerically simulated delay-KE spectrogram of each symmetry is shown in Fig. 6.7e–h. The numbers in parentheses to the right of some of the figures correspond to $[m, n]$, where m and n denote the m-th electronic state of each symmetry and the harmonic order of the probe pulse, respectively. From the calculated transition probabilities, it is expected that the transition from the $A^2\Pi_u$ state to the $4^2\Pi_g$ state is the dominant process when the 9th order harmonic is absorbed in which the final state is dissociated into the L_3 asymptotic limit accompanying the ejection of N^+ with a KE of approximately 2 eV.

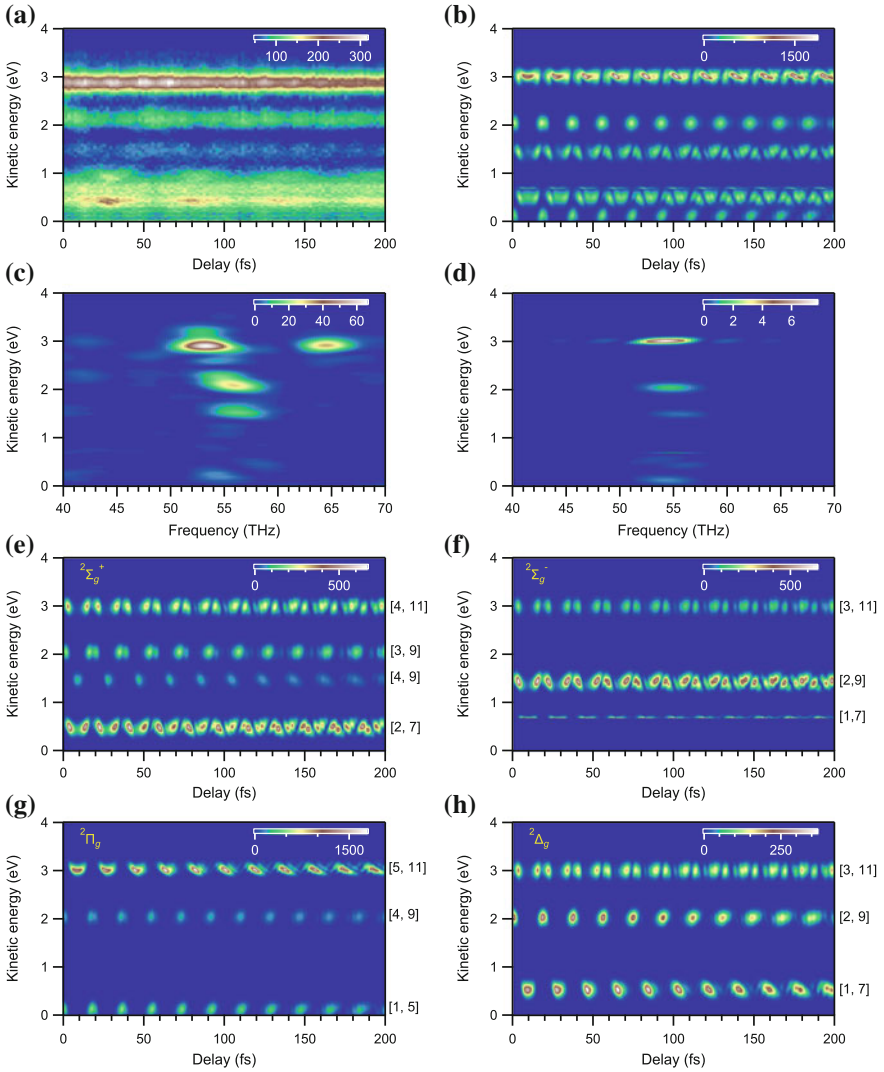

Fig. 6.7 **a** Delay-KE spectrogram (0–200 fs) measured using the normal wavelength condition. **b** Numerically simulated delay-KE spectrogram (0–200 fs). **c** Frequency-KE spectrogram (40–70 THz) obtained via Fourier transformation of (**a**). **d** Numerically simulated frequency-KE spectrogram (40–70 THz) obtained via Fourier transformation of (**b**). **e**–**h** Numerical simulation of time evolution of a VWP probed by the excitation to the (**e**) $^2\Sigma_g^+$ states, (f) $^2\Sigma_g^-$ states, (**g**) $^2\Pi_g$ states, and (h) $^2\Delta_g$ states. The numbers in parentheses to the right shown in (**e**)–(**h**) correspond to $[m, n]$, in which m and n denote the m-th electronic state of each symmetry and the harmonic order of the probe pulse, respectively. The electronic states $1^2\Pi_g$ and $2^2\Sigma_g^+$ are also known as $D^2\Pi_g$ and $F^2\Sigma_g^+$, respectively

However, one-photon absorption of the 11th order harmonic will preferentially excite from the $A^2\Pi_u$ state to the $5^2\Pi_g$ state leading to a dissociation into the L_4 dissociation limit accompanying the ejection of N^+ with a KE of approximately 3 eV. Fig. 6.7b shows the summing of the spectra shown in Fig. 6.7e–h, and Fig. 6.7d shows the Fourier transform of Fig. 6.7b. This Fourier transformed spectrum qualitatively reproduces the experimental result shown in Fig. 6.7c.

6.4.4 *Frequency-Resolved Momentum Imaging of Vibrational Wavepackets*

The frequency-resolved momentum images shown in Fig. 6.8 were extracted based on the data analysis procedure described in the Sect. 6.3. The resultant 2D frequency amplitude map can be regarded as the angular distribution of the fragment ions generated via the pump-probe delay correlated two-photon processes. In other words, the fragment ions generated from the delay-independent one-photon and two-photon processes can be excluded. The 2D frequency-resolved momentum map of the VWP formed in the $b'^1\Sigma_u^+$ state, $M_b(x, y)$, is shown in Fig. 6.8a, in which only one quadrant of the frequency-resolved momentum image is shown. Because the amplitude is large

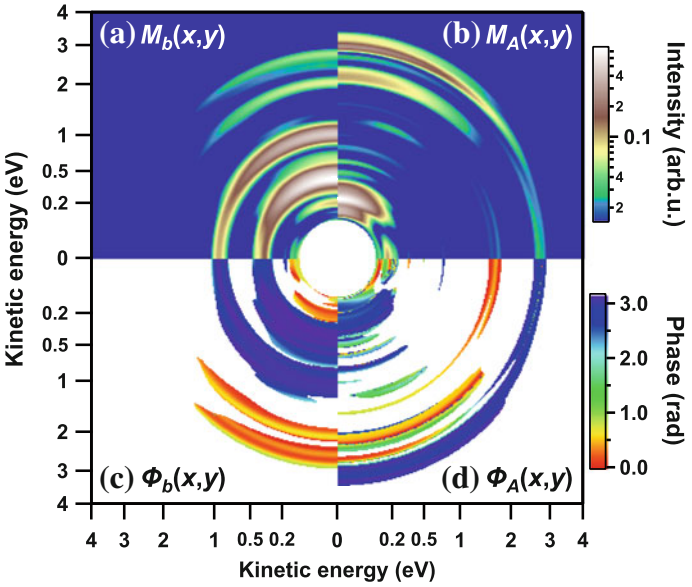

Fig. 6.8 Frequency-resolved momentum imaging of VWPs formed in the $b'^1\Sigma_u^+$ and $A^2\Pi_u$ states. **a** Amplitude map of the $b'^1\Sigma_u^+$ state, $M_b(x, y)$. **b** Amplitude map of the $A^2\Pi_u$ state, $M_A(x, y)$. **c** Phase map of the $b'^1\Sigma_u^+$ state, $\Phi_b(x, y)$. **d** Phase map of the $A^2\Pi_u$ state, $\Phi_A(x, y)$. The amplitudes in (**a**) and (**b**) are shown in a logarithmic scale. The laser polarization direction is the y-axis

for the y-axis, the fragment ions are preferentially ejected along the laser polarization direction. The 2D frequency-resolved momentum map of the VWP formed in the $A^2\Pi_u$ state, $M_A(x, y)$, is shown in Fig. 6.8b. Similar to the case of the map $M_b(x, y)$, the fragment ions are preferentially ejected along the laser polarization direction. However, there are certain signals along the x-axis reflecting that fragment ions are also generated perpendicular to the laser polarization direction.

The 2D phase map of the VWP launched in the $b'^1\Sigma_u^+$ state, $\Psi_b(x, y)$, is shown in Fig. 6.8c. It is clearly seen that fragment ions with low kinetic energy are generated at phase π. The phase of the fragment ions with low kinetic energy is π because they are generated at the outer turning point of the $b'^1\Sigma_u^+$ state. Meanwhile, a 2D phase map of $A^2\Pi_u$ state, $\Psi_A(x, y)$, is shown in Fig. 6.8d. The fragment ions generated with a high kinetic energy of $\sim$3 eV is ascribed to be probed around the outer well of the electronic state because the phase is π. These 2D phase maps correspond to the 2D maps of internuclear distance at the moment of probing for each VWP.

6.5 Summary

In this work, we investigated the VWPs in a nitrogen molecule via pump-probe measurement using a-few-pulse APT. More than one VWP was simultaneously launched both in the neutral and singly charged manifolds via the one-photon absorption of a-few-pulse APT. Their time evolutions were monitored by recording the change in the momentum image of the fragment ions N^+ generated by the probe a-few-pulse APT. From the recorded delay-dependent momentum images of the fragment ions, the frequency-resolved momentum images were extracted. The resultant frequency-resolved momentum images mapped the angular distribution of the fragment ions exclusively generated via the delay-correlated two-photon processes. In addition to the frequency-resolved momentum images, 2D phase maps were extracted for each vibrational wavepacket. There is a one-to-one correspondence between the phase and the internuclear distance at the moment of probing. The reconstructed frequency-resolved momentum and phase maps can show the time evolution of each VWP without integrating any parameters such as the ejection angle and momentum.

Our work presented here is limited to the observation of VWPs in diatomic molecules. For investigating vibrational or electron wavepackets in polyatomic molecules, there are several issues to be solved. One is developing intense attosecond light sources with a higher repetition rate. A repetition rate of more than 1 kHz is necessary for recording the momentum images of fragment ions and photoelectrons in coincidence to extract the delay-dependent photoelectron momentum image in the molecular frame with sufficient statistics. Because the number of pump-probe delay settings exceeds several hundred for measuring the time evolution of VWPs, the repetition rate of the attosecond light source should be as high as possible. Second, the development of an adequate non-volatile sample injection system in an ultrahigh vacuum system is necessary because the vapor pressure will be lower as a general tendency and the molecules will be more easily thermally decomposed as

the molecular size increases. In particular, a standard sample injection method in the molecular beam cannot be applied to the investigation of nuclear and electron dynamics in amino acids.

Acknowledgements This work was supported in part by the Photon Frontier Network Program of the Ministry of Education, Culture, Sports, Science and Technology (MEXT) Japan. T.O., Y.N., and K.M. acknowledge the financial support of JSPS Grants-in-Aid for Scientific Research (Nos. 15H03581, 26247068, and 26220606). T.O. acknowledges the financial support from JST PRESTO Grant Number JPMJPR15P6, Japan.

References

1. C.R. Calvert, W.A. Bryan, W. Newell, I.D. Williams, Time-resolved studies of ultrafast wavepacket dynamics in hydrogen molecules. Phys. Rep. **491**, 1 (2010)
2. B. Feuerstein, Th Ergler, A. Rudenko, K. Zrost, C.D. Schröter, R. Moshammer, J. Ullrich, T. Niederhausen, U. Thumm, Complete characterization of molecular dynamics in ultrashort laser fields. Phys. Rev. Lett. **99**, 153002 (2007)
3. F. Kelkensberg, C. Lefebvre, W. Siu, O. Ghafur, T.T. Nguyen-Dang, O. Atabek, A. Keller, V. Serov, P. Johnsson, M. Swoboda, T. Remetter, A. L'Huillier, S. Zherebtsov, G. Sansone, E. Benedetti, F. Ferrari, M. Nisoli, F. Lépine, M.F. Kling, M.J.J. Vrakking, Molecular dissociative ionization and wave-packet dynamics studied using two-color XUV and IR pump-probe spectroscopy. Phys. Rev. Lett. **103**, 123005 (2009)
4. T. Okino, Y. Furukawa, Y. Nabekawa, S. Miyabe, A.A. Eilanlou, E.J. Takahashi, K. Yamanouchi, K. Midorikawa, Direct observation of an attosecond electron wave packet in a nitrogen molecule. Sci. Adv. **1**, e1500356 (2015)
5. Y. Cheng, M. Chini, X. Wang, A. González-Castrillo, A. Palacios, L. Argenti, F. Martín, Z. Chang, Reconstruction of an excited-state molecular wave packet with attosecond transient absorption spectroscopy. Phys. Rev. A **94**, 023403 (2016)
6. G. Sansone, L. Poletto, M. Nisoli, High-energy attosecond light sources. Nat. Photon. **5**, 655 (2011)
7. F. Lépine, M.Y. Ivanov, M.J.J. Vrakking, Attosecond molecular dynamics: fact or fiction? Nat. Photon. **8**, 195 (2014)
8. M. Nisoli, P. Decleva, F. Calegari, A. Palacios, F. Martín, Attosecond electron dynamics in molecules. Chem. Rev. **117**, 10760 (2017)
9. F. Calegari, D. Ayuso, A. Trabattoni, L. Belshaw, S. De Camillis, S. Anumula, F. Frassetto, L. Poletto, A. Palacios, P. Decleva, J.B. Greenwood, F. Martín, M. Nisoli, Ultrafast electron dynamics in phenylalanine initiated by attosecond pulses. Science **346**, 336 (2014)
10. P.M. Kraus, B. Mignolet, D. Baykusheva, A. Rupenyan, L. Horny, E.F. Penka, G. Grassi, O.I. Tolstikhin, J. Schneider, F. Jensen, L.B. Madsen, A.D. Bandrauk, F. Remacle, H.J. Wörner, Measurement and laser control of attosecond charge migration in ionized iodoacetylene. Science **350**, 790 (2015)
11. A.S. Alnaser, X.M. Tong, T. Osipov, S. Voss, C.M. Maharjan, P. Ranitovic, B. Ulrich, B. Shan, Z. Chang, C.D. Lin, C.L. Cocke, Routes to control of H_2 Coulomb explosion in few-cycle laser pulses. Phys. Rev. Lett. **93**, 183202 (2004)
12. H. Niikura, D.M. Villeneuve, P.B. Corkum, Controlling vibrational wave packets with intense, few-cycle laser pulses. Phys. Rev. A **73**, 021402 (2006)
13. E.J. Takahashi, P. Lan, O.D. Mücke, Y. Nabekawa, K. Midorikawa, Attosecond nonlinear optics using gigawatt-scale isolated attosecond pulses. Nat. Commun. **4**, 2691 (2013)
14. M. Dantus, R.M. Bowman, A.H. Zewail, Femtosecond laser observations of molecular vibration and rotation. Nature **343**, 737 (1990)

15. Ch. Warmuth, A. Tortschanoff, F. Milota, M. Shapiro, Y. Prior, ISh Averbukh, W. Schleich, W. Jakubetz, H.F. Kauffmann, Studying vibrational wavepacket dynamics by measuring fluorescence interference fluctuations. J. Chem. Phys. **112**, 5060 (2000)
16. E.R. Warrick, W. Cao, D.M. Neumark, S.R. Leone, Probing the dynamics of Rydberg and valence states of molecular nitrogen with attosecond transient absorption spectroscopy. J. Phys. Chem. A **120**, 3165 (2016)
17. M.Y. Emelin, M.Y. Ryabikin, A.M. Sergeev, Monitoring long-term evolution of molecular vibrational wave packet using high-order harmonic generation. New J. Phys **10**, 025026 (2008)
18. A. Assion, M. Geisler, J. Helbing, V. Seyfried, T. Baumert, Femtosecond pump-probe photoelectron spectroscopy: mapping of vibrational wave-packet motion. Phys. Rev. A **54**, R4605 (1996)
19. T. Baumert, B. Bühler, M. Grosser, R. Thalweiser, V. Weiss, E. Wiedenmann, G. Gerber, Femtosecond time-resolved wave packet motion in molecular multiphoton ionization and fragmentation. J. Chem. Phys. **95**, 8103 (1991)
20. A. Assion, T. Baumert, M. Geisler, V. Seyfried, G. Gerber, Mapping of vibrational wavepacket motion by femtosecond time-resolved kinetic energy time-of-flight mass spectroscopy. Eur. Phys. J. D **4**, 145 (1998)
21. S. De, M. Magrakvelidze, I.A. Bocharova, D. Ray, W. Cao, I. Znakovskaya, H. Li, Z. Wang, G. Laurent, U. Thumm, M.F. Kling, I.V. Litvinyuk, I. Ben-Itzhak, C.L. Cocke, Following dynamic nuclear wave packets in N_2, O_2, and CO with few-cycle infrared pulses. Phys. Rev. A **84**, 043410 (2011)
22. Y.H. Jiang, A. Rudenko, J.F. Pérez-Torres, O. Herrwerth, L. Foucar, M. Kurka, K.U. Kühnel, M. Toppin, E. Plésiat, F. Morales, F. Martín, M. Lezius, M.F. Kling, T. Jahnke, R. Dörner, J.L. Sanz-Vicario, J. van Tilborg, A. Belkacem, M. Schulz, K. Ueda, T.J.M. Zouros, S. Düsterer, R. Treusch, C.D. Schröter, R. Moshammer, J. Ullrich, Investigating two-photon double ionization of D_2 by XUV-pump-XUV-probe experiments. Phys. Rev. A **81**, 051402 (2010)
23. J. Yang, M. Guehr, X. Shen, R. Li, T. Vecchione, R. Coffee, J. Corbett, A. Fry, N. Hartmann, C. Hast, K. Hegazy, K. Jobe, I. Makasyuk, J. Robinson, M.S. Robinson, S. Vetter, S. Weathersby, C. Yoneda, X. Wang, M. Centurion, Phys. Rev. Lett. **117**, 153002 (2016)
24. Y. Furukawa, Y. Nabekawa, T. Okino, A.A. Eilanlou, E.J. Takahashi, P. Lan, K.L. Ishikawa, T. Sato, K. Yamanouchi, K. Midorikawa, Resolving vibrational wave-packet dynamics of D_2^+ using multicolor probe pulses. Opt. Lett. **37**, 2922 (2012)
25. Y. Nabekawa, Y. Furukawa, T. Okino, A.A. Eilanlou, E.J. Takahashi, K. Yamanouchi, K. Midorikawa, Settling time of a vibrational wavepacket in ionization. Nat. Commun. **6**, 8197 (2015)
26. Y. Nabekawa, Y. Furukawa, T. Okino, A.A. Eilanlou, E.J. Takahashi, K. Yamanouchi, K. Midorikawa, Sub-10-fs control of dissociation pathways in the hydrogen molecular ion with a few-pulse attosecond pulse train. Nat. Commun. **7**, 12835 (2016)
27. A.T.J.B. Eppink, D.H. Parker, Velocity map imaging of ions and electrons using electrostatic lenses: application in photoelectron and photofragment ion imaging of molecular oxygen. Rev. Sci. Instrum. **68**, 3477 (1997)
28. Y. Nabekawa, A.A. Eilanlou, Y. Furukawa, K.L. Ishikawa, H. Takahashi, K. Midorikawa, Multi-terawatt laser system generating 12 fs pulses at 100 Hz repetition rate. Appl. Phys. B **101**, 523 (2010)
29. Y. Nabekawa, T. Shimizu, T. Okino, K. Furusawa, H. Hasewaga, K. Yamanouchi, K. Midorkawa, Conclusive evidence of an attosecond pulse train observed with the mode-resolved autocorrelation technique. Phys. Rev. Lett. **96**, 083901 (2006)
30. D. Proch, T. Trickl, A high-intensity multipurpose piezoelectric pulsed molecular beam source. Rev. Sci. Instrum. **60**, 713 (1989)
31. O. Ghafur, W. Siu, P. Johnsson, M.F. Kling, M. Drescher, M.J.J. Vrakking, A velocity map imaging detector with an integrated gas injection system. Rev. Sci. Instrum. **80**, 033110 (2009)
32. G.A. Garcia, L. Nahon, I. Powis, Two-dimensional charged particle image inversion using a polar basis function expansion. Rev. Sci. Instrum. **75**, 4989 (2004)

33. H.-J. Werner, P.J. Knowles, G. Knizia, F.R. Manby, M. Schütz, P. Celani, T. Korona, R. Lindh, A. Mitrushenkov, G. Rauhut, K.R. Shamasundar, T.B. Adler, R.D. Amos, A. Bernhardsson, A. Berning, D.L. Cooper, M.J.O. Deegan, A.J. Dobbyn, F. Eckert, E. Goll, C. Hampel, A. Hesselmann, G. Hetzer, T. Hrenar, G. Jansen, C. Köppl, Y. Liu, A.W. Lloyd, R.A. Mata, A.J. May, S.J. McNicholas, W. Meyer, M.E. Mura, A. Nicklass, D.P. ÓNeill, P. Palmieri, D. Peng, K. Pflüger, R. Pitzer, M. Reiher, T. Shiozaki, H. Stoll, A.J. Stone, R. Tarroni, T. Thorsteinsson, M. Wang, Molpro, version 2012.1, a package of ab initio programs (2012), http://www.molpro.net
34. A. Lofthus, P.H. Krupenie, The spectrum of molecular nitrogen. J. Phys. Chem. Ref. Data **6**, 113 (1977)
35. U. Thumm, T. Niederhausen, B. Feuerstein, Time-series analysis of vibrational nuclear wave-packet dynamics in D_2^+. Phys. Rev. A **77**, 063401 (2008)
36. M. Magrakvelidze, O. Herrwerth, Y.H. Jiang, A. Rudenko, M. Kurka, L. Foucar, K.U. Kühnel, M. Kübel, N.G. Johnson, C.D. Schröter, S. Düsterer, R. Treusch, M. Lezius, I. Ben-Itzhak, R. Moshammer, J. Ullrich, M.F. Kling, U. Thumm, Tracing nuclear-wave-packet dynamics in singly and doubly charged states of N_2 and O_2 with XUV-pump-XUV-probe experiments. Phys. Rev. A **86**, 013415 (2012)

Chapter 7
From Molecular Symmetry Breaking to Symmetry Restoration by Attosecond Quantum Control

ChunMei Liu, Jörn Manz and Jean Christophe Tremblay

Abstract It is well known that laser pulses can break electronic structure symmetry of atoms and molecules, specifically by superposing two (or more) states with different irreducible representations (IRREPs). Recently, our theory group together with the experimental group of Professor Kenji Ohmori, our partner at the Institute for Molecular Science in Okazaki, have shown that laser pulses can also achieve the reverse process, symmetry restoration. For this purpose, the pulse for symmetry restoration was designed as a copy of the pulse for symmetry breaking, with attosecond precision of the proper time delay. Here we develop the theory for new scenarios coherent molecular symmetry breaking and restoration. The extensions are from previous applications of weak circularly polarized ultrafast (fs) laser pulses with Gaussian shapes to intense linearly polarized ultrafast laser pulses that do not need to be transform-limited, e.g. they may have down- and up-chirps. As a proof-of-principle, quantum dynamics simulations demonstrate restoration of D_{6h} symmetry of the aligned model benzene molecule, after laser induced $D_{6h} \rightarrow C_{2v}$ symmetry breaking. The success depends on two criteria: (i) the laser pulse that restores symmetry is designed as a time-reversed copy of the pulse that breaks symmetry; and (ii) their time delay must be chosen with attosecond precision such that the wavefunction at the central time between the pulses is a superposition of two states with different IRREPs but with the same or with opposite phases (modulo 2π).

C. Liu · J. Manz · J. C. Tremblay
Institut für Chemie und Biochemie, Freie Universität Berlin, 14195 Berlin, Germany
e-mail: chunmei@zedat.fu-berlin.de

J. C. Tremblay
e-mail: jctremblay@zedat.fu-berlin.de

J. Manz (✉)
State Key Laboratory of Quantum Optics and Quantum Optics Devices, Institute of Laser Spectroscopy, Shanxi University, Taiyuan 030006, China
e-mail: jmanz@chemie.fu-berlin.de

J. Manz
Collaborative Innovation Center of Extreme Optics, Shanxi University, Taiyuan 030006, China

© Springer Nature Switzerland AG 2018

K. Yamanouchi et al. (eds.), *Progress in Ultrafast Intense Laser Science XIV*,
Springer Series in Chemical Physics 118,
https://doi.org/10.1007/978-3-030-03786-4_7

7.1 Introduction

The purpose of this chapter is twofold: First, to introduce the reader to attosecond control of coherent symmetry breaking and restoration of the electronic structure of molecules and atoms, a field of research that our theory group has initiated in cooperation with the experimental group of Professor Kenji Ohmori, our partner at the Institute of Molecular Science in Okazaki [1]. Section 7.2 presents a survey of that approach, with the necessary details and explanation of the nomenclature. This survey serves as a reference for the second purpose, namely to develop the theory for new control scenarios that employ ultrafast (<10 fs) intense (up to 10 TW/cm^2) linearly polarized laser pulses, instead of the previous weak (ca 26 MW/cm^2) circularly polarized pulses [1], in order to break and restore electronic structure symmetry in molecules (Sect. 7.3), and also to demonstrate successful applications by means of quantum dynamics simulations for an important model system, the aligned benzene molecule (Sect. 7.4). The new scenarios also include non-transform-limited laser pulses, specifically with down- and up-chirps, whereas the previous approach employed Gaussian pulses. Conclusions are presented Sect. 7.5.

The previous [1] and present investigations are motivated by important processes of breaking and making symmetry in nature. Symmetry breaking is a ubiquitous phenomenon, from elementary particle physics [2] to biology [3] and cosmology [4]. In particular, it is well known that molecular symmetry can be broken by laser pulses, see e.g. [5–8]. After the derivations of fundamental concepts, this effect was demonstrated recently, both experimentally and theoretically [9, 10]. Generation of symmetry is exemplified in chemical synthesis, e.g. the formation of the Buckminster fullerene C_{60} with its beautiful icosahedral symmetry [11].

In retrospect, one can also find examples of laser driven coherent symmetry breaking and restoration in the literature, even though this phenomenon had not been noted by the authors. As an example, consider the celebrated three-step mechanism of laser induced high harmonic generation (HHG) [12–15] applied to molecules that have highly symmetric electronic structures in their ground states: In the first step, the system is photo-ionized by a laser pulse, thus breaking its symmetry. Next the laser pulse drives the photo-emitted electron back to the ion such that it forms a highly excited asymmetric collision pair. In the third step, the system is de-excited to the symmetric ground state by spontaneous emission of high harmonics. This example shows that symmetry breaking and subsequent restoration, starting from and ending up in the symmetric electronic ground state, may be quite useful, e.g. here it induces HHG. Unfortunately, the yields of HHG are typically very small, which implies that the efficiency of symmetry breaking and restoration by means of HHG is much less than 1%. This provides the quantitative challenge for the previous [1] and present investigations: we are heading for the design of laser pulses that achieve 100% coherent symmetry breaking and restoration. The goal had already been achieved in early work on Ramsey fringes in Rydberg atoms by Alber et al. [16] and by Noordam et al. [17], but again, these authors did not note the phenomenon. Recently, Golubev et al. developed concepts of laser control for exciting molecules from the ground

state to excited superposition states, and then de-exciting them back to the ground state, but without aiming at symmetry breaking nor restoration [18].

7.2 Survey of Our Previous Approach to Coherent Symmetry Breaking and Restoration of Molecular Electronic Structure [1]

For reference, the present summary of our previous approach [1] focuses on symmetry breaking and restoration of molecular electronic structure. There are also quite important applications to atoms in [1], but those will not be reported here in any detail. In general, the approach is applied to molecules that have highly symmetric electronic ground (g) states with irreducible representation IRREP_g as well as degenerate pairs of excited (e) states with $\text{IRREP}_e \neq \text{IRREP}_g$. It employs two rather weak circularly polarized laser pulses, the "first" one $\boldsymbol{\epsilon}_b(t)$ breaks (b) the electronic symmetry and the "second" one $\boldsymbol{\epsilon}_r(t)$ restores (r) it. The second pulse centered at t_r is a copy of the first one centered at t_b,

$$\boldsymbol{\epsilon}_r(t + t_r) = \boldsymbol{\epsilon}_b(t + t_b). \tag{7.1}$$

The total electric field of the two pulses is

$$\boldsymbol{\epsilon}(t) = \boldsymbol{\epsilon}_b(t) + \boldsymbol{\epsilon}_r(t), \tag{7.2}$$

with maximum intensity

$$I_{\max} = \max \frac{1}{2} c\varepsilon_0 |\boldsymbol{\epsilon}(t)|^2 \tag{7.3}$$

where ε_0 is the permittivity of the vacuum, and c is the velocity of light. For convenience, we set $t_b < 0$ and

$$t_r = -t_b > 0, \tag{7.4}$$

that means the temporal center (c) of the two pulses is at

$$t_c = \frac{(t_r + t_b)}{2} = 0. \tag{7.5}$$

The two pulses have the same Gaussian envelopes, the same amplitudes ϵ for the electric field, the same pulse durations τ, and the same carrier frequencies ω_c. The time delay

$$t_d = t_r - t_b = 2|t_b| \tag{7.6}$$

between the peaks of the two pulse envelopes is chosen to be much (that means at least several times) larger than their durations,

$$t_d \gg \tau, \tag{7.7}$$

so that the overlap of the two pulses at t_c is negligible. As a consequence, there is a time interval (centered at t_c) between the two laser pulses where the molecule evolves in a quasi-field-free environment.

Initially, at time t_i well before the peak of the laser pulse that breaks symmetry (that means the pulse is negligible), $t_i \ll t_b$, the molecule is in the symmetric electronic ground state

$$\Psi(t_i) = \Psi_g \tag{7.8}$$

with energy E_g. For convenience, E_g is set equal to zero. The first pulse excites the system to a superposition

$$\Psi(t) = c_g(t)\Psi_g + c_e(t)\Psi_e \tag{7.9}$$

of Ψ_g and a degenerate excited state Ψ_e with energy $E_e > E_g$. The corresponding populations are

$$\begin{aligned} P_g(t) &= |c_g(t)|^2, \\ P_e(t) &= |c_e(t)|^2. \end{aligned} \tag{7.10}$$

The superposition (7.9) of the two molecular eigenstates with different IRREPs implies symmetry breaking, e.g. $D_{6h} \to C_s$ in the case of benzene [1]. During the quasi-field-free time interval between the first and second laser pulses, the coefficients evolve as

$$\begin{aligned} c_g(t) &= C_g e^{i\eta_g - iE_g t/\hbar}, \\ c_e(t) &= C_e e^{i\eta_e - iE_e t/\hbar}, \end{aligned} \tag{7.11}$$

with real valued amplitudes C_g, C_e and phases η_g, η_e, respectively. The corresponding populations are perfectly constant

$$\begin{aligned} P_g(t) &= P_g(t_c) = C_g^2, \\ P_e(t) &= P_e(t_c) = C_e^2, \end{aligned} \tag{7.12}$$

and they are normalized,

$$P_g(t_c) + P_e(t_c) = 1. \tag{7.13}$$

The field amplitude and the corresponding maximum intensity applied in [1] are rather weak, $\epsilon = 4.420 \times 10^6$ V/cm, $I_{\max} = 26$ GW/cm^2 such that the population of the excited state at the central time is rather small, $P_e(t_c = 0) = 0.0037$, but this is sufficient for symmetry breaking.

The laser carrier frequency satisfies the resonance condition

$$\hbar\omega_c = E_e - E_g. \tag{7.14}$$

Typical energy gaps are of the order of few eV. The corresponding periods

$$T = \frac{2\pi}{\omega_c} \tag{7.15}$$

are, therefore, in the domain from few fs down to few hundred as. The wavelengths

$$\lambda = c \cdot T \tag{7.16}$$

exceed the molecular scale by two orders of magnitude or more, so that the molecule is in a quasi-homogeneous environment i.e. to a very good approximation, the electric field in the domain of the molecule depends on time but not on spatial coordinates.

After symmetry breaking, the superposition state $\Psi(t)$, (7.9), represents ultrafast circulating charge migration, with period T, similar to the phenomena discovered in [19, 20], see also [21, 22]. The second laser pulse transfers the molecule back to its ground state, i.e. finally at time

$$t_f = -t_i, \tag{7.17}$$

well after the pulse that restores symmetry (that means the pulse is negligible), the molecular wavefunction is

$$\Psi(t_f) = \Psi_g e^{i\tilde{\eta}} \tag{7.18}$$

with irrelevant phase $\tilde{\eta}$, i.e.

$$\begin{aligned} P_g(t) &= P_g(t_f) = 1, \\ P_e(t) &= P_e(t_f) = 0 \text{ for } t \geq t_f \end{aligned} \tag{7.19}$$

This means that the second pulse stops charge migration. For this purpose, the laser pulses should satisfy two conditions [1]. First, the time delay between the two pulses must be chosen such that the phase shift of the two components Ψ_g and Ψ_e of the wavefunction $\Psi(t)$ at the central time t_c are equal to 0 or to π,

$$\begin{aligned} \Delta\eta(t_c) \bmod 2\pi &= (\eta_e - \eta_g) \bmod 2\pi = \{0, \pm\pi\}. \\ \eta = \eta_g \bmod \pi &= \eta_e \bmod \pi. \end{aligned} \tag{7.20}$$

In practice, the ideal condition (7.20) must be satisfied with temporal precision of ca 5 as. The experimental results in [1] show that this is possible, by means of the methods that have been developed in [23], in the limit of weak laser pulses applied to a gas of the system at low temperature and at low density such that interactions between neighboring atoms or molecules are negligible. Control of the time delay between two laser pulses with time resolution even better than 1 as (in the time domain of few hundred zeptoseconds) has been demonstrated in [24].

The second condition is that the laser pulses should be designed such that the matrix representation of the Hamiltonian of the molecule H_m with semiclassical dipole coupling to the laser field,

$$H(t) = H_m - \mathbf{d} \cdot \boldsymbol{\epsilon}(t) \tag{7.21}$$

is adjunct upon time reversal,

$$\mathbf{H}(t) = \mathbf{H}^*(-t). \tag{7.22}$$

The construction of the laser pulse that restores symmetry as properly time-delayed copy of the circularly polarized laser pulse that breaks symmetry, (7.1) and (7.2), guarantees that the condition (7.22) is satisfied [1].

The two key equations (7.20) and (7.22) define two sufficient conditions that guarantee the success of the approach of [1]. If these conditions are not satisfied, it may fail. For example, if the second pulse is not applied at the proper time t_r but at

$$t_r' = t_r + t', \tag{7.23}$$

then the population of the excited state at the final time

$$t_f' = t_f + t' \tag{7.24}$$

is no longer equal to zero. Instead, it varies periodically,

$$P_e(t_f') = 4P_g(t_c)P_e(t_c) \cdot \left[\frac{1}{2} - \frac{1}{2}\cos\left(\frac{2\pi t'}{T}\right)\right], \tag{7.25}$$

between zero and the maximum value

$$\max P_e(t_f') = 4P_g(t_c)P_e(t_c), \tag{7.26}$$

with period T. The applications of the rather weak laser pulses in [1] imply that the populations $P_e(t_c)$ of the excited state at the central time t_c are rather small so that $P_g(t_c) \approx 1$ and

$$\max P_e(t_f') \approx 4P_e(t_c) \tag{7.27}$$

7.3 Theory for New Scenarios of Coherent Breaking and Restoration of the Symmetry of Molecular Electronic Structure

This Section considers coherent symmetry breaking and restoration by means of two laser pulses analogous to Sect. 7.2, but with extensions from ultrafast weak circularly polarized laser pulses to ultrafast intense linearly polarized pulses, and with new

design of the laser pulse that restores symmetry, different from the previous design (7.1) as time delayed copy of the laser pulse that breaks symmetry. For convenience, we shall employ the same nomenclature and similar rules that have been introduced in Sect. 7.2, e.g. the laser pulses are centered at t_b and $t_r = -t_b$, etc. As in Sect. 7.2, the new approach applies to molecules with highly symmetric electronic ground states Ψ_g with energy $E_g(=0)$ and IRREP_g and excited states Ψ_e with energies E_e and $\text{IRREP}_e \neq \text{IRREP}_g$. In contrast to the scenario of Sect. 7.2, however, we no longer require that the excited states should be degenerate. All we assume is that we can employ a linearly polarized laser pulse that is centered at $t_b < 0$ in order to excite the initial state $\Psi(t_i) = \Psi_g$ to the superposition state $\Psi(t)$, (7.9) such that it evolves with coefficients in quasi-field-free environment.

Specifically, we assume that the molecule is located at the origin of a laboratory fixed system of Cartesian coordinates, and the laser pulse that breaks its symmetry propagates along the z axis, taking the form

$$\boldsymbol{\epsilon}_b(t) = \mathbf{e}_y \epsilon e^{-(t-t_b)^2/2\tau^2} \cdot \sin\left[\omega_b(t) \cdot (t - t_b) + \eta_b\right] \tag{7.28}$$

that means it is linearly polarized – as convenient example, we consider the case of linear y-polarization. It has electric field amplitude ϵ and Gaussian shape with the peak at t_b and with the width parameter τ. The carrier envelope phase η_b is set equal to zero. In contrast with Sect. 7.2, the laser frequency may depend on time, e.g.

$$\omega_b(t) = \omega_c + \omega' \cdot (t_b + t) \tag{7.29}$$

where ω_c is the resonant carrier frequency, (7.14), and the parameter ω' allows applications to various scenarios with linear up-chirp ($\omega' > 0$), zero chirp ($\omega' = 0$), or down-chirp ($\omega' < 0$). For reference, the transform-limited laser pulse has mean duration

$$\Delta\tau = \frac{1}{\sqrt{2}}\tau, \tag{7.30}$$

and the uncertainty of the excitation energy is [1]

$$\Delta E = \hbar\Delta\omega = \frac{1}{\sqrt{2}}\hbar/\tau. \tag{7.31}$$

The laser pulse for symmetry restoration centered at t_r is designed as *time–reversed* copy of the pulse that breaks symmetry,

$$\boldsymbol{\epsilon}_r(t_r - t) = \boldsymbol{\epsilon}_b(t + t_b), \tag{7.32}$$

Note that this is quite different from (7.1) that defines $\boldsymbol{\epsilon}_r$ as a copy of $\boldsymbol{\epsilon}_b$. Explicitly,

$$\boldsymbol{\epsilon}_r(t) = -\mathbf{e}_y \epsilon e^{-(t-t_r)^2/2\tau^2} \cdot \sin\left[\omega_r(t) \cdot (t - t_r)\right] \tag{7.33}$$

where

$$\omega_r(t) = \omega_c - \omega' \cdot (t - t_r), \tag{7.34}$$

with the same parameters as for the laser pulse that breaks symmetry. As in Sect. 7.2, we choose $t_r = -t_b$ such that the central time is $t_c = 0$. Comparison of (7.29) and (7.34) shows that if the first laser pulse $\boldsymbol{\epsilon}_b(t)$ is down-chirped, then the second laser pulse $\boldsymbol{\epsilon}_r(t)$ is up-chirped, and vice versa.

The total electric field of the two laser pulses $\boldsymbol{\epsilon}(t)$ is, therefore, time-reversible,

$$\boldsymbol{\epsilon}(t) = \boldsymbol{\epsilon}(-t) \tag{7.35}$$

The matrix representation of the Hamiltonian $H(t)$ (c.f. (7.21)) is, therefore, also time reversible,

$$\mathbf{H}(t) = \mathbf{H}(-t). \tag{7.36}$$

For linearly polarized laser pulses, the matrix representations are real-valued,

$$\mathbf{H}(t) = \mathbf{H}^*(t) \tag{7.37}$$

As a consequence, (7.36) may be re-written using the same form as (7.22), or in other words, (7.36) may be recognized as special case of (7.22). This means that the present design (7.32) of the laser pulse that restores symmetry as a time reversed copy of the linearly polarized pulse that breaks symmetry satisfies at least one of the two important sufficient conditions for symmetry restoration.

Next we show that the other sufficient condition (7.20) can also be satisfied by proper choice of the time delay t_d (7.6) between the two laser pulses. For this purpose, let us start by a rather arbitrary tentative guess t_b' of the temporal center of the pulse that breaks symmetry, again subject to the condition $|t_b'| \gg \tau$. Symmetry is broken by preparation of the superposition (7.9) of two states Ψ_g and Ψ_e, with different IRREPs. In quasi-field free environment, it evolves with coefficients

$$\begin{aligned} c_g(t') &= C_g e^{i\eta_g' - iE_g t'/\hbar} \\ c_e(t') &= C_e e^{i\eta_e' - iE_e t'/\hbar}, \end{aligned} \tag{7.38}$$

analogous to (7.11). In particular, $c_g(t' = 0) = C_g e^{i\eta_g'}$ and $c_e(t' = 0) = C_e e^{i\eta_e'}$ at the tentative central time $t_c' = 0$. Now there are two possibilities: either the phases satisfy the condition $(\eta_e' - \eta_g')$ modulo $2\pi = 0, \pm\pi$ by chance. Then the tentative guess t_b' and the corresponding time delay $t_d' = 2|t_b'|$ already satisfies condition (7.20) by construction. Else the phase difference will decrease linearly such that the condition

$$\Delta\eta(t') \text{ modulo } 2\pi = \left[\eta_e' - \eta_g' - (E_e - E_g)t'/\hbar\right] \text{ modulo } 2\pi = 0, \pm\pi \tag{7.39}$$

will be satisfied at the properly chosen time t' in the time interval $(0, T)$. This allows to define the central time of the laser pulse that breaks symmetry as

$$t_b = t_b' - t'. \tag{7.40}$$

The resulting phases at $t_c = 0$ are

$$\begin{aligned} \eta_g &= \eta_g' - E_g t'/\hbar, \\ \eta_e &= \eta_e' - E_e t'/\hbar \end{aligned} \tag{7.41}$$

such that the condition (7.20) is indeed satisfied, $\Delta\eta(t_c = 0)$ modulo $2\pi = 0, \pm\pi$.

In conclusion, the design of the linearly polarized laser pulse that restores symmetry, centered at $t_r = -t_b$, as the time reversed copy of the laser pulse that breaks symmetry, centered at t_b, with proper time delay

$$t_d = t_r - t_b = 2|t_b| = 2|t_b' - t'| \tag{7.42}$$

satisfies the two sufficient conditions (7.20) and (7.22) that guarantee successful coherent symmetry breaking and restoration.

The mathematical proof for the sufficient conditions of "proper phase" (7.20) and the "temporal symmetry" (7.22)—which includes time reversal of linearly polarized pulses (7.35) – is presented in the Appendix. Here we add an explanation that is motivated by real life. Consider a child on a swing, or in the mathematical sense more ideally a pendulum that initially hangs down from an infinitesimally small hook, with its rope perpendicular to a plane ($C_{\infty v}$ symmetry). Systematic kicks induce periodic swings, thus breaking the initial symmetry ($C_{\infty v} \rightarrow C_{2v}$). In order to restore the $C_{\infty v}$ symmetry, one can apply the reverse set of kicks (analogous to (7.32) and (7.35)), but they must be applied with proper phases (analogous to (7.20)) in order to stop swinging. The proof in the Appendix also includes the derivation of the periodic population of the excited state $P_e(t_f')$, (7.25) for the case where condition (7.20) is not satisfied. This implies that (7.25) applies also to the present new scenarios (or failures) of coherent symmetry breaking and restoration.

To illustrate the concept of symmetry breaking and restoration, quantum simulations of the laser-driven wave packet dynamics in the model benzene (Sect. 7.4) are carried out by means of the numerical techniques that have been developed in [1].

7.4 The New Scenarios for Coherent Breaking and Restoring the Symmetry of Electronic Structure Applied to the Model Benzene: A Proof-of-Principle

In this Section, we present quantum dynamics simulations of the new scenarios of coherent symmetry breaking and restoration that have been developed in Sect. 7.3, with applications to the model benzene. The model is adapted from the fundamental work on laser control of the aromaticity of benzene, developed by Ulusoy and Nest [25]. Previously, we have employed their model in order to demonstrate

quantum control of adiabatic attosecond charge migration and the related electronic fluxes [20], see also [26, 27]. This way we could already show that the rather high D_{6h} symmetry of the electronic structure of benzene's ground state Ψ_g is broken by exciting Ψ_g to superposition states $c_g(t)\Psi_g + c_e(t)\Psi_e$, (7.9), with different excited states Ψ_e, depending on the laser pulses. Specifically, one can design circularly and linearly polarized laser pulses that achieve different symmetry breakings, $D_{6h} \rightarrow C_s$ and $D_{6h} \rightarrow C_{2v}$, respectively [20]. In [1] we have shown how symmetry breaking, $D_{6h} \rightarrow C_s$ can be restored, $C_s \rightarrow D_{6h}$, by means of an ultrashort circularly polarized laser pulse that is designed as a copy of the pulse that breaks symmetry, with attosecond precision of the proper time delay, as summarized in Sect. 7.2. Here we shall show that $D_{6h} \rightarrow C_{2v}$ symmetry breaking can also be restored, $C_{2v} \rightarrow D_{6h}$, namely by means of the approach of Sect. 7.3. Coherent symmetry breaking, $D_{6h} \rightarrow C_{2v}$, and restoration, $C_{2v} \rightarrow D_{6h}$, will be demonstrated for two scenarios: First we shall employ non-chirped ultrafast intense linearly polarized laser pulses with Gaussian shapes, as suggested in [20]. Second, we shall employ non-transform-limited laser pulses with down- and up-chirps, illustrating the theory developed in Sect. 7.3.

The model benzene assumes that the molecular center of mass is fixed at the origin of the laboratory, right-handed set of Cartesian coordinates x, y, z, where z is along the direction of propagation of the laser pulses, y is along their polarizations, and x is perpendicular to y and z. The molecule is aligned with its molecular plane in the laboratory xy- plane, with two carbon nuclei on the positive and negative y-axis [25]. For convenience, these carbon nuclei will be called the "north-pole" and the "south pole", respectively. The nuclear geometry is fixed at the global minimum structure of the electronic ground state $g = S_0$, with D_{6h} symmetry, as specified in [25, 26]. The excited state is $e = S_4$ – this choice is motivated by the results of [20, 25] that show that the model benzene can be excited from S_0 to S_4 by means of a linearly y-polarized laser pulse. Accordingly, S_4 has been called "S_y" in [20]. Another motivation for the choice of $e = S_4$ is that its IRREP$_e = E_{1u}$ is different from IRREP$_g = A_{1g}$ of the ground state $g = S_0$ [25] so that the y-polarized laser pulse will indeed break the symmetry of electronic structure when it excites the ground state (D_{6h}) to a superposition state of S_0 and $S_4(C_{2v})$, as described in Sect. 7.3. The electronic properties of benzene – including the wave functions Ψ_g and Ψ_e, their energies $E_g(=0)$ and E_e, the one-electron densities, and the relevant y-component of the transition dipole moment – are adapted from [20], or they are calculated by means of quantum chemistry methods that are specified in Sect. 2.2 of [20]. The resulting electronic wave functions Ψ_g and Ψ_e are real-valued. The energy gap is equal to 8.210 eV, implying the period $T = 503.735$ as, cf. (7.14) and (7.15). The one-electron density of the initial ground state S_0, with D_{6h} symmetry, is illustrated on the left hand side of Fig. 7.1. All densities are reconstructed from the many-body wavefunction using the detCI [28] module of our open source python toolbox ORBKIT [29].

The ultrafast intense linearly y-polarized laser pulses that break and restore symmetry are designed according to the following criteria: The pulse durations τ should be rather short so that

(i) the entire time interval from the initial time t_i when $\epsilon_b(t)$ is still negligible, via

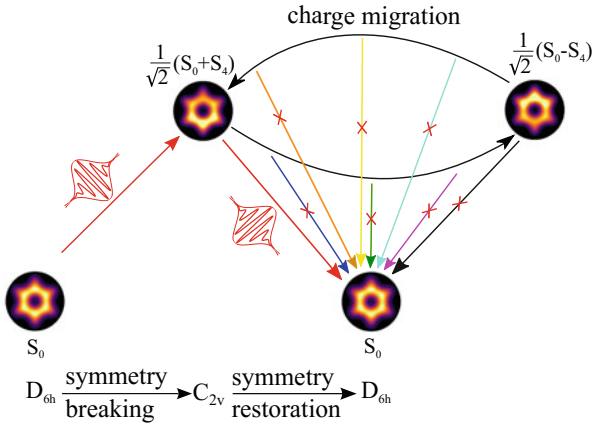

Fig. 7.1 Coherent symmetry breaking $D_{6h} \to C_{2v}$ and restoration $C_{2v} \to D_{6h}$ of the model benzene, by means of two linearly y-polarized ultrashort intense laser pulses (schematic). The first pulse breaks electronic structure symmetry by exciting the molecule from its initial ($t_i = -5$ fs) ground state (S_0) with D_{6h} symmetry to the superposition state $\frac{1}{\sqrt{2}}(S_0 + S_4)e^{i\eta}$ (with irrelevant overall phase factor $e^{i\eta}$) with C_{2v} symmetry at the central time, $t_c = 0$. The second pulse is the time-reversed copy of the first one. It restores symmetry by de-exciting the superposition state back to S_0 at $t_f = 5$ fs. The wave functions of the ground state S_0 (left), the superposition state (top left), and again S_0 (bottom right) are illustrated by snapshots of the one-electron densities, with obvious symmetries D_{6h}, C_{2v}, and D_{6h}, respectively. Successful symmetry breaking and restoration depends on two conditions that are explained in the text, (7.20) and (7.22). In particular, the laser pulses must be fired with attosecond precision of the time delays (red arrows). of the time delay (red arrows). Figure 7.1 also illustrates the pending failures (indicated by arrows with different colors that are crossed out) of the approach if condition (7.20) is violated e.g. by firing the second pulse with additional time delay $t'_d = t_d + t'$, $t' = kT/8$, $k = 1, 2, \ldots, 7$ where T is the period of charge migration on the way from the ideal case ($t' = 0$) for $\frac{1}{\sqrt{2}}(S_0 + S_4)$ (top panel) via the case ($t' = T/2$) for $\frac{1}{\sqrt{2}}(S_0 - S_4)$ (top right panel) $\frac{1}{\sqrt{2}}(S_0 - S_4)$

t_b, t_c, t_r to the final time t_f when $\epsilon_r(t)$ is negligible,

$$t_i < t_b < t_c = 0 < t_r = -t_b < t_f = -t_i \tag{7.43}$$

should be smaller than ca 10 fs,

$$t_f - t_i \leq 10 \text{ fs} \tag{7.44}$$

This condition (7.44) is motivated by the results of [22, 30] that show that effects of nuclear dynamics on the laser driven electronic dynamics of benzene are negligible for times up to 10 fs, that means condition (7.44) justifies the model of Sects. 7.2 (adapted from [1]) and 7.3 that focuses on laser driven electronic dynamics for fixed nuclear geometry;

(ii) the two laser pulses should be well separated from each other such that at the central time $t_c = 0$, the molecule is in a quasi field-free environment.

Accordingly, we set $t_i = -5$ fs, $t_f = 5$ fs, $\tau = 0.5696$ fs. As a consequence, the two laser pulses are ultrashort few-cycle pulses. For reference, consider the case of the transform limited pulses. Their mean durations are $\Delta\tau = 0.403$ fs, c.f. (7.30), and the uncertainty of the excitation energy is $\Delta E = 0.817$ eV, c.f. (7.31). The target state S_4 is the only one that can be excited from S_0 by corresponding one-photon transitions induced by a y-polarized laser pulse. This supports the two-state ($g = S_0, e = S_4$) model of Sects. 7.2 and 7.3.

For the present Chapter focusing on ultrashort intense laser science, the values of the electric field ϵ and the corresponding maximum intensity $I_{\max}$ should be much more intense than for the weak electric field [1]. There, the population $P_e(t_c = 0)$ of Ψ_e in the excited superposition state (7.9) at $t_c = 0$ is so small (=0.0037) that we could use the weak electric field limit (7.27) of the maximum value of $P_e(t_f')$ at the final time t_f' (7.26). Here we go for the opposite limit when max $P_e(t_f')$ approaches its maximum value (=1). As a consequence, we require that

$$P_g(t_c = 0) = P_e(t_c = 0) = \frac{1}{2} \tag{7.45}$$

For this purpose, the laser pulses that break and restore symmetry must be designed as $\pi/2$-laser pulses. This is done as shown in [20]. For the given pulse duration τ, the resulting values of the electric field amplitude and maximum intensity are $\epsilon = 6.650 \times 10^7$ V/cm and $I_{\max} = 5.873$ TW/cm^2, for the first scenario that uses resonant laser pulses. The second scenario uses down- and up-chirped laser pulses to break and restore symmetry, respectively, with chirp parameter $\omega' = -2.495$ fs^{-2}. Here we obtain even larger values of the field strength, $\epsilon = 9.320 \times 10^7$ V/cm, and $I_{\max} = 11.536$ TW/cm^2. As in [20, 25–27], our model neglects multiphoton and ionization processes, even at these high intensities. This is, of course, a serious approximation that should be investigated further in future work.

The time delays between the pulses are determined such that condition (7.20) is satisfied. For the strong field limit (7.45), this means that the wavefunction

$$\Psi(t_c = 0) = \frac{1}{\sqrt{2}}(\Psi_g + \Psi_e)e^{i\eta} = \frac{1}{\sqrt{2}}(S_0 + S_4)e^{i\eta} \tag{7.46}$$

is real-valued, except for the irrelevant overall phase factor $e^{i\eta}$. It is well known that this implies zero electronic fluxes [31], or in other words no charge migration, at the central time $t_c = 0$ between the two pulses. The method for determining the proper time delays has been explained in Sect. 7.3, (7.38)–(7.42). The resulting values are $t_d = 5.035$ fs and $t_d = 5.096$ fs for the scenarios with resonant and chirped pulses, respectively. The corresponding values of the temporal centers of the pulses are $t_b = -t_d/2$ and $t_r = t_d/2$.

Figure 7.1 also illustrates the concept of coherent symmetry breaking and restoration by the new scenarios, using ultrafast intense linearly y-polarized laser pulses,

applied to the model benzene (red arrows): The first laser pulse, which is centered at time $t_b < 0$, breaks symmetry by exciting the ground state (D_{6h}) to the superposition state (7.9) (C_{2v}). The one-electron density of $\Psi(t_c = 0)$ is shown in the top left of Fig. 7.1 – one clearly recognizes its C_{2v} symmetry, with part of the electronic density accumulated near to the "south pole", at the expense of the "north pole". Subsequently, the second laser pulse, which is the time-reversed copy of the first one centered at time t_r, (7.32), restores D_{6h} symmetry of the electronic density, as shown in Fig. 7.1.

Figure 7.1 also illustrates failures of the approach that are pending if one of the two conditions (7.20) and (7.22) is not satisfied. For this purpose, let us consider the case when the second laser is delayed by additional time t' such that

$$\begin{aligned} t'_r &= t_r + t' \\ t'_f &= t_f + t' \\ t'_d &= t_d + t' \\ t'_c &= (t_b + t'_r)/2 = t'/2 \end{aligned} \tag{7.47}$$

The wave function uses this additional time to evolve from the ideal reference (7.46) at t_c to

$$\begin{aligned} \Psi(t) &= \frac{1}{\sqrt{2}} \left[\Psi_g + e^{i(E_e - E_g)t/\hbar} \Psi_e \right] e^{i\eta} \\ &= \frac{1}{\sqrt{2}} \left[\Psi_g + e^{i2\pi t/T} \Psi_e \right] e^{i\eta}, \; 0 \le t \le t' \end{aligned} \tag{7.48}$$

that means it becomes complex so that it describes electronic fluxes that appear as periodic charge migration from the "south pole" (top left snapshot of the one-electron density in Fig. 7.1) to the "north pole" (top right snapshot), and back, with period T [20]. This type of charge migration which is induced by the linearly y-polarized laser pulse (Sect. 7.3) is quite different from circular charge migration that is driven by the circularly polarized laser pulses in [1] (Sect. 7.2). It reminds of periodic charge migration from one site to the opposite one in molecules with linear topology, as discovered in [32–40], but the details are different, i.e. the ring-shaped model benzene with broken C_{2v} symmetry exhibits "pincer-type" charge migration [20].

Specifically, Fig. 7.1 illustrates seven failed attempts to restore symmetry by laser pulses that are fired with additional time $t' = kT/8, k = 1, 2, \ldots, 7$ – that means during charge migration – by arrows with different colors that are "crossed out", because they do not satisfy the condition (7.20). Only the last "attempt" at $t' = T$ is again successful, as indicated by the red arrow from the top left structure to the D_{6h} structure at the bottom right of Fig. 7.1. At this special value of t', the central time has changed from $t_c = 0$ to $t'_c = T/2$.

The results for the first scenario of coherent symmetry breaking ($D_{6h} \rightarrow C_{2v}$) and restoration ($C_{2v} \rightarrow D_{6h}$) of the electronic structure of the model benzene by means of two ultrafast intense linearly y-polarized laser pulses without chirps are shown in Fig. 7.2. The time evolution of the y-component of the total electric field (7.2) is in

the top panel. It consists of two pulses for symmetry breaking and restoration that are centered at $t_b = -2.517$ fs and $t_r = -t_b > 0$, respectively. The laser pulse for symmetry restoration is the time reversed copy of the pulse for symmetry breaking, (7.32). Both pulses have Gaussian envelopes with the same parameters that have been specified above ($\tau = 0.567$ fs, $\epsilon = 6.650 \times 10^7$ V/cm). The middle panel of Fig. 7.2 shows the resulting time evolutions of the probabilities $P_g = P_0$ and $P_e = P_4$, (7.10), of the two components $g = S_0$ and $e = S_4$ of the superposition state (7.9). Initially at time t_i, the model benzene is in the ground state ($P_g(t_i) = 1$) with D_{6h} symmetry, cf. Fig. 7.1. At the central time $t_c = 0$, it is in the superposition state (7.46) with equal

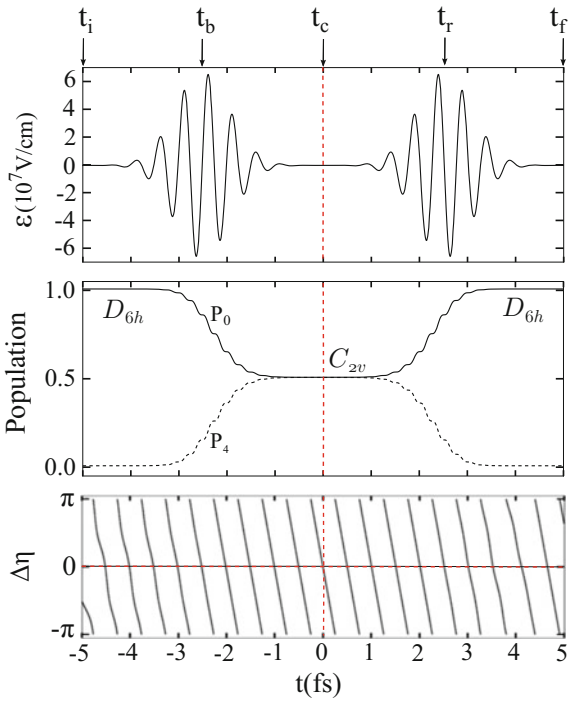

Fig. 7.2 Coherent symmetry breaking $D_{6h} \rightarrow C_{2v}$ and restoration $C_{2v} \rightarrow D_{6h}$ of the electronic structure of the model benzene by means of two ultrafast intense linearly y-polarized laser pulses with Gaussian shapes and zero chirps. Top panel: Time evolution of the y-component of the electric field ϵ of the laser pulses that break and restore symmetry. The pulse for symmetry restoration centered at $t_r = 2.517$ fs is the time reversed copy of the pulse for symmetry breaking centered at $t_b = -t_r$. Middle panel: Time evolution of the populations $P_g = P_0$ and $P_e = P_4$ of the two components, i.e. the ground state $g = S_0$ and the excited state $e = S_4$ of the superposition state (7.9). Initially, $P_0(t_i = -5\,fs) = 1$ i.e. benzene is in its electronic ground state S_0 (D_{6h} symmetry); at the central time $t_c = 0$, the two components have equal weights (C_{2v}); finally $P_0(t_f = 5$ fs$) = 1$, i.e. benzene is back to $S_0(D_{6h})$, compare with Fig. 7.1. Bottom panel: Time evolution of the phase difference ($\Delta\eta$ mod 2π) between the ground and the excited states in the superposition state (7.9). The time delay $t_d = t_r - t_b$ is chosen such that the condition (7.20) for symmetry breaking and restoration, i.e. $\Delta\eta$ mod $2\pi = 0$ at $t_c = (t_b + t_r)/2 = 0$, is satisfied with attosecond precision

weights of the two components ($P_g(t_c = 0) = P_e(t_c = 0) = 1/2$, (7.45)) with C_{2v} symmetry, cf. Fig. 7.1. Finally, at t_f, it is back to the ground state ($P_g(t_f) = 1$), i.e. back to D_{6h} symmetry, cf. Fig. 7.1. The bottom panel shows the time evolution of the phase difference ($\Delta\eta$ mod 2π) between the ground state S_0 and the excited state S_4. Obviously, the time delay $t_d = t_r - t_b$ has been determined such that the important condition for coherent symmetry breaking and restoration, (7.20), is fulfilled, i.e. $\Delta\eta(t_c)$ mod $2\pi = 0$, with precision of attoseconds.

In contrast to Fig. 7.2 that demonstrates successful coherent symmetry breaking and restoration by means of two time reversed ultrashort intense linearly y-polarized non-chirped laser pulse with proper time delay $t_d = t_r - t_b$ that satisfies condition (7.20), Fig. 7.3 documents systematic successes (lines and symbols in red color) and failures (different colors) of the approach that depend on fulfilling or violating condition (7.20), respectively. Specifically, Fig. 7.3 shows the results for the same laser pulse that breaks symmetry as the one shown in Fig. 7.2, together with altogether nine reverse copies of this pulse that are centered at $t'_r = t_r + t'$ with additional times $t' = kT/8, k = 0, 1, \ldots, 7, 8$. These nine cases correspond to the results that have been summarized in Fig. 7.1, i.e. two successful restorations of symmetry ($k = 0, 8$,

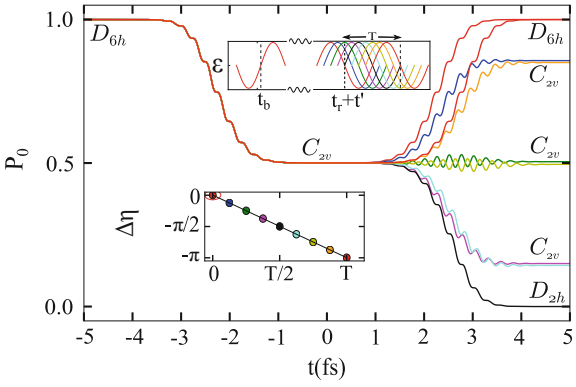

Fig. 7.3 Successes (red lines and red symbols) and failures (other colors) of the approaches to coherent symmetry breaking and restoration by means of two ultrashort intense linearly y-polarized laser pulses. The color codes correspond to those for the arrows shown in Fig. 7.1. In close analogy to the upper, middle, and lower panels of Fig. 7.2, the upper insert illustrates the time evolution of the y-components of the electric fields ϵ of the laser pulses (schematic), the main panel shows the resulting time evolutions of the probability $P_g = P_0$ of the ground state $g = S_0$ in the superposition state (7.9), and the lower insert shows the time evolution of the phase difference $\Delta\eta(t'_c)$ at the central time t'_c (7.47). The laser pulse for symmetry breaking is the same one as in Fig. 7.2. The laser pulse for symmetry restoration shown by the first red line centered at t_r and the resulting $P_0(t)$ and $\Delta\eta(t_c)$ are also the same as in Fig. 7.2. The other laser pulses that are plotted with different colors are centered at $t'_r = t_r + t'$ with additional time $t' = kT/8, k = 1, 2, \ldots, 7$. The resulting phase differences $\Delta\eta(t'_c = t'/2)$ are different from 0 or $\pm\pi$, i.e. they do not satisfy condition (7.20) for symmetry restoration. As a consequence, the resulting $P'_0(t)$ ends up in values $P_0(t'_f) \neq 1$. The final attempt to restore symmetry with additional time $t' = T$ (red curves and symbols) satisfies condition (7.20) ($\Delta\eta(t'_c = T/2) = -\pi$) and is, therefore, successful ($P_0(t'_f) = 1$)

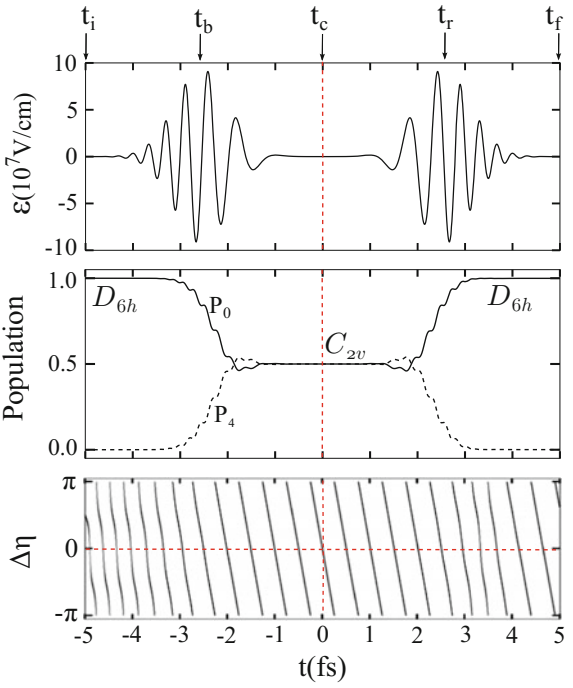

Fig. 7.4 Same as Fig. 7.2, but for time-reversed ultrashort intense laser pulses for coherent breaking ($D_{6h} \rightarrow C_{2v}$) and restoration ($C_{2v} \rightarrow D_{6h}$) of the symmetry of the electronic structure of the model benzene, with down- and up-chirps, respectively

red colors) and seven useless attempts ($k = 1, 2, \ldots, 7$, different colors), see the discussions of (7.47) and (7.48). The case $k = 0$, $t' = 0$ is included here for reference, shown with red color - this is of course the same as the one shown in Fig. 7.2. The other cases include another successful example namely $k = 8$ (that means $t' = T$, $t'_c = T/2$, cf. (7.47), again shown with red color) that satisfies condition (7.20), i.e. $\Delta\eta(t'_c) \bmod 2\pi = -\pi$. As a consequence, the time evolution of $P_g = P_0$ ends up at $P_0(t'_f) = 1$ i.e. the second pulse de-excites the superposition state $\Psi(t'_c) = \frac{1}{\sqrt{2}}(S_0 + S_4)e^{i\eta}$ to the ground state, thus restoring symmetry $C_{2v} \rightarrow D_{6h}$. The other cases $k = 1, 2, \ldots, 7$ turn out to be useless counter-examples i.e. all of them yield phase differences $\Delta\eta(t'_c) \neq 0$ or $\pm\pi$, and hence they violate condition (7.20). As a consequence, the populations P_0 end up in values $P_0(t'_f) \neq 1$—the second pulse cannot de-excite the superposition state completely to the ground state; hence it does not restore D_{6h} symmetry.

Close analysis shows that the numerical results for the final populations of the excited state, $P_e(t'_f = t_f + t') = P_4(t'_f = t_f + t') = 1 - P_0(t'_f = t_f + t')$, agree almost perfectly with the analytical result $4P_g(t_c)P_e(t_c)\left[0.5 - 0.5\cos(2\pi t'/T)\right] = 0.5 - 0.5\cos(2\pi t'/T)$, (7.25). This may be considered as double triumph – first for the derivation of the simple analytical result in the Appendix, see also [1], second for the accuracy and robustness of the numerical techniques for the quantum dynamics simulations of the laser driven wave packet dynamics that are adapted from [1].

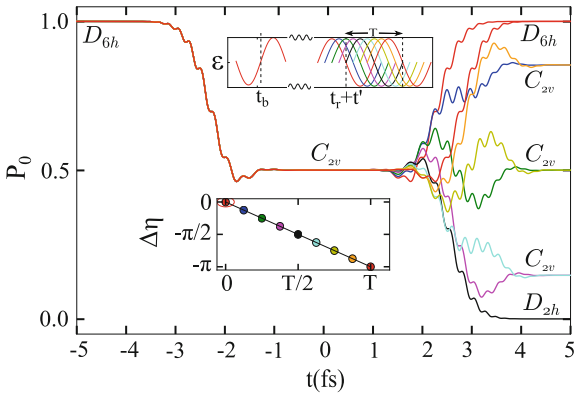

Fig. 7.5 Same as Fig. 7.3, but for time-reversed first and second laser pulses with down- and up-chirps, respectively. For reference, Fig. 7.5 includes results (red lines and red symbols) of Fig. 7.4 that document successful breaking and restoration of the symmetry of the electronic structure of the model benzene

The second scenario for coherent breaking ($D_{6h} \rightarrow C_{2v}$) and restoration ($C_{2v} \rightarrow D_{6h}$) of the symmetry of the electronic structure of the model benzene employs two time-reversed ultrashort intense linearly y-polarized laser pulses with down- and up-chirps, as documented in Fig. 7.4. The parameters of the laser pulses have already been specified above ($\tau = 0.569$ fs, $\epsilon = 9.320 \times 10^7$ V/cm, $\omega' = -2.495$ fs^{-1}, $t_d = t_r - t_b = 5.096$ fs, $t_r = -t_b = t_d/2$). The time reversed down- and up-chirps of the laser pulses that break and restore symmetry are obvious in the top panel of Fig. 7.4. The proper choice of the value of the time delay is verified in the bottom panel, i.e. the phase difference at the central time $\Delta\eta(t_c = 0)$ is equal to zero, that means condition (7.20) is satisfied. As a consequence, the populations $P_g = P_0$ and $P_e = P_4$ of the components of the ground state $g = S_0$ and the excited state $e = S_4$ in the superposition state (7.9) change from $P_0(t_i) = 1, P_4(t_i) = 0$ to $P_0(t_c) = P_4(t_c) = 0.5$ due to the down-chirped laser pulse that breaks symmetry, and finally, they arrive at $P_0(t_f) = 1, P_4(t_f) = 0$ – this demonstrates successful symmetry restoration due to the time-reversed, up-chirped second laser pulse.

Finally, Fig. 7.5 shows the results of a systematic investigation of successful versus useless applications of the second scenario for coherent breaking ($D_{6h} \rightarrow C_{2v}$) and restoration ($C_{2v} \rightarrow D_{6h}$) of the symmetry of the electronic structure of the model benzene, by means of two time-reversed ultrafast intense linearly y-polarized laser pulses with down- and up-chirps, depending on the validity of condition (7.20). The presentation and the results are entirely analogous to those of Fig. 7.3, for the first scenario for non-chirped laser pulses. Again, Fig. 7.5 has two examples ($k = 0, 8$) and seven counter-examples ($k = 1, 2, \ldots, 7$) of useful and useless additional times $t' = kT/8$ for the temporal centers $t'_r = t_r + t'$ of the second laser pulse that fulfill or violate the condition (7.20), thus allowing or forbidding symmetry restoration, respectively.

Close inspection of the numerical results of the final ($t'_f = t_f + t'$) populations of the excited state $P_e(t'_f) = P_4(t'_f) = 1 - P_0(t'_f)$ yields again excellent agreement with the periodic analytical prediction, $0.5 - 0.5\cos(2\pi t'/T)$, (7.25). This confirms the previous (Fig. 7.3) double triumph for both the accuracy and robustness of the

numerical techniques for the quantum dynamics simulations of the laser driven wave packet dynamics that are adapted from [1], and for the analytical derivations in the Appendix, see also [1]. The multiple wiggles in the time evolutions of the populations P_0 documented in Fig. 7.5, with amplitudes that are even larger than those of Fig. 7.3, suggest that this agreement of the numerical and analytical results is by no means trivial.

7.5 Conclusions

The present two examples (Figs. 7.2 and 7.4) of coherent breaking and restoring the symmetry of the electronic structure of the model benzene by means of two well designed laser pulses provide a proof-of-principle. They are different from each other, and they are also different from the pioneering example of [1]. By extrapolation, this suggests that the goal can be achieved by many other scenarios as well, subject to the two conditions for the proper time delay (7.20) and for the temporal symmetry of the matrix presentation of the Hamiltonian (7.22). For example, one could break the molecular symmetry $D_{6h} \rightarrow C_{2v}$ by means of the first laser pulse that is again ultrashort, intense and linearly y-polarized, but it may have non-Gaussian shape, and/or non-linear chirp. The symmetry could then be restored, $C_{2v} \rightarrow D_{6h}$ by the second laser pulse that is designed as time-reversed copy of the first pulse, (7.32), with proper time delay, (7.20), see also (7.36)–(7.40). Violations of conditions (7.20) and/or (7.22) will – in most cases – prohibit successful symmetry restoration (Figs. 7.3 and 7.5). From a mathematical point of view, conditions (7.20) and (7.22) should be satisfied exactly, but in practice, marginal deviations may be acceptable, e.g. the condition (7.20) for the proper time delay should be satisfied with precision of few attoseconds [1]. Lower levels of accuracy would torpedo restoration of the symmetry of electronic structure, and the results may appear intriguing in view of various effects that might prohibit ideal symmetry restoration, such as intermolecular interactions in dense gases [23], or the onset of competing intramolecular processes such as vibrational relaxations [21, 22].

We re-emphasize that according to the derivation in the Appendix, see also [1], the conditions (7.20) and (7.22) are sufficient, but this does not exclude alternative approaches. For example, recent developments of the methods and applications for high harmonic generation HHG suggest that instead of using the criterion of the proper time delay (7.20), one might also use the carrier envelope phase CEP as alternative control knob [13–15, 41].

In conclusion, the present Chapter illustrates the new challenges and opportunities in the field of attosecond coherent control of molecular symmetry breaking and restoration by means of ultrafast intense laser pulses [1]. This adds new effects to the general fields of quantum control [42–45] and attosecond science [13–15, 41]. As some of the next steps, it calls for the discovery of ever new scenarios, and also for more systematic searches for the most efficient and practical approaches.

Acknowledgements One of us (J. M.) would like to express his gratitude to Professor Kenji Ohmori and to Dr. Noboyuki Takei (Institute for Molecular Science IMS, Okazaki, Japan) for stimulating discussions, and also for wonderful hospitality during his visits to the IMS in March and in July, 2017. Generous financial support by the National Key Research and Development Program of China (Grant No. 2017YFA0304203), the Program for Changjiang Scholars and Innovative Research Team (IRT13076), the National Natural Science Foundation of China (Grant No. 11434007), the National Science Foundation of China (Grant No. 61505100), the China Scholarship Council, the Deutsche Forschungsgemeinschaft (project Tr 1109/2-1) are also gratefully acknowledged.

Appendix: From the Conditions of Time Reversibility (7.36) and Phase Matching (7.20) to Symmetry Restoration (7.25)

The purpose of this Appendix is to show that the two conditions (7.20) and (7.36) guarantee that the symmetry of the system's electronic structure is restored by the second linearly polarized laser pulse after it had been broken by the first laser pulse. For the proof, we shall assume that the system is initially in the electronic ground state; the inital symmetry is, therefore, the symmetry of the ground state. The first laser pulse transfers part of the population from the ground state (using Dirac notation: $|\Psi_g\rangle$) to an excited state ($|\Psi_e\rangle$). The system is thus prepared in a superposition of $|\Psi_g\rangle$ and $|\Psi_e\rangle$. We consider the case where $|\Psi_g\rangle$ and $|\Psi_e\rangle$ have different irreducible representations IRREPS - that means the superposition state can no longer have the symmetry IRREP_g of the ground state, nor does it have the symmetry $IRREP_e$ of the excited state—symmetry is broken. Finally, we use (7.20) and (7.36) in order to derive expression (7.25) for the population of $|\Psi_e\rangle$ after the two pulses, depending on the time delay between the pulses. We shall show that for special time shifts of the second pulse ($t' = 0, T, 2T, \ldots$ etc in (7.25)) the population of $|\Psi_e\rangle$ is equal to zero - that means the system is in the ground state; hence it is back to the symmetry of $|\Psi_g\rangle$: the symmetry that was broken by the first pulse is restored by the second pulse.

For a self-contained presentation of this Appendix, let us recall that condition (7.36) means that the matrix representation $\mathbf{H}(t)$ of the Hamiltonian $\hat{H}(t)$ of the laser driven system is time reversed,

$$\mathbf{H}(t) = \mathbf{H}(-t). \tag{7.49}$$

It has been shown in the main text that the time reversibility of the Hamilton matrix (7.49) is a consequence of our design of the laser pulse for symmetry restoration as time reversed, linearly polarized copy of the pulse that breaks symmetry, (7.32). Note that this construction of the second laser pulse yields the time reversibility (7.49) as a general phenomenon that holds irrespectively of the form of the first laser pulse. The special versions that have been employed in the main text i.e. non-chirped as well as chirped laser pulses with Gaussian shapes ((7.28), (7.29), (7.33) and (7.34)) just serve as examples. Their linear polarizations are important, however, because they imply that $\mathbf{H}(t)$ is real-valued, cf. (7.37),

$$\mathbf{H}(t) = \mathbf{H}^*(t). \tag{7.50}$$

This is different from circularly polarized laser pulses that yield complex-valued Hamilton matrices, cf. [1]. As a consequence, the present proof differs slightly from the proof given in [1], even though the concepts and the steps are parallel to each other.

Let us also recall that (7.20) means that at the central time $t_c (= 0)$ between the two laser pulses, the wave function of the system with broken symmetry is a superposition of $|\Psi_g\rangle$ and $|\Psi_e\rangle$ with the same (real-valued) phase η for $|\Psi_g\rangle$ and $|\Psi_e\rangle$, and without populations of any complementary states $|\Psi_d\rangle$, $d \neq g, e$ (the subscript "d" means "different from g and e"),

$$\begin{aligned} |\Psi(t_c = 0)\rangle &= c_g(t_c = 0)|\Psi_g\rangle + c_e(t_c = 0)|\Psi_e\rangle \\ &\equiv e^{i\eta} C_g |\Psi_g\rangle + e^{i\eta} C_e |\Psi_e\rangle \end{aligned} \tag{7.51}$$

with real-valued amplitudes C_g and C_e. (The general version of condition (7.20) has another option, i.e. the phase factor for $|\Psi_e\rangle$ could be $e^{i(\eta \pm \pi)} = -e^{i\eta}$, but this case is equivalent to (7.51) because the minus sign could be used to re-define the amplitude, $C'_e = -C_e$, and this would not change the rest of the derivation.) The amplitudes are normalized, $C_g^2 + C_e^2 = 1$.

Equation (7.51) is a special case of the general expansion of the time dependent electronic wavefunction $|\Psi(t)\rangle$ in terms of electronic eigenstates $|\Psi_k\rangle$,

$$|\Psi(t)\rangle = \sum_k c_k(t)|\Psi_k\rangle \tag{7.52}$$

where the sum over k includes states g, e, and possibly several different states d. The eigenstates $|\Psi_k\rangle$ are solutions of the time independent Schrödinger equation (TISE)

$$H_e|\Psi_k\rangle = E_k|\Psi_k\rangle \tag{7.53}$$

where

$$H_e = T_e + V_C \tag{7.54}$$

is the electronic Hamiltonian of the field-free system, with kinetic energy operator T_e and Coulomb interaction V_C of all particles (electrons and nuclei.) The time dependent wavefunction $|\Psi(t)\rangle$ is evaluated as solution of the time dependent Schrödinger equation (TDSE)

$$i\hbar \frac{\partial}{\partial t} |\Psi(t)\rangle = H(t)|\Psi(t)\rangle \tag{7.55}$$

with model Hamiltonian

$$H(t) = H_e - \mathbf{d} \cdot \boldsymbol{\epsilon}(t) \tag{7.56}$$

where $\mathbf{d}$ is the electronic dipole operator, and

$$\boldsymbol{\epsilon}(t) = \boldsymbol{\epsilon}_b(t) + \boldsymbol{\epsilon}_r(t) \tag{7.57}$$

is the sum of the electric fields of the two laser pulses that break and restore symmetry. The TDSE is solved subject to the initial condition

$$|\Psi(t_i)\rangle = |\Psi_g\rangle \tag{7.58}$$

i.e. initially the system is in its ground state. The initial time $t = t_i < 0$ is chosen well before the laser pulse that breaks symmetry.

Inserting the expansion (7.52) into the TDSE (7.55) yields the algebraic version of the TDSE,

$$i\hbar\frac{d}{dt}\mathbf{c}(t) = \mathbf{H}(t)\mathbf{c}(t) \tag{7.59}$$

where $\mathbf{c}(t) = (c_g(t), c_e(t), c_d(t), \ldots)^\intercal$ denotes the column vector of coefficients $c_k(t)$. The order of the components $c_k(t)$ in $\mathbf{c}(t)$ is arbitrary; for convenience, we use the order $k = g, e$ followed by the components d that are different from g and e. The Hamilton matrix $\mathbf{H}(t)$ in the TDSE (7.59) has elements

$$H_{kl}(t) = \langle\Psi_k|\mathbf{H}(t)|\Psi_l\rangle = E_k\delta_{kl} - \mathbf{d}_{kl}\cdot\boldsymbol{\epsilon}(t) \tag{7.60}$$

where $\mathbf{d}_{kl} = \langle\Psi_k|\mathbf{d}|\Psi_l\rangle$ is the $k \to l$ transition dipole matrix element.

The algebraic version of the initial condition (7.58) is

$$\mathbf{c}(t_i) = (1, 0, 0, \ldots)^\intercal \tag{7.61}$$

Likewise, the algebraic version of condition (7.20) and (7.51) is

$$\mathbf{c}(t_c = 0) = e^{i\eta}(C_g, C_e, 0, 0, \ldots) \tag{7.62}$$

The TDSE (7.59) propagates the initial state (7.61) at t_i to the state (7.62) at t_c that is generated by the laser pulse that breaks symmetry. There are various ways how to express the propagation from (7.61) to (7.62). A rather general expression is

$$\mathbf{c}(t_c = 0) = \mathbf{U}(t_c - t_i)\mathbf{c}(t_i). \tag{7.63}$$

where $\mathbf{U}(t_c - t_i)$ is a unitary transformation that depends on the time interval $t_c - t_i = -t_i$. Condition (7.20) (=(7.51)) implies that $\mathbf{U}(t_c - t_i)$ can be written as block-diagonal unitary matrix,

$$\mathbf{U}(t_c - t_i) = \begin{pmatrix} \mathbf{U}_{ge}(t_c - t_i) & \mathbf{0} \\ \mathbf{0} & \mathbf{U}_d(t_c - t_i) \end{pmatrix} \tag{7.64}$$

The notations of the block diagonal sub-matrices indicate that at the time $t_c - t_i$ after the initial time t_i, the net effect is population transfer between states g and e, as

well as population transfer between the different states labelled d, but without any population transfers from states g or e to d, or *vice versa*. Note that (7.63) does not tell us anything about what has happened between the times t_i and t_c - for example the population transfer between state g and e may well have been mediated by transient populations of state(s) d—see e.g. the experimental example in [1].

The unitarity of $\mathbf{U}(t_c - t_i)$ implies that its block diagonal matrices are also unitary. As a consequence, $\mathbf{U}_{ge}(t_c - t_i)$ takes the form

$$\mathbf{U}_{ge}(t_c - t_i) = e^{i\eta} \begin{pmatrix} C_g & -C_e \\ C_e & C_g \end{pmatrix} \tag{7.65}$$

Another way to express the propagation from (7.61) to (7.62) is

$$\mathbf{c}(t_c = 0) = \hat{T} e^{-i \int_{t_i}^{0} dt' \mathbf{H}(t')/\hbar} \mathbf{c}(t_i). \tag{7.66}$$

where $\hat{T}$ denotes the time-ordering operator. The complex conjugate of (7.66) is

$$\begin{aligned} \mathbf{c}^*(0) &= \hat{T} e^{i \int_{t_i}^{0} dt' \mathbf{H}(t')/\hbar} \mathbf{c}(t_i) \\ &= \hat{T} e^{i \int_{t_i}^{0} dt' \mathbf{H}(-t')/\hbar} \mathbf{c}(t_i) \\ &= e^{-2i\eta} \mathbf{c}(0) \end{aligned} \tag{7.67}$$

In the first (7.67), we use the fact that $\mathbf{H}(t)$ and also $\mathbf{c}(t_i)$ are real-valued, cf. (7.50) and (7.61). The second (7.67) exploits the time reversibility (7.36) of the Hamilton matrix, (7.49). The third (7.67) uses the condition (7.20) for the phases, (7.62). Inversion of (7.67) yields

$$\begin{aligned} \mathbf{c}(t_i) &= \hat{T} e^{-i \int_{0}^{-t_i} dt' \mathbf{H}(t')/\hbar} \mathbf{c}^*(0) \\ &= e^{-2i\eta} \hat{T} e^{-i \int_{0}^{t_f} dt' \mathbf{H}(t')/\hbar} \mathbf{c}(0) \\ &= e^{-2i\eta} \mathbf{c}(t_f) \end{aligned} \tag{7.68}$$

where $t_f = -t_i$ is the final time after the second pulse. As a consequence, the corresponding populations $P_k(t) = |c_k(t)|^2$ of states $k = g, e, d, \ldots$ at $t = t_f$ are the same as the initial probabilities,

$$P_k(t_f) = P_k(t_i), k = g, e, d, \ldots \tag{7.69}$$

In particular, we have

$$P_g(t_f) = 1 \tag{7.70}$$

and

$$P_e(t_f) = 0 \tag{7.71}$$

for the final populations of the ground and excited states. Equation (7.70) implies symmetry restoration by the second laser pulse after symmetry breaking by the first laser pulse—q.e.d.

Next let us consider the case when the second pulse is delayed by time shift t' with respect to the ideal timing—in most cases, this will violate the conditions (7.20) and (7.62). We shall now show that—as one may anticipate—this will prohibit symmetry restoration. The time shift t' has several consequences: (i) The new final time is $t'_f = t_f + t'$. (ii) The system evolves in field-free (*ff*) environment (because the two laser pulses do not overlap), from time $t_c = 0$ till t'. The corresponding unitary matrix $\mathbf{U}_{ff}(t' - t_c)$ for propagation from t_c to t' has elements

$$\mathbf{U}_{ff,kl}(t' - t_c) = e^{-iE_k t'/\hbar}\delta_{kl} \tag{7.72}$$

The diagonality implies that $\mathbf{U}_{ff}(t' - t_c)$ has the same block-diagonal structure as $\mathbf{U}(t_c - t_i)$, (7.64). (iii) The total time evolution operator for propagation from t_i via $t_c = 0$ and t' to t'_f is

$$\begin{aligned}\mathbf{U}(t'_f - t_i) &= \mathbf{U}(t'_f - t')\mathbf{U}_{ff}(t' - t_c)\mathbf{U}(t_c - t_i) \\ &= \mathbf{U}(t_f - t_c)\mathbf{U}_{ff}(t' - t_c)\mathbf{U}(t_c - t_i)\end{aligned} \tag{7.73}$$

In the second (7.73) we use the fact that time evolution operators depend on time intervals (here $t'_f - t' = t_f - t_c$), but not on the initial times (i.e. not on t' or on t_c). Now the first and second (7.68) imply the relation

$$\mathbf{U}^{-1}(t_c - t_i) = \mathbf{U}^{\dagger}(t_c - t_i) = \mathbf{U}(t_f - t_c) \tag{7.74}$$

In (7.74), we use the unitarity of $\mathbf{U}(t_c - t_i)$. Inserting (7.74) into (7.73) yields

$$\begin{aligned}\mathbf{U}(t'_f - t_i) &= \mathbf{U}^{-1}(t_c - t_i)\mathbf{U}_{ff}(t' - t_c)\mathbf{U}(t_c - t_i) \\ &= \mathbf{U}^{\dagger}(t_c - t_i)\mathbf{U}_{ff}(t' - t_c)\mathbf{U}(t_c - t_i)\end{aligned} \tag{7.75}$$

The block-diagonal structure of the unitary time evolution matrices implies that the relation (7.75) holds as well for the block-diagonal sub-matrices. Inserting (7.65) for the sub-matrix $\mathbf{U}_{ge}(t_c - t_i)$ into (7.75) yields the final result for the population of the excited state

$$P_e(t'_f) = 4P_g(t_c)P_e(t_c) \cdot \left[\frac{1}{2} - \frac{1}{2}\cos\left(\frac{2\pi t'}{T}\right)\right] \tag{7.76}$$

cf. (7.25). Apparently, $P_e(t'_f)$ is periodic with period T and with amplitude $2P_g(t_c)$ $P_e(t_c)$. The special case (7.71) is realized for zero time shift $t' = 0$, and then periodically for $t' = T, 2T$, etc. q.e.d..

References

1. C. Liu, J. Manz, K. Ohmori, S. Sommer, N. Takei, J.C. Tremblay, Y. Zhang, Attosecond control of electronic structure symmetry restoration. Phys. Rev. Lett. **121**,173201 (2018)
2. T.D. Lee, C.N. Yang, Phys. Rev. **104**, 254 (1956)
3. M. Quack, Adv. Chem. Phys. **157**, 247 (2014)
4. N.S. Mankoč Borštnik, Phys. Rev. D **91**, 065004 (2015)
5. M. Yu, Ivanov, P.B. Corkum, P. Dietrich, Laser Phys. **3**, 375 (1993)
6. N. Elghobashi, L. González, J. Manz, J. Chem. Phys. **120**, 8002 (2004)
7. Y. Arasaki, K. Takatsuka, Phys. Chem. Chem. Phys. **12**, 1239 (2010)
8. Y. Arasaki, K. Wang, V. McKoy, K. Takatsuka, Phys. Chem. Chem. Phys. **13**, 8681 (2011)
9. A.S. Alnaser, M. Kübel, R. Siemering, B. Bergues, N.G. Kling, K.J. Betsch, Y. Deng, J. Schmidt, Z.A. Alahmed, A.M. Azzer, J. Ullrich, I. Ben-Itzhak, R. Moshammer, U. Kleineberg, F. Krausz, R. de Vivie-Riedle, M.F. Kling, Nat. Commun. **5**, 3800 (2014)
10. Y. Pertot, C. Schmidt, M. Matthews, A. Chauvet, M. Huppert, V. Svoboda, A. Conta, A. Tehlar, D. Baykusheva, J.-P. Wolf, H.J. Wörner, Science **355**, 264 (2017)
11. H.W. Kroto, J.R. Heath, S.C. Obrien, R.F. Curl, R.E. Smalley, Nature **318**, 162 (1985)
12. P.B. Corkum, Phys. Rev. Lett. **71**, 1994 (1993)
13. P.B. Corkum, F. Krausz, Nat. Phys. **3**, 381 (2007)
14. F. Krausz, M. Ivanov, Rev. Mod. Phys. **81**, 163 (2009)
15. T. Schultz, M. Vrakking, *Attosecond and XUV Physics* (Wiley-VCH, Weinheim, 2014)
16. G. Alber, H. Ritsch, P. Zoller, Phys. Rev. A **34**, 1058 (1986)
17. L.D. Noordam, D.I. Duncam, T.F. Gallagher, Phys. Rev. A **45**, 4734 (1992)
18. N.V. Golubev, V. Despré, A.I. Kuleff, J. Mod. Opt. **64**, 1031 (2017)
19. I. Barth, J. Manz, Angew. Chem. Int. Ed. **45**, 2962 (2006)
20. D. Jia, J. Manz, Y. Yang, J. Mod. Opt. **64**, 960 (2016)
21. M. Kanno, H. Kono, Y. Fujimura, Angew. Chem. Int. Ed. **45**, 7995 (2006)
22. H. Mineo, S.H. Lin, Y. Fujimura, Chem. Phys. **442**, 103 (2014)
23. N. Takei, C. Sommer, C. Genes, G. Pupillo, H. Goto, K. Koyasu, H. Chiba, M. Weidemüller, K. Ohmori, Nat. Commun. **7**, 13449 (2016)
24. J. Köhler, M. Wollenhaupt, T. Bayer, C. Sarpe, T. Baumert, Opt. Express **19**, 11638 (2011)
25. I.S. Ulusoy, M. Nest, J. Am. Chem. Soc. **133**, 20230 (2011)
26. G. Hermann, C. Liu, J. Manz, B. Paulus, J.F. Pérez-Torres, V. Pohl, J.C. Tremblay, J. Phys. Chem. A **120**, 5360 (2016)
27. G. Hermann, C. Liu, J. Manz, B. Paulus, V. Pohl, J.C. Tremblay, Chem. Phys. Lett. **683**, 553 (2017)
28. V. Pohl, G. Hermann, J.C. Tremblay, J. Comput. Chem. **38**, 1515 (2017)
29. G. Hermann, V. Pohl, J.C. Tremblay, B. Paulus, H.-C. Hege, A. Schild, J. Comput. Chem. **37**, 1511 (2016)
30. V. Despré, A. Marciniak, V. Loriot, M.C.E. Galbraith, A. Rouzée, M.J.J. Vrakking, F. Lépine, A.I. Kuleff, J. Phys. Chem. Lett. **6**, 426 (2015)
31. E. Schrödinger, Ann. Phys. (Leipzig, Ger.) **81**, 109 (1926)
32. H. Eyring, J. Walter, G.E. Kimball, *Quantum Chemistry* (Wiley, New York, 1944), pp. 198–200
33. R. Weinkauf, P. Schanen, D. Yang, S. Soukara, E.W. Schlag, J. Phys. Chem. **99**, 11255 (1995)
34. L.S. Cederbaum, J. Zobeley, Chem. Phys. Lett. **307**, 205 (1999)
35. S. Chelkowski, G.L. Yudin, A.D. Bandrauk, J. Phys. B.: At. Mol. Opt. Phys. **39**, S409 (2006)
36. F. Remacle, R.D. Levine, PNAS **103**, 6793 (2006)
37. P.M. Kraus, B. Mignolet, D. Baykusheva, A. Rupenyan, L. Horný, E.F. Penka, G. Grassi, O.I. Tolstikhin, J. Schneider, F. Jensen, L.B. Madsen, A.D. Bandrauk, F. Remacle, H.J. Wörner, Science **350**, 790 (2015)
38. D. Jia, J. Manz, B. Paulus, V. Pohl, J.C. Tremblay, Y. Yang, Chem. Phys. **482**, 146 (2017)
39. H. Ding, D. Jia, J. Manz, Y. Yang, Molec. Phys. **115**, 1813 (2017)
40. D.J. Diestler, G. Hermann, J. Manz, J. Phys. Chem. A **121**, 5332 (2017)

41. S. Chelkowski, T. Bredtmann, A.D. Bandrauk, Phys. Rev. A **85**, 033404 (2012)
42. W.P. Schleich, H. Walther (eds.), *Elements of Quantum Information* (Wiley-VCH, Weinheim, 2007)
43. C. Brif, R. Chakrabarti, H. Rabitz, New J. Phys. **12**, 075008 (2010)
44. M. Shapiro, P. Brumer, *Quantum Control of Molecular Processes*, 2nd edn. (Wiley-VCH, Weinheim, 2012)
45. K. Nakajima, H. Abe, Y. Ohtsuki, J. Phys. Chem. A **116**, 11219 (2012)

Chapter 8
Time-Dependent Complete-Active-Space Self-Consistent-Field Method for Ultrafast Intense Laser Science

Takeshi Sato, Yuki Orimo, Takuma Teramura, Oyunbileg Tugs and Kenichi L. Ishikawa

Abstract We present the time-dependent complete-active-space self-consistent-field (TD-CASSCF) method to simulate multielectron dynamics in ultrafast intense laser fields from the first principles. While based on multiconfiguration expansion, it divides the orbital space into frozen-core (tightly bound electrons with no response to the field), dynamical-core (electrons tightly bound but responding to the field), and active (fully correlated to describe highly excited and ejected electrons) orbital subspaces. The subspace decomposition can be done flexibly, conforming to phenomena under investigation and desired accuracy. The method is gauge invariant and size extensive. Infinite-range exterior complex scaling in addition to mask-function boundary is adopted as an efficient absorbing boundary. We show numerical examples and illustrate how to extract relevant physical quantities such as ionization yield, high-harmonic spectrum, and photoelectron spectrum from our full-dimensional implementation for atoms. The TD-CASSCF method will open a way to the ab initio simulation study of ultrafast intense laser science in realistic atoms and molecules.

T. Sato · Y. Orimo · T. Teramura · O. Tugs · K. L. Ishikawa (✉)
Department of Nuclear Engineering and Management,
Graduate School of Engineering, The University of Tokyo, 7-3-1 Hongo,
Bunkyo-ku, Tokyo 113-8656, Japan
e-mail: ishiken@n.t.u-tokyo.ac.jp

T. Sato
e-mail: sato@atto.t.u-tokyo.ac.jp

Y. Orimo
e-mail: ykormhk@atto.t.u-tokyo.ac.jp

T. Teramura
e-mail: teramura@atto.t.u-tokyo.ac.jp

O. Tugs
e-mail: tugs@atto.t.u-tokyo.ac.jp

© Springer Nature Switzerland AG 2018

K. Yamanouchi et al. (eds.), *Progress in Ultrafast Intense Laser Science XIV*,
Springer Series in Chemical Physics 118,
https://doi.org/10.1007/978-3-030-03786-4_8

8.1 Introduction

From atoms and molecules under visible-to-midinfrared laser fields of an intensity $\gtrsim 10^{14}\,\mathrm{W/cm^2}$ emerge highly nonlinear strong-field phenomena, e.g., above-threshold ionization, tunneling ionization, high-harmonic generation (HHG), and nonsequential double ionization (NSDI) [1, 2]. In particular, HHG is more and more widely used as an ultrashort (down to attoseconds) coherent light source in the extreme-ultraviolet (XUV) and soft x-ray spectral ranges [3–5]. In addition, free-electron lasers are now in operation as another type of ultrashort, intense, coherent XUV and x-ray sources. Such a rapid progress in experimental techniques for ultrafast intense laser science has opened new research areas including ultrafast molecular probing [6–8], attosecond science [9–11], and XUV nonlinear optics [12, 13], with the ultimate goal to directly observe, and even manipulate ultrafast electronic motion in atoms, molecules, and solids.

Further advances in these areas require first-principles methods to numerically simulate the real-time dynamics of multielectron atoms and molecules in ultrafast intense laser pulses, or ab initio *strong-field physics*. Although the time-dependent Schrödinger equation (TDSE) [see (8.1) below] rigorously describes these phenomena in principle, its numerical integration in the real space for systems with more than two electrons [14–29] poses a major challenge.

A promising class of approaches is time-dependent multiconfiguration self-consistent field (TD-MCSCF) methods [30, 31], where the total electronic wave function is expressed as a superposition of different electronic configurations or Slater determinants built from a given number of single-electron spin orbitals [see (8.11) and Fig. 8.1]. In the multiconfiguration time-dependent Hartree-Fock (MCTDHF) method [32–34], both the expansion coefficients [configuration-interaction (CI) coefficients] and orbital functions are varied in time, and all the possible realizations to distribute the electrons among the spin orbitals (full CI expansion) are included. Though pioneering and powerful, the computational cost of MCTDHF increases factorially with the number of electrons.

To overcome this difficulty, we have recently developed and successfully implemented a TD-MCSCF method called the time-dependent complete-active-space self-consistent-field (TD-CASSCF) method [35–37], which is the topic of the present chapter. TD-CASSCF classifies the spatial orbitals into doubly occupied and time-independent frozen core (FC), doubly occupied and time-dependent dynamical core (DC), and fully correlated active orbitals. Thanks to this classification, the number of configurations used in simulations and the computational cost are significantly reduced without sacrificing accuracy. The classification can be done flexibly, based on simulated physical situations and desired accuracy. Through comparison of the results from various subspace decompositions, one can analyze the contribution from different shells, the effect of electron correlation, and the mechanism underlying the simulated phenomena. In this sense, TD-CASSCF is even more useful than merely numerically exact black-box simulations.

This chapter proceeds as follows. In Sect. 8.2 we describe the statement of the problem that we are going to treat, i.e., the time-dependent Schrödinger equation for many electron systems in a driving laser field within the dipole and fixed-nuclei approximations. We also briefly mention an important concept of gauge transformation. Section 8.3 explains the formulation of the TD-CASSCF method, the equations of motion for CI coefficients and orbital functions, and its important features of gauge invariance and size extensivity. In Sect. 8.4 we describe how to prepare the initial wave function and absorb the electron wave packet that reaches the simulation box boundary without unphysical reflection. Section 8.5 presents how to extract relevant physical quantities from the wave function obtained by TD-CASSCF simulations, along with representative numerical examples. Summary is given in Sect. 8.6. Hartree atomic units are used throughout unless otherwise stated.

8.2 Problem Statement

8.2.1 Time-Dependent Schrödinger Equation

We consider an atom or molecular system consisting of N electrons subject to an external laser field. Within the electric dipole approximation of laser-electron interaction and the fixed-nuclei or clamped-nuclei approximation that treats nuclei as classical point charges fixed in space, the dynamics of the laser-driven multielectron system is described by the time-dependent Schrödinger equation (TDSE),

$$i\frac{\partial \Psi(t)}{\partial t} = \hat{H}(t)\Psi(t), \tag{8.1}$$

where the time-dependent Hamiltonian,

$$\hat{H}(t) = \hat{H}_1(t) + \hat{H}_2, \tag{8.2}$$

is decomposed into the one-electron part (kinetic energy, nuclear Coulomb energy, and laser-electron interaction),

$$\hat{H}_1(t) = \sum_i \hat{h}(\mathbf{r}_i, t) \tag{8.3}$$

and the two-electron part,

$$\hat{H}_2 = \sum_{i=1}^{N} \sum_{j<i} \frac{1}{|\mathbf{r}_i - \mathbf{r}_j|}, \tag{8.4}$$

for the interelectronic Coulomb interaction. The laser-electron interaction can be expressed either in the length gauge (LG) or velocity gauge (VG): $\hat{h}(\mathbf{r}, t)$ in (8.3) is given by,

$$\hat{h}(\mathbf{r}, t) = \frac{\hat{\mathbf{p}}^2}{2} + \mathbf{r} \cdot \mathbf{E}(t) - \sum_{\alpha} \frac{Z_\alpha}{|\mathbf{r} - \mathbf{R}_\alpha|}, \tag{8.5}$$

in the length gauge, with $\hat{\mathbf{p}} = -i\nabla$, and,

$$\hat{h}(\mathbf{r}, t) = \frac{\left[\hat{\mathbf{p}} + \mathbf{A}(t)\right]^2}{2} - \sum_{\alpha} \frac{Z_\alpha}{|\mathbf{r} - \mathbf{R}_\alpha|}, \tag{8.6}$$

in the velocity gauge, with $\mathbf{A}(t) = -\int \mathbf{E}(t)dt$ being the vector potential. Z_α and $\mathbf{R}_\alpha$ denote the charge and position of nucleus α, respectively.

8.2.2 Gauge Transformation

The wave functions $\Psi_{\mathrm{L}}(t)$ and $\Psi_{\mathrm{V}}(t)$ expressed in the length and velocity gauges, respectively, are transformed into each other through the gauge transformation,

$$\Psi_{\mathrm{V}}(t) = \hat{\mathscr{U}}(t)\Psi_{\mathrm{L}}(t), \tag{8.7}$$

with the unitary operator,

$$\hat{\mathscr{U}}(t) = \exp\left[-i\mathbf{A}(t) \cdot \sum_{i=1}^{N} \mathbf{r}_i\right]. \tag{8.8}$$

If we substitute (8.7) into the TDSE with (8.6), we can easily show that Ψ_{L} indeed satisfies the TDSE with (8.5).

While the operator $\hat{\mathbf{p}}$ corresponds to the kinetic momentum in the length gauge, it corresponds to the canonical momentum in the velocity gauge, and the kinetic momentum is given by $\hat{\mathbf{p}} + \mathbf{A}(t)$. Then, a plane wave state with a kinetic momentum $\mathbf{p}_{kin}$ is $e^{i\mathbf{p}_{kin}\cdot\mathbf{r}}$ in the length gauge and $e^{i\left[\mathbf{p}_{kin}-\mathbf{A}(t)\right]\cdot\mathbf{r}}$ in the velocity gauge, which fulfills (8.7).

The gauge principle states that all physical observables are gauge invariant, i.e., take the same values whether the laser-electron interaction may be represented in the length or velocity gauge [38]. For example, the probability density is gauge invariant, $|\Psi_{\mathrm{V}}(t)|^2 = |\Psi_{\mathrm{L}}(t)|^2$.

One may be surprised to realize that the projection $\langle \Xi | \Psi(t) \rangle$ of the wave function $\Psi(t)$ onto a field-free stationary state Ξ and the population $|\langle \Xi | \Psi(t) \rangle|^2$ are *not* gauge invariant and, thus, *not* a physical observable when $\mathbf{A}(t) \neq 0$, i.e., during the pulse. As a consequence, the degree of ionization is *not* gauge invariant during the pulse,

either. Let us assume that a hydrogen atom under a laser field linearly polarized in the z direction is in the ground state in the length gauge,

$$\psi_{\mathrm{L}}(\mathbf{r}, t) = \frac{e^{-r}}{\sqrt{\pi}}, \tag{8.9}$$

at some moment, e.g., after a complete Rabi oscillation cycle. Then, its velocity gauge wave function is,

$$\psi_{\mathrm{V}}(\mathbf{r}, t) = e^{-iA(t)z}\psi_{\mathrm{L}}(\mathbf{r}, t) = 2e^{-r}\sum_{l=0}^{\infty}\sqrt{2l+1}(-i)^l j_l(A(t)r)Y_{l0}(\theta, \phi), \tag{8.10}$$

which contains not only the $1s$ state but all the angular momenta l including continuum levels unless $A(t) = 0$.

8.3 TD-CASSCF Method

8.3.1 Multicongifuration Expansion

In order to simulate multielectron dynamics, as illustrated in Fig. 8.1, we expand the total wave function $\Psi(t)$ as a superposition of different Slater determinants or configuration state functions,

$$\Psi(t) = \sum_{I}^{\mathsf{P}} \Phi_I(t) C_I(t), \tag{8.11}$$

where expansion coefficients $\{C_I\}$ are called configuration interaction (CI) coefficients and bases $\{\Phi_I\}$ are the Slater determinants built from N spin orbitals out of $2n$ spin orbitals $\{\psi_p(t); p = 1, 2, \ldots, n\} \otimes \{\alpha, \beta\}$ (in the spin-restricted treatment) with $\{\psi_p\}$ being spatial orbital functions and $\alpha(\beta)$ the up- (down-) spin eigenfunction. The summation in (8.11) with respect to configurations I runs through the element of a CI space P, consisting of a given set of determinants.

Multiconfiguration expansion (8.11) can represent a wide variety of different methods; whereas $\{C_I\}$ are usually taken as time-dependent, they can also be fixed [39]. $\{\psi_p\}$, and thus $\{\Phi_I\}$, can be considered either time-independent, as in the time-dependent configuration interaction singles (TDCIS) method [40], or time-dependent, as in the TD-CASSCF, MCTDHF, and time-dependent Hartree-Fock (TDHF) [41] methods described below. While orbital functions are usually assumed to fulfill orthonormality, it is not a necessary condition.

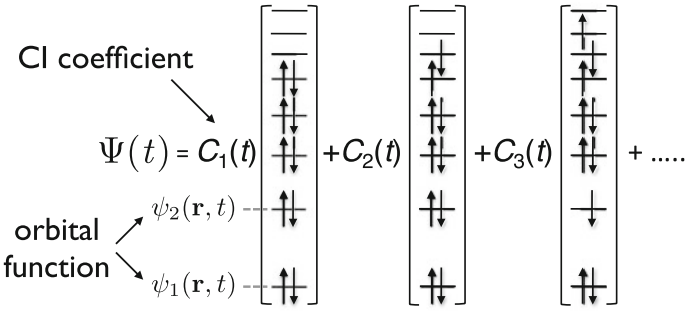

Fig. 8.1 Schematic representation of the multiconfiguration expansion (8.11). Each term on the right-hand side corresponds to a configuration $\Phi_1, \Phi_2, \ldots$ with CI coefficients $C_1, C_2, \ldots$. The first term corresponds to the Hartree-Fock configuration

8.3.2 TD-CASSCF Ansatz

In the TD-CASSCF method, we use orthonormal time-dependent orbital functions. The n occupied orbitals are classified into n_c core orbitals $\{\psi_i : i = 1, 2, \ldots, n_c\}$ that are doubly occupied all the time and $n_a (= n - n_c)$ active orbitals $\{\psi_t : t = n_c + 1, n_c + 2, \ldots, n\}$. This idea is based on a reasonable expectation that only high-lying electrons are strongly driven, while deeply bound core electrons remain nonionized. On the other hand, we consider all the possible distributions of $N_a (= N - 2n_c)$ electrons among n_a active orbitals. It should be noticed that not only the active orbitals but also the core orbitals, though constrained to the closed-shell structure, vary in time, in general, responding to the field formed by the laser and the other electrons. The use of time-dependent (especially active) orbitals that are initially localized near the nuclei but spatially expand in the course of time allows us to efficiently describe excitation and ionization.

It is also possible to further decompose core orbitals into n_{fc} frozen-core (FC) orbitals that do not vary in time and n_{dc} time-dependent dynamical core (DC) orbitals ($n_c = n_{fc} + n_{dc}$). The N-electron CASSCF wave function can be symbolically expressed as,

$$\Psi_{\mathrm{CAS}} : \psi_1^2 \cdots \psi_{n_{fc}}^2 \psi_{n_{fc}+1}^2(t) \cdots \psi_{n_c}^2(t) \{\phi_{n_c+1}(t) \cdots \phi_n(t)\}^{N_A}, \tag{8.12}$$

and given by,

$$\Psi_{\mathrm{CAS}} = \hat{A} \left[\Phi_{\mathrm{fc}} \Phi_{\mathrm{dc}}(t) \sum_I \Phi_I(t) C_I(t) \right], \tag{8.13}$$

where $\hat{A}$ is the antisymmetrization operator, Φ_{fc} and Φ_{dc} are the closed-shell determinants constructed with FC and DC orbitals, respectively, and $\{\Phi_I\}$ are the determi-

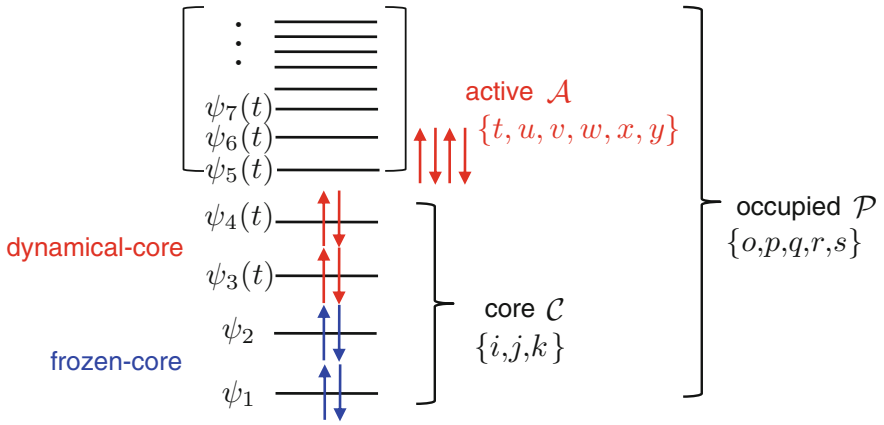

Fig. 8.2 Schematic illustration of the TD-CASSCF concept for a twelve-electron system with two frozen-core, two dynamical-core, and eight active orbitals. The classification of orbitals and the indices we use are also shown

nants formed by active orbitals. In the following, we will denote the level of the CAS approximation employed in Ψ_{CAS} by the integer triple (n_{fc}, n_{dc}, n_a). Hereafter, we use orbital indices $\{i, j, k\}$ for core ($\mathscr{C}$), $\{t, u, v, w, x, y\}$ for active ($\mathscr{A}$), and $\{o, p, q, r, s\}$ for arbitrary occupied (core and active) ($\mathscr{P} = \mathscr{C} + \mathscr{A}$) orbitals (Fig. 8.2). The FC and DC orbitals are distinguished explicitly only when necessary.

There are two limiting cases. On one hand, if we use a single configuration made up of only DC orbitals, i.e., $(0, N/2, 0)$, or equivalently $(0, 0, N/2)$, it corresponds to TDHF [41], where some orbitals can also be frozen in a broader sense. On the other hand, the special case $(0, 0, n)$ $(n > N/2)$, where all the orbitals are fully correlated or treated as active, corresponds to MCTDHF.

8.3.3 TD-CASSCF Equations of Motion

The equations of motion (EOMs) that govern the temporal evolutions of the CI coefficients $\{C_I(t)\}$ and orbital functions $\{\psi_p(t)\}$ have been derived on the basis of the time-dependent variational principle (TDVP) [42–44], which requires the action integral,

$$S[\Psi] = \int_{t_0}^{t_1} \langle \Psi | \left(\hat{H} - i\frac{\partial}{\partial t} \right) | \Psi \rangle, \tag{8.14}$$

to be stationary, i.e.,

$$\delta S = \delta \langle \Psi | \hat{H} | \Psi \rangle - i \left(\langle \delta\Psi | \frac{\partial \Psi}{\partial t} \rangle - \langle \frac{\partial \Psi}{\partial t} | \delta\Psi \rangle \right) = 0, \tag{8.15}$$

with respect to arbitrary variation of CI coefficients and orbitals. By substituting (8.13) into (8.15) and after laborious algebra, one can derive the equations of motion for the CI coefficients and orbital functions.

The form of the resulting EOMs is not unique but can be written in various equivalent ways [36]. Here we present the EOMs in the form convenient for numerical implementation [36]. The EOMs for the CI coefficients read,

$$i\frac{d}{dt}C_I(t) = \sum_J \langle \Phi_I|\hat{H}_2|\Phi_J\rangle C_J(t), \tag{8.16}$$

which describes transitions among different configurations solely mediated by the interelectronic Coulomb interaction. The EOMs of the orbitals are given by

$$i\frac{d}{dt}|\psi_p\rangle = \hat{h}|\psi_p\rangle + \hat{Q}\hat{F}|\psi_p\rangle + \sum_q |\psi_q\rangle R_p^q, \tag{8.17}$$

where $\hat{Q} = 1 - \sum_p |\psi_p\rangle\langle\psi_p|$ is the projector onto the orthogonal complement of the occupied orbital space. $\hat{F}$ is a mean-field operator that describes the contribution from the interelectronic Coulomb interaction, defined by

$$\hat{F}|\psi_p\rangle = \sum_{oqsr} (D^{-1})_p^o P_{or}^{qs} \hat{W}_s^r |\psi_q\rangle, \tag{8.18}$$

where D and P are the one- and two-electron reduced density matrix (RDM) in the orbital representation, respectively (see [35] for their definition and the simplification due to the core-active separation), and $\hat{W}_s^r$ is the electrostatic potential of an orbital product (pair potential),

$$\hat{W}_s^r(\mathbf{r}) = \int d\mathbf{r}' \frac{\psi_r^*(\mathbf{r}')\psi_s(\mathbf{r}')}{|\mathbf{r} - \mathbf{r}'|}. \tag{8.19}$$

The matrix element R_p^q,

$$R_p^q \equiv i\langle\psi_q|\dot{\psi}_p\rangle - h_p^q, \tag{8.20}$$

with $h_p^q = \langle\psi_q|\hat{h}|\psi_p\rangle$, determines the components of the time derivative of orbitals in the subspace spanned by the occupied orbitals . The elements within one subspace, i.e., R_j^i and R_t^u, can be arbitrary Hermitian matrix elements and are set to zero $R_j^i = R_t^u = 0$ in our implementation [36]. The elements between the core and active subspaces are given by,

$$R_i^t = \left(R_t^i\right)^* = \begin{cases} -h_i^t & \text{(LG)} \\ -h_i^t - \mathbf{E}(t) \cdot \mathbf{r}_i^t & \text{(VG)} \end{cases} \qquad \text{(for } i \in \text{frozen core)}, \tag{8.21}$$

$$R_i^t = \left(R_t^i\right)^* = \sum_u [(2-D)^{-1}]_u^t (2F_i^u - \sum_v D_v^u F_v^{i*}) \quad \text{(for } i \in \text{dynamical core)}, \tag{8.22}$$

where $F_i^u = \langle \psi_u | \hat{F} | \psi_i \rangle$, and $\mathbf{r}_i^t$ denotes a matrix element of the position vector $\mathbf{r}$. For the sake of gauge invariance (see Sect. 8.3.5), frozen core orbitals, which are time-independent in the length gauge, are to be varied in time in the velocity gauge as [36],

$$\psi_i(\mathbf{r}, t) = \mathrm{e}^{-i\mathbf{A}(t)\cdot\mathbf{r}} \psi_i(\mathbf{r}, 0) \qquad \text{(for } i \in \text{frozen core)}, \tag{8.23}$$

in spite of their name. Nevertheless, the FC orbital electron density distribution $|\psi_i(\mathbf{r}, t)|^2 = |\psi_i(\mathbf{r}, 0)|^2$ is still time-independent.

It is noteworthy that the laser-electron interaction is explicitly contained only in the first term of the orbital EOM (8.17) and does not directly drive temporal change of the CI coefficients in (8.16). Thus, in the form presented here, we can say that dynamical correlation induced by the laser field manifests itself first in the orbital EOMs and then spreads to the CI coefficients via the temporal change of orbitals (and, thus, of Slater determinants) in (8.16).

8.3.4 Numerical Implementation for Atoms

We have recently numerically implemented the TD-CASSCF method for atoms irradiated by a linearly polarized laser pulse, as detailed in [36]. Our implementation employs a spherical harmonics expansion of orbitals with the radial coordinate discretized by a finite-element discrete variable representation [45–48]. The computationally most costly operation is to evaluate the pair potentials (8.19) contributing to the mean-field (8.18), for which we use a Poisson solver thereby achieving linear scaling with the number of basis functions (or equivalently, grid points) [35, 46, 49–51]. A split-operator propagator is developed with an efficient implicit method for stiff derivative operators which drastically stabilizes the temporal propagation of orbitals. Thanks to the combination of these techniques, we can take full advantage of the TD-CASSCF method.

8.3.5 Gauge Invariance

The TD-CASSCF method is gauge invariant. For a TD-MCSCF method to be gauge invariant, it must meet the following two requirements:

1. Any LG wave function $\Psi_{\mathrm{L}}(t)$ that satisfies a given multiconfiguration ansatz (8.11) can be transformed to a VG wave function $\Psi_{\mathrm{V}}(t)$ that satisfies another multiconfiguration ansatz of the same form, and vice versa.
2. If a LG wave function $\Psi_{\mathrm{L}}(t)$ is optimized on the basis of the TDVP expressed in the length gauge, its VG counterpart $\Psi_{\mathrm{V}}(t)$ satisfies the TDVP in the velocity gauge, and vice versa.

To discuss the first requirement, let us denote the orbital functions calculated with a given multiconfiguration ansatz (8.11) within the length gauge by $\{\psi_p^{\mathrm{L}}(\mathbf{r})\}$. Equation (8.7) is fulfilled if one constructs the wave function $\Psi_{\mathrm{V}}(t)$ of the same ansatz with the CI coefficients unchanged using the orbital functions $\{\psi_p^{\mathrm{V}}(\mathbf{r})\}$ defined by,

$$\psi_p^{\mathrm{V}}(\mathbf{r}) = \exp\left[-i\mathbf{A}(t)\cdot\mathbf{r}\right]\psi_p^{\mathrm{L}}(\mathbf{r}). \tag{8.24}$$

Since this tells us that at least one of $\{\psi_p^{\mathrm{L}}(\mathbf{r})\}$ and $\{\psi_p^{\mathrm{V}}(\mathbf{r})\}$ is necessarily time-dependent, TD-MCSCF methods that use time-independent orbital functions such as TDCIS are, in general, not gauge invariant, i.e., the values of the observables obtained within the length gauge are not equal to those within the velocity gauge. This is because $\Psi_{\mathrm{V}}(t)$ does not necessarily belong to the subspace of the Hilbert space spanned by $\{\Phi_{\mathbf{I}}\}$, in which $\Psi_{\mathrm{L}}(t)$ is optimized. It should be noticed that even if we could use an infinite number of orbitals, TDCIS would not be gauge-invariant; it follows from (8.10) that if we use time-independent orbitals and $\Psi_{\mathrm{L}}(t)$ is expressed as a single (Hartree-Fock) determinant, $\Psi_{\mathrm{V}}(t)$ involves up to N-tuple excitations. (See [52] for a recently reported gauge-invariant formulation of TDCIS with time-dependent orbitals.)

For the second requirement, it should be noticed that the length- and velocity-gauge Hamiltonians $\hat{H}_{\mathrm{L}}(t)$ with (8.5) and $\hat{H}_{\mathrm{V}}(t)$ with (8.6), respectively, are related by [38],

$$\hat{H}_{\mathrm{V}} = \hat{\mathscr{U}}\hat{H}_{\mathrm{L}}\hat{\mathscr{U}}^{\dagger} + i\frac{d\hat{\mathscr{U}}}{dt}\hat{\mathscr{U}}^{\dagger}. \tag{8.25}$$

Then, using the unitarity of the gauge-transformation operator $\hat{\mathscr{U}}(t)$ (8.8), we can show that the TDVP expressions (8.15) in the two representations are equivalent. This guarantees that the wave function transformed via (8.24) from the wave function satisfying the length-gauge TDVP fulfills the velocity-gauge TDVP. Therefore, satisfying both of the above-mentioned conditions, TD-MCSCF methods with time-varying orbital functions, including TDHF, MCTDHF, TD-CASSCF, and the time-dependent occupation-restricted multiple active-space (TD-ORMAS) [53] methods, are gauge invariant in general [30, 35, 53, 54].

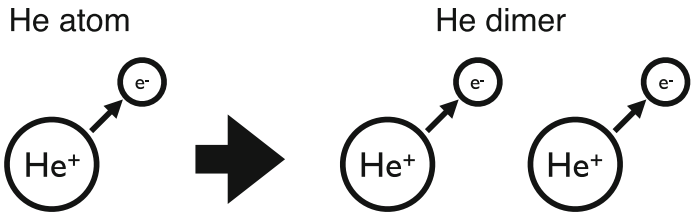

Fig. 8.3 Schematic illustration of size extensivity explained with a He atom and dimer (see text)

8.3.6 Size Extensivity

The TD-CASSCF method is size extensive. Size extensivity[1] states "the method scales properly with the number of particles" [55] or, for the case of the ground-state energy, "if we have k number of noninteracting identical molecules, their total energy must be k times the energy of one molecule" [56]. Roughly speaking, it can be understood as follows.

Let us consider that we simulate photoionization of a He atom for such a laser parameter that He is substantially singly ionized but that double ionization is negligible. Then, what will happen if we simulate photoionization of a He dimer by the identical laser pulse, in which the two He atoms are sufficiently far apart from each other but the dipole approximation is still valid? Physically, we would expect substantial single ionization of each atom, resulting in double ionization in total (Fig. 8.3).

This seemingly obvious requirement is, in general, *not* met by TD-MCSCF methods with truncated expansion such as TDCIS and TD-ORMAS. On the other hand, TD-CASSCF as well as MCTDHF and TDHF fulfills size extensivity.

8.4 Initial-State Preparation and Simulation Boundary

In ab initio simulation study of multielectron dynamics, we usually need to (i) prepare the initial state, (ii) propagate the wave function in time (Sect. 8.3), (iii) absorb electrons that leave the calculation region, and (iv) read out physically relevant information from the wave function (Sect. 8.5). Let us discuss (i) and (iii) in this Section.

[1] It is not to be confused with a similar but different concept of size consistency, which, for the case of the ground-state energy, states "if molecule AB dissociates to molecules A and B, the asymptote of molecule AB at infinite internuclear separation should be the sum of the energies of molecules A and B" [55] and "is only defined if the two fragments are non-interacting" [56].

8.4.1 Imaginary-Time Propagation

While the initial state can also be obtained by a separate time-independent calculation of the ground state, a convenient alternative is imaginary-time propagation (or relaxation) [57]. The solution of the field-free TDSE can be expressed as,

$$\Psi(t) = \sum_{\alpha=0}^{\infty} c_\alpha \Xi_\alpha e^{-iE_\alpha t} = e^{-iE_0 t}\left(c_0\Xi_0 + \sum_{\alpha=1}^{\infty} c_\alpha \Xi_\alpha e^{-i(E_\alpha - E_0)t}\right), \tag{8.26}$$

with eigenstates Ξ_α, of which Ξ_0 is the ground state, and energy eigenvalues E_α. By substituting *imaginary* time $t = -is$ with s being a real number, we obtain,

$$\Psi(-is)e^{E_0 s} = c_0\Xi_0 + \sum_{\alpha=1}^{\infty} c_\alpha \Xi_\alpha e^{-(E_\alpha - E_0)s} \xrightarrow[s\to\infty]{} c_0\Xi_0, \tag{8.27}$$

since $E_\alpha - E_0 > 0$ ($\alpha \geq 1$). Thus, we can obtain the ground state by integrating the field-free EOMs in imaginary time and renormalizing the wave function after every several time steps. The imaginary-time propagation is used for the results presented in this chapter.

8.4.2 Absorption Boundary

Since ionization is essential in the ultrafast intense laser science, it is one of the major issues how to treat electrons that leave the calculation region and suppress unphysical reflections. We use either mask function or infinite-range exterior complex scaling in our numerical implementations.

8.4.2.1 Mask Function and Complex Absorbing Potential (CAP)

One common method is to multiply orbital functions outside a given radius (mask radius) R_0 by a function that decreases from unity and vanishes at the simulation box boundary after each time step [58]. Typical forms of the mask function include $\cos^{1/4}$ and $\cos^{1/8}$.

Another method is to add a complex absorbing potential (CAP), e.g., of the form

$$-i\eta W(r) = -i\eta(r - R_0)^2, \tag{8.28}$$

where η denotes a CAP strength, to the Hamiltonian outside a given radius R_0. In the context of ab initio simulations of strong-field processes, CAP has been used in combination with TDCIS [40].

8.4.2.2 Exterior Complex Scaling (ECS)

Exterior complex scaling [59] analytically continues the wave function outside a given scaling radius R_0 into the complex plane as, for the case of the polar coordinate (Fig. 8.4),

$$r \to R(r) = \begin{cases} r & (r < R_0) \\ R_0 + (r - R_0)e^{\lambda + i\eta} & (r > R_0), \end{cases} \tag{8.29}$$

where λ and scaling angle η are real numbers. Then, the orbital function is transformed via ECS operator $U_{\eta R_0}$ as,

$$(U_{\eta R_0}\psi)(\mathbf{r}) := \begin{cases} \psi(\mathbf{r}) & (r < R_0) \\ e^{\frac{\lambda+i\eta}{2}} \dfrac{R(r)}{r} \psi(\mathbf{R}(r)) & (r > R_0), \end{cases} \tag{8.30}$$

where $\mathbf{R}(r) = \frac{R(r)}{r}\mathbf{r}$. In actual simulations, we numerically store $(U_{\eta R_0}\psi)(\mathbf{r})$ instead of $\psi(\mathbf{r})$ in the scaled region $r > R_0$. We can understand why this works as an absorbing boundary by considering a spherical wave e^{ikr}/r. At $r > R_0$ it becomes $e^{\frac{\lambda+i\eta}{2}} e^{ik[R_0+(r-R_0)e^{\lambda}\cos\eta]-k(r-R_0)\sin\eta}/r$, which exponentially diminishes as $\sim e^{-kr\sin\eta}/r$ at large distance. It should be noticed that ECS modifies neither the wave function nor the system Hamiltonian.

While ECS is usually applied on a finite discretization range, one can infinitely extend the scaled region, thus moving the simulation box boundary to infinity, while using a finite number of exponentially damped basis functions [60]. This method, called infinite-range ECS (irECS), significantly improves the accuracy and efficiency over standard ECS with a considerably smaller number of basis functions. It also has a conceptual advantage of being able to simulate the entire space.

While irECS has originally been formulated for a single-electron system and found only limited use for strongly-driven multielectron systems, we have applied it to our TD-CASSCF numerical implementation, as detailed in [37]. We set $\lambda = 0$ and introduce Gauss-Laguerre-Radau quadrature points [61, 62] to construct discrete-variable-representation basis functions in the last finite element extending to infinity. An essential difference from a single-electron case is the presence of interelectronic Coulomb interaction via mean-field operator (8.18). Its evaluation as well as that of $\hat{Q}$ requires $\hat{U}_{(-\eta)R_0}|\psi_p\rangle$, which is not available in the scaled region. Since the scaled

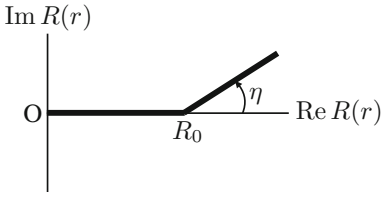

Fig. 8.4 Schematic illustration of radial exterior complex scaling contour $R(r)$ with scaling radius R_0 and scaling angle η

region is far from the origin, it is reasonable to assume that the scaled part of the orbital functions hardly affects the electron dynamics close to the nucleus and that the interaction between electrons residing in the scaled region is negligible. Thus, we neglect $\hat{U}_{(-\eta)R_0}|\psi_p\rangle$ in the scaled region wherever their information is necessary. This treatment roughly corresponds to the neglect of the Coulomb force acting on electrons from scaled-region electrons ($r > R_0$). On the other hand, the Coulomb force acting on scaled-region electrons from unscaled-region electrons ($r < R_0$) is not neglected. Hence, the effect of the ionic Coulomb potential is properly taken into account in the dynamics of departing electrons.

Figure 8.5 compares the electron radial distribution functions after the pulse for the case of a Be atom exposed to a laser pulse with 800 nm wavelength and 3.0×10^{14} W/cm^2 peak intensity, calculated with different absorbing boundaries listed in Table 8.1. The pulse has a sin^2 envelope with a foot-to-foot pulse width of five cycles. We use $(n_{fc}, n_{dc}, n_a) = (1, 0, 4)$. The result of condition A, with $R_0 = 320$ a.u. much larger than the quiver radius 28.5 a.u., is converged and can be considered to be numerically exact. We can see that the irECS delivers much better results (C and E) inside R_0 than the mask function (F). It is remarkable that the irECS works well even with the scaling radius ($R_0 = 28$ a.u.) comparable with the quiver radius. The result of the simulation (condition D) similar to C but neglecting also the interelectronic Coulomb force from the unscaled (inner) to the scaled (outer) region is plotted with a blue dashed curve in Fig. 8.5. We find a large discrepancy from the exact result (A). This indicates that proper account of the Coulomb force acting on scaled-region electrons from unscaled-region ones is crucial for accurate simulations, even though the total momentum of the system is not conserved due to imbalance in counting the interelectronic Coulomb interactions.

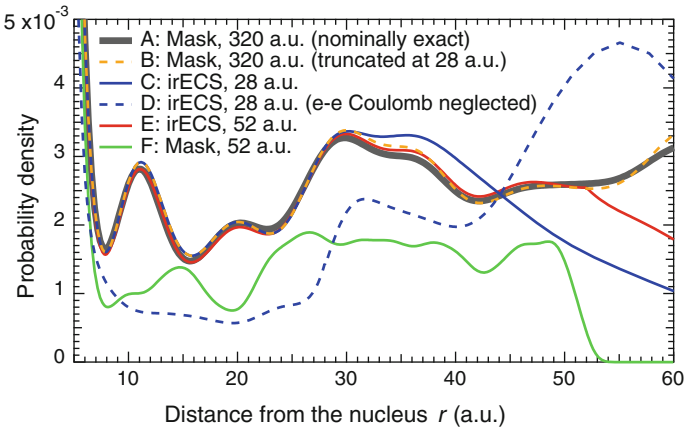

Fig. 8.5 Electron radial distribution function $\rho(r)$ after the laser pulse for the case of Be exposed to a laser pulse with 800 nm wavelength and 3.0×10^{14} W/cm^2 peak intensity, calculated with different absorbing boundaries listed in Table 8.1

Table 8.1 Absorbing boundaries tested for Be

	Absorber	R_0	n_{ua}	L_{a}	n_{a}	Remark
A	Mask	320	1600	80	400	Nominally exact
B	Mask	320	1600	80	400	Truncated at 28 a.u. (see text in Sect. 8.4.2.3)
C	irECS	28	140	∞	40	
D	irECS	28	140	∞	40	Unscaled-to-scaled Coulomb neglected
E	irECS	52	260	∞	40	
F	Mask	52	260	8	40	

8.4.2.3 Which Part of the Total Wave Function is Propagated after One or More Electrons are Absorbed at the Simulation Boundary?

Let us specifically consider a He atom, which is a two-electron system. The (r_1, r_2) space can be divided into four regions, as shown in Fig. 8.6, A: $r_1 < R_0, r_2 < R_0$, B: $r_1 > R_0, r_2 < R_0$, C: $r_1 < R_0, r_2 > R_0$, D: $r_1 > R_0, r_2 > R_0$.

For the case of direct numerical simulation of the two-electron TDSE, e.g., by the time-dependent close-coupling method [16, 17, 21, 22], the wave function only in region A is stored and propagated. Hence, once one electron is absorbed, the dynamics of the other electron is no longer followed even if it is still inside the absorption radius R_0, and, as a consequence, the transition from B or C to D cannot be traced.

In great contrast, not only the two electrons in region A but also the inner electron in regions B and C is simulated in the TD-CASSCF, MCTDHF, and TDHF simulations. In order to understand this prominent feature, we decompose the exact orbital $|\psi_p\rangle$, which would be obtained if we used an infinitely large simulation box, into the part numerically stored and propagated during actual simulation $|\phi_p\rangle$ and the remaining, i.e., absorbed and lost part $|\chi_p\rangle$:

$$|\psi_p\rangle = |\phi_p\rangle + |\chi_p\rangle. \tag{8.31}$$

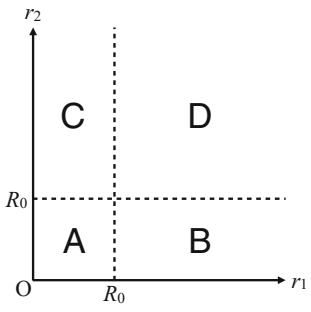

Fig. 8.6 Four regions of the (r_1, r_2) space of the two electrons in He

Roughly speaking, $|\phi_p\rangle$ is the part at $r < R_0$ and $|\chi_p\rangle$ at $r > R_0$. The TD-CASSCF equations of motion are derived on the assumption that $\{|\psi_p\rangle\}$ is orthonormal. On the other hand, $\{|\phi_p\rangle\}$ is *not* orthonormal in general, and its norm decreases. By good use of absorption boundary, $|\phi_p\rangle$ expectedly reproduces $|\psi_p\rangle$ within R_0. In region B, the two-electron wave function is generally expressed as,

$$\Psi(\mathbf{r}_1, \mathbf{r}_2) = \sum_{p,q} C_{pq} \chi_p(\mathbf{r}_1) \phi_q(\mathbf{r}_2), \tag{8.32}$$

with an expansion coefficient C_{pq}. Here we neglect the spin part for simplicity. As (8.32) suggests, even after electron 1 is absorbed, the dynamics of electron 2, still entangled with electron 1, continues to be simulated, though approximately, as long as it stays inside the absorption radius.

In Fig. 8.5 we have seen that the irECS works much better than the mask function. Nevertheless, the irECS results (conditions C and E in Table 8.1) still deviate slightly from the nominally exact solution (condition A). In the present case, Be is nearly totally ionized, and double ionization amounts to 50%, as we will see below in Fig. 8.7. Hence, the deviation may be due to the neglect of the Coulomb interaction in and from the scaled region and/or the loss of information on the wave function in the scaled region.

In order to reveal the effect of the former, we have performed a simulation (condition B in Table 8.1) with a sufficiently large domain as condition A but by truncating the interelectronic Coulomb interaction at $r = 28$ a.u. as in the irECS. The result is plotted in Fig. 8.5. The "truncated" result (B) slightly deviates from the exact one (A) but overlaps with the irECS result (C) at $r < 28$ a.u., which indicates that the difference between the exact and irECS results in Fig. 8.5 originates from the neglect of the Coulomb interaction in and from the scaled region, not from the loss of information.

One may be surprised that the loss of information on orbital functions at the absorption boundary hardly affects simulation results within the absorption radius. It should be noticed that, even if the explicit form of $|\chi_p\rangle$ is unknown, some information on them is still available. At least, we can tell,

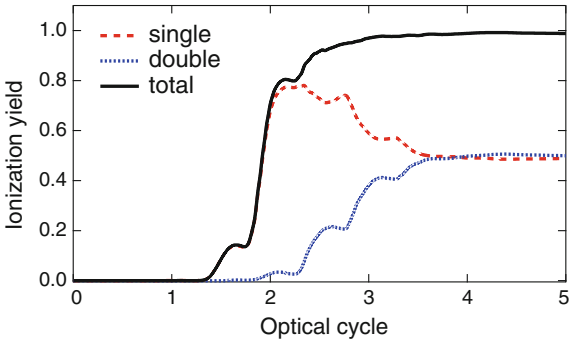

Fig. 8.7 Time evolution of spatial-domain-based single, double, and total ionization probabilities of Be exposed to a laser pulse with 800 nm wavelength and 3.0×10^{14} W/cm^2 peak intensity (the same as for Fig. 8.5). $R_{\text{ion}} = 20$ a.u. is used

$$\langle \phi_p | \chi_q \rangle = 0, \qquad \langle \chi_p | \chi_q \rangle = \delta_{pq} - \langle \phi_p | \phi_q \rangle, \tag{8.33}$$

from the orthonormality of $\{|\psi_p\rangle\}$. This not only helps accurate simulations but also allows to extract useful information such as ionization yields and charge-state-resolved observables, as discussed in the next section.

8.5 Numerical Examples

In this Section, we present how to extract physical observables from the wave function and numerical results obtained with TD-CASSCF and TDHF simulations.

8.5.1 Ionization Yield

One might consider that the ionization yield for charge state n could be obtained through the integration over the population of all possible n-electron continuum states (note that n denotes the ionic charge state in this Section). Unfortunately, however, direct application of this naive idea would encounter difficulties. First, it is not trivial (even more difficult than TD-CASSCF itself) to prepare n-electron continuum wave functions. The ionic core is not necessarily in the ground state and may also be excited. Second, we have to keep the entire wave function within the simulation box, without being absorbed. The computational cost would be prohibitive. Third, as discussed in Sect. 8.2.2, the population of each field-free stationary state is not gauge invariant during the pulse.

Instead, we define ionization in terms of the spatial positions of electrons and introduce ionization probability P_n as a probability to find n electrons in the outer region $|\mathbf{r}| > R_{\mathrm{ion}}$ and the remaining $N - n$ electrons in the inner region $|\mathbf{r}| < R_{\mathrm{ion}}$, with a given distance R_{ion} from the origin,

$$P_n \equiv \binom{N}{n} \int_{>} dx_1 \cdots \int_{>} dx_n \int_{<} dx_{n+1} \cdots \int_{<} dx_N \ |\Psi(x_1, \ldots, x_N)|^2 , \tag{8.34}$$

where $\int_<$ and $\int_>$ denote integrations over a spatial-spin variable $x = \{\mathbf{r}, \sigma\}$ with the spatial part restricted to the domains $|\mathbf{r}| < R_{\mathrm{ion}}$, and $|\mathbf{r}| > R_{\mathrm{ion}}$, respectively. P_n satisfies $\sum_{n=0}^{N} P_n = 1$. This spatial-domain-based ionization probability has an advantage of being gauge invariant. Moreover, it is consistent with our usual perception of ionization as a spatial separation of electron from the parent ion, such as ejection from the surface and arrival of electron at a detector.

If we introduce,

$$T_n \equiv \binom{N}{n} \int dx_1 \cdots \int dx_n \int_{<} dx_{n+1} \cdots \int_{<} dx_N \ |\Psi(x_1, \ldots, x_N)|^2 , \tag{8.35}$$

it is related to P_n as,

$$P_n = \sum_{k=0}^{n} \binom{N-n+k}{k} (-1)^k T_{n-k}, \tag{8.36}$$

due to the orthonormality of orbitals with full-space integration [35] (see also Sect. 8.4.2.3), allowing to calculate the ionization probability only from the information of orbitals inside the radius $R_{\rm ion}$ and CI coefficients. By adopting the multiconfiguration expansion (8.11), and making use of the orthonormality of spin-orbitals in the full-space integration, we have

$$T_n = \sum_{IJ}^{\mathsf{P}} C_I^* C_J D_{IJ}^{(n)}, \tag{8.37}$$

where,

$$\begin{aligned} D_{IJ}^{(0)} &= \sum_{ij}^{N} \det\left(S_{IJ}^{<}\right), \\ D_{IJ}^{(1)} &= \sum_{ij}^{N} \varepsilon_{ij}^{IJ} \det\left(S_{IJ}^{<}[i:j]\right), \\ D_{IJ}^{(2)} &= \sum_{i>j}^{N} \sum_{k>l}^{N} \varepsilon_{ik}^{IJ} \varepsilon_{jl}^{IJ} \det\left(S_{IJ}^{<}[ij:kl]\right), \end{aligned} \tag{8.38}$$

etc., and $S_{IJ}^{<}$ is an $N \times N$ matrix with its $\{ij\}$ element being the inner-region overlap integral,

$$(S_{IJ}^{<})_{ij} = \int_{<} dx \phi_{p(i,I)}^*(x) \phi_{q(j,J)}(x) \equiv \langle \phi_p | \phi_q \rangle_{<}, \tag{8.39}$$

where $\phi_{p(i,I)}$ is the ith (in a predefined order) spin orbital in the determinant I. $S_{IJ}^{<}[ij\cdots:kl\cdots]$ is the submatrix of $S_{IJ}^{<}$ obtained after removing rows $i, j, \ldots$ and columns $k, l, \ldots$ from the latter, and,

$$\varepsilon_{ij}^{IJ} = \delta_{q(j,J)}^{p(i,I)} (-1)^{i+j}. \tag{8.40}$$

The matrix $S_{IJ}^{<}$ and its submatrices are block-diagonal due to the spin-orthonormality, so that, e.g., $\det\left(S_{IJ}^{<}\right) = \det\left(S_{I^\alpha J^\alpha}^{<}\right) \det\left(S_{I^\beta J^\beta}^{<}\right)$, where I^σ is the σ-spin part of the determinant I.

In Fig. 8.7, we show the temporal evolution of thus calculated single, double, and total ionization yields of Be for the same pulse and orbital subspace decomposition as for Fig. 8.5. As an absorption boundary, we have used irECS with $R_0 = 40$ a.u.

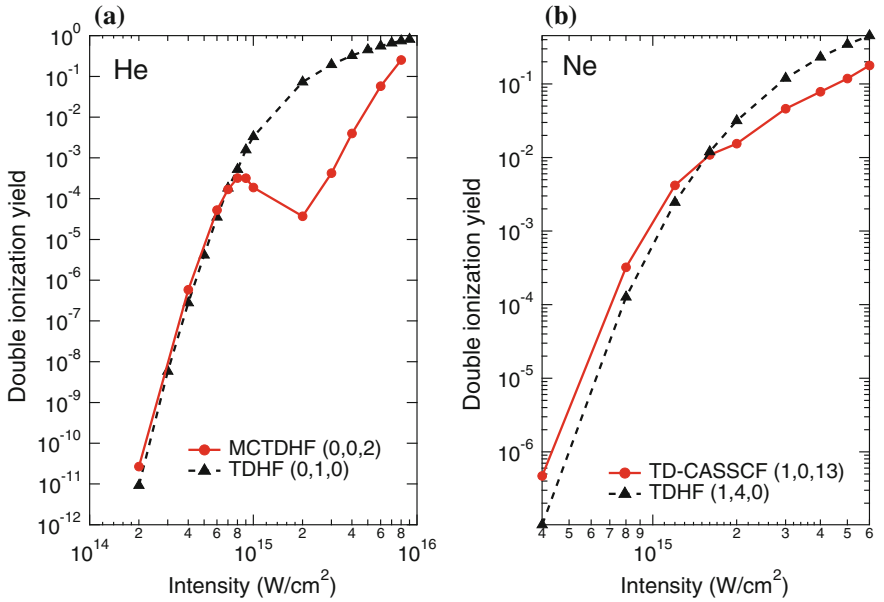

Fig. 8.8 Double ionization yields of **a** He and **b** Ne as a function of intensity of a laser pulse with a wavelength of 800 nm, calculated by the TD-CASSCF and TDHF methods

R_{ion} is set to be 20 a.u. We can see step-like evolution every half cycle typical of tunneling ionization. After the pulse, there is practically no neutral species left, and the double ionization yield is ∼50%. It is remarkable that the neglect of the Coulomb interaction in and from the scaled region is a good approximation and that irECS works excellently even under such massive double ionization.

Figure 8.8 presents the intensity dependence of the double ionization yields of He and Ne irradiated by a laser pulse whose wavelength is 800 nm. Although the results are not converged with respect to the number of orbitals yet, we can already clearly see knee structures in the TD-CASSCF results, but not in the TDHF ones. Thus, the TD-CASSCF method can well reproduce non-sequential double ionization [63, 64], a representative strong-field phenomenon that witnesses electron correlation.

8.5.2 *Charge-State-Resolved Electron Density Distribution*

The usual electron density distribution,

$$\rho(\mathbf{r}) \equiv N \sum_{\sigma} \int dx_2 \cdots \int dx_N \ |\Psi(x, x_2, \ldots, x_N)|^2 \,, \tag{8.41}$$

contains all the different charge states: neutral, singly ionized, doubly ionized, etc. To discuss charge migration following attosecond photoionization, it will be useful to analyze, e.g., a hole distribution inside the cation. Hence, we introduce a charge-state-resolved electron density distribution $\rho^{(n)}(\mathbf{r})$ as a probability to find an electron at $\mathbf{r}$ on condition that n out of the other $N-1$ electrons are at $|\mathbf{r}| > R_{\rm ion}$ and $N-1-n$ at $|\mathbf{r}| < R_{\rm ion}$,

$$\rho^{(n)}(\mathbf{r}) \equiv N\binom{N-1}{n}\sum_{\sigma}\int_{>} dx_2 \cdots \int_{>} dx_{n+1}\int_{<} dx_{n+2}\cdots\int_{<} dx_N \ |\Psi(x, x_2, \ldots, x_N)|^2 . \tag{8.42}$$

Note that the electron density distribution in the neutral species is consistently given by,

$$\rho^{(0)}(\mathbf{r}) \equiv N\sum_{\sigma}\int_{<} dx_2 \cdots \int_{<} dx_N \ |\Psi(x, x_2, \ldots, x_N)|^2 . \tag{8.43}$$

Here, again, we have used domain-based definition of ionization.

$\rho^{(n)}(\mathbf{r})$ can be expressed in terms of orbitals and CI coefficients as well as $S_{IJ}^{<}$ introduced in the previous Subsection. For example, the electron density distribution of the cation can be calculated by,

$$\begin{aligned}\rho^{(1)}(\mathbf{r}) = &\sum_{IJ}^{\Pi} C_I^* C_J \sum_{i,j}^{N} \phi^*_{p(i,I)}(x)\phi_{q(j,J)}(x)(-1)^{i+j} \\ &\left(\sum_{k=1}^{N}\varepsilon_{ik}\varepsilon_{jk}S_{IJ}^{<}[ik;jk] - (N-1)S_{IJ}^{<}[i;j]\right).\end{aligned} \tag{8.44}$$

In Fig. 8.9, we show snap shots of the electron density distribution in Be^+ produced by photoionization of Be by XUV pulses with a photon energy of 150 eV and a FWHM pulse width of 20 and 30 as. The process is simulated with the TDHF method. An isotropic charge density is formed by the superposition of $(1s)^{-1}$ and $(2s)^{-1}$ holes and oscillates with a period of ca. 35 as, consistent with the energy difference ($\sim$120 eV). We also see that its amplitude is larger for the 20 as pulse width than for 30 as, reflecting the wider spectrum of photon energy. The present charge-state-resolved density can also be used to decompose physical observables to contributions from species of different ionic charges, e.g., charge-state-resolved HHG spectra [65].

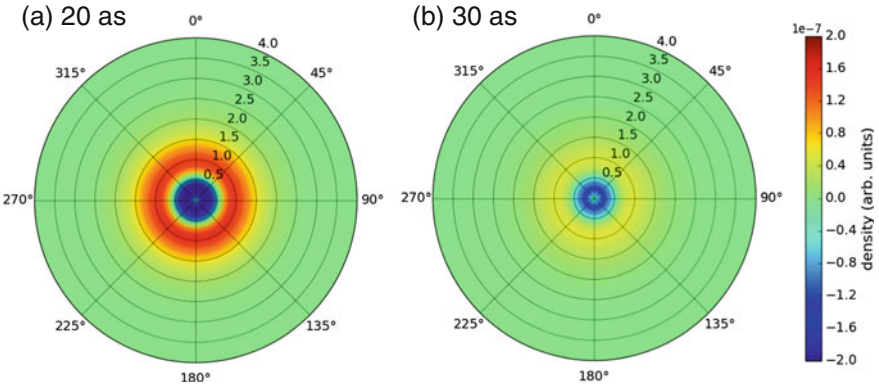

Fig. 8.9 Snap shots of the electron density distribution in Be^+ produced by photoionization of Be by XUV pulses with a photon energy of 150 eV, a peak intensity of 10^{13} W/cm^2, and a FWHM pulse width of **a** 20 as and **b** 30 as. The results of TDHF simulations

8.5.3 Ehrenfest Expression for Dipole Acceleration and High-Harmonic Spectrum

Harmonic spectrum is usually extracted by Fourier transforming the dipole moment,

$$\langle z \rangle(t) = \langle \Psi | z | \Psi \rangle, \tag{8.45}$$

or the dipole acceleration $\langle a \rangle(t)$,

$$\langle a \rangle(t) = \frac{d^2}{dt^2} \langle z \rangle(t). \tag{8.46}$$

As known as the Ehrenfest theorem, one can show, from the TDSE (8.1), that,

$$\langle a \rangle(t) = -\langle \Psi | \left(\frac{\partial \hat{V}_0}{\partial z} + \frac{\partial \hat{V}_{\text{ext}}}{\partial z} \right) | \Psi \rangle. \tag{8.47}$$

The right hand side of this equation is the expectation value of the force acting on the electrons from the nuclei and laser electric field. Equation (8.47), with smaller numerical noise than in (8.45), is widely used in combination with TDSE simulations within the single-active-electron (SAE) approximation, with $\hat{V}_0$ replaced by the effective potential.

The equivalence of (8.46) and (8.47) holds also for the TD-CASSCF methods with all the orbitals time-varying [36], and, hence, the Ehrenfest expression (8.47) can be safely used. However, the use of frozen-core orbitals requires a special care. We have shown that, in the latter case, the following expression should be used instead of (8.47) [36]:

$$\langle a \rangle_{\mathrm{fc}}(t) = -\langle \Psi | \left(\frac{\partial \hat{V}_0}{\partial z} + \frac{\partial \hat{V}_{\mathrm{ext}}}{\partial z} \right) | \Psi \rangle + \Delta(\dot{p}_z). \tag{8.48}$$

In the length gauge and if we neglect the indistinguishability between core and active electrons, the additional term $\Delta(\dot{p}_z)$ can be approximated as [36],

$$\Delta(\dot{p}_z) \approx \langle \Phi_{\mathrm{fc}} | \frac{\partial \hat{V}_0}{\partial z} + \frac{\partial \hat{V}_{\mathrm{ext}}}{\partial z} + \frac{\partial \hat{V}_a}{\partial z} | \Phi_{\mathrm{fc}} \rangle, \tag{8.49}$$

where,

$$V_a(\mathbf{r}) = \int d\mathbf{r}' \frac{\rho_a(\mathbf{r}')}{|\mathbf{r} - \mathbf{r}'|}, \tag{8.50}$$

with ρ_a being the density of active electrons.

The meaning of (8.48) can be interpreted as follows: The Ehrenfest theorem states that the dipole acceleration is given by the expectation value of the total force on the electronic system, made up of the laser electric force acting on the active, f_{la}, and core electrons, f_{lc}, the nuclear Coulomb force on the active, f_{na}, and core electrons, f_{nc}, and the interelectronic forces from the active electrons on the core, f_{ac}, and vice versa, f_{ca}. Then, we obtain the total force,

$$f = (f_{\mathrm{na}} + f_{\mathrm{nc}}) + (f_{\mathrm{la}} + f_{\mathrm{lc}}) + (f_{\mathrm{ac}} + f_{\mathrm{ca}}) = (f_{\mathrm{na}} + f_{\mathrm{nc}}) + (f_{\mathrm{la}} + f_{\mathrm{lc}}), \tag{8.51}$$

where we have used the action-reaction law $f_{\mathrm{ac}} = -f_{\mathrm{ca}}$ in the second equality. We can see correspondence of this expression to (8.47). However, if the core orbitals are frozen, we have to take account of an additional "binding force" f_{b} to fix the frozen core, which is inherent in the variational procedure to derive the EOMs. Since the binding force f_{b} cancels the forces acting on frozen-core electrons from the nuclei, laser field, and active electrons, it is given by,

$$f_{\mathrm{b}} = -f_{\mathrm{nc}} - f_{\mathrm{lc}} - f_{\mathrm{ac}}. \tag{8.52}$$

Consequently, the effective force in the presence of frozen core becomes,

$$f_{\mathrm{eff}} = f + f_{\mathrm{b}} = (f_{\mathrm{na}} + f_{\mathrm{ca}}) + f_{\mathrm{la}}. \tag{8.53}$$

The comparison between (8.49) and (8.52) tells us that the additional term $\Delta(\dot{p}_z)$ in the former represents the binding force f_{b}, and (8.48) is a quantum-mechanical expression of the effective force (8.53).

Figure 8.10 compares the HHG spectra from Be, calculated as the modulus squared of the Fourier transform of the dipole acceleration, extracted from the simulations with a dynamical and frozen core orbital. If we calculate the frozen-core HHG spectrum using the modified formula (8.48), it overlaps with the DC result almost perfectly. This indicates that the use of FC is a good approximation for the circumstances

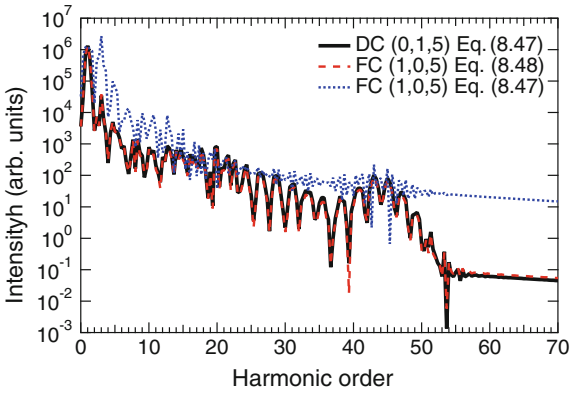

Fig. 8.10 HHG spectra of Be exposed to a laser pulse with a wavelength of 800 nm, an intensity of 3×10^{14} W/cm^2, and a foot-to-foot pulse width of three cycles. Comparison between the simulations with DC $(n_{fc}, n_{dc}, n_a) = (0, 1, 5)$ and FC $(1, 0, 5)$. For the case of FC, we also compare the results extracted via (8.47) and (8.48)

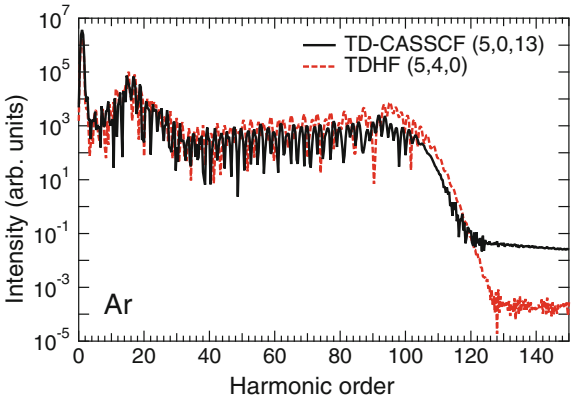

Fig. 8.11 HHG spectra of Ar exposed to a laser pulse with a wavelength of 800 nm, an intensity of 8×10^{14} W/cm^2, and a foot-to-foot pulse width of three cycles. Comparison between the TD-CASSCF $(n_{fc}, n_{dc}, n_a) = (5, 0, 13)$ and TDHF $(5, 4, 0)$

considered here. However, the use of (8.47) with FC leads to an erroneous spectrum. Thus, it is essential to use (8.48) for the calculation of dipole acceleration and, then, HHG spectra from the simulation results with frozen core.

We show in Fig. 8.11 the HHG spectra of Ar calculated with the TD-CASSCF and TDHF methods. These results well reproduce a dip around 53 eV (∼34th order) that originates from the Cooper minimum and has been experimentally observed [66]. Whereas the difference between the TD-CASSCF and TDHF is not large in this case, it is more prominent in the HHG spectrum of Kr shown in Fig. 8.12; the TDHF overestimates the harmonic intensity near the cutoff more than one order of magnitude. Such a quantitative difference is critical when we want to estimate the upper limit of the HHG pulse energy that can be generated with a given experimental setup. It is wonderful that we can now achieve a converged simulation of high-harmonic generation from the thirty-six electron atom.

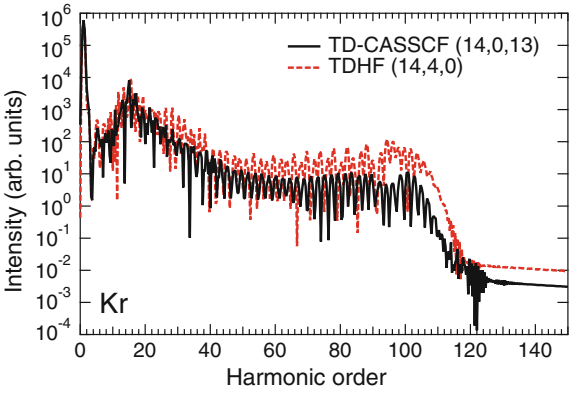

Fig. 8.12 HHG spectra of Kr exposed to a laser pulse with a wavelength of 800 nm, an intensity of 8×10^{14} W/cm^2, and a foot-to-foot pulse width of three cycles. Comparison between the TD-CASSCF $(n_{fc}, n_{dc}, n_a) = (14, 0, 13)$ and TDHF (14, 4, 0)

8.5.4 *Dipole Acceleration Within the Single-Active-Electron Approximation*

The above discussion has important implications also for how to extract harmonic spectra from TDSE simulations of multielectron atoms and molecules within the single-active-electron approximation. As stated above, (8.47) with $\hat{V}_0$ replaced by the effective potential V_{eff}, corresponding to (8.53), is usually used:

$$\langle a \rangle(t) = -\langle \psi | \left(\frac{\partial V_{eff}}{\partial z} + \frac{\partial \hat{V}_{\text{ext}}}{\partial z} \right) | \psi \rangle. \tag{8.54}$$

On the other hand, Gordon et al. [67] have argued that one should rather use (8.47) as is, i.e., with the bare nuclear potential $\hat{V}_0$ $(= -\frac{Z}{r}$ for the atomic case):

$$\langle a \rangle(t) = -\langle \psi | \left(\frac{\partial \hat{V}_0}{\partial z} + \frac{\partial \hat{V}_{\text{ext}}}{\partial z} \right) | \psi \rangle. \tag{8.55}$$

They have taken the action-reaction law into account but ignored the binding force. However, the observation that (8.48) rather than (8.47) has to be used in the presence of frozen-core orbitals, also numerically confirmed in Fig. 8.10, strongly suggests that, at the conceptual level, (8.54) is the correct choice.

8.5.5 *Photoelectron Energy Spectrum*

Time-resolved and angle-resolved photoelectron (photoemission) spectroscopy is becoming more and more important as a tool to probe ultrafast electron dynamics. In principle, (angle-resolved) photoelectron energy spectrum can be calculated through

projection of the departing wave packet onto plane waves or Coulomb waves (the difference in the results is usually negligibly small). To apply this approach, however, we need to keep the wave function within the simulation box without being absorbed, which would lead to a huge computational cost. As a new method that can be used with irECS, requiring a much smaller simulation box, the time-dependent surface flux (t-SURFF) method has recently been proposed [68]. In this method, spectra are computed from the electron flux through a surface, beyond which the outgoing electron wave packet is absorbed by irECS. Instead of analyzing spectra at the end of the simulation, one can record the surface flux in the course of time evolution. We have recently succeeded in applying t-SURFF, originally formulated for SAE-TDSE simulations, to the TD-CASSCF simulations, whose details will be presented in a separate publication.

Figure 8.13 presents the calculated photoionization cross section of Be. Making use of a broadband nature of an ultrashort pulse, one can draw such a plot with a single run, by dividing the photoelectron spectrum by photon energy spectrum. The results, in reasonable agreement with reported measurements [69], well reproduce oscillating features due to the contribution from autoionizing states. We plot three curves extracted at different delays (37, 75, 112 fs) after the pulse. We see that peaks grow around 13 eV with increasing delay, reflecting the evolution of autoionization. Thus, the TD-CASSCF method can properly describe the process induced by electron correlation.

As a demonstration of capability to evaluate photoelectron angular distribution, let us consider a bichromatic XUV pulse whose electric field is of the form,

$$E(t) = F_\omega(t)\cos\omega t + F_{2\omega}(t)\cos(2\omega t - \delta), \tag{8.56}$$

where $F_\omega(t)$ and $F_{2\omega}(t)$ denote the envelopes of the ω and 2ω pulses, respectively, and δ the relative phase. Because of the interference between two-photon ionization by ω and single-photon ionization by 2ω, the photoelectron angular distribution

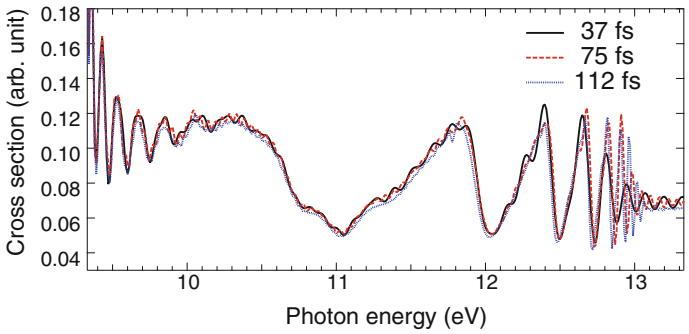

Fig. 8.13 Relative photoionization cross section of Be as a function of photon energy extracted 37, 75, and 112 fs after the pulse from TD-CASSCF simulations with $(n_{fc}, n_{dc}, n_a) = (1, 0, 4)$ for an ultrabroadband three-cycle (foot-to-foot) pulse with 22 eV central photon energy

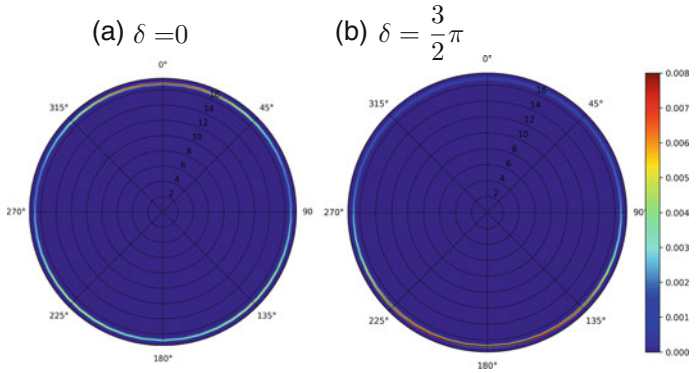

Fig. 8.14 Angle-resolved photoelectron energy spectrum from Ne irradiated by a 10 fs bichromatic XUV pulse (8.56) with $\omega = 19.1$ eV and **a** $\delta = 0$ and **b** $\frac{3}{2}\pi$, calculated with the TDHF simulation. The ω and 2ω intensities are 10^{13} W/cm^2 and 1.5×10^9 W/cm^2, respectively

is expected to vary with δ. This is confirmed by TDHF simulations as shown in Fig. 8.14. Whereas roughly the same number of photoelectrons are emitted to the upper ($\sim 0°$) and lower ($\sim 180°$) hemispheres at $\delta = 0$ (54% to the lower hemisphere), approximately two-thirds (63%) of the electrons are emitted to the lower hemisphere at $\delta = \frac{3}{2}\pi$. Hence, such simulations will be useful to design and analyze, e.g., coherent control experiments that can be realized by use of high-harmonic and free-electron-laser XUV sources with temporal coherence [70, 71].

8.6 Summary

We have compiled our recent development of the time-dependent complete-active-space self-consistent-field method to simulate multielectron dynamics in ultrafast intense laser fields along with numerical examples for atoms. Introducing the concept of frozen core, dynamical core, and active orbital subspace decomposition, TD-CASSCF allows compact and, at the same time, accurate representation of correlated multielectron dynamics in strongly driven atoms and molecules. It also has desirable features of gauge invariance and size extensivity. We can now handle strong-field phenomena in systems containing tens of electrons from the first principles, which was merely a dream several years ago.

While the present work has focused on the TD-CASSCF method, especially, for atoms, we have developed and been actively developing a variety of different ab initio methods. We have numerically implemented the MCTDHF method for molecules, based on a multiresolution Cartesian grid, without need to assume any symmetry of molecular structure [72]. We have developed the TD-ORMAS method [53], which is more approximate and thus computationally even less demanding than TD-CASSCF, and allows one to handle general MCSCF wave functions with

arbitrary CI spaces. We have more recently formulated the time-dependent optimized coupled-cluster method [73], based not on multiconfiguration expansion but on coupled-cluster expansion. This method is gauge invariant, size extensive, and polynomial cost-scaling. Furthermore, as an alternative that can in principle take account of correlation effects and extract any one- and two-particle observable while bypassing explicit use of the wave function, we have reported a numerical implementation of the time-dependent two-particle reduced density matrix method [74, 75]. Whereas the above methods concentrate on the electron dynamics, we have also considered electron-nuclear dynamics and formulated a fully general TD-MCSCF method to describe the dynamics of a system consisting of arbitrary different kinds and numbers of interacting fermions and bosons [76]. All these developments will open various, flexible new possibilities of highly accurate ab initio investigations of correlated multielectron and multinucleus quantum dynamics in ever-unreachable large systems.

Acknowledgements This research was supported in part by a Grant-in-Aid for Scientific Research (Grants No. 23750007, No. 23656043, No. 23104708, No. 25286064, No. 26390076, No. 26600111, No. 16H03881, and 17K05070) from the Ministry of Education, Culture, Sports, Science and Technology (MEXT) of Japan and also by the Photon Frontier Network Program of MEXT. This research was also partially supported by the Center of Innovation Program from the Japan Science and Technology Agency, JST, and by CREST (Grant No. JPMJCR15N1), JST. Y. O. gratefully acknowledges support from the Graduate School of Engineering, The University of Tokyo, Doctoral Student Special Incentives Program (SEUT Fellowship). O. T. gratefully acknowledges support from the Japanese Government (MEXT) Scholarship. We thank I. Březinová, F. Lackner, S. Nagele, J. Burgdörfer, and A. Scrinzi for fruitful collaborations that have greatly contributed to this work.

References

1. M. Protopapas, C.H. Keitel, P.L. Knight, Rep. Prog. Phys. **60**, 389 (1997)
2. T. Brabec, F. Krausz, Rev. Mod. Phys. **72**, 545 (2000)
3. T. Popmintchev, M.C. Chen, D. Popmintchev, P. Arpin, S. Brown, S. Alisauskas, G. Andriukaitis, T. Balciunas, O.D. Mucke, A. Pugzlys, A. Baltuška, B. Shim, S.E. Schrauth, A. Gaeta, C. Hernandez-Garcia, L. Plaja, A. Becker, A. Jaroń-Becker, M.M. Murnane, H.C. Kapteyn, Science **336**, 1287 (2012)
4. Z. Chang, *Fundamentals of Attosecond Optics* (CRC Press, Boca Raton, FL, 2011)
5. L. Plaja, R. Torres, A. Zaïr (eds.), *Attosecond Physics*, vol. 177, Springer Series in Optical Sciences (Springer, Berlin, 2013)
6. J. Itatani, J. Levesque, D. Zeidler, H. Niikura, H. Pépin, J.C. Kieffer, P.B. Corkum, D.M. Villeneuve, Nature **432**, 867 (2004)
7. S. Haessler, J. Caillat, W. Boutu, C. Giovanetti-Teixeira, T. Ruchon, T. Auguste, Z. Diveki, P. Breger, A. Maquet, B. Carré, R. Taïeb, P. Salières, Nat. Phys. **6**, 200 (2010)
8. P. Salières, A. Maquet, S. Haessler, J. Caillat, R. Taïeb, Rep. Prog. Phys. **75**, 062401 (2012)
9. P. Agostini, L.F. DiMauro, Rep. Prog. Phys. **67**, 813 (2004)
10. F. Krausz, M. Ivanov, Rev. Mod. Phys. **81**, 163 (2009)
11. L. Gallmann, C. Cirelli, U. Keller, Annu. Rev. Phys. Chem. **63**, 447 (2013)
12. T. Sekikawa, A. Kosuge, T. Kanai, S. Watanabe, Nature **432**, 605 (2004)
13. Y. Nabekawa, H. Hasegawa, E.J. Takahashi, K. Midorikawa, Phys. Rev. Lett. **94**, 043001 (2005)
14. M.S. Pindzola, F. Robicheaux, Phys. Rev. A **57**, 318 (1998)

15. M.S. Pindzola, F. Robicheaux, J. Phys. B **31**, L823 (1998)
16. J. Colgan, M.S. Pindzola, F. Robicheaux, J. Phys. B **34**, L457 (2001)
17. J.S. Parker, L.R. Moore, K.J. Meharg, D. Dundas, K.T. Taylor, J. Phys. B **34**, L69 (2001)
18. S. Laulan, H. Bachau, Phys. Rev. A **68**, 013409 (2003)
19. B. Piraux, J. Bauer, S. Laulan, H. Bachau, Eur. Phys. J. D **26**, 7 (2003)
20. S. Laulan, H. Bachau, Phys. Rev. A **69**, 033408 (2004)
21. K.L. Ishikawa, K. Midorikawa, Phys. Rev. A **72**, 013407 (2005)
22. J. Feist, S. Nagele, R. Pazourek, E. Persson, B.I. Schneider, L.A. Collins, J. Burgdörfer, Phys. Rev. Lett. **103**, 063002 (2009)
23. R. Pazourek, J. Feist, S. Nagele, E. Persson, B.I. Schneider, L.A. Collins, J. Burgdörfer, Phys. Rev. A **83**, 053418 (2011)
24. K.L. Ishikawa, K. Ueda, Phys. Rev. Lett. **108**, 033003 (2012)
25. S. Sukiasyan, K.L. Ishikawa, M. Ivanov, Phys. Rev. A **86**, 033423 (2012)
26. K.L. Ishikawa, K. Ueda, Appl. Sci. **3**, 189 (2013)
27. W. Vanroose, D.A. Horner, F. Martín, T.N. Rescigno, C.W. McCurdy, Phys. Rev. A **74**, 052702 (2006)
28. D.A. Horner, S. Miyabe, T.N. Rescigno, C.W. McCurdy, F. Morales, F. Martín, Phys. Rev. Lett. **101**, 183002 (2008)
29. T.-G. Lee, M.S. Pindzola, F. Robicheaux, J. Phys. B **43**, 165601 (2010)
30. K.L. Ishikawa, T. Sato, IEEE J. Sel. Top. Quantum Electron. **21**, 8700916 (2015)
31. E. Lötstedt, T. Kato, K. Yamanouchi, in *Progress in Ultrafast Intense Laser Science XIII*, ed. by K. Yamanouchi, W.T. Hill III, G.G. Paulus (Springer, Berlin, 2017), p. 15
32. J. Zanghellini, M. Kitzler, C. Fabian, T. Brabec, A. Scrinzi, Laser Phys. **13**, 1064 (2003)
33. T. Kato, H. Kono, Chem. Phys. Lett. **392**, 533 (2004)
34. J. Caillat, J. Zanghellini, M. Kitzler, O. Koch, W. Kreuzer, A. Scrinzi, Phys. Rev. A **71**, 012712 (2005)
35. T. Sato, K.L. Ishikawa, Phys. Rev. A **88**, 023402 (2013)
36. T. Sato, K.L. Ishikawa, I. Březinová, F. Lackner, S. Nagele, J. Burgdörfer, Phys. Rev. A **94**, 023405 (2016)
37. Y. Orimo, T. Sato, A. Scrinzi, K.L. Ishikawa, Phys. Rev. A **97**, 023423 (2018)
38. A.D. Bandrauk, F. Fillion-Gourdeau, E. Lorin, J. Phys. B **46**, 153001 (2013)
39. R.P. Miranda, A.J. Fisher, L. Stella, A.P. Horsfield, J. Chem. Phys. **134**, 244101 (2011)
40. L. Greenman, P.J. Ho, S. Pabst, E. Kamarchik, D.A. Mazziotti, R. Santra, Phys. Rev. A **82**, 023406 (2010)
41. M.S. Pindzola, D.C. Griffin, C. Bottcher, Phys. Rev. Lett. **66**, 2305 (1991)
42. J. Frenkel, *Wave Mechanics-Advanced General Theory* (Clarendon Press, Oxford, 1934)
43. P.-O. Löwdin, P. Mukherjee, Chem. Phys. Lett. **14**, 1 (1972)
44. R. Moccia, Int. J. Quant. Chem. **7**, 779 (1973)
45. T.N. Rescigno, C.W. McCurdy, Phys. Rev. A **62**, 032706 (2000)
46. C.W. McCurdy, M.B.N. Rescigno, J. Phys. B **37**, R137 (2004)
47. B.I. Schneider, L.A. Collins, S.X. Hu, Phys. Rev. E **73**, 036708 (2006)
48. B.I. Schneider, J. Feist, S. Nagele, R. Pazourek, S.X. Hu, L.A. Collins, J. Burgdörfer, in *Quantum Dynamic Imaging*, ed. by A.D. Bandrauk, M. Ivanov (Springer, New York, 2011), p. 149
49. D. Hochstuhl, M. Bonitz, J. Chem. Phys. **134**, 084106 (2011)
50. J.J. Omiste, W. Li, L.B. Madsen, Phys. Rev. A **95**, 053422 (2017)
51. E. Lötstedt, T. Kato, K. Yamanouchi, Phys. Rev. A **97**, 013423 (2018)
52. T. Sato, T. Teramura, K.L. Ishikawa, Appl. Sci. **8**, 433 (2018)
53. T. Sato, K.L. Ishikawa, Phys. Rev. A **91**, 023417 (2015)
54. H. Miyagi, L.B. Madsen, Phys. Rev. A **89**, 063416 (2014)
55. T. Veszprémi, M. Fehér, *Quantum Chemistry: Fundamentals to Applications* (Springer, Berlin, 1999)
56. F. Jensen, *Introduction to Computational Chemistry* (Wiley, Chichester, 2017)
57. H. Flocard, S.E. Koonin, M.S. Weiss, Phys. Rev. C **17**, 1682 (1978)

58. J.L. Krause, K.J. Schafer, K.C. Kulander, Phys. Rev. A **45**, 4998 (1992)
59. C.W. McCurdy, C.K. Stroud, M.K. Wisinski, Phys. Rev. A **43**, 5980 (1991)
60. A. Scrinzi, Phys. Rev. A **81**, 053845 (2010)
61. W. Gautschi, Math. Comput. Simul. **54**, 403 (2000)
62. M. Weinmbcller, M. Weinmbcller, J. Rohland, A. Scrinzi, J. Comput. Phys. **333**, 199 (2017)
63. B. Walker, B. Sheehy, L.F. DiMauro, P. Agostini, K.J. Schafer, K.C. Kulander, Phys. Rev. Lett. **73**, 1227 (1994)
64. S. Larochelle, A. Talebpour, S.L. Chin, J. Phys. B. **31**, 1201 (1998)
65. I. Tikhomirov, T. Sato, K.L. Ishikawa, Phys. Rev. Lett. **118**, 203202 (2017)
66. H.J. Wörner, H. Niikura, J.B. Bertrand, P.B. Corkum, D.M. Villeneuve, Phys. Rev. Lett. **102**, 103901 (2009)
67. A. Gordon, F.X. Katner, N. Rohringer, R. Santra, Phys. Rev. Lett. **96**, 223902 (2006)
68. L. Tao, A. Scrinzi, New J. Phys. **14**, 013021 (2012)
69. R. Wehlitz, D. Lukić, J.B. Bluett, Phys. Rev. A **68**, 052708 (2003)
70. K.C. Prince, E. Allaria, C. Callegari, R. Cucini, G. De Ninno, S. Di Mitri, B. Diviacco, E. Ferrari, P. Finetti, D. Gauthier, L. Giannessi, N. Mahne, G. Penco, O. Plekan, L. Raimondi, P. Rebernik, E. Roussel, C. Svetina, M. Trovò, M. Zangrando, M. Negro, P. Carpeggiani, M. Reduzzi, G. Sansone, A.N. Grum-Grzhimailo, E.V. Gryzlova, S.I. Strakhova, K. Bartschat, N. Douguet, J. Venzke, D. Iablonskyi, Y. Kumagai, T. Takanashi, K. Ueda, A. Fischer, M. Coreno, F. Stienkemeier, Y. Ovcharenko, T. Mazza, M. Meyer, Nat. Photonics **10**, 176 (2016)
71. D. Iablonskyi, K. Ueda, K.L. Ishikawa, A.S. Kheifets, P. Carpeggiani, M. Reduzzi, H. Ahmadi, A. Comby, G. Sansone, T. Csizmadia, S. Kuehn, E. Ovcharenko, T. Mazza, M. Meyer, A. Fischer, C. Callegari, P. Finetti, E. Allaria, E. Ferrari, E. Roussel, D. Gauthier, L. Giannessi, K.C. Prince, Phys. Rev. Lett. **119**, 073203 (2017)
72. R. Sawada, T. Sato, K.L. Ishikawa, Phys. Rev. A **93**, 023434 (2016)
73. T. Sato, H. Pathak, Y. Orimo, K.L. Ishikawa, J. Chem. Phys. **148**, 051101 (2018)
74. F. Lackner, I. Březinová, T. Sato, K.L. Ishikawa, J. Burgdörfer, Phys. Rev. A **91**, 023412 (2015)
75. F. Lackner, I. Březinová, T. Sato, K.L. Ishikawa, J. Burgdörfer, Phys. Rev. A **95**, 033414 (2017)
76. R. Anzaki, T. Sato, K.L. Ishikawa, Phys. Chem. Chem. Phys. **19**, 22008 (2017)

Chapter 9
Generation of Low-Order Harmonic in Air by Intense Femtosecond Laser Pulses

Jayashree A. Dharmadhikari and Aditya K. Dharmadhikari

Abstract This chapter summarizes some of our recent work on the low-order harmonic generation in air using intense femtosecond pulses. Our results highlight the dependence of experimental conditions such as incident wavelength, external focusing and laser polarization on harmonic generation. For tight focusing condition, third harmonic generation (THG) in air using linearly polarized light 800 nm, yield an efficiency of ~0.5%. Although THG using a circularly polarized light is not possible, in our experiments we do observe weak THG signal due to depolarization of the incident circularly polarized light. For wavelengths longer than 800 nm, easy detection of lower order harmonics in air is possible. Using longer wavelength of 2 μm, we observe generation of third, fifth, and seventh harmonics in the air by tightly focused, femtosecond duration pulses. The ratio of fifth-to-third-harmonic efficiency was found to be 0.28, in agreement with the prediction based on higher-order Kerr effect model. An enhancement in the third harmonic efficiency was observed for co-propagating laser pulses of two different wavelengths when the incident power was lower than the critical power for self-focusing. The third harmonic efficiency at 1.35 μm wavelength was enhanced fourfold in the presence of a second beam at 2.09 μm wavelength. Finally, we discuss enhancement in the spectral extent of supercontinuum generation in air for tight focusing condition relative to the loose focusing condition. Moreover, supercontinuum has a higher yield for incident beam of linear polarization compared to that obtained using circular polarization at the same energy, this difference in yield, reduces for tighter focusing condition.

J. A. Dharmadhikari
Department of Atomic and Molecular Physics, Manipal Academy of Higher Education, Manipal 576104, India

A. K. Dharmadhikari (✉)
Tata Institute of Fundamental Research, 1 Homi Bhabha Road, Mumbai 400005, India
e-mail: aditya@tifr.res.in

© Springer Nature Switzerland AG 2018

K. Yamanouchi et al. (eds.), *Progress in Ultrafast Intense Laser Science XIV*,
Springer Series in Chemical Physics 118,
https://doi.org/10.1007/978-3-030-03786-4_9

9.1 Introduction

The quest for coherent sources at shorter wavelength began after the advent of pulsed lasers via nonlinear optical mixing process. Even though the first experimental observation of third-harmonic generation (THG) in the visible region was observed in 1962, third-harmonic generation in gas and atmospheric air was first reported in 1969 [1]. After the demonstration of the chirp pulse amplification technique [2, 3], intense ultrashort laser pulses were routinely produced opening new avenues for investigation of high-order harmonics and soft X-ray generation in gases [4, 5]. It was realized that the high peak powers associated with ultrashort pulses inevitably give rise to a host of nonlinear optical effects in different media. Corkum et al. first observed supercontinuum in gases using 70 fs laser pulses [6]. Using femtosecond duration pulses, THG was observed in xenon gas [7]. Efficient 266 nm pulses of 16 fs and 1 μJ energy were demonstrated in air that enhanced the prospects for short pulse UV sources, vital for time resolved spectroscopy [8]. One of the manifestations of high peak powers is optical Kerr effect that results in self-focusing of a laser beam. The first measurement on long range self-focusing was carried out using nanosecond pulses in air at atmospheric pressure [9]. Even though spectral broadening in air due to focused femtosecond pulses was known [10], it was Braun et al. who first reported long filaments in air without using any external lens [11]. Nevertheless, the self-focusing action cannot continue indefinitely and is arrested by various mechanisms such as diffraction, group velocity dispersion, pulse self-steepening, higher-order nonlinear effects, multiphoton absorption and defocusing induced by plasma [12, 13].

In the last two decades, supercontinuum (SC) generation, filamentation, and third harmonic generation (THG) in air are thoroughly investigated. Filamentation over long distances is a consequence of a dynamic competition between the optical Kerr effect (OKE) and multiphoton ionization, resulting in a series of focusing-refocusing events. In general, propagation of femtosecond pulses in air cannot be attributed to any single mechanism and the overall propagation dynamics has contributions from various mechanisms mentioned above. It has been experimentally established in air that the intensity within a single filament is clamped to a value of 4.5×10^{13} W cm^{-2} [14, 15]. When the incident power is higher than critical power for self-focusing (P_{cr}) in air, multiple filaments are created [16]. The length of a filament and plasma density are influenced by experimental parameters such as, incident intensity, pulse duration, and external focusing [17].

Figure 9.1 shows schematic of different processes involved in propagation of intense femtosecond pulses in air. Even though most of the experimental and theoretical work pertains to 800 nm central wavelength, there are other experimental handles such as incident wavelength (longer than 800 nm), external focusing and incident polarization that influence filamentation, extent of plasma, supercontinuum generation and lower order harmonic generation in air.

Notwithstanding that lasing in air [18] was demonstrated during the filamentation, it was also shown to be dependent on incident laser polarization [19]. Recently,

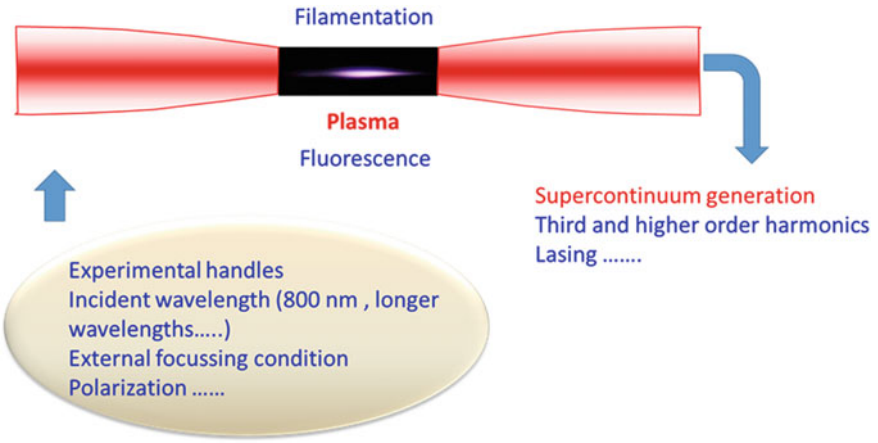

Fig. 9.1 Schematic showing different processes during the propagation of femtosecond laser pulses in air

fluorescence observed during the filamentation of femtosecond duration laser pulses was shown to be dependent on incident polarization; circularly polarized light produced more intense 337 nm fluorescence from neutral nitrogen molecule compared to linearly polarized light [20].

For wavelengths longer than 800 nm, there is an increase in coherence length, which results in a better phase matching with the fundamental wave, resulting in an efficient harmonic generation [21]. In a numerical study using 1.55 μm wavelength, a highly efficient TH conversion of 0.1% was predicted at an incident intensity of 10^{14} W/cm^2 [22]. The P_{cr} scales as λ^2, so at longer wavelengths, the self-focusing occurs at higher powers. At 3.1 μm and higher wavelengths, there is a specific interest in air filamentation as it corresponds to a regime of anomalous group-velocity dispersion (GVD). There have been theoretical investigations in the anomalous GVD regime in air [23] but the experimental investigations are lacking owing to non-availability of sources with sufficient high power in the mid-infrared [24–29]. An important facet of femtosecond filamentation at longer wavelength is that it allows experimentalist a handle for easy detection of low order harmonics in air. Furthermore, it offers an excellent opportunity to examine the role of higher-order Kerr effect and saturating nonlinearities that might arrest self-focusing. In recent years, due to the development of optical parametric amplifier at wavelengths >2 μm, it has become possible to study generation of low order harmonic in the air [30, 31].

It is well known that THG and OKE both are related to the third-order electrical susceptibility. By considering the higher order terms, a more generalised form of Kerr effect has been recently reported [32, 33]. It was proposed that the higher-order Kerr terms, particularly n_4 term might provide an additional mechanism for defocusing, apart from the plasma contribution [12, 32, 33]. There are reports that support and contradict the claim [34–39] that n_4, which has a negative sign, is one of

the defocusing mechanisms in the air. The clamping of intensity inside a filament was thought to be insufficient to access the intensities required for saturation of the Kerr effect. Recently, it was demonstrated that even if the higher-order Kerr terms exist, they are not operative in laser filaments in gases [40–42]. However, in a pump-probe measurement, a transition from plasma-driven to Kerr-driven laser filamentation was observed [43].

In order to confirm the correctness of HOKE model, an experimental test involving comparison of fifth harmonic (FH) and third harmonic (TH) efficiencies in gas media was proposed [44]. The ratio of FH/TH was predicted to be ~0.1 based on HOKE model; in contrast for the standard model (without HOKE) this ratio was predicted to be significantly lower (10^{-5}).

In order to gain better understanding, there has been a renewed interest in the generation of harmonics using intense femtosecond laser pulses, particularly low-orders [32–39] in gases and air. There is also a possibility of direct measurement of nonlinear optical susceptibility from the generated harmonics. Even though there has been an extensive work reported on THG in air using femtosecond pulses, most of these experiments are carried out using laser pulses at 800 nm [45–48]. THG based on filamentation are generated with efficiencies of 3% and 10^{-3} in ring and central part respectively [49–52].

In a combined experimental and theoretical work, Theberge et al. have shown that the electron density and diameter of a filament, depends on the focusing conditions [17]. For a given lens, they observed that the peak electron density initially rises very rapidly and then saturates at an incident power greater than P_{cr}. The diameter of a single filament was found to be dependent on focal length. This was explained by considering an overall balance between laser beam confined by geometric focusing, self-focusing (that depends on OKE) and defocusing action by plasma.

Recently Lim et al. carried out a systematic numerical and experimental study on the effect of focusing condition on filamentation in air [53]. They identified a shift from linear to nonlinear focusing regime that depends on the numerical aperture (NA) of focusing lens. For high NA values, they observed that the geometrical focusing and plasma effects control overall filamentation dynamics. At low values of NA, it is the self-focussing or OKE that governs overall filamentation dynamics.

Consequently, propagation of femtosecond duration intense laser pulses under tight external focusing conditions offers an opportunity not only to improve the efficiency of THG but also for the generation of lower order harmonics. In the first THG measurement in air that utilized tight external focusing geometry, conversion efficiency of ~7×10^{-4} was measured [54]. Ganeev et al. [47] reported an order of magnitude improvement in the THG efficiency (~10^{-3}) in air at a fundamental wavelength of 795 nm and 300 fs laser pulses by using a 10 cm focal length lens. A systematic measurement to study the influence of focusing conditions (focal length in the range 7–100 cm) on THG in the air was investigated by Ionin et al. [55] using laser pulses of 120 fs centered at 744 nm. They reported a higher THG conversion efficiency of 1.6×10^{-3} for incident power that was less than P_{cr}.

In the following sections, we shall summarize some of our recent work on the low-order harmonic generation in air using intense femtosecond laser pulses. We will

first discuss THG in air using 800 nm laser pulses, as a function of tight focusing conditions and incident polarization [56]. Subsequently, using longer wavelengths (up to 2 μm) results of harmonic generation (up to seventh harmonic) and confirmation of the HOKE model, under tight focusing condition will be discussed [57]. Enhancement of THG efficiency, in the presence of two colour longer wavelengths, under tight focusing condition will be also discussed [58]. Finally, we will discuss how the extent of SC generation depends on focusing condition and incident laser polarization [56].

9.2 Low Order Harmonic Generation in the Air

The gaseous medium like air, offers a distinct advantage such as wide transparency, low dispersion and higher incident energy for efficient harmonic generation. It was earlier reported that when the incident power is more than the critical power for self-focussing, there is a significant enhancement of THG because of increase in the effective interaction length due to filamentation [49]. Apart from extended interaction length, it has been established that the plasma formation influences THG in air [50], which scales with interplay of different experimental parameters such as incident intensity, phase mismatch and losses due to ionization of air. It should be noted that with relatively loose focusing conditions, there is a considerable broadening in the TH spectrum [59, 60]. A conversion efficiency of 0.5% for TH emission has been predicted numerically [46, 61] at an incident power sufficient for the onset of filamentation [60]. For tight focussing condition, THG has been observed at incident powers that are lower than P_{cr} [55], with efficiencies of ~0.1% [22, 47]. The typical THG efficiencies are measured to be ~0.2% [49], and there is an ongoing effort to increase this value. The other lower order harmonics might be generated efficiently in atmospheric air, but require wavelengths longer than 800 nm for their easy detection. In subsequent sections, we will discuss THG measurements that were conducted in our laboratory air conditions, i.e. 21 °C temperature and 50% relative humidity.

9.2.1 Polarization and Focusing Dependent Third Harmonic Generation in Air at 800 nm

We first discuss our results of THG in air using two lenses of focal length 10 and 30 cm. The laser utilized had a fundamental wavelength of 800 nm with 1 kHz repetition rate, 10 mm beam size and 40 fs pulse duration. The extinction coefficient of the incident linearly polarized laser was measured using a Glan laser polarizer (extinction ratio 10^5:1) and was found to 10^{-3}. The THG spectrum was measured by reflecting TH signal followed by a 265 nm band pass filter and a collecting lens coupled to a CCD based spectrometer. Figure 9.2 shows a typical data for THG

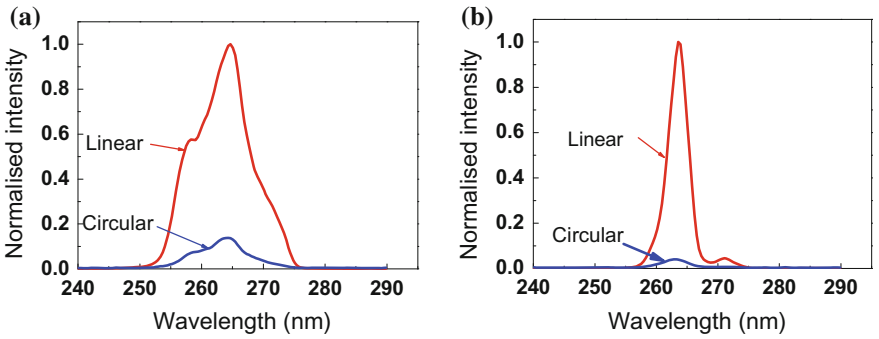

Fig. 9.2 Polarization dependent third harmonic generation in the air using 0.8 μm wavelength using **a** 10 cm lens and **b** 30 cm lens

carried out using both linearly and circularly polarized light at an incident energy of 3 mJ for two different lenses [56]. It should be noted that THG is unlikely to occur in an isotropic medium for a circularly polarized light due to the conservation of spin angular momentum of light [62]. Interestingly, we observe a measurable THG signal in case of circularly polarized light. Furthermore, for a fixed incident energy the intensity of laser light is nine times more for 10 cm lens compared to that for the 30 cm lens. If we compare the ratio of TH intensity for circular to linearly polarized light as a function of lens focusing, we observe the ratio to be $\sim 1.4 \times 10^{-1}$ for the 10 cm lens and 4×10^{-2} for the 30 cm lens [56]. Theoretically, the ratio of TH intensity for circular to linearly polarized light should be zero, but due to depolarization of light, this ratio is nonzero. Concomitantly, it provides a simple measure of the extent of depolarization. The depolarization in air for tight focusing condition may be rationalized as follows. At an incident energy of 3 mJ, the incident laser peak power is 15 P_{cr} (assuming $P_{cr} = 5$ GW for air), sufficient for multiple filamentation to occur. Multiple filamentation within a medium gives rise to a complex refractive index change that may result in a local anisotropy causing the uniformity of polarization in the beam to worsen significantly. In an earlier experiment carried out in BK7 glass, filamentation along the transverse direction was imaged and a correlation between inhomogeneous regions of multiple filamentation and depolarization of the propagated beam was established at incident intensities greater than 1 TW cm^{-2} [63, 64]. Even for gases like Ar, it was reported that with increase in gas pressure (beyond 1.4 atm); there was a detectable degradation in the extinction ratio [65] due to non-uniformities in the refractive index (or electron density) within the filament.

Spectral width of THG is different for two lenses; it is 11 nm for 10 cm lens and 3 nm for 30 cm lens. Broadening is more with 10 cm lens due to the higher electron density. The THG conversion efficiency was found to be 0.03 and 0.5% for 30 and 10 cm lenses, respectively [56]. The length of filamentation in the air was ~5 mm for 10 cm lens and ~12 mm in case of 30 cm lens. The higher THG conversion efficiency

observed for 10 cm lens was attributed to a better phase matching compared to measurement performed with 30 cm lens. We have also carried out THG measurements by keeping the incident intensity fixed at a value of 6×10^{15} W cm^{-2}, by changing the incident energy appropriately for 10 and 30 cm lenses. The ratio of TH intensity for circular to linear polarization was found to be 4×10^{-2} for 30 cm lens; whereas it was 6.4×10^{-2} for 10 cm lens [56]. Note that the plasma length was longer for linearly polarized light compared to circularly polarized light for 30 cm lens; this may be due to a lower self-focusing threshold for linearly polarized light, indicating that filamentation was a dominant process. However, in case of 10 cm lens, the plasma length was nearly same for both the polarizations at same incident energy, indicating that geometric focusing had a greater influence compared to optical Kerr effect induced focusing [17, 53]. Our results bring to the fore, importance of tight focusing condition and polarization for TH generation in the air.

9.2.2 Third Harmonic Generation in Air at Long Wavelengths

We now discuss THG in the air at long wavelengths. Here, we make use of signal and idler beam generated from an optical parametric amplifier (OPA, Palitra, Quantronix) pumped by Ti: Sapphire amplifier (800 nm, 40 fs, 4 mJ pulses) operating at 1 kHz repetition rate [57, 58], and beam diameter of ~6 mm. The signal and idler beams were separated using a set of dielectric mirrors. Figure 9.3 shows schematic of the experimental set up. In our measurements, we use tightly focused signal beam or an idler beam in the air with lenses of focal length in the range 3.5–30 cm. The generated harmonics were reflected using a broadband dielectric mirror and were recorded using USB 4000 and USB 2000 spectrometer (Ocean Optics). For measuring, the harmonic efficiency we use a power/energy meter (Ophir PD10 pJ meter) along with appropriate interference filters.

The incident energies used in our experiments were in the range of 50–400 μJ, the tighter focusing enabled us to reach higher intensities (~270 TW cm^{-2}). In a second set of experiments described in Sect. 9.3, both the signal and the idler beams were simultaneously used (by removing set of dielectric mirrors), and focused using a single lens in air.

Figure 9.4 shows the variation in THG spectra in air as a function of different focal length lens in the range 5–30 cm at incident wavelength of 1.35 μm with incident energy of 400 μJ. We observe a blue shift in the THG peak wavelength. The THG peak wavelength was found to shift from 447.3 to 435.8 nm as the focal length is changed from 30 cm to 5 cm respectively. This blue shift can be attributed to increase in the electron density due to increase in the incident intensity with tighter focusing. The incident power (7.1 GW) was significantly lower than the P_{cr} in air at 1.35 μm (8.2 GW), so the spectral shift is governed by geometric focusing and there is no contribution from OKE induced focusing. We have also measured the absolute THG

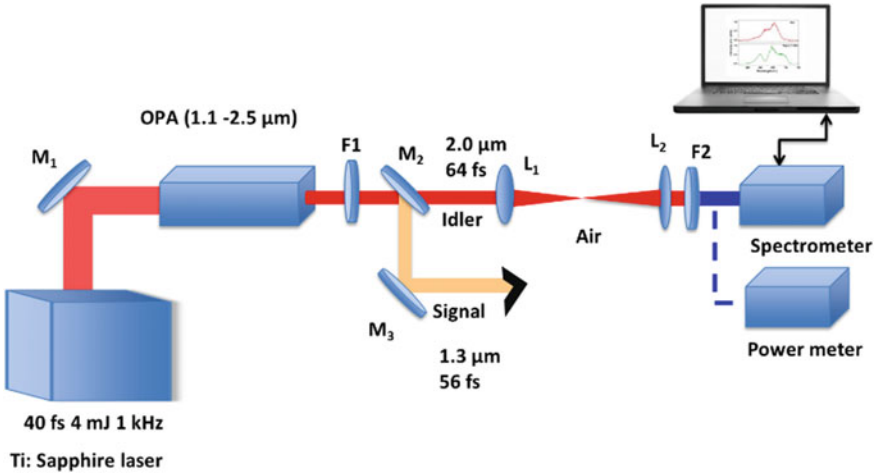

Fig. 9.3 Experimental setup for measuring low-order harmonic in the air

energies: for 5 cm lens THG energy was 30 nJ. By increasing the focal length of lens to 10 cm, THG energy was found to be 70 nJ, with further increase in the focal length to 15 cm an energy of 50 nJ was measured. When a lens of focal length 10 cm was used, we observed a higher conversion to THG compared to 5 cm lens due to longer length of the plasma, even though the incident intensity was four times lesser. Further increase in the plasma length using 15 cm lens did not show enhancement of THG, in fact it reduced by a factor of 1.4 even though the intensity decreased by a higher factor (2.25). This elucidates the role played by plasma length and incident intensity, both controlled by external lens, for efficient generation of THG. We now discuss low order harmonic generation i.e., third, fifth and seventh harmonic generation from fundamental wavelength at 2.05 μm in air using a 5 cm focal length lens.

Figure 9.5 shows variation in THG as a function of incident energy for incident wavelength of 2.05 μm.

The peak wavelength of THG was nearly same for all the energies. However, the bandwidth (full width at half maximum (FWHM)) of THG spectrum broadens from 13 to 25 nm as the incident energy was increased from 80 to 180 μJ, this we attribute to cross-phase modulation effects [64]. The broadening was asymmetric, blue side being significantly broader compared to the red side.

9.2.3 Fifth Harmonic Generation in Air at Long Wavelengths

In an earlier report [21], at an incident wavelength of 3.9 μm and incident intensity of 0.2 TW cm^{-2}, third and fifth harmonic were generated in atmospheric air. Based on fifth harmonic efficiency, $\chi^{(5)}$ value was estimated to be 3.1×10^{-36} cm^4 V^{-4} [21].

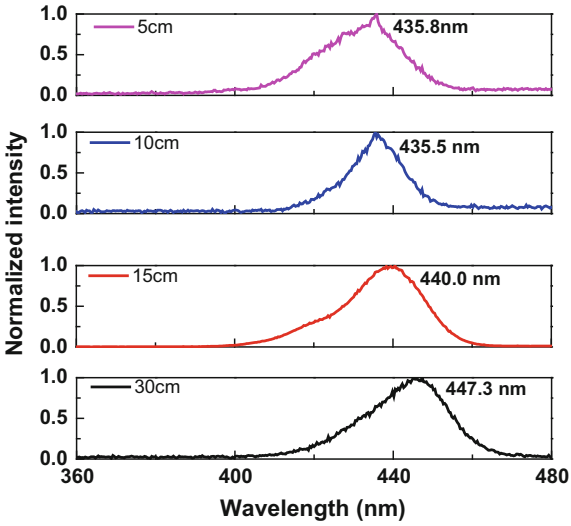

Fig. 9.4 Third harmonic generation in air for different focal length lenses using 1.35 μm incident wavelength (input energy 400 μJ)

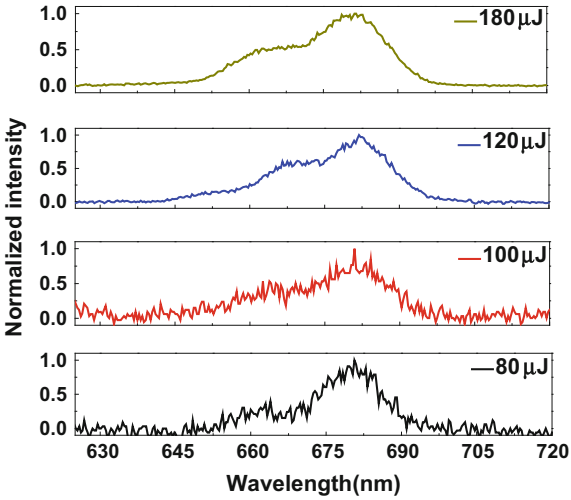

Fig. 9.5 Third harmonic generation in the air using 2.05 μm wavelength

We have carried out experiments using incident wavelength at 2.05 μm to observe fifth harmonic.

At very low energy (60 μJ), we observed only the TH signal. The fifth harmonic appeared at incident energy of 80 μJ as shown in Fig. 9.6. This corresponds to an intensity of ~30 TW cm^{-2}. By increasing the incident energy from 80 to 180 μJ, the fifth harmonic peak wavelength was observed to shift from 409 to 411 nm. The spectral profile had single peak at 410 nm and bandwidth (FWHM) was ~10 nm at incident energies less than 120 μJ. With an increase in the incident energy, a second peak appears, that reduces the width of first peak at ~410–5 nm. The appearance of a

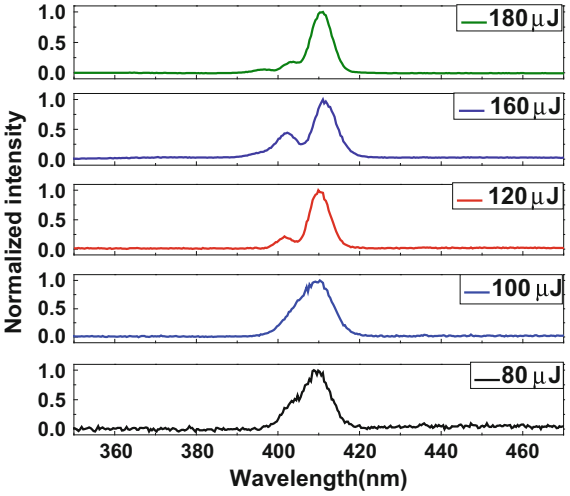

Fig. 9.6 Fifth harmonic generation in air using 2.05 μm wavelength

second peak can be attributed to inhomogeneity within the plasma [58]. At incident energy of 100 μJ, the ratio of FH/TH signal intensity was observed to be 8×10^{-2} [57].

The third and fifth harmonic were simultaneously observed at a fundamental wavelength of 1.3 μm in air. At an intensity of ~220 TW cm^{-2} the ratio of FH/TH was found to be ~0.2 and this ratio saturates at higher intensities [57].

How fifth harmonic is generated? There are two possible scenarios, in the first case, already generated TH mixes with the residual fundamental to generate FH. The ratio of FH/TH efficiency was predicted [44] to be 10^{-5} for a fundamental wavelength of 1.3 μm. In the second case, based on HOKE model, FH is directly generated from the fundamental wavelength through higher order Kerr response, the predicted ratio of FH/TH efficiency was very high (~0.1) [44]. In our measurements that were carried out by employing tight focusing conditions, the ratio of FH/TH was observed to be ~0.2, supporting HOKE model. The advantage of generating harmonics using longer wavelengths is that the coherence length is longer. For 2 μm beam focused using a 5 cm focal length lens, estimated Rayleigh range is 3.8 mm and the coherence lengths were estimated to be 102, 20, and 7 mm between the fundamental and the TH, FH, and the seventh harmonic (SVH), respectively [37, 57]. In case of 1.3 μm beam, coherence lengths are 28 and 5 mm between the fundamental and the TH and the FH, respectively [57]. Thus, for tight focusing condition, Rayleigh range is significantly smaller than the coherence length, which helps in enhancing harmonic generation.

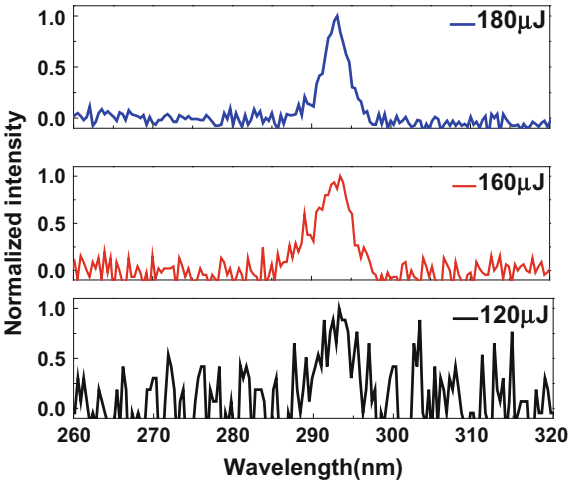

Fig. 9.7 Seventh harmonic generation in the air at the incident wavelength of 2.05 μm

9.2.4 Seventh Harmonic Generation in Air at Long Wavelengths

For incident laser energy greater than 120 μJ, we observed a very weak signal at 293 nm as shown in Fig. 9.7, which corresponds to SVH of 2.05 μm along with TH and FH signals. Further, increase in the incident energy to 180 μJ, SVH signal was very distinctly observed with bandwidth of 3 nm. At this incident energy, ratio of FH/TH signal was ~0.1 and ratio of SVH/FH was ~5×10^{-3} [57].

With further tighter focusing, using a lens of focal length 3.5 cm and incident energy of 280 μJ, efficient TH, FH, and SVH was observed. The ratio of FH/TH was ~0.28 [57]. Weerawarne et al. [38] verified these results for tight focus conditions. Liang et al. generated up to ninth harmonic in air using incident power greater than P_{cr} at 2.1 μm, [66]. In a very recent [39] study based on simulations, it has been shown that, to access a regime that significantly departs from the cubic nonlinearity, incident intensity should be higher than ~1.5×10^{14} W/cm^2.

9.3 Enhancement in Third Harmonic Generation Using Two-Color Long Wavelengths in Air

In earlier section, we discussed that THG in air under tight focusing condition was generated with a conversion efficiency of 0.5%. Even if the phase matching condition is satisfied, for focused Gaussian beam in a homogeneous medium, it is known that THG generated before the focus is out of phase with THG generated after the focus leading to destructive interference resulting in no net THG [67, 68]. To overcome this limitation posed by Gouy phase shift, pump-probe measurement using two beams

of 800 nm wavelength [69], demonstrated an enhanced efficiency by two orders of magnitude in atomic and molecular gases [46, 69–73]. Interestingly, using two crossed laser beams of orthogonal polarizations, it was possible to separate out the fifth order process from the third-order process allowing one to estimate the value of $\chi^{(5)}$ in air [74].

In this section, we will discuss THG measurements using two different wavelengths in the range of 1.35–2.05 μm in atmospheric air under tight focusing condition (focal length 3.5 or 5 cm). These wavelengths are obtained from an OPA as shown in Fig. 9.3.

The signal and idler beams were co-propagating, and were focused using a single lens in air. The two wavelengths are simultaneously generated within an OPA; the lens because of difference in the dispersion introduced a fixed temporal delay.

Even though the P_{cr} in air at 1.35 and 2.09 μm are 8.2 and 20.8 GW [75] respectively (48 GW at 2.09 μm estimated by Bergé [76]), the incident power used in this measurement was smaller (~4 GW at 1.35 μm and 2.5 GW at 2.05 μm). Four different measurements are performed,

(i) TH efficiency in air for signal beam in the wavelength range (1.35–1.55 μm),
(ii) TH efficiency in air for signal beam in the presence of an idler beam,
(iii) TH efficiency in air for idler beam in the wavelength range (1.74–2.09 μm) and
(iv) TH efficiency in air for idler beam in the presence of a signal beam [58].

In Fig. 9.8, we show a typical THG spectrum obtained using an idler beam (upper panel) of 160 μJ (65 TW/cm^2) energy focused in air using 5 cm lens. The TH spectral bandwidth is 18 nm measured at full width at half maximum (FWHM). The lower panel shows TH spectrum of an idler beam in the presence of a co-propagating signal beam. The incident signal energy in this case was 230 μJ.

The TH spectrum of fundamental idler beam in the presence of a signal beam was significantly broadened (FWHM ~ 40 nm) compared to TH spectrum (18 nm) in the

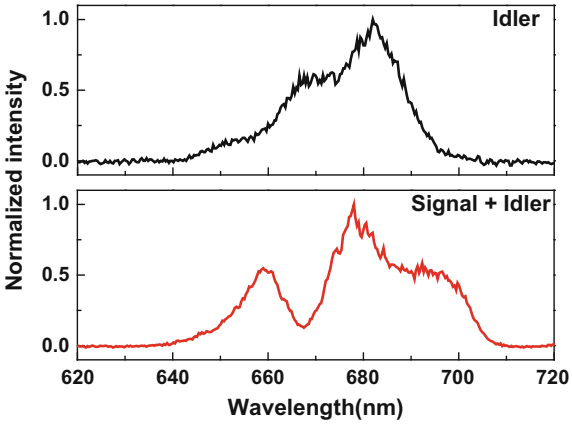

Fig. 9.8 Third harmonic generation in air using (top panel) idler at 2.05 μm (energy 160 μJ) and (bottom panel) idler at 2.05 μm, (energy 160 μJ) and signal at 1.35 μm (230 μJ)

absence of a signal beam. Introduction of a second beam reshapes the spectral profile of THG and broadens it due to cross phase modulation effects [77]. As discussed earlier, for tight focusing geometry and with incident power less than P_{cr}, plasma effects are expected to dominate. Note that the TH peak blue shifts by 4 nm in the presence of a second beam. As already noted, a second peak appearing in Fig. 9.8 (bottom panel) can be attributed to inhomogeneity within the plasma [58]. For 3.5 cm focal length lens, the TH spectrum of the fundamental idler beam at 2.05 μm with 140 μJ incident energy (1×10^{14} W cm^{-2} intensity) had a bandwidth of 11 nm FWHM. The TH energy was ~2.5 nJ, and conversion efficiency was ~1.8×10^{-3}% [58]. In the presence of 190 μJ signal beam (at 1.35 μm), spectral bandwidth of the idler THG was 15 nm. The TH energy was measured to be 5 nJ and its conversion efficiency was ~3.5×10^{-3}%, a factor of two more than that obtained using only the idler beam [58]. We have also made measurements at different idler wavelengths; the corresponding THG energy values in the presence of the signal beam are shown in Fig. 9.9. It should be noted that for the idler wavelengths of 1.74 (72 μJ), 1.84 (114 μJ), 1.94 (120 μJ) and 2.05 μm (140 μJ), corresponding signal wavelengths are 1.55 (105 μJ), 1.48 (140 μJ), 1.42 (170 μJ) and 1.35 μm (190 μJ) respectively. The values within the brackets indicate incident energy at these wavelengths.

By using similar wavelengths and incident energies, we measured THG for fundamental signal wavelength in the presence and absence of an idler beam. Figure 9.10 shows the graph of third harmonic energy plotted as a function of different signal wavelengths in the presence and absence of an idler beam. Interestingly, we obtained a higher TH conversion efficiency for signal beam in the presence of an idler beam. The TH energy was measured to be 8 nJ at a fundamental wavelength of 1.35 μm, yielding a conversion efficiency of ~4×10^{-3}%. In the presence of an idler beam TH energy increases to 30 nJ, an enhancement in the conversion efficiency by factor of ~4 [58]. It should be noted that the incident intensity of the signal beam at 1.35 μm

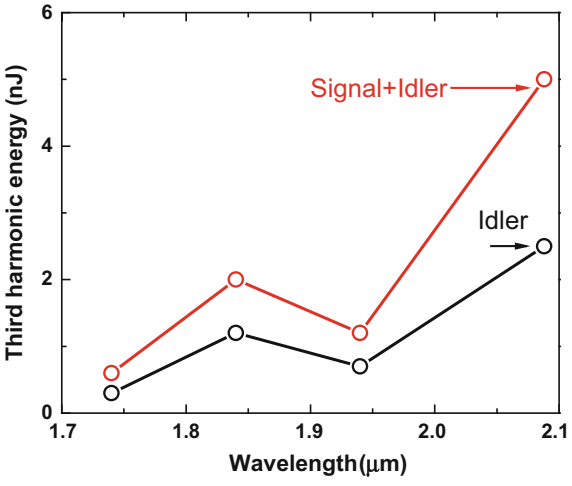

Fig. 9.9 Third harmonic energy as a function of different idler wavelengths in the presence and absence of a signal beam

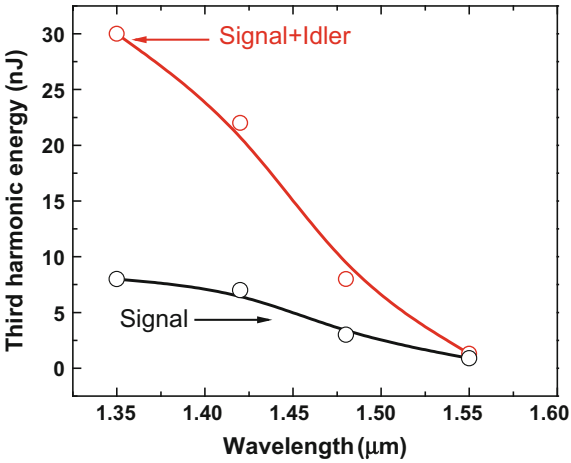

Fig. 9.10 Third harmonic energy as a function of different signal wavelengths in the presence and absence of an idler beam

is four times higher than that of the idler beam at 2.05 μm, thereby yielding a higher efficiency [46].

In a two-beam THG measurement, both beams (signal and idler) are generated simultaneously by an OPA and are co-propagating. The symmetry of Gouy's phase shift breaks in the presence of a second beam, resulting in the enhancement of THG. The length of plasma channel increases due to the addition of a second beam by a factor of 1.2 [58].

The phase mismatch and coherence length are estimated assuming contribution from neutrals [37] and electrons [58]. At 1.35 μm, Δk, the phase mismatch due to electrons is 595 mm^{-1} which is much larger compared to the phase mismatch from neutrals (9.7 mm^{-1}), further coherence length is estimated to be 0.5 mm [58]. For 2.05 μm, the estimate for phase mismatch due to electrons was 246 mm^{-1} compared to 2.7 mm^{-1} from neutrals and the coherence length was 1.2 mm [58]. Thus in the presence of an idler beam at 2.05 μm, TH efficiency of signal beam at 1.35 μm is enhanced because of the reduction in the phase mismatch and hence, an increase in the coherence length [58].

9.4 Supercontinuum Generation in Air

As discussed in the introduction section, electron density and diameter of filament [17] strongly depends on focusing conditions apart from incident power. Liu et al. [78] reported a broadband supercontinuum (SC) in air, with cut-off wavelength around 400 nm for tight external focusing condition, using ~0.8 TW laser pulses of 805 nm wavelength. The cut-off wavelength was attributed to intensity clamping during filamentation. Xu et al. [79] confirmed the experimental validity of intensity clamping under tight external focusing geometry in air. The dependence of laser polarization

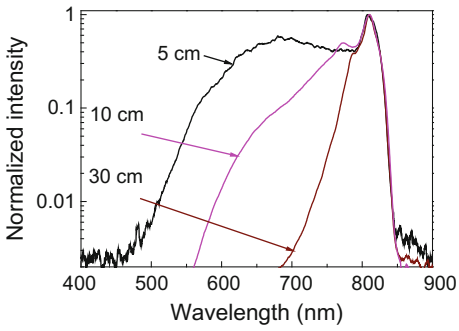

Fig. 9.11 Supercontinuum generation at an incident energy of 3 mJ (40 fs pulses) using different lenses for linearly polarized light

on SC generation in air has been investigated using pulses from a 21 TW femtosecond laser and loosely focused by 2 m lens [80]. A higher SC conversion efficiency was observed for circularly polarized light compared to that for linearly polarized light [80]. The onset of filamentation in air using a linearly polarized light occurs earlier compared to a circularly polarized light. A circularly polarized light thus propagates slightly longer distance, attaining higher intensity and consequently a higher SC.

It is known that value of P_{cr} is higher for circularly polarized light compared to linearly polarized light [81]. In an earlier work, it was shown theoretically, that multiple filamentation is suppressed for circularly polarized light [82]. Recently, it was shown that, loosely focusing circularly polarized light in gas could generate higher SC energy [83], nearly 30% higher energy and better spectral stability compared to linearly polarized light.

We now discuss experimental results of SC generation in air by tight focusing geometry for both linearly and circularly polarized light. In these measurements, the circularly polarized beam was obtained by placing a λ/4 wave plate in the path of linearly polarized laser beam. The focal lengths of the lenses used were in the range 5–30 cm. A diffusely reflecting Teflon sheet placed in the path, scattered SC light that was collected using a lens coupled to a CCD based spectrometer [56]. Figure 9.11 shows SC spectra generated at a fixed incident laser energy of 3 mJ for different lenses [56]. All the spectra were asymmetric with blue side broadened more compared to the red side. For 30 cm lens, the SC cut-off wavelength in the blue side was observed to be around 680 nm, with 10 and 5 cm lens the cut-off wavelength was extended up to ~560 and 480 nm respectively.

Self-steepening [84] and plasma induced self-phase modulation are responsible for such a pronounced asymmetry in the blue side of the SC spectra [85]. The SC spectra generated using 5 and 10 cm lens are broad due to the fact that the incident intensity was high, thereby enhancing the time varying refractive index change that has contribution from optical Kerr effect and plasma. For SC spectra obtained using a 30 cm lens, the extent of SC with circularly polarized light pulses was significantly smaller than that obtained with linearly polarized light. Our observation can be rationalized by considering the fact that the P_{cr} for circularly polarized light is higher compared to linearly polarized light [86], also the ionization rates are lower

for circularly polarized light [87]. The blue side of SC spectrum has contributions from both self-steepening [84] and plasma-induced self-phase modulation at incident power (15 P_{cr}) used in our measurement. Interestingly, by reducing the focal length from 30 to 5 cm, the amplitude of SC signal becomes comparable for linear and circularly polarized light. In fact for 5 cm lens, it was observed that in the spectral region 700–800 nm, circularly polarized light had more signal than linearly polarized light [56]. The length of plasma channel for 5 cm focal length lens was nearly same for circularly and linearly polarized light in air [56]. In a recent report, rotational dynamics of gases such as nitrogen and oxygen, which can be controlled by ellipticity of laser, was found to play a significant role in SC generation [88].

9.5 Summary

In this chapter, we have discussed our experimental results on third harmonic generation in air using fundamental wavelength in the range 800–2050 nm, particularly for tight focusing conditions. The THG conversion efficiency in air for linearly polarized laser light at a fundamental wavelength of 800 nm was found to be higher for 10 cm lens compared to that obtained using a 30 cm lens. A much weaker THG was observed for circularly polarized light. Third, fifth and seventh harmonic generation are observed for long wavelength femtosecond laser pulses that are tightly focused in air with FH/TH ratio as large as ~0.2. This ratio confirms the contribution from HOKE in the generation of low order harmonic. The TH efficiency at a wavelength of 1.35 μm was 4×10^{-3}%, however in the presence of a co-propagating second beam at 2.05 μm, the TH efficiency was 1.6×10^{-2}%. A modest enhancement by a factor of four was attributed to longer coherence length. The extent of supercontinuum generation was observed to be higher for tight focusing conditions. Difference in the supercontinuum for linearly and circularly polarized beam of the same energy reduces with tighter focussing, essentially due to the depolarization effects.

Acknowledgements The Department of Science and Technology is thanked for assistance to JAD under the Women Scientists Scheme. We would like to acknowledge Professor Deepak Mathur for his encouragement. We also acknowledge the skills and continuing enthusiasm of colleagues A. Nath, Stephen Edward and R. Bernard.

References

1. J.F. Ward, G.H.C. New, Phys. Rev. **185**, 57 (1969)
2. D. Strickland, G. Mourou, Opt. Commun. **56**, 219 (1985)
3. M. Pessot, P. Maine, G. Mourou, Opt. Commun. **62**, 419 (1987)
4. A. McPherson, G. Gibson, H. Jara, U. Johann, T.S. Luk, I.A. McIntyre, K. Boyer, C.K. Rhodes, J. Opt. Soc. Am. B **4**, 595 (1987)
5. M. Ferray, A. L'Huillier, X. Li, L. Lomprk, G. Mainfray, C. Manus, J. Phys. B: At. Mol. Opt. Phys. **21**, L31 (1988)

6. P.B. Corkum, C. Rolland, T. Srinivasan-Rao, Phys. Rev. Lett. **57**, 2268 (1986)
7. A. L'Huillier, L.A. Lompre, M. Ferray, X.F. Li, G. Mainfray, C. Manus, Europhys. Lett. **5**, 601 (1988)
8. S. Backus, J. Peatross, Z. Zeek, A. Rundquist, G. Taft, M.M. Murnane, H.C. Kapteyn, Opt. Lett. **21**, 665 (1996)
9. R.I. Miller, T.G. Roberts, Appl. Opt. **26**, 4570 (1987)
10. D. Kuhlke, U. Herpers, D. von der Linde, Opt. Commun. **63**, 275 (1987)
11. A. Braun, G. Korn, X. Liu, D. Du, J. Squier, G. Mourou, Opt. Lett. **20**, 73 (1995)
12. A. Couairon, A. Mysyrowicz, Phys. Rep. **441**, 47 (2007)
13. L. Berge, S. Skupin, R. Nuter, J. Kasparian, J.P. Wolf, Rep. Prog. Phys. **70**, 1633 (2007)
14. J. Kasparian, R. Sauerbrey, S.L. Chin, Appl. Phys. B **71**, 877 (2000)
15. H.R. Lange, A. Chiron, J.F. Ripoche, A. Mysyrowicz, P. Berger, P. Agostini, Phys. Rev. Lett. **81**, 1611 (1998)
16. S.L. Chin, S. Petit, W. Liu, A. Iwasaki, M.C. Nadeau, V.P. Kandidov, O.G. Kosareva, YuK Andrianov, Opt. Commun. **210**, 329 (2002)
17. F. Théberge, W. Liu, P.T. Simard, A. Becker, S.L. Chin, Phys. Rev. E **74**, 036406 (2006)
18. Q. Luo, W. Liu, S.L. Chin, Appl. Phys. B **76**, 337 (2003)
19. S. Mitryukovskiy, Y. Liu, P. Ding, A. Houard, A. Mysyrowicz, Opt. Express **22**, 12750 (2014)
20. S. Mitryukovskiy, Y. Liu, P. Ding, A. Houard, A. Couairon, A. Mysyrowicz, Phys. Rev. Lett. **114**, 063003 (2015)
21. D. Kartashov, S. Ališauskas, A. Pugžlys, A.A. Voronin, A.M. Zheltikov, A. Baltuška, Opt. Lett. **37**, 2268 (2012)
22. S. Skupin, L. Berge, Opt. Commun. **280**, 173 (2007)
23. B. Shim, S.E. Schrauth, A.L. Gaeta, Opt. Express **19**, 9118 (2011)
24. L. Bergé, S. Skupin, Phys. Rev. Lett. **100**, 113902 (2008)
25. I.G. Koprinkov, A. Suda, P. Wang, K. Midorikawa, Phys. Rev. Lett. **84**, 3847 (2000)
26. A.L. Gaeta, F.W. Wise, Phys. Rev. Lett. **87**, 229401 (2001)
27. L. Bergé, A. Couairon, Phys. Rev. Lett. **86**, 1003 (2001)
28. T.T. Xi, X. Lu, J. Zhang, Phys. Rev. Lett. **96**, 025003 (2006)
29. L.M. Kovachev, Opt. Express **15**, 10318 (2007)
30. O. Chalus, A. Thai, P.K. Bates, J. Biegert, Opt. Lett. **35**, 3204 (2010)
31. T. Popmintchev, M. Chen, P. Arpin, M. Gerrity, M. Seaberg, B. Zhang, D. Popmintchev, G. Andriukaitis, T. Balciunas, O.D. Mücke, A. Pugzlys, A. Baltuska, M. Murnane, H. Kapteyn, Science **336**, 1287 (2012)
32. V. Loriot, E. Hertz, O. Faucher, B. Lavorel, Opt. Express **17**, 13429 (2009)
33. V. Loriot, E. Hertz, O. Faucher, B. Lavorel, Opt. Express **18**, 3011 (2010)
34. P. Béjot, J. Kasparian, S. Henin, V. Loriot, T. Vieillard, E. Hertz, O. Faucher, B. Lavorel, J.P. Wolf, Phys. Rev. Lett. **104**, 103903 (2010)
35. C. Brée, A. Demircan, G. Steinmeyer, Phys. Rev. Lett. **106**, 183902 (2011)
36. J. Ni, J. Yo, B. Zeng, W. Chu, G. Li, H. Zhang, C. Jing, S.L. Chin, Y. Cheng, Z. Xu, Phys. Rev. A **84**, 063846 (2011)
37. G.O. Ariunbold, P. Polynkin, J.V. Moloney, Opt. Express **20**, 1662 (2012)
38. D.L. Weerawarne, X. Gao, A.L. Gaeta, B. Shim, Phy. Rev. Lett. **114**, 093901 (2015)
39. A. Bahl, V.P. Majety, A. Scrinzi, M. Kolesik, Opt. Lett. **42**, 2295 (2017)
40. P. Polynkin, M. Kolesik, E.M. Wright, J.V. Moloney, Phys. Rev. Lett. **106**, 153902 (2011)
41. O. Kosareva, J.F. Daigle, N. Panov, T. Wang, S. Hosseini, S. Yuan, G. Roy, V. Makarov, S.L. Chin, Opt. Lett. **36**, 1035 (2011)
42. Y.H. Chen, S. Varma, T.M. Antonsen, H.M. Milchberg, Phys. Rev. Lett. **105**, 215005 (2010)
43. P. Béjot, E. Hertz, J. Kasparian, B. Lavorel, J.P. Wolf, O. Faucher, Phys. Rev. Lett. **106**, 243902 (2011)
44. M. Kolesik, E.M. Wright, J.V. Moloney, Opt. Lett. **35**, 2550 (2010)
45. H. Yang, J. Zhang, L.Z. Zhao, Y.J. Li, H. Teng, Y.T. Li, Z.H. Wang, Z.L. Chen, Z.Y. Wei, J.X. Ma, W. Yu, Z.M. Sheng, Phys. Rev. E **67**, 015401(R) (2003)

46. L. Bergé, S. Skupin, G. Méjean, J. Kasparian, J. Yu, S. Frey, E. Salmon, J.P. Wolf, Phys. Rev. E **71**, 016602 (2005)
47. R.A. Ganeev, M. Suzuki, M. Baba, H. Kuroda, I.A. Kulagin, Appl. Opt. **45**, 748 (2006)
48. S. Suntsov, D. Abdollahpour, D.G. Papazoglou, S. Tzortzakis, Phys. Rev. A **81**, 033817 (2010)
49. N. Aközbek, A. Iwasaki, A. Becker, M. Scalora, S.L. Chin, C.M. Bowden, Phys. Rev. Lett. **89**, 143901 (2002)
50. H. Yang, J. Zhang, J. Zhang, L.Z. Zhao, Y.J. Li, H. Teng, Y.T. Li, Z.H. Wang, Z.L. Chen, Z.Y. Wei, J.X. Ma, W. Yu, Z.M. Sheng, Phys. Rev. E **67**, 015401 (2003)
51. I. Alexeev, A.C. Ting, D.F. Gordon, E. Briscoe, B. Hafizi, P. Sprangle, Opt. Lett. **30**, 1503 (2005)
52. H. Xiong, H. Xu, Y. Fu, Y. Cheng, Z. Xu, S.L. Chin, Phys. Rev. A **77**, 043802 (2008)
53. K. Lim, M. Durand, M. Baudelet, M. Richardson, Sci. Rep. **4**, 7217 (2014)
54. A.K. Rebane, V.N. Krylov, N.I. Koroteev, A.M. Zheltikov, Quantum Electron. **26**, 283 (1996)
55. A.A. Ionin, I. Kudryashov, L.V. Seleznev, D.V. Sinitsyn, E.S. Sunchugasheva, VYu. Fedorov, Laser Phys. **21**, 500 (2011)
56. A.K. Dharmadhikari, S. Edward, J.A. Dharmadhikari, D. Mathur, J. Phys. B: At. Mol. Opt. Phys. **48**, 094012 (2015)
57. A. Nath, J.A. Dharmadhikari, A.K. Dharmadhikari, D. Mathur, Opt. Lett. **38**, 2560 (2013)
58. A. Nath, J.A. Dharmadhikari, D. Mathur, A.K. Dharmadhikari, Appl. Phys. B **122**, 248 (2016)
59. F. Theberge, N. Akozbek, W. Liu, J.F. Gravel, S.L. Chin, Opt. Commun. **245**, 399 (2005)
60. Y. Tamaki, K. Midorikawa, M. Obara, Appl. Phys. B **67**, 59 (1998)
61. N. Aközbec, A. Iwasaki, A. Becker, M. Scalora, S.L. Chin, C.M. Bowden, Appl. Phys. B **77**, 177 (2003)
62. P.P. Bey, J.F. Giuliani, H. Rabin, Phys. Lett. A **26**, 128 (1968)
63. D. Mathur, F.A. Rajgara, A.K. Dharmadhikari, J. Phys. Chem. A **111**, 9399 (2007)
64. A.K. Dharmadhikari, F.A. Rajgara, D. Mathur, Opt. Lett. **31**, 2184 (2006)
65. A.K. Dharmadhikari, J.A. Dharmadhikari, F.A. Rajgara, D. Mathur, Opt. Express **16**, 7083 (2008)
66. H. Liang, D.L. Weerawarne, P. Krogen, R.I. Grynko, C. Lai, B. Shim, F.X. Kärtner, K. Hong, Optica **3**, 678 (2016)
67. L.G. Gouy, C.R. Acad, Sci. Paris **110**, 1251 (1890)
68. R.W. Boyd, J. Opt. Soc. Am. **70**, 877 (1980)
69. Y. Liu, M. Durand, A. Houard, B. Forestier, A. Couairon, A. Mysyrowicz, Opt. Commun. **284**, 4706 (2011)
70. Z.Y. Liu, P.J. Ding, Y.C. Shi, X. Liu, S.H. Sun, X.L. Liu, B.W. Ding, B.T. Hu, Laser Phys. Lett. **9**, 649 (2012)
71. G. Méjean, J. Kasparian, J. Yu, S. Frey, E. Salmon, R. Ackermann, J.P. Wolf, L. Berge, S. Skupin, Appl. Phys. B **82**, 341 (2006)
72. K. Hartingera, R.A. Bartels, Appl. Phys. Lett. **93**, 151102 (2008)
73. X. Yang, J. Wu, Y. Peng, Y. Tong, S. Yuan, L. Ding, Z. Xu, H. Zeng, Appl. Phys. Lett. **95**, 111103 (2009)
74. V. Vaičaitis, V. Jarutis, K. Steponkevičius, A. Stabinis, Phys. Rev. A **87**, 063825 (2013)
75. VYu. Fedorov, V.P. Kandidov, Opt. Spectrosc. **105**, 280 (2008)
76. L. Bergé, Opt. Express **16**, 21529 (2008)
77. N.I. Koroteev, A.M. Zheltikov, Laser Phys. **8**, 512 (1998)
78. X.L. Liu, X. Lu, X. Liu, L. Feng, J. Ma, Y. Li, L. Chen, Q. Dong, W. Wang, Z. Wang, Z. Wei, Z. Sheng, J. Zhang, Opt. Lett. **36**, 3900 (2011)
79. S. Xu, J. Bernhardt, M. Sharifi, W. Liu, S.L. Chin, Laser Phys. **22**, 195 (2012)
80. H. Yang, J. Zhang, Q. Zhang, Z. Hao, Y. Li, Z. Zheng, Z. Wang, Q. Dong, X. Lu, Z. Wei, Z. Sheng, J. Yu, W. Yu, Opt. Lett. **30**, 534 (2005)
81. L. Bergé, C. Gouedard, J. Schjopdt-Eriksen, H. Warda, Physica D **176**, 181 (2003)
82. G. Fibich, B. Ilan, Phys. Rev. Lett. **89**, 013901 (2002)
83. O. Varela, A. Zaır, J. Roman, B. Alonso, I. Sola, C. Prieto, L. Roso, Opt. Express **17**, 3630 (2009)

84. A.L. Gaeta, Phys. Rev. Lett. **84**, 3582 (2000)
85. A.K. Dharmadhikari, F.A. Rajgara, D. Mathur, Appl. Phys. B **82**, 575 (2006)
86. M. Kolesik, J.V. Moloney, E.M. Wright, Phys. Rev. E **64**, 046607 (2001)
87. M.V. Ammosov, N.B. Delone, V.P. Krainov, Sov. Phys. JETP **64**, 1191 (1986)
88. S. Rostami, M. Chini, K. Lim, J.P. Palastro, M. Durand, J.C. Diels, L. Arissian, M. Baudelet, M. Richardson, Sci. Rep. **6**, 20363 (2016)

Chapter 10
Femtosecond Filament-Induced Nonlinear Spectroscopy for Combustion Sensing

Huailiang Xu, Helong Li, Hongwei Zang, See Leang Chin and Kaoru Yamanouchi

Abstract Combustion diagnostics is of particular importance in combustion science for raising the combustion efficiency with low-pollution products as well as for monitoring the nanoparticle growth by combustion synthesis. In this chapter, we discuss the feasibility in the detection and diagnosis of combustion intermediates using femtosecond filament-induced nonlinear spectroscopy (FINS) by referring to our recent studies and determine the critical power for self-focusing of a Ti: Sapphire 800-nm, 35-fs laser pulse in alcohol burner flames in ambient air. We find that the laser filamentation in the flame produces a clamped intensity in the range of 2×10^{13}–3×10^{13} W/cm^2 and the flame filament can induce optical emissions from multiple combustion intermediates such as free radicals CH, CN, NH, OH, and C_2, as well as atomic C and H. We find that the emission intensities vary sensitively dependent on the fuel species as well as on the positions of the filament within the flame and that the filament can induce nonlinear frequency conversion via harmonic generation, which can be efficiently scattered by soot nanoparticles formed inside the flames. Our results show that FINS has a high potential applicability in remote and in situ sensing of spatial distributions of combustion intermediates in flames.

H. Xu (✉)
State Key Laboratory of Precision Spectroscopy, East China Normal University, Shanghai 200062, China
e-mail: huailiang@jlu.edu.cn

H. Xu · H. Li · H. Zang
State Key Laboratory of Integrated Optoelectronics, College of Electronic Science and Engineering, Jilin University, Changchun 130012, China

S. L. Chin
Center for Optics, Photonics and Laser (COPL) and Department of Physics, Engineering Physics and Optics, Laval University, Quebec City G1V 0A6, Canada

K. Yamanouchi
Department of Chemistry, School of Science, The University of Tokyo, 7-3-1 Hongo, Bunkyo-ku, Tokyo 113-0033, Japan

© Springer Nature Switzerland AG 2018

K. Yamanouchi et al. (eds.), *Progress in Ultrafast Intense Laser Science XIV*,
Springer Series in Chemical Physics 118,
https://doi.org/10.1007/978-3-030-03786-4_10

10.1 Introduction

Combustion processes through which we release chemical energy stored in the burning fuels generate heat and power that could greatly benefit people to live on our planet. On the other hand, the combustion can also result in a huge number of pollutants such as soot, SO_x, and NO_x, giving rise to serious environmental problems. Therefore, combustion diagnostics that can help understand combustion processes and enhance combustion efficiencies with low-pollution products is of special importance in combustion science. So far, a variety of measurement techniques have been developed for probing the combustion intermediates and products in various combustion environments [1–5]. Among these methods, laser spectroscopic techniques, such as planar laser induced fluorescence (PLIF), infrared spectroscopy and polarization spectroscopy have been extensively employed for measuring combustion temperature, sensing combustion intermediates, and mapping fuel distributions because of their non-invasive, real-time and high-sensitivity characteristics. For example, the PLIF technique can be applied to obtain directly the two-dimensional distribution of the combustion intermediates of OH, CN, CH and CH_2O in a combustion flame with high detection sensitivity [6]. Nevertheless, there are also some technical limitations on these methods. For instance, because PLIF is a resonant technique, it requires a specific laser wavelength to be in resonance with the species to be probed. Since the excitation wavelengths of different species vary in a wide spectral range, which could not be achieved with only one laser source, PLIF can be applied in most cases for the detection of one species at a time. It is true that Raman spectroscopy is a powerful technique for simultaneous sensing of multiple molecular species, but the strong background emissions from the flame itself could mask the Raman signal, leading to a low signal-to-noise ratio. Laser-induced breakdown spectroscopy (LIBS) is another powerful multiple elemental analysis technique, but LIBS involves detecting various atomic species, which makes it difficult to provide the information on the combustion intermediates that are in most cases molecular species.

Recent progress in high-power femtosecond laser technology can produce laser pulses in a wide power range from a sub-terawatt (TW) up to Petawatt (PW). When such powerful laser pulses propagate in transparent optical medium, filamentation takes place as a result of the dynamic balance between Kerr self-focusing and defocusing induced by plasma generated by multiphoton and/or tunnel ionization of the optical medium, giving rise to a long weak plasma channel [7–9]. In air, the dynamic balance limits the laser intensity to an almost constant value of 10^{13}–10^{14} W/cm^2. This is called clamped intensity in the filament core [9]. The filament could be very long ranging from centimeters to near kilometer and could be formed at a far distance [9]. Filamentation in air can initiate a variety of intriguing phenomena such as remote air lasing, THz radiation and high-harmonic generation [10–15]. In particular, as conceptualized in Fig. 10.1, characteristic optical emissions generated from the ionized or fragmented particles in filaments can be investigated by filament-induced nonlinear spectroscopy (FINS), which was proposed as an efficient technique applicable for remote sensing of trace chemical and biological agents and pollutants in

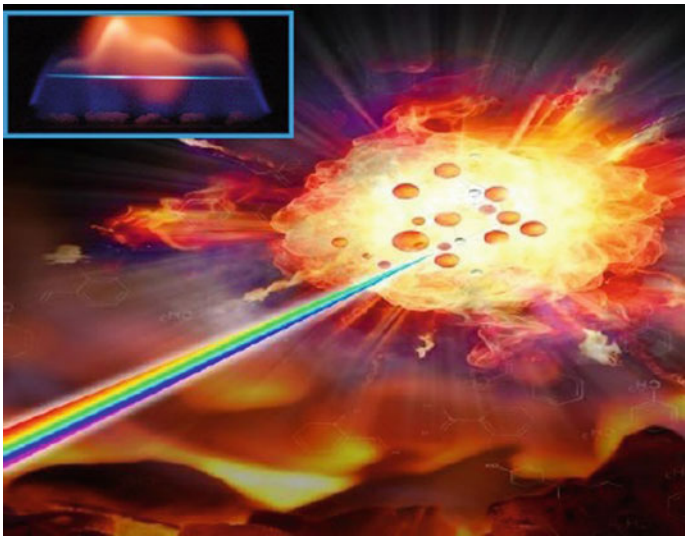

Fig. 10.1 Concept of combustion diagnostic based on femtosecond laser filament-induced nonlinear spectroscopy. The self-channeling laser-induced intense laser intensity induces the ionization and excitation of combustion intermediates which emit characteristic optical radiations. Inset shows a photo of a laser-induced filament in a combustion flame in air with a methanol fuel gas produced by the irradiation of near-IR femtosecond laser pulses (800 nm, 40 fs, and 5.5 mJ/pulse)

the atmosphere [16–20]. This technique is applicable even in a harsh atmospheric environment [9]. Based on the detection characteristics of FINS mentioned above, we recently reported that the FINS technique can have a high potential for a diagnosis of multiple intermediate species generated in complex combustion environments [20].

In this chapter we shall discuss the feasibility of the FINS technique in detection and diagnosis of combustion intermediates by referring to our recent studies of femtosecond laser filamentation in combustion flames. We will first show in Sect. 2 the formation of filamentation in combustion (flames) and the determination of the two fundamental physical properties; i.e. the critical power for self-focusing and the clamped intensity. In Sect. 3, we will present the typical fingerprint spectra induced by laser filamentation in flames and discuss the feasibility of the FINS technique for the detection of combustion intermediates in flames fueled by different alkanol molecules. In Sect. 4, we will show third harmonic generation and scattering in flames using femtosecond laser filaments for sensing soot nanoparticles. Finally, in Sect. 5, a summary will be given.

10.2 Filamentation in Combustion Flames

For the formation threshold and properties of femtosecond laser filamentation in combustion flames, we performed experiments to measure the two fundamental physical parameters: (i) the critical power for self-focusing of Ti: Sapphire 800 nm laser pulses, and (ii) the laser intensity clamped in the filament core [21]. The former determines whether filamentation could be formed, and the latter is crucial for understanding the nonlinear filament-flame interaction. Both of them are sensitive to the propagation media.

10.2.1 Critical Power

It is well known that, when the peak power of the laser pulse is smaller than the critical power, the focal position of the laser beam keeps practically constant at the geometrical focus due to the absence of the Kerr self-focusing effect [9]. However, when it exceeds the critical power, the pulse will collapse towards a self-focus due to the self-focusing that makes the medium equivalent to an additional focal lens [22]. Combined with the external focal lens, it leads to a shift of the focal position from the geometrical focus toward the position of the focusing lens [9, 22, 23]. Therefore, by measuring the focal position as a function of the input laser energy, the critical power can be straightly determined as the power at which the focal position starts to move.

In the measurement, a Ti: Sapphire laser system (Spectra Physics, Spitfire) was used, which produced laser pulses with a central wavelength at 800 nm, a pulse duration of 35 fs and a repetition rate of 1 kHz. A half-wave plate and a Brewster window were inserted into the laser beam for adjustment of the pulse energy. The laser pulses were focused by an $f = 50$ cm fused silica lens into an ethanol-air flame on an alcohol burner array. The flame has a length of about 5 cm, and a height of about 40 mm. The distance between the laser focal position and the burner wick was about 9 mm. The 'fluorescing' filament was imaged onto the entrance slit of a spectrometer coupled with a gated intensified charge coupled device (ICCD, Andor iStar) by using a periscope and a fused silica lens (50.8 mm in diameter, $f = 6$ cm). The fluorescence was then dispersed by a grating with 1200 grooves/mm whose blazed wavelength is 500 nm and recorded by the gated ICCD camera. The ICCD gate was opened for 10 ns prior to the arrival time of the laser pulse at the interaction zone and the gate width was set to be $\Delta t = 210$ ns.

When we focused a 500 μJ femtosecond laser pulse on the ethanol-air flame in the ambient atmosphere, the spectrum in Fig. 10.2a was obtained. The emission signals were assigned to the electronic transitions of free radicals CH, CN, N_2, NH, OH, and C_2. When the pump laser energy was decreased to be lower than the critical power, the intensities of the laser-induced emissions from the combustion free radicals of CH, OH, and C_2 were found to become comparable to or even weaker than their

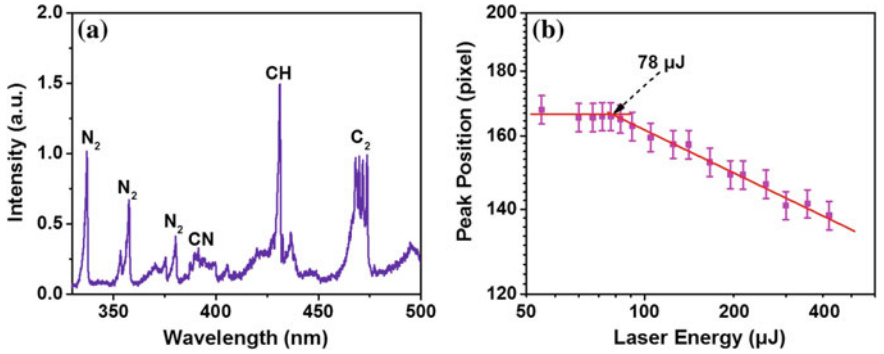

Fig. 10.2 (a) Optical emission spectrum induced by ultrafast filamenting laser pulses in an ethanol-air flame. (b) The focal position determined using the nitrogen fluorescence signals in the flames as a function of the input laser energy

spontaneous emissions in the flame, as explained below in Sect. 10.3. In addition, the fluorescence emission intensities from CN and NH, which are generated mainly through the chemical reactions proceeding in the laser-induced plasma, were found to become too weak when the laser intensity was lowered. Therefore, the fluorescence emission of N_2 at 337 nm was used for monitoring the shift of the self-focal position in response to the variation of the input laser intensity.

In Fig. 10.2b, the focal position determined from the measurements of the spatial distribution of the N_2 fluorescence signals at 337 nm along the laser propagation is plotted as a function of the input laser energy. It can be seen that when the laser power is weaker than a certain value, the focal position keeps at an almost constant position, showing the absence of self-focusing effect. However, when the laser power increases, the focal position moves towards the focusing lens. By fitting the data shown in Fig. 10.2b using two straight lines, the critical energy for the self-focusing of the employed laser pulses in the ethanol-air flame was determined to be ~78 μJ. Therefore, the critical power was calculated be ~2.2 GW, which is about four times smaller than that in air (10 GW for near IR (800 nm) 42 fs laser pulses [23]).

According to the measured critical power and the theoretical relation of $P_c = 3.72\lambda^2/8\pi n_0 n_2$, where n_0 and n_2 are the linear refraction index and the second order nonlinear index coefficients of a pure gas, respectively, we can calculate the numerical value for the effective second order nonlinear index coefficient in the flame. Because the flame was produced in ambient air, we assumed the linear index of refraction to be $n_0 = 1$, and obtained an effective value of $n_2 = 40 \times 10^{-20}$ cm^2/W, which is about four times as large as that of air (12×10^{-20} cm^2/W) [24].

10.2.2 Clamped Intensity

In the determination of the clamped intensity of the filament inside the flame, we adopted a simple method by which the intensity can be calculated from the laser pulse energy transmitted through a pinhole drilled on a metallic foil by the filament and the pinhole area. In this measurement, the laser beam was loosely focused into the ethanol-air flame by a 1-m fused silica lens. The repetition rate of the laser pulses was changed to 100 Hz and the laser energy was fixed at 0.8 mJ. The corresponding peak power was higher than the critical power for the self-focusing. A mechanical shutter was placed just before the focal lens to control the number of laser pulses. A 50 μm-thick copper foil was inserted into the flame with the surface perpendicular to the laser propagation direction. A power meter was used to record the laser energy transmitted through the pinhole drilled by the filament itself on the copper foil. The area of the drilled pinhole was measured by a scanning electron microscope (JEOL JSM-7500F). As a reference, a similar experiment in air was also performed.

In Fig. 10.3, we show the transmitted laser pulse energy as a function of the number of the laser shots, from which we find that the transmitted laser energy increases as the number of laser shots increases. In addition, it can be noted from the linear fits of the data shown in Fig. 10.3 that the transmitted laser pulse energy first increases linearly with a larger slope, and then, after 700 laser shots, the slope becomes shallower. The observation of the two linear regions can be explained as follows. The steeper slope before 700 laser shots shows that the laser energy inside the filament core passes the pinhole as shown by the SEM image in the inset of Fig. 10.3 while the energy in the reservoir surrounding the filament core is blocked by the pinhole, so that the drilled pinhole area can represent the cross section of the filament core. The shallower slope after 700 laser shots reflects the fact that the wandering effect of the filament becomes dominant, which enlarges the area of the drilled pinhole [25]. Therefore, the clamped intensity can be determined from the measured laser energy and the pinhole area at the crossing position of the two slopes at 650 laser shots, which is about $I_{f(\mathrm{obs})} \sim 5.2 \times 10^{13}$ W/cm^2. As a reference, we also performed the same measurement in air by removing the flame from the optical path, which gave a clamped intensity of $I_{a(\mathrm{obs})} \sim 1.2 \times 10^{14}$ W/cm^2. This measured value of I_{a} is 2.4 times as large as the commonly quoted value of $I_a^{(0)} = 5 \times 10^{13}$ W/cm^2 in air [9], which indicates that we overestimated the clamped laser intensity in the flame by a factor of 2.4. Therefore, we obtain $I_{f(\mathrm{obs})}^{(0)} = 2.2 \times 10^{13}$ W/cm^2 as the calibrated clamped intensity inside the frame by dividing $I_{f(\mathrm{obs})} \sim 5.2 \times 10^{13}$ W/cm^2 by 2.4. As a next step, in order to correct the beam wandering effect, which makes the slope shallower when the number of the laser shots becomes larger than 700, the correction factor $r = 1.3$, defined as the ratio of the steeper slope with respect to the shallower slope, was obtained, and the corrected clamped laser intensity in the flame was derived as $I_{f(\mathrm{obs})}^{(\mathrm{cor})} = r \times I_{f(obs)}^{(0)} = 2.8 \times 10^{13}$ W/cm^2. This means that, as has been pointed out in [21], the clamped laser field intensity in combustion flames is about a half of the clamped laser field intensity in air, $I_a^{(0)} = 5 \times 10^{13}$ W/cm^2 [9].

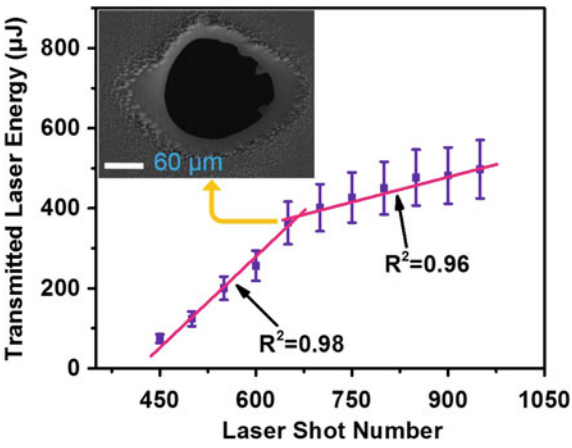

Fig. 10.3 The measured transmitted laser energy as a function of the number of laser shot. Inset: the SEM image of the pinhole drilled on a copper foil by the filament itself with 650 laser shots

10.3 FINS in Combustion Flames

Although the clamped intensity in combustion flames is only a half of that in air, the intensity is high enough to induce nonlinear optical interactions with the combustion species, resulting in characteristic fluorescence emissions. In this section, we investigate the filament-induced fluorescence spectra in combustion flames, and discuss the feasibility of FINS for combustion diagnosis.

10.3.1 Filament-Induced Fluorescence

Figure 10.4 shows a typical filament-induced spectrum of the ethanol-air flame in ambient atmosphere in the spectral range from 240 to 850 nm [26]. This spectrum was obtained by focusing the laser pulses (800 nm, 100 fs, 0.7 mJ) into the alcohol burner flame by a fused silica lens ($f = 200$ mm), which generated a filament of 1 cm. The width and delay of the ICCD gate were set to be $\Delta t = 2000$ ns and $t = 0$ ns, respectively. The distance between the filament and the tip of the burner wick was 18 mm. The total length of the flame from the burner wick to the top of the flame is ~50 mm. The spectral signals are assigned to the Swan band of C_2 radical (563, 516, and 466 nm), CH radical resulting from the $A^2\Delta$-$X^2\Pi$ (431 nm) and $C^2\Sigma$-$X^2\Pi$ (314 nm) band, and CN radical originating from the $B^2\Sigma$-$X^2\Sigma$ (388 and 358 nm) band, respectively [27]. In addition, several weak emission bands assigned to molecular species such as N_2 (337 nm), NH (336 nm) and OH (307 nm) and atomic emission lines assigned to atomic species, C (247.7 nm) and H (Balmer-α, 656 nm), can be seen.

For removing the second order diffraction and the third order diffraction of the fluorescence emission in the UV wavelength range from the spectrum as well as for

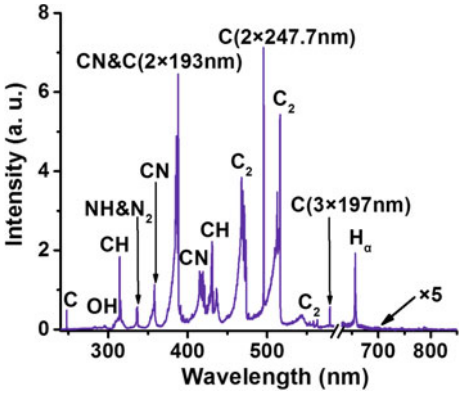

Fig. 10.4 Typical FINS spectrum obtained by focusing a 0.7 mJ femtosecond laser pulse into an ethanol-air flame in ambient air

extracting the spectral information in the long wavelength range with high precision, a high-pass filter was placed before the spectrometer slit to block the signal below 450 nm. As shown in Fig. 10.4, except for H_α (Balmer-α) line at 656 nm, no atomic emission lines such as N (I) at 744 nm and O (I) at 777 and 845 nm are observed, which are typically present in nanosecond laser-induced breakdown spectroscopy, in which optical emission lines from electronically excited fragment species generated from parent molecules. Therefore, we concluded that the fragmentation and electronic excitation processes proceeding in the laser induced filament in the flame are much milder than those in the nanosecond laser induced breakdown. Therefore, FINS is considered to be a promising technique for monitoring the combustion intermediates in flames.

10.3.2 Mechanisms for the Fluorescence Emissions from Radicals in FINS

As described in Sect. 2, the laser intensity in the filament in a combustion flame is clamped to be ~2.8×10^{13} W/cm^2. For a so high intensity, it was questioned whether the filament-induced fluorescence results from the dissociation and fragmentation of parent molecules. Therefore, we performed a comparative study by measuring the flame spectra under different conditions, that is, with the excitation of femtosecond filament, nanosecond laser-induced breakdown as well as without laser excitation [26].

Figure 10.5a shows a typical ns-LIBS spectrum of the ethanol–air flame, which we obtained by focusing 532-nm Nd: YAG laser pulses into the ethanol-air flame using a fused silica lens of 125 mm. The laser pulse duration and energy were 10 ns and 100 mJ, respectively. The width and delay of the ICCD gate were set to be the same as those in the FINS measurement presented in Sect. 3.1. By comparing the LIBS spectrum with that shown in Fig. 10.4, it can be seen that LIBS shows atomic/ionic

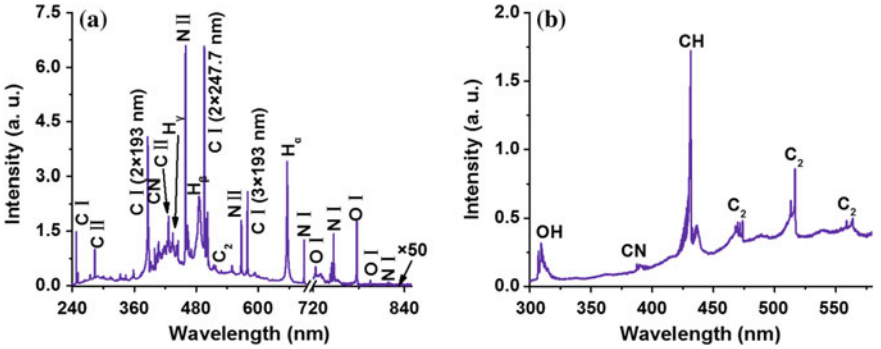

Fig. 10.5 **a** Typical LIBS spectrum obtained when a 100 mJ, 10 ns laser pulses were focused into an ethanol-air flame in ambient air using an $f = 125$ mm lens. **b** Emission spectrum of the flame recorded without any laser excitation

lines, which are superposed on a broad continuum. These intense atomic emission lines can be assigned to the Balmer lines (H_α, H_β, and H_γ), and the emission lines of C(I, II), N (I, II) and O (I). The FINS (Fig. 10.4) spectrum, in which emission lines of molecular species dominate, confirms that the decomposition and electronic excitation do not proceed in an excessive manner in the femtosecond filamentation in the flame, exhibiting a marked contrast with the LIBS (Fig. 10.5a) spectrum, in which emission lines from the electronic excited states of fragment atoms and atomic ions dominate.

The emission spectrum of the ethanol–air flame without laser excitation was also measured as shown in Fig. 10.5b, in which the molecular emission bands of the intermediate molecular species such as OH, CH and C_2 created in the combustion flame can be observed together with a broad continuum originating from the blackbody radiation of the flames. The accumulation time was set to be 450 ms.

As can be seen in the FINS spectrum (Fig. 10.4) and the laser-free flame spectrum (Fig. 10.5b), all of the free radical species appearing in the laser-free flame spectrum appear also in the FINS spectrum, indicating that FINS carries the information on the intermediates of the combustion flame. However, it should be noted that the ratios of the relative signal intensities of combustion species OH, CH, CN and C_2 are obviously different in these two cases. For example, the signal of CN at 388 nm is much stronger in FINS than that in the laser-free flame spectrum, which implies that a part of the CN emission lines appearing in FINS originate from bimolecular chemical reactions, such as $C_2 + N_2$, though which CN is prepared in the electronically excited states in the filament-induced plasma.

It can also be seen that the ratio of the signal intensity of CH at 431 nm with respect to that of C_2 at 516 nm is much smaller in FINS than that in the laser-free frame spectrum. It is well known that the dissociation of the parent ethanol molecule in intense laser fields prefers to form CH than C_2 [28], the smaller ratio of CH/C_2 in FINS may indicate that the CH radical are not produced from the dissociation of the

parent fuel molecule, and that the plasma-assisted collision might give a contribution to the formation of C_2 in FINS.

We also performed the FINS measurements at the different spatial positions in the flames, by moving the burner vertically and found that the intensities of all the free radical species in FINS become weaker when the position becomes closer to the wick of the alcohol burner [29]. Because the concentration of the parent fuel molecules is higher at the positions closer to the burner wick, the observation clearly indicates that the dissociation of the parent fuel molecules induced by the intense laser fields in the femtosecond filament may not contribute to the FINS signals. Therefore, it can be said that the combustion intermediates appearing in FINS are not those created by the fragmentation of parent fuel molecules but those excited electronically by the femtosecond laser light and/or collisions within the laser induced filament in the combustion flame.

10.3.3 Feasibility of FINS for Combustion Diagnostics

In order to further explore the possibility of the application of FINS to the sensing of combustion intermediates, we systematically investigated the FINS phenomena in various environmental conditions. We first measured the FINS spectra at the different spatial positions in the ethanol-air flame along the vertical axis of the central combusting flow, and plotted the signal intensities of different combustion intermediates as a function of the distance between the filament and the wick tip of the alcohol burner [29]. As shown in Fig. 10.6a, the signals of the four species, C_2, CH, CN and C, first increase and then decrease as the distance increases, which reflects the concentration distribution of the four intermediate species in the flame. In the region just above the burner wick the combustion has not been fully developed, resulting in a low concentration of combustion intermediates. As the distance increases, the combustion further develops, resulting in the formation of a large number of combustion intermediates, and thus the increased fluorescence signals. When the distance increases further, the combustion intermediates are consumed in the fully developed combustion zone, resulting in the decreased signals. This result shows the possibility to map the concentration distributions of combustion intermediates using the FINS technique.

We also performed the FINS measurements for five different alkanol-air flames fueled by methanol, ethanol, *n*-propanol, *n*-butanol, and *n*-pentanol [30]. The analysis of the FINS spectra of the five different alkanol-air flames showed that the combustion reactions with the five different fuels produce almost the same combustion intermediate species. This means that the combustion intermediate species can be the same as long as fuel molecules are composed of the same elements, that is, C, H and O. On the other hand, the spectral intensities of the four main combustion intermediates C, C_2, CH, CN increase as the number of carbons contained in a single fuel molecule increases. It was also found that the ratios of the signals of these intermediates produced in the five different alkanol combustion flames exhibit char-

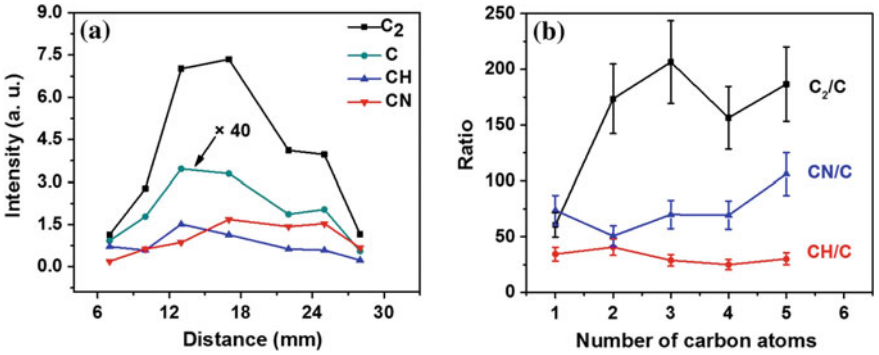

Fig. 10.6 **a** Signal intensities of the four filament-induced combustion intermediates, C_2, C, CH, and CN, in the ethanol flame recorded by the FINS measurements as a function of the distance between the filament and the tip of the alcohol burner wick. **b** The ratios of the signal intensities of the three combustion intermediates with respect to the signal intensity of C for the five different fuel molecules, methanol ($m = 1$), ethanol ($m = 2$), *n*-propanol ($m = 3$), *n*-butanol ($m = 4$), and *n*-pentanol ($m = 5$), where m stands for the number of carbon atoms within a fuel molecule

acteristic dependences on the number of carbon atoms in a fuel molecule as shown in Fig. 10.6b. Therefore, by the FINS measurements, alkanol species that are fueled for producing the alkanol-air flames can be readily identified based on the intensity ratios of the combustion intermediates.

10.4 Third Harmonic Generation in Flames

Femtosecond filamentation generated by 800-nm Ti:Sapphire laser pulses induces not only nonlinear fluorescence emission but also nonlinear frequency conversion. In this section, we investigate third harmonic generation inside the combustion flames using femtosecond laser filaments and show a potential applicability of Rayleigh scattering spectroscopy using the third-harmonics in the UV range to remote and in situ measurements of distributions of soot nanoparticles in combustion flames [31].

10.4.1 Third Harmonic Generation in Flames

Figure 10.7a shows the forward third harmonic spectra induced by the filamentation in air as well as in the alkanol–air flames fueled with methanol, ethanol, *n*-propanol, *n*-butanol, and *n*-pentanol. In this measurement, the laser pulses whose pulse energy is 0.6 mJ was focused by a fused silica lens ($f = 50$ cm) into the flame and a single filament was generated. The filament position was set to be at about 28 mm above the

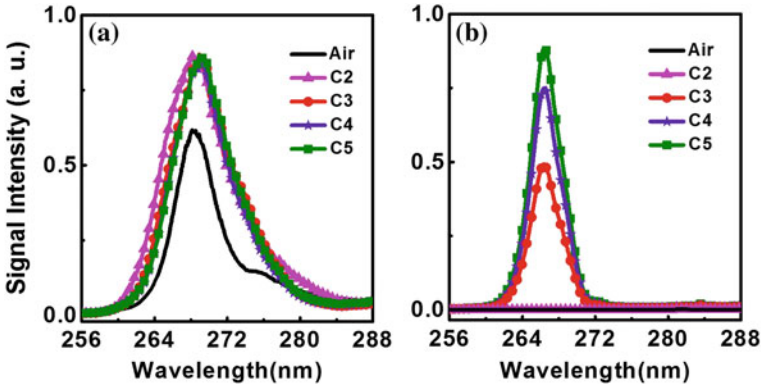

Fig. 10.7 Third harmonic signals measured from the forward direction along the laser propagation (**a**) and those measured from the side of the filament (**b**) for air and the four different flames fueled with ethanol, *n*-propanol, *n*-butanol, and *n*-pentanol

tip of the alcohol burner wick. The third harmonic produced by the femtosecond laser filamentation in the flame was measured in the forward direction after the attenuation using two wedge plates. The width and delay time of the ICCD gate were set to be $\Delta t = 20$ ns and $t = -5$ ns, respectively. As shown in Fig. 10.7, the third harmonic at ~267 nm was generated by the laser induced filament in air as well as in the four different flames.

It can be seen in Fig. 10.7a that the signal intensities of the filament-induced third harmonic in the combustion flames are almost the same for all the four alkanol species, showing that the third harmonic generation is not sensitive to the fuel species used in our experiment. It can also be seen that the third harmonic generated in the flames are stronger than that in air, which may be explained as follows. The intensity of the generated third harmonic is expressed using the clamped laser intensity in the filament I_{clamp} as $I_{\text{harmonic}} \propto (n_0 n_2)^2 (I_{\text{clamp}})^3$. As determined in Sect. 2.1, the value of n_2 in the ethanol-air flame (40×10^{-20} cm^2/W) was about four times larger than that in air (12×10^{-20} cm^2/W), and the clamped laser intensity in the flame filament was about 56% of that in air. Therefore, the intensity of the filament-induced third harmonic in the ethanol-air flames is expected to be roughly twice as large as that in air, which is in good agreement with the experimental observation shown in Fig. 10.7a. The observation shown in Fig. 10.7a that the third harmonic intensities for all the four alkanol-air flames are almost the same indicate that the second order nonlinear refractive index coefficient n_2 and the clamped laser intensity I_{clamp} for these four fuel species are close to each other.

We also examine the dependence of the conversion efficiency in the third harmonic generation in the flame filaments on the polarization state of the fundamental laser light. By rotating a quarter wave plate inserted in the fundamental laser beam with which the polarization of the fundamental laser light can be varied from linear to

circular, we find that the intensity of the third harmonic signals decreases dramatically as the polarization of the fundamental laser changes from linear to circular [31].

10.4.2 Third Harmonic Scattering in Flames

In order to examine the scattering of the third harmonic by the soot particles produced in the combustion flames, we measured the third harmonic from the side of the laser filament. Because the third harmonic propagates along the propagation direction of the fundamental laser pulse, the signal intensity of the third harmonic recorded from the side of the filament can be regarded as the scattering of the particles in the combustion flame. The experimental conditions were the same as in the measurement from the forward direction. For collecting the emission signal, we employed a $2f$–$2f$ imaging scheme with a fused silica lens of $f = 60$ mm.

As shown in Fig. 10.7b, the intensity of the scattered third harmonic signals from the four alkanol-air flames increases as the number of carbon atoms in the fuel molecular species increases whereas no signals of the scattered third harmonic can be seen in air. This is because the third harmonic signals are scattered by carbonous nanoparticles existing in the flames originating from the incomplete combustion, which are typically from a few to tens of nanometers [3, 32], and because the number density of the nanoparticles in the flames increases as the carbon number in the fuel molecule increases. Therefore, the filament-induced third harmonic spectroscopy can be used for monitoring the density distribution of nanoparticles in combustion flames. The observation that no detectable scattering signals of the third harmonic were recorded in air indicates that the number density of carbonous nanoparticles was considerably low in air in the laboratory environment.

10.5 Summary

In this chapter, by referring to our recent studies on femtosecond laser filamentation in combustion flames, we show the feasibility of the detection and diagnosis of combustion intermediates using femtosecond filament-induced nonlinear spectroscopy (FINS). By measuring the focal positions of ultrafast laser pulses versus the laser energy, and comparing the difference of the laser energy transmitted through a pinhole drilled on a metallic foil by the filament itself, we determined the critical power and the clamped intensity of femtosecond laser filaments in combustion flames in ambient air. We further demonstrated that the clamped intensity in combustion flames is high enough to induce characteristic optical emissions from multiple combustion intermediates, and found that the intensities of these intermediate emissions vary sensitively to the fuel species as well as the positions of the filament within the flame. We also introduced the phenomena of the filament-induced third harmonic generation in flames and demonstrated that the third harmonic can be efficiently scattered

by nanoparticles formed in flames. We demonstrated that FINS has a high potential applicability to remote and in situ sensing of the spatial distributions of combustion intermediates in flames as well as to combustion diagnostics for understanding the combustion processes, leading to a new scheme with which the combustion efficiency is to be raised with low-pollution products.

Acknowledgements This work was supported in part by the National Natural Science Foundation of China (61427816, 61625501), the National Basic Research Program of China (2014CB921302) and JSPS KAKENHI grant (JP15H05696). SLC acknowledges the support of Laval University, Quebec City, Canada.

References

1. N. Docquier, S. Candel, Prog. Energy Combust. Sci. **28**, 107 (2002)
2. G. Hagen, C. Feistkorn, S. Wiegärtner, A. Heinrich, D. Brüggemann, R. Moos, Sensors **10**, 1589 (2010)
3. M. Aldén, J. Bood, Z. Li, M. Richter, Proc. Combust. Inst. **33**, 69 (2011)
4. A.C. Eckbreth, *Laser Diagnostics for Combustion Temperature and Species*, 2nd edn. (Gordon & Breach, UK, 1996)
5. S. Svanberg, *Atomic and Molecular Spectroscopy: Basic Principles and Practical Applications* (Springer, Berlin, 2004)
6. J. Sjöholm, J. Rosell, B. Li, M. Richter, Z. Li, X.S. Bai, M. Aldén, Proc. Combust. Inst. **34**, 1475 (2013)
7. A. Couairon, A. Mysyrowicz, Phys. Rep. **441**, 47 (2007)
8. L. Berge, S. Skupin, R. Nuter, J. Kasparian, J.-P. Wolf, Rep. Prog. Phys. **70**, 1633–1713 (2007)
9. S.L. Chin, *Femtosecond Laser Filamentation* (Springer, Berlin, 2010)
10. Q. Luo, W. Liu, S.L. Chin, Appl. Phys. B **76**, 337 (2003)
11. J.P. Yao, B. Zeng, H.L. Xu, G. Li, W. Chu, J. Ni, H. Zhang, S.L. Chin, Y. Cheng, Z.Z. Xu, Phys. Rev. A **84**, 051802 (2011)
12. H.L. Xu, E. Lötstedt, A. Iwasaki, K. Yamanouchi, Nat. Commun. **6**, 8347 (2015)
13. V. Andreeva, O. Kosareva, N. Panov, D. Shipilo, P. Solyankin, M. Esaulkov, P. Martínez, A. Shkurinov, V. Makarov, L. Bergé, S.L. Chin, Phys. Rev. Lett. **116**, 063902 (2016)
14. N. Akozbek, A. Iwasaki, A. Becker, M. Scalora, S.L. Chin, C.M. Bowden, Phys. Rev. Lett. **89**, 143901 (2002)
15. T. Popmintchev, M.C. Chen, D. Popmintchev, P. Arpin, S. Brown, S. Alisauskas, G. Andriukaitis, T. Balciunas, O.D. Mucke, A. Pugzlys, A. Baltuska, B. Shim, S.E. Schrauth, G. Gaeta, C. Hernandez-Garcia, L. Plaja, A. Becker, A. Jaron-Becker, M.M. Murnane, H.C. Kapteyn, Science **336**, 1287 (2012)
16. H.L. Xu, Y. Kamali, C. Marceau, P.T. Simard, W. Liu, J. Bernhardt, G. Mejean, P. Mathieu, G. Roy, J.-R. Simard, S.L. Chin, Appl. Phys. Lett. **90**, 101106 (2007)
17. H.L. Xu, G. Méjean, W. Liu, Y. Kamali, J.-F. Daigle, A. Azarm, P.T. Simard, P. Mathieu, G. Roy, J.-R. Simard, S.L. Chin, App. Phys. B **87**, 151 (2007)
18. H.L. Xu, P.T. Simard, Y. Kamali, J.-F. Daigle, C. Marceau, J. Bernhardt, J. Dubois, M. Châteauneuf, F. Théberge, G. Roy, S.L. Chin, Laser Phys. **22**, 1767 (2012)
19. H.L. Xu, S.L. Chin, Sensors **11**, 32–53 (2011)
20. H.L. Xu, Y. Cheng, S.L. Chin, H.B. Sun, Laser Photonics Rev. **9**, 275 (2015)
21. H.L. Li, W. Chu, H. Zang, H.L. Xu, Y. Cheng, S.L. Chin, Opt. Expr. **24**, 3424 (2016)
22. V.I. Talanov, Sov. Phys. JETP Lett. **11**, 199 (1970); J.H. Marburger, Prog. Quantum Electron. **4**, 35 (1975)
23. W. Liu, S.L. Chin, Opt. Expr. **13**, 5750 (2005)

24. V. Loriot, E. Hertz, O. Faucher, B. Lavorel, Opt. Expr. **18**, 3011 (2010)
25. S.L. Chin, A. Talebpour, J. Yang, S. Petit, V.P. Kandidov, O.G. Kosareva, M.P. Tamarov, Appl. Phys. B **74**, 67 (2002)
26. H.L. Li, X.Y. Wei, H.L. Xu, S.L. Chin, K. Yamanouchi, H.B. Sun, Sens. Actuators B Chem. **203**, 887 (2014)
27. R.W.B. Pearse, A.G. Gaydon, in *The Identification of Molecular Spectra*, 4th edn. (Chapman & Hall, UK, 1976)
28. J. Chen, R. Ma, H. Ren, X. Li, H. Yang, Q. Gong, Int. J. Mass Spectrom. **241**, 25 (2005)
29. H. Li, H. Xu, B. Yang, Q. Chen, T. Zhang, H. Sun, Opt. Lett. **38**, 1250 (2013)
30. H. Li, W. Chu, H.L. Xu, Y. Cheng, S.L. Chin, K. Yamanouchi, H.B. Sun, Sci. Rep. **6**, 27340 (2016)
31. H.W. Zang, H.L. Li, Y. Su, Y. Fu, M.Y. Hou, A. Baltuška, K. Yamanouchi, H.L. Xu, Opt. Lett. **43**, 615 (2018)
32. P. Minutolo, G. Gambi, A. D'Alessio, S. Carlucci, Atmos. Environ. **33**, 2725 (1999)

Chapter 11
Towards Single-Shot XUV-Pump-XUV-Probe Studies

I. Orfanos, I. Makos, N. Tsatrafyllis, S. Chatziathanasiou, E. Skantzakis, D. Charalambidis and P. Tzallas

Abstract During the last decades, systematic efforts in ultra-short pulse generation led to the development of table-top sources with the capability of producing such pulses in the extreme-ultraviolet spectral range (XUV). Such pulses have been extensively exploited in the investigation of ultrafast dynamics in all states of matter. Intense XUV radiation, that can induce non-linear processes in the XUV spectral range, advance such studies through time resolved measurements performed by means of XUV-pump-XUV-probe schemes. Although these schemes, as fully perturbative, are highly beneficial for such studies, they are inherited with spectroscopic limitations held by the stability of the experimental conditions and the delay lines of the pump-probe arrangement. Here, we describe an approach which provides high temporal and spectral resolution realized in a single-shot measurement. The approach is based on a recently developed method for measuring the spatially resolved photoionization yield resulting from the interaction of XUV pulses with gas phase media.

11.1 Introduction

Gas phase high-order-harmonic (HOH) sources have been extensively used for the generation of sub-fs intense XUV pulse trains as well as isolated pulses which upon focus can reach intensities sufficient to induce observable non-linear XUV processes [1–11]. Such sources have been exploited: for quantitative studies both in the linear as

I. Orfanos · I. Makos · N. Tsatrafyllis · S. Chatziathanasiou · E. Skantzakis · D. Charalambidis
P. Tzallas (✉)
Foundation for Research and Technology—Hellas, Institute of Electronic Structure and Laser, PO Box 1527, Heraklion (Crete) 71110, Greece
e-mail: ptzallas@iesl.forth.gr

I. Orfanos · I. Makos · N. Tsatrafyllis · S. Chatziathanasiou · D. Charalambidis
Department of Physics, University of Crete, Heraklion 71103, Greece

D. Charalambidis · P. Tzallas
ELI-ALPS, ELI-Hu Kft, Dugonics Ter 13, Szeged 6720, Hungary

© Springer Nature Switzerland AG 2018

K. Yamanouchi et al. (eds.), *Progress in Ultrafast Intense Laser Science XIV*,
Springer Series in Chemical Physics 118,
https://doi.org/10.1007/978-3-030-03786-4_11

well as in the non-linear XUV spectral range employing an ion-microscope device [12–15]; for pulse metrology by means of 2nd-order volume autocorrelation (2-IVAC) measurements [1, 8, 9, 16–19]; for time-resolved spectroscopy studies [20]; and for XUV-pump-XUV-probe measurements of ~1 fs scale dynamics in atomic [9] and molecular systems [21].

XUV-pump-XUV-probe schemes, as fully perturbative, have notable advantages in studies of ultrafast dynamics compared to the IR-XUV pump-probe schemes. The latter occurs as a result that XUV pulse does not effectively distort the system under investigation, since much less number of photons lead to an XUV-pump-XUV-probe process comparing to that of an IR-XUV pump-probe scheme. However, an XUV-pump-XUV-probe measurement suffers from the intrinsic restrictions that accompany any pump-probe approach which involves an interferometer. In every pump-probe experiment, the evolution of the system is determined by multi-shot measurements at different time delays between the interacting pulses. Therefore, during the data acquisition all characteristics of the pulses and the experimental conditions must remain stable. Additionally, a pump-probe scheme with few-*fs*/*asec* temporal resolution is limited by the spectroscopic resolution originating from the difficulty to maintain the temporal resolution for long data acquisition times and long delay values between the pump-probe pulses.

One way to overcome these obstacles is the utilization of an approach which provides high temporal and spectral resolution revealed from a single-shot measurement. This is feasible by imaging the ion distribution, produced by a two-photon process, along the propagation axis of two focused counter propagating intense XUV pulses. The principle of the approach was reported 20 years ago [22, 23] in studies investigating the dynamics of 'slow' wave packets of coherently excited high lying Rydberg states. The extension to time scales of few-fs or less was not an attainable goal due to the lack of (I) intense ultrashort XUV pulses and (II) high spatial resolution ion imaging detectors.

Here, after a brief overview on the generation and the applications of intense ultrashort XUV pulses, utilized to trace the ultrafast dynamics of atoms and molecules (Sect. 11.2); we will describe the essentials of the "Time gated ion microcopy" (Sect. 11.3) focusing particularly on aspects related to its applicability on single-shot XUV-pump-XUV-probe measurements using counter propagated XUV pulses (Sect. 11.4).

11.2 Generation of Intense XUV Pulses and Applications in Ultrafast Non-linear XUV Optics

High power XUV pulses with duration $\leq$1.5 fs, capable of inducing two-photon processes, have been already produced [9, 11, 19] and implemented in XUV-pump-XUV-probe studies of atomic [9, 11] and molecular [21] dynamics on 1 fs timescale. Figure 11.1a illustrates an experimental set-up used for the generation, character-

ization, and applications of intense ultra-short XUV pulses produced in gas phase media. The enhancement of the pulse energy is achieved by utilizing, high power fs IR pulses, loose focusing geometries, and the proper phase-matching conditions in a single gas jet configuration. Briefly, the high-harmonics are generated by focusing (with an $f = 3$ m focal length lens) a ~30 fs p-polarized IR (centered at 800 nm) laser beam acquiring energy of tens-mJ/pulse into the generation area filled with Xe by a pulsed gas jet (P-GJ). A Silicon (Si) plate, placed after the jet at the Brewster angle for the fundamental (~75°), reflects the harmonics towards the detection area, while substantially attenuating the IR field. After reflection from the Si plate, the XUV radiation passes through an aperture (A) which blocks the residual outer part of the IR beam. Subsequently, the insertion of a ~150 nm thick band pass metal filter (F) allows the spectral selection of the XUV radiation. Finally, the XUV beam is focused into the target gas jet (T-GJ) (filled with gas under investigation) by of a spherical gold mirror (SM) with 5 cm focal length. With this configuration XUV peak intensities up to 10^{14} W/cm^2 have been achieved at the focus of the XUV beam [12]. The energy of the latter in the interaction region was determined by using an XUV calibrated photodiode (PD_{XUV}) considering also the reflectivity of the gold spherical mirror. The harmonic spectrum was obtained by recording energy resolved photoelectron spectra (PE) resulting from the single-photon ionization of Ar after the interaction with the harmonic frequency comb. Figure 11.1b shows the harmonic spectrum filtered by a band pass Sn foil (~150 nm thick). The electron spectra have been recorded by means of a μ-metal shielded time-of-flight (TOF) ion/electron spectrometer, attached to the upper branch of the XUV beam line shown in Fig. 11.1a. The TOF can be operated recording either the photoelectron energy distribution or ion-mass spectrum. The measured PE distribution does not differ significantly from the XUV spectral distribution since in the photon energy range spanning from 15 eV to 30 eV, the single-photon-ionization cross section of Argon does not varies substantially. When a polarization gating (PG) optical arrangement [24] is introduced in the beam line, the spectrum shown in Fig. 11.1b switches form a harmonic frequency comb to continuum (Fig. 11.1c) corresponding to the generation of isolated *asec* pulses.

Using a split spherical mirror (SM) of 5 cm focal length the duration of each *asec* pulse in the pulse train (Fig. 11.1d) as well as the duration of ~1-fs isolated XUV pulses (Fig. 11.1e) were obtained after performing 2-IVAC measurements. Intense XUV continua, generated after implementing the PG approach, have been exploited for tracing the 1-fs ultrafast dynamics in Xe atoms and H_2 molecules (Fig. 11.2). This was achieved by recording the XUV-pump-XUV-probe trace of Xe^{2+} generated by a two-XUV-photon double ionization process and H^+ generated by a two-photon XUV resonant ionization-fragmentation process of H_2 respectively.

Although the split-mirror XUV-pump-XUV-probe arrangement has been successfully implemented for the investigation of the ultrafast dynamics of these systems, intrinsic limitations associated with the stability of the interferometer for long data acquisition as well as delay times between the pump and the probe beams hinder further studies.

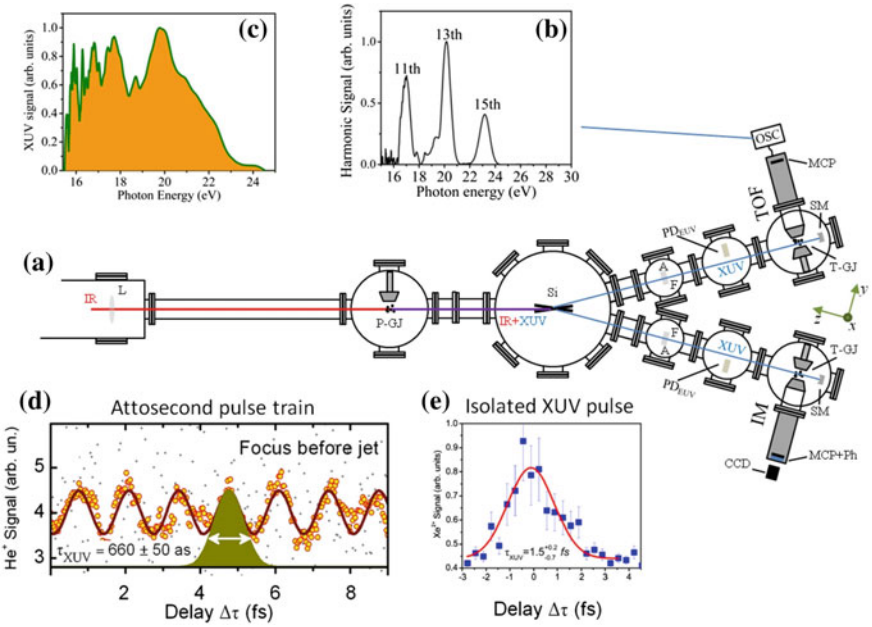

Fig. 11.1 **a** Beam line for the generation of intense XUV pulses in gas phase media. L: Lens; P-GJ: Pulsed gas jet used for the HHG; Si: Silicon plate; A: Aperture; F: Filter; PDEUV: Calibrated XUV photodiode; T-GJ: Target gas jet; TOF: Time of flight ion/electron spectrometer; IM: Ion Microscope; -SM: Split Spherical mirror; MCP: Microchannel plate detector. The y-axis is parallel to the TOF axis and the x-axis is parallel to the plane of the detector (MCP); **b** Harmonic spectrum recorded in case of using Sn filter. **c** Continuum XUV spectrum in the interaction area (Sn filter was used) when the PG optical arrangement [24] is introduced in the beam line. **d** 2nd order AC trace of an *asec* pulse train. **e** 2nd order AC trace of a ~1-fs isolated XUV pulse. Figure **a**, **b** from [12], Figure **c** from [9], Figure **d** from [17] and Figure **e** from [25]

A way to overcome the above obstacles is to utilize a XUV-pump-XUV-probe correlator which provides high temporal and spectral resolution in a single-shot measurement. The correlator relies on an approach named "Time gated ion microscopy" that provides an image of the ion distribution, produced by a two-photon process, along the propagation axis of two focused counter propagating intense XUV pulses. In the following section we present the conditions required for the successful implementation of the approach.

11.3 Time Gated Ion Microscopy

Time gated ion microscopy is a recently developed approach providing the imaging of the photoionization yield resulting from the interaction of IR/XUV ultra-short light pulses in gas phase media [15]. The aforementioned approach has been successfully

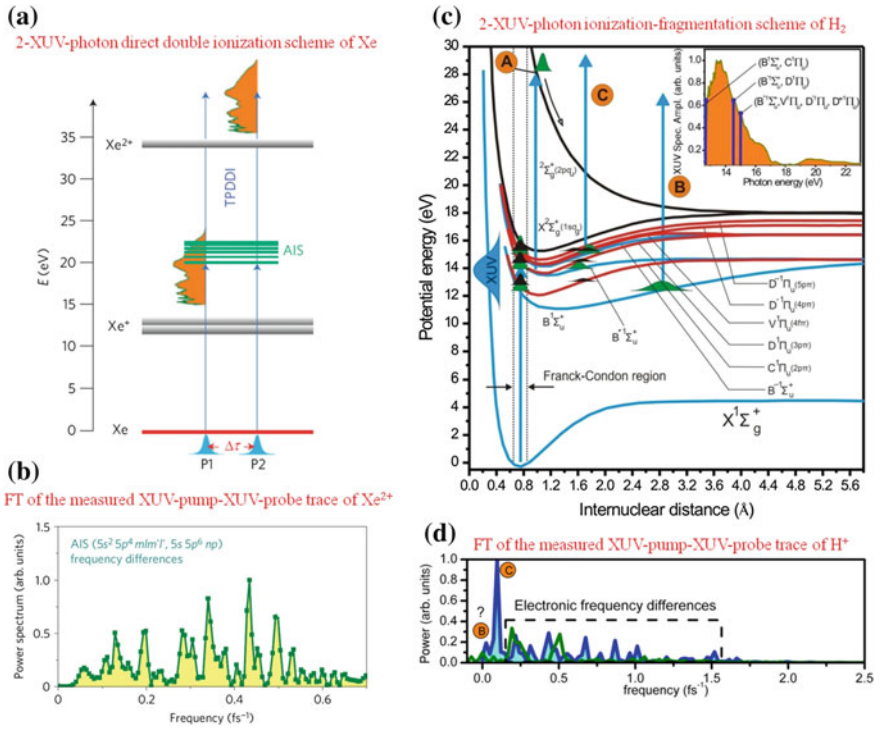

Fig. 11.2 **a** Two-XUV-photon direct double ionization scheme (in part through the autoionizing (AIS) manifold, induced in Xe by the interaction with the sequence of two mutually delayed intense broadband XUV pulses. The green line orange-filled area shows the spectrum used in the experiment. **b** Fourier Transform (FT) spectrum of the XUV-pump-XUV-probe trace of Xe^{2+} which reveals the frequency differences of the excited states. **c** The two-photon XUV resonant ionization-fragmentation scheme of H_2. The inset shows the XUV spectrum (green line (orange-filled area)) used in the experiment. XUV-pump-XUV-probe traces have been measured by recording the total proton yield and the non-zero kinetic energy protons. The XUV-pump-XUV-probe trace of total proton yield depicts minimum at zero delay times which is followed by a maximum at delay times of ~1 fs. The latter is attributed to the dynamics of the of the opening of the dissociation channel through $^2\Sigma_g^+$ $(2p\sigma_u)$ repulsive potential (noted with "A"). **d** FT spectra of the XUV-pump-XUV-probe trace of the total (blue-filled line) and the non-zero kinetic energy (green-line) proton yield. "B" and "C" as in (**c**). The pronounced peak (noted with "C") at 0.09 fs^{-1} corresponds to half of the vibrational period of the $C^1\Pi_u$, $B'\Sigma_u^+$, $D^1\Pi_u$ (unresolved) excited states ($C^1\Pi_u$ being the main contributor). The small peak (noted with "B") at 0.04 fs^{-1} is compatible with half the vibrational period of the $B^1\Sigma_u^+$ state, but due to the limited frequency resolution such a measurement is marginal. The spectroscopic resolution of the FT spectra shown in **b** and **d** was in the range of ~0.1 eV. Figures **a**, **b** from [9] and figures **c**, **d** from [21]

implemented in quantitative studies in the linear and non-linear regime in the XUV spectral range [12–15]. These investigations are based on the "Ion Microscope" (IM), which is an ion imaging device facilitating the observation of the spatial distribution

of the ionization products produced in a focused beam as a function of their mass over charge ratio m/q, i.e. it is an ion mass spectrometer with spatial imaging capability.

A schematic representation of the IM is illustrated in Fig. 11.3a. A spherical mirror focuses the back reflected XUV radiation towards the interaction region filled with the under investigation gas. The ion distribution produced at the focus of the beam (located in the object plane) is mapped onto a position sensitive detector located at the image plane. The ionic species generated in the focusing region of the laser beam are first accelerated by an electric field applied between the repeller (being floated at a voltage of V_{rep}) and extractor electrodes (being floated at a voltage of V_{ext}). The first electrostatic lens (EL1) images the ion distribution on an intermediate ion image plane with a small magnification factor M1. This intermediate image is located at the focal plane of a second electrostatic lens (EL2) that projects a further magnified (a magnification factor of M2) image onto the detector consisting of a pair of MCPs and a phosphor screen. The image of the ion distribution which appears on the phosphor screen is magnified by a factor of $M = M1 \times M2$ and is recorded by a CCD camera. The particular IM configuration, leads to a total magnification in the range of $M \approx 150$ with a field of view ≈ 500 μm and providing spatial resolution in the range of $\approx$ 270 nm. Thus the IM reveals their spatial distribution in a magnified high-resolution manner.

At this point it should be noted that an Abel transformation is required and so applied to obtain the actual size of the produced ion distribution, since the recording images are the projections of the three-dimensional ion cloud, characterized by cylindrical symmetry in the observation plane. Fragments with different times of flight (atomic ions A^+, A^{2+} or molecular ions AB^+ and fragments A^+, B^+), can be selected by gating (G) the detector (Fig. 11.3b and c). Spatially resolved ion distributions produced by one-XUV-photon and two-XUV-photon ionization process of Ar and He are shown in Fig. 11.3d and e, respectively. The ion distributions were recorded at the focus of an XUV radiation consisted from the up-converted harmonic frequencies (11–15th) of a ≈30 fs long IR laser pulse. The XUV beam was focused into the interaction region by a spherical gold mirror of 5 cm focal length.

Although the observation of the two-XUV-photon image in a multi-shot measurement is an important step towards the development of a single-shot XUV-pump-XUV-probe correlator, the single-shot measurement requires further enhancement of the XUV energy. A substantial increase of the XUV energy can be achieved by further improving the design of the table-top laser driven sources, implementing loose focusing geometries and quasi-phase matching conditions. Towards this direction "low" (10 Hz) and "high" (1 kHz) repetition rate XUV sources have been designed at FORTH, Lund, RIKEN, MPQ and ELI-ALPS [14, 26–29].

11.4 Single-Shot XUV-Pump-XUV-Probe Correlator

A schematic illustration of a high spatial resolution single-shot two-photon correlator is shown in Fig. 11.4a. A p-polarized high power XUV beam propagates towards the

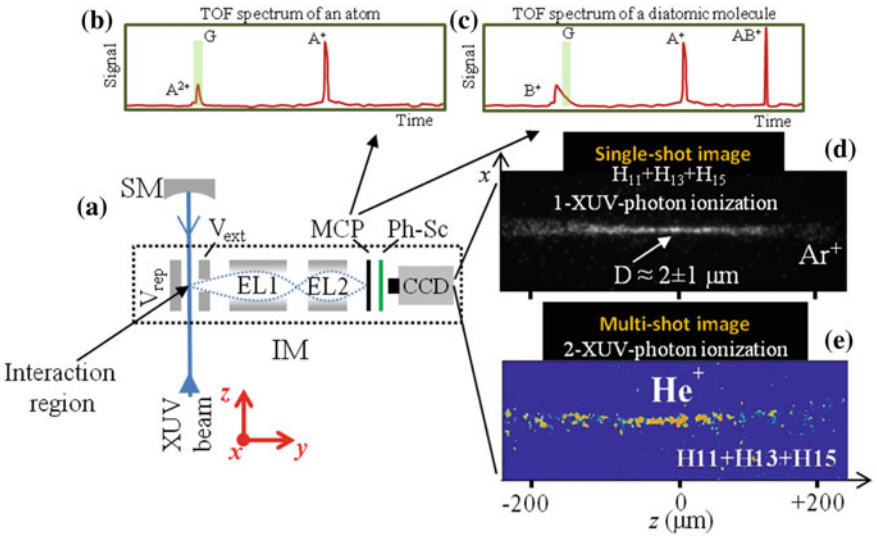

Fig. 11.3 **a** A schematic of the operation principle of the IM. The IM consists of the interaction region where an XUV laser pulse is focused and the electrostatic lenses, EL1, EL2, are used for magnifying and imaging the ion distribution produced in the interaction region on the MCP detector coupled with a phosphor screen (Ph-Sc). The image is recorded by a CCD camera. **b**, **c** A sketch of TOF mass spectra produced by the interaction of the focused beam with atoms (A) and diatomic molecules (AB), respectively. The shaded green area (G) in the mass spectra shows a temporally controlled gate which is applied on the MCP for imaging the ion distribution of a specific mass peak (m/q). **d** Single-shot ion distribution recorded at the focus of an XUV beam which contains the harmonics from 11 to 15th. The ion distribution was produced through 1-XUV-photon ionization of argon. The XUV energy at the focus was in the range of tens-nJ per pulse. In this measurement, the XUV focal spot diameter is found to be ≈2 μm, the spatial resolution of the device being ≈1 μm. **e** He + spatial ion distribution produced by a two-XUV-photon ionization process at the focus of the XUV beam. The XUV energy at the focus was in the range of hundred-nJ per pulse and the image was recorded accumulating 15,000 shots. Figures **a**–**d** from [15] and Figure **e** from [12]

single-shot two-XUV-photon correlator. A Si wedge manufactured with its surfaces at grazing angle incidence is located at the entrance of the correlator in order to split equally the XUV beam and substantially attenuating the IR pulse. The beams reflected by the Si plate XUV are transmitted through thin metal filters (F1, 2), which are implemented for XUV spectral selectivity. The two separated beams propagate towards the arms of the correlator using broadband high reflectivity XUV mirrors (M) and focused in the interaction region of the IM by a pair of gold SM. The sketch of the ion distribution produced by a two-XUV-photon non-linear ionization process in the region where the counter propagating XUV pulses interact with the gas medium is shown in Fig. 11.4b. It is assumed that the optical interference is taking place at $z \approx 0$ and the wave packet evolution is revealed at $z < 0$ and $z > 0$. The applicability of this approach has been explored and so tested out by the investigation of Xe^+ ion distribution resulting from the multi-photon ionization of Xenon atoms under the

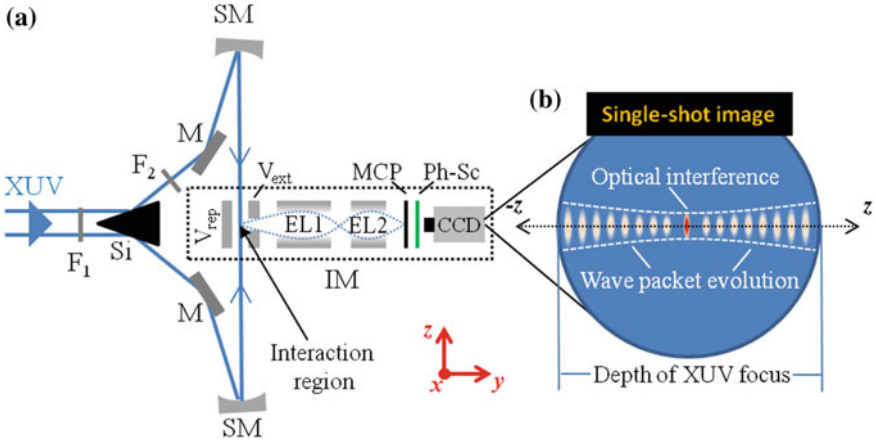

Fig. 11.4 **a** A schematic of the high spatial resolution single-shot two-XUV-photon correlator, showing its XUV optical set-up and the IM. Si, F1,2, M and SM are a silicon wedge, thin metal filters, mirrors and spherical mirrors, respectively. **b** A sketch of the imaged ion distribution along the propagation axis of the counter propagating pulses showing the areas where the optical interference ($z \approx 0$) and the wave packet evolution ($z < 0$ and $z > 0$) is taking place. Figure from [15]

influence of two counter propagating few-cycle mid-IR laser pulses with a central wavelength of 2.1 μm [15] and in UV spectral region by recording O_2^+ using UV pulses in the 20 fs range etc. [30–32].

Using the specifications of the IM as described in Sect. 11.3., a ≈500 μm long ion distribution can be resolved with ≈270 nm resolution i.e. the wave packet evolution can be traced with 2 fs resolution over a few-*psec* delay range resulting in a spectral resolution of ≈1 meV. The feasibility of recording a single-shot image induced by a two-XUV-photon process (hereafter called a 'non-linear single-shot image'), using few-fs XUV pulses with power of about 1 GWatt/pulse ($\tau_{XUV} = 1$ fs and $E_{XUV} = 1$ μJ/pulse), can be evaluated taking into account the conditions at which the image of Fig. 11.3e was recorded. The image of Fig. 11.3e was recorded by accumulating ≈15 000 shots, when an XUV beam with power ∼0.01 GWatt/pulse was focused (with $f = 5$ cm spherical mirror) into a He gas. The peak intensity of this XUV radiation at the focusing region was $\sim 10^{14}$ W/cm^2. In case of implementing an ≈1 GWatt/pulse XUV pulse and the correlator shown in Fig. 11.4 with focusing mirrors of $f = 40$ cm, intensities up to $I_{XUV} \approx 10^{15}$ W/cm^2 can be reached in the interaction region. These levels of intensity can lead to a 'non-linear single-shot image' with a signal much stronger compared to the 'non-linear image' of Fig. 11.3e and sufficient for performing single-shot XUV-pump-XUV-probe studies [for details see 15].

The temporal evolution of the wave packet can be directly obtained from the measured single-shot image induced by the counter propagating XUV beams. This relies on the fact that each position of the image along the propagation axis (z) corresponds to a specific delay value between the pump and the probe pulses according to the relation $\Delta T = 2z/c$ (where ΔT is the difference in the pulse delay for particles

which are separated by a distance z). The ion distribution (Fig. 11.4b) at $z = 0$ (zero delay between the pump and the probe pulses) contains information about the optical interference (i.e. duration of the XUV pulses when the pump and the probe pulses are identical) between the pump-probe pulses. For example, for an IM with spatial resolution of ≈270 nm, XUV pulses with a duration down to ≈2 fs can be measured. The modulation of the ion distribution (Fig. 11.4b) at $z < 0$ and $z > 0$ reflects the wave packet evolution. For identical XUV pulses the image will be symmetric with respect to $z = 0$ position. Considering that a sufficient amount of ions can be produced along a field of view ≈500 μm, it can be estimated that the evolution of the wave packet can be recorded with spectral resolution of ≈1 meV in the range of ≈3 psec. We note that the choice of the SM focal length f is of crucial importance since it is associated with (I) the aberrations of the XUV at the focus, (II) the XUV intensity in the interaction region and (III) the spectral resolution of the measurement which is inversely proportional to the maximum delay values at which the wave-packet evolution can be studied.

11.5 Conclusions

Summarizing, the operation principle and the requirements for the development of a single-shot XUV-pump-XUV-probe correlator which can be used for ultrafast time resolved studies with high spectral resolution is presented. The correlator relies on the imaging of the ion distribution, produced by a two-XUV-photon ionization non-linear process along the propagation axis of two focused counter propagating intense XUV pulses. This is based on the recently developed approach of the "Time gated ion microscopy" that has been successfully implemented for the spatially resolved photoionization yield investigations resulting from the linear and non-linear interaction of gas phase media with XUV harmonic pulses. We estimate, that for ~1 GWatt XUV pulses of ≈1 fs duration, the wave packet evolution can be recorded with temporal and spectral resolution of ≈2 fs and ≈1 meV, respectively, in a single-shot measurement.

References

1. Y. Kobayashi, T. Ohno, T. Sekikawa, Y. Nabekawa, S. Watanabe, Appl. Phys. B **70**, 389 (2000)
2. N.A. Papadogiannis, L.A.A. Nikolopoulos, D. Charalambidis, G.D. Tsakiris, P. Tzallas, K. Witte, Phys. Rev. Lett. **90**, 133902 (2003)
3. N.A. Papadogiannis, L.A.A. Nikolopoulos, D. Charalambidis, G.D. Tsakiris, P. Tzallas, K. Witte, Appl. Phys. B **76**, 721 (2003)
4. N. Miyamoto, M. Kamei, D. Yoshitomi, T. Kanai, T. Sekikawa, T. Nakajima, S. Watanabe, Phys. Rev. Lett. **93**, 083903 (2004)
5. Y. Nabekawa, H. Hasegawa, E.J. Takahashi, K. Midorikawa, Phys. Rev. Lett. **94**, 043001 (2005)
6. E.P. Benis, D. Charalambidis, T.N. Kitsopoulos, G.D. Tsakiris, P. Tzallas, Phys. Rev. A **74**, 051402(R) (2006)

7. E.P. Benis, P. Tzallas, L.A.A. Nikolopoulos, M. Kovacev, C. Kalpouzos, D. Charalambidis, G.D. Tsakiris, New J. Phys. **8**, 92 (2006)
8. K. Midorikawa, Y. Nabekawa, A. Suda, Prog. Quant. Elect. **32**, 43 (2008)
9. P. Tzallas, E. Skantzakis, L.A.A. Nikolopoulos, G.D. Tsakiris, D. Charalambidis, Nat. Phys. **7**, 781 (2011)
10. B. Manschwetus, L. Rading, F. Campi, S. Maclot, H. Coudert-Alteirac, J. Lahl, H. Wikmark, P. Rudawski, C.M. Heyl, B. Farkas, T. Mohamed, A. L'Huillier, P. Johnsson, Phys. Rev. A **93**, 061402(R) (2016)
11. S. Chatziathanasiou, S. Kahaly, E. Skantzakis, G. Sansone, R. Lopez-Martens, S. Haessler, K. Varju, G.D. Tsakiris, D. Charalambidis, P. Tzallas, Photonics **10**, 3390 (2017)
12. N. Tsatrafyllis, B. Bergues, H. Schröder, L. Veisz, E. Skantzakis, D. Gray, B. Bodi, S. Kuhn, G.D. Tsakiris, D. Charalambidis, P. Tzallas, Sci. Rep. **6**, 21556 (2016)
13. G. Kolliopoulos, B. Bergues, H. Schröder, P.A. Carpeggiani, L. Veisz, G.D. Tsakiris, D. Charalambidis, P. Tzallas, Phys. Rev. A **90**, 013822 (2014)
14. B. Bergues, D.E. Rivas, M. Weidman, A.A. Muschet, W. Helml, A. Guggenmos, V. Pervak, U. Kleineberg, G. Marcus, R. Kienberger, D. Charalambidis, P. Tzallas, H. Schröder, F. Krausz, L. Veisz, Optica **5**, 237 (2018)
15. P. Tzallas, B. Bergues, D. Rompotis, N. Tsatrafyllis, S. Chatziathanassiou, A. Muschet, L. Veisz, H. Schröder, D. Charalambidis, J. Opt. **20**, 024018 (2018)
16. P. Tzallas, D. Charalambidis, N.A. Papadogiannis, K. Witte, G.D. Tsakiris, Nature **426**, 267 (2003)
17. J.E. Kruse, P. Tzallas, E. Skantzakis, C. Kalpouzos, G.D. Tsakiris, D. Charalambidis, Phys. Rev. A **82**, 021402(R) (2010)
18. P. Tzallas, E. Skantzakis, D. Charalambidis, J. Phys. B **45**, 7 (2012)
19. E.J. Takahashi, P.F. Lan, O.D. Mucke, Y. Nabekawa, K. Midorikawa, Nat. Comm. **4**, 2691 (2013)
20. E. Skantzakis, P. Tzallas, J.E. Kruse, C. Kalpouzos, O. Faucher, G.D. Tsakiris, D. Charalambidis, Phys. Rev. Lett. **105**, 043902 (2010)
21. P.A. Carpeggiani, P. Tzallas, A. Palacios, D. Gray, F. Martín, D. Charalambidis, Phys. Rev. A **89**, 023420 (2014)
22. M.B. Campbell, T.J. Bensky, R.R. Jones, Opt. Exp. **1**, 197 (1997)
23. M.B. Campbell, T.J. Bensky, R.R. Jones, Phys. Rev. A **59**, 4117(R) (1999)
24. P. Tzallas, E. Skantzakis, C. Kalpouzos, E.P. Benis, G.D. Tsakiris, D. Charalambidis, Nat. Phys. **3**, 846 (2007)
25. P. Tzallas, E. Skantzakis, D. Charalambidis, J. Phys. B **45**, 074007 (2012)
26. A. Nayak, I. Orfanos, I. Makos, M. Dumergue, S. Kühn, E. Skantzakis, B. Bodi, K. Varju, C. Kalpouzos, H.I.B. Banks, A. Emmanouilidou, D. Charalambidis, P. Tzallas, Phys. Rev. A **98**, 023426 (2018)
27. F. Brizuela, C.M. Heyl, P. Rudawski, D. Kroon, L. Rading, J.M. Dahlström, J. Mauritsson, P. Johnsson, C.L. Arnold, A. L'Huillier, Sci. Rep. **3**, 1410 (2013)
28. K. Midorikawa, Y. Nabekawa, A. Suda, Prog. Quant. Electr. **32**, 43 (2008)
29. S. Kühn, M. Dumergue, S. Kahaly, S. Mondal, M. Füle, T. Csizmadia, B. Farkas1, B. Major, Z. Várallyay, E. Cormier, M. Kalashnikov, F. Calegari, M. Devetta, F. Frassetto, E. Månsson, L. Poletto, S. Stagira, C. Vozzi, M. Nisoli, P. Rudawski, S. Maclot, F. Campi, H. Wikmark, C. L Arnold, C. M Heyl, P. Johnsson, A. L'Huillier, R. Lopez-Martens, S. Haessler, M. Bocoum, F. Boehle, A. Vernier, G. Iaquaniello, E. Skantzakis, N. Papadakis, C. Kalpouzos, P. Tzallas, F. Lépine, D. Charalambidis, K. Varjú1, K. Osvay, G. Sansone, J. Phys. B **50**, 132002 (2017)
30. D. Rompotis, A. Baumann, O. Schepp, T. Maltezopoulos, M. Wieland, M. Drescher, Optica **4**, 871 (2017)
31. A. Baumann, S. Bazzi, D. Rompotis, O. Schepp, A. Azima, M. Wieland, D. Popova-Gorelova, O. Vendrell, R. Santra, M. Drescher, Phys. Rev. A **96**, 013428 (2017)
32. D. Rompotis, T. Gebert, M. Wieland, F. Karimi, M. Drescher, Opt. Lett. **40**, 1675 (2015)

Chapter 12
Lightwave-Driven Electronic Phenomena in Solids Observed by Attosecond Transient Absorption Spectroscopy

Katsuya Oguri, Hiroki Mashiko, Akira Suda and Hideki Gotoh

Abstract Steering electronic motion in solid state materials by light with unprecedented speed is the ultimate goal in the field of ultrafast physics and devices. Recent trends toward this goal are promoting extensive exploration of various lightwave-driven electric phenomena whose characteristic response occurs on a time scale comparable to the sub-cycle of lightwaves. Clarifying the comprehensive dynamics of lightwave-driven electric phenomena and pioneering its application to electronic functionality in solid state devices, require development of various diagnostic techniques with attosecond temporal resolution. Currently, attosecond transient absorption spectroscopy based on an isolated attosecond pulse (IAP) source is one of the most promising techniques. In this chapter, we will review a new scheme for lightwave-pulse-pump and IAP-probe attosecond transient absorption spectroscopy for solids. This scheme utilizes a quantum interference effect that appears in IAP absorption, which is induced by the simultaneous transition from the lightwave-coupled valence and conduction bands to a high-energy conduction band. We discuss the scheme based on an intuitively comprehensible approach that approximates a semiconductor band structure as a multi-eigenstate system in a theoretical formulation of the optical Bloch equation. The validity of the scheme is demonstrated by our recent experimental observation of third-order polarization in a wide-gap GaN semiconductor, which is well reproduced by the numerical simulation. This first observation of electronic oscillation beyond 1 PHz in a solid state system clearly shows the potential of future petahertz signal processing technology based on ordinary semiconductor devices.

K. Oguri (✉) · H. Mashiko · H. Gotoh
Quantum Optical Physics Research Group, Optical Science Laboratory,
NTT Basic Research Laboratories, NTT Corporation, 3-1 Morinosato Wakamiya, Atsugi,
Kanagawa 243-0198, Japan
e-mail: oguri.katsuya@lab.ntt.co.jp

A. Suda
Department of Physics, Faculty of Science and Technology, Tokyo University of Science, 2641,
Yamazaki, Noda, Chiba 278-8510, Japan

© Springer Nature Switzerland AG 2018

K. Yamanouchi et al. (eds.), *Progress in Ultrafast Intense Laser Science XIV*,
Springer Series in Chemical Physics 118,
https://doi.org/10.1007/978-3-030-03786-4_12

12.1 Introduction

The current technological fundamentals for high-speed operation in the modern electronics and photonics rely on the ultrafast control of electronic properties in solid state devices by an electric field. This principle is common to various applications from the field-effect transistor, which is one of the building blocks for high-clock rate logic operation in the digital electronics, to the electro-absorption modulator, which is a key component for high-bit rate signal encoding in the optical communication technology. In principle, the operational speed in a single device function is dominantly limited by two electronic parameters. One is the response time of band energy modulation with electric fields in the typical frequency region from gigahertz ($\sim 10^9$ Hz) to terahertz ($\sim 10^{12}$ Hz). The other one is a carrier response parameter such as carrier transit time (mobility) and carrier life time (recombination). As a breakthrough in future unprecedented-speed signal processing, a new concept has arisen from the field of attosecond science [1, 2]: direct sub-cycle electron manipulation in solid state materials by lightwave electric field. Replacing electric gigahertz fields by lightwave fields has the potential to substantially extend the operational frequency of solid state devices to petahertz ($\sim 10^{15}$ Hz), which is very close to the lightwave frequency. Thus, the concept of petahertz electron steering by a lightwave field offers exciting opportunities for ultrafast solid state physics and devises.

Recently, various lightwave-driven electric phenomena have been investigated. They can be classified into two regimes depending on the strength of the lightwave field. One is the non-perturbative regime, where light-matter interactions can be described as a periodic-electric-field action picture [3–12]. A typical example is high-harmonic generation (HHG) in solids driven by strong mid-infrared (MIR), near infrared (NIR), and even terahertz fields [3–7]. Since the essence of the HHG process has been understood as the interband recombination emission of electrons accelerated by a fundamental laser electric field in gaseous atomic systems [13, 14], HHG in solids is also closely related to the sub-cycle lightwave-driven electron dynamics in them. In addition to the interband transition, sub-cycle intraband electron transport plays an important role for HHG in solids [5, 15–18]. Another example is the lightwave-driven intraband current in solids [8–10]. The current, although interpreted as essentially the same as the source for HHG in solids, is interesting from the perspective of its ballistic transport that originates from well-defined phase relation among electrons induced by a lightwave field. In addition, the transient polarizability changes, which are explained by intense lightwave-induced Zener tunneling and Franz-Keldysh effect, are also categorized into this regime [11, 12].

The other is the perturbative regime where the quantized-photon transition picture is valid [19–21]. The light-matter interactions in this regime can be induced by a relatively weaker lightwave than in the non-perturbative regime. Although this regime includes all the conventional linear and nonlinear optical phenomena explained by the photo-transition picture, recent ultrafast measurements with sub-cycle temporal resolution clarify that such optical phenomena are also driven by a lightwave field. Sub-cycle stepwise population transfer from the valence band (VB) to the conduction

band (CB) [19] and sub-cycle oscillation originating from nonlinear polarization between them [20] are the pioneering examples. Conventionally, these perturbative phenomena have been understood as an instantaneous photo-transition induced by a light pulse under the envelope approximation with the oscillatory components of the light electric field neglected. At present, it is becoming appropriate to regard even such perturbative optical phenomena as an interaction between a lightwave field and electrons.

Clarifying the above-mentioned lightwave-driven electric phenomena and pioneering petahertz electronic functionality also entails great challenges regarding diagnostic techniques with attosecond temporal resolution. In this chapter, we introduce our new scheme for attosecond transient absorption spectroscopy [20]. This scheme utilizes the VB absorption induced by an isolated attosecond pulse (IAP) in the extreme ultraviolet (EUV) region as a probe for lightwave-driven electron interband transition. In Sect. 12.2, we describe its theoretical framework based on multi-level Bloch equation, and we show typical numerical simulation results in Sect. 12.3. Then, in Sect. 12.4, we introduce our recent demonstration of the observation of petahertz frequency in wide-gap GaN semiconductor using this scheme [20].

12.2 Attosecond Valence-Band Absorption Spectroscopy

12.2.1 EUV Absorption of Solids and Its Application to Attosecond Spectroscopy

In general, absorption of solid state materials in the EUV region is considerably strong. Figure 12.1 shows a typical EUV transmission spectrum of Si with a thickness of 100 nm. Even at this thickness, the transmission ranges from 0.05 to 0.7, indicating just how strong the absorption is. In this figure, the characteristic spectrum structure at the energy of approximately 100 eV that exhibits a sharp transmission decrease is called the x-ray absorption edge [22]. Since this energy corresponds to the transition from core level to a CB minimum (Fig. 12.2a), the spectrum near the x-ray absorption edge dominantly reflects the occupation of CB. For Si, the absorption edge near 100 eV corresponds to the transition from the $L_{\mathrm{II,III}}$ core level to the CB. The fine structure near and above the x-ray absorption edge is called the x-ray absorption fine structure (XAFS). XAFS spectra are known to be sensitive to local atomic structures for a selected atomic species, such as the distances, coordination number, and species of the atoms surrounding the selected element. Therefore, absorption spectra near x-ray absorption edges have been intensively investigated in the field of solid state physics. From this reason, previous time-resolved (TR) EUV absorption spectroscopy has measured transmission spectra near an x-ray absorption edge conventionally [11, 19, 23–25]. As shown in Fig. 12.2a, EUV absorption near an x-ray absorption edge is modified with the transition from the VB to CB induced

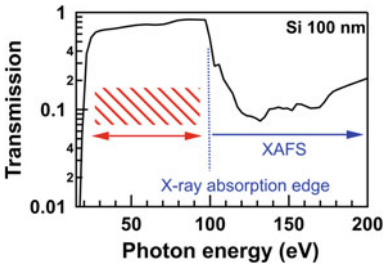

Fig. 12.1 Typical EUV transmission spectrum of Si thin film with a thickness of 100 nm. This is an example of transmission spectrum for solid state materials. The red hatched region corresponds to the absorption band originating from numerous allowed interband transitions in the whole VB and CB area (see text)

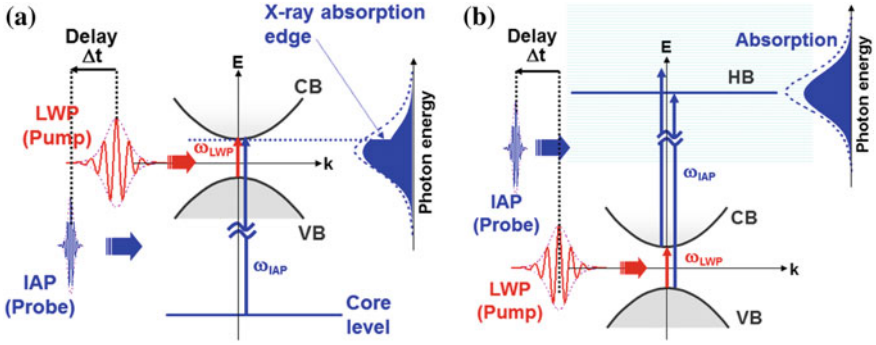

Fig. 12.2 Schematic band diagram pumped by a lightwave pulse (LWP) and probed by the delayed IAP. **a** IAP induces a core-level transition. An edge structure appears in the absorption spectrum. **b** IAP induces the transition from the VB maximum to a high-energy band (HB) in the CB

by the pump light wave. When a EUV IAP is used as the probe, measuring the modification of the core-level EUV absorption as a function of the delay provides us with the temporal evolution of lightwave-driven electron transition. The sub-cycle population transfer from the VB to CB observed in Si is the most obvious example [19]. However, in this scheme, it is necessary to match the photon energy of the probe IAP to the energy of an x-ray absorption edge of the sample. This is a major problem because it is no easy task to change the arbitrarily photon energy of the IAP.

In contrast to the XAFS region, the continuous spectrum region below the x-ray absorption edge corresponding to the lowest-energy core level, which typically ranges from a few to several tens of electron volts, has been outside the scope of interest in the conventional x-ray spectroscopy for solids (the red hatched region in Fig. 12.1). Because of the spectrum is structureless, the EUV absorption spectrum seemingly provides no useful information. However, the absorption spectrum should reflect numerous allowed interband transitions in the whole VB and CB area. The new

attosecond transient absorption scheme we propose here uses the EUV absorption in this region as a probe signal.

Figure 12.2b shows a schematic illustration of our scheme for an intuitive understanding of it. Here, a semiconductor electronic system is given as an example. In this scheme, we simplify the band structure in semiconductors into a two-band model, which consists of an occupied VB and an empty CB with bandgap energy of a few electron volts. When a lightwave pulse (LWP) interacts with the two bands, an interband polarization between them is induced. In addition to the two bands that are dominantly induced by the pump LWP, we assume a high-energy band (HB) with a few tens of electron volts for detecting the LWP-induced electronic polarization by the IAP. The delayed probe IAP induces interband transitions from the VB to HB and from the CB to HB simultaneously. The optical response of the probe IAP is closely linked to the pump LWP-induced electronic polarization via the VB and CB when the IAP and LWP transitions are assumed to have a common wave number. As a result, the absorption of the IAP is modified by the induced interband polarization between the VB and CB. Measuring the modification of the IAP absorption as a function of the delay is expected to provide us with the temporal evolution of the lightwave-driven electron transition between the VB and CB. This is the essence of our new scheme based on IAP absorption from the VB. This scheme only requires that the IAP photon energy is in the energy region where the contribution of core-level absorption is almost negligible. Typically, this photon energy ranges from 10 to 100 eV for solids.

12.2.2 Numerical Simulation Based on Multi-level Bloch Equation

To validate the above concept, we simulate an attosecond transient absorption spectroscopy for semiconductors using the three-level Bloch equation. In this simulation, we simply model the semiconductor two-band system as one with two-discrete levels, where the ground state $|a\rangle$ and the excited state $|b\rangle$ mimic the VB and CB, respectively (Fig. 12.3). We also approximate the HB to an isolated high-energy state $|c\rangle$ for detection, which contributes to the absorption of an IAP. The energy of each eigenstate is represented by E_a, E_b, and E_c. The electric field of the LWP, $\boldsymbol{E}_{LWP}(t)$, with the frequency of ω_{LWP} and that of the delayed IAP, $\boldsymbol{E}_{\mathrm{IAP}}(t-\Delta t)$, with the frequency of ω_{IAP} interact with the three-level system. In this simple approach, we focus on the interband effects between the VB and CB induced by the pump LWP. Intraband effects such as the lightwave-driven electron transport are ignored in the present analysis. This formulation basically follows the one presented in previous work [26–28], and we extend the previous two-level formalism to a three-level system [20].

The time-dependent Hamiltonian of the system within the dipole approximation is described as

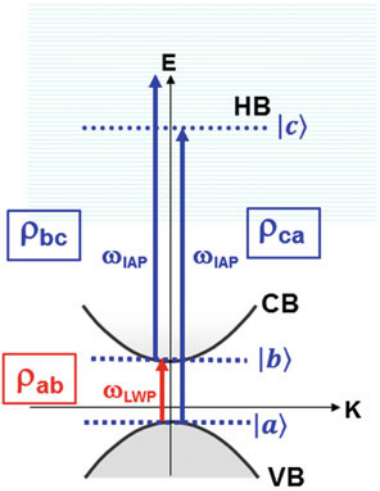

Fig. 12.3 Schematic illustration of the three-level model which mimics the VB and CB, and the high-energy conduction band (HB). The density matrix elements ρ_{ij} and the dipole matrix element d_{ij} at each transition are defined

$$\hat{H}(t) = \hat{H}_0 + \hat{H}_{\text{dip}}(t) \tag{12.1}$$

$$\hat{H}_0 = \begin{pmatrix} E_a & 0 & 0 \\ 0 & E_b & 0 \\ 0 & 0 & E_c \end{pmatrix} \tag{12.2}$$

$$\hat{H}_{\text{dip}}(t) = \begin{pmatrix} 0 & d_{ab}\boldsymbol{E}_{\text{NIR}}(t) & d_{ac}\boldsymbol{E}_{\text{IAP}}(t-\Delta t) \\ d_{ba}\boldsymbol{E}_{\text{NIR}}(t), & 0 & d_{bc}\boldsymbol{E}_{\text{IAP}}(t-\Delta t) \\ d_{ca}\boldsymbol{E}_{\text{IAP}}(t-\Delta t) & d_{cb}\boldsymbol{E}_{\text{IAP}}(t-\Delta t) & 0 \end{pmatrix}, \tag{12.3}$$

where $\hat{H}_0$ denotes the unperturbed Hamiltonian and $\hat{H}_{\text{dip}}$ denotes the interaction energy of the system with an electric field of the LWP and IAP. The dipole moment, d_{ij}, should be a real number, hence $d_{ij} = d_{ji}$. The time delay of the probe IAP with respect to the pump LWP is denoted as Δt. To describe the temporal evolution of each state with this Hamiltonian, we introduce the time-dependent density matrix of the system, $\rho_{ij}(t)$ (Fig. 12.3). The equation of motion for the density matrix is written as

$$\dot{\rho_{ij}} = \frac{1}{i\hbar}\left[\hat{H}(t), \rho\right]_{ij}, \tag{12.4}$$

where the dot represents the derivative with respect to time t. We solve the (12.4) based on a formalism of the optical Bloch equation. The density matrix elements are converted into Bloch vectors $u(t)$, $v(t)$, and $w(t)$, i.e.,

$$u_{ij}(t) = \rho_{ji}(t) + \rho_{ij}(t), \tag{12.5}$$

$$v_{ij}(t) = -i\left[\rho_{ji}(t) - \rho_{ij}(t)\right] \tag{12.6}$$

$$w_{ij}(t) = \rho_{jj}(t) - \rho_{ii}(t). \tag{12.7}$$

For the dipole matrix elements, we use the expression derived from $k{\cdot}p$ perturbation theory as follows [29]:

$$d_{ij} = \sqrt{\frac{\hbar^2 e^2}{2E_{ij}}\left(\frac{1}{m_0} - \frac{1}{m_e}\right)}, \tag{12.8}$$

with the elementary charge e, the conduction band effective mass m_e, and the free electron mass m_0. The energy difference between the three states is given by $E_{ij} = |E_i - E_j|$. In addition, we add phenomenological damping terms γ_{ij} for the dephasing rate and Γ_{ij} for the energy relaxation rate to the optical Bloch equation. We numerically solve the Bloch equation without employing the slowly varying envelope approximation and the rotating wave approximation at each delay time. The initial conditions for the Bloch vectors are $u(0) = v(0) = 0$ and $w(0) = -1$. Since we assume that the LWP and IAP are linearly polarized in parallel, the calculation is a one-dimensional problem.

After solving the Bloch equation, we calculate the macroscopic polarization $P(t)$, which is induced by the IAP. Since this polarization consists of transitions from $|a\rangle$ to $|c\rangle$ and from $|b\rangle$ to $|c\rangle$, it is given in terms of the Bloch vectors by

$$P(t) = N_0[\mathrm{d}_{ca}(u_{ca}(t) - i\,v_{ca}(t)) + \mathrm{d}_{cb}(u_{cb}(t) - i\,v_{cb}(t))], \tag{12.9}$$

where N_0 denotes the number of systems per unit volume. Then, we evaluate the complex amplitude absorption coefficient α of the IAP [28],

$$\alpha = -\frac{iK}{2\varepsilon}\frac{P(\omega)}{E_{\mathrm{IAP}}(\omega)} = -\frac{K}{2\varepsilon}\frac{N_0}{E_{\mathrm{IAP}}(\omega)}[V(\omega) + iU(\omega)] \tag{12.10}$$

where $U(\omega)$ and $V(\omega)$, using the Fourier transform of the real and imaginary part of the polarization given by

$$U(\omega) = \int \mathrm{Re}[P(t)]\mathrm{e}^{-i\omega t}\mathrm{d}t, \tag{12.11}$$

$$V(\omega) = \int Im[P(t)]\mathrm{e}^{-i\omega t}\mathrm{d}t. \tag{12.12}$$

$E_{\mathrm{IAP}}(\omega)$ denotes the Fourier amplitude of the input IAP. Using the Beer's law for the intensity,

$$I(z) = I(0)\mathrm{Exp}[-2\mathrm{Re}(\alpha)], \tag{12.13}$$

where $I(0)$ and $I(z)$ correspond to the intensity of the input beam before and after transmission of sample, respectively, we can evaluate the modification of the IAP absorption. Consequently, we calculate the imaginary part of the polarization of the

IAP with and without the LWP irradiation, $|V_{\mathrm{LWP}}(\omega, \Delta t)|$ and $|V_0(\omega)|$, as a function of time delay Δt.

12.3 Numerical Simulation for GaAs

In this section, we present several numerical simulation results to show what kind of information can be obtained with our scheme. Here, we simulate GaAs as an example of a two-band semiconductor, which is resonantly excited by an LWP in the perturbative excitation regime. The band gap of GaAs ranges from 1.4 to 1.5 eV [30]. When a Ti:sapphire laser with a photon energy near 1.5 eV is used as a pump LWP source, the band near the Γ point can be excited resonantly.

12.3.1 Linear Polarization in GaAs

Figure 12.4a shows typical behavior of the Bloch vectors induced by the LWP a with photon energy of 1.55 eV in the temporal domain. The LWP duration and its peak intensity correspond to 7 fs and 1×10^9 W/cm^2, respectively. From the experimental value reported in previous work [20], we assume the dephasing rate to be $\gamma_{ba} = 3 \times 10^{14}$ Hz, which corresponds to 3.3 fs of dephasing time. The energy damping rate, which corresponds to the recombination rate, is assumed to be $\Gamma_{ba} = 1 \times 10^{12}$ Hz (1 ps). Since the interband recombination time is generally long enough compared to the time scale of interest in the simulation, this value does not affect the result. The LWP induces the dipole oscillation between the VB and CB with the same frequency as the LWP [$u_{ba}(t)$ and $v_{ba}(t)$ in Fig. 12.4a]. The oscillation continues for the duration of the input LWP because the dephasing time is shorter than the LWP duration of 7 fs. In addition, Fig. 12.4a shows that the peak of the dipole oscillation is formed slightly later than that of the LWP. This is because the amplitude of the dipole oscillation is proportional to the population inversion, $w_{ba}(t) = \rho_{bb} - \rho_{aa}$, which reaches the maximum after the LWP peak. The population difference, $w_{ba}(t)$, also shows a slight stepwise increase with a half period of the LWP cycle. This is typical temporal behavior of the Bloch vectors for a resonantly excited two-level system.

Figure 12.4b shows the IAP electric field, IAP-induced Bloch vectors which consists of the macroscopic polarization, and the population inversion. We set the IAP duration and photon energy as 650 as and 21 eV to match the experimental parameters described in Sect. 12.4. The dipole moments from $|a\rangle$ to $|c\rangle$ and from $|b\rangle$ to $|c\rangle$, d_{ca} and d_{cb}, are assumed to be 1×10^{-28} and 5×10^{-30} m C. Since the dephasing rate of the IAP-induced polarization should be much higher than γ_{ba}, it is assumed to be $\gamma_{ca} = \gamma_{cb} = 4 \times 10^{15}$ Hz. In this case, the duration of the dipole oscillation induced by the IAP is comparable to that of the IAP. The population inversion $w_{ca}(t) = \rho_{cc} - \rho_{aa}$ shows the same half-cycle stepwise increase as $w_{ba}(t)$. Thus, the LWP-induced

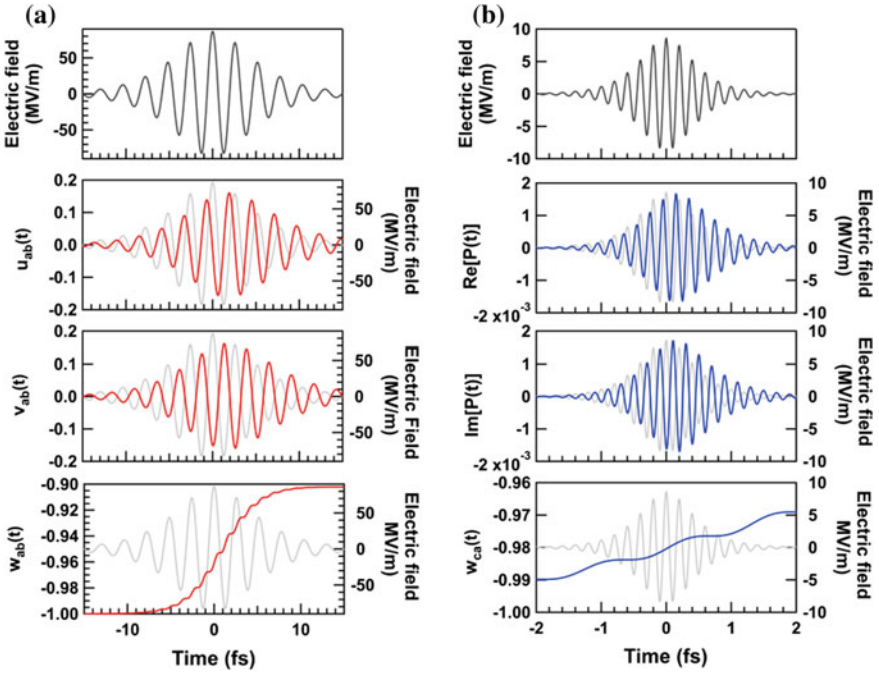

Fig. 12.4 **a** Solutions of time-dependent the Bloch vectors $u_{ab}(t)$, $v_{ab}(t)$, and $w_{ba}(t)$ for the VB-CB transition induced by the LWP with photon energy of 1.55 eV. The input LWP electric field is also shown (top panel, fine gray curves). **b** Probe IAP electric field (top panel, fine gray curves) and time-dependent macroscopic polarization $P(t)$ induced by the IAP. The real and imaginary parts of the polarization and the population inversion $w_{ca}(t)$ are shown

population transfer affects the IAP population transfer due to the transition from the bands common to the both the LWP and IAP excitation.

Figs. 12.5a and b show the absorption profiles obtained from the imaginary part of the IAP-induced polarization as a function of the time delay with and without the LWP irradiation. Although no temporal modification is observed without the LWP as expected (Fig. 12.5a), a clear oscillatory structure with a decrease in absorption appears when the LWP is irradiated (Fig. 12.5b). The oscillation period is 2.6 fs, suggesting that the temporal behavior of the linear dipole oscillation induced by the LWP can be transferred to the delay-time-dependent IAP absorption profile. It is interesting that our simple approach based on the three-level Bloch equation demonstrates the potential for directly probing the most fundamental light-matter interaction in the time domain. From the viewpoint of the experimental feasibility using attosecond transient absorption spectroscopy, the LWP-induced IAP absorption modification is expected to be observed as a differential optical density as a function of the time delay. This is given by

$$\Delta OD(\omega, \Delta t) = \log[I_0(\omega, \Delta t)/I_{\mathrm{LWP}}(\omega, \Delta t)], \tag{12.14}$$

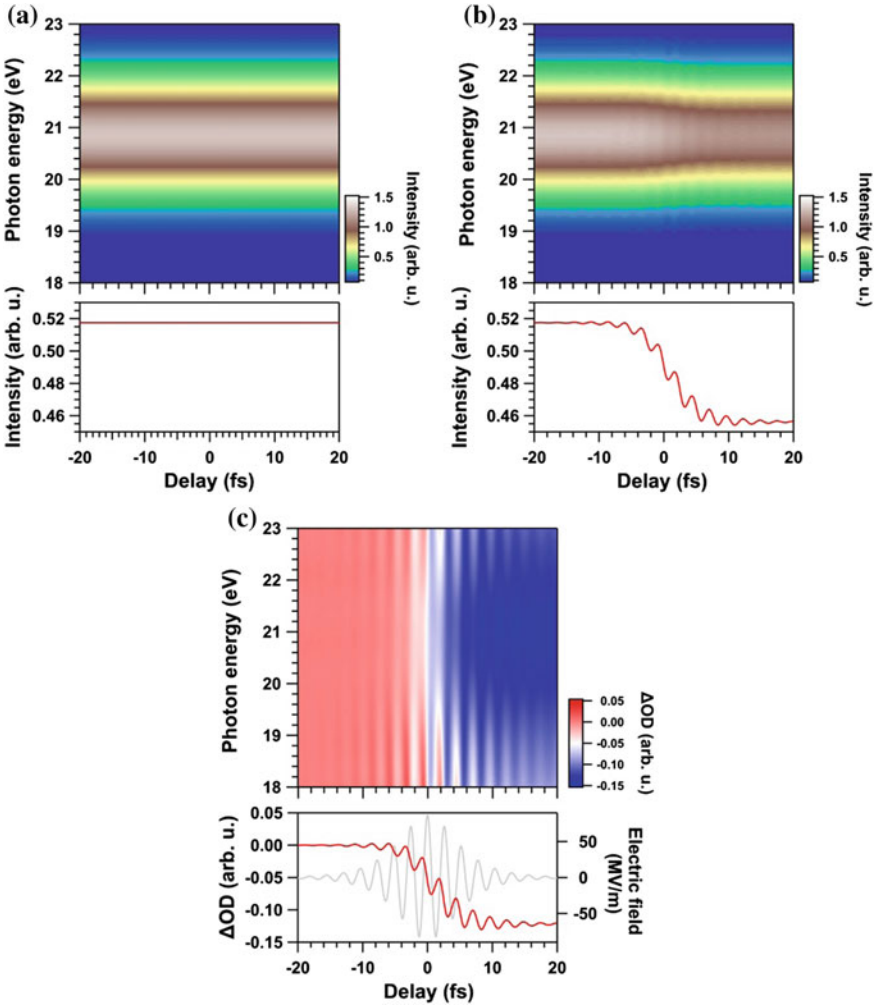

Fig. 12.5 Absorption profile obtained from the imaginary part of the IAP-induced polarization as a function of the time delay **a** with and **b** without LWP irradiation. **c** Temporal evolution of the differential absorption spectrum and its averaged profile

where $I_0(\omega, \Delta t)$ and $I_{\mathrm{LWP}}(\omega, \Delta t)$ correspond to the IAP transmission spectra through a sample without and with the LWP irradiation, respectively. To compare numerical simulations with experimental results, we approximate the differential optical density by the differential absorption expressed by

$$\Delta OD(\omega, \Delta t) \propto [-V_0(\omega) + V_{\mathrm{LWP}}(\omega, \Delta t)]/E_{\mathrm{IAP}}(\omega). \tag{12.15}$$

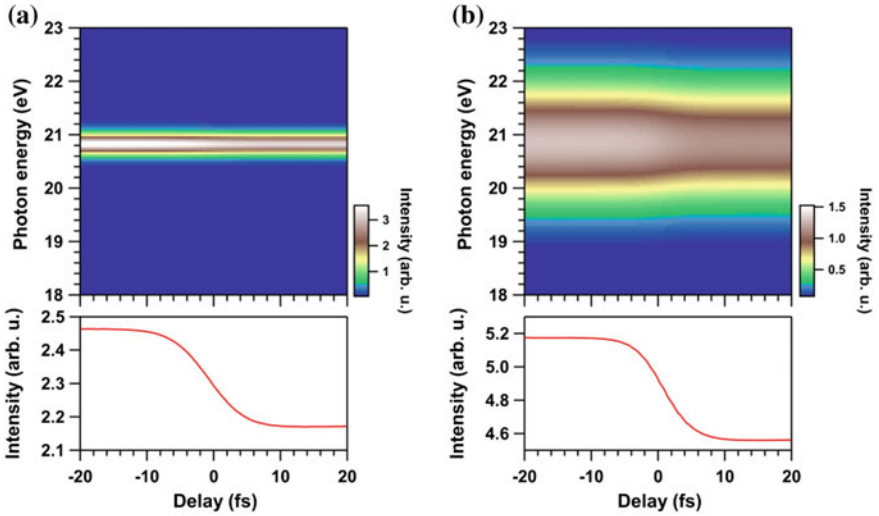

Fig. 12.6 Temporal evolution of the absorption profile when **a** the IAP duration is assumed to be 2600 as and when **b** the quantum path is blocked by setting the dipole matrix elements d_{cb} to zero. Other parameters are the same as those used in the simulations shown in Figs. 12.4 and 12.5

The calculated results are shown in Fig. 12.5c. The oscillation structure originating from the LWP-induced linear polarization is clearly seen. In addition, a decrease of the differential absorption is observed in the delay from −5 to +5 fs, which corresponds to the population transfer from VB to CB. The dephasing of the linear polarization oscillation can be clearly observed as a decrease in the contrast of the oscillatory structure. Thus, this simulation result strongly confirms the experimental feasibility of our scheme.

12.3.2 Quantum Beat Appeared in IAP Absorption

To clarify the origin of the IAP absorption modulation corresponding to the polarization oscillation shown in Fig. 12.5c, we focus two possible effects. One is the temporal duration of the probe IAP. Figure 12.6a shows the temporal evolution of the absorption profile when we assume an IAP with duration of 2600 as, which is comparable to one-cycle of the LWP-induced polarization oscillation. When the IAP duration is increased from 650 to 2600 as, the bandwidth of the IAP absorption spectrum decreases as shown in this figure. The considerable decrease in the temporal resolution of the probe IAP results in the disappearance of the oscillatory modulation as expected.

As the second effect, we investigated the quantum transition path from the CB (the state $|b\rangle$) to the HB (the state $|c\rangle$) induced by the IAP. Figure 12.6b shows

simulation results when the quantum path is blocked by setting the dipole matrix elements between $|b\rangle$ to $|c\rangle$ zero ($d_{cb} = 0$). In this case, the oscillatory modulation also disappeared, suggesting that the simultaneous transition from the two different initial states, $|a\rangle$ and $|b\rangle$, to the same final state, $|c\rangle$, is essentially important for detecting the LWP-induced polarization oscillation as an IAP absorption modulation. Therefore, this effect is explained by a kind of quantum beat of the imaginary part of the polarization between $v_{ca}(t)$ and $v_{cb}(t)$. Since the bandwidth of the IAP is broad enough to cover the frequency difference between $v_{ca}(t)$ and $v_{cb}(t)$, a quantum interference appears as the intensity modulation of the IAP absorption. In other words, the bandwidth of the probe IAP should be broader than the energy difference between the two states which correspond to the VB and CB. It is equivalent to IAP duration of less than one cycle of the LWP-induced polarization between the VB and CB. To date, a quantum interference effect between two quantum paths has been observed in various material systems [31–33]. Although the physical mechanism is common among them, the quantum beat frequency detectable with our scheme is significantly higher than these previous works.

12.3.3 Carrier-Wave Rabi Flopping

In the above discussion, we have seen that the LWP-induced linear polarization oscillation can be observed as IAP absorption modulation. In addition to linear optical effects, our scheme can be applied to extreme nonlinear optical effects. In this section, we address carrier-wave Rabi flopping (CWRF), which is a typical nonlinear effect expected in a resonantly excited two-level system [26, 34]. Figure 12.7 shows the temporal evolution of the differential absorption spectrum when the peak intensity of the LWP is assumed to be 3×10^{11} W/cm^2. The temporal evolution shows a strong oscillatory modulation with a period of approximately 6 fs, which corresponds to CWRF. The oscillation rapidly damps due to the dephasing time of 3.3 fs in this simulation. In addition, weak linear polarization oscillation can be seen in the leading edge of the trace. Previously, a signature of CWRF was observed in the spectral domain as a peak splitting of the third harmonic emission from GaAs by irradiating a 5-fs near infrared pulse with peak intensity of $10^{11} \sim 10^{12}$ W/cm^2 [34]. By using the attosecond transient spectroscopy, the CWRF oscillation can be directly detected in the time domain. Since the CWRF originates from the coherent behavior of light-matter interactions, it has the potential to become ultrafast gating with a few-femtosecond gate width, which is not limited by the slow carrier recombination time. From this point of view, time-domain control of CWRF is an important research target.

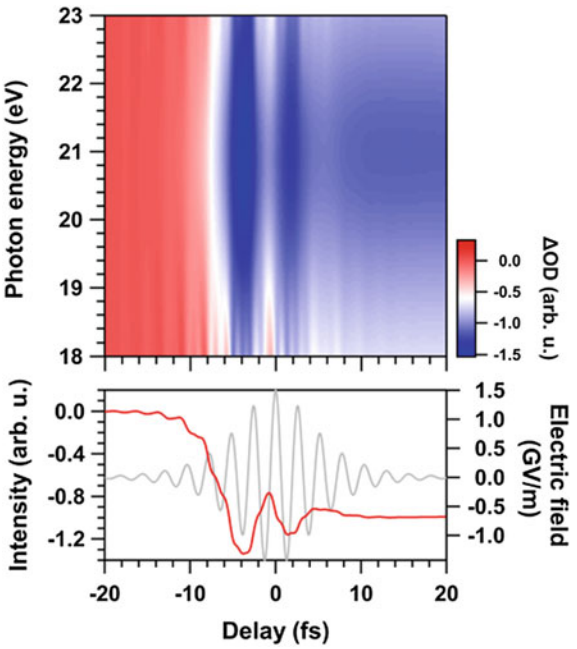

Fig. 12.7 Temporal evolution of differential absorption spectrum when the peak intensity of the pump LWP is assumed to be 3×10^{11} W/cm^2

12.4 Attosecond Transient Spectroscopy for GaN

In this section, we introduce the first experiment for directly measuring lightwave-induced interband polarization in the time domain based on attosecond transient absorption spectroscopy [20]. This experiment clearly demonstrated that our scheme enables us to observe an oscillatory modulation in a time evolution of IAP differential absorption spectrum that originates from LWP-induced nonlinear interband polarization.

12.4.1 Experimental Setup

Details of the experimental setup are described in the supplementary material of [20]. Figure 12.8 shows a schematic illustration of our pump and probe attosecond transient absorption spectroscopy setup for GaN thin crystal. Basically, this setup measures IAP-probe transmission spectra of the GaN sample pumped by a few-cycle-NIR pulse as a function of the time delay between the two pulses. In this experiment, the duration and central photon energy of IAP were 660 as at the FWHM and 21 eV. The GaN sample was pumped by the NIR pulse with 7-fs duration and 1.6-eV photon energy. The peak intensity of the pump NIR pulse was estimated to be approximately

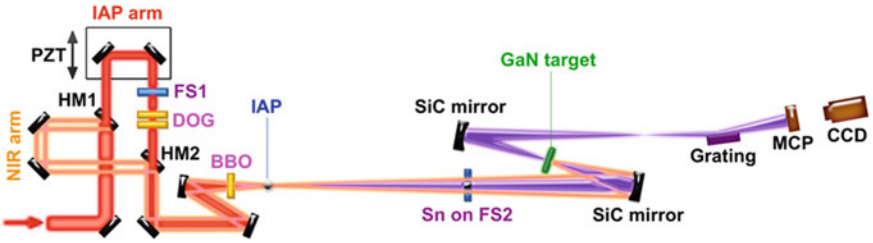

Fig. 12.8 Attoseocnd transient absorption spectroscopy setup. HM1 and HM2: annular hole mirrors. FS1: fused silica plate. PZT: piezo-electronic transducer stage for delay control between IAP and NIR pulse. DOG: double optical gating (DOG) optics (two quartz plates). BBO: β-BaB_2O_4 crystal of final DOG optics. Sn on FS2: tin filter mounted on annular fused silica plate. SiC: silicon carbide mirror. MCP: micro-channel plate. CCD: cooled charge-coupled device

1×10^{10} W/cm^2. We measured the differential absorption spectrum as a function of the time delay, $\Delta OD(\omega, \Delta t)$, which is defined in Sect. 3.1.

The direct bandgap of the GaN sample was measured to be 3.35 eV. Therefore, the linear polarization cannot be induced resonantly. Instead, the most probable nonlinear effect resonantly induced by the NIR pump pulse should be a three-photon transition with transition energy of 4.8 eV. The band that satisfies such an energy gap between the VB and CB has been confirmed in the M-Γ-A direction of the GaN band structure [36]. Thus, this experiment is expected to provide us with a direct measurement of the third-order polarization oscillation in the time domain.

12.4.2 Simulation for Third-Order Polarization

To simulate the above experiment, we fundamentally use the three-level Bloch equation consisting of the VB, CB, and HB as we described in the previous sections. However, we have to consider situations where the system nonlinearly interacts with the pump NIR LWP for this experiment. In previous work [20], we simplified the pump electric field as the third harmonic pulse of the NIR to simulate the three-photon transition. Here, to extend this treatment to more realistic one, we assume two intermediate virtual states, $|j\rangle$ and $|k\rangle$, between $|a\rangle$ and $|b\rangle$ states (Fig. 12.9a). We assume that the three-photon transition between $|a\rangle$ and $|b\rangle$ states is allowed only by a cascade transition through the intermediate states, i.e., $|a\rangle$ to $|j\rangle$, $|j\rangle$ to $|k\rangle$, and $|k\rangle$ to $|b\rangle$, and that its direct transition is prohibited ($d_{ab} = 0$) [28, 35]. We also assume the energy relaxation time of the $|j\rangle$ and $|k\rangle$ intermediate virtual states to be extremely large ($\Gamma = 10^{17}$ Hz). The transition from the intermediate virtual states to $|c\rangle$ with the IAP is ignored. The dephasing rate and energy relaxation rate related to the cascade transition are assumed to be very large, $\gamma = 2\times10^{15}$ Hz. The interaction energy $\hat{H}_{dip}$ is given by

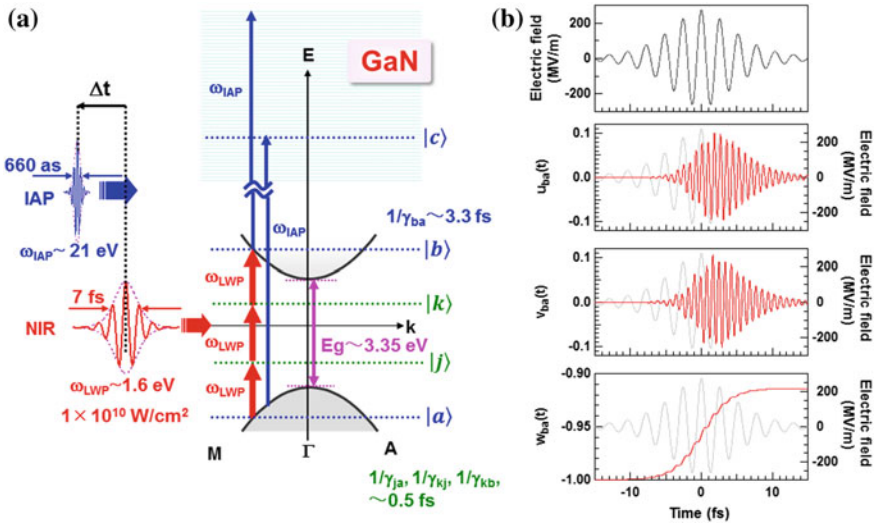

Fig. 12.9 **a** Schematic band diagram of GaN with direct band gap energy of 3.35 eV. This band structure is simplified with an approximation of a five-level system. Third-order nonlinear polarization should be strongly induced when the energy difference between the valence and conduction bands matches three-photon energy of $3\omega_{\mathrm{LWP}}$. We approximate this situation by assuming $|a\rangle$ and $|b\rangle$ levels with an energy difference of $3\omega_{\mathrm{LWP}}$. The system is pumped by a 1.6-eV LWP with a duration of 7 fs and a peak intensity of 1×10^{10} W/cm^2 and is probed by a 21-eV IAP with 650-as duration. These parameters are same as the experimental values. **b** Time-domain solutions of the Bloch vectors for VB and CB transition, $u_{ab}(t)$, $v_{ab}(t)$, and $w_{ba}(t)$ for the 5-level Bloch equation. The input LWP electric field is also shown (top panel, fine gray curves)

$$\hat{H}_{\mathrm{dip}} = \begin{pmatrix} 0 & d_{aj}E_{\mathrm{NIR}} & 0 & 0 & d_{ac}E_{\mathrm{IAP}} \\ d_{ja}E_{\mathrm{NIR}} & 0 & d_{jk}E_{\mathrm{NIR}} & 0 & 0 \\ 0 & d_{kj}E_{\mathrm{NIR}} & 0 & d_{kb}E_{\mathrm{NIR}} & 0 \\ 0 & 0 & d_{bk}E_{\mathrm{NIR}} & 0 & d_{bc}E_{\mathrm{IAP}} \\ d_{ca}E_{\mathrm{IAP}} & 0 & 0 & d_{cb}E_{\mathrm{IAP}} & 0 \end{pmatrix}. \tag{12.11}$$

The dipole matrix elements involving the three-photon transition, d_{aj}, d_{jk}, and d_{kb}, are unknown parameters. We estimate these parameters from the transmissivity of the IAP under the assumption of $d_{aj} = d_{jk} = d_{kb}$. Since the intermediate virtual levels, j and k, should be sufficiently nonresonant to ω_{LWP}, we assume each energy difference to be $E_{ja} = E_{kj} = E_{bk} = 2.0$ eV. Moreover, in order to estimate the effect of three-photon resonance on the transition between $|a\rangle$ and $|b\rangle$, we introduce enhancement parameter β for Bloch vectors $\beta v_{ja}(t)$ and $\beta v_{kj}(t)$. We evaluate this parameter to agree with the experimental result for GaN. After the density matrix elements are converted into the Bloch vectors, we solve the five-level Bloch equation at each time delay. This treatment enables us to simulate the interband polarization between $|a\rangle$ and $|b\rangle$, $u_{ba}(t)$ and $v_{ba}(t)$, with the third-harmonic frequency of the NIR

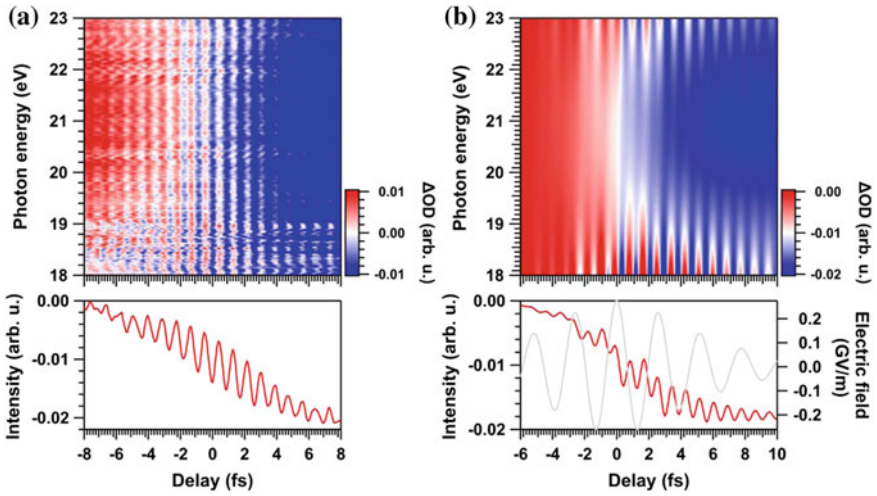

Fig.12.10 **a** Temporal evolution of the differential optical density trace of the GaN sample measured by attosecond transient absorption spectroscopy using a 21-eV IAP. We assume the delay time as 0 when the amplitude of the oscillatory modulation is maximum. **b** Simulated GaN differential optical density trace, assuming that the enhancement factor $\beta = 10$, and the dipole moment for the IAP transition, $d_{ca} = d_{cb}$, $= 1 \times 10^{-28}$ m C. The simulation well reproduced the experimental result where the 1.16-PHz oscillation accompanied by the gradual absorption decrease appeared in the whole energy region of the differential optical density trace

pulse, which are shown in Fig. 12.9b. Since this situation is almost same as the case of linear polarization discussed in previous sections, the third-harmonic oscillation will appear in the temporal evolution of the IAP differential absorption spectrum.

12.4.3 Comparison of Experimental Results with Simulation

Figure 12.10a shows the measured differential absorption trace of the GaN sample as a function of time delay. A characteristic temporal oscillatory modulation is clearly observed in the whole energy region from 18 to 23 eV as we expected from the simulation. The oscillation periodicity corresponds to 860 as, corresponding to 1.16 PHz in the frequency domain. This frequency corresponds to triple of the NIR frequency, thus indicating that the third-order interband polarization is dominantly detected. In addition, this figure also shows a gradual decrease in the differential absorption trace for about 15 fs. This corresponds to an increase in transmission of the IAP due to the population transfer from the VB to CB induced by the NIR pulse.

The simulated absorption trace as a function of time delay in Fig. 12.10b clearly shows the oscillatory modulation induced by the third-order polarization and the absorption decrease due to the population transfer, thus well reproducing the experimental result shown in Fig. 12.10a. With the differential absorption decrease, gradual

decrease in the contrast of the oscillatory modulation was also observed in the experiment in Fig. 12.10a. The decrease in the contrast corresponds to the dephasing of the induced interband polarization. From the comparison with simulation, the dephasing time is estimated to be 3.3 fs, which is almost same dephasing time for an interband transition in bulk GaAs at room temperature [37]. In this a few femtosecond time scale, electron-electron scatterings are likely to induce the dephasing process dominantly. In addition, the energy relaxation of the excited carrier due to carrier recombination process hardly occurs because recovery of the differential absorption decrease is not observed in this time scale. Long energy relaxation time of 1 ps assumed in the simulation also supports this experimental result. This good agreement between the experiment and the simulation results strongly confirms that our simple quantum interference picture essentially contributes to the appearance of the interband polarization on the IAP differential optical density.

The experiment and the simulation showed that the third-order polarization is only observed as an oscillatory modulation in IAP absorption. However, linear polarization should be induced non-resonantly in addition to the third-order polarization. One possible reason the linear polarization was not observed is that the most dominant process of IAP absorption is likely to be the transition from the real state, $|a\rangle$ and $|b\rangle$, to $|c\rangle$. The transition probability of the IAP from the virtual states, $|j\rangle$ and $|k\rangle$, should be considerably smaller than that from the real state. When the peak intensity of the LWP becomes much higher than that in this experiment, such as ~10^{12} W/cm^2, coupling between the linear polarization and IAP could be induced.

Although the formulation we discussed above ignores the intraband effects, we can consider the combination effect by incorporating intraband displacement terms with the optical Bloch equation [16, 38, 39]. In particular, in the case of an LWP with a high peak intensity that is intense enough to induce HHG in solids, the combination effect between the interband and intraband electronic dynamics plays a dominant role. Although it has been investigated with the spectral features of the HHG [5, 15], our understanding of such extreme nonlinear phenomena in solids will benefit from a direct time-domain measurement of the source dynamics of the HHG process based on attosecond transient absorption spectroscopy.

Thus, we have demonstrated that the lightwave-driven electronic response of a well-known semiconductor in the PHz frequency regime is detectable with the attosecond transient absorption spectroscopy from the theoretical and experimental viewpoint. The most important difference between the conventional GHz electronic response and the PHz one revealed in the present is that the induced electronic coherence is maintained in the PHz frequency regime. This characteristic will enable us to manipulate electronic system between VB and CB in solids without limitation of physical properties such as carrier recombination time. Coherent control of electronic system in solids has conventionally been investigated using exciton states in low-dimensional materials such as semiconductor quantum wells, dots, wires, carbon nanotubes, and nanoparticles under a low-temperature condition comparable to a few K. The observation of PHz electronic response reviewed in this chapter opens the door to the coherent control of electronic system in bulk solids at room temperature by taking advantage of the current evolution of the PHz lightwave control technology.

12.5 Conclusion

We reviewed the new attosecond transient absorption spectroscopy that provides us with a direct measurement in the time domain for LWP-driven electronic polarization in solid state materials. For the analysis, we demonstrated that an approach using multi-level optical Bloch equation formulation gives us a clear and simple picture of the interband electronic phenomena induced by the LWP and their detection by IAP absorption. The first experimental observation of electronic polarization oscillation with beyond 1-PHz frequency clearly validated the proposed concept. This technique will become a powerful diagnostic tool for novel electronic motion occurring on a time scale comparable to sub-cycle of lightwaves.

A promising extension of our scheme is attosecond transmissivity or reflectivity measurement that is combined with various detection techniques with high signal to noise ratio. Although the first experiment presented here used an energy-dispersive spectrometer, the most important information is an intensity modulation of the probe IAP. Therefore, measuring the IAP intensity of the whole bandwidth with a lock-in detection or differential detection technique will drastically improve the signal to noise ratio for the measurements. Such high-sensitivity measurement with attosecond resolution is expected to provide us with richer and more detailed information regarding with lightwave-driven coherent motion of electronic systems on an attosecond time scale.

Acknowledgements This work was partially supported by JSPS KAKENHI Grant No. 25706027, 23310086, 16H05987, and 16H02120.

References

1. F. Krausz, M.I. Stockman, Attosecond metrology: from electron capture to future signal processing. Nature Photon. **8**, 205–213 (2014)
2. O.D. Mücke, Petahertz electronics: Pick up speed. Nature Phys. **12**, 724–725 (2016)
3. S. Ghimire, A.D. Dichiara, E. Sistrunk, P. Agostini, L.F. Dimauro, D.A. Reis, Observation of high-order harmonic generation in a bulk crystal. Nat. Phy. **7**, 138–141 (2011)
4. T.T. Luu, M. Garg, SYu. Kruchinin, MTh Hassan, E. Goulielmakis, Extreme ultraviolet high-harmonic spectroscopy of solids. Nature **521**, 498–502 (2015)
5. G. Vampa, T.J. Hammond, N. Thiré, B.E. Schmit, F. Légaré, C.R. McDonald, T. Brabec, P.B. Corkum, Linking high harmonics from gases and solids. Nature **522**, 462–466 (2015)
6. O. Schubert, M. Hohenleutner, F. Langer, B. Urbanek, C. Lange, U. Huttner, D. Golde, T. Meier, M. Kira, S.W. Koch, R. Huber, Sub-cycle control of terahertz high-harmonic generation by dynamical Bloch oscillations. Nat. Photon. **8**, 119–123 (2014)
7. N. Yoshikawa, T. Tamaya, K. Tanaka, High-harmonic generation in graphene enhanced by elliptically polarized light excitation. Science **356**, 736–738 (2017)
8. A. Schiffrin, T. Paasch-Colberg, N. Karpowicz, V. Apalkov, D. Gerster, S. Mühlbrandt, M. Korbman, J. Reichert, M. Schultze, S. Holzner, J.V. Barth, R. Kienberger, R. Ernstorfer, V.S. Yakovlev, M.I. Stockman, F. Krausz, Optical-field-induced current in dielectrics. Nature **493**, 70–74 (2013)
9. T. Rybka, M. Ludwig, M.F. Schmalz, V. Knittel, D. Brida, A. Leitenstorfer, Sub-cycle optical phase control of nanotunnelling in the single-electron regime. Nat. Photon. **10**, 667–671 (2016)

10. T. Higuchi, C. Heide, K. Ullmann, H.B. Weber, P. Hommelhoff, Light-field-driven currents in graphene. Nature **550**, 224–228 (2017)
11. M. Schultze, E.M. Bothschafter, A. Sommer, S. Holzner, W. Schweinberger, M. Fiess, M. Hofstetter, R. Kienberger, V. Apalkov, V.S. Yakovlev, M.I. Stockman, F. Krausz, Controlling dielectrics with the electric field of light. Nature **493**, 75–78 (2013)
12. M. Lucchini, S.A. Sato, A. Ludwig, J. Herrmann, M. Volkov, L. Kasmi, Y. Shinohara, K. Yabana, L. Gallmann, U. Keller, Attosecond dynamical Franz-Keldysh effect in polycrystalline diamond. Science **353**, 916–919 (2016)
13. P.B. Corkum, Plasma Perspective on Strong-Field Multiphoton Ionization. Phys. Rev. Lett. **71**, 1994–1997 (1993)
14. P.B. Corkum, F. Krausz, Attosecond Science. Nat. Phys. **3**, 381–387 (2007)
15. M. Garg, M. Zhan, T.T. Luu, H. Lakhotia, T. Klostermann, A. Guggenmos, E. Gouliermakis, Multi-petahertz electronic metrology. Nature **538**, 359–363 (2016)
16. D. Golde, T. Meier, and S.W. Koch, High harmonics generated in semiconductor nanostructures by the coupled dynamics of optical inter- and intraband excitations. Phys. Rev. B **77**, 075330-1-6 (2008)
17. T. Higuchi, M.I. Stockman, and P. Hommelhoff, Strong-Field Perspective on High-Harmonic Radiation from Bulk Solids. Phys. Rev. Lett. **113**, 213901-1-5 (2014)
18. M. Wu, S. Ghimire, D.A. Reis, K.J. Schafer, M.B. Gaarde, High-harmonic generation from Bloch electrons in solids. Phys. Rev. A **91**, 043839-1-11 (2015)
19. M. Schultze, K. Ramasesha, C.D. Pemmaraju, S.A. Sato, D. Whitmore, A. Gandman, J.S. Prell, L.J. Borja, D. Prendergast, K. Yabana, D.M. Neumark, S.R. Leone, Attosecond band-gap dynamics in silicon. Science **346**, 1348–1352 (2014)
20. H. Mashiko, K. Oguri, T. Yamaguchi, A. Suda, H. Gotoh, Petahertz optical drive with wide-bandgap semiconductor. Nat. Phys. **12**, 741–745 (2016)
21. A. Sommer, E.M. Bothschafter, S.A. Sato, C. Jakubeit, T. Latka, O. Razskazovskaya, H. Fattahi, M. Jobst, W. Schweinberger, V. Shirvanyan, V.S. Yakovlev, R. Kienberger, K. Yabana, N. Karpowicz, M. Schultze, F. Krausz, Attosecond nonlinear polarization and light–matter energy transfer in solids. Nature **534**, 86–90 (2016)
22. P.A. Lee, P.H. Citrin, P. Eisenberger, B.M. Kincaid, Extended x-ray absorption fine structure-its strengths and limitations as a structural tool. Rev. Mod. Phys. **53**, 769–806 (1981)
23. H. Nakano, Y. Goto, P. Lu, T. Nishikawa, N. Uesugi, Time-resolved soft x-ray absorption spectroscopy of silicon using femtosecond laser plasma x rays. Appl. Phys. Lett. **75**, 2350–2352 (1998)
24. C. Bressler, M. Chergui, Ultrafast X-ray absorption spectroscopy. Chem. Rev. **104**, 1781–1812 (2004)
25. Y. Pertot, C. Schmidt, M. Matthews, A. Chauvet, M. Huppert, V. Svoboda, A. Conta, A. Tehlar, D. Baykusheva, J.-P. Wolf, H.J. Wörner, Time-resolved x-ray absorption spectroscopy with a water window high-harmonic source. Science **355**, 264–267 (2017)
26. S. Hughes, Breakdown of the area theorem: carrier-wave rabi flopping of femtosecond optical pulses. Phys. Rev. Lett. **81**, 3363–3366 (1998)
27. T. Tritschler, O.D. Mücke, M. Wegener, Extreme nonlinear optics of two-level systems. Phys. Rev. A **68**, 033404 (2003)
28. P. Meystre, and M. Sargent III, *Elements of Quantum Optics* (Springer, 1998)
29. M. Wegener, Extreme nonlinear optics in semiconductors, in *Optics of Semiconductors and Their Nanostructures* (H. Kalt and M. Hetterich (Eds.), Springer 2004)
30. M. Rohlfing, P. Kriiger, J. Pollmann, Quasiparticle band-structure calculations for C, Si, Ge, GaAs, and SiC using Gaussian-orbital basis sets. Phys. Rev. B **48**, 17791–17805 (1993)
31. N.H. Bonadeo, J. Erland, D. Gammon, D. Park, D.S. Katzer, D.G. Steel, Coherent optical control of the quantum state of a single quantum dot. Science **282**, 1473–1476 (1998)
32. F. Rossi, T. Kuhn, Theory of ultrafast phenomena in photoexcited semiconductors. Rev. Mod. Phys. **74**, 895–950 (2002)
33. E. Goulielmakis, Z.-H. Loh, A. Wirth, R. Santra, N. Rohringer, V.S. Yakovlev, S. Zherebtsov, T. Pfeifer, A.M. Azzeer, M.F. Kling, S.R. Leone, F. Krausz, Real-time observation of valence electron motion. Nature **466**, 739–744 (2010)

34. O.D. Mücke, T. Tritschler, M. Wegener, U. Morgner, F.X. Kärtner, Signatures of carrier-wave Rabi flopping in GaAs. Phys. Rev. Lett. **87**, 057401-1-4 (2001)
35. M. Sargent III, S. Ovadia, M.H. Lu, Theory of two-photon multiwave mixing. Phys. Rev. B **32**, 1596–1604 (1985)
36. Y.C. Yeo, T.C. Chong, M.F. Li, Electronic band structures and effective-mass parameters of wurtzite GaN and InN. J. Appl. Phys. **83**, 1429–1436 (1998)
37. P.C. Becker, H.L. Fragnito, C.H. Brito Cruz, R.L. Fork, J.E. Cunningham, J.E. Henry, C.V. Shank, Femtosecond photon echoes from band-to band transitions in GaAs, Phys. Rev. Lett. **61**, 1647–1649 (2016)
38. M.S. Wismer, S. Yu. Kruchinin, M. Ciappina, M.I. Stockman, V.S. Yakovlev, Strong-field resonant dynamics in semiconductors, Phys. Rev. Lett. **116**, 197401-1-5 (2016)
39. T. Tamaya, A. Ishikawa, T. Ogawa, K. Tanaka, Diabatic mechanisms of higher-order harmonic generation in solid-state materials under high-intensity electric fields. Phys. Rev. Lett. **116**, 016601-1-5 (2016)

Chapter 13
Intra- and Interband Transitions in High-Order Harmonic Generation from Solids

Xue-Bin Bian, Tao-Yuan Du, Guang-Rui Jia and Xiao-Huan Huang

Abstract We introduced a quasi-classical step-by-step model for interband transitions in the k space to reveal the mechanisms of high-order harmonic generation (HHG) in solids. The ultrafast dynamics are also investigated in the real space by solving the time-dependent Schrödinger equations. The inter- and intraband dynamics in k space correspond to the local and global oscillations of the Bloch electron wave packet in the coordinate space moving at phase and group velocities, respectively. Their contributions can be controlled by different laser parameters, such as chirp, pulse duration, carrier-envelope phase, two-color field, and so on. We also introduced an efficient way to enhance the yield of HHG in inhomogeneous laser fields below the damage threshold.

13.1 Introduction

High-order harmonic generation (HHG) in plasma was observed by laser-solid interaction as early as 1977 [1]. The nonlinear effect for HHG from laser-gas interaction was demonstrated in 1987 [2]. The energy of HHG from atoms and molecules in the gas phase can reach up to hundreds of eV. It has been studied extensively [3, 4] and utilized to produce attosecond laser pulses. The mechanism for HHG in the gas phase is well described by the three-step recollision model [5]. This model gives the cutoff law of HHG in linearly polarized lasers: $I_p + 3.17U_p$, where I_p is the ionization potential, $3.17U_p$ is the maximum recollision energy of the returning electrons

X.-B. Bian (✉) · T.-Y. Du · G.-R. Jia
State Key Laboratory of Magnetic Resonance and Atomic and Molecular Physics, Wuhan Institute of Physics and Mathematics, Chinese Academy of Sciences, Wuhan 430071, China
e-mail: xuebin.bian@wipm.ac.cn

X.-H. Huang
Hubei Key Laboratory of Pollutant Analysis and Reuse Technology, College of Chemistry and Chemical Engineering, Hubei Normal University, Huangshi 435002, China
e-mail: xhuang@hbnu.edu.cn

© Springer Nature Switzerland AG 2018

K. Yamanouchi et al. (eds.), *Progress in Ultrafast Intense Laser Science XIV*, Springer Series in Chemical Physics 118,
https://doi.org/10.1007/978-3-030-03786-4_13

driven by the external laser fields. U_p is the ponderomotive energy, proportional to laser intensity and wavelength square, i.e. $\propto I\lambda^2$. The intensity I can not be too high due to the saturation ionization threshold of atoms and molecules. Recently, more attention has been attracted to extend the wavelength λ of the driving lasers. The HHG in solids [6–15] with the development of long-wavelength lasers was studied. Solid HHG demonstrates novel features different from the HHG from gases. For example, linear cutoff energy dependence on the amplitude of the laser field [6], multiplateau structure in the HHG spectra [12], and different HHG yield dependence on laser ellipticity [6]. However, mechanisms of HHG from solids are still under debate. Inter- and intraband transition models [16–21] are proposed. Three-step model in coordinate space [20] and step-by-step model in vector k space [22–26] are investigated. The former requires that the electron and hole have the same displacement, i.e., $x_e - x_h = 0$, whereas the latter requires that they have the same wave vector, i.e., $k_e - k_h = 0$. Solid HHG is a promising way for compact Ultraviolet (UV) sources due to the high density of solid materials. However, the damage threshold of solids is usually low, which restricted the maximum energy of HHG. Many efforts have been undertaken to enhance the yield of HHG. For example, two-color laser fields [27, 28] and plasmon-enhanced inhomogeneous laser fields [19, 29–31] are used to manipulate the HHG processes, especially for the enhancement of the second plateau of the HHG spectra [19].

In this chapter, we will review the theoretical models for intra- and interband transitions and their roles in HHG. Atomic units ($e = m_e = \hbar = 1$) are used throughout unless stated otherwise.

13.2 Quasi-Classical Step-by-Step Model for HHG

Based on Bloch's theorem, the electron dynamics in periodic potentials can be described in the reduced Brillouin zone (BZ) in the wavevector space. As shown in Fig. 13.1, the intraband transitions describe the electron oscillations in each band, while the interband transitions mean the polarization between different bands.

For intraband transitions, after neglecting the periodic Coulomb field, the electron motion in semiconductors driven by external laser field can be described in the momentum space as

$$k(t) = k(0) + A(t), \tag{13.1}$$

where $A(t)$ is the vector potential of the laser fields. Compared to a classical particle, the photonemission from electrons in solids comes from its acceleration, i.e., $a(t) = dk(t)/dt = dA(t)/dt = -E(t)$. The maximum value of the acceleration $a(t)$ is only determined by the amplitude of laser field $E(t)$, i.e. E_0. In other words, the cutoff energy of the HHG from intraband transitions is linearly dependent on the strength of the laser field E_0, independent on laser frequency ω. This is in agreement with the one-band model [16, 17].

For interband transitions, we developed a step-by-step model for HHG in the tunnel ionization regime by involving multiband transitions [22–24] to reveal the

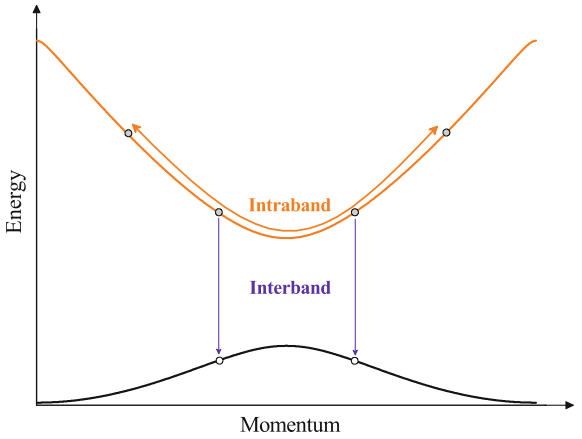

Fig. 13.1 Schematic illustration of intra- and interband transitions in the momentum space

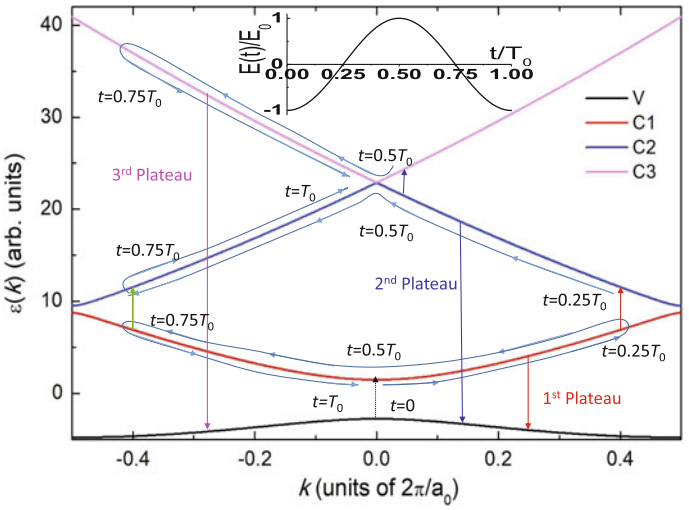

Fig. 13.2 Step-by-step model for HHG by involving multiband contributions

mechanism for multiplateau structure in HHG spectra [12]. Figure 13.2 illustrates a typical band structure for periodic potentials. At the peak of laser fields ($A(t) = 0$), the electron on the top of the valence band V is pumped by tunnel ionization to the first conduction band C1 at $k(t = 0) \approx 0$, where the band gap between them is minimal. Then the electrons on C1 conduction band follow the driving laser by intraband transition in (13.1) and move toward the positive edge of the first BZ. After around a quarter optical cycle $0.25T_0$ (T_0 is the period of the laser field), part of the electrons is pumped to the conduction band C2 by tunnel ionization where the band gap between C1 and C2 is small as shown in Fig. 13.2. The electron then

oscillates in the C2 band driven by the external laser field. Following the evolution of the vector potential of the laser field, the electrons remaining on the conduction band C1 oscillate along the same band to $k(t) = 0$ at $t = 0.5T_0$, then go to the negative edge of the BZ at $t = 0.75T_0$, and return to its original position $k \approx 0$ at $t = T_0$. The transition from C1 to V bands is responsible for the first plateau in HHG spectra. In the first optical cycle, the number of channels for HHG in the first plateau from the transition between C1 and V bands is four by counting the times of electron passing the transition points with the same energy gap between C1 and V bands within T_0. For the electrons pumped to C2 band at $t = 0.25T_0$ in Fig. 13.2, they propagate along C2 band and may be pumped to C3 band at around $t = 0.5T_0$ with a small band gap between C2 and C3 bands. The electrons remaining on C2 band evolve in the laser fields to the negative edge of the BZ at $t = 0.75T_0$, and return to $k = 0$ at the end of this cycle. Part of the electrons on C2 band may come from the transition from C1 band at around $t = 0.75T_0$. The transition from C2 to V bands corresponds to the second plateau of HHG spectra. The emission time of HHG from C2 should be delayed for $0.25T_0$ intrinsically compared to those from C1 band due to the step-by-step excitation processes. For the same reason, C3 band is populated from around $t = 0.5T_0$ and the emission of HHG from C3 band is around $0.5T_0$ delayed compared to that from C1 band. The numbers of HHG channels in the second and third plateaus are three and two, respectively.

To quantitatively describe the above HHG process, the wavevector of electrons and holes is determined by (13.1), and we assume $k(0) = 0$. After tunneling into the conduction bands, the electrons are still attracted by the long-range periodic potentials, i.e., the energy of the electron is not like free particle energy $k(t)^2/2$, but conduction band energy $\varepsilon_c(k(t))$ computed based on Bloch's theorem. The HHG emissions synchronize with the Bloch electron wave packet motions. The HHG emission $\Omega(t)$ is determined by

$$\Omega(t) = \varepsilon_c(k(t)) - \varepsilon_v(k(t)), \tag{13.2}$$

where ε_v represents the energy of the hole in the valence band. The above equation indicates the condition for harmonic emission: $k_e = k_h$. Once we know the band structure of the system and the parameters of the laser fields, the HHG emission times from each band can be obtained inversely by (13.2) [23]. Based on this quasi-classical model, the cutoff energy Ω_{cutoff} is determined by the maximum band gap between the conduction (including higher bands) and valence bands in the range of $k \in [0, k_{\max}]$. For ZnO, its energy band structure along the Γ-M direction has been well studied as illustrated in Fig. 13.3a. One may find that the energy gap ΔE between the first conduction band and the top valence band is approximately linearly dependent on k as presented in Fig. 13.3b. Due to the fact that the wave vector of the Bloch electron wave packet has a maximum value $k_{\max}$, which is determined by the amplitude of laser vector potential A_0 from (13.1) if we adopt the initial condition $k(0) = 0$. As a result, the cutoff energy of HHG

$$\Omega_{\text{cutoff}} = \Delta\varepsilon_{k_{\max}} \propto k_{\max} \propto A_0 \propto E_0\lambda \tag{13.3}$$

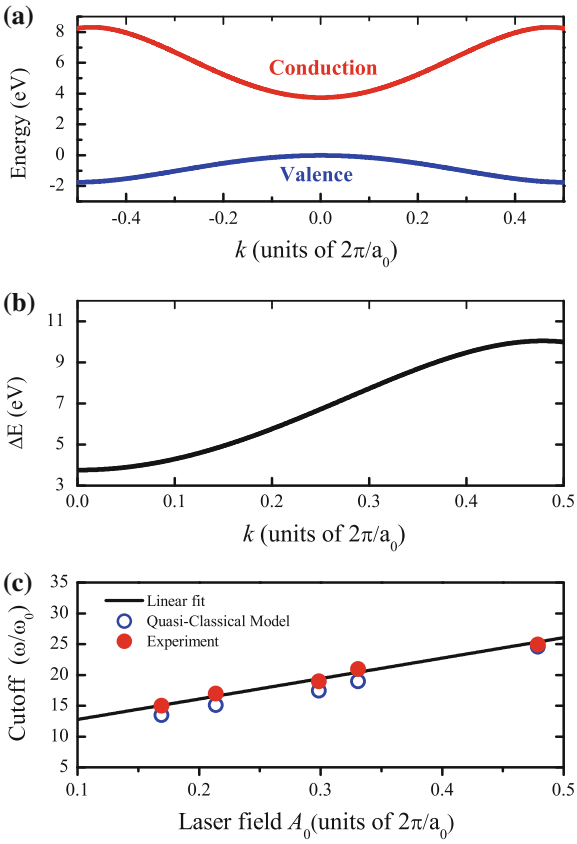

Fig. 13.3 **a** The lowest conduction (red line) and the top valence (blue line) bands of ZnO along the Γ-M direction in the reduced BZ [23]. **b** The band gap between the two bands along the Γ-M direction as a function of wave vector k. **c** Comparison of the cutoff energies of HHG obtained from the experimental measurement [6] and the calculation by the proposed quasi-classical model

From the above analysis, one can conclude that the cutoff energy of HHG induced by interband transtions depends linearly on both the strength and the wavelength of the laser field if the band structure is parabolic.

A comparison of the predicted cutoff energies of HHG to the experimental results [6] is shown in Fig. 13.3c. One can find very good agreement after considering the reflection of lasers from the surface of ZnO. Once the parameters of driving fields and cutoff energies are given, the energy bands can be reconstructed by this model. However, if the band gap between the conduction band and valance band is not linearly dependent on k in other solid materials, the linear cutoff law in HHG will be broken. In addition, if $A_0 > \pi/a_0$, the cutoff energy will be the maximum band gap between the valence and conduction bands, independent on field strength or wavelength in the two-band model [32]. However, if multibands are involved, the cutoff may be extended [36].

Based on the above step-by-step model, we predicted [24] the nonadiabatic redshift of HHG and even-order harmonic generation due to the relaxation of the system by involving multibands. It may stimulate related experimental studies in the future.

13.3 Numerical Methods

To include quantum effects, we developed a numerical method based on the single-active-electron model [18], in which we simulate the laser-crystal interaction in one-dimensional systems with laser polarization along the periodic potentials. The time-dependent Hamiltonian in the length gauge is written as

$$\hat{H}(t) = \hat{H}_0 + xE(t), \tag{13.4}$$

where $\hat{H}_0 = \frac{\hat{p}^2}{2} + V(x)$, $\hat{p}$ is the momentum operator, x is the coordinate, and $V(x)$ is the periodic potential of the lattice. Here we choose the Mathieu-type periodic potential [33, 34]. The specific expression is $V(x) = -V_0[1 + \cos(2\pi x/a_0)]$, with $V_0 = 0.37$ a.u., and lattice constant $a_0 = 8$ a.u. It mimics the band structure of AlN [33].

In absence of the external laser fields, the time-independent Schrödinger equation (TIDSE) can be written as

$$H_0\phi_n(x) = E_n\phi_n(x). \tag{13.5}$$

We use B-spline basis [35] to expand the field-free eigen-wave function,

$$\phi_n(x) = \sum_{i=1}^{N_{\max}} c_i B_i(x). \tag{13.6}$$

Substituting (13.6) into (13.5), one can obtain a matrix equation in the following form:

$$HC = ESC, \tag{13.7}$$

where C is the column coefficient matrix, H and S are $N \times N$ square Hamiltonian and overlap matrices, respectively. The H and S matrix elements are

$$H_{ji} = \int B_j(x)\left[-\frac{1}{2}\frac{d^2}{dx^2} + V(x)\right]B_i(x)dx, \tag{13.8}$$

$$S_{ji} = \int B_j(x)B_i(x)dx. \tag{13.9}$$

3600 B-spline functions are used to calculate the eigenvalues of the system in the spacial range $[-244, 244]$ a.u. The energy bands are obtained and illustrated in Fig. 13.4. As is well known, the Bloch-state basis is widely utilized in periodic systems. It can be further expanded in plane waves. All calculations based on this basis can be carried out in the wavevector k space, and the integral of laser-induced currents involves the whole first BZ. In contrast, here we use B-spline functions in the coordinate space to perform all the calculations, in which the periodic property

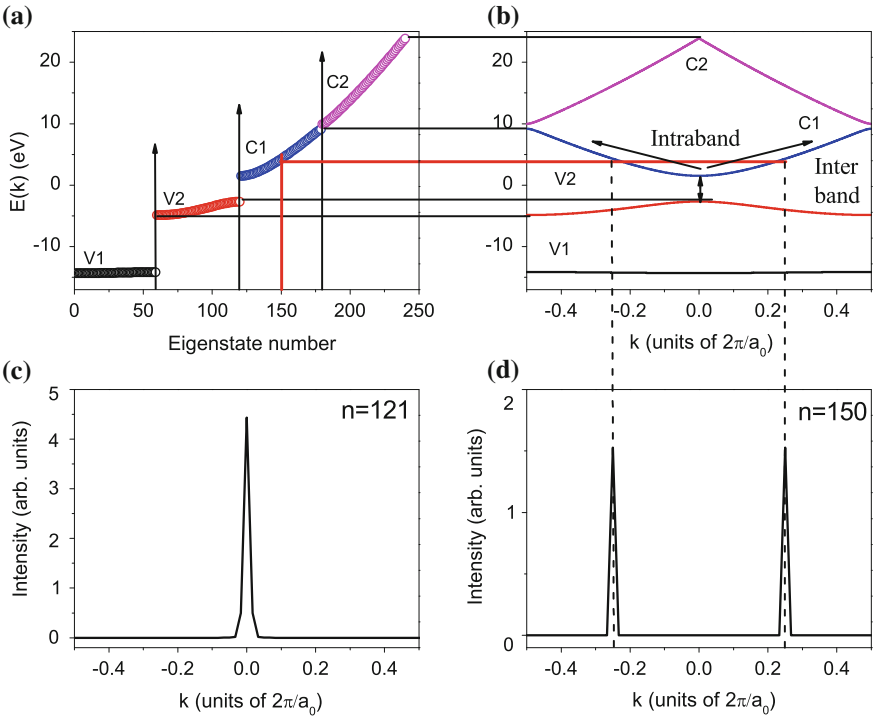

Fig. 13.4 Band structures calculated by B-spline-basis method (**a**) compared to results obtained by Bloch states expansion (**b**) [18]. Fourier transformation (FT) of the initial state in our TDSE calculations and FT of the 150th eigenstate are presented in (**c**) and (**d**), respectively

is not explicitly indicated in the basis. However, we will show that the results in the wavevector k space and the real space are equivalent. To demonstrate this equality, we present the energy bands calculated by the Bloch-state expansion in k space, and by the B-spline basis method described above. We may find that the number of energy bands, the width of each band, and band gaps agree perfectly with each other in Fig. 13.4a, b. In our proposed coordinate-space method, the wavevector is not explicitly shown in the wavefunction. However, it can be directly extracted by Fourier transformation (FT) of the eigenfunction in the real space to the vector space. We choose the state on top of the V2 band and the 150th eigenstate and transform them from coordinate space to wavevector space by FT. We can see in Fig. 13.4c, d that the transformed wavevectors agree well with the wavevectors in Bloch-state expansion [34]. It is worth noting that the wavevectors obtained by FT exist in all extended BZs separated by $2\pi/a_0$. It means that the electron dynamics in real space automatically account for the electron motion in extended BZs. It may be used to investigate the multichannel HHG at the edge of BZ and the Landau-Zenner-Stückelberg interference [36].

For the time-dependent wavefuntion in laser fields, we use the Crank-Nicolson (CN) method [37] to numerically calculate the evolution of the time-dependent coefficients $C(t)$.

$$C(t+\triangle t) = \frac{S - iH(t+\triangle t/2)\triangle t/2}{S + iH(t+\triangle t/2)\triangle t/2} C(t). \tag{13.10}$$

After obtaining the wavefunction at an arbitrary time, the time-dependent laser-induced currents can be calculated by

$$j(t) = -\langle \psi(t)|\hat{p}|\psi(t)\rangle. \tag{13.11}$$

We calculate the HHG spectra by using the above method in real space [18]. An absorbing function is used at the boundaries to remove artificial reflection. Its effect is negligible if the range of the real space is big enough. A comparison to the results by Bloch-state basis in the momentum space is shown in Fig. 13.5. One can find very good agreement between them, suggesting the validity of our methods. One can also see the double-plateau structure, agreeing well with the experimental measurements [12] and our prediction in the step-by-step model [22–24] in the above section. We also calculated the HHG cutoff energy dependence on E_0 and λ. From Fig. 13.6, the cutoff energy of HHG in both the first and the second plateau linearly depends on $E\lambda$, in accord with the step-by-step model [22, 23].

There are a number of bands in solid crystals, we have to extract the contribution of each band to HHG from the eigensystem. The band group can be distinguished easily because of the energy discontinuity as illustrated in Fig. 13.4. For instance, the state number 0–59 corresponds to band V1, the state number 60–121 corresponds

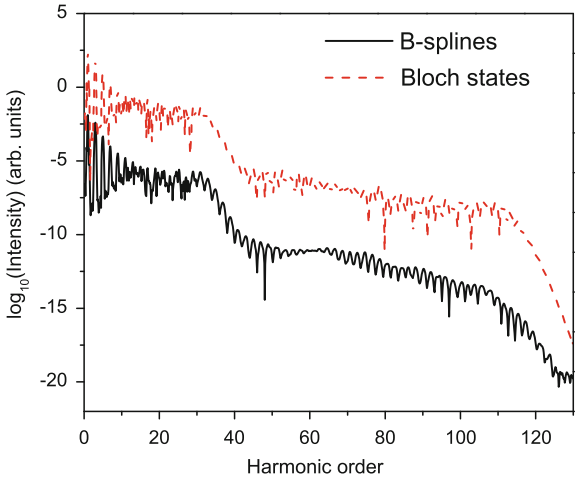

Fig. 13.5 Harmonic spectra of laser-induced currents [18] calculated by Bloch-state basis (dashed line) and B-spline basis (solid line), respectively. For clarity, the latter is down shifted. The laser parameters: $I = 8.087 \times 10^{11}\,\mathrm{W/cm^2}$, and $\lambda = 3.2\,\mu\mathrm{m}$

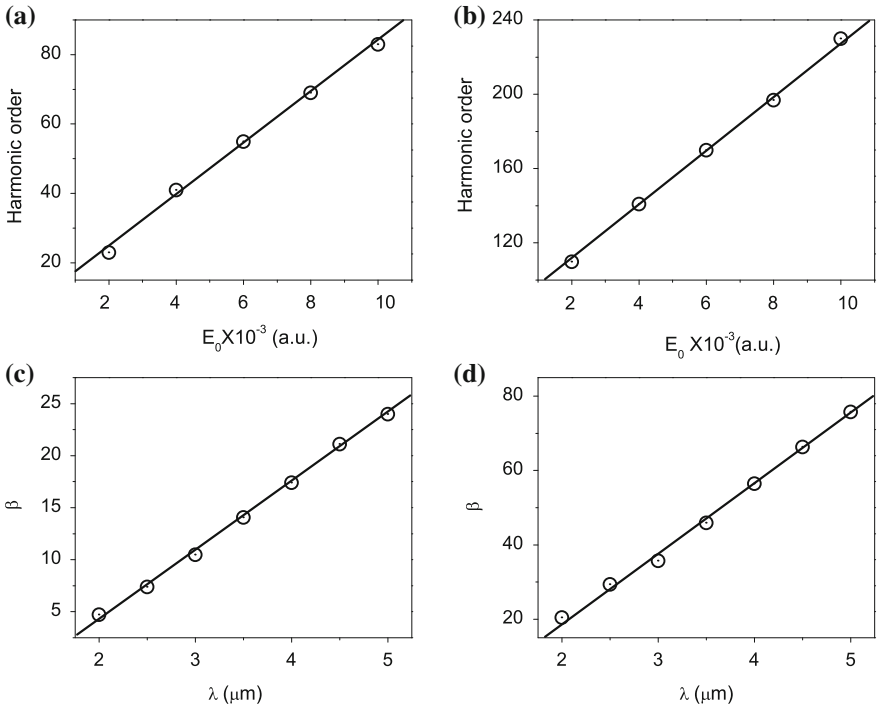

Fig. 13.6 The cutoff energy of the first (**a**, **c**) and second (**b**, **d**) plateaus in HHG as a function of the laser field strength E_0 and wavelength λ. β is in unit of Bloch frequency [18]

to band V2. The interband contribution comes from transitions between states in different bands, while the intraband contribution to the current involves transitions between states in the same band.

The time-dependent wave function can be projected on the eigenstates

$$|\psi(t)\rangle = \sum_b \sum_n a_n^b(t)|\phi_n^b\rangle, \tag{13.12}$$

where b is the band index.

By substituting (13.12) into (13.11), the total photoelectron current can be written as

$$j(t) = -\sum_{bb'} \sum_{nn'} \langle\psi(t)|\phi_n^b\rangle\langle\phi_n^b|\hat{p}|\phi_{n'}^{b'}\rangle\langle\phi_{n'}^{b'}|\psi(t)\rangle. \tag{13.13}$$

There are many eigenstates in each band, so the interband currents involving transitions between different states in different bands can be written as

$$j_{\text{inter}} = -\sum_{\substack{bb' \\ b\neq b'}}\sum_{nn'}\langle\psi(t)|\phi_n^b\rangle\langle\phi_n^b|\hat{p}|\phi_{n'}^{b'}\rangle\langle\phi_{n'}^{b'}|\psi(t)\rangle. \tag{13.14}$$

The intraband currents involving transitions between states in the same band can be written as

$$j_{\text{intra}} = -\sum_{b}\sum_{nn'}\langle\psi(t)|\phi_n^b\rangle\langle\phi_n^b|\hat{p}|\phi_{n'}^{b}\rangle\langle\phi_{n'}^{b}|\psi(t)\rangle. \tag{13.15}$$

We divided the HHG spectra in Fig. 13.5 into intra- and interband contributions as illustrated in Fig. 13.7. A comparison to the results by time-dependent Houston states in the velocity gauge [34] is presented. Very good agreement is achieved. One can find that the intraband transitions dominate the HHG below the bandgap, while the interband transitions contribute the most for harmonics above the bandgap. When their contributions are comparable at some special laser conditions, the intra- and interband currents may interfere with each other [38].

Many numerical methods for HHG in solids are in the momentum space based on Bloch's theorem. However, the total potential in (13.4) is not periodic by including the external laser fields. Our method in the coordinate space is not restricted. It is universal and naturally applicable for the non-periodic fields, even complex fields in Sect. 13.5.

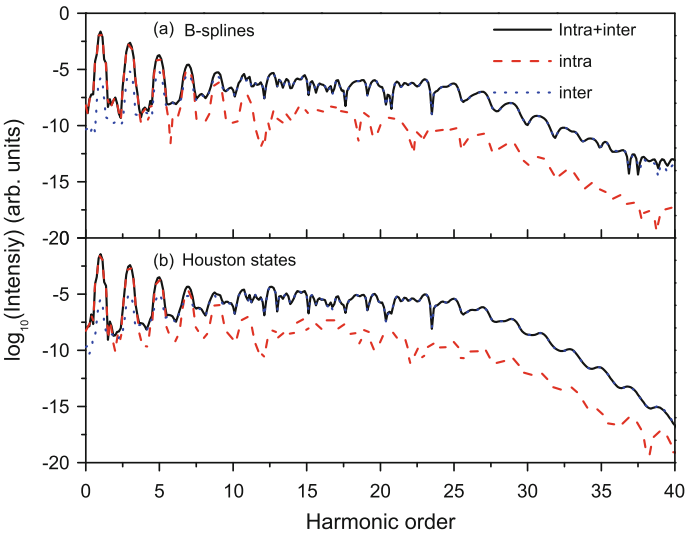

Fig. 13.7 Intraband and interband HHG obtained by B-spline and Houston basis method [18]. The band gap is 4.2 eV. The laser intensity is $I = 4.5 \times 10^{11}\,\text{W/cm}^2$ and the other parameters are the same as those in Fig. 13.5

13.4 Intra- and Interband Transitions in Real Space

The intra- and interband transitions are always described in the momentum space as illustrated in Fig. 13.1. In this section, we provide an alternative physical picture to describe the transitions in real space [21].

The time-dependent wavepacket can be written as [39, 40]

$$\psi_k^n(x,t) = e^{i[kx-\varepsilon_n(k)t]}u_k^n(x), \tag{13.16}$$

where $\varepsilon_n(k)$ is the eigen-energy, and $u_k^n(x)$ is a periodic function with period in a_0 (the lattice constant). In band n, the Bloch wavepacket with a given central wavevector k_0 can be a superposition of wavefunctions in a range of Δk near k_0 in the same band. It can be written as

$$\Psi_{k_0}^n(x,t) = \frac{1}{\Delta k}\int_{k_0-\frac{\Delta k}{2}}^{k_0+\frac{\Delta k}{2}} u_k^n(x)e^{i[kx-\varepsilon_n(k)t]}dk. \tag{13.17}$$

The Taylor series expansion of $\varepsilon_n(k)$ near the central vector k_0 can be written as

$$\varepsilon_n(k) = \varepsilon_n(k_0) + [\nabla_k\varepsilon_n(k)]_{k_0}\cdot\delta k + \cdots. \tag{13.18}$$

The change of amplitude modulation factor $u_k^n(x)$ is slow with k. So the (13.17) can be rewritten in the following form as

$$\Psi_{k_0}^n(x,t) \approx \frac{u_{k_0}^n(x)}{\Delta k}e^{i[k_0x-\varepsilon_n(k_0)t]}\int_{-\frac{\Delta k}{2}}^{\frac{\Delta k}{2}} e^{i[\delta k\cdot(x-[\nabla_k\varepsilon_n(k)]_{k_0}t)]}d(\delta k), \tag{13.19}$$

Finally, we come to

$$\Psi_{k_0}^n(x,t) \approx \psi_{k_0}^n(x,t)\frac{\sin\frac{\Delta k}{2}\zeta}{\frac{\Delta k}{2}\zeta} = \psi_{k_0}^n(x,t)\Phi(x,t), \tag{13.20}$$

where $\zeta = x - (\frac{\partial\varepsilon_n(k)}{\partial k})_{k_0}t$. The wavefunction can be divided into a product of two parts naturally. The probability of finding electrons in coordinate space is defined by

$$|\Psi_{k_0}^n(x,t)|^2 = |\psi_{k_0}^n(x,t)|^2|\Phi(x,t)|^2. \tag{13.21}$$

It indicates that the electronic probability is the modulus square of the periodic lattices function ($|\psi_{k_0}^n(x,t)|^2$) multiplied by the envelope function ($|\Phi(x,t)|^2$). The envelope includes the information of the derivative of energy bands.

We use the numerical method introduced in the above section to solve the time-dependent Schrödinger equation (TDSE) in the coordinate space [18]. We choose an initial wavefunction in the valence band which is superposed by the Δk Bloch eigenstates near $k_0 = 0$ [34]. After the time-dependent wave function $\Psi_{k_0}^n(x,t)$ at

an arbitrary time is obtained, one can divide the laser-induced currents into two contributions according to (13.20). It can be written as

$$j_{\text{phase}}(t) = \frac{i}{2}\sum_{s=1}^{N}\int_{x_s}^{x_{s+1}} [\psi_{k_0}^{n^*}(x,t)\frac{\partial}{\partial x}\psi_{k_0}^{n}(x,t) - \psi_{k_0}^{n}(x,t)\frac{\partial}{\partial x}\psi_{k_0}^{n^*}(x,t)]dx \tag{13.22}$$

and

$$j_{\text{group}}(t) = \frac{i}{2}\int [\Phi^{*}(x,t)\frac{\partial}{\partial x}\Phi(x,t) - \Phi(x,t)\frac{\partial}{\partial x}\Phi^{*}(x,t)]dx, \tag{13.23}$$

where N is the index of the lattice site, and x_s are the coordinates of the periodic lattice. Equations (13.22) and (13.23) indicate that the above two nonlinear photoelectron currents describe the Bloch wavepacket moving respectively at phase and group velocities in the laser fields. The current j_{phase} is a sum of the electron polarization between each two neighboring lattice sites, which is illustrated in the inset of the upper panel in the Fig. 13.8b. The HHG intensity $|j(\omega)|^2$ is proportional to the modulus square of Fourier transform of the time-dependent currents in (13.22) and (13.23).

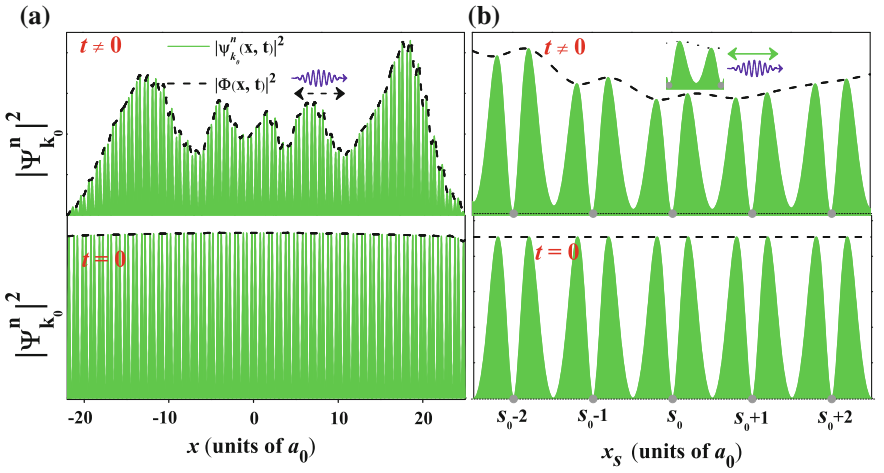

Fig. 13.8 Schematic of the evolution process of time-dependent electron wavepacket in a periodic lattice crystal [21]. The lower panel (**a**) shows the distribution of the initial wavepacket with k_0 = 0 at the top of the valence band V_2, while the upper panel (**a**) illustrates a snapshot of the electron wavepacket driven by the laser fields. The envelope ($|\Phi(x,t)|^2$) function is shown by the dashed line, while the fine structure term ($|\psi_n^{k_0}(x,t)|^2$) is filled by green color. Panel (**b**) illustrates the details of the wavepacket. The atomic sites are shown by gray circles at the bottom of the figure. The polarization of the electron wavepacket between neighboring atomic sites gives rise to the emission of interband HHG, while the back and forth global oscillation of the wavepacket leads to the emission of intraband HHG

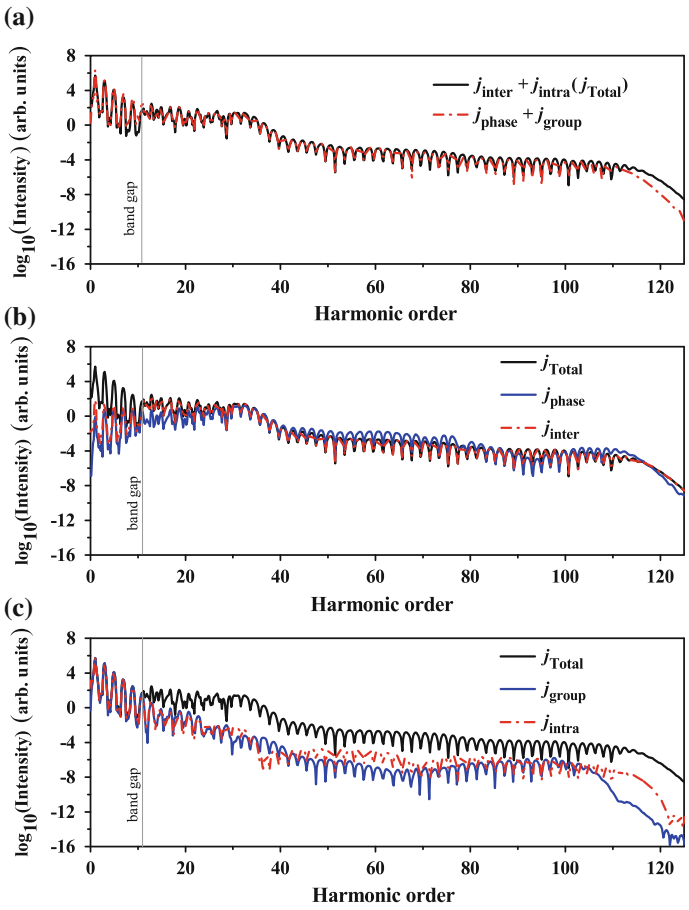

Fig. 13.9 Comparison of HHG spectra obtained by different models [18–21]. **a** Comparison of HHG obtained by $j_{\text{phase}} + j_{\text{group}}$ and $j_{\text{inter}} + j_{\text{intra}}$. **b** Comparison of HHG obtained by j_{phase} and j_{inter}. **c** Comparison of HHG obtained by j_{group} and j_{intra}. The driving laser pulse parameters: $I = 0.87\,\text{TW/cm}^2$, and $\lambda = 3.2\,\mu\text{m}$ [21]

The results are shown in Fig. 13.9. In Fig. 13.9a, one can find that the total HHG spectra obtained by $j_{\text{phase}} + j_{\text{group}}$ agree with that by $j_{\text{inter}} + j_{\text{intra}}$. We also compare the HHG spectra obtained by j_{phase} and j_{inter} in Fig. 13.9b and by j_{group} and j_{intra} in Fig. 13.9c, respectively. For harmonics below the bandgap, the contributions from j_{group} and j_{intra} agree with each other and are dominant in the total spectra. While the harmonics above the band gap are mainly from the contributions by j_{phase} or j_{inter}. One can conclude that the intraband and interband transitions in the momentum space correspond to the electron wavepackets in the real space moving at the group and phase velocities, respectively. The laser intensity, wavelength, CEP, chirp, and other

parameters will definitely change the relative contributions between the intra- and interband transitions [21].

13.5 HHG in Inhomogeneous Fields

Recently, a new technique, namely the spatially inhomogeneous field (based on plasmonic enhancement induced by bow-tie nanostructures), has attracted much attention both in experiments and theories [41–55]. It has been used to assist the enhancement of HHG in atoms and molecules. Compared to the homogeneous external field, the electron trajectories are greatly changed in the inhomogeneous fields. This alternative technique provides us an efficient way to enhance the effective intensity of the input laser pulses by almost two orders. It is well known that the HHG from solid materials suffers from the very low damage-threshold laser intensity. This plasmon-enhanced scheme by growing nano-structure array on the semiconductor substrate as illustrated in Fig. 13.10 can be employed to overcome the shortage [19].

Here we study HHG in the periodic systems interacting with a mid-infrared laser pulse. The peak intensity is $I = 8.774 \times 10^{11}\,\mathrm{W/cm^2}$, and the wavelength of the driving laser pulse is $\lambda = 3.2\,\mu\mathrm{m}$. As described in [43], an additional interaction term in (13.4) induced by the bow-tie structure is approximated as $\varepsilon x^2 E(t)$ (similar to Taylor expansion). ε in unit of length inverse is a parameter describing the inhomogeneity. It can be tuned by changing the distance between the bow-tie structure or their shape. Its value can be obtained by FDTD simulations [55]. The laser intensity used in this work is low, and the choice of the numerical values of ε is rationalized for the system we are treating here. We present the harmonic spectra in the homogeneous and in the case of the inhomogeneous fields with different inhomogeneity parameters ε in Fig. 13.11a. The double-plateau structure in the harmonic spectra appears in both the homogeneous field and the inhomogeneous field. However, with a small $\varepsilon = 0.0005$ in the inhomogeneous fields, the intensity of the second HHG plateau shows two-three orders enhancement compared with the case of the homogeneous field. In order to identify the physics behind the enhancement in the harmonic

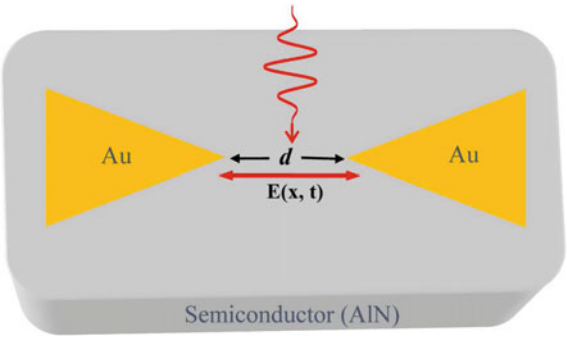

Fig. 13.10 Schematic illustration of plasmon-enhanced harmonic generation by using bow-tie nanostructure elements growing on the substrate of semiconductors [19]. The incident direction of the laser pulses is perpendicular to the semiconductor substrate

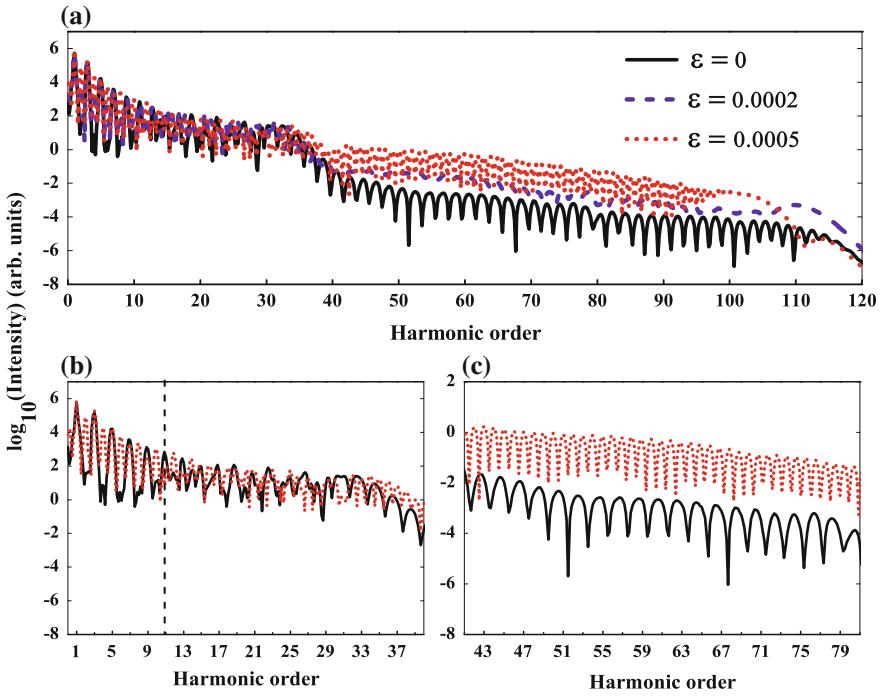

Fig. 13.11 Comparison of HHG spectra obtained in homogeneous (solid line) and inhomogeneous fields. The inhomogeneous parameters are $\varepsilon = 0.0002$ (dashed curve) and $\varepsilon = 0.0005$ (red dotted curve), respectively. **a** HHG in the full range. The first and second HHG plateaus with $\varepsilon = 0.0005$ are shown in (**b**) and (**c**), respectively. The vertical dashed line represents the minimum bandgap. The laser parameters are: $I = 8.77 \times 10^{11}$ W/cm^2, $\lambda = 3200$ nm [19]

spectra, we illustrate HHG spectra in the first plateau in Fig. 13.11b, and the second plateau in Fig. 13.11c. Both the even- and odd-order harmonics can be clearly observed in the HHG spectra in the case of inhomogeneous fields. The occurrence of the even-order harmonic generation is due to the fact that the system symmetry is broken. The first few harmonics decay fast, their energies are lower than the band gap. It is similar to the below-threshold harmonics in the gas phase [56], which are in the perturbative regime.

To reveal the mechanism of the enhancement of HHG, we calculated the transition probabilities between the valence and the conduction bands in Fig. 13.12. The spatial-inhomogeneity-induced transition probabilities can be described by $|\langle\phi_{n_0}|x^2|\phi_n\rangle|^2$, in which n_0 is the initial valence band state and n stands for the conduction band states. In the case of homogeneous field (solid curve), one can find two minima of transition probabilities at the energy about 10 and 24 eV, which correspond to the two band gaps in Fig. 13.4a, b. The total transition probability in the first conduction band (energy below 10 eV) changes little, while a one-two orders enhancement of transition probability in the conduction bands C2 and C3 (energy range from 10 to

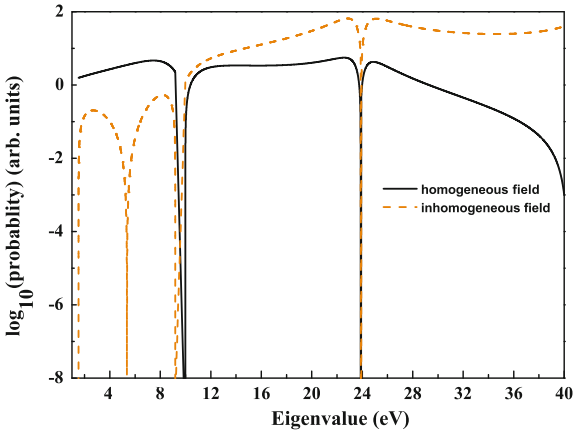

Fig. 13.12 Transitional probabilities to conduction bands calculated by $|\langle\phi_{n_0}|\hat{x}|\phi_n\rangle|^2$ (solid curve) for homogeneous field and the term $|\langle\phi_{n_0}|x^2|\phi_n\rangle|^2$ (dashed curve) for spatial inhomogeneous field [19]

40 eV) can be obtained due to the effect of spatial inhomogeneity. This provides us a deep physical insight into the obvious enhancement of HHG intensity in the second plateau.

The plasmon-enhanced HHG from solids have been experimentally studied recently [29, 31]. One order enhancement of low-order harmonics has been achieved. Our results suggest that this scheme is applicable to enhance the higher order harmonics by involving higher conduction bands. Doped nanostructures are also proposed to enhance the HHG yields [30].

13.6 Summary

We introduced a step-by-step model by combining intraband oscillation and interband transitions of electron wavepacket to explain the experimentally measured HHG spectra. This model can interpret the linear HHG cutoff energy dependence on the laser field strength E_0. This model also predicts that the maximum HHG photon energy should also linearly depend on the wavelength of the lasers, provided that the band structure of the solid material is parabolic. The multiple bands involved in the HHG processes lead to the multiplateau structure of HHG measured experimentally. We also introduced a numerical method for solving TDSE in real space to simulate the electron dynamics in HHG. Although it is very simple, it reproduced most of the novel features of HHG from solids. We studied the intra- and interband transitions in real space. It is found that they correspond to electron wavepackets moving at group and phase velocities, respectively. We also studied the mechanisms of plasmon-enhanced HHG by using nano structures. It may increase the efficiency of HHG in solids.

Acknowledgements The authors thank Zhong Guan, Xiao-Xin Zhou, Hui-Hui Yang, Cheng Gong, Tian-Jiao Shao, Ling-Jie Lv and Ming-Hu Yuan very much for valuable discussions. This work is supported by the National Natural Science Foundation of China (NSFC) (Grants No. 21501055, and No. 11674363), and NSFC-FRQNT Exchange Program (Grant No.11811520120).

References

1. N.H. Burnett, H.A. Baldis, M.C. Richardson, G.D. Enright, Appl. Phys. Lett. **31**, 172 (1977)
2. A. McPherson, G. Gibson, H. Jara, U. Johann, T.S. Luk, I.A. McIntyre, K. Boyer, C.K. Rhodes, J. Opt. Soc. Am. B **4**, 595 (1987)
3. F. Krausz, M. Ivanov, Rev. Mod. Phys. **81**, 163 (2009)
4. L.-Y. Peng, W.-C. Jiang, J.-W. Geng, W.-H. Xiong, Q. Gong, Phys. Rep. **575**, 1 (2015)
5. P.B. Corkum, Phys. Rev. Lett. **71**, 1994 (1993)
6. S. Ghimire, A.D. DiChiara, E. Sistrunk, P. Agostini, L.F. DiMauro, D.A. Reis, Nat. Phys. **7**, 138 (2011)
7. K.F. Lee, X. Ding, T.J. Hammond, M.E. Fermann, G. Vampa, P.B. Corkum, Opt. Lett. **42**, 1113 (2017)
8. U. Huttner, M. Kira, S.W. Koch, Laser Photonics Rev. **11**, 1700049 (2017)
9. O. Schubert, M. Hohenleutner, F. Langer, B. Urbanek, C. Lange, U. Huttner, D. Golde, T. Meier, M. Kira, S.W. Koch, R. Huber, Nature Photonics **8**, 119 (2014)
10. T.T. Luu, M. Garg, SYu. Kruchinin, A. Moulet, MTh Hassan, E. Goulielmakis, Nature **521**, 498 (2015)
11. G. Vampa, T.J. Hammond, N. Thiré, B.E. Schmidt, F. Légaré, C.R. McDonald, T. Brabec, D.D. Klug, P.B. Corkum, Phys. Rev. Lett. **115**, 193603 (2015)
12. G. Ndabashimiye, S. Ghimire, M. Wu, D.A. Browne, K.J. Schafer, M.B. Gaarde, D.A. Reis, Nature **534**, 520 (2016)
13. H. Liu, Y. Li, Y.S. You, S. Ghimire, T.F. Heinz, D.A. Reis, Nat. Phys. **13**, 262 (2017)
14. C. Yu, X. Zhang, S. Jiang, X. Cao, G. Yuan, T. Wu, L. Bai, R. Lu, Phys. Rev. A **94**, 013846 (2016)
15. C. Liu, Y. Zheng, Z. Zeng, R. Li, Phys. Rev. A **93**, 043806 (2016)
16. K.A. Pronin, A.D. Bandrauk, A.A. Ovchinnikov, Phys. Rev. B **50**, R3473 (1994)
17. K.A. Pronin, A.D. Bandrauk, Phys. Rev. Lett. **97**, 020602 (2006)
18. Z. Guan, X.X. Zhou, X.B. Bian, Phys. Rev. A. **93**, 033852 (2016)
19. T.Y. Du, Z. Guan, X.X. Zhou, X.B. Bian, Phys. Rev. A **94**, 023419 (2016)
20. G. Vampa, C.R. McDonald, G. Orlando, P.B. Corkum, T. Brabec, Phys. Rev. B **91**, 064302 (2015)
21. T.Y. Du, X.H. Huang, X.B. Bian, Phys. Rev. A **97**, 013403 (2018)
22. T. Y. Du, X.B. Bian (2016), arXiv:1606.06433
23. T.Y. Du, X.B. Bian, Opt. Express **25**, 151 (2017)
24. G.R. Jia, X.H. Huang, X.B. Bian, Opt. Express **25**, 23654 (2017)
25. M. Wu, D.A. Browne, K.J. Schafer, M.B. Gaarde, Phys. Rev. A **94**(6), 063403 (2016)
26. T. Ikemachi, Y. Shinohara, T. Sato, J. Yumoto, M. Kuwata-Gonokami, K.L. Ishikawa, Phys. Rev. A **95**(4), 043416 (2017)
27. X. Liu, X. Zhu, P. Lan, X. Zhang, D. Wang, Q. Zhang, P. Lu, Phys. Rev. A **95**, 063419 (2017)
28. J.B. Li, X. Zhang, S.J. Yue, H.M. Wu, B.T. Hu, H.C. Du, Opt. Express **25**, 18603 (2017)
29. G. Vampa, B.G. Ghamsari, S.S. Mousavi, T.J. Hammond, A. Olivieri, E.L. Skrek, A.Y. Naumov, D.M. Villeneuve, A. Staudte, P. Berini, P.B. Corkum, Nat. Phys. **13**, 659 (2017)
30. J.D. Cox, A. Marini, F.J.G.D. Abajo, Nat. Commun. **8**, 14380 (2016)
31. S. Han, H. Kim, Y.W. Kim, Y.-J. Kim, S. Kim, I.-Y. Park, S.-W. Kim, Nat. Commun. **7**, 13105 (2016)
32. Z. Wang et al., Nat. Commun. **8**, 1686 (2017)

33. P.G. Hawkins, M.Y. Ivanov, V.S. Yakovlev, Phys. Rev. A. **91**, 013405 (2015)
34. M. Wu, S. Ghimire, D.A. Reis, K.J. Schafer, M.B. Gaarde, Phys. Rev. A **91**, 043839 (2015)
35. H. Bachau, E. Cormier, P. Decleva, J.E. Hansen, F. Martín, Rep. Prog. Phys. **64**, 1815 (2001)
36. T.Y. Du, D. Tang, X.H. Huang, X.B. Bian, Phys. Rev. A **97**, 043413 (2018)
37. X.B. Bian, Phys. Rev. A **90**, 033403 (2014)
38. X.Q. Wang, Y. Xu, X.H. Huang, X.B. Bian, Phys. Rev. A **98**, 023427 (2018)
39. K. Huang, *Solid State Physics* (Higher Education Press, Beijing, China, 1988)
40. J.M. Ziman, *Principles of the Theory of Solids* (Cambridge University Press, Cambridge, England, 1972)
41. S. Kim, J. Jin, Y.J. Kim, I.Y. Park, Y. Kim, S.W. Kim, Nature **453**, 757 (2008)
42. M. Sivis, M. Duwe, B. Abel, C. Ropers, Nature **485**, 7397 (2012)
43. T. Shaaran, M.F. Ciappina, M. Lewenstein, Phys. Rev. A **87**, 053415 (2013)
44. T. Shaaran, M.F. Ciappina, R. Guichard, J.A. Pérez-Hernández, L. Roso, M. Arnold, T. Siegel, A. Zaïr, M. Lewenstein, Phys. Rev. A **87**, 041402(R) (2013)
45. T. Shaaran, M.F. Ciappina, M. Lewenstein, Phys. Rev. A **86**, 023408 (2012)
46. M.F. Ciappina, T. Shaaran, M. Lewenstein, Ann. Phys. **525**, 97 (2013)
47. M.F. Ciappina, S.S. Acimovic, T. Shaaran, J. Biegert, R. Quidant, M. Lewenstein, Opt. Express **20**, 26261 (2012)
48. I. Yavuz, E.A. Bleda, Z. Altun, T. Topcu, Phys. Rev. A **85**, 013416 (2012)
49. L.X. He, Z. Wang, Y. Li, Q.B. Zhang, P.F. Lan, P.X. Lu, Phys. Rev. A **88**, 053404 (2013)
50. X. Cao, S.C. Jiang, C. Yu, Y.H. Wang, L.H. Bai, R.F. Lu, Opt. Express **22**, 26153 (2014)
51. I.Y. Park, S. Kim, J. Choi, D.H. Lee, Y.J. Kim, M.F. Kling, M.I. Stockman, S.W. Kim, Nature Photon. **5**, 677 (2011)
52. A. Husakou, S.J. Im, J. Herrmann, Phys. Rev. A **83**, 043839 (2011)
53. J.A. Pérez-Hernández, M.F. Ciappina, M. Lewenstein, L. Roso, A. Zaïr, Phys. Rev. Lett. **110**, 053001 (2013)
54. J. Wang, G. Chen, S.Y. Li, D.J. Ding, J.G. Chen, F.M. Guo, Y.J. Yang, Phys. Rev. A **92**, 033848 (2015)
55. M.F. Ciappina et al., Rep. Prog. Phys. **80**, 054401 (2017)
56. W.H. Xiong, J.W. Geng, J.Y. Tang, L.Y. Peng, Q. Gong, Phys. Rev. Lett. **112**, 233001 (2014)

Chapter 14
Extreme States of Matter by Isochoric Heating

Dimitri Batani

Abstract Extreme states of matter, characterized by very high temperatures and pressure, are common in the laboratory and in nature, including laser-produced plasmas, controlled thermonuclear fusion, the interior of planets, brown dwarfs, burning stars, up to supernova explosions. The advent of high-intensity short-pulse lasers offers a new tool for this kind of studies. Extreme states can be created using the "isochoric heating" approach in which matter is rapidly heated by the fast energy deposition from the laser before any significant expansion takes place. Laser beams are unable to penetrate deeply inside matter but the fast electrons produced by laser-matter interaction can be the "carriers" allowing heating in-depth of the target. X-ray imaging and X-ray spectroscopy allow for characterization of the produced states of matter.

14.1 Introduction

Extreme states of matter, characterized by extreme temperature and pressure, are common to many physical situations taking place in the laboratory or in nature. These include laboratory experiments on laser-produced plasmas, controlled thermonuclear fusion, high-energy-density experiments. In nature such states are common in the interior of planets and are useful to describe many astrophysical phenomena from burning stars, to brown dwarfs, up to supernova explosions. In order to provide realistic modeling of such phenomena, or in order to try to achieve the goal of thermonuclear fusion, we need a precise characterization of such states, including data on the equation of state of matter and data on the absorption and emission of radiation (opacities). Therefore we need experiments to create such extreme states in the laboratory and measure their physical properties.

D. Batani (✉)
Université Bordeaux, CNRS, CEA, CELIA, UMR 5107, Talence 33405, France
e-mail: dimitri.batani@u-bordeaux.fr

D. Batani
Department of Plasma Physics, National Research Nuclear University MEPhI, Moscow, Russia

© Springer Nature Switzerland AG 2018

K. Yamanouchi et al. (eds.), *Progress in Ultrafast Intense Laser Science XIV*,
Springer Series in Chemical Physics 118,
https://doi.org/10.1007/978-3-030-03786-4_14

Historically, the first experiments to produce and measure matter in extreme states have been done by dynamical compression of samples by shock waves produced by chemical (or even nuclear) explosions. Starting from the 90s such experiments have been usually replaced by experiments with shock waves produced by ns-lasers, which of course offer a more "practical" laboratory tool. In this approach, an intense laser, of typical duration in the nanosecond range, is focused on the target surface producing laser-ablation and plasma generation. Such hot plasma expands rapidly in vacuum and by conservation of momentum an intense shock is produced and travels inside the material. Such approach has proven to be quite successful and has brought to precise measure of the equation-of-state (EOS) of many materials in the Megabar or multi-Megabar pressure [1–3] range.

These include measurements of iron [4, 5] (the main component of the core of earth-like rocky planets), hydrogen (the main component of giant planets and stars), water [6, 7] and carbon [8, 9] (making up the mantle of giants planets like Uranus and Neptune), but also materials of interested for inertial confinement fusion experiments like brominated plastics [10], foams [11], etc.

The recent advent of high-intensity short-pulse lasers offers a new tool for this kind of studies. Such lasers allow creating extreme states of matter with relatively small systems as compared to the kJ-class lasers needed to drive intense shocks in the ns-regime. The intrinsic advantage is that such lasers are relatively cheaper and easier to manage, which means that they are much more common and available also to university laboratories.

Short-pulse lasers can be used to create extreme states of matter in two different ways. The first is the so-called "isochoric heating" approach, which will be described in this chapter. Here matter is rapidly heated by the fast energy deposition from the laser before any significant expansion takes place. Clearly the challenge in this approach is the real capability of preforming significant measurements on a very short time-scale, before matter is set in motion by hydrodynamics. Luckily, X-ray diagnostics are in a way "self-gated" since X-ray emission takes mainly place when matter is hot and dense, or when fast electrons are present (see later). Hence they can be used to get relevant information on the created states of matter at very early times.

The second approach relies on developments at longer time-scales, i.e. on the fact that following energy deposition from the laser, strong temperature and pressure gradient are created inside matter, quickly bringing to the creation of shock waves. This approach is in a way "more similar" to the standard use of laser-driven shock waves with however the important difference that, due to the short duration of the laser pulse, now the shock pressure is not maintained and the shock immediately becomes a blast wave, i.e. a thin pressure front, which travels in the material gradually losing its strength. This approach is described in the chapter of this book written by K. Jakubowska.

14.2 Principle of Isochoric Heating

Matter can be taken to extreme states by fast delivery of energy. By definition high-energy-density states are obtained for an energy density larger than 0.1 MJ/cm^3 (corresponding to a pressure of 1 Mbar). This corresponds to deposition of $\approx$10 J in a cubic sample of size $\approx$0.5 mm. However, in order to get such "isochoric heating", the deposition of energy must be very fast. This is due to several reasons.

First, hydrodynamic expansion takes place at a velocity corresponding to the sound velocity of the heated material, i.e. is increasing with the square root of the temperature of the sample. Therefore, rapid delivery of energy must take place over a time, which is much shorter than hydro timescale in order to maintain the density. Sometimes, in order to limit the hydro expansion, experiments use "tampered targets" in which a buffer material constraints expansion and keeps the density of an intermediate layer of the material to be studied. The problem of this approach is that the buffer material also absorbs the energy deposited by the laser.

Second, in order to achieve isochoric heating, it is important that the sample is homogeneously heated, i.e. no strong temperature gradients are created inside matter (otherwise one would only get an "average" measurement).

An additional issue is that laser beams are unable to penetrate deeply inside matter. Preplasma is always formed in front of the solid material and the laser penetrates only up to the critical density (of the order of 10^{21} electrons/cm^3). Therefore, an intermediate "carrier" must be used to deposit the energy in depth into the material. Such a carrier is naturally provided by laser-induced secondary emission of particle and radiation. Therefore isochoric heating of matter can be produced by laser-accelerated (relativistic) electrons, by X-rays produced from laser-plasmas, or by proton beams from ultra-high-intensity laser-matter interaction.

In this chapter, we will exclusively focus on the use of fast electrons since indeed this is the approach, which has been more extensively used and reported in the scientific literature. It must be noticed that, in this case, the heating takes place on a very fast time scale since relativistic electrons practically travel at the speed of light. Also they have a large penetration range, allowing the heating of relatively thick samples without creating strong temperature gradients. Finally, an important aspect of these experiments is that the bulk of fast electrons are effectively prevented from escaping the target due to the confinement produced by the huge electrostatic fields that are created by charge separation as soon the some electrons leave the target. This produces multiple "refluxing" of the electrons inside the targets, which further contribute to heating and smoothing of temperature gradients.

14.3 Early Experiments

Early experiments typically used multilayer planar targets with one or more "tracer" layers, which emitted Kα radiation following inner-shell ionization induced by the passage of fast electrons.

In one of such experiments [12] the LULI 100 TW laser system, delivering about 10 J on target at a wavelength $\lambda = 1.06$ microns, with 400 fs pulse duration, was focused at normal incidence onto the target by an f/3 off-axis parabola. The laser intensity on target was 5×10^{17} W/cm^2 and the contrast ratio 1–2 $\times$ 10^7 with a typical 2 ns duration yielding a prepulse intensity of less than a few 10^{11} W/cm^2. The relatively weak prepulse intensity is expected to minimize preplasma formation in front of the target before the arrival of the main pulse. At the intensity of the main laser pulse, the expected hot electron "temperature" was approximately 170 keV following well-known scaling laws [13].

Different kind of multi-layer targets were used in the experiment. The first corresponds to millimeter-size targets (typically 2–3 mm-size square) comprising three layers: Al (d μm)-Cu (20 μm)-Al (20 μm). The front ("propagation") layer, of variable thickness «d», permits both to characterize the fast electron beam, and change the conditions reached in the last two layers. The second kind of targets were small "mass-limited" targets, consisting of square double-layer foils Cu (20 μm)-Al (20 μm) of varying transverse sizes (from 250 μm to 1 mm-wide). These targets were irradiated by the laser on the Cu side.

Several diagnostics have been simultaneously implemented. In particular, a spherical Bragg crystal located at 30° with respect to the target normal at the rear side, produces a monochromatic 2D image of the Cu-Kα emission (8.04 keV). In addition a conical Bragg crystal spectrometer recorded Cu-Kα and Al-Kα emission respectively in the 5th order and the 1st order. A schematic experimental set-up is shown in Fig. 14.1.

The results shown in Fig. 14.2 represent Kα images obtained with the spherical Bragg crystal, for different sizes of the irradiated target. In all cases, we see a bright spot corresponding to the focusing spot of the laser from which fast electrons originate. In addition we see a background diffused emission which corresponds to the Kα emission from fast electron circulating inside the targets. As expected, the intensity of this Kα signal decreases with target surface. However the total signal integrated over the whole target surface is approximately constant corresponding to the fact that fast electrons make the same number of collision with target atoms before completely losing their energy.

Figure 14.3 shows the spectrum obtained from a multilayered target showing the Kα emission from Al and Cu. We notice that the "cold" Kα line is accompanied by an emission line at higher energy. This corresponds to "hot" or "shifted" Kα emission from ionized Al. Indeed as ionization increases, the fewer electrons in the ions are less effective in screening the nuclear charge. This results in "shrinking" of the energy level of the ion. The Kα emitted from ions then shifts to higher and higher energies as the ionization degree increases. With thermal ionization, this results in a diagnostics

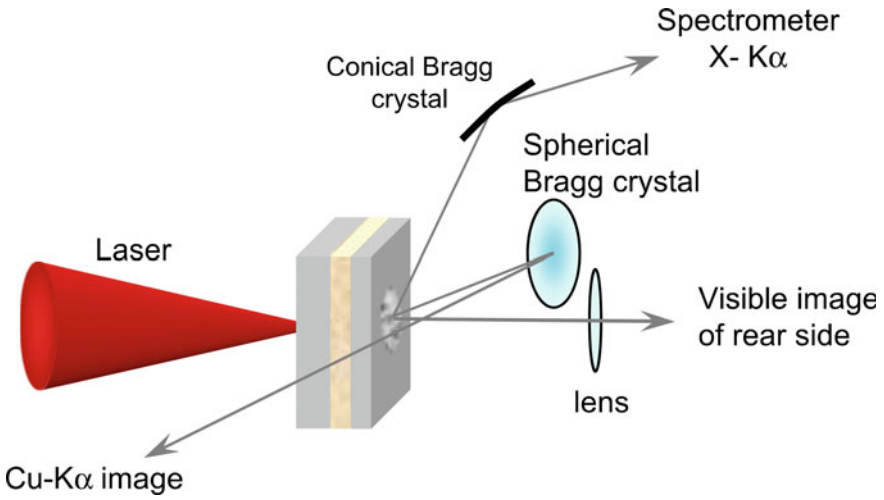

Fig. 14.1 Schematic experimental set-up

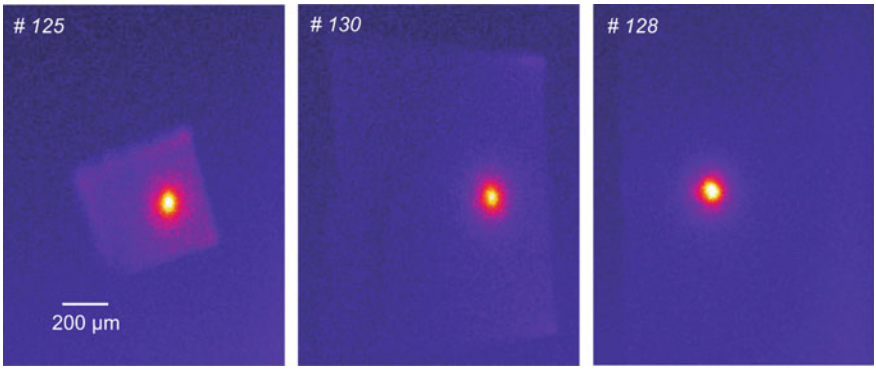

Fig. 14.2 Cu-Kα (8.04 keV) images of mass-limited targets as measured from the rear side at 30° from normal. Respective sizes: #125 (450 × 390 mm^2), #130 (700 × 910 mm^2), #128 (2100 × 900 mm^2). The on-target laser energy was kept constant within 10%. The same color scale is used in all images

of temperature (hot Kα spectroscopy [14]). In the case of Al, the first 3 ionization stages are very close and the respective Kα lines superimpose. Instead the Kα line from Al^{5+} is clearly visible (this line originates from inner-shell ionization of the ion Al^{4+} following collision with fast electrons). Figure 14.4 shows the populations of the different ion stages for solid density Al as a function of temperature. In the case of the reported experiment, the presence of the cold Kα and the Al^{5+} Kα lines but the absence of Al^{6+} Kα above noise level implies that the back Al layer is heated to temperatures of the order of 10 eV.

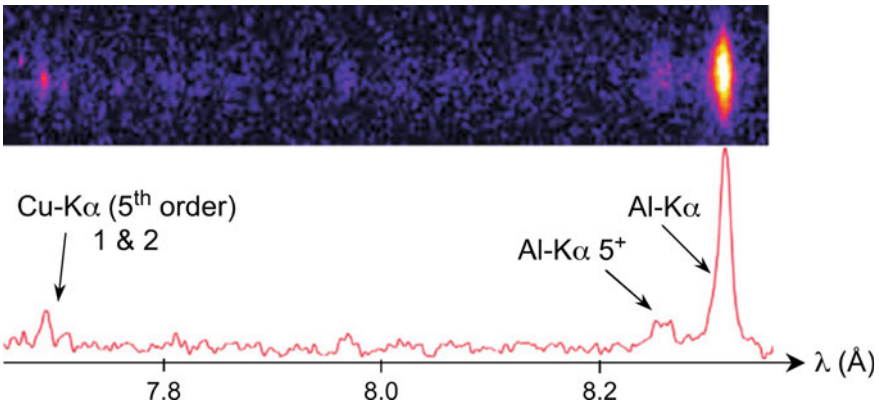

Fig. 14.3 X-ray spectrum recorded on a DEF film from the rear side of the target at 45° to the equatorial plan. It zooms in on the 7.65–8.4 Å range, so as to highlight the Al and Cu lines. This typical spectrum exhibits the Cu-Kα doublet (7.7–7.72 Å, 5th order) and the Al-Kα lines (8.269–8.3396 Å, 1st order). This spectrum corresponds to the shot #125 (charge-insulated, 20 μm Cu/20 μm Al target)

Fig. 14.4 Ion populations in solid Al versus temperature, calculated with the UBCAM atomic physics code [15]

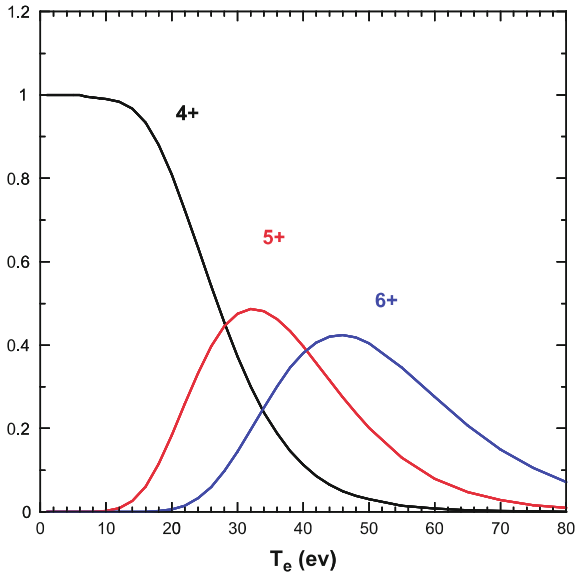

In conclusion, this experiment showed that matter in extremes states characterized by solid-state density and T ≈ 10 eV can be created by the propagation of laser-accelerated fast electron with the target. Since in principle laser absorption should not depend on target size, one could conclude that very high temperatures (a few 100 eV) could be reached by reducing the target size. This was indeed the goal of a following experiment [16], which, however, showed how obtaining isochoric heating

conditions is all but easy. Reducing target size does indeed dramatically increase the target sensitivity to hydrodynamic expansion.

In the experiment, low-Z (C_8H_8) mass limited targets were heated by fast electrons produced in laser matter interaction at ultra-high-intensity. A buried chlorinated plastic thin layer was used as a tracer. The X-ray emission was collected by a high resolution Bragg spectrometer, and the spectral analysis was mainly based on the Cl Heα line and its Li-like satellites. Complementary optical, X-ray, and proton diagnostics have been used to measure the prepulse effects on target (i.e. preplasma formation and target expansion). The target heating of the Cl-doped layer was only produced by fast electron refluxing in the target, being the 10 μm C_8H_8 overcoating thick enough to prevent any possible direct irradiation of the tracer layer even taking into account mass-ablation due to the prepulse.

The experiment has been performed at CEA/CESTA using the 100 TW Alisé Laser Facility. The laser delivered up to 12 J and 1053 nm pulses with 1 ps duration. Pulses were focused on target using a f/3 off axis parabola with an expected mean intensity in the focal spot between 6×10^{17} and 3×10^{18} W/cm^2. The prepulse was 6 ns long growing linearly from the noise to a final contrast ratio of 5×10^{-5} (much better contrast ratios can be obtained nowadays by using non-linear optics techniques in the laser chain or plasma mirrors).

The chlorine X-ray spectrum has been collected by a toroidally bent Bragg quartz crystal spectrometer looking at the target front side and recorded on a back illuminated CCD. The spectrometer was operated in the second order of reflection, giving spectral range from 4.40 to 4.75 Å and recording Cl lines from the "cold" Kα at 4.7286 Å to the Heα at 4.4438 Å (this being reflected at a 41.7° Bragg angle). Figure 14.5 shows the spectrum recorded with a simple PVC target. In this case, the chlorinated target is directly irradiated by the laser giving a very strong thermal emission showing the Heα$_1$ resonance line, the Heα$_2$ line (overlapped to some Li-like satellite lines) and all the Li-like and B-like satellites. The chlorine Kα line at lower energy than the Heα is relatively weaker due to depletion of Cl-atoms, which are directly irradiated, heated and ionized by the laser.

With a multi-layer targets, the Kα line was relatively stronger (Cl atoms are not directly irradiated by the laser). Figure 14.6 shows the experimental data obtained in this case (only the part corresponding to the Heα and satellite lines is shown). The simulation of the X-ray spectrum was performed with a detailed kinetic code taking into account all the possible transition among all different energy levels and collisional radiative equilibrium conditions [17, 18]. Also the presence of fast electrons was taken into account (since they can act as a preferential way to populate high-energy levels and can thus affect the spectrum shape). The "optimal" simulation corresponds to a background electron temperature of 250 eV, an electron density of 10^{21} cm^{-3}, and a fast electron fraction of 0.05%.

These density and temperature conditions do correspond to "extreme states"; i.e. the experiment demonstrated that the fast electrons are suitable to heat up plasmas to a very large temperature, as required to generate high energy density states. However, the electron density is of the order of the laser critical density, i.e. very far from solid density. This shows that the conditions for isochoric heating were not achieved in the

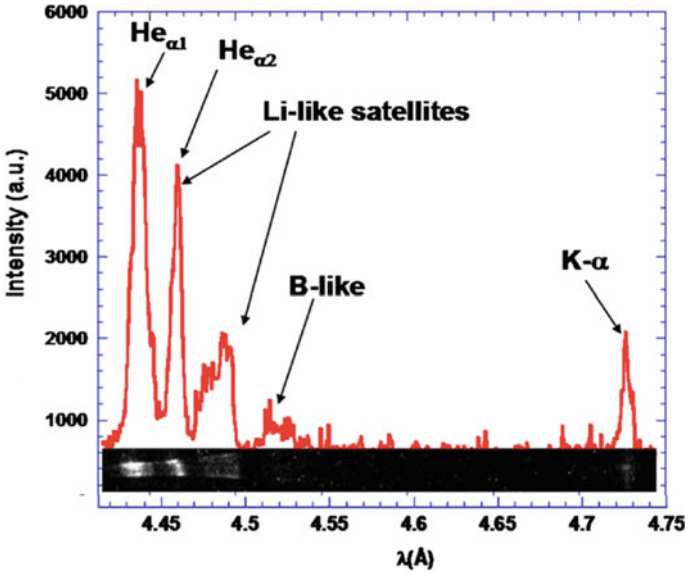

Fig. 14.5 Chlorine high-energy spectrum from the Kα line (right) to the $He\alpha_1$ resonance line (left). The $He\alpha_2$ line is overlapped to some Li-like satellite lines (Bottom: the experimental spectrum as recorded on the X-ray CCD)

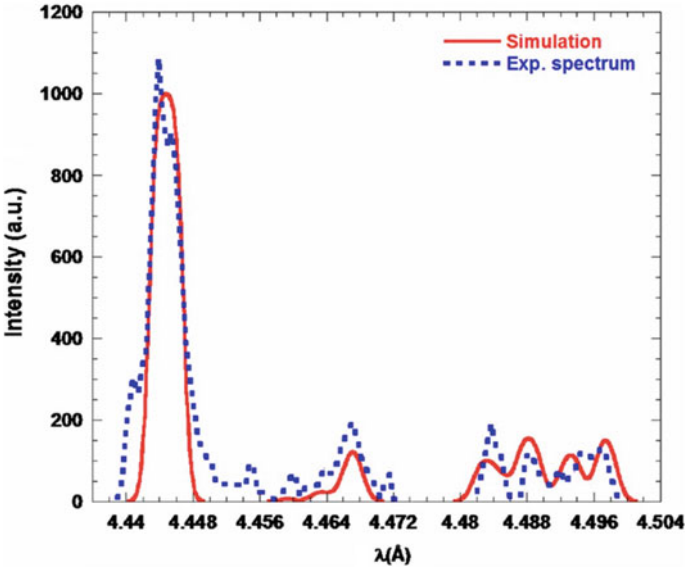

Fig. 14.6 Experimental data (dashed line) and best simulation (solid line) for mass limited target. The simulation corresponds to a background electron temperature of 250 eV, an electron density of 10^{21} cm^{-3}, and a fast electron fraction of 0.05%

present experiment, consistently with the high level of laser prepulse, a result that was un-doubtfully confirmed by other diagnostics (X-ray pin-hole camera and visible interferometry) directly showing a significant target expansion before the arrival of the main pulse on target.

14.4 Recent Experiments

Thin foils targets have proven to be useful to produce extreme states of matter as most of the electrons are confined in the target owing to the large electrostatic fields produced by charge separation along the target's borders. The trapped electrons reflux several times through the target on the ps time scale, which is below the hydrodynamic expansion time, hence producing a soft longitudinal temperature gradient [19].

However, these foil experiments have several drawbacks. The main limitation to this approach arises from the fact that high-intensity short-pulses are always accompanied by a prepulse, generated through the amplification of spontaneous emission (ASE) in the laser main amplifier. As in the previously described experiment, this laser intensity pedestal may have durations of several ns and capable to produce plasma and create shocks that travel in the material, finally inducing a substantial decompression of matter before the arrival of the main pulse. Also, even if refluxing strongly limits the longitudinal temperature gradients, gradients are still important in the radial direction.

A way to overcome, at least partially, such problems has been recently implemented in an experiment with the laser Phelix [20], based on the use of wire targets irradiated by short-pulse high-intensity lasers. There are several advantages in using a wire—target with respect to a thin foil. First, provided it is long enough, the wire releases the constraint upon the laser prepulse. Secondly, the laser heating (up to several keV) occurs over several microns near the critical density surface whereas the relativistic electrons can heat the target along hundreds of microns, in several hundreds of fs, which means they are the only factor governing heating of the target deep along the wire. Thirdly, for a wire radius comparable to the electron source, the radial electrostatic field generated by the charge separation is sufficiently high to confine most of the hot electron population. The energy flux is hence constrained to flow along the wire. By contrast, in the case of planar targets, the electron current density rapidly decreases with target depth because of the natural divergence of the fast electron beam. Hence, the heating of target induced by hot electron propagation rapidly becomes negligible far away from the interaction region. Instead in the wire, a high current density is maintained even at large depths (along hundreds of microns).

Last, unlike for planar targets where matter in extreme states is screened by nearly opaque layers of cold matter, the wire-target offers easy access to diagnostics all along its length. With length comparable or larger than the typical penetration range of the electrons, the energy flow decreases and a temperature gradient is created along the wire, allowing to simultaneously study states at different temperatures. Indeed, while the electric and magnetic field confinement act to reduce the radial temperature

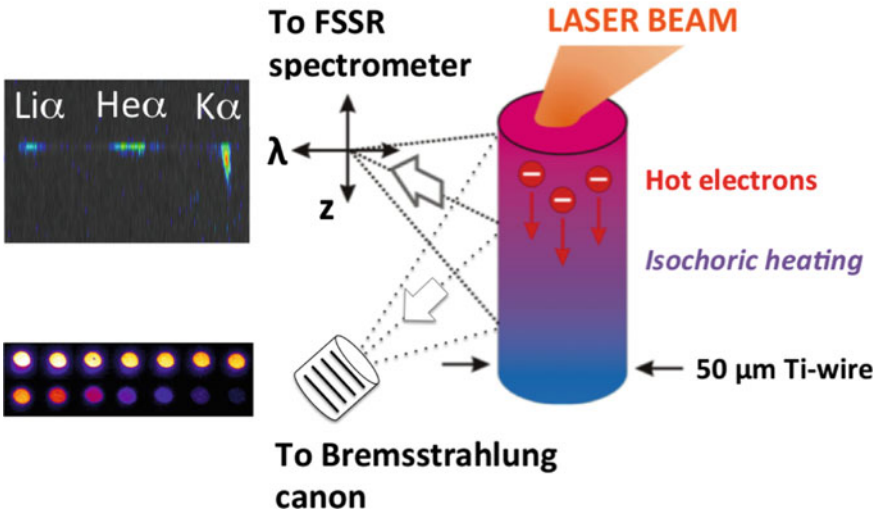

Fig. 14.7 Layout of the experimental setup including example images of the FSSR and the "bremsstrahlung cannon"

gradients, the use of spatially resolved diagnostics, as in our experiment, allows to simultaneously measure the propagation of fast electrons along the wire and the target heating at every position. This constitutes an important crosscheck for the models used to simulate the experiment.

In the experiment, Ti-wires with a diameter of 50 μm and a length up to 8 mm were used. The PHELIX-laser beam (E = 150 J, 50% of which on target, duration 500 fs, λ = 1064 nm) was focused by an off-axis parabola to about 5 μm FWHM focal spot, with an incident angle of 22.5° on the tip of the wire, leading to a maximum intensity of 7×10^{20} W/cm^2. The laser-target interaction produces relativistic electrons that ionize target atoms inducing radiative electronic transitions from outer shells into K-shell vacancies. This X-ray emission offers the possibility to determine the temperature of the wire by analysis of the Kα broadening and makes the propagation of the electrons experimentally traceable. In addition, the electrons produce bremsstrahlung radiation, which is related to the hot electron spectrum. The scheme of the experimental set-up is shown in Fig. 14.7.

Figure 14.8 shows the recorded Kα, He-like and Ly-like emission profile as a function of the wire depth, measured by using a FSSR spectrometer (with 1D spatial resolution [21]) for a high intensity ($I = 7 \times 10^{20}$ W/cm^2) and high contrast (10^{-10}) laser shot. Here "cold Kα" means that a wavelength corresponding to the "cold part" of the Kα line only was selected. Instead the "Kα group" corresponds to all shifted Kα emission lines. The difference is hence that the cold Kα group corresponds to small ionization degrees only, while the "Kα group" implies integration over a wider range of wavelengths and all ionization states.

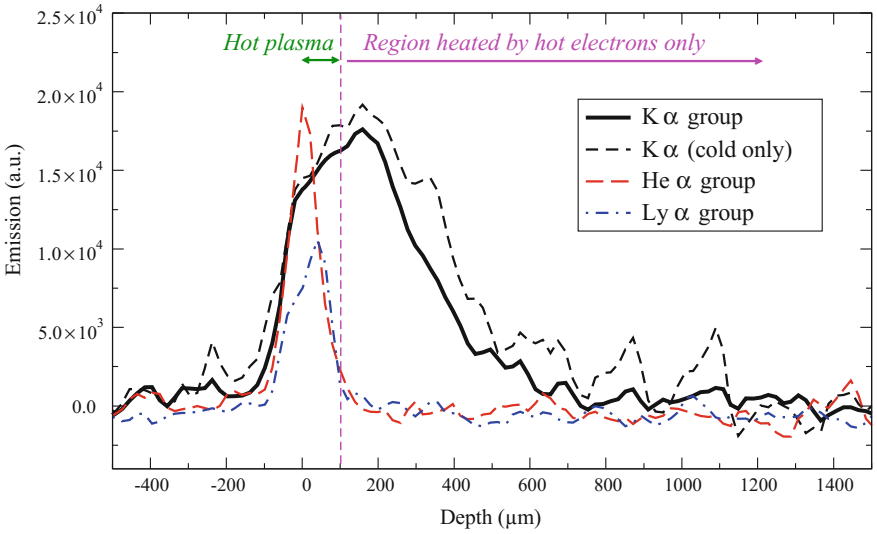

Fig. 14.8 Kα, He-like and Ly-like emission profile as a function of the wire depth, measured by the FSSR for a high intensity ($I = 7\times10^{20}$ W/cm^2) and high contrast (10^{-10}) laser shot. Cold Kα means that we select a wavelength corresponding to the "cold part" of the Kα line only, i.e. we look at small ionization degrees only, while Kα group means that we perform the integration over a wider range of wavelengths

We see that Heα and Li-like satellite emission are concentrated at the top of the wire, directly heated by the laser up to a depth of about 100 μm. Kα emission goes down to about 1 mm. At shallow depths, this is mainly given by shifted Kα lines (corresponding to intense heating of the wire material) while at larger depth it is mainly given by the cold Kα. We notice that at these intensities, fast electrons with temperature of the order of 1–2 MeV, as confirmed by measurements from the bremsstrahlung cannon. Their collisional penetration range in solid density Ti is expected to be much less than 1 mm. This shows indeed the impact of strong collective effects related to fast electron propagation and energy deposition in the target [22].

Figure 14.9 shows the measured Kα shape corresponding to depth of 200 and 350 μm into the wire. Rather then showing separate hot Kα lines, here the Kα lines are broaden, implying moderate background temperatures. The experimental results are compared to calculation of Kα lines broadening using the code FLYCHK [23] where the temperature has been varied. In this case, the best matching is obtained for temperatures of 50 and 28 eV, respectively. The calculation can be repeated at any depth providing the temperature profile along the wire axis, shown in Fig. 14.9 on the right.

In conclusion, by using a laser-irradiated wire as target and spatially-resolved X-ray diagnostics, this experiment has shown the possibility of measuring the penetration depth of laser-accelerated relativistic electrons, as well as the temperature of mat-

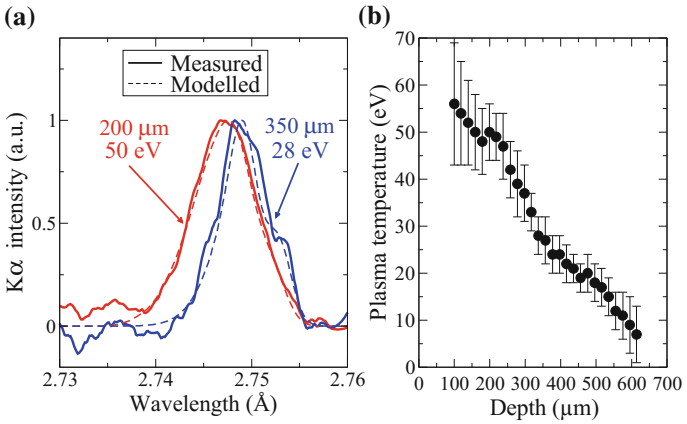

Fig. 14.9 **a** Measured (solid) Kα broadening for 200 and 350 µm depth into the wire compared to the modeled (dashed) Kα broadening for 50 and 28 eV, respectively. **b** Deduced bulk electron temperature along the wire axis

ter deep inside the target, isochorically heated to extreme states. In addition, detailed simulations were performed to reproduce the hot electron source (constrained by Bremsstrahlung Cannon data) and heating inside the target [24]. They unravel a very efficient confinement of the electron current along hundreds of microns. In comparison to the usual foil-target geometry, we have a substantial increase of energy deposition both from resistive and from collisional effects. This can then provide an efficient isochoric heating of the target with soft temperature gradients. The wire-target also allows for an easier diagnostic of the obtained states and clearly allows discriminating the hot plasma from the in-depth solid density regions, which is critical in this kind of experiments.

14.5 Conclusions

In recent years, short-pulse lasers have allowed producing and studying extreme states of matter, either by isochoric heating or by producing blast waves (see the chapter by K. Jakubowska in this book). These are becoming useful tools, complementary to shocks driven by high-energy ns-laser systems.

Despite the experiments are still in their infancy, significant progress has been made and more is expected in next years. Control of laser parameters, use of novel diagnostics approaches, new target configurations have already allowed getting significant results. The availability of short-pulse high-intensity laser systems in many laboratories around the world looks promising for the future expansion of this domain of physics.

Acknowledgements The experiments described in this chapter have been possible thanks to collaborations with many scientists from different laboratories and countries: G. Boutoux, J. J. Santos (University of Bordeaux, France), O. N. Rosmej, A. Schönlein (Goethe University, Frankfurt, Germany), L. Antonelli (University of York, UK), J. J. Honrubia (Universidad Politécnica de Madrid, Spain), S. Pikuz (JIHT, Moscow, Russia), D. Khaghani, P. Neumayer (GSI Darmstadt. Germany), A. Debayle, Ch. Rousseaux, L. Gremillet (CEA DAM DIF, Bruyères-le-Chatel, France), Ch. Spindloe, M. Tolley (Rutherford Appleton Laboratory, UK), A. Magunov (General Physics Institute, Moscow, Russia), W. Nazarov (University of St. Andrews, UK), S. D. Baton, A. Benuzzi-Mounaix (LULI, Ecole Polytechnique, France), A. Morace, Y. Okano, Y. Inubushi, H. Nishimura, R. Kodama (Osaka University, Japan) Y. Aglitskiy (Science Applications International Corporation, USA), K. Jakubowska (IPPLM, Warsaw, Poland). The work was also partially supported by the Competitiveness Program of NRNU MEPhI, Russia.

References

1. D. Batani, Matter in extreme conditions produced by lasers. Perspect. Europhys. Lett. **114**, 65001 (2016)
2. A. Benuzzi, T. Lower, M. Koenig, B. Faral, D. Batani, D. Beretta, C. Danson, D. Pepler, Indirect and direct laser driven shock waves and applications to copper equation of state measurements in the 10–40 Mbar pressure range. Phys. Rev. E **54**, 2162 (1996)
3. D. Batani, A. Balducci, D. Beretta, A. Bernardinello, T. Lower, M. Koenig, A. Benuzzi, B. Faral, T. Hall, Equation of state data for gold in the pressure range <10 TPa. Phys. Rev. B **61**, 9287 (2000)
4. D. Batani, A. Morelli, M. Tomasini, A. Benuzzi-Mounaix, B. Faral, M. Koenig, P. Baclet, B. Cathala, B. Marchet, I. Masclet, M. Rebec, C. Reverdin, R. Cauble, P. Celliers, G. Collins, L. Da Silva, T. Hall, M. Moret, B. Sacchi, Equation of state data for iron at pressure beyond 10 Mbar. Phys. Rev. Lett. **88**, 235502 (2002)
5. A. Benuzzi-Mounaix, M. Koenig, G. Huser, B. Faral, N. Grandjouan, D. Batani, E. Henry, M. Tomasini, B. Marchet, T.A. Hall, M. Boustie, T. De Rességuier, M. Hallouin, F. Guyot, Absolute equation of state measurements of iron using laser driven shocks. Phys. Plasmas **9**, 2466 (2002)
6. P.M. Celliers, G.W. Collins, D.G. Hicks, M. Koenig, E. Henry, A. Benuzzi-Mounaix, D. Batani, D.K. Bradley, L.B. Da Silva, R.J. Wallace, S.J. Moon, J.H. Eggert, K.K.M. Lee, L.R. Benedetti, R. Jeanloz, I. Masclet, N. Dague, B. Marchet, M. Rabec Le Gloahec, C. Reverdin, J. Pasley, O. Willi, D. Neely, C. Danson, Electronic conduction in shock-compressed water. Phys. Plasmas **11**, L41 (2004)
7. D. Batani, K. Jakubowska, A. Benuzzi-Mounaix, C. Cavazzoni, C. Danson, T. Hall, M. Kimpel, D. Neely, J. Pasley, M. Rabec Le Gloahec, B. Telaro, Refraction index of shock compressed water in the megabar pressure range. Europhys. Lett. **112**, 49901 (2015)
8. D. Batani, H. Stabile. M. Tomasini, G. Lucchini, A. Ravasio, M. Koenig, A. Benuzzi-Mounaix, H. Nishimura, Y. Ochi, J. Ullschmied, J. Skala, B. Kralikova, M. Pfeifer, C. Kadlec, T. Mocek, A. Präg, T. Hall, P. Milani, E. Barborini, P. Piseri, Hugoniot data for carbon at megabar pressures. Phys. Rev. Lett. **92**, 065503 (2004)
9. S. Paleari, D. Batani, T. Vinci, R. Benocci, K. Shigemori, Y. Hironaka, T. Kadono, A. Shiroshita, P. Piseri, S. Bellucci, A. Mangione, A. Aliverdiev, A new target design for laser shock-compression studies of carbon reflectivity in the megabar regime. Eur. J. Phys. D **67**, 136 (2013)
10. M. Koenig, A. Benuzzi, B. Faral, J. Krishnan, J.M. Boudenne, T. Jalinaud, C. Remond, A. Decoster, D. Batani, D. Beretta, T. Hall, Brominated plastic equation of state measurement using laser driven shocks. Appl. Phys. Lett. **72**, 1033 (1998)

11. R. Dezulian, F. Canova, S. Barbanotti, F. Orsenigo, R. Redaelli, T. Vinci, G. Lucchini, D. Batani, B. Rus, J. Polan, M. Kozlová, M. Stupka, A.R. Praeg, P. Homer, T. Havlicek, M. Soukup, E. Krousky, J. Skala, R. Dudzak, M. Pfeifer, H. Nishimura, K. Nagai, F. Ito, T. Norimatsu, A. Kilpio, E. Shashkov, I. Stuchebrukhov, V. Vovchenko, V. Chernomyrdin, I. Krasuyk, Hugoniot data of plastic foams obtained from laser-driven shocks. Phys. Rev. E **73**, 047401 (2006)
12. S. Baton, M. Koenig, P. Guillou, B. Loupias, A. Benuzzi-Mounaix, J. Fuchs, Ch. Rousseaux, L. Gremillet, D. Batani, A. Morace, M. Nakatsutsumi, R. Kodama, Y. Aglitskiy, Relativistic electron transport and confinement within charge-insulated, mass-limited targets. High Energy Density Phys. **3**, 358 (2007)
13. F. N. Beg, A. R. Bell et al., Phys. Plasmas 4, 447 (1997)
14. E. Martinolli, M. Koenig, S.D. Baton, J.J. Santos, F. Amiranoff, D. Batani, E. Perelli-Cippo, F. Scianitti, L. Gremillet, C. Rousseaux, T.A. Hall, M.H. Key, R. Snavely, A. MacKinnon, R.R. Freeman, J.A. King, D. Neely, R.J. Clark, Fast electron transport and heating of solid targets in high intensity laser interaction measured by Kα fluorescence. Phys. Rev. E **73**, 046402 (2006)
15. G. Chiu, A. Ng, Phys. Rev. E **59**, 1024 (1999)
16. A. Morace, A. Magunov, D. Batani, R. Redaelli, C. Fourment, J.J. Santos, G. Malka, A. Boscheron, A. Casner, W. Nazarov, T. Vinci, Y. Okano, Y. Inubushi, H. Nishimura, A. Flacco, C. Spindloe, M. Tolley, Study of plasma heating induced by fast electrons. Phys. Plasmas **16**, 122701 (2009)
17. V.A. Boiko, J. Sov. Laser Res. **6**, 85 (1985)
18. J. Abdallah Jr., A.Y. Faenov, IYu. Skobelev, A.I. Magunov, T.A. Pikuz, T. Auguste, P. D'Oliveira, S. Hulin, P. Monot, Phys. Rev. A **63**, 032706 (2001)
19. H. Nishimura, R. Mishra, S. Ohshima, H. Nakamura, M. Tanabe, T. Fujiwara, N. Yamamoto, S. Fujioka, D. Batani, M. Veltcheva, T. Desai, R. Jafer, T. Kawamura, Y. Sentoku, R. Mancini, P. Hakel, F. Koike, K. Mima, Energy transport and isochoric heating of a low-Z, reduced-mass target irradiated with a high intensity laser pulse. Phys. Plasmas **18**, 022702 (2011)
20. A. Schönlein, G. Boutoux, S. Pikuz, L. Antonelli, D. Batani, A. Debayle, A. Franz, L. Giuffrida, J.J. Honrubia, J. Jacoby, D. Khaghani, P. Neumayer, O.N. Rosmej, T. Sakaki, J.J. Santos, A. Sauteray, Generation and characterization of warm dense matter isochorically heated by laser-induced relativistic electrons in a wire target. EPL **114**, 45002 (2016)
21. T.A. Pikuz, et al., Laser-generated and other laboratory X-ray and EUV sources, optics, and applications, in *Proceedings of SPIE*, vol. 5196, ed. by G. Kyrala, J.C. Gauthier (2004), p. 362
22. F. Pisani, A. Antonicci, A. Bernardinello, D. Batani, E. Martinolli, M. Koenig, L. Gremillet, F. Amiranoff, S. Baton, T. Hall, D. Scott, P. Norreys, A. Djaoui, C. Rousseaux, P. Fews, H. Bandulet, H. Pepin, Experimental evidence of electric inhibition in the propagation of fast electrons in solid matter. Phys. Rev. E **62**, R5927 (2000)
23. H.K. Chung, M.H. Chen, W.L. Morgan, Y. Ralchenko, R.W. Lee, High Energy Density Phys. **1**, 3 (2005)
24. J.J. Honrubia et al., Laser Part. Beams **24**, 217 (2006)

Chapter 15
Short-Pulse Laser-Driven Strong Shock Waves

Katarzyna Jakubowska

Abstract Warm Dense Matter (WDM) or the High Energy Density (HED) states are useful for instance, to describe properties in giant planets. They are usually achieved in laboratory conditions by using high energy (hundreds of J) and long duration (ns) lasers. An alternative for creating matter in extreme states is described in this chapter. It relies on the formation of strong shocks driven by highly energetic electrons generated by low-energy short-pulse duration laser interacting with the solid target. Such approach opens new pathways in studies and benchmarking of matter in extreme conditions, including study of Equation of State (EOS), structural dynamics on smaller installations, which are easier accessible for researchers.

15.1 Introduction

Realistic modelisation of the conditions in supernova precursors, giant planets, Inertial Confinement experiments, in particular Fast Ignition [1, 2] and Shock Ignition [3–6] requires deep knowledge of matter reaching extreme values of density, temperature and pressure. Warm Dense Matter (WDM) defines matter near solid density ($\rho \sim 0.01$–100 g/cm^3) and temperature of a few eV. Instead High Energy Density (HED) defines states with an energy density above 0.1 MJ/cm^3. Usually such kinds of conditions are achieved in laboratory by using high energy (several hundreds of J) and long (ns) duration lasers. The generated shock pressure (Mbar) can be estimated according to the following equation as a function of laser intensity I_L (W/cm^2) and wavelength λ (μm) [7]:

$$P(\text{Mbar}) = 8.6\left(\frac{I_L(\text{W/cm}^2)}{10^{14}}\right)^{2/3}\lambda^{-2/3}(\mu\text{m}) \tag{15.1}$$

K. Jakubowska (✉)
IPPLM, Warsaw, Poland
e-mail: k.jakubowska2@gmail.com

© Springer Nature Switzerland AG 2018

K. Yamanouchi et al. (eds.), *Progress in Ultrafast Intense Laser Science XIV*,
Springer Series in Chemical Physics 118,
https://doi.org/10.1007/978-3-030-03786-4_15

A novel and alternative approach to create HED states relies on the generation strong shocks driven by highly energetic electrons generated by low-energy short-pulse duration interacting with the solid target. Such kind of study opens new pathways in studies and benchmarking of matter Equation of State (EOS) and structural dynamics models on smaller laser installations, which are more easily accessible for researchers, and which can also be coupled to novel facilities like XFEL, allowing for advanced diagnostics of the created states.

15.2 Shocks and Blast Waves

Strong shock waves can be produced by focusing intense laser light on the surface of the target. This causes ablation of the target material and creation of plasma, which rapidly expands in vacuum. At the same time, due to conservation of momentum, a strong shock wave is generated and propagates inward. As shown in formula (15.1) the pressure increases when the laser intensity is increased or when the laser wavelength is decreased (due to the fact that shorter wavelength lasers penetrate to higher electron density inside the plasma, following the dependence of the critical density on wavelength). Also formula (15.1) shows that very high pressures (>10 Mbar) are already created for relatively low laser intensities (of the order of 10^{14} W/cm^2).

Shocks are discontinuity fronts, which travel in the material satisfying the conservation law for momentum, mass flux and energy [8], which are constant on the two sides of the shock front. In the reference frame co-moving with the shock front, these conservation laws, known as Rankine-Hugoniot relations, have the form:

$$\begin{aligned} &\rho_0 u_0 = \rho u \\ &P_0 + \rho_0 u_0^2 = P + \rho u^2 \\ &\varepsilon_0 + \frac{P_0}{\rho_0} + \frac{u_0^2}{2} = \varepsilon + \frac{P}{\rho} + \frac{u^2}{2} \end{aligned} \tag{15.2}$$

where ρ, P, u are the density, pressure and fluid velocity of the compressed material, and ρ_0, P_0, u_0 are the same quantities in the unperturbed material. In this reference frame, the unperturbed material "enters" the shocked region with velocity u_0. In the laboratory reference frame this hence corresponds to the shock velocity, which is usually indicated by D and, in the perfect gas approximation, is given by:

$$D = \left(\frac{\gamma + 1}{2} \frac{P}{\rho_0} \right)^{1/2} \tag{15.3}$$

where γ is the adiabatic coefficient of the perfect gas defined as C_p/C_v. C_p is the heat capacity at constant pressure and C_v at constant volume.

The shock pressure P and the shock velocity D are maintained as long as the laser pulse continues to produce ablation. After the duration of the laser pulse (τ_L), the

shock is not maintained and a rarefaction wave is generated at the target front side. This relaxation (decompression) wave moves in the target at the sound speed C_s:

$$C_s = \left(\gamma \frac{P}{\rho}\right)^{1/2} \tag{15.4}$$

The velocity of this rarefaction wave is smaller than D because it depends on ρ (and the density of compressed material is $\rho > \rho_0$). However it moves in matter which has been compressed and has now a reduced thickens $d = d_0\ \rho_0/\rho$. Therefore the relaxation wave will reach the shock front at the time t^* determined by the equation:

$$D\ t^* = \tau_L + C_s\ t^* \rho_0/\rho \tag{15.5}$$

After this time, the shock degenerates in a blast wave, i.e. a thin shock front, which travels in the material gradually losing its strength. For times $t \gg \tau_L$, the blast wave dynamics can be described by using the equation of Sedov-Taylor model [9, 10]. These equations are self-similar solutions of the hydrodynamic equations, which correspond to an instantaneous and localized release of energy. Therefore they correctly describe the behavior of blast wave for $R \gg R_{\text{LaserSpot}}$ and $t \gg \tau_{\text{L}}$ i.e. when the system has completely "forgotten" the initial conditions (therefore they correspond to an instantaneous and localized release of energy E). These conditions are easily achieved when using laser pulses with very short duration, which are tightly focused to reach high intensity.

According to Sedov-Taylor model [9, 10] the position of the shock front evolves in time as:

$$R = \varepsilon_0 \left(\frac{E}{\rho_0}\right)^{1/2+k} t^{2/2+k}; \quad \left(\varepsilon_0 = 1.2 \quad \text{for } \gamma = \frac{3}{5}\right) \tag{15.6}$$

where ρ_0 is the density of the propagation medium and E is the energy released in shock creation. Also k represents the dimensionality of the problem, i.e. $k = 1$ for planar wave and $k = 3$ for spherical shocks.

Blast waves are common to many physical phenomena including supernova explosions (astrophysics), nuclear explosions… Hence blast waves initiated by relativistic laser-plasma interaction have been extensively studied in physics, and there have been already several experiments and theoretical calculations where the blast waves were studied [11–15]. All of these works studied blast waves generated in gases. An exception, addressing the study of shocks generated in solid is the work of Budil et al. [16]. However they used a laser pulse with a very large energy (400 J) and 20 ps pulse duration. Also, in their work, the physical mechanisms of blast wave creation are not investigated and discussed.

In the following we will describe recently obtained experiential results, which used short-pulse, low-energy lasers to create blast wave in solid targets. In this experiment, the generation of the shock is the indirect effect following the generation of fast electrons in the ultra-high-intensity interaction of the laser beam with the target. These

electrons travel in the target material and gradually deposit their energy producing a temperature and pressure gradient. Due to pressure gradient in the target, the material expands locally with a different velocity in each point. This expansion compresses the material ahead. At a given time, all such compression wave moving at the local sound waves catch up with each other producing a shock wave.

Therefore the mechanism of shock generation follows the energy deposition from fast electrons producing a pressure/density gradient across the target thickness.

15.3 Experimental Set-up

As an example of blast wave created by short pulse laser propagating in solid material, we will present experimental results obtained in LOA, Palaiseau [17] using the Ti:Sa laser providing 3 J of energy during 24 fs by irradiation at 810 nm with contrast of 10^8. As the intensity of the laser was very high ($I \sim 10^{21}$ W/cm^2) the laser plasma interaction took place in the relativistic regime, which is dominated by the creation of the hot electrons. In the experiment aluminum foils of several thicknesses (3, 6, 10, 15, 50 μm) were used as targets. The measurement of the shock breakout time was realized by detecting the emission at two wavelengths (405 and 532 nm) at the rear side of the target with a streak camera (Hamamatsu C7700). The detection with the streak camera provided time and space resolved measurement. The laser was focused on the target at 45° and the measurement was taken under 15.4° to the target normal. The emission was transferred to the streak camera via a triplet 3″ lens and 4 mirrors (see Fig. 15.1).

The choice of the two observation wavelengths (405 and 532 nm) is related to the possible different mechanism for emission of radiation at the target rear side. 405 nm corresponds to the second harmonic of the irradiated laser. This could contain signals

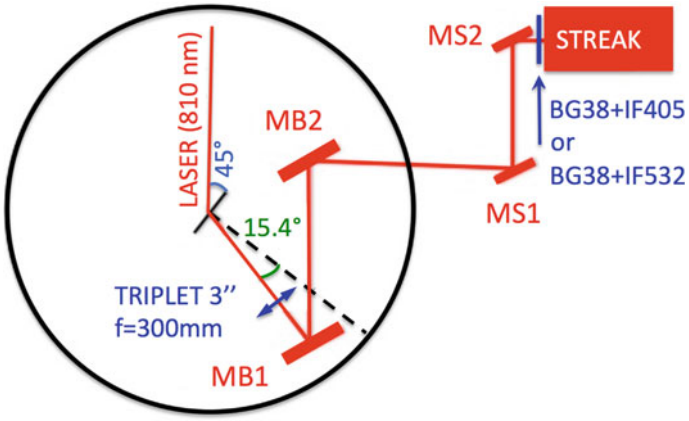

Fig. 15.1 Scheme of experimental set-up

from CTR (Coherent Transition Radiation), which is peaked at the harmonics of the laser wavelength. Instead we expect the channel at 532 nm to contain thermal emission only.

15.4 Experimental Results

The interaction of the laser light with the surface of the aluminum target does not only lead to ablation of the surface of the target and creation of the plasma expanding in front of the target, but due to high intensity of the laser (above 10^{18} W/cm^2) it is creating a beam of highly energetic electrons (superthermal), which propagate practically at light speed within the target. Such superthermal electrons deposit part of their energy causing sudden change of the pressure and temperature of the material.

In calculations of the target rear-side luminance, we took into account the optical transmission and density of all elements in the optical path, the geometry and magnification of the system, the slit size and finally the sensitivity of the streak camera. The temporal evolution of the luminance signal includes several characteristic features, which evolve in a different manner depending on the thickness of the target, as shown in Fig. 15.2.

In the first streak camera image and in the corresponding time-profile (Fig. 15.2a), showing the signal emitted at the rear side of the 3 μm thick target, we observe sharp increase of the emission corresponding to the arrival of the hot electrons on target

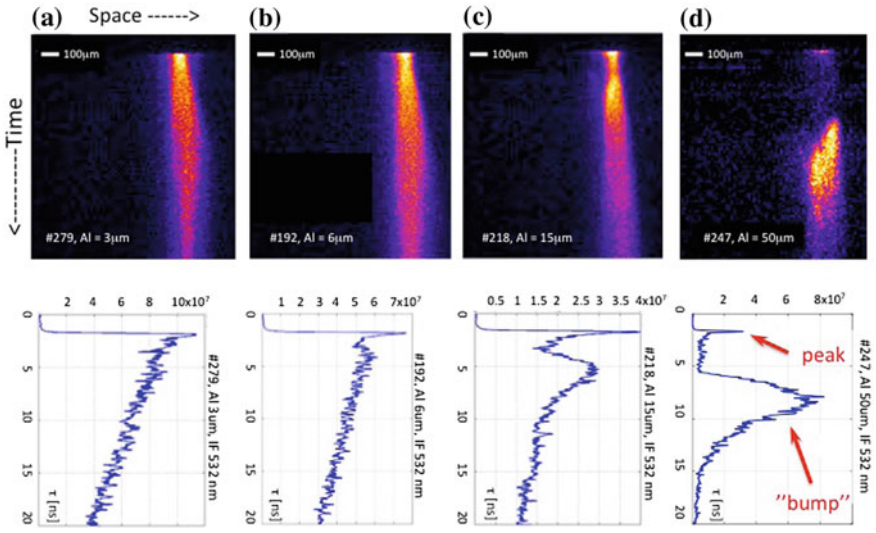

Fig. 15.2 The temporal signal of the streak signal for aluminum target **a** 3 μm, **b** 6 μm, **c** 15 μm and **d** 50 μm. All shown images were taken with an interferential filter at 532 nm plus a BG38 filter and with the slit of the streak camera open to 100 μm. The time window is 20 ns for all images

rear side, followed by a slow decay in time. This rapid emission is probably a mixture of thermal radiation, following the intense heating of material at target rear side, and of CTR, characteristic for relativistic electrons crossing the interface between two materials with different refraction index [18, 19].

After the initial peak we have a rapid decrease of emissivity that is on one side due to the end of CTR emission (which lasts as long as there are travelling fast electrons, i.e. a time of the order of τ_L) and on the other side due to the rapid expansion and cooling of the heated material.

In our case, we can probably infer that the initial peak is dominated by thermal emission and not by CTR. Indeed CTR is peaked at the harmonics of the laser wavelength while thermal emission is spectrally much flatter. In the experiment, emission measured at 405 nm (which contains CTR) was almost the same of (thermal) emission at 532 nm.

Also let's notice that the initial peak is stronger for thinner targets (see Fig. 15.2: the value in the peak decreases from 10 to 2×10^7 (W m^{-2} sr^{-1}) with increasing target thickness from 3 to 50 μm). This corresponds to the fact that CTR decreases (more fast electrons lose energy before reaching the target rear side) and thermal emission decreases because thicker targets are heated less.

In the last 3 figures of Fig. 15.2b, after the initial peak and the signal drop, emission increases again later, forming a characteristic "bump". This increase is the characteristic signature of the shock breakout at target rear side, as observed in many works related to shock dynamics in solid targets performed with higher-energy lasers [20–22].

The time resolved detection of emission from the rear side allows determining the velocity of such "heating wave" by measuring its arrival time and by knowing the thickness of the target. Comparing this velocity to the sound speed in cold aluminum (6.4 km/s) shows that the wave has higher velocity, which strongly suggest that the observed heating wave is indeed a (supersonic) shock wave (this conclusion is true also if we consider the sound velocity of Al heated to temperatures of several eV).

In the following we will describe the mechanism originating the shock wave. This takes place in two steps:

- In the first step we will study hot electrons and their dynamics inside the target, bringing to the formation of a temperature gradient;
- In the second step, such temperature gradient will be used to initialize 2D hydro simulations describing the creation and the propagation of the shock.

15.5 Theoretical Calculations

Ultra-high-intensity laser-matter interaction produces hot electron beams [23], which are of interest for many applications, including laser-driven ion acceleration [24], warm dense matter generation [25, 26] or fast ignition approach to inertial confinement fusion [27–30].

The experimental results presented here were confirmed [17] by theoretical calculations based on CHIC code [31, 32] showing the dynamics of the shock front and shape/structure of the shock wave (blast wave evolving in time). The initial temperature profile used to initialize the simulations was reconstructed on basis of a model of electron energy deposition, which includes collisional effects [33] and collective effects [34, 35]. Collective effects [34, 36, 37] produced by the intense self-generated electric and magnetic fields and are important due to high intensity of the laser. Additionally the hydrosimulations with CHIC code were performed.

15.5.1 Electron Energy Deposition

At relatively low laser intensities ($I \leq 10^{17}$ W/cm^2) the energy transfer, the energy deposition range and the divergence of the hot electrons are dependent only on collisions with ions and electrons in the material. However at relativistic laser intensities ($I > 10^{18}$ W/cm^2) the energy deposition is simultaneously dependent on collisional and electromagnetic processes. The electromagnetic processes are resulting from the charge separation during the passage of the highly energetic electrons via target thickness, and the resulting "return current" taking place in the material [35]. These are "collective" effects in the sense that they cannot be treated considering single particles one by one (as it is the case of collisional propagation of hot electrons in the target). Indeed their strength depends on the strength of the electromagnetic fields, i.e. depends on the total charge separation, i.e. on the total number of created hot electrons. Many experimental results has even proven that for the superthermal electrons such collective electromagnetic effect become dominating mechanism [28–30].

The collisional effects are described in terms of stopping power $\mathrm{d}E/\mathrm{d}x$, which characterize the energy loss as the electron propagates in the material up to a penetration range R_P where they stop due to complete loss of the energy. This can be calculated on basis of the Spencer's model valid for the collisional range of the electrons [33]:

$$\frac{\mathrm{d}E}{\mathrm{d}x} = \frac{E}{R_P(E)} P\left(\frac{x}{R_P(E)}\right) \tag{15.7}$$

where P is a universal function (see Fig. 15.3) and the collisional range R_P represents the total distance travelled by the electron with initial energy E before it completely loses its energy. The values of values $R_P(E)$ were taken from the NIST database [38].

One should note here that the collisional penetration range for electrons between 1 and 3 MeV is 0.2 and 0.69 cm, which is several orders of magnitude bigger than the target thickness (thickest target used in the experiment was 50 μm). This indeed already shows that in the case of this experiment the collective effects are dominant because they reduce the range from cm to sub mm.

The collective effects define a propagation range as a function of energy given by [34]:

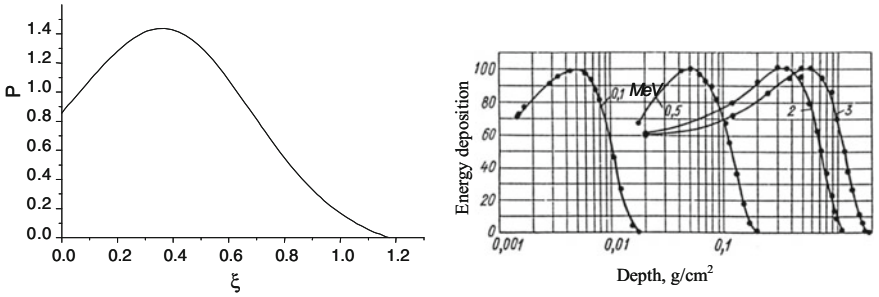

Fig. 15.3 (Left) Universal function P. (Right) Energy deposition profile for different energies of electrons [39]

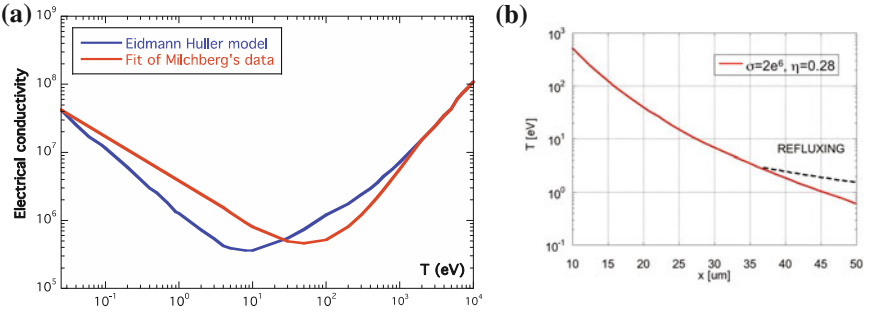

Fig. 15.4 **a** Comparison of the experimental and theoretical electrical conductivity dependency on the temperature [40]; **b** Initial resulting temperature profile in the 50 μm Al target showing in particular the effect of hot electron refluxing at the target rear side

$$R_C(E) = z_0\left(\mathrm{e}^{E/(2T_{\mathrm{hot}})} - 1\right) \tag{15.8}$$

where T_{hot} is the temperature of the distribution of fast electrons and z_0 represents the average penetration range given by Bell's formula [35]:

$$z_0(m) = 3 \times 10^{-16} \frac{T_{\mathrm{hot}}^2(\mathrm{keV})\sigma(\Omega^{-1}\mathrm{m}^{-1})}{\eta I_{18}(\mathrm{W/cm}^2)} \tag{15.9}$$

where η is the conversion of energy from laser to fast electrons, I_{18} is the laser intensity (in units of 10^{18} W/cm^2) and σ is the resistivity of the material, which is a function of the temperature as shown in Fig. 15.4.

In all the calculations we have taken into account the geometry of the electron beam increasing from the initial radius of about 10 μm (compatible with the laser focal spot size, i.e. with the hot electron source) to 40 μm, which was corresponding to the size of the initial signal on streak camera images (Fig. 15.2). Finally we have included correction describing the refluxing of hot electrons [34], which increases the temperature at target rear side.

In calculating the temperature profile from the energy deposition profile, we have used equipartition of energy among atoms and free electrons and calculated ionization in the Al target (i.e. number of free electrons) using a simplified model confirmed in [17]. We took care that the resulting average temperature is consistent with target resistivity (Fig. 15.4) and hence with the propagation range.

The resulting initial temperature profile in the 50 μm Al target is shown in Fig. 15.4b. This has been used as input data for hydrodynamics simulations performed with the code CHIC.

15.5.2 Hydrosimulations (CHIC)—Shock Wave

Hydrosimulations, done with the CHIC code [31, 32], unrevealed the structure and basic parameters (pressure, density) of the wave propagating in 50 μm thick aluminum target. Cylindrical geometry (axial symmetry) was used in such simulations.

Observation of the 3D plots related to spatial distribution of pressure show that at the beginning ($t = 0.5$ ns, Fig. 15.5a) the formed blast wave is sharp and thin but spherical (due to small focal spot). As the time is passing, the blast wave advances but at the same time not only the target front side, but also the rear side of the target expands fast. This leads to decrease of the pressure on the axis ($t = 2$ ns, Fig. 15.5c), which finally causes the division of the blast wave in two waves travelling almost in vertical direction (in the real 3D cylindrical geometry, they correspond to an annular blast wave). Finally around 4 ns (Fig. 15.5d) the front of the blast wave riches the edge of the target and breaks out.

The profile on the horizontal axis in Fig. 15.5 is presented in Fig. 15.6 as a 2D plot of pressure (a)/density (b) dependence on the time and target thickness. The heating of the target in the very early stage of the laser-target interaction, leads to the target expansion on both sides of the target. The fast expansion ($v_{\mathrm{exp}} = 28$ km/s) of the target causes change in thickness from 50 μm to about 180 μm at 5 ns. One can also observe that the shock is breaking out from the target at around 4 ns. The shock velocity calculated from the slope of the shock propagation has a constant value of 34 km/s. The expansion of the target implies a shock velocity (34 km/s), which is about 3 times higher than what can be estimated from the relation $D = d/t$ where d is the target thickness and t the shock breakout time (this would be just about 11 km/s).

Figure 15.7 is the result of the hydrodynamic simulation. The time evolution of the pressure along the horizontal axis indicates that the fast electron emission/interaction with the target material has created a very strong shock wave (with pressure initially higher than 100 Mbars). At the early stage ($t < 1$ ns) the shock wave has a clear blast wave structure, which in time ($t \geq 1$ ns) is becoming broader and finally completely vanishes becoming flatter.

Clearly in our experiment we generate a shock, which for early times is very strong. We recall that in hydrodynamics (see for instance [8]) a shock is "very strong" when its pressure is much bigger than the initial pressure ($P \gg P_{\mathrm{O}}$) or, equivalently, the shock velocity is much bigger than the initial sound velocity in the material ($D \gg c_s$).

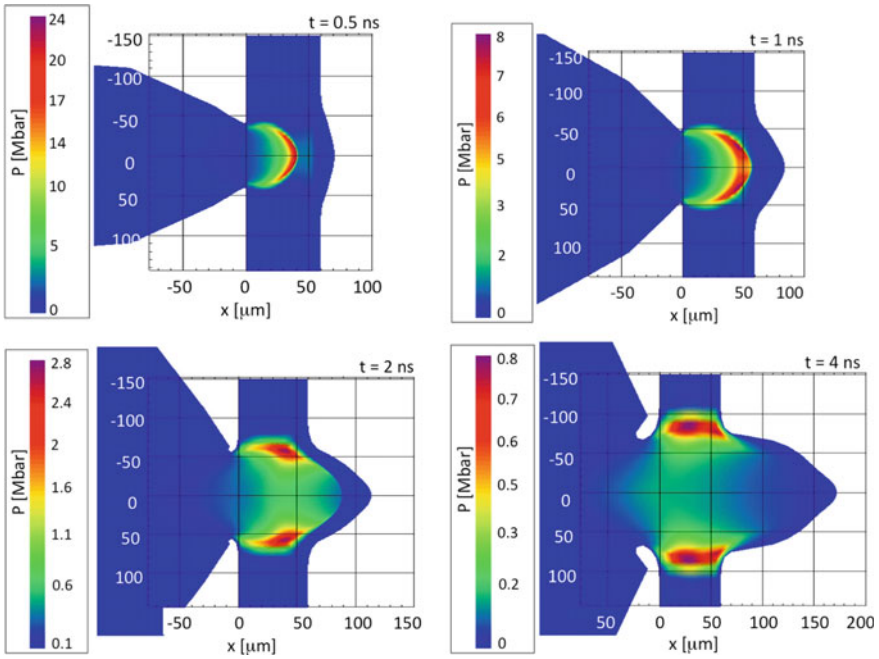

Fig. 15.5 3D plot showing distribution of pressure in space for different times (50 μm aluminum target) [17]

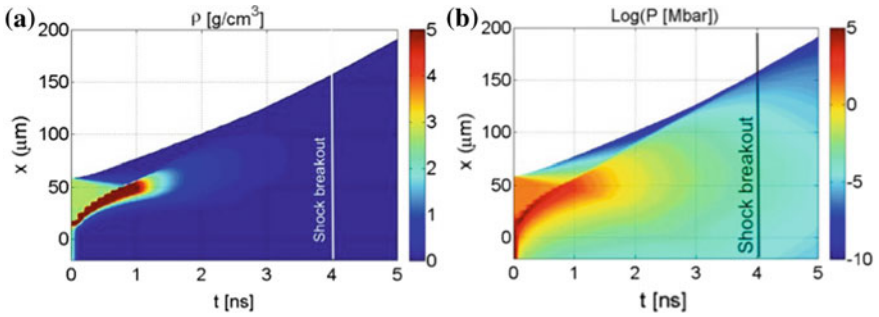

Fig. 15.6 Density (**a**), and pressure (**b**) dynamics in time and space for a 50 μm aluminum target along the horizontal axis [17]

Such shocks are able to produce a substantial change in the thermodynamic state of shocked matter and induce phase transitions.

As just noticed, at later times the shock gradually attenuates and the shock velocity (which is constant in our case) becomes more comparable to the plasma sound velocity (which indeed increases because the density decreases). Typically the Mach number of the shock, defined by the ratio D/c_s varies between initial values as high

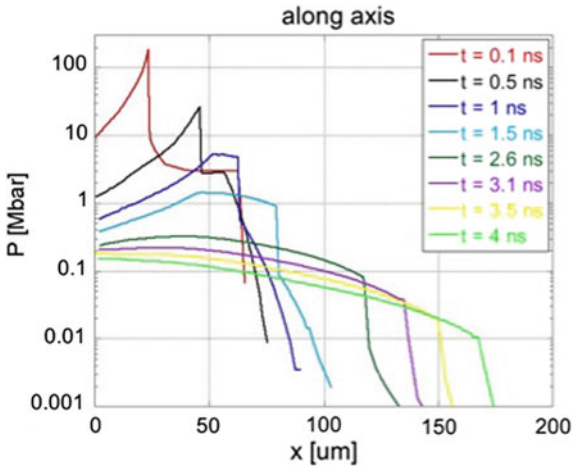

Fig. 15.7 The time evolution for chosen times along the horizontal axis

as 10^4 to final values of the order of 1.7 (corresponding to the final shock velocity of 34 km/s and a sound velocity in the final expanded Al of the order of 0.7–2 $\times$ 10^7 cm/s).

The decrease in shock pressure is due on one side the density decrease due to expansion of the target and on the other side to the fact that the shock is not maintained because of the short duration of the laser pulse (24 fs). However the simulation results of Fig. 15.6 show that the shock velocity D is constant from about 0.7 ns up to shock breakout. This results from to the interplay of two counteracting effects, as described in the following.

15.5.3 Shock Dynamics

The shock velocity is proportional to square root of the pressure over density, as shown in formula (15.2). Then, when the shock pressure is constant, but the shock moves in a material with a decreasing density profile, the shock accelerates [41].

Instead, in the case of a non-stationary shock moving in a constant density medium, the velocity decreases following the decrease of pressure (again in agreement with 15.2).

In the case of the simulations presented in Figs. 15.5 and 15.6, the pressure is decreasing, but the density is decreasing even faster due to the fast expansion of the target. In conclusion the two counteracting effects produce a shock moving at constant velocity.

Shock acceleration due to density decrease can be calculated by using the impedance mismatch relations. When a shock moves from a medium of density ρ_1 to a medium of lover density ρ_2, pressure reduces as [42]:

$$P_2 = \frac{4\rho_2 P_1(\gamma_1+1)}{\left[(\gamma_2+1)^{1/2}\rho_1^{1/2} + (\gamma_1+1)^{1/2}\rho_2^{1/2}\right]^2} \tag{15.10}$$

For a continuous density gradient, this brings to:

$$P + dP = \frac{4(\rho+d\rho)P}{\left[\rho^{1/2} + (\rho+d\rho)^{1/2}\right]^2} \tag{15.11}$$

which finally gives:

$$\frac{dP}{P} = \frac{d\rho}{2\rho} \Rightarrow P \propto \sqrt{\rho} \tag{15.12}$$

similarly to the result previously obtained by [41] (and also by [43] and by [44]).

On the other side, the decrease of shock velocity for a non-maintained shock pressure can be modeled using the Sedov-Taylor self-similar model [9, 10] for blast wave propagation (15.6). Let's notice that self-similar solutions, like those provided by Sedov-Taylor's model, are well-known to apply for long times, when the system under investigation has «forgotten» the initial conditions. In our case the laser pulse duration is only 40 fs, which indeed implies that the observation times (ns time scale) are "infinitely long" with respect to the duration of laser energy deposition. However, if we consider comparison of the simulation shock trajectory with the Sedov-Taylor prediction (Fig. 15.8) assuming $k \sim 3$ (spherical expansion, 3 degrees of freedom). The equation for shock front position and shock front velocity are then:

$$\begin{aligned} R &= \varepsilon_0 \left(\frac{E}{\rho_0}\right)^{1/5} t^{2/5} \\ D \equiv \dot{R} &= \varepsilon_0 \left(\frac{E}{\rho_0}\right)^{1/5} t^{2/5-1} \propto t^{-3/5} \end{aligned} \tag{15.13}$$

Clearly a decrease of D as $t^{-3/5}$ is non-compatible with the observation of the constant shock velocity. In our case shock dynamics is really strongly affected by the preheating implying the propagation of a non-maintained shock in a decreasing density profile.

Simulations show that pressure decrease is linear with the density (rather than following 15.12), which leads to constant shock velocity.

However we can still use Sedov-Taylor model to interpolate the points for $t < 1$ ns before the relaxation wave meets the shock front, i.e. before appreciable target decompression takes place. Figure 15.8 shows that the initial shock trajectory is in good agreement with Sedov-Taylor model. In this case we can use the fit to estimate the absorbed energy E (which is the only free parameter in 15.5). The obtained coefficient is 0.219, which is quite close to what obtained from applying Sedov-Taylor (0.249) assuming a conversion efficiency of $\eta \approx 30\%$ (this provides support to our assumptions).

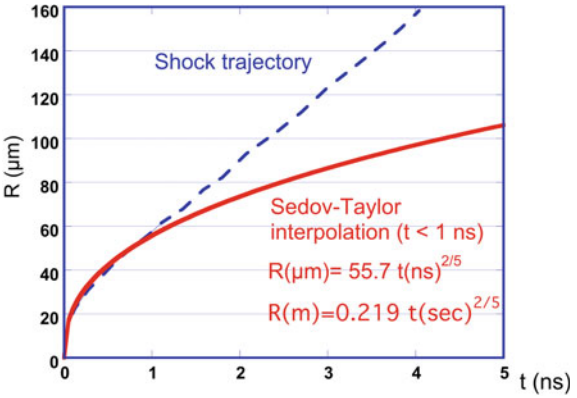

Fig. 15.8 Blue curve: shock trajectory derived from the hydro simulations of Fig. 15.6. Red curve: interpolation of the trajectory corresponding to $t < 1$ ns, using the dependence of Sedov-Taylor's model

15.6 Temperature

In the following, we tried to measure the temperature of aluminum at the target rear side and compare it to the prediction of hydrosimulations (incorporating a model for Al EOS).

In order to measure the rear side target temperature we used the "color temperature" approach following [45], i.e. we recorded emission at two different wavelengths using interference filters that pass through the light of selected different wavelength. Then, by assuming that the emitted light is following a black body radiation spectrum, we can calculate the "color temperature". In case of dense matter eV or sub-eV temperatures, this can be shown to approach the real temperature of the material (see for instance [17, 45–48]).

The procedure is explained in Fig. 15.9. Black body radiation is described by Planck's equation [8], which gives the irradiance as a function of wavelength (Fig. 15.9 left). From this one can calculate the ratio of emission at the two wavelengths (in our case 405 and 532 nm) as shown in Fig. 15.9 (right).

In our case the ratio of the luminance $I(405)/I(532)$ from experimental data (Fig. 15.10) at the time of breakout (4 ns in respect to the first peak, which marks the arrival of the laser on the target) is equal to 1.1. According to Fig. 15.9 (right), this ratio corresponds to a temperature $T \sim 0.57$ eV, measured color temperature). This corresponds fairly well to the temperature predicted by CHIC simulations ($T \sim 0.52$ eV). The agreement of the two results not only support the confidence in the used method, but even more importantly, suggests that such blast waves can be used to perform significant measurements of the physical properties of matter in extreme states.

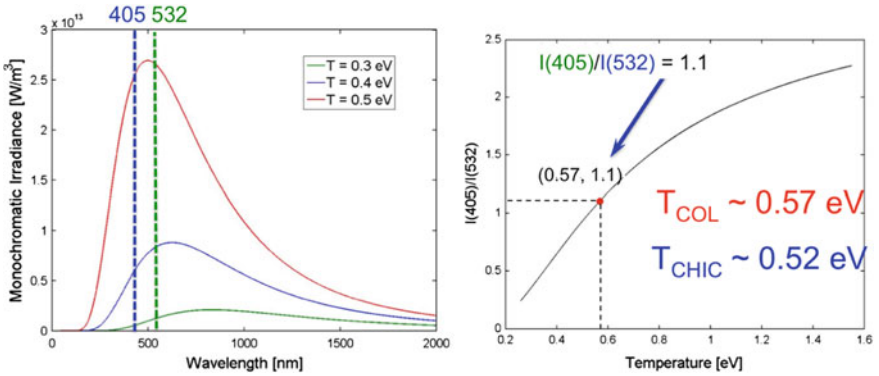

Fig. 15.9 (Left) The black body radiation corresponding to different temperatures. (Right) The dependence of irradiance ratio $I(405)/I(532)$ on the temperature

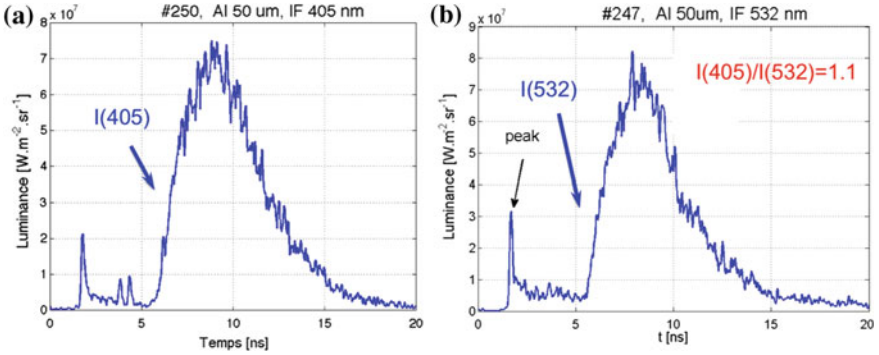

Fig. 15.10 The emission from the rear side of the aluminum target (50 μm) after passing through interference filters **a** IF 405 nm and **b** IF 532 nm

15.7 Conclusions

In this chapter we have demonstrated the generation of strong shocks driven by hot electrons produced when an ultra-short low-energy laser pulse (*fs*) interacts with a solid target. We would like to stress that our work is very different from the several papers dealing with "isochoric heating" of matter induced by laser-generated hot electrons. In our work the energy deposition from hot electrons produces a significant temperature gradient, which, in turn, originates a strong shock wave. Therefore, in our experiment, HED states are produced by the shock wave and not by direct electron isochoric heating.

Also, our case is different from shock generation using long laser pulses with high energy where the laser energy is absorbed in the target producing a plasma, which expands outwards. Following momentum conservation, this expansion is compensated by a compression (shock) wave traveling inside the target material. So shock

generation takes place at the "ablation front", i.e. can be considered as a "surface effect". Here instead the hot electron energy is deposited in depth in the material producing a temperature gradient, which finally originates the shock. Therefore we could consider that this is rather a "volume effect".

We have shown that the rear side emission evidences the breakout of a shock propagating through the target. The temporal evolution of the recorded emission changes with the thickness of the target.

Simulations performed with the 2D hydro code CHIC confirm and explain the mechanism of shock creation due to hot electron heating.

The color temperature, defined by luminance ratio for two different wavelength, allowed to recover a value of temperature very close to the prediction of hydro simulations, which consolidates our experiment interpretation.

This study shows the pertinence of the approach to study matter in extreme states. Such approach opens new path in studies and benchmarking of matter in extreme conditions, including study of Equation of State (EOS), structural dynamics on smaller installations, which are easier accessible for researchers, as well as on novel facilities like XFEL.

References

1. M. Roth, T.E. Cowan, M.H. Key, S.P. Hatchett, C. Brown, W. Fountain, J. Johnson, D.M. Pennington, R.A. Snavely, S.C. Wilks, K. Yasuike, H. Ruhl, F. Pegoraro, S.V. Bulanov, E.M. Campbell, M.D. Perry, H. Powell, Phys. Rev. Lett. **86**, 436 (2001)
2. R. Kodama, P.A. Norreys, K. Mima, A.E. Dangor, R.G. Evans, H. Fujita, Y. Kitagawa, K. Krushelnick, T. Miyakoshi, N. Miyanaga, T. Norimatsu, S.J. Rose, T. Shozaki, K. Shigemori, A. Sunahara, M. Tampo, K.A. Tanaka, Y. Toyama, T. Yamanaka, M. Zepf, Nature **412**, 798 (2001)
3. R. Betti, C.D. Zhou, K.S. Anderson, L.J. Perkins, W. Theobald, A.A. Solodov, Phys. Rev. Lett. **98**, 155001 (2007)
4. L.J. Perkins, R. Betti, K.N. LaFortune, W.H. Williams, Phys. Rev. Lett. **103**, 045004 (2009)
5. D. Batani, S. Baton, A. Casner, S. Depierreux, M. Hohenberger, O. Klimo, M. Koenig, C. Labaune, X. Ribeyre, C. Rousseaux, G. Schurtz, W. Theobald, V.T. Tikhonchuk, Nucl. Fusion **54**, 054009 (2014)
6. D. Batani, L. Antonelli, S. Atzeni, J. Badziak, F. Baffigi, T. Chodukowski, F. Consoli, G. Cristoforetti, R. De Angelis, R. Dudzak, G. Folpini, L. Giuffrida, L.A. Gizzi, Z. Kalinowska, P. Koester, E. Krousky, M. Krus, L. Labate, T. Levato, Y. Maheut, G. Malka, D. Margarone, A. Marocchino, J. Nejdl, Ph Nicolai, T. O'Dell, T. Pisarczyk, O. Renner, Y.J. Rhee, X. Ribeyre, M. Richetta, M. Rosinski, M. Sawicka, A. Schiavi, J. Skala, M. Smid, Ch. Spindloe, J. Ullschmied, A. Velyhan, T. Vinci, Phys. Plasmas **21**, 032710 (2014)
7. J. Lindl, Phys. Plasmas **2**(11), 3933 (1995)
8. Ya. Zeldovich, YuP Raizer, *Physics of Shock Waves and High Temperature Hydrodynamic Phenomena* (Academic Press, New York, 1967)
9. G. Taylor, Proc. R. Soc. A **201**, 159–174 (1950)
10. E. de Posada et al., J. Phys: Conf. Ser. **274**, 012078 (2011)
11. J.L. Giuliani Jr., M. Mulbrandon, E. Hyman, Phys. Fluids B **1**, 1463 (1989)
12. J.J. MacFarlane, G.A. Moses, R.R. Peterson, Phys. Fluids B **1**, 635 (1989)
13. Y.T. Li, J. Zhang, H. Teng, K. Li, X.Y. Peng, Z. Jin, X. Lu, Z.Y. Zheng, Q.Z. Yu, Phys. Rev. E: Stat. Nonlin. Soft Matter Phys. **67**, 056403 (2003)

14. D.R. Farley, K. Shigemori, H. Azechi, Laser Part. Beams **23**(4), 513 (2005)
15. M.J. Edwards, A.J. MacKinnon, J. Zweiback, K. Shigemori, D. Ryutov, A.M. Rubenchik, K.A. Keilty, E. Liang, B.A. Remington, T. Ditmire, Phys. Rev. Lett. **87**, 085004 (2001)
16. K.S. Budil et al., Astrophys. J. Suppl. Ser. **127**, 262 (2000)
17. K. Jakubowska, D. Batani et al., EPL **119**, 35001 (2017)
18. J.J. Santos et al., Phys. Rev. Lett. **89**, 025001 (2002)
19. M. Manclossi et al., Phys. Rev. Lett. **96**, 125002 (2006)
20. M. Koenig et al., Phys. Rev. E **50**, R3314 (1994)
21. D. Batani et al., Plasma Phys. Control. Fusion **41**, 93 (1999)
22. A. Benuzzi et al., Phys. Plasmas **5**, 2410 (1998)
23. F.N. Beg, A.R. Bell, A.E. Dangor, C.N. Danson, A.P. Fews, M.E. Glinsky, B.A. Hammel, P. Lee, P.A. Norreys, M. Tatarakis, Phys. Plasmas **4**, 447 (1997)
24. R.A. Snavely, M.H. Key, S.P. Hatchett, T.E. Cowan, M. Roth, T.W. Phillips, M.A. Stoyer, E.A. Henry, T.C. Sangster, M.S. Singh, S.C. Wilks, A. MacKinnon, A. Offenberger, D.M. Pennington, K. Yasuike, A.B. Langdon, B.F. Lasinski, J. Johnson, M.D. Perry, E.M. Campbell, Phys. Rev. Lett. **85**(14), 2945–2948 (2000)
25. D. Batani, M. Koenig, S. Baton, F. Perez, L.A. Gizzi, P. Koester, L. Labate, J. Honrubia, L. Antonelli, A. Morace, L. Volpe, J. Santos, G. Schurtz, S. Hulin, X. Ribeyre, C. Fourment, P. Nicolai, B. Vauzour, L. Gremillet, W. Nazarov, J. Pasley, M. Richetta, K. Lancaster, Ch. Spindloe, M. Tolley, D. Neely, M. Kozlova, J. Nejdl, B. Rus, J. Wolowski, J. Badziak, F. Dorchies, Plasma Phys. Control. Fusion **53**, 124041 (2011)
26. P.K. Patel, A.J. Mackinnon, M.H. Key, T.E. Cowan, M.E. Foord, M. Allen, D.F. Price, H. Ruhl, P.T. Springer, R. Stephens, Phys. Rev. Lett. **91**, 125004 (2003)
27. M. Tabak, J. Hammer, M.E. Glinsky, W.L. Kruer, S.C. Wilks, J. Woodworth, E.M. Campbell, M.D. Perry, R.J. Mason, Phys. Plasmas **1**, 1626 (1994)
28. R.R. Freeman, D. Batani, S. Baton, M. Key, R. Stephens, Fusion science & technology (FS&T). Fast Ignition Special Issue **49**(3), 297 (2006)
29. D. Batani, Nukleonika **56**(2), 99–106 (2011)
30. P. Norreys, D. Batani, S. Baton, F. Beg, R. Kodama, Ph Nilson, P. Patel, F. Perez, J.J. Santos, R. Scott, V.T. Tikhonchuk, M. Wei, J. Zhang, Fast electron energy transport in solid density and compressed plasma. Nucl. Fusion **54**, 054004 (2014)
31. J. Breil et al., J. Comp. Phys. **224**, 785 (2007)
32. P.-H. Maire et al., SIAM JSC **29**, 1781 (2007)
33. L.V. Spencer, Natl. Bur. Std. (U.S.) Monograph 1 (1959)
34. L. Volpe et al., Phys. Plasmas **20**, 013104 (2013)
35. A.R. Bell, J.R. Davies, S. Guerin, H. Ruhl, Plasma Phys. Control. Fusion **39**, 653 (1997)
36. F. Pisani, A. Antonicci, A. Bernardinello, D. Batani, E. Martinolli, M. Koenig, L. Gremillet, F. Amiranoff, S. Baton, T. Hall, D. Scott, P. Norreys, A. Djaoui, C. Rousseaux, P. Fews, H. Bandulet, H. Pepin, Phy. Rev. E Rapid Commun. **62**(5), R5927–R5930 (2000)
37. D. Batani, A. Antonicci, F. Pisani, T.A. Hall, D. Scott, F. Amiranoff, M. Koenig, L. Gremillet, S. Baton, E. Martinolli, C. Rousseaux, W. Nazarov, Phys. Rev. E **65**, 066409 (2002)
38. https://physics.nist.gov/PhysRefData/Star/Text/ESTAR.html
39. V. Gann et al., in *Proceedings of EPAC 2004*, Lucerne, Switzerland (2004)
40. D. Batani et al., EPL **114**, 65001 (2016)
41. R. Teyssier et al., Astrophys. J. Suppl. Ser. **127**, 503 (2000)
42. D. Batani et al., Phys. Rev. E **63**, 046410 (2001)
43. R. Chevalier et al., ApJ **359**, 463 (1990)
44. T. Grover, J. Hardy, ApJ **143**, 48 (1966)
45. T. Hall et al., Phys. Rev. E **55**, R6356 (1997)
46. D.G. Hicks et al., Phys. Rev. Lett. **91**, 035502 (2003)
47. G. Huser et al., Phys. Plasmas **12**, 060701 (2005)
48. J.H. Eggert et al., Nat. Phys. **6**, 40 (2010)

Index

© Springer Nature Switzerland AG 2018

K. Yamanouchi et al. (eds.), *Progress in Ultrafast Intense Laser Science XIV*,
Springer Series in Chemical Physics 118,
https://doi.org/10.1007/978-3-030-03786-4